U.S. Department of the Interior
U.S. Geological Survey

Prepared in cooperation with the National Science Foundation

The Loma Prieta, California, Earthquake of October 17, 1989—Geologic Setting and Crustal Structure

Professional Paper 1550–E

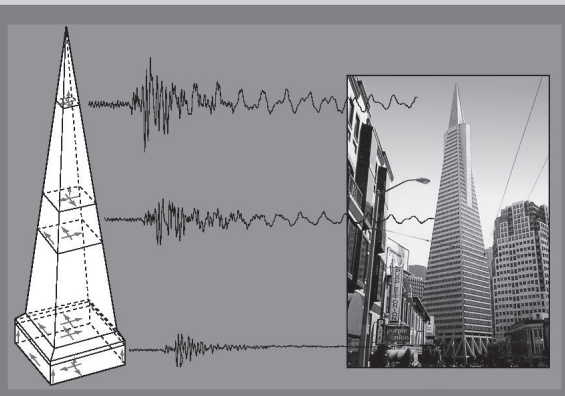

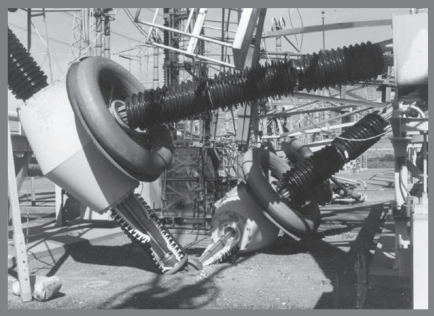

USGS
science for a changing world

The Loma Prieta, California, Earthquake of October 17, 1989—Geologic Setting and Crustal Structure

RAY E. WELLS, *Editor*

EARTHQUAKE OCCURRENCE
William H. Bakun and William H. Prescott, *Coordinators*

U.S. GEOLOGICAL SURVEY PROFESSIONAL PAPER 1550–E

Prepared in cooperation with the National Science Foundation

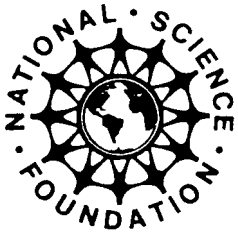

U.S. DEPARTMENT OF THE INTERIOR

GALE A. NORTON, Secretary

U.S. GEOLOGICAL SURVEY

Charles G. Groat, Director

U.S. Geological Survey, Reston, Virginia: 2004

For additional copies please contact:

USGS Information Services
Box 25286
Denver, CO 80225

This report and any updates to it are available at
http://pubs.usgs.gov/pp/p1550e/

Additional USGS publications can be found at
http://geology.usgs.gov/products.html

For more information about the USGS and its products:

Telephone: 1–888–ASK–USGS (1–888–275–8747)
World Wide Web: http://www.usgs.gov/

Produced in the Western Region, Menlo Park, California
Manuscript approved for publication, May 14, 2003
Text edited by George A. Havach
Layout and design by Stephen L. Scott

Library of Congress catalog-card No. 92–32287

CONTENTS

PLATES

[Plates are in pocket]

1. Geologic map of the Loma Prieta region, California
2. Stratigraphic columns across the San Andreas fault in the Loma Prieta region, California, comparing differences in thickness, lithology, and basement rock types in major fault blocks
3. Maps showing residual-magnetic fields, isostatic-residual-gravity fields, and generalized geology of the southern San Francisco Bay and Loma Prieta regions, California

EARTHQUAKE OCCURRENCE

INTRODUCTION

By Ray E. Wells, U.S. Geological Survey

CONTENTS

BACKGROUND

Although some scientists considered the M_S=7.1 Loma Prieta, Calif., earthquake of 1989 to be an anticipated event, some aspects of the earthquake were surprising. It occurred 17 km beneath the Santa Cruz Mountains along a left-stepping restraining bend in the San Andreas fault system. Rupture on the southwest-dipping fault plane consisted of subequal amounts of right-lateral and reverse motion but did not reach the surface. In the area of maximum uplift, severe shaking and numerous ground cracks occurred along Summit Road and Skyland Ridge, several kilometers south of the main trace of the San Andreas fault. The relatively deep focus of the earthquake, the distribution of ground failure, the absence of throughgoing surface rupture on the San Andreas fault, and the large component of uplift raised several questions about the relation of the 1989 Loma Prieta earthquake to the San Andreas fault: Did the earthquake actually occur on the San Andreas fault? Where exactly is the San Andreas fault in the heavily forested Santa Cruz Mountains, and how does the fault relate to ground ruptures that occurred there in 1989 and 1906? What is the geometry of the San Andreas fault system at depth, and how does it relate to the major crustal blocks identified by geologic mapping?

Subsequent geophysical and geologic investigations of crustal structure in the Loma Prieta region have addressed these and other questions about the relation of the earthquake to geologic structures observed in the southern Santa Cruz Mountains. The diverse papers in this chapter cover several topics: geologic mapping of the region, potential-field and electromagnetic modeling of crustal structure, and the velocity structure of the crust and mantle in and below the source region for the earthquake. Although these papers were mostly completed between 1992 and 1997, they provide critical documentation of the crustal structure of the Loma Prieta region. Together, they present a remarkably coherent, three-dimensional picture of the earthquake source region—a geologically complex volume of crust with a long history of both right-lateral faulting and fault-normal compression, thrusting, and uplift.

GEOLOGIC SETTING

McLaughlin and Clark (this chapter) place the earthquake within the context of the Late Cenozoic geologic history of strike-slip faulting, folding, and thrusting in the southern Santa Cruz Mountains. They present detailed geologic maps and cross sections covering a 700-km^2 area of the Loma Prieta region and note that the geologic histories on either side of the San Andreas fault differ considerably. The San Andreas fault is defined by a clear bedrock trace which separates terranes that have undergone hundreds of kilometers of right-lateral motion.

Late Cenozoic displacements on the San Andreas and its subsidiary faults have juxtaposed three major geologic terranes in the region. West of the Zayante-Vergeles fault, Tertiary marine strata overlie Salinian granodiorite basement that has been transported northward from southern California. Between the Zayante and San Andreas faults, the thick, folded Cenozoic marine-basin sequence of the La Honda block is underlain by the gabbro of Logan, a Jurassic terrane of oceanic affinity that is also displaced northward 300 km from Eagle Rest Peak near the Tehachapi Mountains. East of the San Andreas fault, McLaughlin and Clark map a series of fault slivers consisting of Franciscan Complex subterranes and overlying Mesozoic Great Valley sequence and Tertiary sedimentary strata.

The mapped terrane-boundary faults, with the possible exception of the San Andreas fault itself, are largely southwest-dipping thrust or reverse faults that have accommodated significant shortening normal to the plate boundary, in addition to strike-slip motion. Some of these faults—for example, the Monte Vista, Berrocal, and Shannon faults—are associated with shallow seismicity, have youthful geomorphic features, and are interpreted by McLaughlin and Clark to be active structures accommodating uplift of the eastern Santa Cruz Mountains. During the earthquake, triggered

slip occurred on some of the foothills thrust faults along the southern margin of the Santa Clara Valley. McLaughlin and Clark view the uplift and shortening associated with the Loma Prieta earthquake to be consistent with the history of recent thrust faulting in the Santa Cruz Mountains.

Coseismic ground cracking along Summit Road and Skyland Ridge followed a zone of previously mapped echelon faults along ridgetops south of the San Andreas fault. McLaughlin and Clark note that this was also the zone of maximum uplift during the earthquake and suggest that lateral and vertical inhomogeneities in fault slip and crustal composition near the northern tip of the rupture zone could have contributed to focusing of tectonic deformation in the Summit Road area. They also note, however, that postearthquake investigations demonstrated that the displacements on ground cracks tended to follow the regional slope and that many of these ground cracks were associated with large landslide complexes. In the San Andreas rift valley, the mapped bedrock trace of the San Andreas fault is sinuous, and the bends correlate with the toes of large, coherent-block landslide complexes and zones of detachment faulting along the valley walls. For example, at the Wrights railroad tunnel, right-lateral displacement of the tunnel in 1906 was almost 400 m south of the mapped bedrock trace of the San Andreas fault. McLaughlin and Clark's mapping suggests that a history of gravitational collapse of topography during seismic shaking has left a substantial imprint on the tectonic geomorphology of the San Andreas fault in the Santa Cruz Mountains.

CRUSTAL STRUCTURE FROM POTENTIAL-FIELD AND ELECTROMAGNETIC METHODS

Guided by geologic constraints, Jachens and Griscom (this chapter) interpret gravity and magnetic-field anomalies to construct a model of the subsurface crustal structure and composition beneath the Santa Cruz Mountains and southern Santa Clara Valley. In their model, the Loma Prieta region consists of seven crustal blocks juxtaposed by faults in the San Andreas system. Southwest of the San Andreas fault, two nonmagnetic basement terranes of Salinian granodiorite are separated by a magnetic basement terrane correlated with the Jurassic gabbro of Logan. A Tertiary sedimentary-basin sequence, as much as 10 km thick, overlies the gabbro, and both blocks are interpreted to be thrust beneath the Ben Lomond block along a southwest-dipping Zayante-Vergeles fault. All three blocks are truncated by the San Andreas fault on the east and by the San Gregorio fault on the west.

Northeast of the San Andreas fault, curvilinear magnetic anomalies delineate the boundaries of four tectonic blocks consisting of Franciscan Complex and overlying Coast Range ophiolite, Great Valley sequence, and Tertiary strata. Jachens and Griscom interpret these terranes to be the uplifted remnants of a regional Franciscan tectonic wedge emplaced onto Sierran basement along the 600-km-long Coast Range-Great Valley contact to the east. Its exposure in the Santa Cruz Mountains resulted from Late Cenozoic northward transport by the San Andreas fault system.

A comparison of the crustal model with the aftershock distribution suggests that most events are attributable to the San Andreas, Zayante-Vergeles, and Sargeant faults. Epicenters of aftershocks that plot off the main fault traces are commonly associated with dipping fault segments, and the San Andreas fault is interpreted to dip steeply southwest to vertical at depth. Within 1 km of the surface, the fault may locally dip gently to the northeast, putting nonmagnetic rocks over magnetic Purisima Formation on the northeast side of the surface trace. This unusual geometry coincides with southward-dipping Tertiary detachment faults northeast of the San Andreas fault (see McLaughlin and Clark, this chapter). One possible explanation for this relation is suggested by the widespread, structurally controlled ground cracking, extension, and downslope ground displacements that have occurred along ridgetops in the Loma Prieta region. During major earthquake shaking, the detachment faults are appropriately oriented to accommodate downslope transport of tectonic slivers across the San Andreas fault.

A deep geoelectric survey of the Loma Prieta region by Rodriguez and others (this chapter) confirms that lithologically distinctive crustal blocks are bounded by the San Andreas and Zayante-Vergeles faults at depth. High resistivities are characteristic of the Salinian granodiorite block southwest of the Zayante-Vergeles fault and of a large block of Franciscan rocks to the northeast of the San Andreas fault. A low-resistivity region in the uppermost 7 km of crust between the Zayante and San Andreas faults correlates with the thick, folded Tertiary marine sedimentary sequence mapped between the two faults. At midcrustal depths, a low-resistivity channel that extends to 19-km depth beneath the San Andreas fault is interpreted to represent fluids in the fault zone. The heterogeneity of the crust in the Loma Prieta region contrasts with the more uniform geoelectric structure observed in the Gabilan Range profile across the creeping section of the San Andreas fault to the south.

SEISMIC-VELOCITY STRUCTURE OF THE CRUST AND MANTLE

Brocher and others (this chapter) have used onshore recordings of airgun profiles offshore of Santa Cruz and Año Nuevo to construct a velocity model of the continental margin in the Loma Prieta region west of the San Andreas fault. The crust consists of two major components: a landward-thickening wedge of rocks with 6.0- to 6.5-km/s velocities that is consistent with the granitic or quartz monzonite crust of the Salinia terrane, and an underlying 5-km-thick, 6.8- to 7.1-km/s-velocity mafic unit, dipping gently east beneath the continental margin and apparently continuous with the offshore Pacific

plate. Brocher and others consider that this mafic layer may be arc-derived lower crust or a magmatically underplated layer, but they prefer to interpret this high-velocity layer as a slab of oceanic crust, possibly Pacific plate, that has underthrust the margin during Pliocene-Quaternary plate reorganization and crustal extension in the Basin and Range Province. They note that similar relations are found along the coast southward to Morro Bay. The hypocenter of the earthquake at about 17-km depth occurred in the high-velocity layer in the lower crust, consistent with previous correlations of high-velocity regions and earthquake rupture zones.

The westward-tapering tectonic wedge west of the San Andreas fault zone mirrors the tectonic wedge of Franciscan Complex emplaced eastward over Sierran basement on the east side of the San Andreas fault, and is thought to accommodate some of the shortening perpendicular to the San Andreas fault. The resulting concave-upward Moho may help to focus seismic energy from earthquakes along the San Andreas fault zone.

In a series of three papers on the seismic tomography of the Loma Prieta region, Shalev and Lees (this chapter), Atre and Thurber (this chapter), and Eberhart-Phillips and Michael (this chapter) investigate the relation between the three-dimensional velocity structure of the source region, its geologic structure, and the earthquake process. Shalev and Lees used raypaths from 844 aftershocks to generate a three-dimensional *P*-wave-velocity model of the Loma Prieta region. Their model clearly images a low-velocity region in the uppermost 10 km of crust between the San Andreas and Zayante-Vergeles faults. This feature coincides with tightly folded Tertiary strata of the La Honda Basin as mapped by McLaughlin and Clark (this chapter), a deep sedimentary basin also characterized by its low density and low resistivity (see Jachens and Griscom, this chapter; Rodriguez and others, this chapter). Between 6-km depth and the lower limit of the model at 16-km depth, a high-velocity prism dips steeply westward beneath the San Andreas fault and coincides with the zone of aftershocks below 6-km depth. Shalev and Lees offer two interpretations of the high-velocity body: a more rigid, high-velocity rock that acts as an asperity along the fault, or, as suggested by its low resistivity, a weaker, serpentinite-bearing fault zone.

Atre and Thurber (this chapter) recognize significant three-dimensional variations in V_P/V_S ratio in the Loma Prieta region. By combining their results with independent V_P data and the gravity and magnetic constraints, they examine variations in crustal composition across the major faults. Southwest of the Zayante-Vergeles fault, high V_P values and low V_P/V_S ratios in the upper 7 km of the crust are consistent with the granodioritic composition of the Salinian terrane and support the existence of a Zayante-Vergeles fault to at least 7-km depth. High V_P/V_S ratios at 3-km depth northeast of the Zayante-Vergeles fault correlate with porous Tertiary sedimentary rocks of the La Honda Basin and continue across the San Andreas fault into heterogeneous, ophiolite-bearing thrust packages of the Franciscan Complex. At 7-km depth, high V_P/V_S ratios of 1.84 to 2.0 suggest gabbroic compositions beneath the sedimentary layers, consistent with geologic and potential-field data indicating gabbro of Logan beneath the La Honda Basin. A major transition to low V_P/V_S ratios below 11-km depth could reflect a Salinian lower crust or may reflect healing of microcracks and a relative increase in *S*-wave velocities.

In a major synthesis, Eberhart-Phillips and Michael (this chapter) present three-dimensional V_P and V_P/V_S models of the Loma Prieta region derived from inversion of earthquake and explosive source traveltimes recorded at 1,700 permanent and temporary stations. The *P*-wave-velocity model and the relocated earthquake hypocenters reveal a high-*P*-wave-velocity body below 6-km depth that extends the length of the Loma Prieta rupture and separates it from a near-vertical San Andreas fault 5 km to the northeast. Eberhart-Phillips and Michael suggest that this body controlled not only the extent of the rupture but also the pattern of background seismicity on the adjacent San Andreas and Sargent faults, thus explaining how the earthquake filled in a gap in the regional microseismicity. As in their previous studies, the asperities with the greatest moment release correspond to regions where higher velocity material is in contact with the fault. The upward termination of the Loma Prieta rupture correlates with its propagation into a volume of low-density Tertiary sedimentary rocks with low *P*-wave velocities and high V_P/V_S ratios, possibly reflecting high pore pressures and different frictional behavior.

Northeast of the San Andreas fault, the *P*-wave-velocity model images a southwest-dipping thrust zone correlative with the southwestern Santa Clara Valley thrust belt, which places Franciscan Complex and other Mesozoic terranes over Late Cenozoic and Quaternary valley fill (see McLaughlin and Clark, this chapter). Loma Prieta aftershocks tend to be concentrated in the hanging wall of this thrust, and most events have thrust mechanisms. Aftershock focal mechanisms in the main-shock rupture zone indicate a completely heterogeneous stress field after the main shock and do not support the uniform fault-normal compressional-stress field expected after total stress drop on the main-shock plane. Eberhart-Phillips and Michael consider both the Loma Prieta fault surface and the San Andreas fault to be parts of a complex, 5-km-wide San Andreas fault zone with several potential rupture surfaces. They also conclude that this section of the San Andreas fault zone does not have a single type of characteristic earthquake.

Takauchi and Evans (this chapter) use teleseismic travel time residuals to determine the velocity structure of the lower crust and upper mantle in the Loma Prieta region. They find horizontal velocity gradients across the San Andreas fault at all depths, including the upper mantle, suggesting that the fault has been a steep, narrow locus of shear. A low-velocity feature near the Moho beneath Loma Prieta peak is interpreted as a crustal root, 2 to 5 km thick, at the base of the crust. Two upper-mantle low-velocity features between 45- and

70 -km depth are separated by 45 km right-laterally across the San Andreas fault. Takauchi and Evans note that this offset is small in comparison with the total offset across the fault and is compatible with models in which deep mantle slip is now accommodated beneath the Hayward-Calaveras faults to the east.

CONCLUDING REMARKS

Geologic and geophysical investigations of the crustal structure in the Loma Prieta region indicate that this region consists of a complex assemblage of crustal blocks, juxtaposed by hundreds of kilometers of right-lateral displacement and related imbricate thrusting along the San Andreas fault system. The structural complexities extend to depth. Although the San Andreas fault can be mapped as a throughgoing dextral-slip fault, the southwest-dipping Loma Prieta rupture surface appears to be a separate strand and is one of several southwest-dipping thrusts along this section of the San Andreas fault system. Several fault strands are capable of accommodating plate motion, and more than one type of characteristic earthquake is probable along this section of the San Andreas fault system.

At depth, the composition of geologic materials in the fault zone may have controlled the distribution of fault slip during the earthquake. High-velocity and high-density rocks correlate with asperities, or zones of high slip, on the fault plane, whereas the updip termination of the Loma Prieta rupture correlates with weak, low-density sedimentary fill in the La Honda Basin.

Near the surface, tectonic mountain-building processes in the Santa Cruz Mountains compete with partial gravitational collapse of the topography during intense seismic shaking. The abundant coseismic extensional ground cracking along ridgetops, a correlation between the trace sinuosity of the San Andreas fault and large slope failures along the rift-valley wall, and geophysical evidence for shallow thrusting in the bottom of the rift-valley all suggest that large-scale downslope movement along preexisting geologic structures may characteristically overprint tectonic deformation in the Loma Prieta region.

EARTHQUAKE OCCURRENCE

STRATIGRAPHY AND STRUCTURE ACROSS THE SAN ANDREAS FAULT ZONE IN THE LOMA PRIETA REGION AND DEFORMATION DURING THE EARTHQUAKE

By Robert J. McLaughlin, U.S. Geological Survey;
and
Joseph C. Clark, Indiana University of Pennsylvania

CONTENTS

ABSTRACT

The Loma Prieta region is divided by the San Andreas and Zayante faults into three structural blocks with different basement terranes. Tertiary strata that overlie the basements of these structural blocks record separate but overlapping histories of uplift, shortening, and strike-slip events, the most recent of which was the 1989 Loma Prieta earthquake.

Cretaceous (≥91 Ma) granitic rocks intrusive into older high-grade metasedimentary rocks of the Salinia terrane are exposed locally in the Ben Lomond block southwest of the Zayante fault. Northeast of the Zayante fault, in the La Honda block, the basement is covered by a Tertiary sedimentary section, as much as 6 km thick. High magnetization and high density suggest that this buried basement probably represents the northwestward continuation of the bodies of Jurassic (165–161 Ma) gabbro and undated anorthositic gabbro near Logan and San Juan Bautista.

The juxtaposition of continental Salinian basement with oceanic Logan basement along the Zayante fault apparently required significant latest Cretaceous to early Eocene dip-slip displacement. As much as 3 to 4 km of additional dip slip along the Zayante fault during Oligocene (Zemorrian) to early Miocene (Relizian) time resulted in unroofing of the Salinia terrane to the south and thick sediment accumulation and volcanism in the La Honda block to the north. Regional transpression during the Miocene and Pliocene (when it was most pronounced) reactivated this fault. Aftershocks of the 1989 Loma Prieta earthquake associated with the Zayante fault at 7- to 10-km depth suggest secondary fault reactivation, but that slip did not propagate to the surface.

The San Francisco Bay block northeast of the San Andreas fault and southwest of the Silver Creek fault consists of a composite basement of Franciscan Complex, Coast Range ophiolite, and Great Valley sequence. Seismic data suggest that these geologic units occur from the surface to 8- to 10-km depth beneath the Loma Prieta region. Early Jurassic to

Late Cretaceous metaclastic, metaigneous, and pelagic rocks of the Bald Mountain-El Sombroso and Permanente terranes of the Franciscan Central belt, and Jurassic (181?–156 Ma) ophiolitic rocks of the Coast Range ophiolite, compose most of the exposed basement. Beneath Loma Prieta peak, a thin fault sliver of slate and phyllite resembling Jurassic rocks of the Sierra Nevada foothills in metamorphic grade, composition, and texture is interpreted to have been thrust upward and northeastward from a separate metamorphic basement that may underlie Coast Range ophiolite and Franciscan rocks.

The San Francisco Bay block is broken into five subsidiary fault blocks by a system of dextral reverse-slip faults that include the Sargent, Hooker Gulch, Soda Springs, Sierra Azul, Berrocal, and Shannon faults. Most of these boundary faults are delineated by discontinuous lenticular bodies of mafic to ultramafic igneous rocks derived from the Coast Range ophiolite.

A major change in Oligocene to Miocene stratigraphy occurs across the Berrocal and Sargent faults, which partly form the boundary between the El Sombroso and Sierra Azul subsidiary blocks to the southwest and the Uvas, Los Capitancillos, and Santa Teresa subsidiary blocks to the northeast. Along the Sargent fault, as much as 1.4 km of uplift, 1.5 to 1.8 km of reverse slip, and 0.5 to 1.1 km of shortening probably began in the early Miocene (18 Ma) and may have been largely completed by the early late Miocene (10 Ma).

The southwestern Santa Clara Valley thrust belt contains several anastomosing faults northeast of the Sargent fault, including the Lime Kiln, Berrocal, Shannon, and Monte Vista faults. As much as 3.0 km of shortening and uplift and 4.2 km of reverse slip have occurred across this thrust belt since the early late Miocene (10 Ma). Faults of the thrust belt locally exhibit evidence for surface displacement within the past 15–18 k.y. Compressional deformation along the Monte Vista and Berrocal-Shannon fault zones during the earthquake suggests that these thrusts interact with the San Andreas fault and (or) that uplift and shortening across the San Andreas fault zone is accommodated by these thrust faults.

Tectonic evolution of the Loma Prieta region has included 13 to 15 km of unroofing of the Coast Ranges, which occurred largely from 95 to 70 Ma southwest of the San Andreas fault and from about 65 to 56 Ma northeast of the fault. Southwest of the San Andreas fault, as much as 4 km of uplift and basaltic volcanism occurred during the Oligocene to early Miocene across the Zayante fault. Northeast of the San Andreas fault, Oligocene to early Miocene uplift and erosion was associated with low-angle attenuation faulting. Oblique transpressional deformation began in the early Miocene southwest and northeast of the San Andreas fault and became most pronounced during the late Pliocene (3 Ma), producing cumulative uplift of about 6 km and shortening of about 5 km. This transpressional deformation was largely concurrent with 480 km of Miocene and later aggregate dextral slip across the San Andreas, Pilarcitos, and San Gregorio faults and faults of the eastern San Francisco Bay region. About 136 km of this slip is attributable to displacement along the Pilarcitos fault and the Peninsular segment of the San Andreas fault.

A model involving tectonic wedging is here invoked to explain the relation between uplift, blind thrusting, and strike-slip faulting during the earthquake. The 17-km depth of the main shock approximates the postulated depth to the floor-thrust zone of a tectonic wedge complex. The Loma Prieta rupture, therefore, may have propagated upward to 8- to 10-km depth along a steeply dipping dextral reverse fault from a reactivated segment of the flat floor of the tectonic wedge complex. Secondary extensional surface deformation was focused along the Summit Road-Skyland Ridge fault zone, southwest of the principal trace of the San Andreas fault, and less intense compressional deformation was accommodated along eastward-vergent thrust faults of the southwestern Santa Clara Valley thrust belt.

Data collected by other workers indicate that the Summit Road-Skyland Ridge fault zone was activated in the 1906 San Francisco earthquake. Other evidence indicating the partitioning of secondary slip to preexisting Quaternary faults of the southwestern Santa Clara Valley thrust belt during the 1989 Loma Prieta earthquake further suggests that Loma Prieta-type events have occurred in the past and should be expected to recur in this region in the future.

INTRODUCTION

The epicenter of the 1989 Loma Prieta earthquake was located in the Santa Cruz Mountains (fig. 1), a structurally complex region of heavy vegetation and limited rock exposures. The San Andreas fault bisects the region, displacing rocks to the southwest hundreds of kilometers northwestward relative to rocks on the northeast side of the fault. These juxtaposed rocks are further divided into subsidiary fault blocks with different basements and different stratigraphic and structural histories.

The purpose of this paper is to describe the tectonic histories and geometries of the major structural blocks of the Loma Prieta region, as recorded by the stratigraphy and structure. This information places constraints on the timing of past movements and rates of slip on major faults in the region and suggests their relations to the San Andreas fault system. An understanding of these relations is important in evaluating the significance of the earthquake and of the potential for future damaging earthquakes in the San Francisco Bay region.

The essential features of the geology of the Loma Prieta region (fig. 1), including the existence of major reverse-slip faults linked with the San Andreas fault system, were well known by at least 1980. It was pointed out in 1974 that thrust faults along the southwest side of the Santa Clara Valley are linked at depth to the San Andreas fault and that these thrust faults, if linked to each other, would be capable of an $M \geq 7.0$ event, on the basis of the half-length of the thrust system (McLaughlin, 1974; Sorg and McLaughlin, 1975). However,

the 70° SW.-dipping fault on which the 1989 Loma Prieta earthquake occurred was completely unknown until that event.

The seismic potential of thrust faults in northern California was unclear until the 1983 Coalinga, Calif., earthquake, which occurred on an eastward-vergent blind thrust beneath the Coast Ranges northeast of the heavily monitored Parkfield segment of the San Andreas fault (Wentworth and Zoback, 1990). The possible significance of that earthquake to the potential for a major thrusting event in the San Francisco Bay region was still not fully appreciated until the 1989 Loma Prieta earthquake.

Since then, geologists have begun to view faulting in the northern Coast Ranges, including the San Francisco Bay region (fig. 1), much differently, in light of the enormous number of new data that have been accumulated regarding deep crustal structure. Much has been also learned about the distribution of blind thrusts. Previously unrecognized buried thrusts have been found to underlie areas of recently folded rocks in several areas. Buried thrusts could be more youthful and could pose a greater seismic hazard than thrusts that are mapped at the surface; however, the details of their earthquake recurrence and of how these faults interact with the major strike-slip faults of the North American plate transform boundary remain unclear and controversial. The 1989 Loma Prieta earthquake pointed out to us that a more thorough knowledge of the dynamics of these interactions is essential to predicting the timing or locations of future earthquakes in the San Francisco Bay region.

Just 2 years before the earthquake, we began a detailed mapping of four 7½-minute quadrangles astride the San Andreas fault in the southern Santa Cruz Mountains. The structural and stratigraphic relations discussed herein are based on this timely recent work, together with many years of previous U.S. Geological Survey investigations.

STRATIGRAPHY SOUTHWEST OF THE SAN ANDREAS FAULT

The San Andreas fault in the Santa Cruz Mountains (figs. 1, 2) juxtaposes a Mesozoic plutonic basement southwest of the fault with a different Mesozoic composite basement northeast of the fault, composed of the accretionary Franciscan Complex, ophiolitic rocks, and forearc-basin deposits of the Great Valley sequence. Since the early Miocene, these Mesozoic basement terranes have been displaced hundreds of kilometers across the San Andreas fault (fig. 1). Southwest of the San Andreas fault, the area that includes the Los Gatos, Laurel, and Loma Prieta quadrangles is divided by the Zayante and Vergeles faults into two structural blocks: the Ben Lomond block to the southwest and the La Honda block to the northeast (figs. 1, 2). In the Ben Lomond block, crystalline rocks of the Salinia terrane are locally exposed and occur at relatively shallow depths beneath Tertiary strata that are tilted and deformed into broad open folds. Except for a thin sliver of gabbro along the San Andreas fault between Logan and San Juan Bautista (fig. 1*A*), the basement northeast of the Zayante-Vergeles fault is completely buried by a Tertiary section, as much as 6 km thick, that is tightly folded and locally overturned (see pl. 1).

BASEMENT ROCKS OF THE SALINIA TERRANE SOUTHWEST OF THE ZAYANTE FAULT (CRETACEOUS AND OLDER)

In the Loma Prieta region, granitic intrusive and high-grade metasedimentary rocks of the Salinia terrane form the basement southwest of the Zayante fault. Small isolated exposures in the Laurel quadrangle indicate that the granitic rocks range in composition from quartz diorite on the west to granodiorite and quartz monzonite on the east (see pl. 1). Pelitic schist crops out locally in the southwest corner of the quadrangle. These crystalline rocks have been mapped westward into the adjoining Felton quadrangle, where quartz diorite predominates in the more extensive exposures of Ben Lomond Mountain (fig. 1*B*; Clark, 1981, pl. 2). Exploratory wells south of the Zayante fault and its southeastward extension, the Vergeles fault, confirm the subsurface continuity of basement rocks of the Salinia terrane with granitic rocks in the northern Gabilan Range, 30 km to the southeast (Clark and Rietman, 1973, pl. 1; Ross and Brabb, 1973, fig. 2).

Radiometric (Rb-Sr and U-Pb) ages and structural data (Compton, 1966; Ross, 1978; Mattinson and James, 1985; James, 1992) suggest that granitic rocks of the Salinia terrane in the Santa Cruz Mountains were emplaced 103–91 Ma (mid-Cretaceous) at ≥18-km depths (Hansen and others, 1991) and unroofed to less than 3- to 5-km depth from late Maastrichtian to early Paleocene (67–61 Ma) time (fig. 3; Arrowsmith and others, 1992; Bürgmann and others, 1994). Similarities in lithology and metamorphic grade suggest that the metasedimentary rocks are correlative with the Sur Series of Trask (1926). Although the depositional age of the Sur Series is uncertain, analysis of detrital zircons from schist and quartzite from Ben Lomond Mountain northwest of the city of Santa Cruz (fig. 1) indicates a mid-Cretaceous metamorphism for these metasedimentary rocks. The detrital zircons originally crystallized from an igneous melt as early as the Precambrian (1.7 Ga; James, 1984, 1992).

MAFIC BASEMENT ROCKS OF THE SALINIA TERRANE BETWEEN THE ZAYANTE AND SAN ANDREAS FAULT ZONES (JURASSIC)

Northeast of the Zayante fault and southwest of the San Andreas fault (fig. 1), the crystalline basement is buried beneath as much as 6 km of Tertiary rocks. A greater depth

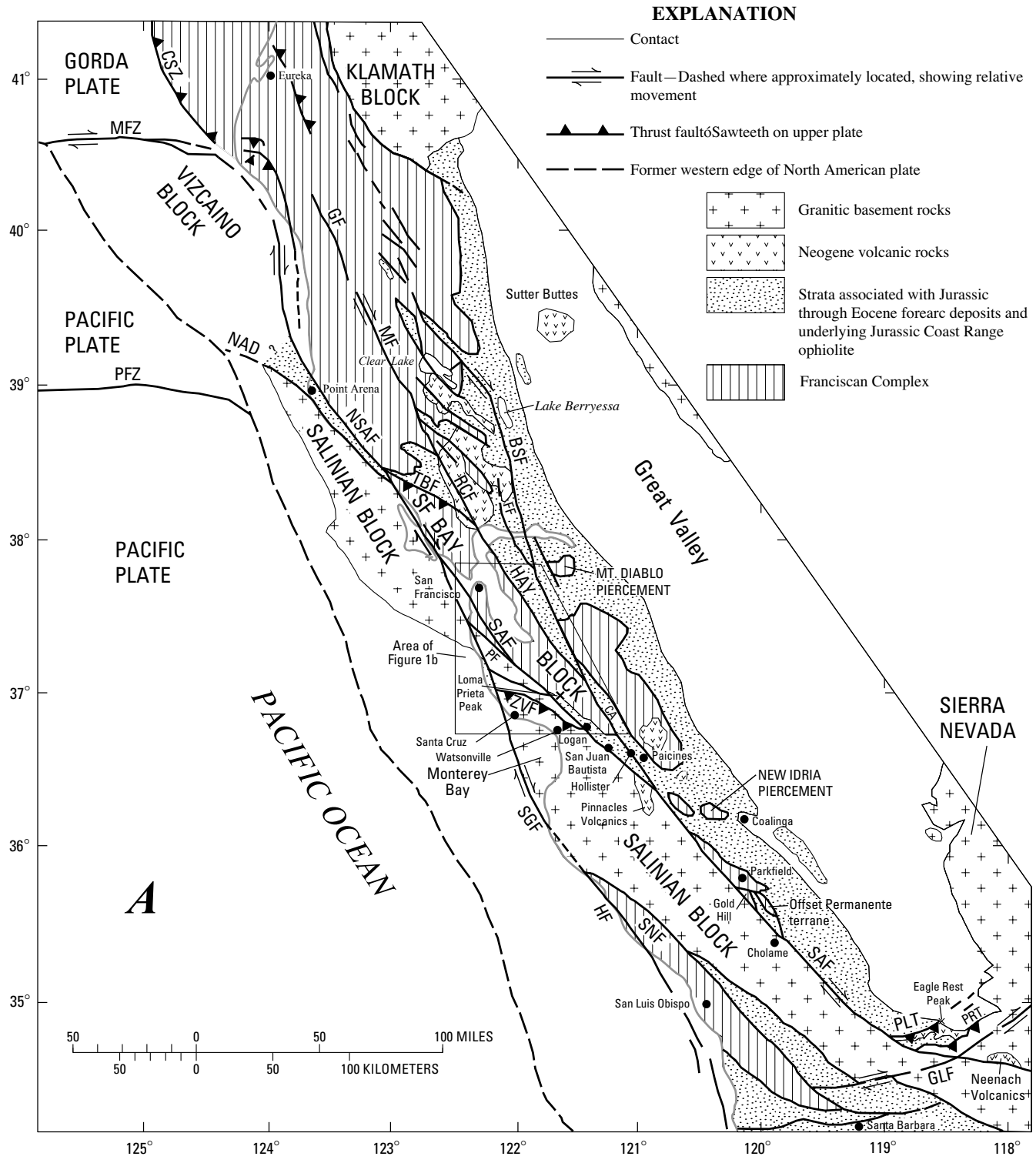

Figure 1.—Loma Prieta region, Calif., showing major fault blocks and fault zones. *A*, Regional setting. BSF, Bartlett Springs fault; CA, Calaveras fault; CSZ, Cascadia subduction zone; FF, Franklin fault; GF, Garberville fault; GLF, Garlock fault; HAY, Hayward fault; HF, Hosgri fault; MF, Maacama fault; MFZ, Mendocino Fracture Zone; NAD, Navarro discontinuity; NSAF, northern section of the San Andreas fault (north of the San Francisco peninsula); PF, Pilarcitos fault; PFZ, Pioneer Fracture Zone; PLT, Pleito thrust; PRT, Pastoria-Rand thrust zone; RCF, Rodgers Creek fault; SAF, San Andreas fault, including Peninsular segment; SGF, San Gregorio fault; SNF, Sur-Nacimiento fault; TBF, Tolay-Bloomfield fault; ZVF, Zayante-Vergeles fault. *B*, San Francisco Bay block, showing locations of plate 1 and figure 2*A*. Star, epicenter of October 18, 1989, main shock.

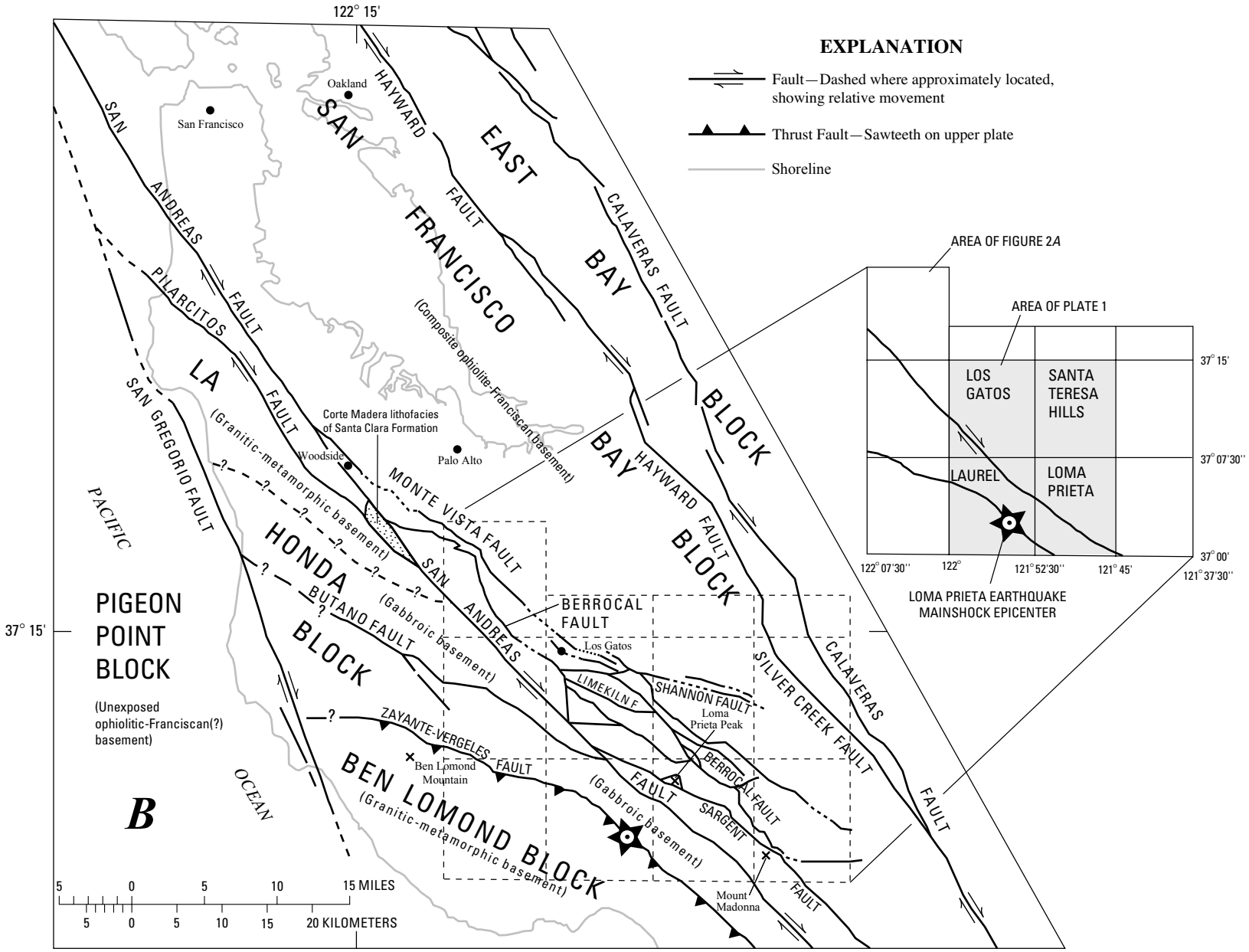

Figure 1.—Continued

is suggested by recent velocity and resistivity models that include a low-velocity, low-resistivity unit between these faults that extends to more than 8-km depth. This unit is interpreted to be largely Tertiary marine sedimentary rocks (Eberhart-Phillips and others, 1990), although highly fractured basement may produce similar low resistivity.

Deep exploratory wells between the San Andreas and Zayante-Vergeles faults (fig. 1) have failed to reach basement. One well (Union Teresa Hihn No. 2), located about 600 m northeast of the mapped surface trace of the Zayante fault, deviated southward across a buried strand of the Zayante fault to reach quartz monzonite at 1,047-m depth (Ross

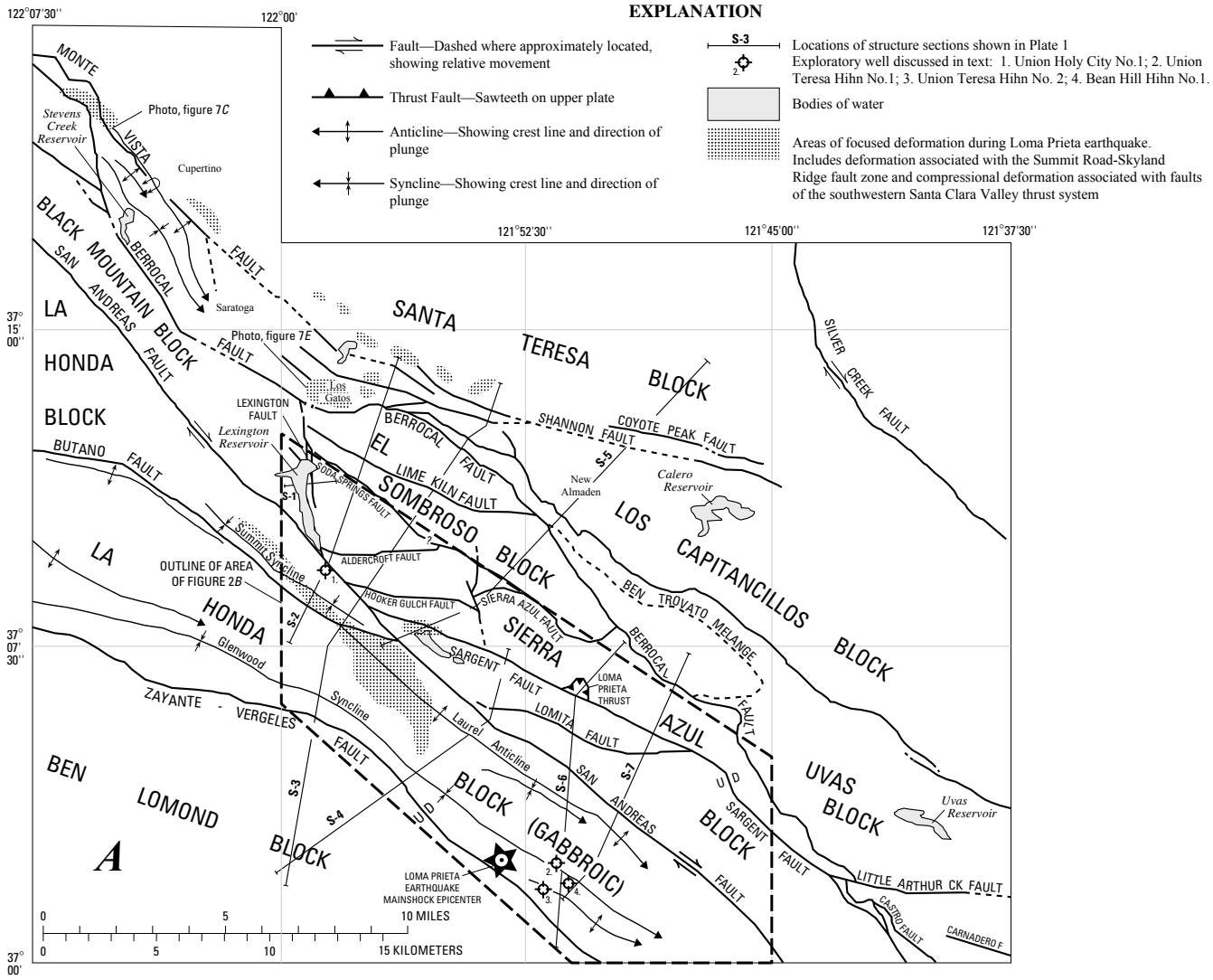

Figure 2.—Epicentral area in the Loma Prieta region, Calif. (fig. 1). Star, epicenter of October 17, 1989, main shock. *A*, Part of the San Francisco Bay block, showing locations of major and subsidiary fault blocks, fold axes, lines of cross sections S–2 through S–7 (see pls. 1, 2), exploratory wells discussed in text (numbered crossed circles), and distribution of focused surface deformation (stippled areas) from earthquake. *B*, Summit Road-Skyland Ridge area, showing locations of Pliocene and younger fold axes, areas of the Purisima Formation (dark shaded), faults in Summit Road-Skyland Ridge fault zone (red lines), principal trace of the San Andreas fault, the abandoned Wrights Railroad Tunnel (which was damaged in 1906 San Francisco earthquake), and distribution of landslides along the San Andreas fault. Circled numbers 1–4, exposures of principal trace of San Andreas fault discussed in text: 1, Spanish Ranch Road; 2, beneath landslide in tributary to Los Gatos Creek; 3, tributary to Los Gatos Creek adjacent to Holy City No.1 exploratory well, which penetrated the San Andreas fault at 1,108-m depth; 4, Moody Gulch. Circled numbers 5–11, other localities discussed in text: 5, north portal of the Wrights Railroad Tunnel; 6, Moody Gulch oil field (cross hachured area); 7, Lexington fault zone; 8, trenched 1989 coseismic cracks and faults in the Summit Road-Skyland Ridge fault zone on California Highway 17 at Summit Road; 9, trenched 1989 and older coseismic-deformation features associated with sag locality in the Summit Road-Skyland Ridge fault zone south of Summit Road; 10, coseismic cracks along Morrell Road that exhibited sinistral displacement in October, 1989 and April 1906; 11, 1989 coseismic cracks exhibiting dextral extension along the Sargent fault at Lake Elsman.

and Brabb, 1973; McLaughlin and others, 1988b, sheet 2). Union Hihn No. 1 well (cross sec. S–6, pl. 1) to the east failed to reach basement at a total depth of 2,361 m, where it bottomed in lower Miocene rocks (Ross and Brabb, 1973, p. 277; McLaughlin and others, 1988b). If the subsurface thickness of the pre-lower Miocene sedimentary section here approximates the 3,260 m of composite Eocene and Oligocene section exposed in the central Santa Cruz Mountains to the northwest, then the top of basement in this area would be at a depth of as much as 5.4 km. If Paleocene strata are also preserved here beneath Eocene rocks, the thickness of this Tertiary section could be almost 6 km.

An elongate body of distinctive gabbro crops out southwest of the San Andreas fault at Logan (fig. 2). Surface exposures of these crystalline basement rocks extend southeastward for 10 km to the vicinity of San Juan Bautista (fig. 1*A*), where the exposures are largely of undated, banded anorthositic gabbro containing conspicuous secondary fibrous amphibole (Ross, 1970; Dibblee and others, 1979). On the southwest, the anorthositic gabbro is locally faulted against green marine mudstone beds that yield foraminifers and nannofossils diagnostic of lower-bathyal to abyssal depths and an early Eocene age (Bukry and others, 1975; Kristin McDougall, written commun., 1991). At Logan, the gabbroic unit includes hornblende-quartz gabbro with a granular texture and a Pb-U age of 161 to 165 m.y. (Johnson and O'Neil, 1988; James and others, 1994). An initial $^{87}Sr/^{86}Sr$ ratio of 0.7039 (table 1) suggests that the hornblende-quartz gabbro has oceanic affinities.

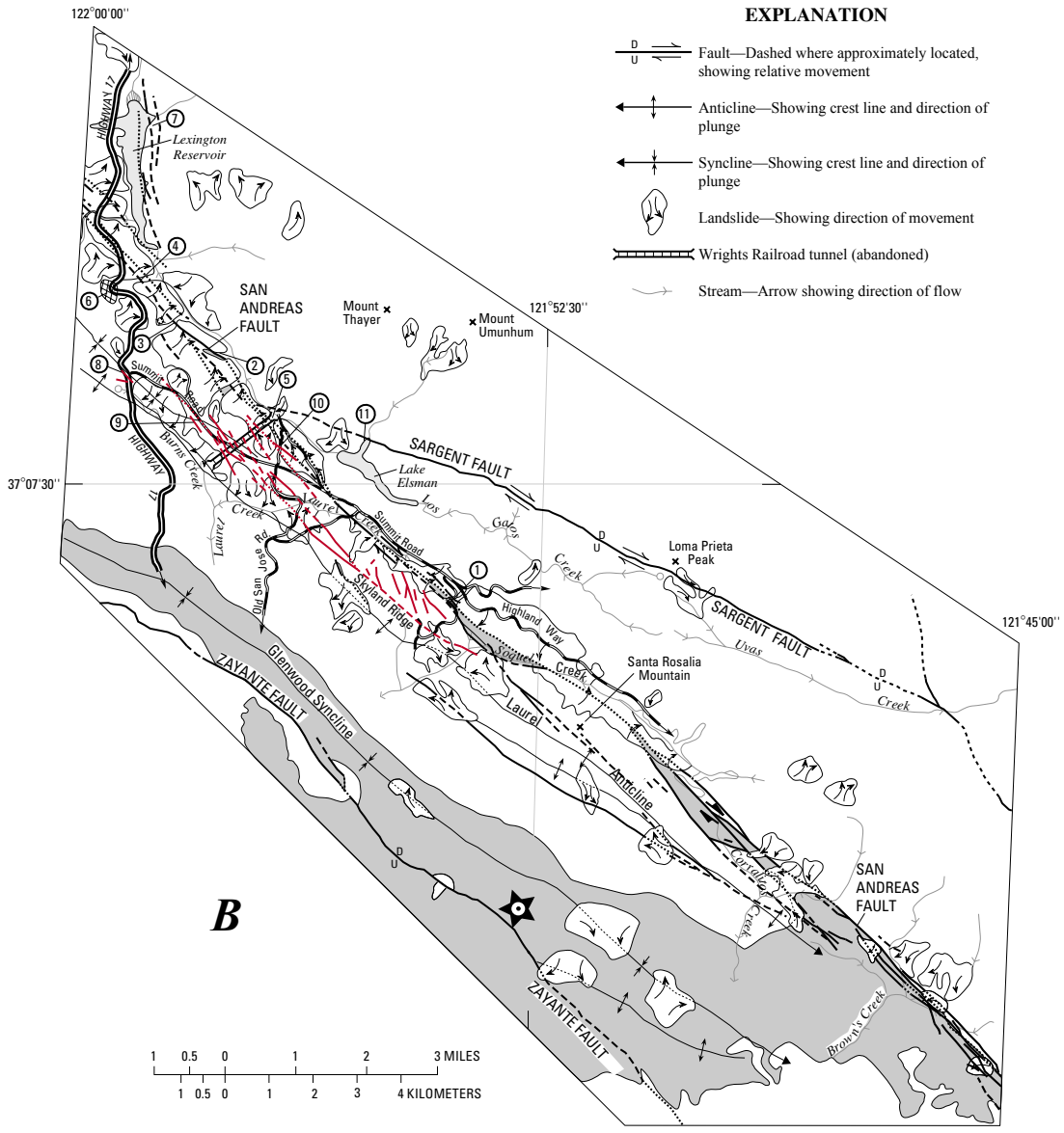

Figure 2.—Continued

Past geophysical and geologic studies have postulated that the basement between the Zayante-Vergeles and San Andreas faults consists of granitic and metamorphic rocks (Clark and Rietman, 1973), Jurassic gabbro (Hanna and others, 1972), Franciscan rocks (Ross and Brabb, 1973; Coppersmith, 1990), or mafic oceanic rocks (Ross, 1984; Clark and others, 1991). Recent gravity and magnetic models (see Jachens and Griscom, this chapter), however, indicate that these basement rocks have a high magnetization and high density, consistent with northwestward subsurface continuation of the Jurassic hornblende-quartz gabbro of Logan and the undated anorthositic gabbro near San Juan Bautista.

The northern part of the La Honda block is underlain by rocks that are less magnetic and less dense than the gabbro of Logan (see Jachens and Griscom, this chapter) and that presumably represent a southeastward extension of the granitic rocks exposed to the northwest at Montara Mountain southwest of the Pilarcitos fault (fig. 1*B*). The north magnetic boundary of the Logan gabbroic basement with this granitic basement (fig. 1*B*) is about 5 km north and subparallel to the

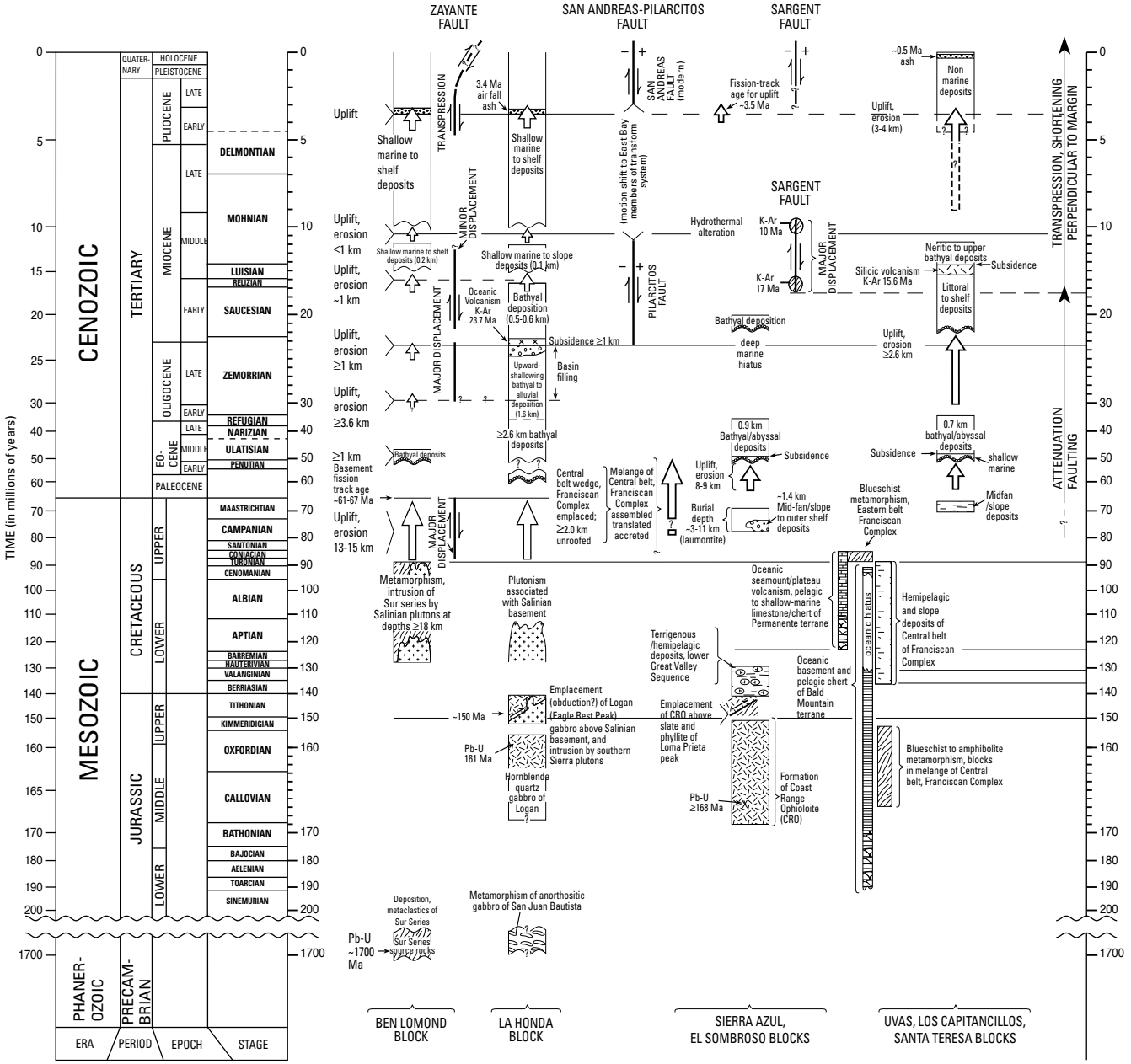

Figure 3.—Summary of tectonic history across the San Andreas fault in the Loma Prieta region, Calif. (fig. 1), comparing differences in timing and amount and style of tectonism in major fault blocks. CRO, Coast Range ophiolite.

Table 1.—*Summary of $^{87}Sr/^{86}Sr$ and radiometric age data for igneous rocks of the Loma Prieta region, Calif., and related areas along the San Andreas fault*

[Data sources: 1, James and others (1994), with age of 161 Ma assumed in calculating $^{87}Sr/^{86}Sr$ (initial) ratio; 2, Kistler and others (1973); 3, R.W. Kistler (written commun., 1990), with age of 160 Ma assumed in calculating $^{87}Sr/^{86}Sr$ (initial) ratio; 4, J.L. Wooden (written commun., 1992), with true age interpreted as ≥168 Ma; 5, R.W. Kistler (written commun., 1990), with age of 143 Ma assumed in calculating $^{87}Sr/^{86}Sr$ (initial) ratio; 6, R.W. Kistler (written commun., 1990), with age of 20 Ma assumed in calculating $^{87}Sr/^{86}Sr$ (initial) ratio; 7, R.W. Kistler(written commun., 1990), with age derived from Rb/Sr isochron; 8, Turner (1970)]

Lithologic unit	Age, method of dating, and mineral dated, where known	Source of age date	$^{87}Sr/^{86}Sr$ ratio	$^{87}Sr/^{86}Sr$ data sources
(Hornblende-quartz) gabbro of Logan.	161–165 Ma, Pb-U, zircon.	1	0.7039 (initial)	1, 2
Hornblende-quartz gabbro of Eagle Rest Peak.	159–177 Ma, Pb-U, zircon.	1	.7034–0.7039 (initial)	1, 2
Hornblende-quartz gabbro of Gold Hill.	144 Ma, Pb-U, zircon	1	.7038 (initial)	1, 2, 5
Coast Range ophiolite of Sierra Azul block (hornblende-albite pegmatite in dikes and sills).	144–168 Ma, Pb-U, zircon.	4	.70242–0.70404 (initial)	3
Franciscan Complex, Permanente terrane (basalt and tuff).	136–120 Ma, $^{87}Sr/^{86}Sr$ initial, whole rock.	7	.70394–0.70998 (0.70365 initial)	7
Diabase of Laurel Creek and Morrell Cutoff Road.	Unknown, possibly Oligocene to Miocene.	This report	.70439–0.70596 (0.70437 initial)	6
Tertiary basalt flows of the Felton quadrangle.	23.7 Ma, K-Ar, plagioclase.	8	.70360 (initial)	6
Diabase and gabbro of Highland Way and Diablo Gulch.	Unknown, possibly Mesozoic.	This report	.70403–0.70692 (initial)	3

surface trace of the Butano fault (see Jachens and Griscom, this chapter). Thus, the gabbro of Logan and the anorthositic gabbro near San Juan Bautista (fig. 1*A*) appear to compose an elongate block of mafic oceanic rocks within the Salinia terrane that is juxtaposed with granitic and metamorphic rocks of the terrane. This block of mafic rocks of the Salinia terrane is bounded on the northeast by the San Andreas fault, on the southwest by the Zayante-Vergeles fault, on the west by the San Gregorio fault, and on the north by a presumed buried fault (fig. 1*B*). On the basis of gravity and magnetic models (see Jachens and Griscom, this chapter), the gabbroic basement appears to be truncated at depth by a flat boundary interpreted to be a low-angle fault. The rocks beneath this low-angle fault are less magnetic than the gabbro and are also believed to be crystalline basement (see Jachens and Griscom, this chapter).

TERTIARY SECTION SOUTHWEST OF THE SAN ANDREAS FAULT

Cretaceous strata are unknown in the Santa Cruz Mountains between the San Andreas fault and the San Gregorio fault to the southwest (fig. 1). The Tertiary section exposed there consists largely of marine clastic sedimentary rocks ranging in age from Paleocene to Pliocene, with a composite thickness of more than 10 km (Clark and Brabb, 1978). This section is divisible into four major sequences separated by regional unconformities (see pl. 1). The exposed basal beds of each sequence locally rest on crystalline rocks of the Salinia terrane.

POSSIBLE BURIED PALEOCENE SEQUENCE

Paleocene rocks are exposed west of the study area (fig. 1*B*) near Ben Lomond Mountain, where erosional remnants of the Locatelli Formation that rest on the crystalline basement consist of basal, shallow-marine arkosic sandstone overlain by bathyal to abyssal siltstone. As much as 275 m thick, the sequence is of late Paleocene (Ynezian) age (Clark, 1981). Paleocene strata may occur in the subsurface above the basement of the La Honda block (see pl. 1), but coeval rocks have not been penetrated by exploratory wells in this area, and the oldest sedimentary rocks exposed at the surface northeast of the Zayante fault are Eocene.

EOCENE TO LOWER MIOCENE SEQUENCE

The Eocene to lower Miocene sequence consists of the Butano Sandstone, the Twobar Shale and Rices Mudstone

Members of the San Lorenzo Formation, the Zayante Sandstone, the Vaqueros Sandstone, and the Lambert Shale. Basaltic flows locally are included in the Vaqueros Sandstone. Only the lower part of this sedimentary sequence is exposed in the Ben Lomond block south of the Zayante fault (fig. 1), where as much as 1.1 km of conglomeratic beds of the Butano Sandstone rests nonconformably on basement rocks of the Salinia terrane (see pl. 1).

Northeast of the Zayante fault, in the La Honda block, the base of the sequence is not exposed, but as much as 3.1 km of the section is preserved along the Glenwood syncline and Laurel anticline south of the Butano fault (see pl. 1). These rocks also crop out along the Summit syncline north of the Butano fault and in fault blocks southwest of and near the San Andreas fault.

The Butano Sandstone is interpreted to have been deposited at lower-bathyal to abyssal depths by northward-flowing currents as the midfan and interchannel facies of a submarine fan (Nilsen, 1984). Its arkosic composition suggests derivation from a granitic source terrane that lay to the south, probably in the vicinity of present-day Monterey Bay (fig. 1*A*).

The overlying mudstone beds of the Twobar Shale Member of the San Lorenzo Formation record undisturbed marine deposition at lower-bathyal depths in an anoxic basin. Benthic foraminifers are assignable to the Narizian Stage of the middle to late Eocene (Smith, 1971), and planktic foraminifers indicate open-ocean connections.

The Rices Mudstone Member of the San Lorenzo Formation locally records shallower marine conditions. Along Soquel Creek in the Laurel quadrangle and to the east in the Loma Prieta quadrangle, the lower part of this unit is massive, fine-grained glauconitic sandstone, containing locally abundant Pitar and other mollusks characteristic of inner-neritic depths and a Refugian (late Eocene) age (Smith, 1971; Clark and others, 1989). The upper part of the Rices Mudstone Member is nodular mudstone that yields benthic foraminifers diagnostic of upper-middle-bathyal (500–1,500 m) depth and an early Zemorrian (Oligocene) age (McDougall, 1989, 1991).

The Vaqueros Sandstone is restricted to the La Honda block, where it was laid down in environments ranging from shallow-marine shelf to deep-sea fan (Stanley, 1990). In this area, benthic foraminifers from mudstone interbeds in the lower part of the formation are diagnostic of bathyal depths and an early Zemorrian (Oligocene) age (Clark and others, 1989). To the south, along Hinckley Creek in the Laurel quadrangle, the upper 92 m of the Vaqueros Sandstone contains thick *Dosinia* and *Ostrea* biostromes indicative of shallow-marine conditions (Clark and others, 1989). Locally, along the Glenwood syncline, the Vaqueros Sandstone encloses conglomeratic interbeds of the Zayante Sandstone, a nonmarine facies that was deposited in alluvial fans along the Zayante fault at the southern margin of the La Honda Basin (see pls. 1, 2).

The limited areal extent of the Zayante Sandstone, together with the absence of the marine San Lorenzo Formation and Vaqueros Sandstone southwest of the Zayante fault, was interpreted by Clark and Rietman (1973) to be the result of regional uplift of the Ben Lomond block along this fault during Oligocene time (fig. 3). Arkosic debris shed from the emergent Salinia terrane to the south resulted in nonmarine deposition of the Zayante Sandstone along the fault and a rapid northeastward facies change within the Vaqueros Sandstone from marine shelf to deep-sea fan.

Mafic igneous rocks that occur in isolated exposures and in the subsurface of this part of the La Honda block are probably correlative with the more voluminous Oligocene and (or) Miocene Mindego Basalt of the central La Honda block and with nearby basalt flows in the Felton quadrangle to the west. These basalt flows, as much as 60 m thick (Clark, 1981), have been dated by K-Ar methods at 23.7±0.7 Ma (late Oligocene or early Miocene; Turner, 1970; age recalculated by Fox and others, 1985, using currently accepted International Union of Geological Sciences constants). Their low $^{87}Sr/^{86}Sr$ ratio of 0.70360 (R.W. Kistler, written commun., 1991) suggests an oceanic magmatic source (table 1). The Mindego Basalt was believed by Stanley (1990) to have been erupted in an extensional tectonic setting, concurrent with displacement along the Zayante fault, which served to localize the less voluminous volcanic activity in this area.

In the study area (fig. 1), basaltic flows and (or) sills are locally exposed along the Glenwood syncline, along California Highway 17 north of the Zayante fault in the Laurel quadrangle, and near the west edge of the Los Gatos quadrangle (see pl. 1). Basaltic rocks that are also reported as intrusive into the San Lorenzo Formation both in surface exposures and in the subsurface of the Moody Gulch oil field in the Los Gatos quadrangle (Krueger, 1943) were penetrated by Union Hihn No. 1 well (cross sec. S–6, pl. 1; fig. 2*A*) in the Loma Prieta quadrangle (McLaughlin and others, 1988b).

Altered fine- to coarse-grained diabase and gabbro also occur in fault slivers along Laurel Creek in the Laurel quadrangle and along Morrell Cutoff Road in the Los Gatos quadrangle. The diabase and gabbro are of oceanic composition ($^{87}Sr/^{86}Sr$ ratio, 0.70437–0.70596) and geochemically (TiO_2 content versus FeO/MgO ratio, and Ti versus Cr contents) are nearly identical to the Mindego Basalt.

In the Loma Prieta quadrangle, fine- to medium-grained, locally titaniferous diabase, basalt, and gabbro (cross sec. S–7, pl. 1) occur in fault-bounded slivers along the northeast side of the San Andreas fault. The geochemistry of these rocks and a $^{87}Sr/^{86}Sr$ ratio of 0.707 (table 1) suggest an oceanic-ridge or offridge formational setting. Their position just to the northeast of the principal trace of the San Andreas fault, however, suggests that these exposures may be more closely associated with the Mesozoic basement northeast of the fault rather than with the Mindego Basalt to the southwest.

The Lambert Shale is conformable above the Vaqueros Sandstone along the Glenwood syncline, where from 460 to as much as 550 m of the shale crops out in the Laurel quadrangle (Clark and others, 1989). Throughout this area, the upper part of the Lambert Shale has been removed by erosion.

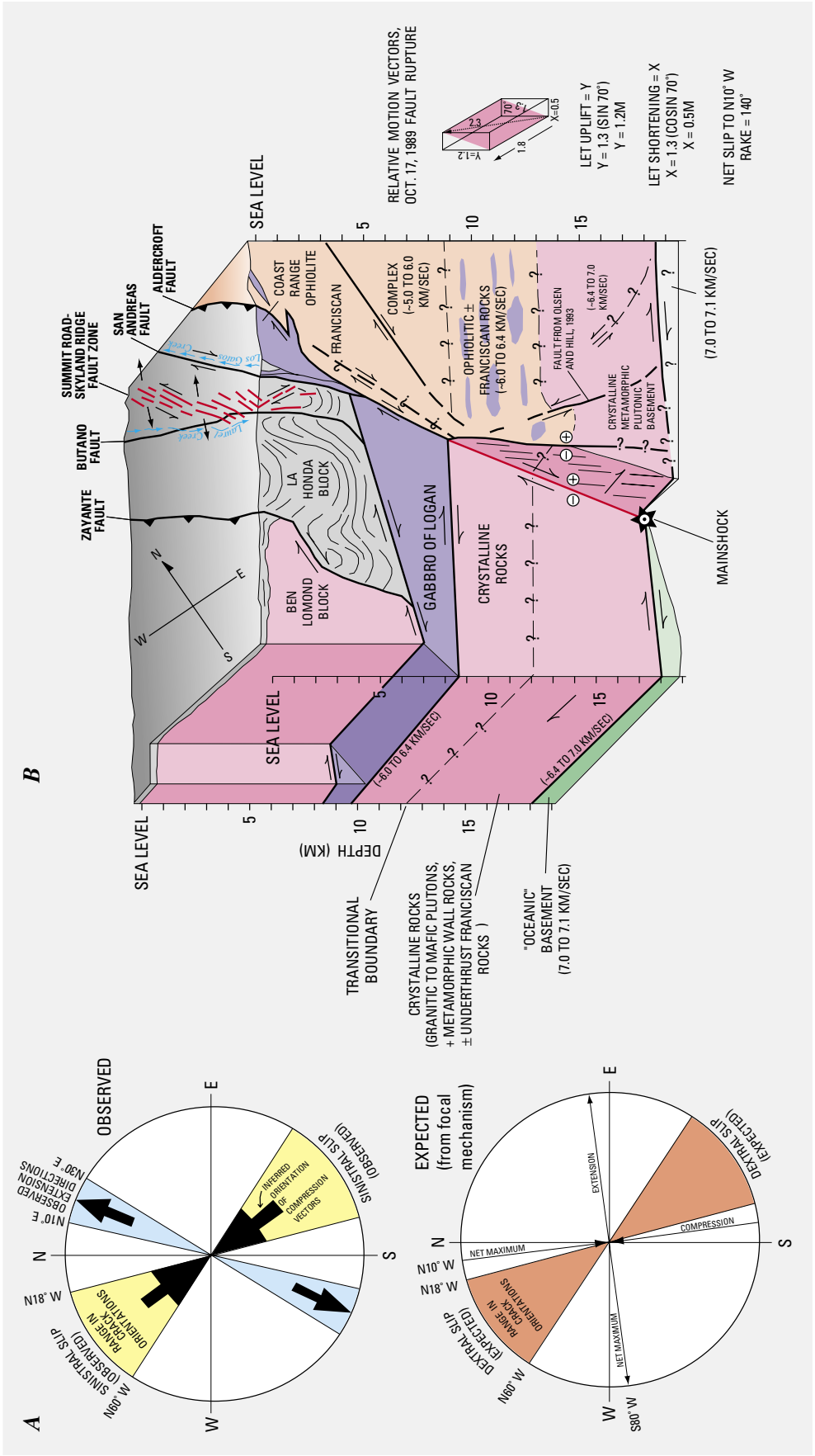

Figure 4.—Surface deformation and crustal structure in the Summit Road-Skyland Ridge area (fig. 2*B*). *A*, Rose diagrams comparing observed and expected horizontal surface-deformation fields during 1989 Loma Prieta earthquake. *B*, Block diagram showing inferred crustal structure across the San Andreas fault and possible relation to primary and secondary slip during 1989 Loma Prieta earthquake. Red echelon faults at surface and shallow subsurface are fissures in the Summit Road-Skyland Ridge fault zone. Loma Prieta rupture is shown in red at depth, extending upward from main shock to base of the gabbro of Logan. Deep configuration of the San Andreas fault is partly inferred from Olson and Hill (1993). Crustal structure to about 10-km depth is partly inferred from Jachens and Griscom (this chapter), and below about 10-km depth is highly speculative and inferred from indicated seismic velocities (Fuis and Mooney, 1990; Rufus Catchings, oral commun., 1993; see Brocher and others, this chapter).

A decrease in the influx of coarse detritus, together with subsidence of the La Honda Basin, resulted in deposition of organic and phosphatic mudstone beds of the Lambert Shale at upper-middle-bathyal (500–1,500 m) depths (see pl. 1), largely under anoxic conditions (Clark, 1981). Arkosic sandstone interbeds in the upper part of the Lambert Shale were probably derived from the Salinia terrane to the south and laid down by occasional turbidity flows. Benthic foraminifers in the Lambert Shale in the Laurel quadrangle are diagnostic of the Saucesian to early Relizian Stages of the early Miocene (Clark, 1981; McDougall, 1991).

LOWER TO MIDDLE MIOCENE SEQUENCE

The lower to middle Miocene sequence consists of a widely transgressive basal sandstone unit, the Lompico Sandstone, and an overlying organic mudstone unit, the Monterey Formation. This marine sedimentary sequence is best preserved in the Ben Lomond block and locally occurs in the subsurface of the La Honda block (see pls. 1, 2; fig. 3).

Surface exposures of this sequence in the study area (see pls. 1, 2) are restricted to the western part of the Laurel quadrangle, where 192 m of section is locally exposed south of the Zayante fault. There, the Lompico Sandstone rests unconformably on the Butano Sandstone and includes a coquina bed containing mollusks, barnacles, and foraminifers diagnostic of near-shore, shallow-marine conditions and an early to middle Miocene (Relizian to Luisian) age, according to Clark and others (1989). The conformably overlying micaceous siltstone and subsiliceous organic mudstone beds of the Monterey Formation yield pelecypods and benthic foraminifers characteristic of neritic depths and a Luisian (middle Miocene) age.

Northeast of the Zayante fault, where the sequence is not exposed, 17 m of siliceous strata of the Monterey Formation and 70 m of the Lompico Sandstone was penetrated by Bean Hill Ltd. Hihn No. 1 well (cross sec. S–7, pl. 1) in the Loma Prieta quadrangle (McLaughlin and others, 1988b). Thus, the lower to middle Miocene sequence probably extended over all of this area but is now restricted to erosional remnants beneath the upper Miocene-Pliocene unconformity.

UPPER MIOCENE TO PLIOCENE SEQUENCE

The upper Miocene to Pliocene sequence consists of a transgressive, shallow-marine sandstone unit, the Santa Margarita Sandstone; a deeper-marine siliceous organic mudstone unit, the Santa Cruz Mudstone; and a shallow-marine unit, the Purisima Formation (see pl. 1). The Purisima Formation records late Miocene and Pliocene continuation of the marine transgression that began with deposition of the Santa Margarita Sandstone during earlier late Miocene time. The transgression spread more widely during the early Pliocene, probably recording the major global sea-level rise at about 5–4.2 Ma (Haq and others, 1987).

The Purisima Formation includes distinctive lithic sandstone containing abundant andesitic detritus and a heavy-mineral assemblage characterized by hypersthene, augite, basaltic hornblende, and green and brown hornblende (Clark, 1981). Locally, it includes rhyolitic tuff interbeds. One tuff bed that crops out in Forest of Nisene Marks State Park in the eastern part of the Laurel quadrangle is interpreted to be of air-fall origin and is tentatively correlated with the Nomlaki Tuff Member (of the Tehama, Tuscan, and Laguna Formations), which was erupted from the southern Cascade Range and K-Ar dated at 3.4 Ma (late Pliocene; A.M. Sarna-Wojcicki, written commun., 1978).

The sequence rests unconformably on all older units and is widely distributed in both the Ben Lomond and La Honda blocks. In the Laurel quadrangle, as much as 1,000 m of this sequence is preserved along the Glenwood syncline. In this quadrangle, the Santa Margarita Sandstone and Santa Cruz Mudstone pinch out to the east, and the Purisima Formation is more widespread (see pl. 1). The Purisima Formation also is preserved in fault slivers along the San Andreas fault zone. Throughout the study area (see pl. 1), the upper part of the Purisima Formation has been removed by erosion, and locally this formation is overlain unconformably by Quaternary deposits.

STRATIGRAPHY NORTHEAST OF THE SAN ANDREAS FAULT

The area northeast of the San Andreas fault is underlain by a composite Mesozoic basement consisting of Franciscan rocks, Coast Range ophiolite, and Great Valley sequence (see pl. 1). Seismic reflection and refraction data for the Loma Prieta region have been interpreted as indicating that these formations occur from the surface to 8- to 12-km depth (Fuis and Mooney, 1990). Newer data to the north in the San Francisco Bay region suggest that rocks with seismic velocities compatible with this those of this composite basement may extend to 16- to 18-km depth (Hole and others, 1993). To the east beneath the Diablo Range, the composite Franciscan, Great Valley, and ophiolitic basement is interpreted as extending to about 12-km depth, gradually shallowing and thinning farther to the east beneath the western San Joaquin Valley (Wentworth and others, 1984; Fuis and Mooney, 1990; Wentworth and Zoback, 1990). Below this eastward-thinning basement, rocks with seismic velocities like those of the metamorphic and plutonic rocks exposed in the Sierra Nevada foothills slope southwest to the San Andreas fault (Fuis and Mooney, 1990).

The composite basement consisting of Franciscan Complex, Coast Range ophiolite, and Great Valley sequence is broken at the surface into several structural blocks by major late Cenozoic faults. Displacements across these faults have resulted in

different stratigraphic sections within each block (see pl. 1). A major change in Oligocene to Miocene stratigraphy occurs across the Berrocal and Sargent faults, which define part of the northeast boundaries of the El Sombroso block of Bailey and Everhart (1964) and the Sierra Azul block of this paper (see pl. 2; fig. 2). The Sierra Azul block is bounded along its northwest side by parts of the Aldercroft, Soda Spring, and Sierra Azul faults (fig. 2). The study area northeast of the San Andreas fault is divided into several additional fault blocks, modified after the study by Bailey and Everhart.

FRANCISCAN COMPLEX (JURASSIC AND CRETACEOUS)

Northeast of the San Andreas fault and southwest of the Silver Creek fault (see pl. 1), Franciscan rocks compose most of the exposed structural basement. The Franciscan Complex consists predominantly of what is termed its Central belt, which is largely a melange of igneous and pelagic oceanic rocks and clastic sedimentary rocks derived from two highly disrupted tectonostratigraphic terranes. Pelagic rocks of the Bald Mountain-El Sombroso terrane (McLaughlin and others, 1991a, b) include radiolarian chert of Early Jurassic to Early Cretaceous age that formed at equatorial latitudes (Hagstrum and Murchey, 1991). This chert was deposited on an Early Jurassic or older basaltic basement formed in near-ridge-seamount to midocean-ridge-basalt (MORB)-like settings (McLaughlin and others, 1991a, c). The younger Permanente terrane includes both radiolarian chert and pelagic limestone of mid-Cretaceous (Aptian) to Late Cretaceous (Turonian) age formed at equatorial latitudes and deposited on basaltic rocks whose geochemistry and $^{87}Sr/^{86}Sr$ ratios (table 1) suggest an intraplate, seamount or oceanic-plateau formational setting (Sliter and others, 1991; McLaughlin and others, 1991a, c).

The depositional age of the sandstone component of the Bald Mountain-El Sombroso terrane is Early to mid-Cretaceous, on the basis of the ages of radiolarians in clasts of chert in conglomerate and on the inferred 90-Ma age of high-pressure metamorphism of some weakly foliated metaclastic rocks of the terrane (McLaughlin and others, 1991a). The depositional age of terrigenous rocks associated with the Permanente terrane is poorly constrained, except that locally they depositionally overlie and so are considered to postdate the pelagic limestone. Thus, the metaclastic rocks of the Permanente terrane are Late Cretaceous (Turonian) or younger.

Tectonic disruption of the Bald Mountain-El Sombroso and Permanente terranes and their mixing into melange of the Central belt along the continental margin followed earlier metamorphism and uplift of older Franciscan rocks in the melange. The later disruption and mixing of the Bald Mountain-El Sombroso and Permanente terranes at the California margin occurred sometime between the Late Cretaceous (Campanian) and early Eocene, when the rocks were accreted, unroofed, and overlain by early Tertiary deposits (fig. 3).

The Franciscan Complex also includes minor blocks of garnet-bearing glaucophane schist, eclogite, amphibolite, and other sedimentary and volcanic rocks metamorphosed to high-pressure-metamorphic-mineral assemblages, as well as local thin, lenticular bodies of serpentinite. These rocks generally are associated with argillic zones considered to be the matrix of the melange. The serpentinite is at least partly derived from nearby rocks of the Coast Range ophiolite, and some unmetamorphosed terrigenous sedimentary rocks sheared into the melange are derived from Upper Jurassic to Lower Cretaceous parts of the Great Valley sequence.

Rocks of these Franciscan terranes are imbricated by several faults at low angles both to bedding and to lithologic contacts. These faults appear to repeat and thicken the section, and are folded. Thus, they are probably deformed thrusts, although no detailed kinematic data are available. Locally, outcrop-scale asymmetric isoclinal and recumbent folds and axial-planar cleavage are associated with the thickened section. These structures probably reflect contraction at the California margin during the Late Cretaceous and early Tertiary accretion of the Franciscan Complex (fig. 3).

SLATE AND PHYLLITE OF LOMA PRIETA PEAK (JURASSIC?)

A thin unit of slate and phyllite (Jlpp, pl. 1) is exposed at one locality beneath Loma Prieta peak (cross sec. S–6, pl. 1; figs. 1*B*, 2*A*) in the sole of the Loma Prieta thrust. The coarse-grained and pelitic clastic components of this unit are flattened, and the rocks exhibit a strong penetrative, slaty cleavage. The metapelite also is highly siliceous and locally tuffaceous. Flattened lenses of metaconglomerate include mostly clasts of metachert, fine-grained porphyritic andesitic to rhyolitic volcanic rocks, and granitic rocks. The unit is distinguished from rocks of the Franciscan Complex by its lithology and geochemistry, as well as by the absence of any high-pressure/temperature-metamorphic-mineral phases, which almost always occur in Franciscan rocks that have undergone equivalent flattening and cleavage development (McLaughlin and others, 1991b). On the basis of vitrinite reflectance and petrography, the slate and phyllite of Loma Prieta peak has, instead, undergone much higher temperature and lower pressure metamorphism to greenschist facies, at temperatures of ≥310°C (Underwood and others, 1991). These rocks are similar in composition and metamorphism to the Jurassic Mariposa Slate of the western Sierra Nevada metamorphic belt, the Galice Formation of the western Klamath Mountains, and the Santa Monica Slate of the Santa Monica Mountains in the Transverse Ranges. The slate and phyllite of Loma Prieta peak also is similar to rocks that occur along the Coast Range fault in the northern Sacramento Valley that have been correlated with the Galice Formation (Jayko and Blake, 1986). We interpret these rocks to have been faulted upward from a deep (≥10 km) sub-Franciscan

crystalline basement that may underlie structurally shallower Franciscan rocks and Coast Range ophiolite (figs. 3, 4), as implied in interpretations of deep crustal structure by Fuis and Mooney (1990).

COAST RANGE OPHIOLITE (JURASSIC)

Rocks of the Jurassic Coast Range ophiolite, the oceanic basement on which Jurassic and Cretaceous clastic marine strata of the Santa Teresa and Sierra Azul blocks were deposited, structurally overlie the Franciscan Complex and the slate and phyllite of Loma Prieta peak. Gravity and magnetic modeling and seismic reflection and refraction data further suggest that similar ophiolitic rocks may underlie the Franciscan Complex below about 8-km depth. Field exposures in the Loma Prieta region suggest that the ophiolite section ranges in thickness from about 400 to 1,700 m (see pl. 1). A composite section, on the basis of maximum thicknesses for each ophiolite unit (see pl. 1), permits a thickness of as much as 2,135 m, although nowhere is this much continuous section exposed at the surface. Interpreted aeromagnetic data (see Jachens and Griscom, this chapter) suggest that buried parts of the ophiolite section could be as much as 3 km thick in the eastern part of the study area (fig. 1), and more than 2 km thick at depth elsewhere.

Although we recognize that magnetic models imply an ophiolite section as much as 2.0 to 3.0 km thick at depth, the thickness depicted in our structure sections is based on surface exposures (see pl. 1). Aeromagnetic modeling, however, also indicates the ophiolite section to be complexly segmented by wedge-shaped bodies of nonmagnetic rocks interpreted to be part of the Franciscan Complex (see Jachens and Griscom, this chapter).

From bottom to top, the Coast Range ophiolite is composed of varying thicknesses of cumulate ultramafic rocks, cumulate gabbro, diabase to diorite dikes and sills, basaltic to andesitic flows, andesitic to quartz-keratophyric tuff with local thin intercalations of recrystallized radiolarian chert, and coarse-grained quartz-keratophyre pyroclastic breccia (McLaughlin and others, 1991a). Initial $^{87}Sr/^{86}Sr$ ratios for the igneous section of the ophiolite range from a primitive value of 0.70242 in the cumulate ultramafic rocks, upward to a higher value of 0.70404 at the top of the more highly evolved volcanic section (table 1).

A zircon separate from dikelets of hornblende-albite pegmatite in the noncumulate intrusive rocks yielded Pb-U ages that lie on concordia between 144 and 168 Ma (J.L. Wooden, written commun., 1992). Hornblende from the same sample yielded a discordant K-Ar age of 138.5 Ma (Nakata and others, 1993). Two alteration events, one in the Cretaceous and one in the Miocene, appear to have completely or partially reset the K-Ar and Pb-U ages. Therefore, the upper concordia Pb-U age of 168 Ma is considered to be closest to the true cooling age for the intrusive section of the ophiolite. Elsewhere in California, Pb-U ages of zircons from plagiogranite in cumulate and intrusive sections of the Coast Range ophiolite range from 163 to 173 Ma (Hopson and others, 1981, 1991; Mattinson and Hopson, 1992).

On the basis of radiolarians contained in interbedded chert and tuff in the upper part of the volcanic sequence, the volcanic pelagic rocks are as young as Oxfordian (160–156 Ma) and possibly as old as Bajocian (181–175 Ma) in their lower part (Bonnie Murchey, written commun., 1990). Radiolarians from the volcanic pelagic section of the Coast Range ophiolite at other localities in the Coast Ranges are dated at early Oxfordian to late Tithonian (163–145 Ma; Hull and others, 1992).

The exposed ophiolitic sequence of the El Sombroso and Sierra Azul blocks has been attenuated along high- to low-angle detachment faults that displace structurally higher parts of the ophiolite downward onto structurally lower parts of the section (see pl. 1). These attenuation faults, which may be related to Mesozoic and Tertiary unroofing of the Coast Ranges, have had a complex history of reactivation.

GREAT VALLEY SEQUENCE (UPPER JURASSIC TO UPPER CRETACEOUS)

The Great Valley sequence was defined by Bailey and others (1964) as the Upper Jurassic through Cretaceous sedimentary strata and associated outlier strata originally deposited in the marine depositional basin of the Great Valley of California. In the northern and central Coast Ranges, most upper Mesozoic marine clastic sequences overlying ophiolitic rocks, which also structurally overlie the Franciscan Complex, have been assigned to the Great Valley sequence. Some outlier sections have no established depositional connection to the Great Valley, including the section described herein, and are not similar lithologically to any known coeval marine sections in the Sacramento or San Joaquin parts of the Great Valley sequence or to any coeval rocks of the Great Valley sequence in the Diablo Range. For example, the framework-grain compositions of sandstone and the clast compositions of conglomerate in Upper Cretaceous rocks of the Sierra Azul block reflect a mafic to intermediate-composition volcanic and plutonic provenance devoid of chert, with only minor quartzite. Coeval rocks along the southwest side of the Great Valley have a more quartzose provenance, with conglomerate that contains fewer mafic igneous clasts and significantly more chert and quartzite (Seiders and Blome, 1988; Seiders and Cox, 1991). For this reason, the term "Great Valley sequence" is used herein to indicate only that rocks of this age and structural setting occur in the Sierra Azul, Santa Teresa, and Los Capitancillos blocks. We do not imply original structural or depositional continuity with rocks directly to the east in the Diablo Range or Great Valley. Any original connection with rocks to the east has been disrupted by Miocene to Holocene large strike-slip displacement across the Hayward-Calaveras and San Andreas faults, and by additional pre-San Andreas (Campanian to early

Eocene) strike-slip displacement along the Sur-Nacimiento and ancestral Calaveras fault systems (McLaughlin and others, 1990). In addition, the upper Mesozoic clastic section of the Sierra Azul block, as with the underlying ophiolite and overlying lower Tertiary rocks, is highly attenuated along faults at low angles to bedding. Most of the Lower and Upper Cretaceous section of the Great Valley sequence of the Sacramento-San Joaquin Valley and Diablo Range is missing in the Loma Prieta region (see pls. 1, 2; fig. 1).

UPPER JURASSIC AND LOWER CRETACEOUS ROCKS

A thin unit of dark-green to black argillite overlies the Coast Range ophiolite discontinuously along attenuation faults in the Loma Prieta region (see pls. 1, 2; fig. 1). The rocks commonly are penetratively deformed, but numerous megafossils indicate a Late Jurassic (Tithonian) and Early Cretaceous (Berriasian? to Valanginian) age (McLaughlin and others, 1988b, 1991a, b). The rocks contain local, lenticular to nodular, phosphatized or silicified carbonate concretions. The basal beds of this unit are tuffaceous. In one place north of the Calero Reservoir, a thin lens of fossiliferous mudstone and sandstone composed of serpentinite detritus overlies a slice of Coast Range ophiolite (see pl. 1). This argillite unit in the lower part of the Great Valley sequence is generally no more than 100 to 200 m thick and is bounded above by another low-angle attenuation fault and locally by younger southwest-side-up reverse faults.

UPPER CRETACEOUS ROCKS

Overlying the lower part of the Great Valley sequence above a sheared contact, which is interpreted as another low-angle normal fault, is a unit of sandstone, shale, and conglomerate, as much as 1,615 m thick in the Sierra Azul block and as much as 335 m thick in the Santa Teresa block. From bottom to top (see pl. 1), the sedimentary section consists of conglomerate, lithic arkosic wacke, thinly interbedded arkosic wacke and shale turbidites, and massive shale and fine-grained sandstone containing local carbonate concretions.

Locally, the concretionary massive shale and sandstone near the top of the unit are overlain by a few meters of thinly interbedded, graded feldspathic sandstone and interbedded shale. Strata assigned to this unit in the Santa Teresa block are thin-bedded concretionary shale and sandstone that are undated but lithologically resemble the upper part of Upper Cretaceous rocks of the Sierra Azul block (see pl. 1). In the Sierra Azul block, megafossils occur in conglomerate of the lower part of the unit and in massive concretionary shale and sandstone of the upper part. These megafossils indicate a Late Cretaceous (Campanian) age, and the sedimentology of the enclosing strata suggests their deposition in a submarine-fan or slope setting (Elder, 1990). The conglomerate and thick-bedded arkosic sandstone suggest a proximal or channeled, upper-midfan or slope setting, whereas overlying thin-bedded turbidites may have been deposited in deeper water in an interchannel, midslope region. Megafossils in the conglomerate were apparently transported downslope from a near-shore high-energy habitat; fossils in overlying concretionary shale and sandstone also were moved downslope, but from a more offshore shelf setting (Elder, 1990). Limited paleocurrent data suggest transport to the west-southwest. Tangentially crossbedded sandstone, locally interbedded with argillite in the uppermost beds of the succession, may record marine regression after deposition of the underlying transgressive succession (see pl. 1).

The conglomerate clast suite of the Sierra Azul block is generally well rounded and consists predominantly of cobbles to boulders of mafic and intermediate-composition porphyritic volcanic rocks, porphyritic silicic volcanic rocks, mafic to granitic plutonic rocks, and various minor sedimentary and metasedimentary rocks (McLaughlin and others, 1988b, 1991a, b). The rocks of this unit are extensively deformed by fracturing, shearing, and folding; and in the Sierra Azul block, the unit is extensively laumontitized.

EOCENE SEQUENCE

In the Sierra Azul and Santa Teresa blocks, a sequence of shale and sandstone, mudstone, and bioclastic limestone overlies the Jurassic and Cretaceous Great Valley sequence and the Franciscan Complex. This younger sequence, possibly as much as 1,110 m thick, may be structurally repeated in the Sierra Azul block. In the Santa Teresa block, the sequence is as much as 670 m thick (see pl. 1). The base of the sequence is a sheared low-angle contact interpreted to be an attenuation fault, which places Eocene rocks over Great Valley sequence, Coast Range ophiolite, or Franciscan rocks.

Locally at the faulted base of the Eocene sequence is a unit that varies in composition from bioclastic limestone in the Santa Teresa block to glauconitic calcareous lithic grit or conglomerate in the Sierra Azul block. The unit commonly contains clastic material derived from the underlying Coast Range ophiolite and Franciscan Complex, indicating significant unroofing of this area of the Coast Ranges before the early Eocene. In addition, the unit locally contains shallow-marine mollusks, algal debris, and discocyclinid foraminifers. In the Santa Teresa and Sierra Azul blocks, shallow-water foraminifers are mixed with deeper-water fauna, indicating downslope displacement from a near-shore to bathyal setting. These foraminifers indicate that the basal unit is early Eocene (planktic zone upper P6b or P7; McDougall, 1989, 1991).

These basal beds are overlain by as much as 200 m of distinctive olive-green and red-and-green-mottled foraminiferal mudstone containing an early Eocene (planktic zones P8, P9) foraminiferal fauna indicative of a lower-bathyal to abyssal depositional setting (McDougall, 1989, 1991). The mottled mudstone and sandstone of Mount Chual (see pl. 1) is recog-

nized over much of the Eocene California margin northeast and southwest of the San Andreas fault (McLaughlin and others, 1990, 1991b).

Overlying the Mount Chual unit is as much as 915 m of interbedded quartzofeldspathic sandstone and micaceous brown carbonaceous mudstone (see pl. 1), here called the sandstone and shale of Loma Chiquita Ridge, which typically are deeply weathered and locally are hydrothermally altered. Sparse foraminiferal faunas and rare, poorly preserved megafossils from these strata suggest an early Eocene (planktic zone P6b) to late Eocene age for the rocks, which overlaps the age of underlying Eocene strata. Paleobathymetry of the foraminifers indicates deposition in a middle- to lower-bathyal-slope setting. In most places, these rocks are in contact with underlying formations along attenuation faults, which locally cut out the underlying rocks at a low angle to bedding.

LOWER EOCENE TO LOWER MIOCENE SEQUENCE

The lower Eocene to lower Miocene sequence is recognized only along the southwest side of the Sierra Azul block adjacent to the San Andreas fault. This sequence is bounded to the northeast by a poorly defined fault that places the rocks over partly coeval Eocene strata of the Sierra Azul block. This northeast contact is interpreted to be a reverse or thrust fault (fig. 3) because of its southwestward dip and the apparent repetition of the lower Eocene part of the sequence across the boundary (cross secs. S–6, S–7, pl. 1; see pl. 2).

The lower Eocene to lower Miocene sequence consists of as much as 1,100 m of hard carbonaceous to cherty shale with minor interbeds of locally glauconitic quartzofeldspathic sandstone, a unit that is here referred to as the shale and sandstone of Highland Way. Microfossils from carbonaceous shale in the lower part of the sequence indicate an early Eocene (planktic zones P8 and P9 and nannofossil zone CP 11) age (McDougall, 1989), indicating that the shale and sandstone of Highland Way is coeval with, but lithologically dissimilar from, the two structurally underlying Eocene marine units. Foraminifers from the upper beds of this sequence indicate a late Oligocene to early Miocene (Zemorrian to Saucesian) age, whereas the intervening strata are poorly dated. The benthic foraminifers suggest deposition at bathyal or greater depths, consistent with a midslope to lower-slope setting. These strata also are partly coeval with the Temblor Sandstone north of the Sierra Azul block (see pl. 1) but were deposited in a much deeper marine setting.

PRE-PLIOCENE SEQUENCE NORTHEAST OF THE EL SOMBROSO AND SIERRA AZUL BLOCKS

Two formations ranging in age from Oligocene to Miocene are exposed only in the area northeast of or along the Berrocal and Sargent faults.

TEMBLOR SANDSTONE (OLIGOCENE TO MIDDLE MIOCENE)

The Temblor Sandstone, about 200 m thick, consists of thick-bedded to massive subfeldspathic to arkosic sandstone, minor mudstone, unsorted conglomerate, and dacitic tuff. The conglomerate occurs locally at or near the base of the formation, where it nonconformably overlies the Franciscan Complex and Coast Range ophiolite and contains locally derived angular detritus from the uplifted Franciscan Complex and Coast Range ophiolite and from the Eocene sequence of the Sierra Azul block (McLaughlin and others, 1991a, b). Reeflike accumulations of fragmented oysters, barnacles, bryozoans, and pectens occur locally within the basal conglomerate, suggesting a littoral to inner-shelf depositional setting and an Oligocene or early Miocene age (see pl. 1). In the New Almaden area (see pl. 1; fig. 2*A*), the upper beds of the Temblor are tuffaceous and grade upward into dacite tuff and tuff breccia. Map relations depicted by Bailey and Everhart (1964) imply that some of the dacite could be intrusive and postdate the volcaniclastic rocks. The tuff has been dated at about 15.6 Ma (D.H. Sorg and P.C. Russell, written commun., 1990). Locally, this tuff is hydrothermally altered and contains mercury mineralization (Bailey and Everhart, 1964).

MONTEREY SHALE (MIDDLE MIOCENE)

The Monterey Shale consists of yellowish-white-weathering, hard, brown diatomaceous mudstone, porcelanite, and cherty porcelanite, as much as 424 m thick. The rocks conformably overlie the Temblor Sandstone and contain nannofossils and benthic foraminifers diagnostic of middle Miocene (nannofossil zone CN3 or CN4, Luisian) age (David Bukry and Kristin McDougall, written commun., 1989) and indicative of deposition at 500- to 1,500-m depth. The Monterey Shale is lithologically distinct from, and represents a shallower marine setting than, the lower Eocene to lower Miocene sequence in the Sierra Azul block (see pl. 2; fig. 3).

QUATERNARY AND TERTIARY NONMARINE DEPOSITS NORTHEAST OF THE SAN ANDREAS FAULT

SANTA CLARA FORMATION (PLIOCENE AND PLEISTOCENE)

The Santa Clara Formation consists predominantly of fluvial coarse-grained gravel and fanglomerate; silty sandstone; silty, locally lithic carbonaceous mudstone; and laminated lacustrine mudstone. Cummings (1968) recognized eight lithofacies in the Santa Clara Formation, three of which crop out in the Loma Prieta region (see pl. 1). The Los Gatos

lithofacies (and its right-laterally offset equivalent, the Corte Madera lithofacies near Portola Valley), which is exposed in the Los Gatos area (figs. 1*B*, 2*A*), consists of fluvial gravel and fanglomerate containing clasts reworked from Upper Cretaceous conglomerate of the Sierra Azul block. The Stevens Creek lithofacies consists of gravel and fanglomerate, with a clast suite of graywacke and minor basalt, diabase, red and green metachert, and vein quartz, derived from adjacent uplands of the Franciscan Complex south of the Santa Clara Valley (see pl. 1). The Arastradero lithofacies consists of moderately well sorted, sandy, crossbedded pebble gravel and minor claystone and mudstone, deposited in braided-stream and flood-plain/overbank settings (Vanderhurst and others, 1982).

The Arastradero lithofacies, which is the stratigraphically lowest part of the Santa Clara Formation, includes laminated lacustrine mudstone adjacent to the San Andreas fault west of the Lexington Reservoir (see pl. 1). In the Saratoga area (fig. 2*A*), the Arastradero lithofacies locally contains fossil-plant debris, freshwater mollusks, and vertebrate-fossil remains, including *Felis (Cheetah) studeri* of Blancan (1.9–4.8 Ma) age (Adam and others, 1982; Repenning and others, 1990). Beds overlying the Blancan part of the Santa Clara Formation are poorly dated because of their coarse, unfossiliferous, nonmarine characteristics, but the overlying section is dated at Pleistocene, partly on the basis of a 250-ka age assigned to the older fluvial-terrace and alluvial-fan deposits of Santa Clara Valley that unconformably overlie the Santa Clara Formation (McLaughlin and others, 1991a), and the presence of a 500–600-ka ash horizon (Rockland ash bed of Sarna-Wojcicki and others, 1991; Sarna-Wojcicki, 2000) in marine intertongues in the Santa Clara Formation near Woodside, Calif. (fig. 1*B*). If additional time is considered for deposition of the clastic section overlying the Rockland ash bed, then the age of Santa Clara Formation is approximately constrained to the range 0.3–4.8 Ma. Santa Clara strata adjacent to the San Andreas fault and along the frontal thrust-fault system bounding the east side of the Santa Cruz Mountains are steeply tilted and deformed into open, high-amplitude, northwest-trending folds. In the lowland areas and subsurface northeast of the mountain front, gravel mapped as the Santa Clara Formation shows little, if any, discordance to overlying, undeformed to mildly tilted fluvial deposits.

ALLUVIAL AND LANDSLIDE DEPOSITS (PLEISTOCENE AND HOLOCENE)

Extensive alluvial-fan and stream deposits, younger than about 250 ka (McLaughlin and others, 1992), overlie the Santa Clara Formation with marked discordance. These deposits generally consist of poorly to moderately well sorted pebble to boulder gravel, sand, silt, and mudstone, deposited along ancient to modern stream channels and flood plains. The maximum age assigned to these deposits is based partly on the estimated 0.3-Ma age for the deformed upper part of the unconformably underlying Santa Clara Formation, and partly on the degree of weathering of the terrace materials (McLaughlin and others, 1992). In addition, oxygen-isotopic ratios plotted against time and correlated with eustatic sea-level fluctuations indicate global warming and eustatic highstands at 250 and 120 ka (Sarna-Wojcicki and others, 1991). This relation further constrains the age of the post-Santa Clara alluvial deposits. These highstands are the most likely times for cutting of the two highest and oldest post-Santa Clara fluvial terraces. Thus, the high terraces cut into the Santa Clara Formation along Los Gatos Creek between Los Gatos and the Lexington Reservoir are dated at about 250 ka. The upper part of the Pleistocene alluvial-fan- and stream-deposit section around the present San Francisco Bay margin locally contains vertebrate (Rancholabrean) fossils and radiocarbon-dated wood and plant materials dated at about 22 ka. Overlying Pleistocene to Holocene alluvial deposits have yielded radiocarbon ages of about 14 ka and younger (Wright, 1971; Lajoie and Helley, 1975).

Numerous large composite landslide deposits, ranging from rotational blocks of coherent rocks with intact internal stratigraphy to incoherent, unsorted, rubbly debris flows, occur in the Loma Prieta region (fig. 1), particularly along the San Andreas fault between the Lexington Reservoir and the divide between Soquel and Corralitos Creeks. Surface deformation in this area during the 1989 Loma Prieta earthquake probably resulted partly from reactivation of some of these landslides (Cotton and others, 1990; Spittler and Harp, 1990; Ponti and Wells, 1991).

STRUCTURE SOUTHWEST OF THE SAN ANDREAS FAULT

The exposed structure southwest of the San Andreas fault zone consists of a series of nearly parallel faults and folds that trend more westerly than the San Andreas fault zone itself (see pl. 1; fig. 2). The more important folds are the Glenwood syncline and the Laurel anticline, between the Zayante and Butano faults, and the Summit syncline to the north (see pl. 1; fig. 2). These folds apparently developed concurrently with displacements on the major faults. Major faults displacing the Tertiary section are the Zayante-Vergeles fault, which also forms the boundary between two major structural blocks, and the Butano fault. Hundreds of meters to more than 1 km south of the bedrock San Andreas fault in the Los Gatos and Laurel quadrangles are the faults in the Summit Road-Skyland Ridge area, which were reactivated during the 1989 Loma Prieta earthquake. The fault zone there consists of a series of geomorphically youthful echelon faults that trend more northerly or subparallel to the throughgoing San Andreas fault zone and locally appear to offset the Butano fault. The faults of the Summit Road-Skyland Ridge area are discussed below in the section entitled “San Andreas Fault Zone.”

ZAYANTE-VERGELES AND RELATED BURIED FAULTS

The Zayante fault zone is the most important structure present between the San Andreas and San Gregorio faults. In the Santa Cruz Mountains (see pl. 1; fig. 1*A*), it is mapped for 55 km from west of Ben Lomond Mountain, where it is covered by upper Miocene strata of the Santa Margarita Sandstone and Santa Cruz Mudstone, southeastward to the vicinity of Watsonville, where locally it is covered by Quaternary deposits (Brabb, 1989). A gravity investigation (Clark and Rietman, 1973) demonstrated the continuity of this fault southeastward beneath Quaternary cover to the Vergeles fault in the northern Gabilan Range. The Vergeles fault, in turn, continues southeastward to the San Andreas fault south of San Juan Bautista. The combined Zayante-Vergeles fault is 82 km long (figs. 1, 2).

Although the throughgoing strand of the Zayante fault is confined to a narrow zone, branching lineaments locally occupy a zone as much as 1 to 2 km wide (Clark, 1981, pl. 2; McLaughlin and others, 1988b, sheet 2). The relatively straight course of this fault across canyons and ridges in the study area (see pl. 1) suggests that the fault plane dips steeply. Shear zones along the Vergeles fault south of San Juan Bautista dip 65°–85° S.(Ross, 1984, fig. 10). Gravity and aeromagnetic data (see Jachens and Griscom, this chapter) in the Santa Cruz Mountains suggest a southwestward dip to a depth of a few kilometers that steepens to near vertical at greater depth (cross sec. S–3, pl. 1; fig. 4).

South of the Zayante-Vergeles fault, the basement of the Salinia terrane is exposed or relatively shallow. Between the Zayante and San Andreas faults, the basement is not exposed in this part of the Santa Cruz Mountains, but gravity and magnetic data (see Jachens and Griscom, this chapter) suggest that the buried basement is most probably the northwestward continuation of the hornblende-quartz gabbro that crops out at Logan (figs. 1, 4). Thus, the Zayante-Vergeles fault appears to be a major structure in the Loma Prieta region juxtaposing continental and oceanic basements, truncated by the San Andreas fault at its southeast end (see pl. 1; figs. 1, 4).

Ross (1970, 1984) postulated that the gabbroic rocks at Logan may be right-laterally offset some 300 to 350 km by the San Andreas fault from petrographically and chemically similar gabbroic rocks at Eagle Rest Peak (fig. 1*A*) in the San Emigdio Mountains at the southern tail of the Sierra Nevada. A south-dipping fault of the Pleito thrust zone (fig. 1*A*) bounds the north side of the gabbroic rocks of Eagle Rest Peak; this fault could be equivalent to, or may at depth root into, a fault equivalent to the buried fault at the base of the gabbro of Logan (fig. 4). Although the gabbroic rocks of Eagle Rest Peak are covered to the south by Eocene marine strata, a southern segment of the Pleito thrust zone that cuts Miocene strata is aligned with the south contact of the gabbro. Faults of the Pastoria-Rand thrust system also are aligned with the south contact of the gabbroic rocks. Thus, the Pleito or Pastoria-Rand fault zones may correspond to the offset continuation of an ancestral Zayante-Vergeles fault (Ross, 1970, 1984). To juxtapose the Zayante-Vergeles fault with the Pleito thrust requires the restoration of about 350 km of right slip on the San Andreas fault.

The juxtaposition of ≥91-Ma continental basement of the Ben Lomond block with 165–161-Ma oceanic gabbroic basement of the La Honda block along the Zayante-Vergeles fault (see pl. 1; fig. 1) seems to require major up-to-the-south dip-slip fault displacement. Geobarometric and fission-track data suggest that the basement of the Salinia terrane in the Ben Lomond block, southwest of the fault, was uplifted more than 13 km to within 5 km of the surface between 90 and 61 Ma (Hansen and others, 1991; Arrowsmith and others, 1992; Bürgmann and others, 1994). South of the Zayante-Vergeles fault and outside the study area (fig. 1*A*), depositional remnants of the shallow- to deep-marine upper Paleocene Locatelli Formation overlie the basement of the Salinia terrane in the Ben Lomond block (Clark, 1981). The Locatelli Formation may also be present in the subsurface north of the Zayante-Vergeles fault. The basements of the La Honda and Ben Lomond blocks are also overlain north and south of the Zayante-Vergeles fault by about the same thicknesses of bathyal-marine strata of the lower to upper Eocene Butano Sandstone (see pl. 2; Clark, 1981). These data all suggest that initial juxtaposition of the La Honda and Ben Lomond blocks occurred between about 90 and 61 Ma.

Juxtaposition of the gabbro of Logan with Ben Lomond basement across the Zayante-Vergeles fault corresponds to a period of general uplift and unroofing in the Coast Ranges that seems to have begun southwest of the San Andreas fault (and thus farther south) as early as 91–60 Ma. From the latest Cretaceous (60 Ma) to the early Tertiary (52 Ma), oblique dextral convergence is believed to have occurred in northern California along the interface between the continental margin and rocks composing the Central belt of the Franciscan Complex (McLaughlin and others, 1988a). Some of this oblique strike-slip movement may have been accommodated within the Salinia terrane along the Zayante-Vergeles-Pastoria fault.

As much as 3 to 4 km of vertical displacement along the Zayante fault during Oligocene time (see pl. 2; fig. 3) resulted in emergence of the Salinia terrane to the south, in deposition of the terrestrial Zayante Sandstone along and north of the fault, and in restriction of marine conditions to a northeast-sloping La Honda Basin (Clark, 1981). Mafic volcanism was localized along this fault during late Oligocene to early Miocene time. Allen (1946) reported a remarkably similar history along the Vergeles segment of the fault in the San Juan Bautista area to the southeast.

In the Laurel quadrangle, the Purisima Formation and the lower part of the Butano Sandstone are juxtaposed along the Zayante fault, indicating at least 3.7 km of dip-slip separation, with the north side relatively downthrown. Model stud-

ies of the gravity field (Clark and Rietman, 1973) suggest that the basement is displaced as much as 2.7 km by this fault in the southern Santa Cruz Mountains near Corralitos, but in their modeling these workers assumed a density of 2.67 g/cm^3 for the Salinian basement between the Zayante and San Andreas faults. More recent modeling (see Jachens and Griscom, this chapter), which takes into account the greater density and magnetic contrasts across the fault and assumes these contrasts to define the Zayante-Vergeles fault at depth, suggests as much as 4 to 6 km of vertical dip-slip displacement (up on the southwest), with at least 6 km of horizontal shortening.

Most displacement along the Zayante fault at the surface is in rocks older than middle Miocene. The fine clastic deposition recorded by the Lambert Shale north of the fault suggests that by early Miocene (Saucesian) time, the uplifted Ben Lomond block was no longer supplying coarse detritus and thus had been reduced to a lowland. Subsequent transgression by middle Miocene seas led to deposition of the Lompico Sandstone-Monterey Formation sequence. Although most displacement appears to have occurred in Oligocene and earlier time, late Pliocene regional transpression reactivated the Zayante fault, because the Purisima Formation is offset along the Zayante fault in the southern part of the study area (see pl. 1). Late Pleistocene and possible Holocene displacement has been suggested for strands of the Zayante fault near Watsonville (Hall and others, 1974; Coppersmith, 1990), but in the Santa Cruz Mountains to the north, the Zayante fault lacks youthful geomorphic expression.

Aftershocks associated with the southwest-dipping Zayante fault at 7- to 10-km depth may indicate reactivation of the deep part of this fault during the earthquake. This deep slip did not propagate to the surface in the Santa Cruz Mountains (fig. 4).

Widespread basaltic volcanic rocks of Oligocene to early Miocene age in the Coast Ranges (including the Mindego Basalt and associated volcanic rocks of the La Honda Basin) have been cited as evidence for regional crustal extension resulting from a component of divergent motion (transtension) between the Pacific and North American plates during early development of the San Andreas transform fault (Clark and Rietman, 1973, pl. 1; Stanley, 1985, 1990; Atwater, 1989; Tennyson, 1989). The stratigraphic record across the Zayante-Vergeles fault indeed indicates major up-on-the-southwest dip-slip movement during the Oligocene (see pl. 1; fig. 3). The volcanism in the La Honda Basin also seems to be best explained within the context of horizontal extension above thin crust. The present reverse-slip geometry of the Zayante-Vergeles fault both at the surface (see pl. 1; fig. 4) and at depth (see Jachens and Griscom, this chapter) is, however, difficult to relate to an extensional setting. Interpretation of the Zayante-Vergeles fault as a transtensional structure seemingly requires either that (1) the fault dips northeast at some depth or that it dipped northeast before about 18 Ma and has since rotated to its present orientation, (2) an earlier normal fault has been overprinted by the present vertical to southwest-dipping Zayante-Vergeles thrust fault, or (3) the transtensional displacement was accommodated by faults not situated along the Zayante-Vergeles fault zone. This problem is presently unresolved and needs further study.

Compressional-deformation events were imposed on La Honda Basin fill deposits along the Zayante-Vergeles fault zone from 17 to 16 Ma (early Relizian), from 14 to 10 Ma (late Luisian to early Mohnian; Clark, 1981), and during the late Oligocene (fig. 3). Pliocene compression across the Zayante-Vergeles fault may have resulted from a change in plate-motion vectors between the Pacific and North American plates that caused conspicuous transpression across the entire transform margin (Atwater, 1989; Harbert and Cox, 1989).

BUTANO FAULT

The Butano fault is poorly exposed in the southwestern part of the Los Gatos quadrangle, where it trends southeast into the San Andreas fault (see pl. 1; figs. 1*B*, 2*A*). In this area, the Butano fault lacks geomorphic expression and is mapped with difficulty, on the basis of the juxtaposition of different parts of the lower Eocene to lower Miocene sequence through which it passes. Where the Butano Sandstone is faulted against the Vaqueros Sandstone, dip separation is as much as 1.3 km, with the north side relatively downthrown. The Butano fault has been mapped northwestward from the study area as a series of bifurcating faults for a distance of as much as 37 km. In the northern Santa Cruz Mountains, these faults are reported to dip steeply southwest and to have a combined dip separation of as much as 1.8 km (Cummings and others, 1962).

Although the pre-Eocene slip history of the Butano fault is uncertain, sedimentary units of the lower Eocene to lower Miocene sequence that are almost identical across this fault have been offset by post-early Miocene reverse slip. Displacement may have occurred during the two Miocene compressional deformations that may have activated the Zayante-Vergeles fault, and during late Pliocene transpression. A lower member of the Purisima Formation in the northern Santa Cruz Mountains is the youngest stratigraphic unit cut by the Butano fault; in that area, stream terraces of Pleistocene age appear to extend across the fault zone without interruption (Brabb and Olson, 1986). The Butano fault does not appear to have moved during the earthquake, nor is there evidence for Holocene activity on the Butano fault in the study area (fig. 1). Its eastern trace appears to be offset by the geomorphically youthful echelon faults in the Summit Road-Skyland Ridge area (see next section).

SAN ANDREAS FAULT ZONE

The San Andreas fault is the principal member of a transform-fault system that has accommodated as much as 460 km of right-lateral motion between the Pacific and North

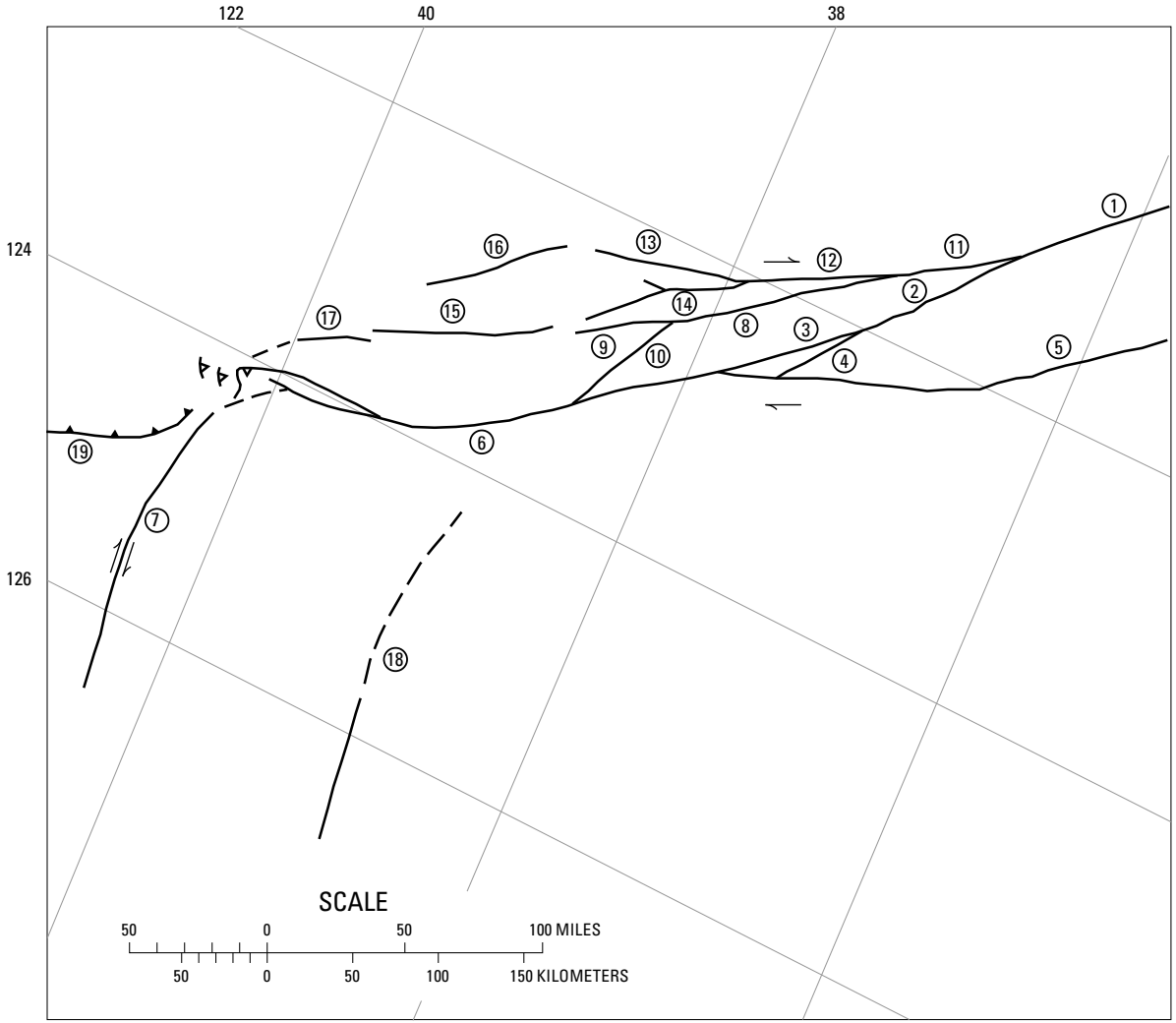

	FAULT NAME	DISPLACEMENT (km)
1.	Southern section of the San Andreas fault	310
2.	San Andreas and Pilarcitos faults	136
3.	Peninsular segment of the San Andreas fault	22-30
4.	Pilarcitos fault	106-114
5.	San Gregorio fault	115-170
6.	Northern section of the San Andreas fault	251-306
7.	Mendocino Fracture Zone	- -
8.	Hayward fault	174 (East Bay fault system)
9.	Rodgers Creek fault	
10.	Bloomfield-Tolay fault zone	
11.	Calaveras fault	
12.	Calaveras and Sunol faults	
13.	Concord fault	
14.	Franklin fault	
15.	Maacama fault	- -
16.	Bartlett Springs fault	- -
17.	Garberville fault	- -
18.	Pioneer Fracture Zone	- -
19.	Cascadia subduction zone	- -

Figure 5.—Schematic map of northwestern California and adjacent offshore area, showing partitioning of Miocene and younger dextral slip on faults of the San Andreas fault system.

Table 2.—*Miocene and younger offsets and slip rates for faults of the San Andreas fault system*

Fault member	Total displacement (km)	Duration of faulting (Ma)	Slip rate (mm/yr)
San Andreas fault south of intersection with the east-bay fault system.	310	0–18	17
East-bay fault system----------	174	0–12	14
Peninsular segment of the San Andreas fault.	22–30	0–3	10
Northern section of the San Andreas fault system (Pilarcitos fault+San Gregorio fault+Peninsular segment of the San Andreas fault).	251–306	~13 (0–3 and 8–18)	~19–22 (but 14–17 if slip occurred between 18 Ma and present
Total, San Andreas fault system (includes the San Gregorio fault, the Pilarcitos fault, the Peninsular segment of the San Andreas fault, and the east bay fault system)	425–480	0–18	24–27
Total, Pilarcitos fault ----------	106–114	~13 (18–5)	~8–9 (but 5.8–6.3 if slip occurred between 18 Ma and present
San Gregorio fault ----------	115–170	0–12	10–13

American plates since the early Miocene as it extended northward along the California margin (Huffman, 1972; Ross and others, 1973; Mathews, 1976; Fox and others, 1985; Stanley, 1987; Irwin, 1990). In northern and central California, the San Andreas fault system consists of numerous fault segments (fig. 5; table 2) that have accommodated different components of the total displacement at different times. Estimates of the amount and timing of slip that is partitioned to various segments of the fault system vary, partly owing to a poor understanding of the slip histories of the San Gregorio and Pilarcitos faults and faults in the eastern San Francisco Bay region.

Estimates of slip on the San Gregorio fault range from 115 to 170 km (Graham and Dickinson, 1978; Clark and others, 1984; Ross, 1984; Jachens and others, 1998). This slip is added to that in the San Andreas-Pilarcitos fault zone in the offshore area north of San Francisco (fig. 5; table 2).

At the intersection of the San Andreas and Calaveras faults near Hollister (fig. 1*A*), part of the remaining 310 km of slip on the San Andreas fault system is partitioned to the Calaveras fault (McLaughlin and others, 1990; Jones and Curtis, 1991). About 160 to 170 km of slip is partitioned to faults in the eastern San Francisco Bay region from the Calaveras fault, on the basis of offsets of the trend in ages of volcanic rocks and hydrothermal mineralization and displacement of the distinctive Permanente terrane of the Franciscan Complex across the Calaveras fault (McLaughlin and others, 1996). Additional evidence from gravity and aeromagnetic data refines the estimated offset on the southern section of the Calaveras fault (R.C. Jachens, oral commun., 2000) to about 174 km. With this refinement, the remaining 136 km of right slip on the San Andreas fault system is apparently taken up by the San Andreas and Pilarcitos faults and (or) other unidentified faults on the San Francisco peninsula. Dextral offset of the Corte Madera lithofacies of the Santa Clara Formation across the Peninsular segment of the San Andreas fault from its source area in the Sierra Azul block (Cummings, 1968), together with displacement of the axis of a linear magnetic low associated with the Permanente terrane (Robert C. Jachens, oral commun., 2000), indicates that only 22 to 30 km of the remaining slip is attributable to the Peninsular segment of the San Andreas fault system. Thus, about 106 to 114 km of Miocene to Pliocene right slip remains to be accommodated by the Pilarcitos fault.

Most right-lateral slip across the Peninsular segment of the San Andreas fault appears to have occurred since 3 Ma. Modern right-lateral-strain rates on this segment based on geodetic measurements beginning before the earthquake (Thatcher and Lisowski, 1987; Thatcher, 1990) range from 5 to 12 mm/yr. The slip rate across the entire transform margin at this latitude is about 30 mm/yr, apparently within the range indicated by geologic offsets (Brown, 1990).

SAN ANDREAS FAULT IN THE LOMA PRIETA REGION

The San Andreas fault zone trends northwesterly through the study area (fig. 1) as a zone of deformation, ranging in width from about 610 m in the southeast to as much as 1,220 m to the northwest (see pl. 1). The surface geology, as well as gravity and magnetic data (see Jachens and Griscom, this chapter), suggests that the fault zone is vertical or dips steeply southwest in the northwestern part of the study area. In the Loma Prieta quadrangle to the southeast, the upper part of the fault zone locally is considered to have a northeastward dip, on the basis of gravity and magnetic modeling (see Jachens and Griscom, this chapter), but the mapped fault zone follows a straight, apparently steep course at the surface (see pl. 1).

The San Andreas fault zone in the Loma Prieta region consists of two components. First, we recognize a "principal" or "main bedrock" component of the fault zone, on the basis of major differences in Pliocene and older stratigraphy across the fault. Thus, the principal trace of the fault zone corresponds to the long-term fault across which as much as 136 km of right-lateral displacement is accommodated. Second, we recognize faults of the San Andreas fault zone that exhibit little evidence of large strike-slip offset but do exhibit strong evidence of repeated Quaternary surface displacements, on the basis of youthful geomorphic features (for example, aligned closed depressions and sag ponds, aligned narrow linear valleys, scarps, captured drainages).

Northwestward along the San Andreas fault zone from the southeast border of the study area (see pl. 1; fig. 2*B*) to the drainage divide between Corralitos and Soquel Creeks, youthful geomorphic features correspond closely to the principal trace of the San Andreas fault.

From the divide between Corralitos and Soquel Creeks northwestward to the boundary of the Los Gatos quadrangle, however, the San Andreas fault zone is obscured by extensive landslide deposits. In this area, the principal trace of the San Andreas fault forms the northeast boundary of the fault zone (see pl. 1; fig. 2*B*), and geomorphically youthful fault traces are mapped noticeably southwest of the principal fault trace (Sarna-Wojcicki and others, 1975; U.S. Geological Survey staff, 1989). The active, geomorphically youthful fault traces appear as photolineaments that cross the landslides and commonly align with structural and lithologic discordances in the Tertiary sedimentary section of the La Honda block exposed beneath the landslides.

From the divide between Corralitos and Soquel Creeks to the west boundary of the Los Gatos quadrangle, the principal trace of the San Andreas fault is exposed at only a few localities. Along Spanish Ranch Road in the northeast corner of the Laurel quadrangle, the fault is located to within 15 m, where it juxtaposes Pliocene marine sandstone of the Purisima Formation on the southwest against lower to upper Eocene sandstone and shale sequences of the Mount Chual and Loma Chiquita Ridge areas to the northeast, and is draped by perched Quaternary alluvium (see pl. 1). The principal trace of the San Andreas fault is also exposed at several other isolated localities in tributary canyons south of Los Gatos Creek (see pl. 1; fig. 2*B*). At the southeast end of these localities (see pl. 1; fig. 2*B*), an 8-m-wide zone of gouge, including sheared serpentinite, separates the Rices(?) Mudstone Member of the San Lorenzo Formation on the southeast from Upper Cretaceous sandstone and shale of the Sierra Azul block to the northeast. In the two tributaries to the northwest (one adjacent to the community of Holy City and the other in Moody Gulch), the principal trace of the San Andreas fault separates Oligocene marine strata of the Vaqueros Sandstone on the southwest from lower Eocene sandstone and shale of the Sierra Azul block to the northeast.

At Holy City, Los Nietos (Union Oil) Holy City No. 1 well, located about 91 m southwest of the mapped principal surface trace of the San Andreas fault (see pl. 1; fig. 2*B*), apparently penetrated the fault at 1,108-m depth, indicating a dip of 84° SW. (cross sec. S–2, pl. 1).

No convincing evidence exists for primary coseismic movement along the mapped principal surface trace of the San Andreas fault from the drainage divide between Corralitos and Soquel Creeks to California Highway 17 during the 1989 Loma Prieta earthquake, nor clear evidence that the main bedrock trace of the fault ruptured the surface in this area during the 1906 San Francisco earthquake. Although 1.4 m of right-lateral offset was recorded in the Wrights Railroad Tunnel (Lawson, 1908; Sarna-Wojcicki and others, 1975; Prentice and Ponti, 1994), this displacement was along a fault strand 150 to 300 m southwest and parallel to the principal trace of the San Andreas fault (see pl. 1; fig. 2B). Most of the surface deformation in 1989 and, possibly, 1906 was in the La Honda block, along secondary faults in the Summit Road-Skyland Ridge area, 1 to 2 km southwest of the principal trace of the San Andreas fault.

FAULTS IN THE SUMMIT ROAD-SKYLAND RIDGE AREA

Geomorphically youthful faults in the Summit Road-Skyland Ridge area form a 6-km-wide zone trending N. 18°–65° W. Most of these faults trend N. 30°–40° W., subparallel to the principal trace of the San Andreas fault, and are more northerly than the Butano fault (trend, N. 65°–70° W.) and the axes of the Laurel anticline and Summit syncline. Most of the faults in this zone range from 300 to 800 m in length. One fault that cuts Morrill (Morrell) Road extends 3 km southeastward of Summit Road; another fault to the west of the Morrill Road fault appears to be the northwestward extension of a more nearly continuous fault that trends southeast into the Loma Prieta quadrangle (see pl. 1; fig. 2*B*).

These faults are mapped on the basis of structural discordances in the Butano Sandstone, San Lorenzo Formation, and Vaqueros Sandstone and, locally, of the juxtaposition of

different rock units (see pl. 1). Several of the faults, which were trenched in the vicinity of C.T. English School and Loma Prieta School along Summit Road, were found to juxtapose colluvium and Paleogene bedrock units of the La Honda block (Sarna-Wojcicki and others, 1975; Johnson and Associates, 1989). Most of the faults display youthful geomorphic features, such as closed depressions, swales, scarps, and vegetation lineaments along their extent (Sarna-Wojcicki and others, 1975), that have resulted from repeated displacements. Radiocarbon dating of offset soil horizons along one of these faults that trends beneath the Loma Prieta School grounds shows that some of the displacements are Holocene (Johnson and Associates, 1989).

Several faults along the west side of the Summit Road-Skyland Ridge area trend more westerly and parallel the strike of the Vaqueros Sandstone on the south limb of the Summit syncline (see pl. 1; fig. 2*B*). One of these faults is well exposed on the east side of California Highway 17, about 120 m south of Summit Road (see pl. 1; fig. 2*B*), and another was trenched south of Summit Road (670 m south of the NE. cor. sec. 21, T. 9 S., R. 1 W.; see pl. 1). Both are bedding-plane normal faults, with the north sides relatively downthrown, and both faults slipped during the 1989 Loma Prieta earthquake. Multiple episodes of normal slip have occurred on these faults during the late Quaternary; the California Highway 17 fault has undergone about 8 m of cumulative displacement during the past 20 k.y. (Cotton, 1990; Cotton and others, 1990).

EARTHQUAKE DEFORMATION IN THE SUMMIT ROAD-SKYLAND RIDGE FAULT ZONE

During the earthquake, numerous linear coseismic cracks and fissures, some as much as 600 m long, formed along the Summit Road-Skyland Ridge fault zone (Sarna-Wojcicki and others, 1975; Clark and others, 1989; Johnson and Associates, 1989; McLaughlin and others, 1991a). Many of the coseismic cracks underwent sinistral extension during the 1989 Loma Prieta earthquake, and some also were shown to have undergone sinistral extension during the 1906 San Francisco earthquake (Prentice and Schwartz, 1991). The overall surface orientation and sense of displacement of these coseismic cracks and fissures in the Summit Road-Skyland Ridge fault zone is inconsistent with the expected deformation field for the 1989 Loma Prieta earthquake inferred from first-motion studies of the main shock (fig. 4). The net updip-slip vector of the hanging-wall fault block, as determined from the rake of the first motion at the focal depth of 17 km, was toward N. 10° W. Net maximum horizontal extension at this depth was, therefore, at about N. 80° E.–S. 80° W. The direction of maximum horizontal extension derived from the observed surface-deformation field along Summit Road and Skyland Ridge was about N. 10°–30° E. to S. 10°–30° W. (Ponti and Wells, 1991)—a significant rotation from the expected orientation (fig. 4*A*).

Ponti and Wells (1991) analyzed and modeled the 1989 deformation field of the Summit Road-Skyland Ridge fault zone. They found that the total extension across this zone after the earthquake was at least 35 times that predicted from the geodetically measured uplift and that the azimuths of extension statistically point downslope. They concluded that the coseismic cracking and fissuring was predominantly gravity driven and that recurrent ridgetop spreading and downslope movement of near-surface materials was triggered by seismic shaking. Other workers (for example, Cotton, 1990; Cotton and others, 1990) interpreted the cracks and fissures as predominantly bedding-parallel, bending-moment tension faults associated with preexisting folds in the flexed hanging-wall block of the Loma Prieta rupture, and discounted slope processes as a major cause of the deformation.

The large-scale collapse of the northeast-facing slopes between the Lexington Reservoir and Santa Rosalia Mountain (fig. 2*B*) that is indicated in our geologic mapping is consistent with long-term uplift and recurrent focused seismic shaking of the relatively soft, incompetent Tertiary rocks in the steeply dipping hanging-wall block southwest of the San Andreas fault. Numerous coseismic cracks and fissures in this area crossed large landslides whose headwalls are along the crests of Summit and Skyland Ridges.

Other coseismic cracks, however, are not so obviously relatable to landslide activation. Some of these coseismic cracks have straight traces that cross ridgecrests, are aligned for distances of 1 km or more with other subparallel features (see pl. 1; fig. 2*B*), and appear to cut across, and root into bedrock outside of and below, the basal-slip surfaces of landslides (see pl. 1). Other cracks with straight traces that are confined to landslides may have originated as faults before their incorporation into landslides and so are probably displaced downslope from inplace faults beneath the landslide basal-slip planes.

Prentice and Ponti (1994) suggested that previous interpretations of data from a post-1906 survey (Lawson, 1908) of the now-inaccessible Wrights Railroad Tunnel located beneath Summit Ridge erroneously concluded that the tunnel was deformed over a broad zone. They showed that the data can be reinterpreted to indicate that slip occurred along a single fault trace near the northeast end of the tunnel. If correct, this reinterpretation makes it unlikely that the Summit Road-Skyland Ridge fault zone ruptured to more than 200-m depth (the depth of the tunnel below Summit Ridge) in 1906 or 1989, although deeper seated earlier faulting is possible.

A prominent bulge, or convex-northeastward bend, in the principal trace of the San Andreas fault northeast of Summit Ridge is apparent from the fault configuration revealed in exposures beneath large landslides dissected by tributaries to Los Gatos Creek (see pl. 1; fig. 2*B*). If the mapped exposures of the San Andreas fault are in place beneath these landslides, as implied by our mapping, then this bulge may be local flexure or warping of the fault plane due to lateral spreading and extension within the adjacent Summit Road-Skyland Ridge fault zone. Alternatively, if the exposures of the San Andreas

fault mapped as in place are, in fact, underlain by deeper seated landslide slip surfaces, then the mapped fault is displaced downslope, and the principal trace is buried upslope beneath the overriding landslides.

Features mapped as faults on Summit Road and Skyland Ridge, which are not within landslides (see pl. 1; fig. 2*B*), imply some unknown component of sinistral extension unrelated directly to slope failure. A more thorough study of the composition, material properties, and deep structure beneath the Loma Prieta region may provide some further basis for interpreting how deformation was propagated from depth to the surface, as well as for separating tectonic from slope-driven components of deformation. Pertinent topics include the following data.

1. *Vertical and lateral inhomogeneities in the crust*.—The main shock and most aftershocks of the 1989 Loma Prieta earthquake occurred in crystalline basement rocks beneath the gabbro of Logan, and primary slip did not propagate above about 8-km depth but, instead, stopped below the gabbro (see Jachens and Griscom, this chapter). The compositions, seismic velocities, and inferred material properties of rocks above the earthquake focus also vary nonuniformly with depth, as well as laterally across the Zayante fault and the principal trace of the San Andreas fault (Eberhart-Phillips and others, 1990; T.M. Brocher and R.D. Catchings, oral commun., 1993; see Brocher and others, this chapter; Jachens and Griscom, this chapter). Furthermore, consideration of vertical changes in crustal composition can be important in reconciling disparities between seismically and geodetically derived fault-plane-rupture models (Lisowski and others, 1990; Marshall and others, 1991; Eberhart-Phillips and Stuart, 1992). Thus, these data raise the issue of how the deep focus of the main shock (17 km) and the complex vertical and lateral variations in crustal composition between the focus and surface might have affected the orientation of the surface-deformation field.
2. *Heterogeneous slip*.—Another factor that could have significantly affected the location, orientation, amount, and sense of surface deformation is heterogeneous slip within the Loma Prieta rupture zone. Beroza (1991) showed that the earthquake ruptured primarily in a reverse sense to the northwest, beneath the Summit Road-Skyland Ridge area, and primarily right laterally to the southeast. One possible interpretation of these data would be that the hanging-wall block underwent significant clockwise rotation in the plane of rupture. If such rotation were substantial, sinistral extension conceivably could occur in the hanging-wall block at the surface—an interpretation consistent with the observed deformation on Summit Road and Skyland Ridges (fig. 4*B*).
3. *Rupture-end effect*.—The hanging-wall rocks above an oblique dextral-reverse rupture that terminates before reaching the surface must accommodate the vertical slip that occurred along the underlying rupture plane. The horizontal component of motion must also be accommodated at the northwest and southeast ends of the rupture, so that horizontal stress is focused at the rupture ends. Some component of the sinistral extension exhibited in the Summit Road-Skyland Ridge surface-deformation field, therefore, might be viewed as an accommodation effect of horizontal and vertical stresses focused at the northwest termination of the Loma Prieta rupture.

Although these data do not establish a tectonic origin for the Summit Road-Skyland Ridge surface-deformation field, they do suggest a reasonable basis for suspecting the existence of a tectonic component to this deformation that could involve the interplay of one or more of the above factors.

STRUCTURE NORTHEAST OF THE SAN ANDREAS FAULT

Northeast of the San Andreas fault, the San Francisco Bay region is also dominated by large fault-bounded blocks. The faults bounding these blocks trend west-northwest and have poorly constrained and differing displacement histories (figs. 1*B*, 2*A*). The exposed basements of these fault blocks are composite units, consisting of Franciscan rocks, Coast Range ophiolite, and Great Valley sequence. Most of the faults bounding the major structural blocks are delineated by discontinuous lenticular bodies of mafic to ultramafic igneous rocks derived from the Coast Range ophiolite that have conspicuous associated aeromagnetic anomalies. Although the tectonostratigraphy may vary in detail between the fault blocks, some elements of the pre-Quaternary stratigraphy are similar in most of the blocks between the San Andreas fault and the Silver Creek fault zone to the east. Northeast of the Silver Creek fault, however, many of the Cretaceous and younger rocks are dissimilar in age and tectonostratigraphic history to age-equivalent rocks southwest of the fault. Rocks northeast of the Silver Creek fault are, therefore, considered here to have undergone major displacement (probably dextral) relative to rocks to the southwest. The rocks present between the Silver Creek and San Andreas faults are herein referred to as the "San Francisco Bay block," which is considered to include all of the subsidiary fault blocks between the San Andreas and Silver Creek faults. We discuss here only those faults between the San Andreas fault zone and the southwest side of the Santa Clara Valley.

Folds are poorly expressed in pre-Miocene rocks of the San Francisco Bay block and mainly occur within the thin Miocene to Pleistocene cover of marine and nonmarine deposits. These units locally display high-amplitude, open to tightly appressed, upright to northeastwardly overturned folds.

We have divided the San Francisco Bay block into several subsidiary fault blocks (figs. 1, 2), modified after the original subdivisions introduced by Bailey and Everhart (1964). In the following subsections, we describe the faults that bound major subsidiary fault blocks of the San Francisco Bay block,

and discuss the constraints on their geometries, the style and timing of their displacements, and, where evident, the geometry of the folding and its relation to the faulting.

SARGENT FAULT

The Sargent fault was first described by Allen (1946) in the area northwest of San Juan Bautista (fig. 1*A*), where it dips nearly vertically. In the Loma Prieta region, the Sargent fault dips 55°–85° SW. and generally strikes N. 60°–74° W. throughout most of the Los Gatos, Laurel, and Loma Prieta 7½-minute quadrangles. Beneath Loma Prieta peak, a segment of the Sargent fault zone dips 25°–35° SW. (Loma Prieta thrust fault) and places Jurassic rocks of the Coast Range ophiolite and a thin sliver of (Jurassic?) slate and phyllite of Loma Prieta peak over Eocene rocks. This low-angle thrust segment is truncated against a trace of the younger, geomorphically youthful, more steeply dipping Sargent fault that crosses the divide between the Los Gatos Creek and Uvas Creek drainages on the southwest side of Loma Prieta peak (fig. 2*B*). Moderately shallow to subhorizontal rakes of slickensides on some shear surfaces along the steeply dipping segment of the fault zone indicate a conspicuous component of dextral strike slip; other shear surfaces indicate dip slip (Sebrier and others, 1992). Thus, the Sargent fault is predominantly a reverse fault, up on the southwest side, overprinted by later dextral slip. Locally, faults that are subsidiary, parallel, and adjacent to the Sargent fault, particularly in the vicinity of Loma Prieta peak, display conspicuous silicified, slickensided, quartz-lined surfaces with multilayered fault mullion of different orientations, suggesting episodic changes in the relative amounts of dip slip and strike slip. Also, the presence of a geomorphically youthful, steeper, south-dipping segment of the Sargent fault that cuts the thin thrust sheet of ophiolitic and metamorphic basement suggests that fault movement has been distinctly episodic and has shifted to more steeply dipping fault segments during late Cenozoic time.

The Sargent fault displaces early Miocene rocks along its course. Linear geomorphology, entrainment of young alluvium, sag ponds, and trenchlike topography indicate that the fault has been active during late Quaternary time. The youngest topographic expression of the fault occurs along the most steeply dipping segments of the fault zone, notably southeast of California Highway 152, and to the northwest along the 15-km-long segment between Sveadal and Lake Elsman (see pl. 1; fig. 2*B*).

At the northwest end of this segment of the Sargent fault, for a distance of approximately 2.4 km, surface rupturing occurred during the 1989 Loma Prieta earthquake. East-west-oriented tension cracks in this area had components of dextral extension of as much as about 10 cm, with approximately equal components of vertical displacement (figs. 6*A*, 6*B*). Other east-west-oriented tension cracks with components of vertical displacement of as much as 76 cm had smaller components of dextral extension of about 2 to 3 cm. Many of the extensional cracks with large components of vertical displacement were relatable to slumps and slope failures. Less abundant, southwest-side-up, N. 55° W.-oriented compressional cracks, including "popups" and one mole track, also occurred. The reverse-sense compressional cracks typically indicated components of vertical displacement of 5 to 6 cm. On the basis of more detailed mapping of this deformation zone, Aydin and others (1990, 1992) concluded that the overall deformation pattern indicates southwest-side-up reverse-dextral slip.

Along most of its length, the Sargent fault entrains a thin zone, ranging from less than 30 to about 300 m in thickness, of mafic to ultramafic rocks assigned to the Coast Range ophiolite. Aeromagnetic data (see Jachens and Griscom, this chapter) indicate that a thicker magnetic body than that exposed at the surface underlies the Sierra Azul block at depth. We therefore infer that the surface exposures of ophiolitic rocks have been sliced away and displaced upward from the thicker slab of buried magnetic rocks which underlies the Mesozoic to Tertiary sedimentary section of the Sierra Azul block north of the Sargent fault. On the basis of modeling of the buried magnetic slab from northeast-southwest-oriented gravity and magnetic profiles (see Jachens and Griscom, this chapter) and our geologic mapping of the ophiolitic section (cross secs. S–3, S–5, pl. 1), the top of the ophiolite slab in the footwall of the Sargent fault is estimated at 1.4-km depth. The magnetic models alone suggest a somewhat greater depth to the top of the magnetic source, closer to 2.0 km, possibly owing to the presence of less magnetic rocks in the upper part of the ophiolite. The magnetic models also suggest that the ophiolite slab is generally thicker (1.5–3.0 km) than the 0.8- to 1.7-km-thick slab depicted in our structure sections based on surface geology (see pl. 1). The downdip separation measured on the Sargent fault (cross secs. S–5, S–6, pl. 1) is at least 1.5 to 1.8 km. On the basis of a dip range of 50°–70°, the minimum horizontal shortening across the fault is estimated at 0.5 to 1.1 km.

The timing of most displacement across the Sargent fault is constrained by the youngest offset rocks, by K-Ar dating of hydrothermal alteration in the fault zone, and by fission-track data. Youthful geomorphology and faulted Miocene to Pliocene rocks along the fault between Gilroy and Mount Madonna (fig. 1*B*) indicate that the Sargent fault has remained active into the Quaternary (McLaughlin, 1974).

Potassic hydrothermal alteration that locally occurs along the Sargent fault zone is a result of fluids channeled along the fault, and so the age of the hydrothermal mineralization is a minimum for the age of faulting. Alteration in the fault zone northeast of Mount Madonna (fig. 1*B*) is K-Ar dated at about 17 Ma (McLaughlin and others, 1990, 1991b), indicating that slip was initiated by at least 17 Ma. To the northwest at Loma Prieta peak, where a thrust segment of the Sargent fault underlies the peak, potassic hydrothermal alteration in the hanging wall and footwall of the thrust is K-Ar dated at about 10 Ma (McLaughlin and others, 1990, 1991b).

Fission-track data (Arrowsmith and others, 1992; Bürgmann and others, 1994) in the vicinity of Loma Prieta peak indicate that the rocks northeast and southwest of the Sargent fault have been uplifted about 3.5 to 4.0 km since 4.0 Ma. Any major vertical displacement accommodated by the Sargent fault, therefore, must have predated 4.0 Ma (fig. 3).

The occurrence of potassic hydrothermal alteration in both the hanging wall and footwall of the Sargent fault zone at Loma Prieta peak indicates that vertical displacement across the fault since 10 Ma has been less than the vertical extent of the hydrothermal system. Fission-track data and radiometric ages indicate that the presently exposed quartz-adularia veins composing the hydrothermal zone at Loma Prieta peak were at a depth of at least 3 km at 4 Ma. Well-studied quartz-adularia vein systems elsewhere in the northern California Coast Ranges and in New Zealand have generally formed in upper-mesothermal and epithermal depth ranges of 0 to 2 km (Browne and Ellis, 1970; McLaughlin and others, 1985; Peabody and Einaudi, 1992; Rytuba, 1993). At 3- to 4-km depth, veins in the hanging wall and footwall of the thrust fault beneath Loma Prieta peak thus are probably in the lowermost part of the hydrothermal system. This hydrothermal system probably could not have been appreciably deeper when it formed at 10 Ma, and so most vertical displacement may have been accommodated by the Sargent fault between 17 and 10 Ma.

In summary, the Sargent fault has accommodated at least 1.4 km of uplift, 1.5 to 1.8 km of reverse slip, and 0.5 to 1.1 km of shortening. This deformation began as early as 17 Ma and may have largely ceased by 10 Ma (fig. 3).

In the sections above on stratigraphy, we noted that the slate and phyllite of Loma Prieta peak occurs in a thin fault sliver along the sole of the Loma Prieta thrust and that these metamorphic rocks have no known Coast Range source. The composition, metamorphic texture, and low greenschist metamorphic grade of these rocks are nearly identical to those of rocks of the Jurassic Mariposa Slate in the western Sierra Nevada foothills. It therefore was proposed (Blake and others, 1991; McLaughlin and others, 1991b) that the slate and phyllite of Loma Prieta peak is part of the western Sierra Nevada metamorphic belt of crystalline rocks, which continues from the Sierra Nevada foothills southwestward beneath the Franciscan Complex of the Coast Ranges (Wentworth and others, 1987; Fuis and Mooney, 1990). If this model is valid, then the slate and phyllite of Loma Prieta peak has undergone considerable vertical displacement because basement rocks with a velocity structure (Fuis and Mooney, 1990; Blake and others, 1991) similar to that of crystalline basement in the Sierra Nevada foothills lie at 12- to 15-km depth just northeast of the San Andreas fault. The Sargent fault, however, appears to have accommodated no more than about 1.4 km of offset of the ophiolitic basement of the Sierra Azul block. Thus, any uplift of the slate and phyllite of Loma Prieta peak from more than about 1.4-km depth and accompanying shortening must largely predate 17 Ma and probably occurred on a fault(s) other than the Sargent. The results from fission-track studies (Arrowsmith and others, 1992; Bürgmann and others, 1994) suggest that the fault block between the Sargent and San Andreas faults has been uplifted about 3 to 4 km since 5–3 Ma, yielding uplift rates of 0.6 to 1.3 mm/yr—almost 3 times that determined across the Sargent fault and, therefore, possibly related to deeper seated structures.

Kinematic data suggest that subequal or larger amounts of strike slip have occurred along the Sargent fault during the latest stages of its offset history, although, as determined from the surface geology, the amount of dextral strike slip on the fault is relatively unconstrained and, therefore, unresolvable at this time.

HOOKER GULCH-SIERRA AZUL FAULT ZONE

The Hooker Gulch fault is a reverse fault, about 4.8 km long, that is truncated by the San Andreas fault on the west. The Hooker Gulch fault dips vertically to about 60° SW. and is offset by a younger, north-south-trending normal fault south of Mount Umunhum (fig. 1*A*). To the east of the offsetting normal fault, the continuation of the Hooker Gulch fault is known as the Sierra Azul fault. Reverse separation across the Hooker Gulch-Sierra Azul fault, measured from structure sections (cross sec. S–5, pl. 1), may be about 1.8 km, on the basis of separation of the top of the Coast Range ophiolite across the fault. Shortening of the Sierra Azul section across the fault is about 1 km, and the associated uplift or vertical displacement of the section is about 1.5 km. Thus, the amounts of reverse slip, uplift, and shortening across the Hooker Gulch and Sargent faults are similar. The Hooker Gulch fault appears to be a part of the same reverse-slip-fault system as the Sargent fault, as indicated by its subparallel orientation and nearly identical sense and amount of displacement. The relative component of dextral strike slip, if any, is unknown because no kinematic indicators were measured.

The dextral normal fault that offsets the Hooker Gulch-Sierra Azul fault zone appears to have a dip-slip component of about 2 km. The fault extends into the basal part of the Coast Range ophiolite and locally, at its north end, extends into, and dies out in, underlying metaclastic rocks of the Franciscan Complex, as indicated in exposures on Mount Umunhum (cross sec. S–5, pl. 1). Here, the crossfault dips about 60° SW., with slickensides that rake 20° NW. and suggest that, at least locally, about 80 percent of the slip is dextral. Elsewhere, along the trend of the fault, slip vectors indicate components of strike slip in the range 50–90 percent.

The timing of displacement on the Hooker Gulch-Sierra Azul fault is post-early Eocene, on the basis of offset of the Eocene sequence. The similarity of the fault zone in its orientation and displacement to the Sargent fault suggests that it may be of the same Miocene or younger generation. The timing of movement along the oblique-normal crossfault south of Mount Umunhum

also is Miocene or younger, possibly considerably later than that along the Hooker Gulch-Sierra Azul fault zone.

ALDERCROFT FAULT

The Aldercroft fault is the principal local boundary between rocks of the Sierra Azul block on the south and the Franciscan Complex to the north, and as such, it occupies the same structural position as the Coast Range fault of Jayko and others (1987), which extends throughout the Coast Ranges. As pointed out by Jayko and others, the Coast Range fault is a highly modified subduction boundary with an early record of Jurassic and Cretaceous compressional tectonism associated with oblique subduction of the Franciscan Complex. During the latest Cretaceous to early Eocene, low-angle normal faulting associated with uplift and attenuation of the Coast Range ophiolite and with unroofing of the Franciscan Complex was focused along this boundary. In the study area (fig. 1), the Aldercroft fault exhibits compressional and extensional structures that correspond to those described along the Coast Range fault (Jayko and others, 1987). In the Sierra Azul block, the extensional structures may be as young as Oligocene because subparallel extensional faults at a low angle to bedding cut Eocene, but not Miocene, rocks higher in the section. Thus, the Aldercroft fault is here presumed to have been coextensive with the Coast Range fault until the time of extensional deformation from the Late Cretaceous (possibly Campanian) to the Oligocene.

On the geologic map and structure sections (cross secs. S–3, S–5, pl. 1), the lowest fault in the Aldercroft fault zone is depicted as a southwest-dipping thrust fault, because it places older (Jurassic) ophiolitic rocks over younger (Cretaceous) Franciscan rocks along its length. However, structurally higher faults in the zone, which locally form the upper contact of the ultramafic section of the Coast Range ophiolite, either consistently place younger rocks down on the ophiolite or cut out intervening ophiolite section. These faults are extensional rather than compressional structures and were superposed on and, in places, may root into or below the basal thrust of the Aldercroft fault zone (cross secs. S–3, S–5, pl. 1).

Although the Aldercroft fault is similar in orientation to the Hooker Gulch-Sierra Azul fault zone and merges with these faults along strike, no convincing field evidence exists for early Miocene or younger reactivation of the Aldercroft fault as a thrust. The latest observed displacement along the segment of the Aldercroft fault between its intersection with the San Andreas fault and Mount Umunhum is normal, up on the north side. Locally, the fault is overturned and dips 45° NE. Near Mount Umunhum (fig. 1*A*), where the fault dips 75° SW., some of this normal displacement may be accommodated by the Soda Springs fault, although the Soda Springs fault appears to have only minor displacement.

The amount of normal slip on the Aldercroft fault is undetermined in the study area (fig. 1), partly because slip mostly predated displacements along other faults (including the Sierra Azul, Soda Springs, and Berrocal faults) that cut or merge with the Aldercroft fault and break the Sierra Azul block into several subsidiary blocks. Late (Miocene and younger) offsetting compressional faults that followed earlier extensional deformation along the Aldercroft fault (cross sec. S–3, pl. 1) suggest that the Aldercroft fault is presently inactive.

Structure sections drawn across the Aldercroft fault and the Coast Range ophiolite northeast of Mount Thayer (fig. 2), based on an interpretation of the surface geology (cross sec. S–3, pl. 1), depict the Aldercroft fault as dipping about 55° SW., intersecting the San Andreas fault at about 6-km depth. This configuration generally agrees with the magnetic models of Jachens and Griscom (this chapter), although interpretation of aeromagnetic data suggests a more complex "wedging" relation between the Coast Range ophiolite and underlying Franciscan Complex at depth.

Gravity and magnetic models (see Jachens and Griscom, this chapter) suggest that the Coast Range ophiolite is segmented at depth by wedges of nonmagnetic rocks interpreted to be part of the Franciscan Complex. Jachens and Griscom's interpretation of the aeromagnetic data implies that the surface trace of the Aldercroft fault may be the steeply tilted roof thrust to one such wedge of Franciscan rocks. Their model further suggests that the wedge composed of Franciscan Complex originally was emplaced eastward into a thick subhorizontal slab of ophiolite. This wedge then peeled up and incorporated thinner slabs of the ophiolite into the roof of the wedge complex. The present southwestward dip of the Aldercroft fault zone would have resulted from later southwestward tilting superimposed on the wedge complex.

This structural style is consistent with the interpretation (McLaughlin and others, 1988a) that the Coast Range ophiolite and Great Valley sequence are interleaved with rocks of the Central belt of the Franciscan Complex along folded imbricate low-angle faults. A model for eastward "wedge" emplacement (see Jachens and Griscom, this chapter) is also consistent with the field observation that the present Aldercroft fault indicates down-to-the-southwest displacement. The gravity and magnetic models do not agree, however, with our interpretation that this down-to-the-southwest displacement is due to extension, as suggested by structures (boudinage and attenuation) in the ophiolite. If the displacement resulted from thrusting associated with emplacement of a wedge, we would expect to see evidence of compression, such as eastward-vergent folds or duplexing, which are unrecognized.

FAULTS OF THE SOUTHWESTERN SANTA CLARA VALLEY THRUST BELT

The thrust belt along the southwest side of the Santa Clara Valley includes several anastomosing and branching fault zones, including the Lime Kiln, Berrocal, Shannon, and Monte

Vista faults. Focused compressional deformation occurred across the Monte Vista and Berrocal-Shannon fault zones during the earthquake (Haugerud and Ellen, 1990; D.H. Sorg and F.J. Groffie, unpub. data, 1990), strongly suggesting that these thrust zones root into the San Andreas fault and (or) that reverse slip on these thrusts is driven by horizontal shortening across the San Andreas fault zone. The faults of this thrust belt dip predominantly southwest at moderately low to steep angles (35°–60°), as judged from the curvilinear upcanyon V-patterns of their surface traces, the measured attitudes of shear surfaces in the fault zones, and the subsurface exposures of faults in mines of the New Almaden mercury district (Bailey and Everhart, 1964). These faults vary in dip along strike, however, and locally are overturned to the northeast. Faults of the Berrocal and Shannon fault zones include those dipping 40°–55° NE. that can mostly be interpreted as subsidiary normal faults in the hanging-wall blocks of the major southwest-dipping reverse faults (cross secs. S–1, S–2, S–5, pl. 1). Map relations along the Berrocal, Shannon, and Lime Kiln fault zones suggest that these faults include segments of older, folded, sheetlike fault slivers, whose boundaries are commonly delineated by thin serpentinite bodies (cross sec. S–2, pl. 1). Some of the thin, deformed serpentinite bodies in these fault zones are derived from the lower part of the Coast Range ophiolite.

The various faults of the southwestern Santa Clara Valley thrust belt traverse some of the more densely populated areas of the San Francisco peninsula and locally display relatively clear evidence of Quaternary displacement. The relation of the thrust belt to the San Andreas fault, however, has remained unclear. In particular, crustal shortening and related deformation that occurred across the Berrocal, Shannon, and Monte Vista fault zones during the 1989 Loma Prieta earthquake have raised the questions of (1) earthquake potential, (2) the extent to which faulting along the thrust belt coincides with large earthquakes on the San Andreas fault (Haugerud and Ellen, 1990; D.H. Sorg and F.J. Groffie, unpub. data, 1990), and (3) whether faulting and seismicity may occur independently of events on the San Andreas fault.

The Berrocal, Shannon, and Monte Vista faults have offset Pliocene and Pleistocene strata of the Santa Clara Formation at numerous localities, including exposures observed in several trenches (fig. 6). The distribution, lithofacies variations, and deformation of the Santa Clara Formation and some younger nonmarine Quaternary deposits indicate that the deposition of these largely fluvial units was penecontemporaneous with uplift, shortening, and faulting across the thrust belt. The youngest deposits observed to be cut by faults of the thrust system are present along a northeast-dipping normal-fault segment of the Shannon fault zone, exposed in a trench at the Senator Mine, west of New Almaden, in 1989 (figs. 2*A*, 6). At this locality, a 15- to 18-ka paleosol (Emcon Associates, 1990) that formed on the eroded Temblor Sandstone is cut by a north-dipping shear whose sense and amount of displacement are uncertain (fig. 6). This fault is subsidiary to a conspicuous northeast-dipping normal fault within the hanging-wall block of the main southwest-dipping segment of the Shannon fault. Radiocarbon ages from an overlying lower Holocene colluvial unit that is uncut by shearing suggest that the faulting probably was pre-Holocene.

At another locality, along the Berrocal fault zone, near the intersection of Wood Road and Santa Cruz Avenue in the town of Los Gatos (figs. 2*A*, 6), undated Pleistocene terrace sand and gravel, estimated at 120–250 ka (see sections above on stratigraphy), are cut by a 58°– 60° SW.-dipping segment of the Berrocal fault, which thrusts volcanic rocks of the Franciscan Complex upward and northeastward over the terrace gravel. The hanging-wall Franciscan rocks have a postterrace reverse-slip component of ≥0.7 m. The fault scarp is draped with Holocene colluvium, which is unfaulted.

The Lime Kiln fault in this thrust belt is not as well studied as the Berrocal and Shannon faults. However, the Lime Kiln fault locally exhibits moderately strong physiographic linearity in the vicinity of Lime Kiln Canyon southeast of the Lexington Reservoir (fig. 2*A*). In this area, poorly exposed elevated terrace gravel may be offset along the fault (see pl. 1), but more detailed study of these exposures is needed to determine whether offset has occurred.

Thus, the southwestern Santa Clara Valley thrust belt locally exhibits evidence for surface faulting during the latest Pleistocene (20–12 ka). The fault that exhibits this evidence is a secondary north-dipping normal fault. A widespread pulse of faulting appears to have occurred since the late Pleistocene (250–120 ka) along the length of the thrust belt. Several of the faults now exposed at the surface within the thrust belt appear not to have ruptured to the surface during all or part of the Holocene, as suggested by colluvial draping of Pleistocene fault scarps. We note, however, that many of the thrust faults of this northeastward-vergent fault system deform Miocene to Pleistocene hanging-wall rocks into open to tightly appressed folds with axes that parallel the curvilinear trend of the thrust belt. Many of the faults now exposed at the surface may have propagated upward from depth as blind thrusts within the range-front thrust belt. In a fold-and-thrust belt, blind thrusts generally propagate upward, deforming the overlying sedimentary package into folds that take up vertical and compressional components of slip above the depth of rupture propagation. Typically, such faults steepen as they propagate to the surface and (or) rotate to steeper positions after reaching the surface, as newly active blind thrusts begin propagating upward and outboard from the root zone of the thrust system at depth. The open, high-amplitude folds in the Santa Clara Formation and underlying Miocene strata in the low uplands between the Monte Vista and Berrocal fault zones (Cupertino-Saratoga area, fig. 2*A*) probably owe their origin to slip on blind thrusts of the Monte Vista and Berrocal fault zones during the late Pleistocene (Sorg and McLaughlin, 1975). The Monte Vista fault zone is probably a former blind thrust that has breached the axis of its hanging-wall anticline, broken the surface, and rotated into a steeper, southwest-dipping orientation. If this interpretation

is correct, then active blind thrusts that root into the San Andreas or Monte Vista fault at depth might exist beneath the Santa Clara Valley northeast of the main exposures of the Monte Vista fault.

Sebrier and others (1992) reported that the southwestern Santa Clara Valley thrust belt has undergone a multiphase kinematic history. The chronology of outcrop-scale fault features and fault-slip indicators in the Monte Vista, Berrocal, and Shannon fault zones indicates that the earliest slip along these faults was reverse and up to the southwest. This primary reverse slip is overprinted by a later generation of predominantly strike slip features, which include both dextral and sinistral components. Excluding the 1989 coseismic compressional deformation (Haugerud and Ellen, 1990), a late pre-Loma Prieta generation of features indicative of normal (transtensional) displacement is also recorded at localities in the Monte Vista and Shannon-Berrocal fault zones (Sebrier and others, 1992). The chronology of change in slip modes on these faults, from dominantly thrusting to strike slip, is interpreted to have occurred as faults within the thrust belt propagated toward the surface and rotated into more steeply dipping orientations. The late, extensional indicators are questionably related by Sebrier and others to secondary extension associated with hanging-wall folds or to transfer of slip from older, structurally high thrust faults to structurally lower, more recently activated blind thrusts beneath the Santa Clara Valley.

AGE OF THRUST-BELT INITIATION AND AMOUNT OF DISPLACEMENT

Earliest slip on the Berrocal and Sargent faults is constrained by structural relations and by the ages of hydrothermal K-feldspar veinlets along the Sargent fault zone, as previously discussed. The 17.8-Ma K-Ar age on adularia from the fault zone near Mount Madonna (fig. 1*B*) was determined on rocks from within a thin fault sliver bounded to the northeast by the southwest-dipping Berrocal fault and to the southwest by the structurally higher Sargent fault. Hydrothermal alteration occurs sporadically northward along both the Sargent and Berrocal faults, as indicated by local concentrations of silica-carbonate rock, an alteration product of serpentinite, and by hydrothermally bleached and veined clastic rocks. We interpret this alteration to indicate that the Sargent and Berrocal faults were both conduits for hydrothermal circulation at 18–17 Ma. Juxtaposition of rocks in the Sierra Azul block with the Temblor Sandstone and the Monterey Shale along the Berrocal fault also indicates that major reverse-slip displacement postdated the middle Miocene.

Local unroofing and uplift of the Coast Ranges before late early Miocene time is reflected in an unconformity at the base of the Temblor Sandstone in the New Almaden area (fig. 2*A*). Low-angle attenuation faults that cut Eocene and older rocks in this area are unrecognized in the Miocene section, suggesting that a change from extensional faulting to northeastward-vergent thrusting occurred during the Oligocene to early Miocene. Although the data are equivocal, we find no convincing evidence in the depositional or structural record to indicate that displacements or hydrothermal circulation occurred along the Sargent or Berrocal faults any earlier than 17.8 Ma. We therefore speculate that deep-seated thrusting was initiated on the Sargent and Berrocal faults at 18–17 Ma. This early contractional deformation apparently was overprinted by younger thrusting by 3.0 Ma along the Monte Vista, Berrocal, and Shannon faults that cut strata of the Santa Clara Formation.

A major episode of Miocene to Pliocene shortening, accompanied or followed by strike-slip faulting along the thrust belt, is suggested by major structural and depositional discordance between the Santa Clara Formation and underlying Miocene rocks, as well as by the depositional-facies contrasts between coeval Miocene deposits northeast and southwest of the Berrocal-Sargent fault zone, as noted above in the sections on stratigraphy. The contrast in depositional settings across the thrust belt indicates that the Miocene deep-water margin was displaced relatively landward (northeastward) over the adjacent Miocene continental slope and shelf. By analogy with the average width of the modern Continental Shelf and upper slope of California and Oregon, as much as 50 km of the Miocene shelf and slope width appear to have been tectonically removed. Since the Berrocal and Sargent faults both lie within 6 to 10 km of the San Andreas fault, we conclude that a considerable amount of the missing Miocene shelf to slope must have been removed by strike-slip motion along and (or) within the thrust belt. If the missing margin were completely the result of horizontal shortening, considerably greater topographic relief should be present northeast of the San Andreas fault. Nevertheless, a major unconformity between the Miocene section and the overlying Santa Clara Formation suggests that major erosion, probably associated with uplift and horizontal shortening, occurred after deposition of the Monterey Shale before and concurrent with the onset of Santa Clara deposition (5–2 Ma).

The aggregate components of reverse and strike slip across the southwestern Santa Clara Valley thrust belt are relatively large, although the amount of strike slip remains obscure. A gravity study across the Monte Vista segment of the thrust belt in the Cupertino and Los Altos Hills areas suggests that Franciscan rocks are thrust eastward at least 2.3 km over low-density Miocene and Pliocene to Pleistocene strata along a 9.7-km-long segment of the fault zone (Fleck, 1967; McLaughlin, 1974), indicating at least 2 to 3 km of horizontal shortening in those areas since the Miocene (10 Ma). Assuming this amount of horizontal shortening, as well as an average dip of 45° across the Monte Vista segment of the thrust belt (Sorg and McLaughlin, 1975), about 3 km of uplift and 4 km of reverse slip have been accommodated along the Monte Vista fault zone. Uplift and horizontal shortening rates have thus been about 0.3 mm/yr, if displacement is distributed over

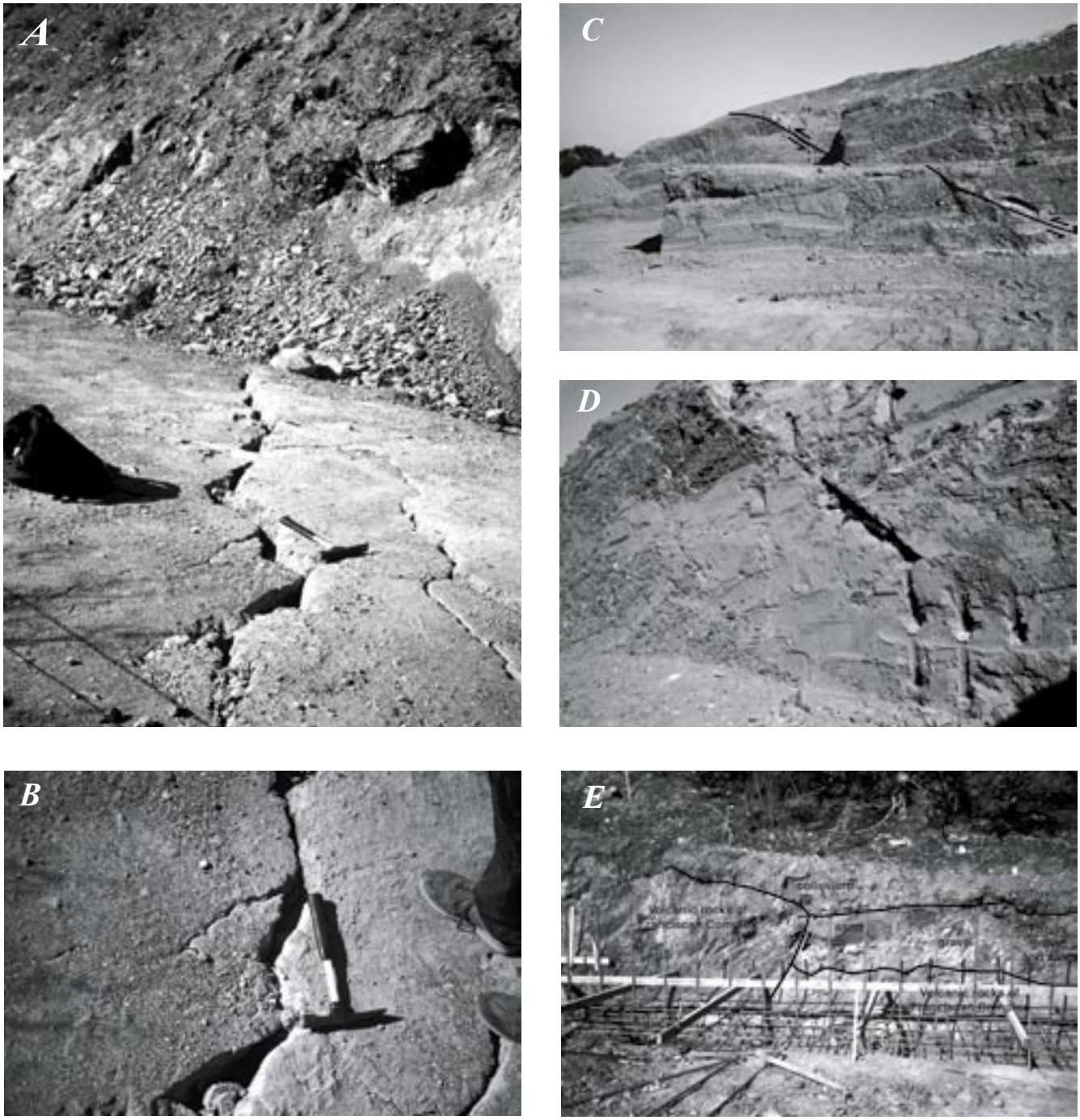

Figure 6.—Pleistocene and younger faulting along reverse faults northeast of the San Andreas fault in the Loma Prieta region, Calif. (fig. 1). *A*, Coseismic surface rupture during the 1989 Loma Prieta earthquake along the Sargent fault on north side of the Elsman Reservoir. Right-stepping cracks within fault zone indicate dextral extension with a 10-cm right-slip component of up-to-the-north slip. View westward. *B*, Closeup of coseismic surface rupture in figure 6*A*, showing right-stepping dextral cracking along the Sargent fault at the Elsman Reservoir. Extension direction is N. 75° E.–S. 75° W. C, Thrust faulting within the Santa Clara Formation at construction site along Permanente Road in Cupertino (fig. 2*A*). Main trace of the Monte Vista fault is to southwest (right). Photograph taken in 1973. *D*, Closeup of thrust fault in figure 6*C*. View southeastward. E, Faulted Pleistocene fluvial gravel and sand along the Berrocal fault at construction site on Wood Road near downtown Los Gatos (fig. 2*A*). Fault is up on southwest (left) side. Photograph taken in October 1989. *F*, Closeup of faulted fluvial deposits in figure 6*E*. Colluvium overlies faulted contact between Franciscan volcanic rocks and Pleistocene deposits. *G*, South strand of the Shannon fault trenched by Emcon Associates at the Guadalupe Landfill on the site of the Senator Mine, 1.3 km west of Guadalupe Creek. Hammer straddles north (left)-dipping fault in the Temblor Sandstone, which extends upward into dark paleosol, estimated at 15–18 ka. View southeastward.

the past 10 m.y. (that is, if uplift began soon after deposition of the Miocene strata). If most of the uplift and horizontal shortening have occurred since the onset of deposition of the Santa Clara Formation, about 5–2 Ma, then late Quaternary uplift and horizontal shortening rates could have approached or exceeded 1.0 mm/yr, an interpretation supported by youthful topographic relief, by tight high-amplitude folds in the Santa Clara Formation, and by locally conspicuous angular depositional discordance of the Santa Clara Formation with Miocene and older rocks.

Studies along the Monte Vista fault zone in Cupertino (fig. 2*A*; Sorg and McLaughlin, 1975; E.J. Helley, oral commun., 1991) show that a 120-ka fluvial terrace is vertically displaced about 43 m across the Monte Vista fault at the mouth of Stevens Creek Canyon, yielding a post-120-ka uplift rate of about 0.4 mm/yr. This uplift rate is close to that indicated by gravity-derived horizontal shortening in the past 10 m.y. (Fleck, 1967) and supports an interpretation that the uplift rate has been relatively constant since the late middle Miocene. Alternatively, the data could be interpreted as indicating a high uplift and horizontal-shortening rate of about 1.0 mm/yr between 3 and 0.12 Ma, which subsequently decreased to 0.3 mm/yr.

In summary, structural relations and gravity data suggest that as much as 3 km of uplift and horizontal shortening and 4 km of reverse slip have been accommodated across the southwestern Santa Clara Valley thrust belt since 10 Ma. Uplift and horizontal-shortening rates have been about 0.4 mm/yr since 120 ka, about the same as those calculated by assuming a constant slip rate since 10 Ma (0.3 mm/yr). The stratigraphic and structural discordance between the Santa Clara Formation and Miocene and older formations, however, strongly suggests that uplift and horizontal-shortening rates increased markedly with the initiation of deposition of the Santa Clara Formation between 4.8 and 1.9 Ma. If most of the observed uplift and horizontal shortening were accommodated during this later episode of deformation (4.8–0.12 Ma), then

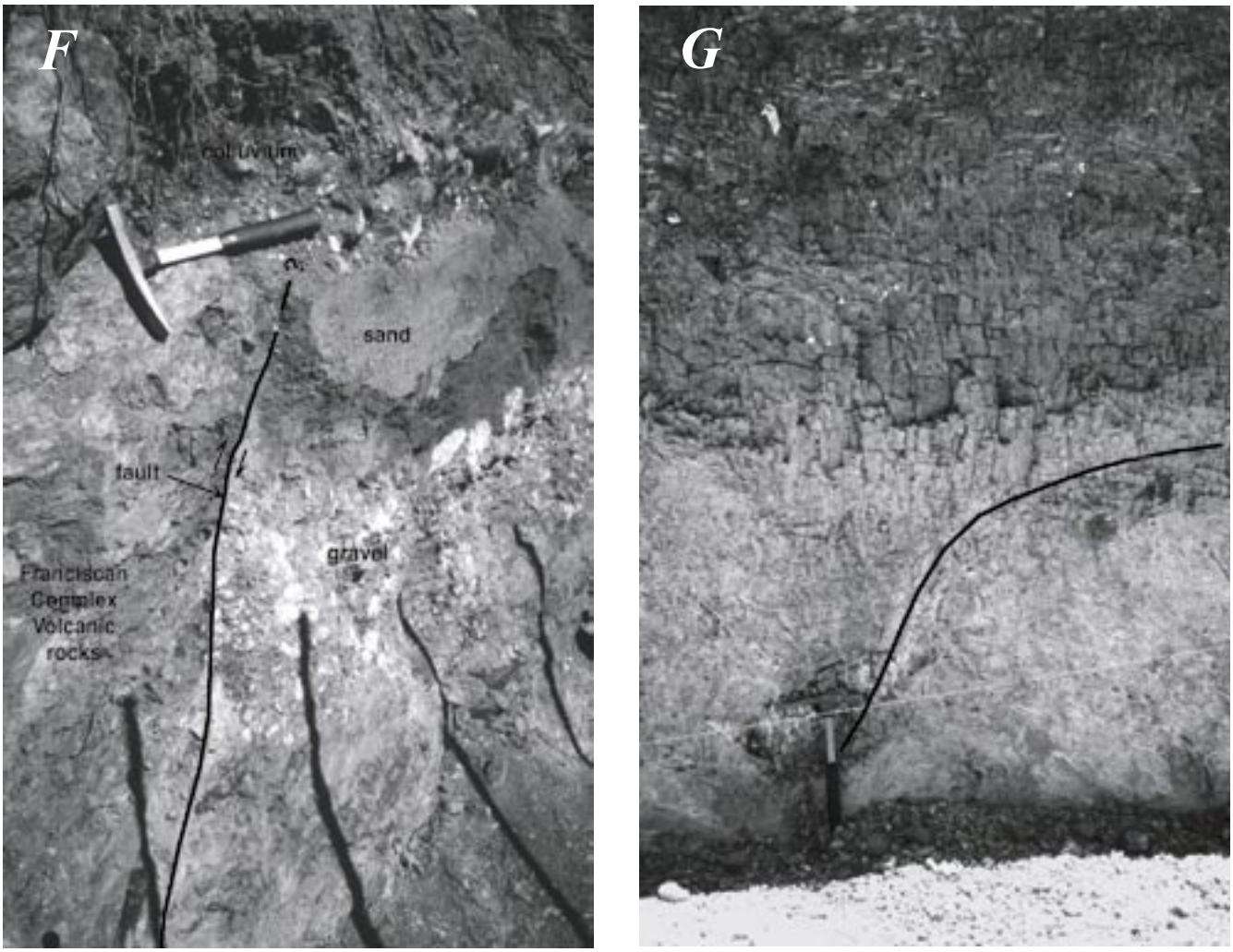

Figure 6.—Continued

Table 3.—*Estimated parameters for faults located between the San Andreas fault and the southwestern Santa Clara Valley thrust belt*

[Values for the Lexington fault were not added to total fault displacement. The Lexington fault is nearly orthogonal to the main thrust front, and so its displacement may merely be partitioned off from the other fault zones]

Fault zone	Shortening (km)	Uplift (km)	Reverse slip (km)	Duration of faulting (Ma)
Sargent fault	1.1	1.4	1.8	18–10
Hooker Gulch fault	.9	1.6	1.8	18–10
Southwestern Santa Clara Valley thrust belt.	3.0	3.0	4.2	10–0 or 4.8–0
Total	5.0	6.0	7.8	18–0
Lexington fault	1.1–1.4	2.9–3.8	3.1–4.0	4.8–0

rates were about 0.6 to 1.7 mm/yr and decreased to about 0.3 mm/yr after 120 ka.

The amounts of horizontal shortening, uplift, and reverse slip across the major thrust zones between the southwestern margin of the Santa Clara Valley and the San Andreas fault are listed in table 3 in an attempt to estimate the total Miocene and later contractional deformation. These data suggest that approximately 5 km of horizontal shortening, 6 km of uplift, and 8 km of reverse slip have been accommodated between the southwestern Santa Clara Valley thrust belt and the San Andreas fault (fig. 7). The observed amounts of horizontal shortening and uplift clearly do not approach what would be necessary to cause the observed loss of the Miocene marine margin, and so we conclude that a 45-km-wide segment of this margin has been eliminated through a large, but as yet ill-defined, component of strike slip. The total uplift and horizontal-shortening rates of 0.4 to 0.5 mm/yr since 18 Ma are consistent with regional uplift rates of less than 1 mm/yr for Quaternary marine terraces southwest of the San Andreas fault (Lajoie and others, 1979), with rates calculated for the southwestern Santa Clara Valley thrust belt since 10 Ma, and with the rate calculated from uplift of the 120-ka fluvial terrace across the Monte Vista fault. These rates are low, however, in comparison with uplift rates near the San Andreas and Sargent faults based on fission-track studies, which are about 0.8 to 1.0 mm/yr since 5–3 Ma (Arrowsmith and others, 1992; Bürgmann and others, 1994), and in comparison with uplift and horizontal-shortening rates of 0.6 to 1.7 mm/yr for the thrust belt based on the assumption that most deformation occurred between 4.8 and 0.12 Ma. Structural relations and K-Ar dating of hydrothermal alteration suggest that most vertical and contractional displacement across the Sargent fault may have occurred before 10 Ma. Similar fission-track-derived uplift rates northeast and southwest of the Sargent fault must, therefore, reflect displacement above deeper faults beneath the Sargent fault. Correspondence of the 4.8–0.12-Ma uplift rate for the southwestern Santa Clara Valley thrust belt with the fission-track rate for approximately the same time frame suggests that rapid uplift adjacent to the San Andreas fault could have been accommodated by the southwestern Santa Clara Valley thrust belt. In figure 7, we suggest a model for the partitioning of contractional deformation normal to the San Andreas fault among faults of the Sierra Azul block and those of the southwestern Santa Clara Valley thrust belt.

LEXINGTON FAULT ZONE

The Lexington fault zone (see pl. 1; figs. 1, 2) strikes north-south and is approximately 4 km long by 0.4 km wide. This fault zone is of particular interest because it appears to link the dextral-slip San Andreas fault zone with the southwestern Santa Clara Valley thrust belt (McLaughlin and others, 1991a, 1992). Faults of the Lexington fault zone dip both east and west, but the principal slip has been along a reverse fault at the east side of the zone dipping about 70° E. Thus, the fault zone is regarded as predominantly contractional (McLaughlin and others, 1991a, 1992; Sebrier and others, 1992). Los Gatos Creek is incised along the Lexington fault zone, and the main fault is mappable as a conspicuous north-south lineament on aerial photographs.

The Lexington fault zone cuts the Santa Clara Formation. Near the Lexington Reservoir (fig. 2), the Santa Clara Formation consists of a basal lacustrine lithofacies, which dips southwest toward the San Andreas fault. The lacustrine lithofacies interfingers eastward with coarse-grained fanglomerates that are tilted steeply, truncated, and juxtaposed with Franciscan rocks

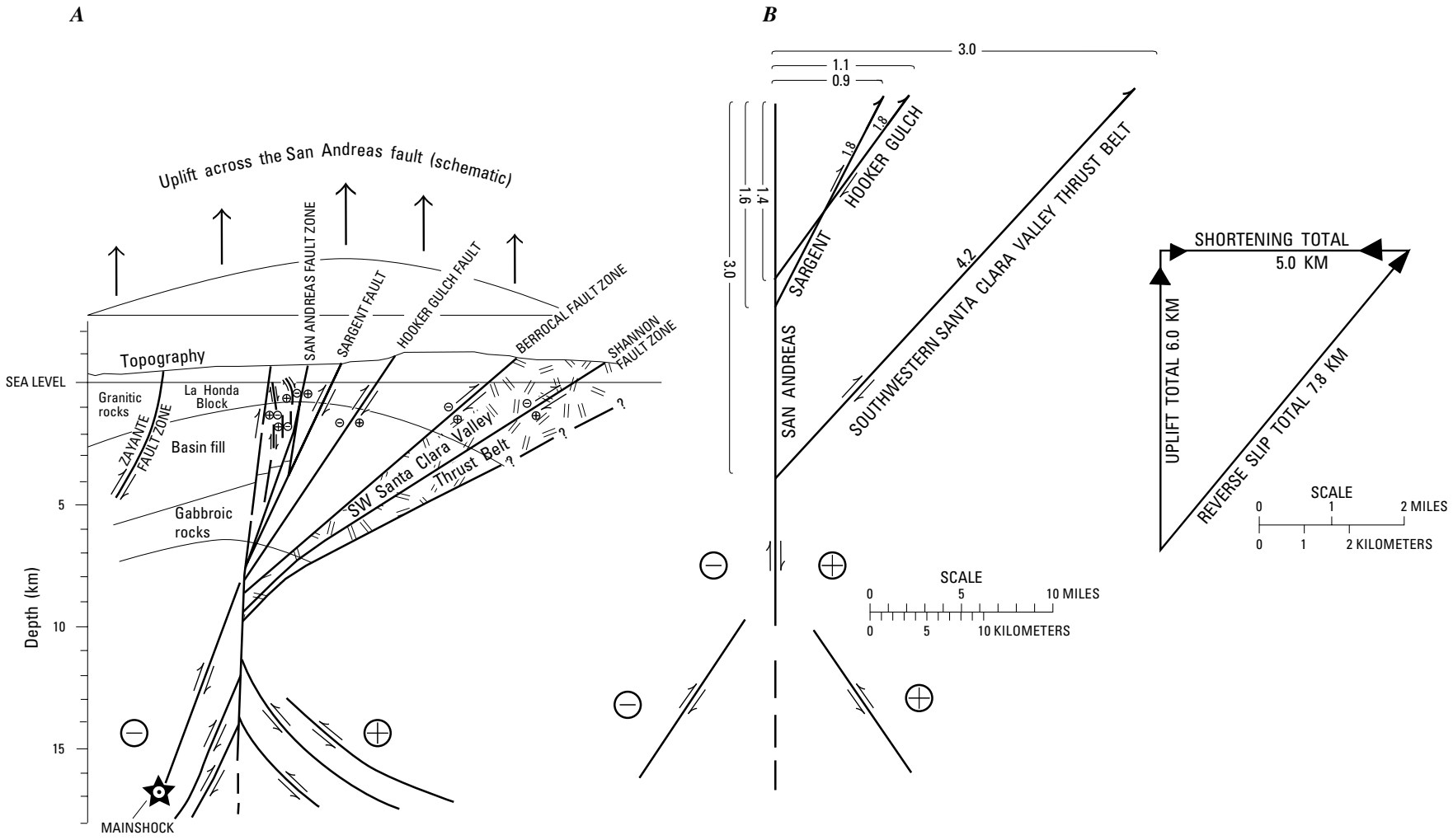

Figure 7.—San Andreas fault system in the Loma Prieta region, Calif. (fig. 1). Plus, movement into plane; minus, movement out of plane. *A*, Hypothetical depth configuration of the San Andreas fault zone, showing deep southwest- and northeast-dipping components inferred from seismic evidence (Olson and Hill, 1993). *B*, Schematic cross section showing partitioning of shortening, reverse slip, and uplift to thrust faults between the San Andreas fault and the southwestern Santa Clara Valley thrust belt since 18 Ma.

along the main trace of the Lexington fault on the east side of the reservoir. These relations suggest that the Lexington fault was active, and that vertical displacement occurred, during the deposition of fanglomerates of the Santa Clara Formation. The fanglomerates apparently were shed westward from the growing Lexington fault scarp into a large deep lake along the San Andreas fault. The depression in which the lacustrine sediment was deposited may have been formed by a landslide dam or, alternatively, a structural barrier that blocked northward drainage along the San Andreas fault.

Flat-lying fluvial-terrace gravel unconformably overlies folded and tilted strata of the Santa Clara Formation along the Lexington fault zone. These younger Pleistocene gravel deposits are incised by Los Gatos Creek and are now at an elevation of about 200 m. The high elevation of this terrace relative to other fluvial terraces in the Santa Clara Valley that postdate the 0.3–4.8-Ma Santa Clara Formation, the degree of soil development, and the degree of weathering of terrace clasts suggest that the terrace was cut during the 250-ka eustatic highstand (see sections above on stratigraphy). This age may also mark the time of capture of northwestward drainage along the San Andreas fault by the headward incision of northeastwardly draining Los Gatos Creek. As along the southwestern Santa Clara Valley thrust belt, uplift and faulting of the Santa Clara Formation occurred between about 4.8 and 0.25 Ma (McLaughlin and others, 1992). Subsequently, the 250-ka terrace gravel was incised approximately 152 m along the fault zone by Los Gatos Creek, yielding an incision rate and an approximate uplift rate of about 0.6 mm/yr. If continuous for 4.8 m.y., this rate would result in about 2.9 km of uplift accommodated across the Lexington fault zone. This much uplift, however, is likely a minimum because deformation of the Santa Clara Formation appears to have been focused between 4.8 and 0.25 Ma. If the high uplift rates calculated from fission-track data near the San Andreas fault also apply here, then the amount of uplift could be as much as 3.8 km. Similarly, shortening accommodated across the Lexington fault zone since 4.8 Ma may be 1.1 to 1.4 km, and reverse slip has been 3.1 to 4.0 km, on the basis of minimum and maximum uplift rates, respectively. Kinematic data from the Lexington fault zone (Sebrier and others, 1992) confirm that the principal early slip occurred no earlier than 4.8 Ma within the fault zone and that it was reverse slip. On the basis of kinematic indicators on fault surfaces, a distinctly later episode of dextral slip has been superposed on the reverse slip (Sebrier and others, 1992).

MODELING THE STRUCTURAL EVOLUTION OF THE LOMA PRIETA REGION

STRUCTURAL AND STRATIGRAPHIC CONSTRAINTS

The areas to the northeast and southwest of the principal trace of the San Andreas fault in the Loma Prieta region were as much as 150 km apart when movement on the San Andreas fault was initiated during the early Miocene (20 Ma). Stratigraphic units of the two fault blocks, especially those that were deposited before 20 Ma, therefore, have different stratigraphic and structural histories.

The structural and stratigraphic data suggest that pre-Tertiary plutonic and metamorphic basement rocks southwest of the San Andreas fault underwent 13 to 15 km of unroofing between 95 and 61 Ma (fig. 3). Additional uplift (≤4 km) and erosion southwest of the San Andreas fault occurred during the Oligocene to early Miocene in association with major dip slip on the Zayante fault and with volcanism. Transpressional deformation (see pl. 2; fig. 3) could have been active southwest of the San Andreas fault as early as the Oligocene, although widespread volcanic rocks of this age suggest that extensional tectonism was dominant during the Oligocene to early Miocene (Stanley, 1987).

Northeast of the San Andreas fault, Franciscan rocks underwent unroofing during the Paleocene (65–56 Ma). This deformation may have been accompanied by extension that continued into the Oligocene, as indicated by widespread low-angle attenuation faults in rocks of Eocene age. Transpressional tectonism has been active northeast of the San Andreas fault zone only since the early Miocene; most transpression occurred during the Pliocene to middle Pleistocene (4.8–0.3 Ma). Since the Miocene, a cumulative uplift of about 6 km and horizontal shortening by about 5 km have occurred between the San Andreas fault and the southwestern Santa Clara Valley thrust belt. Oligocene and younger transpressional deformation across the San Andreas fault zone apparently occurred largely in conjunction with the 460 km of Miocene and younger aggregate right slip across faults of the modern San Andreas fault system (fig. 5; table 2).

Late Cretaceous and early Cenozoic unroofing and attenuation of rocks along the length of the Coast Ranges were taken up by low-angle detachment faults and accompanying folds that predated the San Andreas fault system. These attenuation faults probably were driven at greater depths by thrust faults along the Late Cretaceous to early Cenozoic convergent margin between the North American and Farallon plates. These low-dipping early Cenozoic structures strongly influenced the orientation of later compressional structures, and some of the early faults probably have been reactivated during the Neogene and Quaternary as compressional low-angle faults with accompanying folds.

DEEP-CRUSTAL CONSTRAINTS

Deep seismic reflection and refraction data from recent surveys in central and northern California (Wentworth and others, 1984, 1987), first-motion studies of earthquakes (Oppenheimer and others, 1988), and borehole-breakout data (Mount and Suppe, 1987) indicate that the northern and central Coast Ranges are presently being deformed

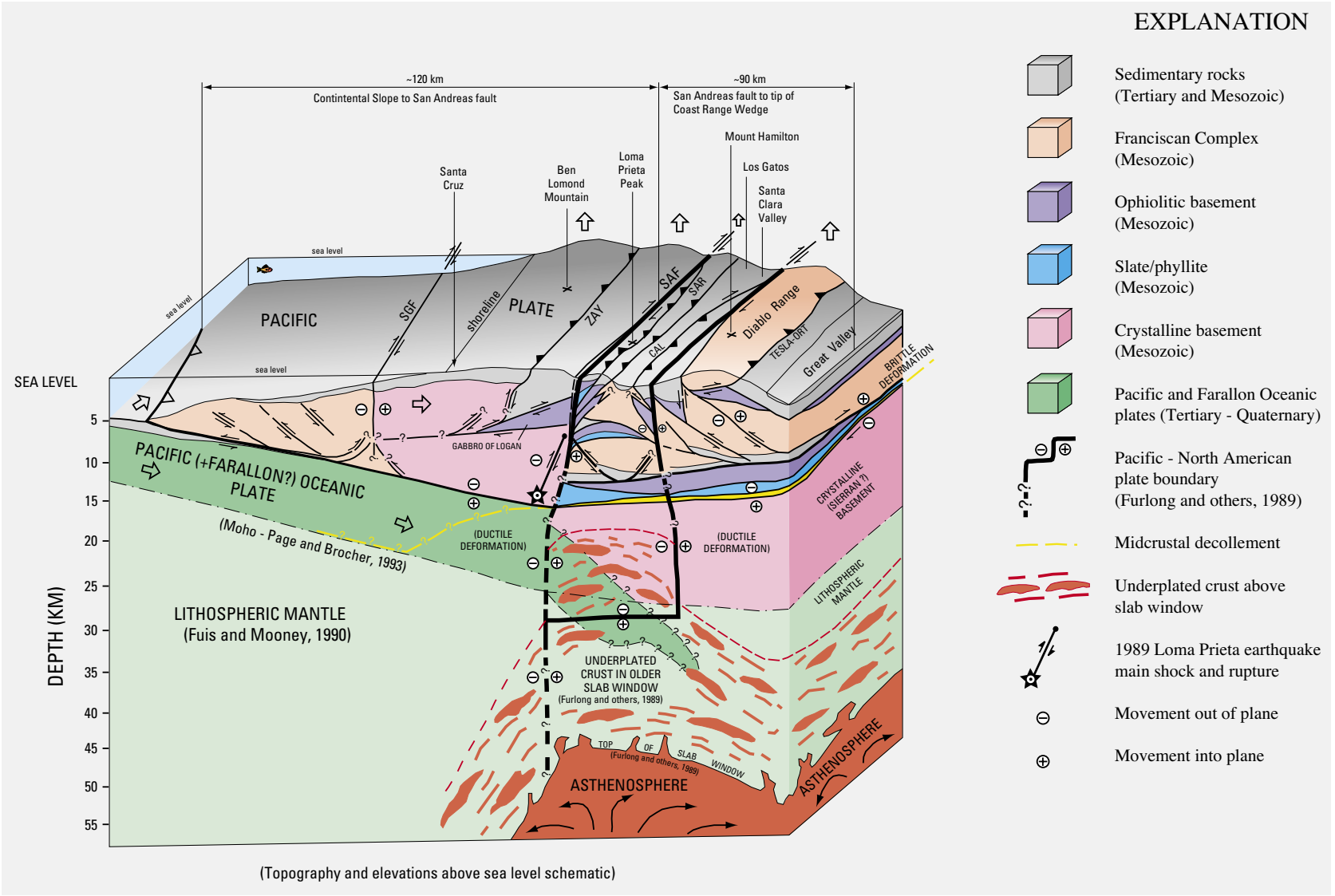

Figure 8.—Schematic cross section across the California margin at latitude of Loma Prieta (fig. 1), showing hypothetical deep structure of the San Andreas fault system, tectonic wedging, and plate boundary relations. Depth, thickness, and compositions of crust and mantle units and location of midcrustal decollement are partly inferred from seismic reflection and refraction models of Fuis and Mooney (1990), Page and Brocher (1993), and Brocher and others (this chapter). Depth to present top of slab window (Dickinson and Snyder, 1979), configuration of lithified materials underplated in older, shallower roof area of window, and hypothetical boundary relation between the Pacific and North American plates are based on thermal and seismic models of Furlong and others (1989). CAL, Calaveras fault; SAF, San Andreas fault; SAR, Sargent fault; SGF, San Gregorio fault; TESLA–ORT, Tesla-Ortigalita fault; ZAY, Zayante fault.

by compression normal to the San Andreas fault (Zoback and others, 1987). Interpretations of the seismic reflection and refraction data suggest that significant compression is accommodated by blind thrust faults within an eastwardly tapered, composite series of tectonic wedges which are herein referred to as the "wedge" or wedge complex. The "wedge" is thought to consist largely of the Franciscan Complex and to have been driven northeastward into the lower part of the Great Valley sequence and the Coast Range ophiolite during the Late Cretaceous to early Tertiary. The wedge complex is also considered to be presently active under the eastern Coast Ranges (Wentworth and others, 1984; Wentworth and Zoback, 1990; Unruh and Moores, 1992). Roof thrusts of the "wedge" dip east near its tip and root into a master zone of west-dipping floor thrusts (fig. 8).

A major unresolved uncertainty is the question of how major strike-slip faults in the San Andreas fault system interact with the basal floor-thrust zone of the wedge complex. Details of the deformation history of the wedge complex also remain obscure. Nevertheless, such a model provides a reasonable mechanism to unify relations among strike-slip, uplift, and crustal shortening in the Coast Ranges.

WEDGE TECTONIC MODEL

A hypothetical wedge tectonic model for the Loma Prieta region and adjacent San Francisco Bay region is illustrated in figure 8. In this model, faults of the southwestern Santa Clara Valley thrust belt represent a part of the roof thrust zone of the wedge complex. The southwestward dip of the thrust belt is explained as an effect of southwestward tilting and northeast-southwestward shortening in the roof-thrust zone of the wedge complex, resulting from eastward "wedge" propagation.

The geometry of the "wedge" tip, the thickness of the "wedge," and the depth to its tip are based on reflection and refraction profiling (Fuis and Mooney, 1990; Wentworth and Zoback, 1990). These models suggest that the tip of the wedge complex is about 90 km east of the San Andreas fault, beneath the San Joaquin Valley. The 5- to 6-km/s-velocity material that is assumed to be Franciscan Complex, which composes the bulk of the "wedge," is interpreted to be underlain below its floor-thrust zone by higher-velocity mafic oceanic rocks, including rocks correlative with the Coast Range ophiolite and (or) the gabbro of Logan. From the seismic refraction and reflection modeling (Fuis and Mooney, 1990), we also infer that rocks of the Jurassic western Sierra Nevada slate belt continue in the subsurface from their outcrops east of the Great Valley to the San Andreas fault, where they underlie the Sierra Azul block and rocks of the Coast Range ophiolite at 12- to 15-km depth. The slate and phyllite of Loma Prieta peak and overlying ophiolitic section in the hanging-wall block of the Sargent fault zone at Loma Prieta peak are interpreted in this model to be a part of this sub-Franciscan basement. Aeromagnetic data (see Jachens and Griscom, this chapter) and structure sections (see pl. 1), however, constrain the total vertical displacement of the Coast Range ophiolite by the Sargent fault to less than 2 km. Uplift of the slate and phyllite of Loma Prieta peak and overlying ophiolitic section from greater depths, therefore, must have occurred along another, possibly flatter fault beneath the Sierra Azul block.

Further support for this interpretation is indicated by the widespread occurrence of laumontite in the Cretaceous and older section of the Sierra Azul block but its absence in younger rocks, and by the occurrence in the Eocene sequence of the Sierra Azul area of detritus derived from high-pressure-metamorphic rocks of the Franciscan Complex. The distribution of laumontite and of high-pressure mineral detritus in the section requires burial of the Cretaceous and older rocks to 3- to 11-km depth (Dickinson and others, 1969; Blake and others, 1988), followed at 70–56 Ma by 8 to 9 km of unroofing, to raise the eroded top of the Cretaceous and older section to a depth shallower than the stability field of laumontite. Attenuation faulting, which downfaulted the unlaumontitized Eocene sequence onto various pre-Eocene rock units, appears to have occurred as late as 30 Ma but also earlier, during unroofing of the pre-Eocene section (Jayko and others, 1987).

Interpreted within the context of a wedge tectonic model, the late Mesozoic and Cenozoic uplift pattern was related to oblique northeastward emplacement of a wedge complex, resulting in 13 to 15 km of uplift by 61 Ma and an additional 8 to 9 km of uplift by 56 Ma. Speculatively, the slate and phyllite of Loma Prieta peak was uplifted along flat thrusts in the roof of the wedge complex from a sub-Franciscan basement position to within 4 km of the surface during this pre-early Eocene stage of "wedge" formation. Concurrent with northeastward "wedge" propagation, folding and tilting occurred above blind thrusts in the roof- and floor-thrust zones of the wedge complex, beneath the shallower attenuation structures.

Movement on the San Andreas transform fault was initiated about 18 Ma as the Mendocino Fracture Zone propagated to the north end of the Salinia terrane. Concurrently, hot asthenosphere moved upward into the lower crust and upper mantle (fig. 8) beneath the North American plate south of the Mendocino triple junction, to form a slab window in place of the subducted Farallon plate north of the triple junction (Dickinson and Snyder, 1979). At that time, the La Honda and Ben Lomond blocks were about 300 km to the south, and the San Francisco Bay block was about 170 km south of its present position. The northeastward-vergent Sargent and Berrocal faults, as well as faults of the southwestern Santa Clara Valley thrust belt, may also have formed at this time in response to transpression across the propagating north end of the triple junction. Surface fault offsets, Quaternary terrace-uplift rates, and fission-track data (Bürgmann and others, 1994) northeast of the San Andreas fault suggest that cumulative uplift of about 6 km and shortening of about 5 km have been accommodated by these thrusts in the roof-thrust zone of the wedge complex. In the Loma Prieta region (see pl. 1), these thrusts root in the main San Andreas transform boundary at

8- to 10-km depth and activate parts of the buried Oligocene and older roof-thrust zone of the wedge complex. Southwest of the San Andreas fault, fission-track data (Bürgmann and others, 1994), stratigraphy, and paleobathymetry suggest as much as 3 km of uplift since 30–24 Ma.

From at least 18 Ma to the present, dextral slip along the Pilarcitos fault, faults of the east-bay fault system, and the Peninsular segment of the San Andreas fault have broken the "wedge" into the Salinia terrane, the San Francisco Bay block, and the eastern San Francisco Bay block. Strike-slip motion between the San Andreas and east-bay fault systems may partly be accommodated by oblique slip along the floor-thrust zone of the "wedge." An undetermined, but probably small, component of the 5 km of horizontal shortening and 8 km of uplift west of the east-bay fault system also may be accommodated by movement along reactivated parts of this floor-thrust zone.

The Pacific-North American plate boundary has migrated eastward to the east-bay fault system (that is, the Calaveras, Hayward, and related faults) since the late Miocene. This eastward step in the plate boundary was facilitated by underplating and cooling of the lithospheric mantle and lower crust above the slab window formed south of the Mendocino triple junction (fig. 8), as the transform and locus of asthenospheric upwelling propagated northward and the plate boundary became increasingly transpressional (Furlong and others, 1989).

1989 LOMA PRIETA EARTHQUAKE

The main shock of the 1989 Loma Prieta earthquake was initiated southwest of the San Andreas fault, with rupture occurring from 17- to 8-km depth, along a 70° SW.-dipping blind dextral-reverse fault (U.S. Geological Survey staff, 1990). The faulting was initiated near the base of the North American plate (figs. 4, 8), near the floor-thrust zone of the wedge complex. Seismicity above 10-km depth is considered to have resulted from accommodation of the deeper slip by upwarping and secondary slip on the thrust-fault system northeast of the San Andreas fault. Beneath the Sargent fault, secondary slip was taken up to within 4 km of the surface.

Within the context of a wedge tectonic model, the 1989 Loma Prieta earthquake may be interpreted as resulting from activation of the hypothetical floor-thrust zone of the wedge complex, in response to transpression across the Pacific-North American plate boundary. The earthquake rupture propagated steeply upward and northeastward from the floor thrust to 8–10-km depth. At shallower levels to the northeast, distributed secondary slip was accommodated across eastward-vergent oblique-dextral thrusts of the southwestern Santa Clara Valley thrust belt. Southwest of the principal bedrock trace of the San Andreas fault, secondary slip was accommodated by extensional faults in the Summit Road-Skyland Ridge area that appear to have ruptured from the surface downward to less than 200-m depth and that may not have roots in the deep crust.

CONCLUSIONS

1. The Loma Prieta earthquake of October 17, 1989 occurred on a steep, southwest-dipping, right-lateral reverse fault that did not rupture to the surface. The fault rupture was initiated southwest of the principal trace of the San Andreas fault at about 17-km depth, near or at the base of the continental crust and, possibly, along the floor-thrust zone of a tectonic wedge complex. The primary rupture propagated upward to 8- to 10-km depth beneath the principal surface trace of the San Andreas fault. Whether this primary rupture was on the principal trace of the San Andreas fault or on a subsidiary fault that merges upward with a vertical San Andreas zone is still undetermined.
2. Geophysical modeling (see Brocher and others, this chapter; Jachens and Griscom, this chapter) indicates that the primary rupture occurred entirely within buried crystalline basement rocks beneath a slab of magnetic rocks, as much as 5 km thick, believed to represent the subsurface continuation of the gabbro of Logan.
3. Above the 8- to 10-km depth of primary rupture, slip was accommodated southwest of the principal trace of the San Andreas fault (a) by upwarping in the hanging-wall block of the fault; (b) by secondary shallow extension, sinistral slip, and associated ridgetop spreading in the Summit Road-Skyland Ridge fault zone; and (c) by shaking-induced massive slope failure. Most of the secondary surface deformation during the earthquake was focused in the Summit Road-Skyland Ridge fault zone, off and southwest of the principal surface trace of the San Andreas fault. Geologic data indicate that similar deformation occurred in the Summit Road-Skyland Ridge area both in 1906 and earlier in the Quaternary, and so it should be expected to recur here during earthquakes of similar magnitude in the future.
4. The Sargent fault immediately northeast of the principal trace of the San Andreas fault shows evidence of major reverse slip that occurred from about 18–10 Ma. A late phase of right-lateral slip indicated from slip-surface data may be later than 10 Ma. During the 1989 Loma Prieta earthquake, a small component of right-lateral extension and compression occurred near the northwest end of the Sargent fault near Lake Elsman.
5. Fission-track data (Bürgmann and others, 1994) suggest that about 3 to 4 km of uplift have occurred beneath the Sierra Azul block northeast of the San Andreas fault since 3 Ma, indicating a post-3-Ma uplift rate of about 1 mm/yr. Constraints on the timing and duration of movement on the Sargent fault and on the southwestern Santa Clara Valley thrust belt suggest that uplift since 3 Ma has been largely accommodated by the southwestern Santa Clara Valley thrust belt and that most uplift and shortening occurred

before about 250 ka. Speculatively, younger blind thrusts could be present beneath the Santa Clara Valley that root southwestward into the exposed southwestern Santa Clara Valley thrust belt or the San Andreas fault. Other southwestward-vergent blind thrusts might also exist beneath the Santa Clara Valley that merge at depth with the Calaveras fault or a more eastward segment of the floor- or roof-thrust zone of the active tectonic wedge complex believed to underlie this region.

ACKNOWLEDGMENTS

We are particularly grateful to Earl Brabb, who participated in parts of the mapping and provided much unpublished biostratigraphic information. We thank Robert Jachens and Andrew Griscom for extensive discussions and insights into the implications of their geophysical studies of crustal structure, and Robert Jachens and Carl Wentworth for their reviews of the manuscript. Zenon Valin prepared digital files for many of the figures and for the geologic map and structure sections (see pl. 1). Some of the illustrations were originally prepared by Kathryn Nimz. Finally, we are particularly indebted to Carl Wentworth for the many hours he spent helping the first author edit and simplify the digital map (see pl. 1).

REFERENCES CITED

Adam, D.P., McLaughlin, R.J., Sorg, D.H., Adams, D.B., Forester, R.M., and Repenning, C.A., 1982, An animal and plant-fossil assemblage from the Santa Clara Formation (Pliocene and Pleistocene), Saratoga, California, *in* Ingersoll, R.V., and Woodburne, M.O., eds., Cenozoic nonmarine deposits of California and Arizona: Los Angeles, Society of Economic Paleontologists and Mineralogists, Pacific Section, p. 105–110.

Allen, J.E., 1946, Geology of the San Juan Bautista quadrangle, California: California Division of Mines Bulletin 133, 112 p.

Arrowsmith, Ramón, Bürgmann, Roland, and Dumitru, Trevor, 1992, Uplift of the southern Santa Cruz Mountains deduced from fission-track dating and geomorphic analyses [abs.]: Eos (American Geophysical Union Transactions), v. 73, no. 44, p. 588.

Atwater, Tanya, 1989, Plate tectonic history of the northeast Pacific and western North America, *in* Winterer, E.L., Hussong, D.M., and Decker, R.W., eds., The eastern Pacific Ocean and Hawaii, v. N *of* The geology of North America: Boulder, Colo., Geological Society of America, p. 21–72.

Aydin, Atilla, Johnson, A.M., and Fleming, R.W., 1990, Field evidence for right-lateral/reverse tectonic surface rupture along the San Andreas/Sargent fault systems associated with the 1989 Loma Prieta earthquake [abs.]: Eos (American Geophysical Union Transactions), v. 71, no. 43, p. 1460.

———1992, Right-lateral-reverse surface rupture along the San Andreas and Sargent faults associated with the October 17, 1989, Loma Prieta, California, earthquake: Geology, v. 20, no. 12, p. 1063–1067.

Bailey, E.H., and Everhart, D.L., 1964, Geology and quicksilver deposits of the New Almaden district, Santa Clara County, California: U.S. Geological Survey Professional Paper 360, 206 p.

Bailey, E.H., Irwin, W.P., and Jones, D.L., 1964, Franciscan and related rocks, and their significance in the geology of western California: California Division of Mines and Geology Bulletin 183, 177 p.

Beroza, G.C., 1991, Near-source modeling of the Loma Prieta earthquake; evidence for heterogeneous slip and implications for earthquake hazard: Seismological Society of America Bulletin, v. 81, no. 5, p. 1603–1621.

Blake, M.C. Jr., Jayko, A.S., McLaughlin, R.J., and Underwood, M.B., 1988, Metamorphic and tectonic evolution of the Franciscan Complex, northern California, *in* Ernst, W.G., ed., Metamorphism and crustal evolution of the Western United States (Rubey volume 7): Englewood Cliffs, N.J., Prentice-Hall, p. 1036–1060.

Blake, M.C., Jr., Jones, D.L., McLaughlin, R.J., and Wentworth, C.M., 1991, Tectonic significance of fragments of Sierran basement in the northern Coast Ranges, California [abs.]: Geological Society of America Abstracts with Programs, v. 23, no. 2, p. 7.

Brabb, E.E., and Olson, J.A., 1986, Map showing faults and earthquake epicenters in San Mateo County, California: U.S. Geological Survey Miscellaneous Investigations Series Map I–1257–F, 2 sheets, scale 1:62,500.

Brown, R.D., 1990, Quaternary deformation, chap. 4 *of* Wallace, R.E., ed., The San Andreas fault system: U.S. Geological Survey Professional Paper 1515, p. 83–114.

Browne, P.R.L., and Ellis, A.J., 1970, The Ohaki-Broadlands hydrothermal area, New Zealand; mineralogy and related geochemistry: American Journal of Science, v. 269, no. 2, p. 97–131.

Bukry, David, Brabb, E.E., and Vedder, J.G., 1975, Correlation of Tertiary nannoplankton assemblages from the Coast and Peninsular Ranges of California, *in* Congreso Latinoamericano de Geología, 2d, Caracas, 1973, Memoir: Venezuela Boletin de Geología Publicación Especial 7, v. 3, p. 1461–1483.

Bürgmann, Roland, Arrowsmith, Ramon, Dumitru, Trevor, and McLaughlin, Robert, 1994, Rise and fall of the southern Santa Cruz mountains, California, from fission tracks, geomorphology, and geodesy: Journal of Geophysical Research, v. 99, no. B10, p. 20181–20202.

Clark, J.C., 1981, Stratigraphy, paleontology, and geology of the central Santa Cruz Mountains, California Coast Ranges: U.S. Geological Survey Professional Paper 1168, 51 p.

Clark, J.C., and Brabb, E.E., 1978, Stratigraphic contrasts across the San Gregorio fault, Santa Cruz Mountains, west central California, *in* Silver, E.A., and Normark, W.R., eds., San Gregorio-Hosgri fault zone, California: California Division of Mines and Geology Special Publication 137, p. 3–12.

Clark, J.C., Brabb, E.E., Greene, H.G., and Ross, D.C., 1984, Geology of Point Reyes Peninsula and implications for San Gregorio fault history, *in* Crouch, J.K., and Bachman, S.B., eds., Tectonics and sedimentation along the California margin: Los Angeles, Society of Economic Paleontologists and Mineralogists, Pacific Section Field Trip Guidebook, v. 38, p. 67–85.

Clark, J.C., Brabb, E.E., and McLaughlin, R.J., 1989, Geologic

map and structure sections of the Laurel 7½′ Quadrangle, Santa Clara and Santa Cruz Counties, California: U.S. Geological Survey Open-File Map 89–676, 30 p., 2 sheets, scale 1:24,000.

Clark, J.C., McLaughlin, R.J., Kistler, R.W., Champion, D.E., and Franck, C.R., 1991, Basement structure southwest of the San Andreas fault, Loma Prieta, Laurel, and Los Gatos Quadrangles, California [abs.]: Geological Society of America Abstracts with Programs, v. 23, no. 2, p. 13.

Clark, J.C., and Rietman, J.D., 1973, Oligocene stratigraphy, tectonics, and paleogeography southwest of the San Andreas fault, Santa Cruz Mountains and Gabilan Range, California Coast Ranges: U.S. Geological Survey Professional Paper 783, 18 p.

Compton, R.R., 1966, Granitic and metamorphic rocks of the Salinian block, California Coast Ranges, *in* Bailey, E.H., ed., Geology of northern California: California Division of Mines and Geology Bulletin 190, p. 277–287.

Coppersmith, K.J., 1990, The Zayante-Vergeles fault zone, *in* Schwartz, D.P., and Ponti, D.J., eds., Field guide to neotectonics of the San Andreas fault system, Santa Cruz Mountains, in light of the 1989 Loma Prieta earthquake: U.S. Geological Survey Open-File Report 90–274, p. 14–16.

Cotton, W.R., 1990, Highway 17 deformation, *in* Schwartz, D.P., and Ponti, D.J., eds., Field guide to neotectonics of the San Andreas fault system, Santa Cruz Mountains, in light of the 1989 Loma Prieta earthquake: U.S. Geological Survey Open-File Report 90–274, p. 31–32.

Cotton, W.R., Fowler, W.L., and Velsor, J.E., 1990, Coseismic bedding plane faults and ground fissures associated with the Loma Prieta earthquake of October 17, 1989, *in* McNutt, S.R., and Sydnor, R.H., eds., The Loma Prieta (Santa Cruz Mountains), California earthquake of 17 October 1989: California Division of Mines and Geology Special Publication 104, p. 95–103.

Cummings, J.C., 1968, The Santa Clara Formation and possible post-Pliocene slip on the San Andreas fault in central California, *in* Dickinson, W.R., and Grant, Art, eds., Proceedings of conference on geologic problems of San Andreas fault system: Stanford, Calif., Stanford University Publications in Geological Sciences, v. 11, p. 191–206.

Cummings, J.C., Touring, R.M., and Brabb, E.E., 1962, Geology of the northern Santa Cruz Mountains, California, *in* Bowen, O.E., Jr., ed., Geologic guide to the gas and oil fields of northern California: California Division of Mines and Geology Bulletin 181, p. 179–220.

Dibblee, T.W., Jr., Nilsen, T.H., and Brabb, E.E., 1979, Preliminary geologic map of the San Juan Bautista Quadrangle, San Benito and Monterey Counties, California: U.S. Geological Survey Open-File Report 79–375, scale 1:24,000.

Dickinson, W.R., Ojakangas, R.W., and Stewart, R.J., 1969, Burial metamorphism of the late Mesozoic Great Valley sequence, Cache Creek, California: Geological Society of America Bulletin, v. 80, no. 3, p. 519–526.

Dickinson, W.R., and Snyder, W.S., 1979, Geometry of triple junctions related to San Andreas transform: Journal of Geophysical Research, v. 84, no. B2, p. 561–572.

Eberhart-Phillips, D.M., Labson, V.F., Stanley, W.D., Michael, A.J., and Rodriguez, B.D., 1990, Preliminary velocity and resistivity models of the Loma Prieta earthquake region: Geophysical Research Letters, v. 17, no. 8, p. 1235–1238.

Eberhart-Phillips, D.M., and Stuart, W.D., 1992, Material heterogeneity simplifies the picture; Loma Prieta: Seismological Society of America Bulletin, v. 82, no. 4, p. 1964–1968.

Elder, W.P., 1990, An unusual Late Cretaceous fauna from an oyster-rich interval in the Santa Cruz Mountains of California: U.S. Geological Survey Bulletin 1934, 18 p.

Emcon Associates, 1990, Shannon fault study, Guadalupe disposal site, Santa Clara County, California: San Jose, Calif., report, p. 2–19 to 2–25.

Fleck, R.J., 1967, Structure significance of the contact between Franciscan and Cenozoic rocks, southern San Francisco Peninsula, California: Stanford, Calif., Stanford University, M.S. thesis, 43 p.

Fox, K.F., Jr., Fleck, R.J., Curtis, G.H., and Meyer, C.E., 1985, Implications of the northwestwardly younger age of the volcanic rocks of west-central California: Geological Society of America Bulletin, v. 96, no. 5, p. 647–654.

Fuis, G.S., and Mooney, W.D., 1990, Lithospheric structure and tectonics from seismic-refraction and other data, chap. 8 *of* Wallace, R.E., ed., The San Andreas fault system, California: U.S. Geological Survey Professional Paper 1515, p. 207–236.

Furlong, K.P., Hugo, W.D., and Zandt, George, 1989, Geometry and evolution of the San Andreas fault zone in northern California: Journal of Geophysical Research, v. 94, no. B3, p. 3100–3110.

Graham, S.A., and Dickinson, W.R., 1978, Evidence for 115 kilometers of right-slip on the San Gregorio-Hosgri fault trend: Science, v. 199, no. 4325, p. 179–181.

Hagstrum, J.T., and Murchey, B.L., 1991, Paleomagnetism of Lower Jurassic chert within the Franciscan Complex, northern California, indicates deposition at the paleoequator and accretion near 7° north paleolatitude [abs.]: Geological Society of America Abstracts with Programs, v. 23, no. 2, p. 33.

Hall, C.A., Jr., Sarna-Wojcicki, A.M., and Dupré, W.R., 1974, Faults and their potential hazards in Santa Cruz County, California: U.S. Geological Survey Miscellaneous Field Studies Map MF–626, 3 sheets, scale 1:62,500.

Hanna, W.F., Brown, R.D., Jr., Ross, D.C., and Griscom, Andrew, 1972, Aeromagnetic reconnaissance and generalized geologic map of the San Andreas fault between San Francisco and San Bernardino, California: U.S. Geological Survey Geophysical Investigations Map GP–815, scale 1:250,000.

Hansen, E.C, Bingham, Norman, Dryer, David, Heistand, Patricia, Mys, Courtney, Stuk, Matt, and Van Appledorn, Kurt, 1991, High-grade metamorphism of the Santa Lucia Range, California [abs.]: Geological Society of America Abstracts with Programs, v. 23, no. 5, p. A445.

Haq, B.U., Hardenbol, Jan, and Vail, P.R., 1987, The new chronostratigraphic basis of Cenozoic and Mesozoic sea level cycles, *in* Ross, C.A., and Haman, Drew, eds., Timing and depositional history of eustatic sequences; constraints on seismic stratigraphy: Cushman Foundation for Foraminiferal Research Special Publication 24, p. 7–13.

Harbert, William, and Cox, Allan, 1989, Late Neogene motion of the Pacific Plate: Journal of Geophysical Research, v. 94, no. B3, p. 3025–3064.

Haugerud, R.A., and Ellen, S.D., 1990, Coseismic ground deformation along the northeast margin of the Santa Cruz Mountains, *in* Schwartz, D.P., and Ponti, D.J., eds., Field guide to neotectonics of the San Andreas fault system, Santa Cruz Mountains,

in light of the 1989 Loma Prieta earthquake: U.S. Geological Survey Open-File Report 90–274, p. 32–36.

Hole, J.A., Holbrook, W.S., Klemperer, S.L., Ten Brink, U.S., and Brocher, T.M., 1993, Crustal structure in the San Francisco Bay Area from wide-angle seismic refraction data [abs.]: Eos (American Geophysical Union Transactions), v. 74, no. 43, p. 445.

Hopson, C.A., Mattinson, J.M., Luyendyk, B.P., and Pessagno, E.A., Jr., 1991, California Coast Range ophiolite; Middle Jurassic/Central Tethyan and latest Jurassic/Southern boreal episodes of ocean-ridge magmatism [abs.]: Eos (American Geophysical Union Transactions), v. 72, no. 44, p. 443.

Hopson, C.A., Mattinson, J.M., and Pessagno, E.A., Jr., 1981, Coast Range ophiolite, western California, *in* Ernst, W.G., ed., Geotectonic development of California (Rubey volume 1): Englewood Cliffs, N.J., Prentice-Hall, p. 418–510.

Huffman, O.F., 1972, Lateral displacement of upper Miocene rocks and the Neogene history of offset along the San Andreas fault in central California: Geological Society of America Bulletin, v. 83, no. 10, p. 2913–2946.

Hull, D.M., Blome, C.D., and Pessagno, E.A., Jr., 1992, Chronostratigraphic assignment of volcanopelagic strata above the Coast Range ophiolite: American Association of Petroleum Geologists Bulletin, v. 76, no. 3, p. 422.

Irwin, W.P., 1990, Geology and plate tectonic development, chap. 3 *of* Wallace, R.E., ed., The San Andreas fault system, California: U.S. Geological Survey Professional Paper 1515, p. 61–82.

Jachens, R.C., Wentworth, C.M., and McLaughlin, R.J., 1998, Pre-San Andreas location of the Gualala block, inferred from magnetic and gravity anomalies, *in* Elder, W.P., ed., Geology and tectonics of the Gualala block, northern California: Los Angeles, Society of Economic Paleontologists and Mineralogists, Pacific Section Field Trip Guidebook, v. 84, p. 27–64.

James, E.W., 1984, U/Pb ages of plutonism and metamorphism in part of the Salinian block, Santa Cruz and San Mateo Counties, California [abs.]: Geological Society of America Abstracts with Programs, v. 16, no. 5, p. 291.

———1992, Cretaceous metamorphism and plutonism in the Santa Cruz Mountains, Salinian block, California, and correlation with the southernmost Sierra Nevada: Geological Society of America Bulletin, v. 104, no. 10, p. 1326–1339.

James, E.W., Kimbrough, D.L., and Mattinson, J.M., 1994, Evaluation of displacements of pre-Tertiary rocks on the northern San Andreas fault using U-Pb zircon dating, initial Sr, and common Pb isotopic ratios, chap. 7 *of* Powell, R.E., Weldon, R.J., II, and Matti, J.C., eds., The San Andreas fault system; displacement, palinspastic reconstruction, and geologic evolution: Geological Society of America Memoir 178, p. 257–271.

Jayko, A.S., and Blake, M.C., Jr., 1986, Significance of Klamath rocks between the Franciscan Complex and Coast Range Ophiolite, northern California: Tectonics, v. 5, no. 7, p. 1055–1071.

Jayko, A.S., Blake, M.C., Jr., and Harms, T.A., 1987, Attenuation of the Coast Range ophiolite by extensional faulting and nature of the Coast Range "thrust," California: Tectonics, v. 6, no. 4, p. 475–488.

Johnson, C.M., and O'Neil, J.R., 1988, Constraints on pre-Tertiary movement on the San Andreas fault system (SAF); stable and radiogenic isotope and trace element data from Jurassic gabbros [abs.]: Geological Society of America Abstracts with Programs, v. 20, p. A381.

Johnson, R.E., and Associates, 1989, Fault investigation report, Loma Prieta Elementary School, Santa Clara County, California: Santa Clara County, Calif., Loma Prieta School District Open-File Report, 50 p.

Jones, D.L., and Curtis, Garniss, 1991, Guide to the geology of the Berkeley Hills, Central Coast Ranges, California, *in* Sloan, Doris, and Wagner, D.L., eds., Geologic excursions in northern California; San Francisco to the Sierra Nevada: California Division of Mines and Geology Special Publication 109, p. 63–74.

Kistler, R.W., Peterman, Z.E., Ross, D.C., and Gottfried, David, 1973, Strontium isotopes and the San Andreas fault, *in* Kovach, R.L., and Nur, Amos, eds., Proceedings of the conference on tectonic problems of the San Andreas fault system: Stanford, Calif., Stanford University Publications in Geological Sciences, v. 13, p. 339–347.

Krueger, M.L., 1943, Moody gulch oil field, in Santa Maria Basin and southern Coast Ranges, chap. 10 *of* Geologic formations and economic development of the oil and gas fields of California: California Division of Mines Bulletin 118, p. 477.

Lajoie, K.R., and Helley, E.J., 1975, Differentiation of sedimentary deposits for purposes of seismic zonation, *in* Borcherdt, R.D. ed., Studies for seismic zonation of the San Francisco Bay region: U.S. Geological Survey Professional Paper 941–A, p. A39–A51.

Lajoie, K.R., Weber, G.E., Mathieson, S.A., and Wallace, J.B., 1979, Quaternary tectonics of coastal Santa Cruz and San Mateo Counties, California, as indicated by deformed marine terraces and alluvial deposits, *in* Weber, G.E., Lajoie, K.R., and Griggs, G.B., eds., Coastal tectonics and coastal geologic hazards in Santa Cruz and San Mateo Counties, California: Geological Society of America field trip guidebook, p. 61–80.

Lawson, A.C., chairman, 1908, the California earthquake of April 18, 1906; report of the State Earthquake Investigation Commission: Carnegie Institution of Washington Publication 87, 2 v.

Lisowski, Michael, Prescott, W.H., Savage, J.C. and Johnston, M.J.S., 1990, Geodetic estimate of coseismic slip during the 1989 Loma Prieta, California, earthquake: Geophysical Research Letters, v. 17, no. 9, p. 1437–1440.

Marshall, G.A., Stein, R.S., and Thatcher, Wayne, 1991, Faulting geometry and slip from co-seismic elevation changes; the 17 October, 1989, Loma Prieta, California, earthquake: Seismological Society of America Bulletin, v. 81, no. 5, p. 1660–1643.

Mathews, Vincent, III, 1976, Correlation of Pinnacles and Neenach Volcanic Formations and their bearing on San Andreas fault problem: American Association of Petroleum Geologists Bulletin, v. 60, no. 12, p. 2128–2141.

Mattinson, J.M., and Hopson, C.A., 1992, U/Pb ages of the Coast Range ophiolite; a critical re-evaluation based on new high-precision Pb/Pb ages [abs.]: American Association of Petroleum Geologists Bulletin, v. 76, no. 3, p. 425.

Mattinson, J.M., and James, E.W., 1985, Salinian block U/Pb age and isotopic variations; implications for origin and emplacement of the Salinian terrane, *in* Howell, D.G., ed., Tectonostratigraphic terranes of the Circum-Pacific region: Houston, Tex., Circum-Pacific Council for Energy and Mineral Resources,

v. 1, p. 215–226.

McDougall, Kristin, 1989, Paleogene benthic foraminifers from the Loma Prieta Quadrangle, California: U.S. Geological Survey Open-File Report 89–649, 90 p.

———1991, Benthic Foraminifera from the Laurel Quadrangle, California: U.S. Geological Survey Open-File Report 91–13, 66 p.

McLaughlin, R.J., 1974, The Sargent-Berrocal fault zone and its relation to the San Andreas fault system in the southern San Francisco Bay region and Santa Clara Valley, California: U.S. Geological Survey Journal of Research, v. 2, no. 5, p. 593–598.

McLaughlin, R.J., Blake, M.C., Jr., Griscom, Andrew, Blome, C.D., and Murchey, Bonnie, 1988a, Tectonics of formation, translation, and dispersal of the Coast Range Ophiolite of California: Tectonics, v. 7, no. 5, p. 1033–1056.

McLaughlin, R.J., Clark, J.C., and Brabb, E.E., 1988b, Geologic map and structure sections of the Loma Prieta 7½′ Quadrangle, Santa Clara and Santa Cruz Counties, California: U.S. Geological Survey Open-File Map 88–752, 30 p., 2 sheets, scale 1:24,000.

McLaughlin, R.J., Clark, J.C., Brabb, E.E., and Helley, E.J., 1991a, Geologic map and structure sections of the Los Gatos 7½′ quadrangle, Santa Clara and Santa Cruz Counties, California: U.S. Geological Survey Open-File Report 91–593, 45 p., 3 sheets, scale 1:24,000.

McLaughlin, R.J., Clark, J.C., Brabb, E.E., Helley, E.J., and Colón, C.J., 2001, Geologic maps and structure sections of the southwestern Santa Clara Valley and southern Santa Cruz Mountains, Santa Clara and Santa Cruz Counties, California: U.S. Geological Survey Miscellaneous Field Studies Map MF–2373, 3 pamphlets, 8 sheets, scale 1:24,000

McLaughlin, R.J., Elder, W.P., and McDougall, Kristin, 1991b, Tectonic framework of the Loma Prieta area, *in* Sloan, Doris, and Wagner, D.L., eds., Geologic excursions in northern California; San Francisco to the Sierra Nevada: California Division of Mines and Geology Special Publication 109, p. 45–54.

McLaughlin, R.J., Kistler, R.W., Sliter, W.V., Murchey, B.L., and Franck, C.R., 1991c, Structure and character of Coast Range ophiolite and oceanic Franciscan terranes, Loma Prieta, Laurel, and Los Gatos quadrangles, California [abs.]: Geological Society of America Abstracts with Programs, v. 23, no. 2, p. 77.

McLaughlin, R.J., Oppenheimer, D.H., Helley, E.J., and Sebrier, Michel, 1992, The Lexington fault zone; a north-south link between the San Andreas fault and range front thrust system, Los Gatos, California [abs.]: Geological Society of America Abstracts with Programs, v. 24, no. 5, p. 69.

McLaughlin, R.J., Sliter, W.V., Elder, W.P., McDougall, Kristin, Russell, P.C., Sorg, D.H., Sims, J.D., and Blake, M.C., Jr., 1990, 190 km post-Middle Miocene offset on the Tolay-Hayward-Calaveras fault system superposed on large-scale Late Cretaceous to early Eocene translation [abs.]: Geological Society of America Abstracts with Programs, v. 22, no. 3, p. 67.

McLaughlin, R.J., Sliter, W.V., Sorg, D.H., Russell, P.C., and Sarna-Wojcicki, A.M., 1996, Large-scale right-slip displacement on the East San Francisco Bay Region fault system, California; implications for location of late Miocene to Pliocene Pacific plate boundary: Tectonics, v. 15, no. 1, p. 1–18.

McLaughlin, R.J., Sorg, D.H., Morton, J.L., Theodore, T.G., Meyer, C.E., and Delevaux, M.H., 1985, Paragenesis and tectonic significance of base and precious metal occurrences along the San Andreas fault at Point Delgada, California: Economic Geology, v. 80, no. 2, p. 344–359.

Mount, V.S., and Suppe, John, 1987, State of stress near the San Andreas fault; implications for wrench tectonics: Geology, v. 15, no. 12, p. 1143–1146.

Nakata, J.K., Sorg, D.H., Russell, P.C., Meyer, C.E., Wooden, J.L., Lanphere, M.A., McLaughlin, R.J., Sarna-Wojcicki, A.M., Saburomaru, J.Y., Pringle, M.S., and Drinkwater, J.L., 1993, New radiometric ages and tephra correlations from the San Jose and the northeastern part of the Monterey 1:100,000 map quadrangles, California: Isochron/West, no. 60, p. 19–32.

Nilsen, T.H., 1984, Submarine-fan facies associations of the Eocene Butano Sandstone, Santa Cruz Mountains, California: Geo-Marine Letters, v. 3, no. 2–4, p. 167–171.

Olson, J.A., and Hill, D.P., 1993, Seismicity in the southern Santa Cruz Mountains during the 20 year period before the earthquake, *in* Johnston, M.J.S., ed., The Loma Prieta, California, earthquake of October 17, 1989—preseismic observations: U.S. Geological Survey Professional Paper 1550–C, p. C3–C16.

Oppenheimer, D.H., Reasenberg, P.A., and Simpson, R.W., 1988, Fault-plane solutions for the 1984 Morgan Hill, California, earthquake sequence; evidence for the state of stress on the Calaveras fault: Journal of Geophysical Research, v. 93, no. B8, p. 9007–9026.

Page, B.M., and Brocher, T.M., 1993, Thrusting of the central California margin over the edge of the Pacific plate during the transform regime: Geology, v. 21, no. 7, p. 635–638.

Peabody, C.E., and Einaudi, M.T., 1992, Origin of petroleum and mercury in the Culver-Baer cinnabar deposit, Mayacmas district, California: Economic Geology, v. 87, no. 4, p. 1078–1103.

Ponti, D.J., and Wells, R.E., 1991, Off-fault ground ruptures in the Santa Cruz Mountains, California; ridge-top spreading versus tectonic extension during the 1989 Loma Prieta earthquake: Seismologic Society of America Bulletin, v. 81, no. 5, p. 1480–1510.

Prentice, C.S., and Ponti, D.J., 1994, The Wrights Tunnel is not an example of a broad shear zone; a re-examination of the documentation of the tunnel deformation associated with the 1906 earthquake [abs.]: Eos (American Geophysical Union Transactions), v. 75, no. 16, p. 343.

Prentice, C.S., and Schwartz, D.P., 1991, Re-evaluation of 1906 surface faulting, geomorphic expression, and seismic hazard along the San Andreas fault in the southern Santa Cruz Mountains: Seismological Society of America Bulletin, v. 81, no. 5, p. 1424–1479.

Repenning, C.A., Fejfar, Oldrich, and Heinrich, W.-D., 1990, Arvicolid rodent biochronology of the Northern Hemisphere, *in* International symposium; evolution, phylogeny, and biostratigraphy of arvicolids (Rodentia, Mammalia): Prague, Geological Survey, p. 385–418.

Ross, D.C., 1970, Quartz gabbro and anorthositic gabbro; markers of offset along the San Andreas fault in the California Coast Ranges: Geological Society of America Bulletin, v. 81, no. 12, p. 3647–3661.

———1978, The Salinian block—a Mesozoic granitic orphan in the California Coast Ranges, *in* Howell, D.G., and McDougall,

K.A., eds., Mesozoic paleogeography of the Western United States (Pacific Coast Paleogeography Symposium 2): Los Angeles, Society of Economic Paleontologists and Mineralogists, Pacific Section, p. 509–522.

———1984, Possible correlations of basement rocks across the San Andreas, San Gregorio-Hosgri, and Rinconada-Reliz-King City faults, California: U.S. Geological Survey Professional Paper 1317, 37 p.

Ross, D.C., and Brabb, E.E., 1973, Petrography and structural relations of basement rocks in the Monterey Bay area, California: U.S. Geological Survey Journal of Research, v. 1, no. 3, p. 273–282.

Ross, D.C., Wentworth, C.M., and McKee, E.H., 1973, Cretaceous mafic conglomerate near Gualala offset by San Andreas fault from oceanic crustal source near Eagle Rest Peak, California: U.S. Geological Survey Journal of Research, v. 1, no. 1, p. 45–52.

Rytuba, J.J., 1993, Active geothermal systems and gold-mercury deposits in the Sonoma-Clear Lake volcanic fields, California: Society of Economic Geology Guidebook 16, 361 p.

Sarna-Wojcicki, A.M., 2000, Revised age of the Rockland tephra, northern California; implications for climate and stratigraphic reconstructions in the western United States—comment and reply: Geology, v. 28, no.3, p. 286–287.

Sarna-Wojcicki, A.M., Lajoie, K.R., Meyer, C.E., Adam, D.P., and Rieck, H.J., 1991, Tephrochronologic correlation of upper Neogene sediments along the Pacific margin, conterminous United States, *in* Morrison, R.B., ed., Quaternary nonglacial geology; conterminous U.S. (Decade of North American Geology, v. K–2): Boulder, Colo., Geological Society of America, p. 117–140.

Sarna-Wojcicki, A.M., Pampeyan, E.H., and Hall, N.T., 1975, Map showing recently active breaks along the San Andreas fault between the central Santa Cruz Mountains and the northern Gabilan Range, California: U.S. Geological Survey Miscellaneous Field Investigations Map MF–650, 2 sheets, scale 1:24,000.

Sebrier, Michel, McLaughlin, R.J., Lajoie, Kenneth, and Oppenheimer, D.H., 1992, Fault kinematics in the San Francisco peninsular area; is the 1989 Loma Prieta earthquake anomalous? [abs.]: Eos (American Geophysical Union Transactions), v. 73, no. 44, p. 589.

Seiders, V.M., and Blome, C.D., 1988, Implications of upper Mesozoic conglomerate for suspect terranes in western California and adjacent areas: Geological Society of America Bulletin, v. 100, no. 3, p. 374–391.

Seiders, V.M., and Cox, B.F., 1991, Place of origin of the Salinian block of California, inferred from conglomerate clast compositions [abs.]: Geological Society of America Abstracts with Programs, v. 23, no. 2, p. 96.

Sliter, W.V., Murchey, B.L., McLaughlin, R.J., and Kistler, R.W., 1991, Permanente terrane; history of early Cretaceous seamount formation in the eastern Pacific [abs.]: Geological Society of America Abstracts with Programs, v. 23, no. 2, p. 98.

Smith, R.K., 1971, Foraminiferal studies in the lower and middle Tertiary of Soquel Creek, Santa Cruz County, California: Berkeley, University of California Publications in Geological Sciences, v. 91, p. 1–111.

Sorg, D.H., and McLaughlin, R.J., 1975, Geologic map of the Sargent-Berrocal fault zone between Los Gatos and Los Altos Hills, Santa Clara County, California: U.S. Geological Survey Miscellaneous Field Investigations Map MF–643, scale 1:24,000.

Spittler, T.E., and Harp, E.L., compilers, 1990, Preliminary map of landslide features and coseismic fissures triggered by the Loma Prieta earthquake of October 17, 1989: California Division of Mines and Geology Open-File Report 90–6, scale 1:48,000.

Stanley, R.G., 1985, Middle Tertiary sedimentation and tectonics of the La Honda basin, central California: U.S. Geological Survey Open-File Report 85–596, 263 p.

———1987, Implications of the northwestwardly younger age of the volcanic rocks of west-central California; alternative interpretation: Geological Society of America Bulletin, v. 98, no. 5, p. 612–614.

———1990, Evolution of the Tertiary La Honda basin, California, *in* Garrison, R.E., Greene, H.G., Hicks, K.R., Weber, G.E., and Wright, T.L., eds., Geology and tectonics of the central California coastal region, San Francisco to Monterey: American Association of Petroleum Geologists, Pacific Section Guidebook 67, p. 1–29.

Tennyson, M.E., 1989, Pre-transform early Miocene extension in western California: Geology, v. 17, no. 9, p. 792–796.

Thatcher, Wayne, 1990, Present-day crustal movements and the mechanics of cyclic deformation, chap. 7 *of* Wallace, R.E., ed., The San Andreas fault system, California: U.S. Geological Survey Professional Paper 1515, p. 189–206.

Thatcher, Wayne, and Lisowski, Michael, 1987, Long-term seismic potential of the San Andreas fault southeast of San Francisco, California: Journal of Geophysical Research, v. 92, no. B6, p. 4771–4784.

Trask, P.D., 1926, Geology of the Point Sur quadrangle, California: Berkeley, University of California, Department of Geological Sciences Bulletin, v. 16, no. 6, p. 119–186.

Turner, D.L., 1970, Potassium-argon dating of Pacific Coast Miocene foraminiferal stages, *in* Bandy, O.L., ed., Radiometric dating and paleontologic zonation: Geological Society of America Special Paper 124, p. 91–129.

Underwood, M.B., Shelton, K.L., Laughland, M.M., Solomon, R.M., McLaughlin, R.J., Russell, P.C., and Sorg, D.H., 1991, Miocene thermal-maturity anomalies at Loma Prieta, Mt. San Bruno, and Bolinas, central California coast [abs.]: Geological Society of America Abstracts with Programs, v. 23, no. 2, p. 105.

Unruh, J.R., and Moores, E.M., 1992, Quaternary blind thrusting in the southwestern Sacramento Valley, California: Tectonics, v. 11, no. 2, p. 192–203.

U.S. Geological Survey staff, 1989, Preliminary map of fractures formed in the Summit Road-Skyland Ridge area during the Loma Prieta, California, earthquake of October 17, 1989: U.S. Geological Survey Open-File Report 89–686, scale 1:12,000.

———1990, The Loma Prieta, California, earthquake; an anticipated event: Science, v. 247, no. 4940, p. 286–293.

Vanderhurst, W.C., Cummings, J.C., and Anderson, D.W., 1982, The Santa Clara Formation as a record of late Cenozoic uplift of the Santa Cruz Mountains, Santa Clara County, California, *in* Ingersoll, R.V., and Woodburne, M.O., eds., Cenozoic nonmarine deposits of California and Arizona: Los Angeles, Society of Economic Paleontologists and Mineralogists,

Pacific Section, p. 23–32.

Wentworth, C.M., Blake, M.C., Jr., Jones, D.L., Walter, A.W., and Zoback, M.D., 1984, Tectonic wedging associated with emplacement of the Franciscan Assemblage, California Coast Ranges, *in* Blake, M.C., Jr., ed., Franciscan geology of northern California: Los Angeles, Society of Economic Paleontologists and Mineralogists, Pacific Section Field Trip Guidebook, v. 43, p. 163–174.

Wentworth, C.M., and Zoback, M.D., 1990, Structure of the Coalinga area and thrust origin of the earthquake, *in* Rymer, M.J., and Ellsworth, W.L., eds., The Coalinga, California, earthquake of May 2, 1983: U.S. Geological Survey Professional Paper 1487, p. 41–67.

Wentworth, C.M., Zoback, M.D., Griscom, Andrew, Jachens, R.C, and Mooney, W.D., 1987, A transect across the Mesozoic accretionary margin of Central California: Royal Astronomical Society Geophysical Journal, v. 89, no. 1, p. 105–110.

Wright, R.H., compiler, 1971, Map showing locations of samples dated by radiocarbon methods in the San Francisco Bay region: U.S. Geological Survey Miscellaneous Field Studies Map MF–317, scale 1:500,000.

Zoback, M.L., Mount, V.S., Eaton, J.P., Healey, J.H., Oppenheimer, D.H., Reasenberg, P.A., Jones, L.M., Raleigh, C.B., Wong, I.G., Scotti, Oona, and Wentworth, C.M., 1987, New evidence on the state of stress of the San Andreas fault system: Science, v. 238, no. 4830, p. 1105–1111.

EARTHQUAKE OCCURRENCE

GEOPHYSICAL AND GEOLOGIC SETTING OF THE EARTHQUAKE, INFERRED FROM GRAVITY AND MAGNETIC ANOMALIES

By Robert C. Jachens and Andrew Griscom, U.S. Geological Survey

CONTENTS

ABSTRACT

To characterize the geophysical and geologic setting of the 1989 Loma Prieta earthquake, we have constructed a model for the subsurface structure and composition of the midcrust and upper crust beneath the Santa Cruz Mountains and adjacent southern Santa Clara Valley. This study was based mainly on an interpretation of local anomalies in the gravity and magnetic fields, relying heavily on geologic information to constrain the gravity and magnetic modeling, and on velocity and structural information from seismic tomography. We subdivide the study area into seven distinctive basement blocks on the basis of geophysical and geologic expression, provide a three-dimensional description of each basement block and its bounding faults by using calculated models, discuss implications about the tectonic development of the Loma Prieta region, and analyze the relation between the aftershock distribution and our crustal model.

Southwest of the San Andreas fault, from southwest to northeast, are three basement blocks: the nonmagnetic Ben Lomond block, a terrane of Mesozoic granitic and metamorphic rocks; the Logan block, with a Mesozoic basement of magnetic, high-density gabbro that is separated from the Ben Lomond block by the Zayante fault, which dips southwest at an average angle, in places, of less than 45°; and, to the north, another nonmagnetic block, presumably composed of granitic rocks, interpreted to be in fault contact with the Logan block. The Zayante fault may be a former Mesozoic thrust fault reactivated by Cenozoic tectonism. The western parts of these three basement blocks are terminated by the San Gregorio fault, which locally dips 50°–70° E. The eastern parts of all three blocks are terminated by the San Andreas fault. Magnetic Pliocene sedimentary rocks in the shallow subsurface are thrust as much as 1 km northeastward beneath the rocks on the opposite side of the San Andreas fault. To the south, near exposures of the gabbro of Logan, the fault is nearly vertical, but a few kilometers farther south it dips 70° SW. to at least 6-km depth, where low-density Pliocene sedimentary rocks are thrust beneath Mesozoic granitic rocks.

Northeast of the San Andreas fault, the area extending to the Silver Creek fault is subdivided into four blocks of Franciscan Complex that, in turn, are overlain near the two bordering faults by the Mesozoic Great Valley sequence (including the Coast Range ophiolite) and Tertiary sedimentary rocks. These faulted blocks are primarily delineated by curvilinear magnetic boundaries. The two southwestern blocks dip southwest and contain thick (2–4 km) slabs of magnetic serpentinite (Coast Range ophiolite) separated by northeastward-directed tectonic wedges of Franciscan rocks. The two northeastern blocks, though deformed in detail, are interpreted from their geophysical expression to be regionally horizontal, each block underlain by a subhorizontal floor thrust. These subhorizontal floor thrusts are interpreted to be wedge faults on the basis of their associations with the Coast Range ophiolite.

The geologic units northeast of the San Andreas fault, their geophysical expression, and their history and style of tectonic wedging are similar to those along the 600-km-long Franciscan-Great Valley contact 40 km east of the study area. We suggest that the blocks of Franciscan rocks in the Loma Prieta region were originally situated along the Franciscan-Great Valley contact near its present truncation by the San Andreas fault (at lat approx 36° N.) and were offset northwestward

during post-middle Miocene time along the San Andreas fault system to their present positions.

Comparison of our crustal model with the aftershock distribution indicates that nearly all hypocenters can be assigned to only three major faults: the San Andreas, Zayante, and Sargent faults. Many aftershocks whose epicenters plot away from the traces of these faults are associated with dipping fault segments. In particular, the San Andreas fault surface is locally curved, dipping gently northeast in the uppermost part of the crust and then bending back steeply southwest in the deeper parts. Epicenters of aftershocks on the curved segments of the San Andreas fault plot on both sides of its trace. Hypocenters appear to avoid our modeled configuration of the gabbro of Logan, but the mechanism by which this basement block influences the regional seismicity is unknown.

INTRODUCTION[1]

The 1989 Loma Prieta earthquake and its aftershocks occurred in a region of marked crustal complexity and diversity. The San Andreas fault itself marks a first-order break between a moderately deformed Mesozoic plutonic terrane (Salinia terrane) to the southwest and a highly deformed complex of accretion-related terranes (Franciscan Complex) and the Great Valley sequence to the northeast. Past movements on other major faults on both sides of the San Andreas fault have juxtaposed numerous crustal blocks with contrasting histories and properties. The crust that has resulted from assembly of these diverse blocks is characterized by profound variations in composition and physical properties, both laterally and vertically.

In a broad sense, the 1989 Loma Prieta earthquake and its aftershocks are a manifestation of continuing movement on the San Andreas fault system in the Santa Cruz Mountains. In detail, however, the specific relation of these events to the San Andreas fault proper is not so clear. No throughgoing pattern of surface rupture on the San Andreas fault was observed after the earthquake, and the aftershock distribution shows strong planar alignments that in some places lie well off the presumed subsurface fault position (Dietz and Ellsworth, 1990).

Because of the discrepancies noted above, questions have been raised concerning which fault actually ruptured during the earthquake and what role crustal structure may have played in localizing or modifying the rupture pattern. To address these questions and to provide a general picture of the geophysical and geologic setting of the earthquake, we have constructed a model for the subsurface structure and composition of the midcrust and upper crust beneath the Santa Cruz Mountains and adjacent southern Santa Clara Valley. This study was based mainly on an interpretation of local anomalies in the gravity and magnetic fields, relying heavily on the geologic information of McLaughlin and Clark (this chapter) and R.G. Coleman (written commun., 1991) to constrain our modeling. We also used some velocity and structural information from seismic tomography (Foxall and others, 1993). Our model by no means completely characterizes the midcrust and upper crust in the Loma Prieta region because it focuses mostly on those features that are reflected in the gravity and magnetic fields. Everywhere, however, we have attempted to link our crustal model directly to the surface geology and, in so doing, have projected the geology into the subsurface rather than simply inferring physical properties. In addition to providing structural information about the midcrust and upper crust, the resulting image of the subsurface carries important implications previously unrecognized about the tectonic development of the Loma Prieta region, as discussed below.

DATA SOURCES

GEOLOGY

The geologic maps (pls. 3A, 3B) were compiled principally from the data of Wentworth and Blake (1991; C.M. Wentworth and M.C. Blake, Jr., written commun., 1991) and from 7 1/2-minute quadrangle maps (McLaughlin and others, 1988b, 1991; Clark and others, 1989). Additional information was compiled from the geologic map of California (Jennings and Strand, 1958; Jennings and Burnett, 1961; Rogers, 1966) and from the reports by Clark and Rietman (1973), McCulloch and Greene (1990), and Wagner and others (1991). Information on the terranes consisting of Franciscan Complex was provided by R.J. McLaughlin (written commun., 1992). We have considerably simplified these geologic maps by generalizing the stratigraphy into only a few units that are relevant to our geophysical interpretation, by eliminating many faults deemed to be relatively minor, and by enlarging certain serpentinite masses to sizes that can be depicted at these map scales.

MAGNETIC FIELD

The primary source of magnetic-field data for this study is a detailed aeromagnetic survey of a 25-km-wide transect across the Santa Cruz Mountains, the southern Santa Clara Valley, and the southern Diablo Range flown by the U.S. Geological Survey (USGS) (Abrams and others, 1991) during late 1989 and early 1990 (see pl. 3A). Total-magnetic-field data were collected with a fixed-wing aircraft along flightlines (N. 75° W.) spaced 400 m apart at a nominal height of 150 m above the ground. Actual flight heights varied, depending on the ruggedness of the topography and the local population density (nominal flight height, 300 m over populated areas). This aeromagnetic survey covers the epicentral area of the 1989 Loma

[1]This study and the composition of the manuscript were completed in November 1993, and so this paper uses only the data and cited references that were available at that time.

Prieta earthquake and its aftershocks. Detailed profiles were extracted from the aeromagnetic survey to serve as the basis for most of the magnetic modeling discussed below.

Additional magnetic-field data of generally lower quality and less detail were assembled to provide a regional geophysical context for the detailed aeromagnetic survey described above. These data, which were from aeromagnetic surveys with a wide variety of flight heights and flightline spacings, were analytically merged into a consistent single data set that represents the magnetic field at 300 m above the ground (see pl. 3B). Jachens and Roberts (1993) provided details of the aeromagnetic surveys and merging procedures used to produce the regional magnetic map (pl. 3B).

GRAVITY FIELD

The regional gravity map of the southern San Francisco Bay region (pl. 3C), including the Loma Prieta region, was constructed mainly from data compiled for the isostatic-residual-gravity map of California and offshore southern California (Roberts and others, 1990), supplemented by more than 1,100 new observations on the San Francisco peninsula and in the mountains surrounding the southern San Francisco Bay region. More complete descriptions of the original data and their sources were given by Clark and Rietman (1973) or can be traced through the references listed on the following sheets of the California Division of Mines and Geology's "Bouguer Gravity Map of California": San Francisco sheet (Chapman and Bishop, 1968), San Jose sheet (Robbins and others, 1976), and Santa Cruz sheet (Bishop and Chapman, 1967).

The data are plotted on plate 3C as isostatic-residual-gravity values to emphasize those anomalies caused by density distributions in the midcrust and upper crust (uppermost approx 10–15 km) at the expense of anomalies from deeper density distributions that buoyantly support the topography in a manner consistent with the concept of isostasy (Jachens and Griscom, 1985). Standard procedures and formulas (for example, Telford and others, 1976) were used to reduce the observed gravity data to complete Bouguer gravity values, and an Airy-Heiskanen model of isostatic compensation (Heiskanen and Moritz, 1967) was used to further reduce the data to isostatic-residual-gravity values. Details of the gravity reduction procedures applied to the data were given by Roberts and Jachens (1993).

PHYSICAL PROPERTIES

Information on the densities and magnetic susceptibilities of the major lithologic units within the study area (see pls. 3A, 3B) was obtained mainly from measurements on hand specimens (table 1), although in a few places magnetic-susceptibility measurements were made directly on outcrops with portable susceptibility meters. The data of Ross (1972) on Mesozoic granitic rocks, of Bailey and others (1964) on sandstone and metasandstone of the Great Valley sequence and the Franciscan Complex, and of Brabb (1960) on Tertiary sedimentary rocks of the Santa Cruz Mountains, together with about 200 measurements by V.E. Langenheim (unpub. data, 1992) and additional measurements on about 500 samples from the collections of various U.S. Geological Survey geologists, constitute the 1,269-element physical-property data base available to this study. Summaries of density data relevant to this study were published by Chapman and Bishop (1968), Clark and Rietman (1973), Robbins and others (1976), and Carle and Langenheim (1990).

BASEMENT BLOCKS OF THE LOMA PRIETA REGION

A convenient way of characterizing the crustal structure of the Loma Prieta region is in terms of distinct basement blocks, defined on the basis of their geophysical and geologic expressions. At least seven such basement blocks occur in the study area (see pl. 3A). These basement blocks are not necessarily tectonostratigraphic terranes according to the standard definition (Howell and others, 1985), although some of them satisfy that definition and encompass such terranes. Many of the basement blocks are bounded by faults or probable faults, but others have bounding structures whose nature remains unclear.

CRUST SOUTHWEST OF THE SAN ANDREAS FAULT

Three major basement blocks make up the crust southwest of the San Andreas fault: (1) the Ben Lomond block (see McLaughlin and Clark, this chapter), bounded on the west by the San Gregorio fault and on the northeast by the Zayante fault and its southwestward continuation, the Vergeles fault (hereinafter referred to simply as the Zayante fault) and floored by Late Cretaceous granitic rocks that are exposed in the Ben Lomond pluton and the northern Gabilan Range (see pl. 3A; Clark and Rietman, 1973; Ross, 1984); (2) another block in the northern part of the study area, floored by unknown basement that might be a southward continuation of Late Cretaceous granitic rocks of the Montara pluton exposed on the San Francisco peninsula; and (3) the Logan block, an intervening block whose basement is almost totally concealed beneath Cenozoic sedimentary rocks and deposits but whose geophysical signature implies a primarily mafic igneous composition (figs. 1–3). The second and third blocks compose the La Honda block of McLaughlin and Clark (this chapter).

The basement of the Ben Lomond block, where exposed in the Ben Lomond pluton and the northern Gabilan Range (see pl. 3B), is composed of minor amounts of metasedimentary rocks intruded by Late Cretaceous plutons varying widely in

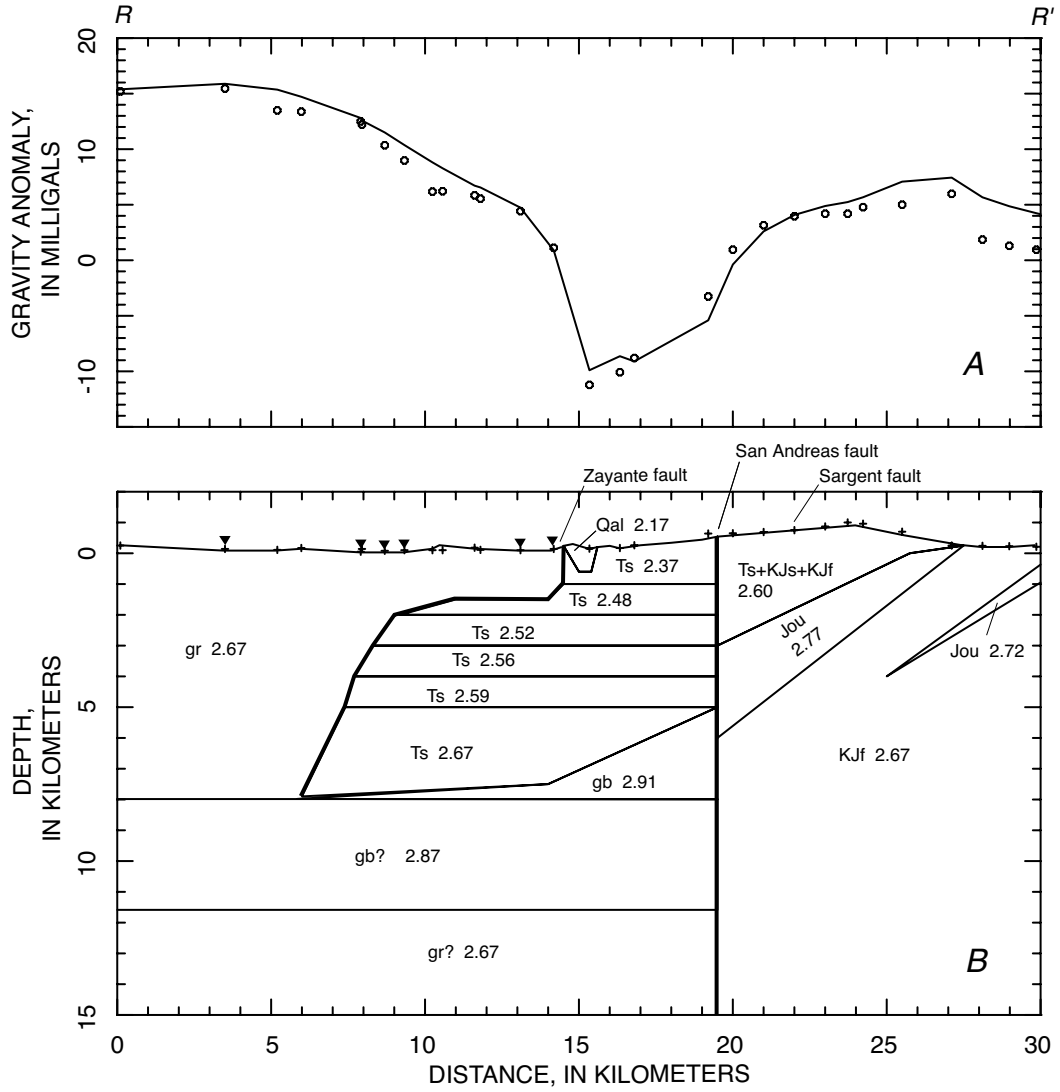

Figure 1.—Isostatic-residual-gravity profile (*A*) (circles, measured data; curve, calculated values) and density model (*B*) along line *R–R′* (pl. 3) across the Logan block between the Zayante and San Andreas faults. Most reliable part of density model is between km 0 and 25. Pluses, locations of gravity observations. Inverted triangles, gravity stations on granitic basement. Numbers on units are densities (in grams per cubic centimeter). Vertical density structure for Tertiary sedimentary rocks here and in figures 3, 5, 9, and 16 was determined by using variation in seismic velocity with depth (Foxall and others, 1993), converting to a variation of density with depth (Gardner and others, 1974) after adjusting resulting curve on the basis of densities of samples collected from surface outcrops and from cores from base of a 3.4-km-deep drill hole. Most important features of density model include the contorted Zayante fault, the vertical San Andreas fault, and a wedge-shaped mass of high-density (2.91 g/cm^3) gabbro (gb) below basin of low-density Tertiary sedimentary rocks between these two faults. High-density slab at base of model is included to account for high background gravity values over the Salinia terrane; actual density distribution responsible for this high background level may be a thin gabbroic body or may include entire lower crust. No vertical exaggeration. gr, granitic and older metamorphic rocks; Jou, Jurassic ultramafic rocks and serpentinite of the Coast Range ophiolite; KJf, Cretaceous and Jurassic Franciscan complex; KJs, Cretaceous and Jurassic sedimentary rocks; Qal, Quaternary alluvium; Ts, Tertiary sedimentary rocks.

composition, mainly quartz diorite in the Ben Lomond pluton and the northernmost Gabilan Range but more felsic farther south in the Gabilan Range (Ross, 1972, 1984; Clark and Rietman, 1973). Similar crystalline basement rocks penetrated by drill holes in the onshore area between the Ben Lomond pluton and the northern Gabilan Range (Clark and Rietman, 1973) are evidence for the continuity of this basement block in the subsurface between the two outcrop areas. The crystalline rocks of the Ben Lomond block are effectively nonmagnetic and produce no magnetic anomalies (see pl. 3B). The basement is overlain by a thin section of Cenozoic strata (typically <1 km thick), mainly of middle Miocene age and younger except along the north edge of the block, where the Butano Sandstone of Eocene age is exposed (Clark and Rietman, 1973; Wagner and others, 1991).

The Logan block is bounded at the surface on the northeast by the San Andreas fault, on the west by the San Gregorio fault, and on the southwest by the Zayante fault. Its north boundary is covered by Tertiary sedimentary rocks and defined by a magnetic gradient (see pl. 3B; fig. 2) but is difficult to locate precisely. The Logan block is not clearly associated with any major exposed structures. Its basement is exposed only as a thin sliver along the San Andreas fault near the southeast end of the block (see pls. 3B, 3C) where it is composed primarily of

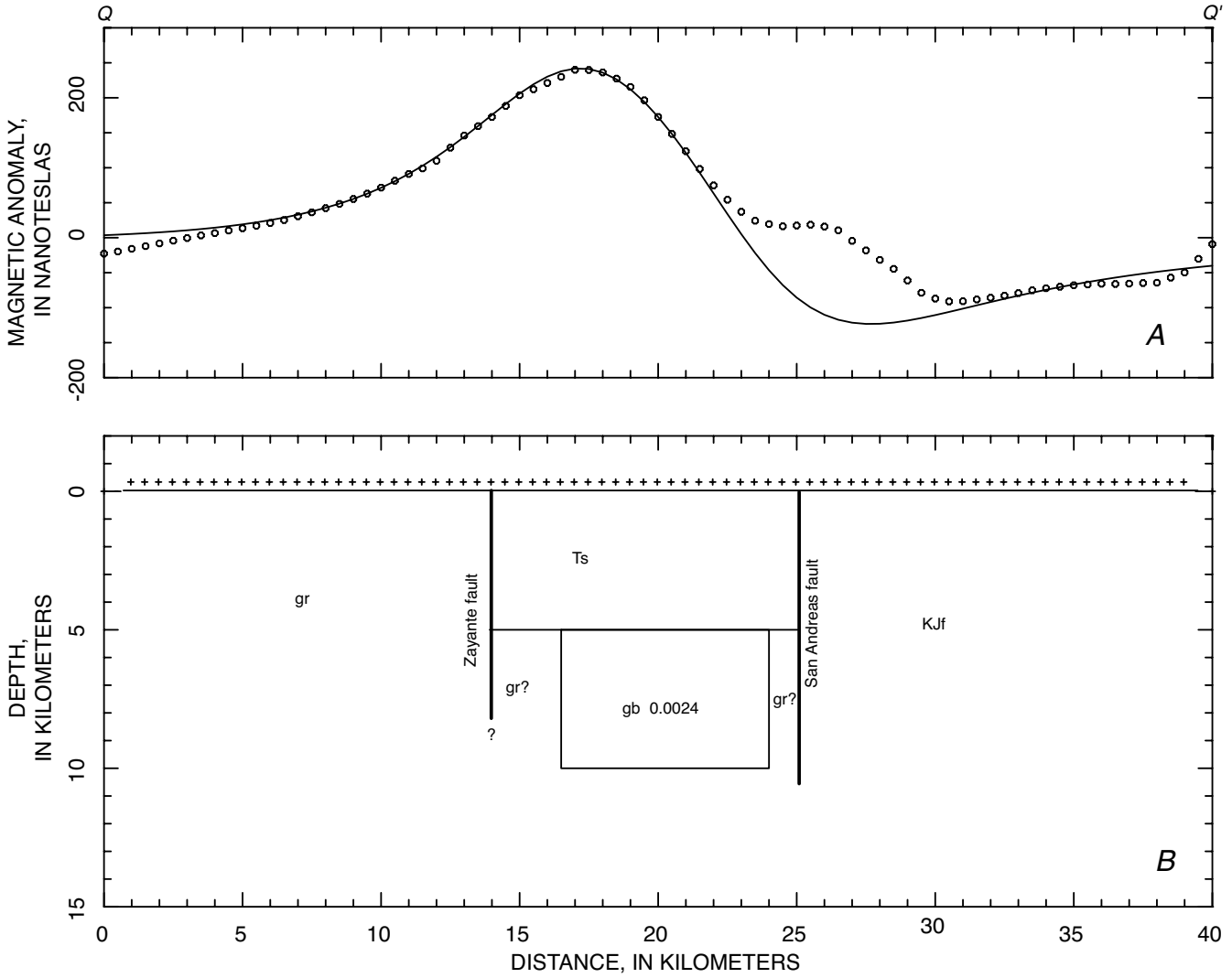

Figure 2.—Magnetic profile (*A*) (circles, measured data; curve, calculated values) and magnetic model (*B*) along line *Q*–*Q′* (pl. 3) across the Logan block between the Zayante and San Andreas faults. Pluses, locations of magnetic observations. In figure 2*B*, rectangular body of magnetic gabbro (gb) underlies sedimentary basin bounded by the Zayante and San Andreas faults; number is magnetization (in electromagnetic units per cubic centimeter). Anomaly between km 24 and 29 is caused by an ophiolitic body bounded by magnetic boundary 1A and is located northeast of the San Andreas fault. No vertical exaggeration. gr, granitic and older metamorphic rocks; KJf, Cretaceous and Jurassic Franciscan complex; Ts, Tertiary sedimentary rocks.

two unusual plutonic rock types: a hornblende-quartz gabbro and a less common, foliated anorthositic gabbro (Ross, 1970, 1972). According to Ross (1970, 1972), these rocks are unlike any other plutonic rocks in the Coast Ranges southwest of the San Andreas fault (Salinia terrane). A U-Pb zircon age of 161 Ma for these gabbros (James and others, 1986), significantly older than the Late Cretaceous ages typical of granitoids of the Salinia terrane, is additional evidence for the unusual composition of these rocks. Both types of gabbro are extremely dense relative to other plutonic rocks of the Salinia terrane (table 1). Although the hornblende-quartz gabbro also is highly magnetic (as implied by the strong magnetic anomaly over its outcrop area), the anorthositic gabbro appears to be, at most, only weakly magnetic, on the basis of the absence of a strong magnetic anomaly over the southern part of its outcrop area. The magnetic properties inferred from the magnetic map (pls. 3A, 3B) are supported by magnetic-susceptibility measurements on a few samples of both types of gabbro (table 1).

The highly magnetic properties of the hornblende-quartz gabbro relative to other plutonic and sedimentary rocks in the study area (see pls. 3A, 3B) permit this body to be traced by its magnetic anomaly even where concealed beneath many

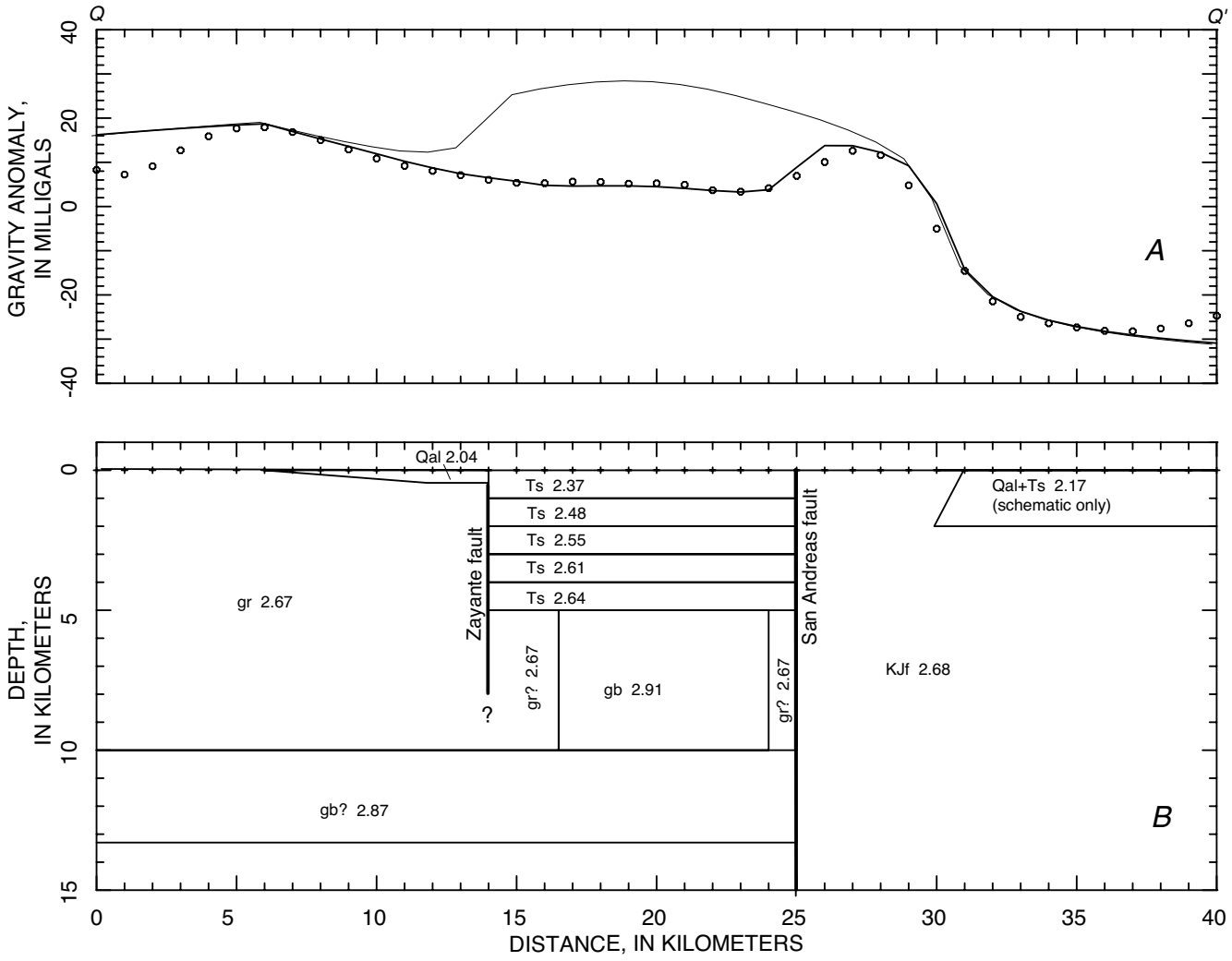

Figure 3.—Isostatic-residual-gravity profile (*A*) (circles, measured data sampled from gridded gravity map; curve, calculated values) and density model (*B*) along line *Q*–*Q′* (pl. 3) across the Logan block between the Zayante and San Andreas faults. Pluses, locations where gravity was calculated. Numbers on units are densities (in grams per cubic centimeter). Density model is consistent with magnetic model (fig. 2*B*) and with sedimentary-rock densities modeled in figure 1. See figure 1 for explanation of high-density slab at base of density model. The Zayante fault does not cause a gravity gradient, because of young thin sedimentary basin shown on left side of fault. In figure 3*A*, thin curve is gravity calculated from density model with sedimentary section stripped away—that is, with all density contrasts in sedimentary section set to zero. No vertical exaggeration. gb, gabbro; gr, granitic and older metamorphic rocks; KJf, Cretaceous and Jurassic Franciscan complex; Qal, Quaternary alluvium; Ts, Tertiary sedimentary rocks.

Table 1.—*Densities and magnetic susceptibilities of rock samples collected in the San Francisco Bay area, Calif.*
[Do., ditto]

Rock type	Number of samples	Density (g/cm^3)		Magnetic susceptibility (10^{-3} cgs units)	
		Mean±1σ	Median	Mean±1σ	Median
Franciscan Complex					
Chert	13	2.62±0.06	2.63	0.0	0.0
Greenstone	29	2.88±0.09	2.90	.1±0.2	.1
Limestone	7	2.66±0.05	2.67	.0	.0
Sandstone and metasandstone	448	2.66±0.11	2.66	– – –	– – –
Do	75	– – –	– – –	.0±0.0	.0
Salinia terrane					
Ben Lomond Mountain pluton	80	2.68±0.06	2.66	– – –	– – –
Do	47	– – –	– – –	.0±0.1	.0
Gabilan Range plutons	74	2.67±0.04	2.66	– – –	– – –
Montara Mountain pluton	48	2.68±0.06	2.69	– – –	– – –
Do	25	– – –	– – –	.1±0.1	.1
Gabbro of Logan	11	2.91±0.08	2.92	– – –	– – –
Do	3	– – –	– – –	1.4±0.4	1.3
Coast Range ophiolite					
Mafic rocks	8	2.68±0.10	2.85	.3±0.5	.1
Serpentinite	56	2.42±0.27	2.41	1.3±0.9	1.2
Cenozoic and Mesozoic sedimentary rocks					
Sandstone (Miocene and Oligocene)	40	2.30±0.22	2.29	.0	.0
Sandstone (Eocene)	61	2.49±0.12	2.53	.0	.0
Sandstone (Cretaceous)	14	2.59±0.07	2.59	– – –	– – –
Do	4	– – –	– – –	.0	.0
Sandstone of the Purisima Formation	15	– – –	– – –	.7±0.3*	.6

*Values of 0.4×10^{-3} to 0.6×10^{-3} cgs units were obtained from modeling the topography magnetically where sandstone of the Purisima Formation makes up the topography, and then comparing the results to the aeromagnetic map (pls. 3A, 3B). Similar values were obtained from more than 100 direct measurements on outcrops and in roadcuts.

kilometers of nonmagnetic material. Modeling of the magnetic data along line *S*–*S′* across the gabbro outcrop (fig. 4) indicates that, as Ross (1972) speculated, the outcrop is the top of a thin (1–2 km wide) sliver within the San Andreas fault zone. Our model also shows, however, that this thin sliver connects at depth with a more extensive, flat-lying gabbro body (in places nearly 5 km thick) that makes up, in part, the basement of the Logan block. Similar modeling and inferences based directly on the magnetic map (pl. 3B) indicate that the magnetic gabbro extends in the subsurface westward from the San Andreas fault to approximately the location of the major magnetic boundary (dashed line, pl. 3B). Note that this magnetic boundary represents the inferred minimum westward extent of the hornblende-quartz gabbro and, as such, indicates the minimum westward extent of the Logan block in the subsurface. Nonmagnetic basement rocks or deeper magnetic basement rocks of the Logan block could extend beyond this limit.

All the magnetic models of the basement of the Logan block indicate that the magnetic gabbro of Logan is a slablike body which does not extend below about 10-km depth. The crust immediately below the gabbro is significantly less magnetic, has a density that is poorly constrained by gravity data (most likely avg >2.67 g/cm^3), and has a *P*-wave velocity of more

than 6 km/s (Michael and Eberhart-Phillips, 1991; Foxall and others, 1993). Although the magnetic properties of the crust immediately beneath the gabbro of Logan serve to distinguish it from the gabbro, the seismic velocity and poorly defined density of the gabbro of Logan are compatible with those of several different rock types (Christensen, 1982).

Most of the basement of the Logan block is overlain by a thick Tertiary section of predominantly marine clastic rocks, ranging in age from Paleocene or Eocene to Pliocene, that, in turn, is covered in places by a thin mantle of Quaternary deposits (Clark and Rietman, 1973). The Tertiary section alone is more than 6 km thick and has been deformed into both broad and tight folds with axes subparallel to the trend of the San Andreas fault and the long axis of the Logan block. The Tertiary sedimentary rocks, which are significantly less dense than either granitic rocks of the Ben Lomond block or basement rocks of the Logan block (table 1), are the source of the linear gravity low over the Logan block that extends northwestward from the north edge of the Gabilan Range, a distance of more than 45 km. As discussed below, the absence of a pronounced gravity low over the north and, to some extent, south ends of the Logan block probably reflects a thickening of the slab of high-density gabbro basement rather than a thinning of the overlying sedimentary sequence. The sedimentary rocks are mostly nonmagnetic except for the Pliocene Purisima Formation, which, on the basis of field observations, contains high concentrations of detrital magnetite. Sedimentary rocks of the Purisima Formation are the source of both the linear magnetic anomaly that lies just northeast of and parallel to the Zayante fault (see pl. 3A), and the linear magnetic anomaly 8 km to the east, immediately southwest of the San Andreas fault, as well as of most of the low-amplitude, short-wavelength magnetic anomalies on the Ben Lomond block (see pl. 3A), because here Purisima rocks make up the topography and the magnetic anomalies reflect this topographic surface.

The northernmost block within the study area (see pl. 3A), southwest of the San Andreas fault, abuts the Logan block to the south and is bounded by the San Gregorio fault on the southwest and by the San Andreas and Pilarcitos faults on the northeast. The basement boundary between these two blocks is completely concealed beneath Tertiary sedimentary strata. The gravity and magnetic maps (pl. 3), however, indicate by their gradients that the basement rocks of the northernmost block are significantly less magnetic and probably less dense than those of the Logan block, properties similar to those of Late Cretaceous granitic rocks of the Montara pluton (see pl. 3B), the nearest basement outcrop north of the Logan block. The contact, which trends northwest, is interpreted to be a fault because of its linearity and the greater age of the gabbro of the Logan block relative to other nearby plutonic rocks of the Salinia terrane (James, 1992). The associated magnetic anomaly indicates that this contact is subparallel to the Butano fault but offset from it by about 4 to 5 km to the north-northeast. Although the parallelism between the Butano fault trace and the buried north-northeast edge of gabbroic basement of the Logan block suggests that the two features are related, their coincidence at depth is difficult to support because the relative positions of the Butano fault and the buried basement contact would require a moderate northeastward dip, whereas geologic evidence indicates that the Butano fault dips steeply southwest (Cummings and others, 1962).

BLOCK BOUNDARIES SOUTHWEST OF THE SAN ANDREAS FAULT

The faults or other structures that separate the crustal blocks southwest of the San Andreas fault typically are sites of abrupt changes in density and (or) magnetic susceptibility and so are generally characterized by gravity and (or) magnetic anomalies. Where such anomalies occur, the potential-field data provide the means for defining the subsurface position and configuration of the block boundaries through modeling. Although all such model interpretations are inherently ambiguous, within the study area (see pl. 3C) independent constraints on the modeling imposed by measured lithologic properties, geologic mapping, and other geophysical interpretations effectively reduce the ambiguity, such that meaningful geologic conclusions can be reached. The following geophysical discussion of the subsurface configuration of block boundaries progresses from southwest to northeast.

The San Gregorio fault at the mouth of Monterey Bay (see pl. 3A) is marked over a distance of more than 60 km by a magnetic gradient (high to the southwest), indicating that nonmagnetic basement rocks of the Ben Lomond block are in contact with a magnetic crustal block to the southwest (see pl. 3B). The magnetic gradient extends northwestward and continues even to where the Logan block abuts the San Gregorio fault, probably because the top of magnetic crust southwest of the fault is much shallower than the magnetic basement of the Logan block. Models along the lines crossing this anomaly (for example, fig. 6) indicate that within the study area the magnetic boundary, presumably the San Gregorio fault, dips 50°–70° NE. Seismic-reflection surveys of the offshore area immediately southwest of the San Gregorio fault reveal a 15-km-wide zone of young folds and similar northeast-dipping thrust faults that approximately parallels the San Gregorio fault (Lewis, 1996).

Both gravity and magnetic modeling require that the Logan block extends southwestward beneath the Ben Lomond block, implying that the Zayante fault dips southwest. The inferred minimum southwest limit of magnetic basement rocks of the Logan block (see pl. 3B) in places is more than 10 km southwest of the trace of the Zayante fault. Because the top of crystalline basement of the Logan block lies at about 5- to 7-km depth, on the basis of seismic tomography (Foxall and others, 1993; see Eberhart-Phillips and Michael, this chapter) and magnetic modeling (fig. 2), we conclude that the Zayante fault dips southwest along much of its length, in places at an average angle of less than 45°. This conclusion is supported

by the gravity profile along line *R–R′* (fig. 1), which shows that early Tertiary sedimentary rocks of the Logan block here continue laterally at least 6 km beneath a thin lip of granitic basement of the Ben Lomond block (see pl. 3C). Also, a three-dimensional velocity model of this area (Foxall and others, 1993; Eberhart-Phillips and Michael, this chapter) shows low-velocity (<5 km/s) material continuing southwestward of the Zayante fault trace to 3- to 5-km depth, where drill-hole logs indicate crystalline basement to be generally less than 1 km deep (Clark and Rietman, 1973). The Zayante fault, however, lies near the southwest limit of the crustal volume that is well resolved in the velocity models.

Although both gravity and magnetic data indicate that the Logan block continues in the subsurface southwestward of the Zayante fault, the two data sets reflect different elements of this block. Specifically, the magnetic anomalies indicate the shape and position of the gabbroic basement, whereas the gravity anomalies primarily reflect the distribution of Tertiary sedimentary rocks.

Although the San Andreas fault does not produce conspicuous, continuous geophysical anomalies in the study area (see pl. 3), isolated gravity and magnetic anomalies provide important information on the subsurface configuration of the fault surface. The gravity profile along the line *R–R′* (fig. 1)

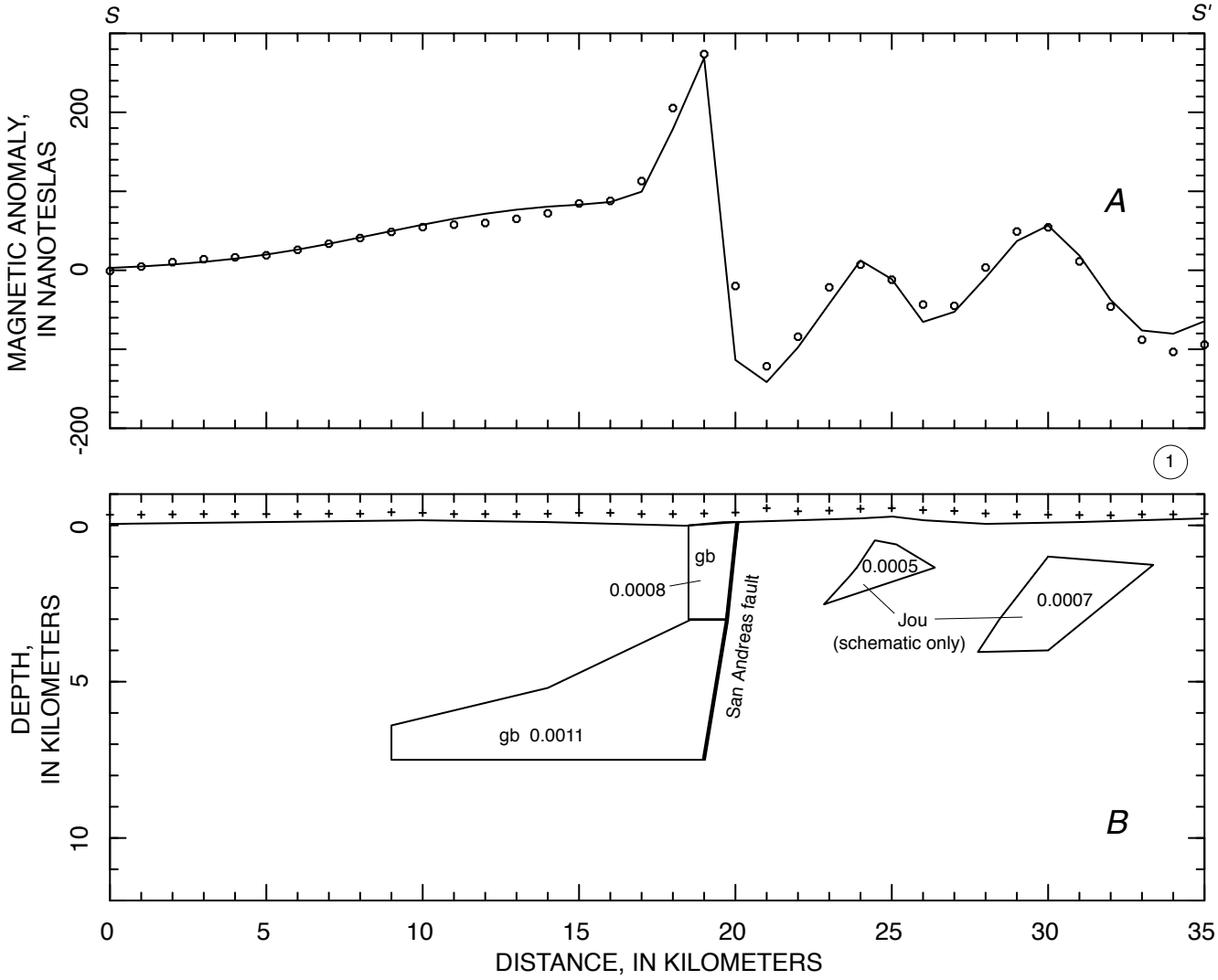

Figure 4.—Magnetic profile (*A*) (circles, measured data; curve, calculated values) and magnetic model (*B*) along line *S–S′* (pl. 3) across the Logan block between the Zayante and San Andreas faults. Pluses, locations of magnetic observations. Numbers on units are magnetizations (in electromagnetic units per cubic centimeter). Most important features of magnetic model include calculated dip of the San Andreas fault and shapes of sliver of gabbro (gb) and wedge-shaped mass of gabbro beneath basin of Tertiary sedimentary rocks. Note magnetic boundary 1, magnetic slab southwest (left) of it, and absence of magnetic slab extending to the San Andreas fault—that is, "hole" in slab near San Andreas fault. No vertical exaggeration. Jou, Jurassic ultramafic rocks and serpentinite of the Coast Range ophiolite.

indicates that the San Andreas fault is vertical in the upper 3 to 4 km of the crust and probably remains vertical to at least 6- to 7-km depth. Starting about 4 km southeast of the point where line *R*–*R′* crosses the San Andreas fault, and extending southeastward along the fault a distance of about 10 km, a linear magnetic anomaly (see pl. 3A) indicates that magnetic sedimentary rocks of the Purisima Formation, which here are confined to the Logan and Ben Lomond blocks southwest of the fault, extend in the shallow subsurface as much as 1 km northeastward of the fault trace (see pl. 3A). The magnetic sedimentary rocks here are only 1 to 1.5 km thick, and so the deeper parts of the fault are undefined. Nevertheless, the fact that Purisima rocks are thrust beneath older sedimentary rocks northeast of the fault suggests that, in places, the near-surface position of the San Andreas fault could be well to the northeast of its mapped position, although the distribution of aftershocks (Dietz and Ellsworth, 1990) suggests that, at depth, the fault dips steeply southwest. Farther southeast, the San Andreas fault forms the northeast face of the sliver of magnetic basement rocks of the Logan block exposed along the fault zone. The magnetic model along line *S*–*S′* (fig. 4*B*), which crosses the northwest end of this sliver, indicates that in the well-constrained upper 3 km of the model, the fault dips steeply southwest. Near the north end of the Gabilan Range,

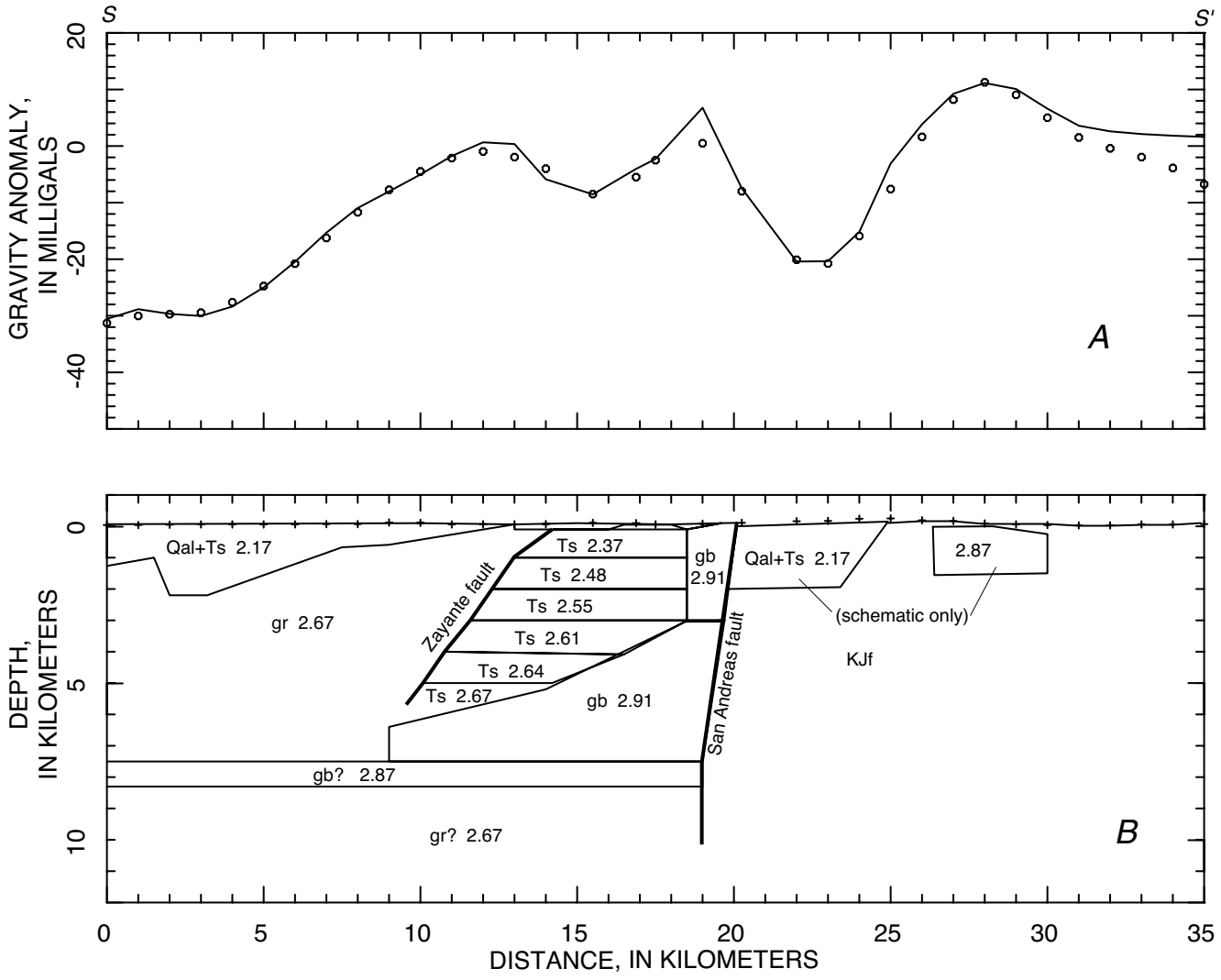

Figure 5.—Isostatic-residual-gravity profile (*A*) (circles, measured data sampled from gridded gravity map; curve, calculated values) and density model (*B*) along line *S*–*S′* (pl. 3) across the Logan block between the Zayante and San Andreas faults. Pluses, locations where gravity was calculated. Numbers on units are densities (in grams per cubic centimeter). Model is consistent with magnetic model (fig. 4*B*) and with sedimentary-rock densities modeled in figure 1. Most important features of density model include dip of the Zayante fault and configuration of sedimentary basin of the Logan block. Block of low-density material to right (northeast) of the San Andreas fault is schematic. See figure 1 for explanation of high-density slab at base of model. No vertical exaggeration. gb, gabbro; gr, granitic and older metamorphic rocks; KJf, Cretaceous and Jurassic Franciscan complex; Qal, Quaternary alluvium; Ts, Tertiary sedimentary rocks.

about 15 to 20 km southeast of line *S–S′*, the San Andreas fault separates Cenozoic sedimentary rocks on the northeast from plutonic rocks of the Ben Lomond block (see pl. 3C). The fault trace lies near the bottom of the gravity low caused by Cenozoic sedimentary rocks (see pl. 3C), indicating that these sedimentary rocks extend in the subsurface southeastward beneath the plutonic rocks. Modeling of this gravity anomaly (Pavoni, 1973) suggests that the fault dips about 70° SW. at least to the depth resolved by this model, about 6 km.

CRUST NORTHEAST OF THE SAN ANDREAS FAULT

The part of the study area (see pl. 3B) northeast of the San Andreas fault is difficult to subdivide clearly into crustal blocks because it is structurally much more complex than that to the southwest. Using a combination of gravity, magnetic, and geologic data, however, we can subdivide the exposed crust northeast of the San Andreas fault and southwest of the Silver Creek and Calaveras faults into four major basement blocks bounded by faults. Although these basement blocks, to some extent, appear to be represented by tectonostratigraphic terranes as mapped by Blake and others (1984) and McLaughlin and others (1991), detailed geologic mapping of terranes in this area is by no means without uncertainties, and the final movements along some or, possibly, all of our block-bounding faults appear to postdate faulting that took place when the terranes were originally amalgamated.

We summarize the geology of this part of the study area (see pl. 3B) principally from the work of McLaughlin and others (1991) (see McLaughlin and Clark, this chapter). Adjacent to the San Andreas fault and bounded on the northwest side by segments of the Aldercroft, Sierra Azul, and Berrocal faults and the southern section of the Sargent fault (see pl. 3A) is an isolated layered sequence of Mesozoic and Cenozoic rocks (Sierra Azul block of McLaughlin and Clark, this chapter; see McLaughlin and others, 1991) consisting of (1) the basal Coast Range ophiolite (unit Jou), with its lower part of serpentinized ultramafic rocks and its upper mafic part overlain

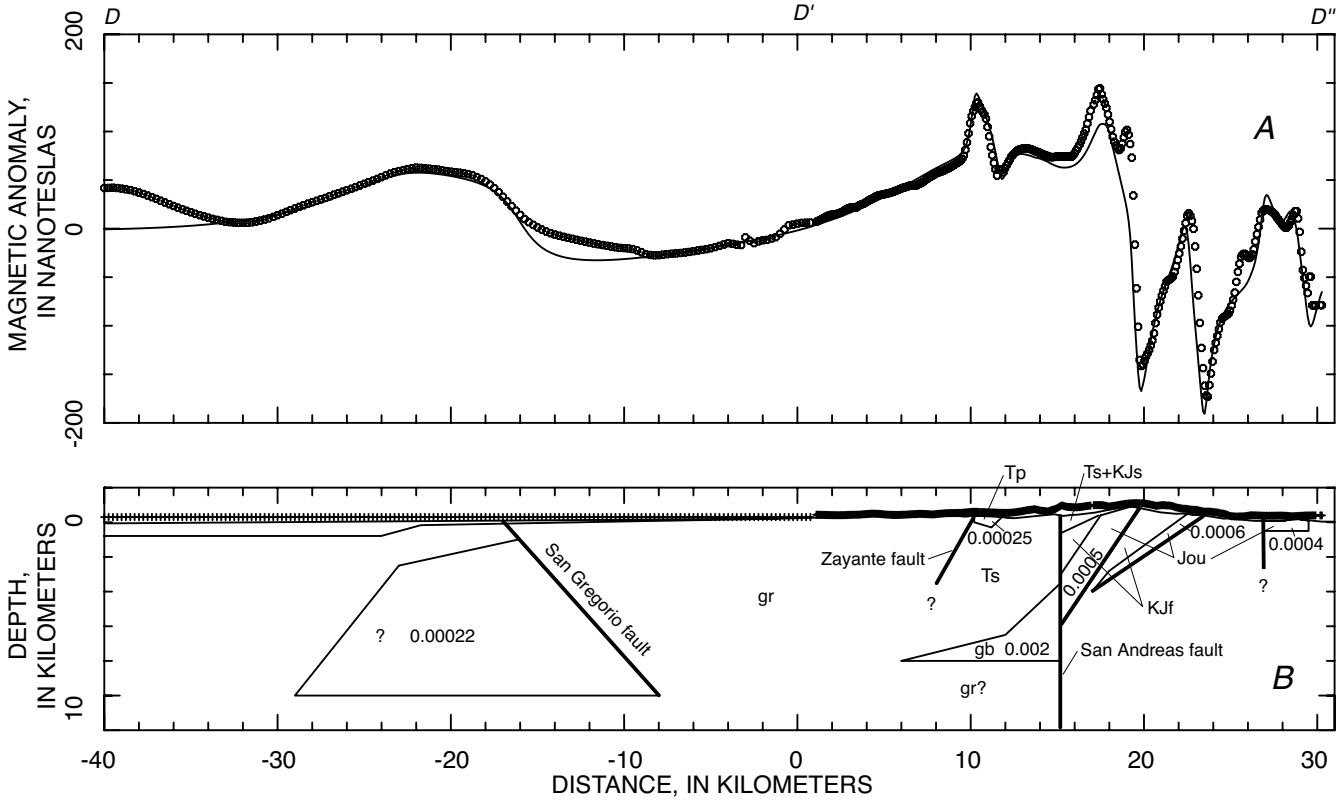

Figure 6.—Magnetic profile (*A*) (circles, measured data; curve, calculated values) and magnetic model (*B*) along line *D–D′–D″* (pl. 3) across the San Gregorio fault. Pluses, locations of magnetic observations. Numbers on units are magnetizations (in electromagnetic units per cubic centimeter). Magnetic-anomaly sources west (to left) of the San Andreas fault appear to have considerable depth extent. Most important feature is unexpectedly shallow northeastward dip of the San Gregorio fault. See figure 7 for details in northeast half of model. No vertical exaggeration. gb, gabbro; gr, granitic and older metamorphic rocks; Jou, Jurassic ultramafic rocks and serpentinite of the Coast Range ophiolite; KJf, Cretaceous and Jurassic Franciscan complex; KJs, Cretaceous and Jurassic sedimentary rocks; Qal, Quaternary alluvium; Ts, Tertiary sedimentary rocks.

by (2) sequences of Jurassic and Cretaceous sedimentary rocks (unit KJs) that include as much as about 200 m of the lower part of the Great Valley sequence, overlain by as much as 1,600 m of Late Cretaceous sedimentary rocks, which, in turn, are overlain by (3) a sequence of Tertiary sedimentary rocks (unit Ts) of Eocene and Oligocene or early Miocene age. Northeast of this isolated block is a series of terranes that here collectively form the Franciscan Complex, a Late Jurassic to Cretaceous subduction complex consisting predominantly of metamorphosed turbiditic graywacke, siltstone, shale, and lesser amounts of chert and volcanic rocks. Additional rocks that characteristically occur in melange of the complex are serpentinite, limestone, and blocks of high-pressure-metamorphic rocks. All, or nearly all, of the serpentinite is considered to be derived from the Coast Range ophiolite (R.G. Coleman, written commun., 1991; McLaughlin and others, 1991). For structural reasons, following McLaughlin and others (1991), we have subdivided the Franciscan Complex on our geologic maps (pls. 3A, 3B) into three northwest-trending belts of rocks, described as follows, from southwest to northeast: (1) the Bald Mountain-El Sombroso terrane (unit KJf_1), predominantly metasandstone and argillite, with associated metabasalt flows and radiolarian chert, especially along the eastern part of the belt; (2) the Permanente terrane (unit KJf_2), predominantly metabasalt flows, with lesser amounts of limestone, chert, argillite, and graywacke (Sliter and others, 1991); and (3) unspecified terranes (unit KJf_3), predominantly argillite and graywacke, metabasalt, and serpentinite.

In the northeast corner of this part of the study area are two smaller patches of Mesozoic sedimentary rocks (unit KJs, pl. 3A) correlative with the Great Valley sequence and in fault contact with the Franciscan Complex. Overlying the larger of these two patches (in the Santa Teresa Hills) are Tertiary (Eocene) sedimentary rocks, similar to those in the isolated block (previously described) adjacent to the San Andreas fault. In this northeast corner near the Silver Creek fault are also several small patches of mafic rocks associated with serpentinite (unit Jou); collectively, these rocks are considered to be Coast Range ophiolite (R.G. Coleman, oral commun., 1991) Small isolated patches of younger Tertiary (early to middle Miocene) sedimentary rocks (unit Ts) that are distributed irregularly throughout this part of the study area lie unconformably and (or) are faulted over Franciscan rocks. A series of Pliocene mafic volcanic rocks (unit Tv) are locally associated with the Silver Creek and Calaveras faults. Pliocene and Quaternary alluvial deposits (unit Qal) cover some older rocks.

Magnetic properties of the lithologic units in this part of the study area (see pls. 3A, 3B) are reflected both in magnetic-susceptibility measurements on rock samples and in the distribution of magnetic anomalies relative to the underlying rocks. Magnetic-susceptibility measurements on rock samples (table 1) indicate that the serpentinite and serpentinized ultramafic rocks are highly magnetic, whereas the mafic rocks of the Coast Range ophiolite are only weakly magnetic. The metavolcanic rocks (greenstone) of the Franciscan Complex mostly range from nonmagnetic to weakly magnetic because the low-grade metamorphism has destroyed the bulk of their original magnetite. The sedimentary rocks and deposits of all ages are essentially nonmagnetic, with the local exception of the Pliocene Purisima Formation, as described above in the subsection entitled "Crust Southwest of the San Andreas Fault." These results from rock samples are fully confirmed by examining the correlation of the magnetic map with the geologic map (pl. 3A). Nearly all outcrops of serpentinized ultramafic rocks produce magnetic anomalies, whereas the large areas of Franciscan metavolcanic rocks (not shown on pl. 3) within the Permanente terrane do not produce significant magnetic anomalies. The mafic components of the Coast Range ophiolite near the San Andreas fault do not display conspicuous magnetic anomalies, even where the rocks form topographic highs and so were close to the magnetometer. The much younger volcanic rocks in restricted amounts near the Silver Creek and Calaveras faults produce high-amplitude, narrow magnetic highs and lows, attesting to their intense remanent magnetizations.

The densities of the rock types that occur northeast of the San Andreas fault are listed in table 1. Metavolcanic rocks (greenstone) of the Franciscan Complex and mafic rocks of the Coast Range ophiolite are significantly denser than most other rocks in the study area (see pl. 3). The densities of serpentinite samples (serpentinized ultramafic rocks) vary widely, as indicated by the large standard deviation associated with the measurements on 56 samples, but on average are lower than those of most pre-Tertiary rocks. The sedimentary rocks generally increase in density with increasing age; the average densities of Pliocene and Quaternary deposits are lower than those shown for Oligocene and Miocene sandstones.

BLOCK BOUNDARIES NORTHEAST OF THE SAN ANDREAS FAULT

Certain major curvilinear magnetic anomalies (see pls. 3A, 3B) extend across the part of the study area northeast of the San Andreas fault. To locate the boundaries of the anomaly sources, we used an automatic technique (Cordell and Grauch, 1985; Blakely and Simpson, 1986). After integrating the magnetic map to produce the pseudogravity map, this technique calculates the locations of the maximum horizontal gradients on the anomaly margins and at these locations plots a sinuous series of dots that represents the pseudodensity boundaries—in other words, the boundaries of the magnetic rocks. This method depends on the theoretical observation that gravity-anomaly (or pseudogravity) gradients tend to be steepest over the edges of gravity sources. These boundaries were then extended and connected visually on an overlay of the magnetic map (pl. 3A) to form the magnetic boundaries that subdivide the northeastern part of the study area into four major blocks; these magnetic boundaries are numbered from 1 to 3 and display two lesser branches numbered 1A and 2A. We consider these three magnetic boundaries to represent major faults, and the subsequent calculated geophysical models display our interpretation of their geologic significance.

Comparisons of these magnetic boundaries and blocks with the geologic map (pl. 3A) yield the following associations and relations.

1. The block between the San Andreas fault and magnetic boundary 1 is characterized by a major magnetic high and is composed of two different structural elements: (1) the northwestern part of the block, which consists of an isolated geologic terrane of Mesozoic ophiolite and sedimentary rocks overlain by Tertiary sedimentary rocks collectively referred to as the Sierra Azul structural block by McLaughlin and others (this chapter); and (2) the southeastern part of the geophysically defined block, which is composed of the Franciscan Complex. Magnetic boundary 1 is defined as the northeast contact of a large mass of magnetic rocks and closely follows parts of the Aldercroft, Sierra Azul, and Berrocal faults where they bound the Sierra Azul structural block. Moderately continuous masses of serpentinite occur along these parts of magnetic boundary 1, apparently in association with the lower part of the Coast Range ophiolite. Nevertheless, along magnetic boundary 1 to the southeast, its southeast end diverges eastward from the Berrocal fault and extends across the Franciscan Complex, approximately (but not exactly) following the southeast side of the Permanente terrane. The magnetic high associated with this block (see pl. 3B) is terminated in the southeast by the Calaveras fault, which also terminates magnetic boundary 1. Magnetic boundary 1 is probably the strongest and most consistent magnetic feature within the study area northeast of the San Andreas fault, and we regard its substantial southeastward divergence from the Berrocal fault as an important factor in our structural interpretations of this part of the study area. This divergence indicates that it is incorrect to interpret the source of the magnetic high simply to be serpentinite in the layer of Coast Range ophiolite at the base of the lower part of the Great Valley sequence (combined in unit KJs, pl. 3A) because to the southeast the magnetic rocks mostly underlie the Franciscan Complex. A separate northwesterly branch off magnetic boundary 1 (magnetic boundary 1A, pl. 3A) extends into the next block to the northeast but, as for magnetic boundary 1, forms the northeast boundary of a mass of magnetic rocks. This magnetic boundary follows the Berrocal fault and then swings westward along the Lime Kiln fault in a bend similar to that in magnetic boundary 1 at the Aldercroft fault; the similarity in shape thus suggests a relation between these two boundaries. Farther northwest (see pl. 3B), magnetic boundary 1A converges with and is ultimately truncated by the San Andreas fault. Along much of its northern part, magnetic boundary 1A appears to follow the southwest side of the Permanente terrane and is intermittently associated with small serpentinite masses.
2. The block between magnetic boundaries 1 and 2 is composed of the Franciscan Complex, specifically the Permanente terrane and the Bald Mountain-El Sombroso terrane. Magnetic boundary 2 approximately follows the northeast geologic contact of the Permanente terrane and correlates with the northeast side of a zone of sheared melange originally mapped by Bailey and Everhard (1964) that contains numerous blocks of blueschist. Magnetic boundary 2 is defined geophysically as the southwest border of a series of nearly continuous magnetic anomalies that are caused by nearly continuous curvilinear masses of serpentinite associated with the third block and lying northeast of magnetic boundary 2. Northwest of line *D–D′* (pl. 3A), the magnetic boundary is located within the Permanente terrane because here the magnetic serpentinite masses lie within the terrane. The block bounded by magnetic boundaries 1 and 2 contains few magnetic anomalies other than those along the southwest side of magnetic boundary 1A, which are caused by a belt of serpentinite.
3. The block between magnetic boundaries 2 and 3 consists of an assemblage of Franciscan metavolcanic and metasedimentary rocks and abundant small masses of serpentinite, which cause various small, irregular magnetic highs. Magnetic boundary 2A, which is located within this block, is similar to magnetic boundary 2 in that both are located as the south or southwest boundaries of magnetic serpentinite belts. The north boundary of the block (magnetic boundary 3) is a continuous linear magnetic boundary on the south side of a coherent magnetic feature. Where it coincides with the south margin of exposed serpentinite, this magnetic boundary may partly correspond to the Shannon fault.
4. The block between magnetic boundary 3 and the Silver Creek fault is composed predominantly of magnetic serpentinite and mafic components of the Coast Range ophiolite, together with metasedimentary rocks of the Franciscan Complex and, importantly, some sedimentary rocks of the Great Valley sequence (lower part of unit KJs, pl. 3*A*) that are not unexpected, considering the large amount of basal Coast Range ophiolite exposed in this block. The metasedimentary rocks were mapped as part of the Central belt of the Franciscan Complex by Blake and others (1984), which they defined as the melange matrix enclosing other Franciscan terranes.

In addition to the curvilinear magnetic features and the obvious correlations of magnetic highs with serpentinite, a smaller but significant number of other subcircular and irregular magnetic anomalies are associated with the localities of Franciscan rocks northeast of the San Andreas fault. We suggest that most of these other anomalies are caused by isolated masses of serpentinite that have not yet been mapped or are buried but that, on the basis of magnetic-gradient studies, are present at depths of less than a few hundred meters below the surface.

THREE-DIMENSIONAL STRUCTURE NORTHEAST OF THE SAN ANDREAS FAULT

In the preceding section, we described the magnetic map (pls. 3A, 3B) and its relations to geology mainly in terms of

plan view. Here, we show two-dimensional geophysical models of the data in order to describe the geologic and geophysical structure of the study area in three dimensions. We display about half of the models that we have actually calculated, using those that best illustrate the subsurface structure.

The magnetic anomaly bounded to the northeast by magnetic boundary 1 is modeled from the magnetic profiles along lines *D–D′* (fig. 7*A*) and *E–E′* (fig. 8*A*). The magnetic models show a magnetic slab, 2 to 3 km thick, that dips 45°–55° SW. until cut off by the San Andreas fault. The slab is too magnetic to contain significant amounts of weakly magnetic mafic material from the Coast Range ophiolite, and so is presumed to be composed substantially of serpentinite or partially serpentinized ultramafic rocks. This slab cannot contain significant amounts of unserpentinized ultramafic rocks, or it would produce a correlative gravity high. Examination of the gravity map (pl. 3C) shows that at the northwest end of magnetic boundary 1 (along the Aldercroft fault), the gravity high in this area (12- and 14-mGal contours) extends northward of both magnetic boundaries 1 and 1A, indicating that the source of the gravity high is not the magnetic slab but must, in fact, lie below both it and the dipping magnetic slab forming magnetic boundary 1A (fig. 7). The southeastward extension of magnetic boundary 1 into the Franciscan Complex shows that here the dipping magnetic slab is both overlain and underlain by Franciscan rocks—that is, it is embedded within the Franciscan Complex. Additionally, in those areas where the slab underlies the Great Valley sequence (figs. 7, 8), this Cretaceous sequence and ophiolite are stratigraphically so thin (McLaughlin and others, 1991) that they presumably rest in fault contact on a wedge-shaped mass of the Franciscan Complex that, in turn, overlies the magnetic slab. We similarly interpret the magnetic slab southwest of magnetic boundary 1A (fig. 7), and magnetic models indicate that this second slab is thinner (1 km thick) and probably branches off from the main slab of magnetic boundary 1. In summary, the magnetic anomalies bounded on the northeast by magnetic boundaries 1 and 1A are interpreted to be caused by southwest-dipping serpentinite slabs that are generally embedded within the Franciscan Complex, but locally the northeast tip of the major slab contacts (or coincides with) mafic and ultramafic components of the Coast Range ophiolite where they are exposed near the southwest side of magnetic boundary 1.

In the southeastern part of the magnetic slab of magnetic boundary 1, adjacent to the San Andreas fault, is a broad magnetic low (−100-nT contour, pl. 3B), about 20 km long and 10 km wide. The magnetic model across this low (fig. 4B) indicates that the magnetic slab is either missing here or of negligible thickness. The northeast boundary of this hole in the slab is shown on plate 3, and its southwest boundary is the San Andreas fault (fig. 9).

The magnetic profile along line *M–M′* (fig. 9) demonstrates some complexities in the geophysical expression of the rocks lying southeast of magnetic boundary 1. Magnetic boundary 1, which is determined from magnetic data, is located about 1 km northeast of the calculated (from gravity data) northeast contact of the concealed, but near-surface, Coast Range ophiolite. This discrepancy is the result of a local steep circular magnetic feature, caused by a small, near-circular mass of magnetic rocks, probably serpentinite, located at approximately km 19 on the profile (see pl. 3A; fig. 9). Another complicating factor, lying directly above the ophiolite slab, is a concealed mass of high-density (2.87 g/cm^3) rocks (probably basaltic volcanic rocks) that also correlate with a moderate magnetic anomaly caused by a near-surface source and located between approximately km 15 and 17 on the profile (see pl. 3A; fig. 9). Although this presumed magnetic basalt is shown to be very near the surface by both gravity and magnetic data, the geologic maps (pls. 3A, 3B) show only a broad area of Franciscan sedimentary rocks (Wentworth and Blake, 1991) in this area. This unusual rock type (high density, moderately magnetic) may be a mafic component of the Coast Range ophiolite or, less likely, a mafic volcanic rock type within the Franciscan Complex.

Magnetic boundary 2 is located near the northeastern margin of the Permanente terrane. This geologic contact corresponds well to the lower part of a locally steep gravity gradient (see pl. 3C) near the 2- to 4-mGal contours to the northwest and the 6-mGal contour to the southeast. Because of this correspondence between the geologic contact and the gravity gradient, and because rocks of the Permanente terrane have a relatively high average density (estimated at 2.83 g/cm^3), we consider that both the gravity high southwest of magnetic boundary 2 and the gravity gradient are caused primarily by exposed rocks of the Permanente terrane and its inferred buried southwestward extension. This gravity high is a conspicuous feature that extends along the northeast side of the San Andreas fault (see pl. 3C) for about 100 km. In the density model along line *M–M′* (fig. 9B), we show that the gravity anomaly can be modeled by a slab of the Permanente terrane, about 2 km thick and dipping about 30° SW., approximately parallel to the magnetic slab (magnetic boundary 1) that on this cross section overlies the Permanente terrane.

The magnetic models crossing magnetic boundary 2, along line *E–E′* (fig. 8*B*), indicate that the magnetic rocks forming a nearly continuous belt on the northeast side have a moderate depth extent relative to their width. Similarly, modeling of magnetic anomalies in the area between magnetic boundaries 2 and 3 indicates that they have shallow sources with a vertical extent of generally less than 1 km. Examination of the geologic map (pl. 3B; Wentworth and Blake, 1991) between magnetic boundaries 2 and 3 shows large, relatively equidimensional areas of metavolcanic rocks that are 1.5 by 2.0 km in plan view or larger; however, the gravity map (pl. 3C) displays no significant gravity highs here, even though a thickness of only 1 km of basalt (density, 2.88 g/cm^3) should produce an anomaly of nearly 10 mGal. Indeed, the gravity field here is relatively featureless and has a background level of about 0 mGal, not much different from levels over metasedimentary rocks of the Franciscan Complex in the Diablo Range 25 km farther east. We conclude that the exposed units of the block between

magnetic boundaries 2 and 3 must generally be relatively flat lying, that the serpentinite and metavolcanic rocks are less than 1 km thick, and that the underlying material is nonmagnetic and composed of moderate-density, presumably metasedimentary rocks. Because gravity levels are slightly higher (6 mGal) in the eastern part of this block between magnetic boundaries 2 and 3, we conclude that here the metavolcanic rocks may be as much as 1 to 2 km thick.

The major change in structural style across magnetic boundary 2, southwest-dipping units to the southwest and different, relatively flat lying rocks to the northeast, indicates a structural boundary as well as a fold in this area and confirms the importance of the shear zone of melange on the southwest side of boundary 2.

Magnetic models across magnetic boundary 3 and the block to the north are shown in figures 7*B* and 8*B*. Again, the structures are flat lying, except close to the Silver Creek fault. As shown in figure 8*B*, the serpentinite sheet is essentially continuous across the Santa Clara Valley beneath the alluvium, as previously inferred from geologic studies (R.G. Coleman, written communs., 1990, 1991). Magnetic boundary 3 is thus the south edge of a nearly continuous subhorizontal sheet of

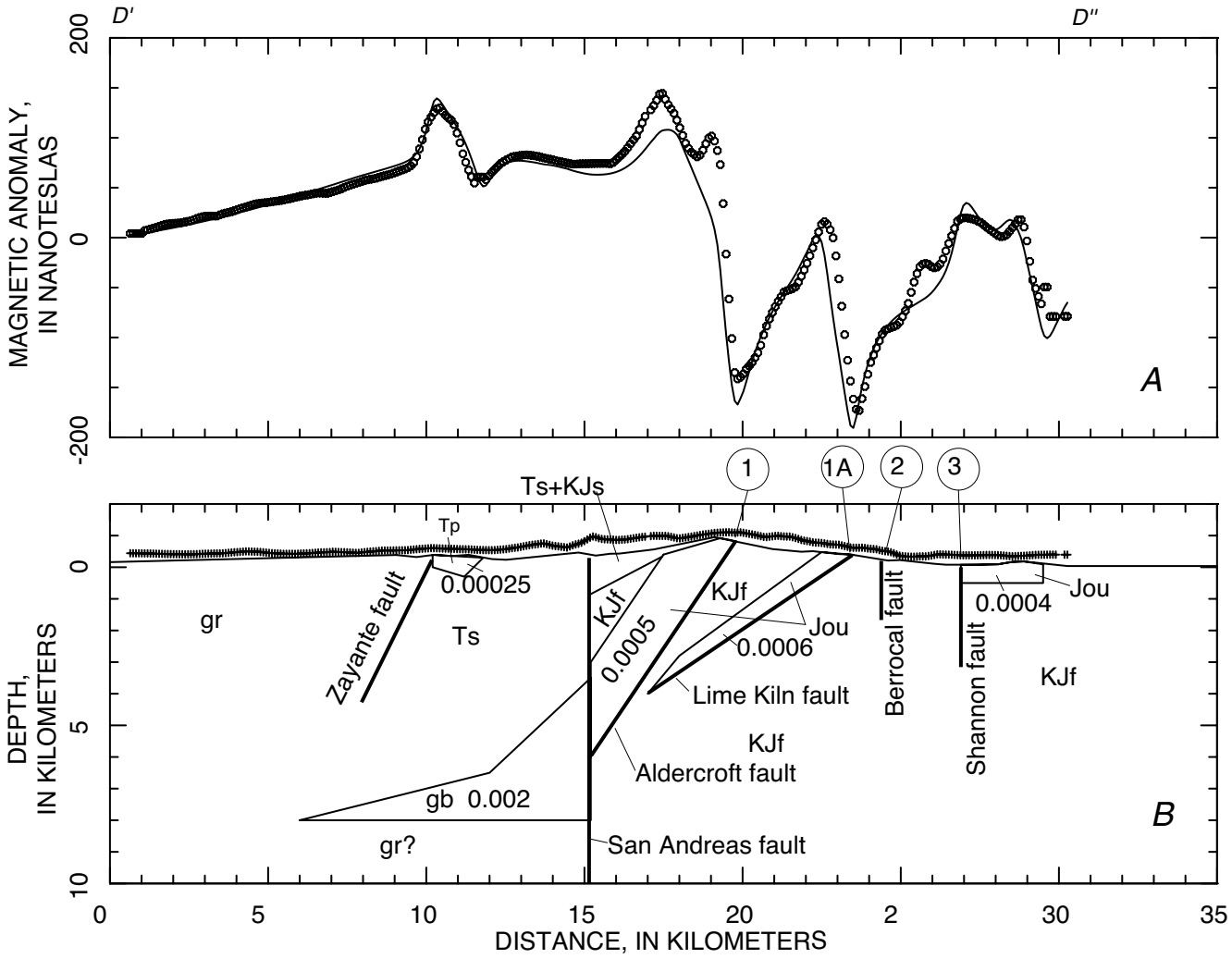

Figure 7.—Magnetic profile (*A*) (circles, measured data; curve, calculated values) and magnetic model (*B*) along line *D′–D″* (pl. 3) across the Logan block and area northeast of the San Andreas fault. Pluses, locations of magnetic observations. Numbers on units are magnetizations (in electromagnetic units per cubic centimeter). Gabbroic body southwest of the San Andreas fault is consistent with other models (figs. 1, 4–6) across the Logan block. Three areas of the Franciscan Complex surrounding thick, dipping slab (km 15–19) and thin, dipping slab (km 18–23) are considered to be wedges. Magnetic boundary 3 corresponds here to the Shannon fault; to the northeast, a horizontal slab of Coast Range ophiolite overlies a horizontal wedge contact with Franciscan rocks. No vertical exaggeration. gb, gabbro; gr, granitic and older metamorphic rocks; Jou, Jurassic ultramafic rocks and serpentinite of the Coast Range ophiolite; KJf, Cretaceous and Jurassic Franciscan complex; KJs, Cretaceous and Jurassic sedimentary rocks; Tp, Pliocene Purisima Formation; Ts, Tertiary sedimentary rocks.

serpentinite, the lower part of a mass of Coast Range ophiolite. This sheet may originally have extended southwestward to magnetic boundary 2 but has since been mostly eroded away to leave the thin small serpentinite masses presently observed here. This interpretation implies that magnetic boundary 3 is a fault with a throw of about 1 km down to the north to account for the missing 1 km of serpentinite on the south side. This interpreted fault at least partly correlates with the Shannon fault. The gravity field in the area northeast of magnetic boundary 3 is a gradient that is caused by a large mass of low-density rocks on the northeast side of the Silver Creek fault. These rocks, possibly Tertiary sedimentary rocks, extend in the subsurface as far as 6 km southwestward horizontally beneath the Franciscan terranes along the southwest-dipping Silver Creek fault (Jachens and others, 1990), but the details are beyond the scope of this paper.

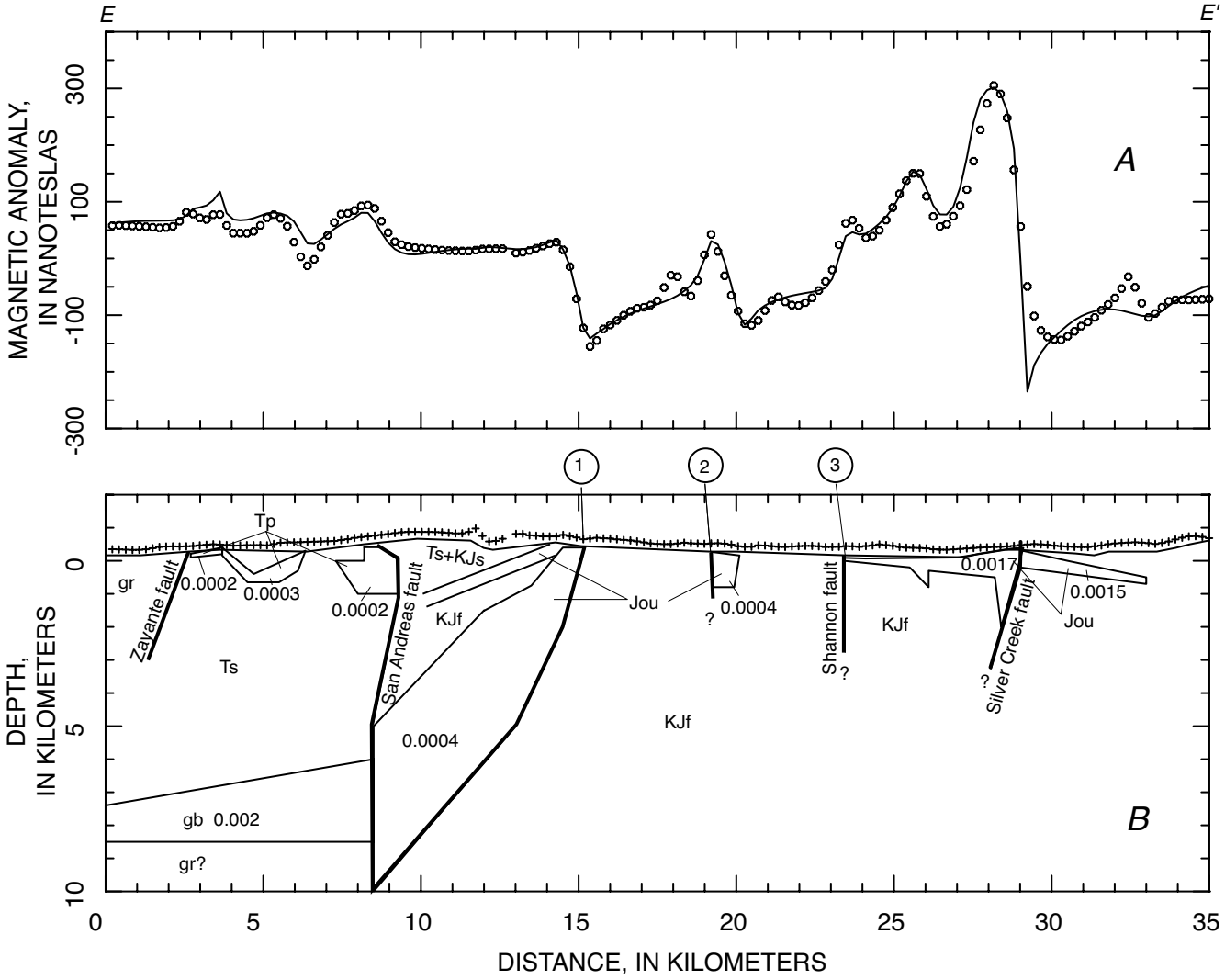

Figure 8.—Magnetic profile (*A*) (circles, measured data; curve, calculated values) and magnetic model (*B*) along line *E–E'* (pl. 3) across the Logan block and area northeast of the San Andreas fault. Pluses, locations of magnetic observations. Numbers on units are magnetizations (in electromagnetic units per cubic centimeter). Gabbroic body southwest of the San Andreas fault is consistent with other models (figs. 1, 4–7) across the Logan block. Thick, dipping slab bounded by magnetic boundary 1 between km 9 and 15 is considered to have wedge contacts on each side. Magnetic boundary 3 at km 23 may correspond to the Shannon fault. Horizontal slab of Coast Range ophiolite overlying a horizontal wedge contact is between magnetic boundary 3 and the Silver Creek fault. Note wedge of magnetic Purisima Formation (sandstone) projecting in subsurface northeastward beneath trace of the San Andreas fault. No vertical exaggeration. gb, gabbro; gr, granitic and older metamorphic rocks; Jou, Jurassic ultramafic rocks and serpentinite of the Coast Range ophiolite; KJf, Cretaceous and Jurassic Franciscan complex; KJs, Cretaceous and Jurassic sedimentary rocks; Tp, Pliocene Purisima Formation; Ts, Tertiary sedimentary rocks.

IMPLICATIONS FOR ORIGIN AND TECTONIC EVOLUTION

CRUST SOUTHWEST OF THE SAN ANDREAS FAULT

Ross (1970) pointed out the unusual petrology of the gabbroic rocks exposed at the southeast end of the Logan block in comparison with granitoids of the rest of the Salinia terrane and with gabbros within the Franciscan Complex. He also drew attention to the striking similarities between the gabbro of Logan and gabbroic rocks exposed on the opposite side of the San Andreas fault at Gold Hill and near Eagle Rest Peak, about 150 and 300 km, respectively, southeast along the fault. On the basis of these observations, he proposed that

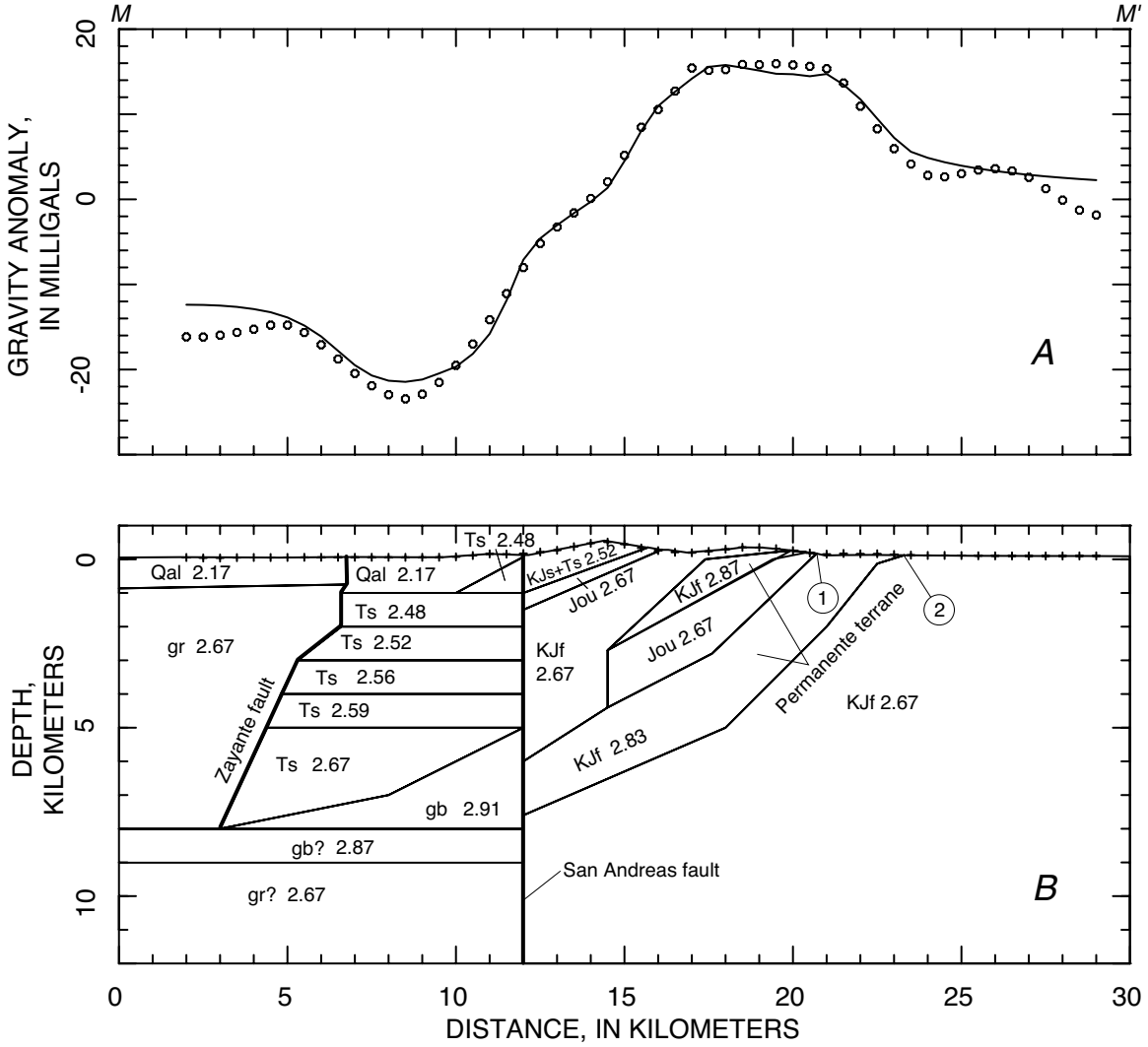

Figure 9.—Isostatic-residual-gravity profile (*A*) (circles, measured data sampled from gridded gravity map; curve, calculated values) and density model (*B*) along line *M–M′* (pl. 3) across the Logan block and area northeast of the San Andreas fault. Pluses, locations where gravity was calculated. Numbers on units are densities (in grams per cubic centimeter). Most important features are two southwest-dipping bodies with densities of 2.83 and 2.87 g/cm^3. 2.83-g/cm^3 body, which is the Permanente terrane of the Franciscan Complex, is here shown to be main source of gravity high (pl. 3) extending 100 km along northeast side of the San Andreas fault. 2.87-g/cm^3, moderately magnetic body may be Permanente terrane or a mafic part of the Coast Range ophiolite. Intervening material is magnetic slab associated with magnetic boundary 1 at km 20.5 and terminated by hole in slab at km 14.5. Circled numbers, magnetic boundaries. Bodies southwest of the San Andreas fault (sedimentary rocks on gabbro) are somewhat schematic because the Zayente fault is concealed here. No vertical exaggeration. gb, gabbro; gr, granitic and older metamorphic rocks; Jou, Jurassic ultramafic rocks and serpentinite of the Coast Range ophiolite; KJf, Cretaceous and Jurassic Franciscan complex; KJs, Cretaceous and Jurassic sedimentary rocks; Tp, Pliocene Purisima Formation; Qal, Quaternary alluvium; Ts, Tertiary sedimentary rocks.

the gabbroic bodies had once been part of a continuous belt which was dismembered by movement along the San Andreas fault system. The fact that the gabbros of Logan and Gold Hill are thin slivers within the fault zone led him to mention an alternative interpretation, namely, that the entire Salinia terrane is underlain by similar gabbro and that these two outcrops represent thin slivers that leaked up along the fault zone. Identical U-Pb ages of 161 Ma on zircon from samples of the gabbros of Logan and Eagle Rest Peak (James and others, 1986) are older than those of Salinian granitoids and support the correlation proposed by Ross (1970). Stable- and radiogenic-isotopic and trace-element data from samples of the gabbros of Logan, Gold Hill, and Eagle Rest Peak (Johnson and O'Neil, 1988) also support this correlation, suggesting that these rocks represent oceanic crust subjected in the past to seawater hydrothermal alteration. Recent isotopic studies (James, 1992) show that the timing of plutonism and metamorphism, initial Pb- and Sr-isotopic ratios, and the style of zircon discordance of basement rocks of the Ben Lomond block are nearly identical to those of basement rocks in the southern Sierra Nevada, supporting the idea that these rocks also were once closer together.

The geophysical data and interpretations presented here provide further support for the idea that the gabbros of Logan and Eagle Rest Peak were once joined. First, the magnetic anomaly over Eagle Rest Peak (Youngs and Mattison, 1989) is nearly identical in shape and amplitude to the elliptical magnetic anomaly over the northern part of the Logan block (see pl. 3B), especially when the depth of burial of the Logan source (relative to the exposed Eagle Rest Peak source) is taken into account. Second, gravity values over Eagle Rest Peak and the northern part of the Logan block are nearly identical, again when the effects of depth of burial are taken into account. In the vicinity of Eagle Rest Peak, the isostatic-residual-gravity values over granitic rocks of the southern Sierra Nevada average about +20 mGal but increase to more than +30 mGal near the outcrop of the gabbroic body (Roberts and others, 1990). Corresponding granitic rocks in the Ben Lomond pluton (+20 mGal) and the inferred gabbroic body (+30 mGal) show gravity values nearly identical to those in the vicinity of Eagle Rest Peak when the gravity effects of the overlying thickness of Cenozoic deposits are removed (fig. 3). Finally, though not directly supporting the proposed former connection between the gabbros of Logan and Eagle Rest Peak, the magnetic data do show that the thin sliver of the exposed gabbro of Logan is actually part of a basement block, 90 km long and as much as 20 km wide, which is separated from the Ben Lomond block to the south by the Zayante fault. These magnetic data indicate that the gabbro of Logan is restricted to a single structural block within the Salinia terrane. The absence of deep-source magnetic anomalies associated with granitoids of the Salinia terrane argues against an interpretation that magnetic gabbro everywhere underlies the Salinia terrane.

An additional implication of the probable pre-San Andreas tie between the gabbros of Logan and Eagle Rest Peak stems from the interpretation, based on magnetic anomalies, that the basement of the gabbro of Logan abuts the San Andreas fault for a horizontal distance of about 65 km (see pl. 3C), whereas the gabbro of Eagle Rest Peak appears to abut the San Andreas fault for a maximum horizontal distance of only 35 km (Youngs and Mattison, 1989). Immediately northwest of the gabbro of Eagle Rest Peak, an approximately 30-km-wide, northwest-trending magnetic anomaly terminates at the San Andreas fault (Youngs, 1989). This anomaly is the south end of the Great Valley magnetic anomaly (Griscom, 1966), a huge feature that extends northwestward along the entire Great Valley for a distance of 700 km and whose source is completely concealed beneath sedimentary fill. The combined San Andreas fault-bounded length of the gabbro of Eagle Rest Peak and the adjacent source of the Great Valley magnetic anomaly is about 60 to 70 km, similar to the San Andreas fault-bounded length of the gabbro of Logan. Therefore, we speculate that the gabbro of Eagle Rest Peak is correlated with the source of the Great Valley magnetic anomaly and that the gabbroic basement of the Logan block is also correlated with this source. The general form of the mass causing the Great Valley magnetic anomaly is that of a thick, west-dipping slab; interpreted to represent ophiolite obducted from the west onto the North American Continent during Jurassic time (Griscom, 1982; Griscom and Jachens, 1990).

Geophysical modeling of the Zayante Fault (figs. 1, 4, 5) indicates substantial uplift and horizontal shortening across this fault. Crystalline basement is uplifted at least 4 to 6 km probably along most of the length of the fault, and the southward continuation of Tertiary sedimentary rocks beneath the granitic basement (fig. 1) suggests horizontal shortening of at least 6 km in this area. Gravity and magnetic models along line *S*–*S*′ (figs. 4*B*, 5*B*) also show sedimentary rocks extending southward beneath granitic basement near the south end of the Logan block, but in this area the overlap is not well constrained by the gravity data. Magnetic basement of the Logan block extends in the subsurface more than 10 km southward of the surface trace of the Zayante fault (see pl. 3B), suggesting horizontal shortening of at least this amount. As discussed below, however, some of this horizontal shortening may reflect pre-Tertiary movement on a predecessor to the Zayante fault and thus predate thrusting of the sedimentary rocks beneath the block to the south. The timing of offset on the Zayante fault, as summarized by Clark and Rietman (1973), indicates that dip-slip movement affecting the Tertiary sedimentary section began in early Oligocene time and had mostly ended by early Miocene time, although some movement continued at least into the Pliocene. Furthermore, correlation of clasts in sedimentary rocks north of the Zayante fault with source rocks in the northern Gabilan Range suggests no major strike-slip movement along this fault since late Oligocene time (Clark and Rietman, 1973).

An unusual feature of the Zayante fault revealed by the geophysical data is that although this fault bounds the Logan block and its highly magnetic gabbroic basement for a distance of more than 90 km, no magnetic gabbro occurs in the

upthrown block—that is, no appropriate magnetic anomalies are present even in covered areas. This feature indicates that if the Zayante fault originated in Tertiary time after deposition of the Eocene Butano Sandstone, then either it broke outboard of all gabbro or subsequent movement, or erosion has effectively eliminated all gabbro locally from the Ben Lomond block, or both. Alternatively, Tertiary movement on the Zayante fault merely reflects reactivation of an older fault that, by Eocene time, already had juxtaposed the markedly different basement rocks of the Logan and Ben Lomond blocks. We suggest that the absence of magnetic gabbro in the Ben Lomond block argues against an Eocene or later origin for the Zayante fault.

That the Zayante fault may have fortuitously cut the basement outboard of all gabbro seems unlikely in light of the fact that the mapped or inferred trace of the fault is quite close to (never more than 10 km from and typically much closer to) the southwest edge of gabbroic basement along the entire 90 km reach of the fault. Eocene or later uplift and erosion sufficient to strip off all the gabbro also seems unlikely because, at least along the north third of the fault, Eocene sedimentary rocks of the Butano Sandstone are preserved on the upthrown block (Clark and Rietman, 1973). Furthermore, erosion of gabbroic basement that in places would have been at least 2 km thick should have supplied mafic sedimentary debris into the basin to the north, but the Tertiary sedimentary rocks do not contain such debris.

An explanation of the absence of gabbro south of the Zayante fault by strike-slip movement along this fault is possible but would constrain the allowable timing and magnitude of such movement. The proposed movement must have occurred earlier than the late Oligocene clast-source-rock crossfault tie identified by Clark and Rietman (1973), and probably earlier than the early Oligocene initiation of uplift south of the fault. Right-lateral offset of at least 100 km on the Zayante fault would have carried all gabbro (including counterparts to the gabbro of Eagle Rest Peak) westward of the current trace of the San Gregorio fault, and subsequent movement on the San Gregorio and San Andreas faults would have swept the outboard block northward to the vicinity of Point Reyes (Griscom and Jachens, 1989), where detailed aeromagnetic coverage west of the San Andreas fault is limited to a strip about 20 km wide paralleling the fault (Chase and Youngs, 1979). In the entire strip extending from about 30 km south to about 70 km north of Point Reyes, only one small magnetic anomaly is present (on the Point Reyes Peninsula), associated with a pendant of magnetic metamorphic rocks within the Cretaceous pluton, not with gabbro. Although the absence of gabbroic bodies in this strip does not rule out right-lateral strike-slip offset as an explanation for the absence of gabbro southwest of the Zayante fault, it does suggest that for this explanation to be viable, the offset would probably have to greatly exceed 100 km. Similarly, the absence of magnetic gabbro or any large unexplained magnetic anomalies in the southern Sierra Nevada batholith south of the gabbro of Eagle Rest Peak and its associated magnetic anomaly (Youngs, 1989; Youngs and Mattison, 1989) indicates that hundreds of kilometers of left-lateral offset would be required to explain the absence of gabbro in the Ben Lomond block. Therefore, lacking any positive evidence for gabbro in places compatible with Eocene or later offset across the Zayante fault, we favor the interpretation that a proto-Zayante fault existed which was subsequently reactivated during Tertiary time.

The existence of a proto-Zayante fault is uncertain because, in the Santa Cruz Mountains, it would have been severely modified by later movement and its counterpart in the southern Sierra Nevada may be concealed. The contact between the gabbro of Eagle Rest Peak and Sierran granitoids to the south occupies a structural position comparable to that of the Zayante fault, is buried beneath Tertiary sedimentary rocks, and dips south, according to the aeromagnetic data (Youngs and Mattison, 1989). This contact could be a reverse or thrust fault that juxtaposed deep-seated batholithic rocks against the gabbro by large-scale vertical movement, possibly along an earlier suture between the gabbro and Sierran country rocks. According to McLaughlin and Clark (this chapter), evidence from fission-track data suggests that by about 70 Ma, Ben Lomond granitic rocks were within 3 to 5 km of the surface, even though geobarometry of intrusive rocks and metamorphic roof pendants suggests earlier intrusion at 20- to 30-km depth. Regardless of the possible existence of a proto-Zayante fault, reactivation of a south-dipping structure by north-southward compression in the middle Tertiary would account both for the northward-directed thrusting indicated by geophysical models and for the absence of gabbroic basement south of the Zayante fault in the Santa Cruz Mountains.

CRUST NORTHEAST OF THE SAN ANDREAS FAULT

In previous sections, we have described the four geophysically defined crustal blocks and their three-dimensional structure northeast of the San Andreas fault. Here, we briefly describe the structure of the contact between the Franciscan Complex and the Great Valley sequence where it has been mapped along the east side of the California Coast Ranges, emphasizing the recent discovery of eastward-tapering tectonic wedges that underlie the western parts of the Great Valley sequence (Wentworth and others, 1984; Wentworth and Zoback, 1990). Then, we show that the structures deduced in the study area (see pl. 3A) are largely similar to those deduced to be caused by tectonic wedging, and we conclude that the part of the study area between the San Andreas and Silver Creek faults consists of tilted and broadly folded wedge structures presently exposed at the surface.

The contact between the Franciscan Complex (a subduction complex) and the Great Valley sequence (a forearc-basin complex) extends for 600 km along the east side of the Coast

Ranges and passes about 40 km east of the study area (see pl. 3A). This contact is a fault, situated at the base of the fragmented Coast Range ophiolite, which forms the former oceanic basement of forearc-basin strata of the Great Valley sequence. This fault, according to plate-tectonic theory, was originally believed to represent an exposed east-dipping subduction zone (Hamilton, 1969; Ernst, 1970). More recently, seismic reflection and refraction data (Wentworth and others, 1984; Walter, 1990; Wentworth and Zoback, 1990), together with gravity and magnetic data (Griscom and Jachens, 1990), have shown that this contact is rather more complex. In the subsurface below and east of the contact are a series of two or more eastward-tapering wedges, with dimensions measured in kilometers, probably composed of both Franciscan rocks and locally, to the east, Great Valley rocks thrust eastward into (that is, intruding) rocks of the forearc basin. Geophysical evidence also shows that the basement of the Great Valley sequence dips relatively smoothly west from the middle of the valley at least as far as the Franciscan-Great Valley contact, where the basement lies commonly at 10- to 15-km depth. Thus, the previously inferred subduction zone associated with the accretionary Franciscan Complex must lie still farther west, because tectonic wedging has transported Franciscan rocks eastward over the Great Valley basement, which necessarily lies east of the subduction zone.

A characteristic feature of the Franciscan-Great Valley contact is a magnetic anomaly, 15 to 30 km wide, that extends nearly continuously for 600 km along the contact (Griscom, 1966, 1983; Griscom and Jachens, 1990). The anomaly is caused by a huge subhorizontal slab composed of the magnetic Coast Range ophiolite (15–30 km wide, max 4 km thick) that extends along the contact, mostly concealed at shallow (<5 km) depth and generally lying beneath the much smaller exposed and fragmented part of the Coast Range ophiolite. The western part of this slab always is structurally embedded within the Franciscan Complex (unit KJf, pl. 3), whereas the east edge of the slab approximately contacts the Coast Range ophiolite (unit Jou) at the base of the Great Valley sequence. We have modeled this slab (fig. 10) from magnetic data obtained near Coalinga (Griscom and Jachens, 1990) and interpret it to be caused by two successive wedges of Franciscan Complex that advanced eastward along or near the top of the Great Valley basement, the slab having been peeled up from the Great Valley basement by the advancing lower wedge. We infer that the 600-km length of this magnetic slab may have resulted from the wedge beheading a preexisting elongate parallel-to-basin structure, such as a faulted antiform, on the floor of the Great Valley basin and that eastward movement of the two wedges was subsequently halted by rapid shallowing of the basin to the east. Regionally, the slab is cut off obliquely at its southeast end (lat approx 35°30′ N.) by the San Andreas fault, which has sliced off a major part of the Franciscan-Great Valley contact at the south end of the Great Valley.

In the Loma Prieta region (see pl. 3A), the block structure between the San Andreas fault and magnetic boundary 1 (fig. 8) is remarkably similar to the structure of the magnetic slab described in the previous paragraphs. Structural similarities include the facts that (1) a substantial magnetic anomaly is associated with the block, caused by a large, thick, west-dipping magnetic slab; (2) the western part of the slab (fig. 8) is surrounded by the Franciscan Complex, yet its northeast edge contacts the Coast Range ophiolite which is basement for the Great Valley sequence; (3) the slab has dimensions (in cross section) similar to those of the slab shown in figure 10; and (4) the geologic and structural associations of the two slabs are similar. In figure 10, we show which part of our 1990 cross section is similar to figure 8 by schematically adding the San Andreas and Silver Creek faults at the locations corresponding to the structures shown in figure 8. The schematic topographic surface shown in figure 8 is also added to figure 10 to demonstrate that our corresponding area near Loma Prieta has been tilted westward and antiformally folded, in good agreement with conclusions reached in the field.

We conclude that magnetic boundary 1 is a wedge fault lying along the base of the thick, west-dipping magnetic slab and marking the top of a wedge composed of Franciscan Complex beneath the slab. A second wedge composed of Franciscan Complex (fig. 8) lies above this magnetic slab and beneath the Great Valley sequence. Magnetic boundary 1 in plan view to the southeast extends into the area of Franciscan Complex because here the magnetic slab is structurally lower, that is, embedded in the Franciscan rocks, such that the acute angle between magnetic boundary 1 and the exposed base of the Great Valley sequence identifies the tip of this upper wedge. This feature (the acute angle) we consider to be one of the most important geophysical and geologic clues establishing the existence of wedge structures in this area. Similarly, magnetic boundary 1A can then be explained as another, less important wedge boundary (see magnetic slab outcropping at km 23 on magnetic profile along line *D–D′*, fig. 7*B*) that may have resulted from a minor shift in the trace of the wedge fault of magnetic boundary 1, and so the acute angle between magnetic boundaries 1 and 1A is interpreted to mark the side edge of a wedge, assuming that the wedges were thrust northeastward. Another wedge boundary is located at and northeast of magnetic boundary 3, where a now-horizontal wedge fault is interpreted to lie at the base of the horizontal sheet of serpentinite (unit Jou, pl. 3) north of magnetic boundary 3 (see fig. 8*B*).

Our geophysical method is, of course, able to define only wedges that have magnetic serpentinite along their boundaries, and so other wedge faults may remain unrecognized, including those within the Great Valley sequence. Other geologic boundaries within the Franciscan Complex are major shear zones or terrane boundaries that probably developed during formation of the Mesozoic subduction complex or during right-lateral faulting in the early Tertiary (McLaughlin and others, 1988a), although the positions of wedges may be partly controlled by preexisting terrane boundaries. We assign magnetic boundary 2 to this category of earlier boundaries

formed primarily before wedging (although a postwedging change in dip occurs here), and magnetic boundary 3 primarily to postwedging offset of the wedge fault.

The geophysical evidence for tectonic wedges in this part of the study area (see pl. 3C) is of great interest because, so far, most previously identified wedge structures elsewhere are concealed beneath the surface and have been inferred primarily from seismic data. We conclude here that the tilted rocks southwest of magnetic boundary 2 contain a series of major wedges and wedge boundaries and that these structures are substantially exposed at the surface, offering a splendid opportunity for observation and study. Because the relative thrust motion on wedge boundaries is in opposite directions at the top or bottom of a wedge (fig. 10), mapping of small-scale structures may help determine whether a specific fault forms the top or bottom of a wedge.

Most of the large amount of wedging inferred to have taken place in the study area (see pl. 3A) must predate the profound early Miocene erosion (McLaughlin and others, 1991) that exposed the wedged rocks. Early Miocene subsidence and deposition then covered the unconformity with flat-lying Miocene marine sedimentary strata. Initial movement on the San Andreas fault in earliest Miocene time (summarized by Stanley, 1987) began faulting these Great Valley and Franciscan rocks away from their original position on the west side of the southern Great Valley. Somewhat more recently, a strand of the San Andreas fault must here for a while have branched off eastward of its present position, probably along the Calaveras and Silver Creek faults, and moved this block of Great Valley and Franciscan rocks to their present position between the Silver Creek and San Andreas faults.

The continuities of magnetic anomalies, curvilinear magnetic boundaries, and geologic units seem to preclude that any major linear strike-slip faults of the San Andreas system may have cut across the area between the San Andreas and Silver Creek faults. Even the Sargent fault (see pl. 3B), whose length and linearity suggest a possible exception, appears to cut across magnetic gradients on both sides of the hole in the magnetic slab southwest of magnetic boundary 1 without laterally offsetting the magnetic boundary by more than 3 km. Furthermore, although we are aware of relatively recent thrust faulting, reactivation of wedge faults, and possible transpression within the two blocks to the southeast of magnetic boundary 2 (see McLaughlin and Clark, this chapter), presumably in response to local stresses created by the San Andreas fault, we infer these movements to be relatively minor

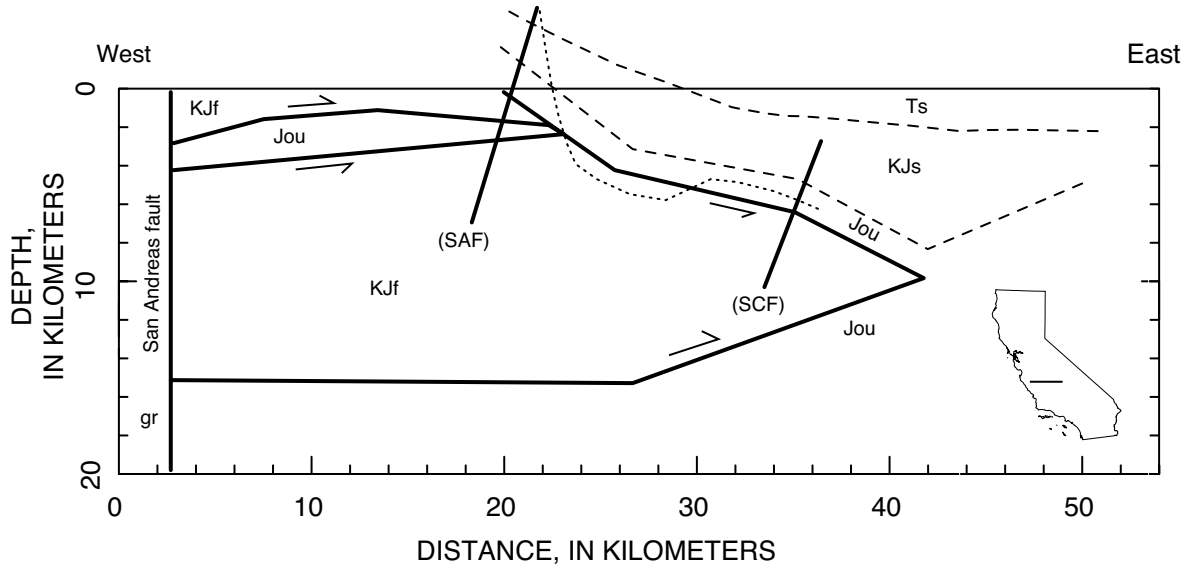

Figure 10.—Geologic cross section across contact between the Franciscan Complex (KJf) and the Great Valley sequence (KJs) at lat approx 36°10′ N. Two wedges of Franciscan Complex have successively intruded eastward along basement of the Coast Range ophiolite and thus isolated an intervening slab of ophiolite. Part of this contact is now represented by geologic relations between the San Andreas fault (SAF) and the Silver Creek fault (SCF) in the San Jose area (see pl. 3). Adapted from magnetic model of Griscom and Jachens (1990, fig. 5.3). Solid lines, faults; dashed lines, sedimentary contacts. Short heavy bars (labeled in parentheses) denote positions of SAF and SCF shown in magnetic model along line *E–E′* (fig. 8*B*). Shape of dotted line, which denotes present-day erosional surface (topography) along line *E–E′*, indicates that corresponding area near San Jose (which has relatively flat topography at this scale) has been tilted westward and anticlinally folded. Vertical exaggeration, ×2. gb, gabbro; gr, granitic and older metamorphic rocks; Jou, Jurassic ultramafic rocks and serpentinite of the Coast Range ophiolite; KJf, Cretaceous and Jurassic Franciscan complex; KJs, Cretaceous and Jurassic sedimentary rocks; Ts, Tertiary sedimentary rocks.

in comparison with the amount of wedge faulting that took place before Miocene time.

Finally, we call attention to a curious problem observed along magnetic boundary 1 and its lesser extension, magnetic boundary 1A. Although the magnetic anomalies and models indicate that an essentially continuous magnetic mass, presumably of serpentinite, is present along the southwest side of these magnetic boundaries, the geologic map (pl. 3A) shows only discontinuous irregular exposures of this magnetic rock, none especially wide in comparison with the model dimensions. In fact, the southeastward extension of magnetic boundary 1 displays no associated serpentinite at all, even though the magnetic feature is exceptionally strong there and the magnetic gradients indicate a large, continuous magnetic mass within about 0.2 km of the surface. The question therefore arises, why is so much of the serpentinite only a short distance below the present irregular erosional surface, a surface that moves downward with erosion over time, such that we would expect a continuous belt of these magnetic rocks to have been exposed after a relatively small amount of erosion? We speculate that when a dipping layer of low-density, well-sheared serpentinite is exposed by erosion at the surface, the upper few hundred meters may, in some relatively unconfined environments, expand and become even less dense, leading to instability. This instability, driven by the surrounding denser country rock, results in extrusion of the serpentinite to the surface in a relatively short time and its subsequent erosion. In this model, the voids left by the extruded serpentinite would simply collapse. Thus, by means of such an intermittent dynamic process, at any moment in the erosional history only parts of a serpentinite belt might actually crop out at the surface, even though the other unexposed parts lie only a short distance below the surface.

CRUSTAL STRUCTURE AND SEISMICITY

As discussed in this section, the structural details provided by potential-field interpretations can aid the interpretation of seismicity. We compare the crustal model calculated during this study with the distribution of aftershocks in an attempt to determine which faults moved during the earthquake. The comparison is based mainly on pattern recognition (separating the aftershocks into subsets that seem to define coherent, approximately planar distributions) and the spatial coincidence of the distribution of hypocenters with inferred subsurface faults or other block boundaries. As a result of this comparison, we argue that most aftershocks are associated with three main faults: the Zayante, San Andreas, and Sargent faults. Within the context of this discussion, the Zayante and San Andreas faults are the geologic boundaries that separate rocks of the Logan block from Salinian plutonic rocks to the southwest, and from Franciscan and related rocks to the northeast, respectively. Furthermore, in many places, the aftershocks that we associate with a particular fault occupy a relatively wide (max 2 km) zone and evidently include events both on the fault plane and in the volume immediately surrounding the fault plane, a volume such as the San Andreas fault zone that studies of exhumed major faults show to be highly deformed.

The distribution of aftershocks for the period October 18, 1989, through 1991 is plotted on a base that includes major faults (fig. 11). Figures 12 through 16 show various modeled cross sections presented previously in this paper, along with the locations of hypocenters of aftershocks that occurred within 2.5 km of each cross section. Only well-located aftershocks (horizontal uncertainty, <1.5 km; vertical uncertainty, <2.5 km) of M>1.0 recorded by eight or more stations are shown. The uncertainties do not reflect possible systematic errors introduced by limitations in the velocity model used to locate the earthquakes. A comparison between the aftershock data set mapped in figure 11 and a smaller set located by using a three-dimensional velocity model (D.M. Eberhart-Phillips, written commun., 1993) shows that the main effect of using a more realistic crustal velocity model is to systematically shift the hypocenters about 1 km southwestward, normal to the San Andreas fault. This shift is most pronounced for aftershocks located northeast of the San Andreas fault or beneath the La Honda Basin.

Aftershocks that we identify as associated with the Zayante fault are shown on our map inside an elliptical region (Z, fig. 11). The epicenters for this group of aftershocks plot as far as 5 km southwest of the surface trace of the Zayante fault but close to the inferred southwest limit of the gabbro of Logan, a limit that we believe marks the position of the southwest-dipping Zayante fault at midcrustal depths (for example, figs. 4*B*, 7). Hypocenters superposed on the magnetic profile along line *D–D′*, together with a schematic representation of the Zayante fault from the adjacent isostatic-residual-gravity profile along line *R–R′* (fig. 1) where the fault geometry is tightly constrained by the gravity data, are plotted in figure 12*B*. Aftershocks that we identify as associated with the Sargent fault zone are shown inside two elliptical regions (S, fig. 11). The Sargent fault has, at most, only a very weak geophysical expression, and so we were unable to infer its subsurface configuration on the basis of gravity or magnetic anomalies. Therefore, our association of these aftershocks with the Sargent fault zone is based simply on the distribution of hypocenters in relation to the mapped fault trace (figs. 13, 14). By this analysis, the Sargent fault dips steeply southwest and was active along only part of its length. Interestingly, the gap between the two clusters of aftershocks corresponds to a marked change in the Sargent fault trace, from long, straight, seismically active segments at the ends to a seismically quiet central segment where the fault is geomorphically less distinct and appears to be irregular in strike (fig. 11).

Region SA (fig. 11) includes those aftershocks that we tentatively associate with the San Andreas fault. In the southern part of this region, the hypocenters define a band that dips steeply southwest and projects to the surface close the San Andreas fault trace (fig. 15). The apparent southwestward dip

of the aftershock zone could be an artifact resulting from the use of an incorrect velocity model to locate the hypocenters (W.L. Ellsworth, written commun., 1992). However, the facts that the magnetic model (fig. 15) indicates a similar dip to the fault-bounded northeast face of the gabbro of Logan (well constrained only in the top 3 km), and that hypocenters in the southeastern part of the area of figure 11 located with a three-dimensional velocity model suggest a similar dip (Michael and Eberhart-Phillips, 1991) and show little change from the locations shown in figure 11 (D.M. Eberhart-Phillips, written commun., 1993), argue against such an interpretation. Farther northwest along the fault, the distribution of epicenters widens, with epicenters plotting on both sides of the San Andreas fault trace. Those epicenters that plot southwest of the fault mainly represent deep-focus earthquakes that define a southwest-dipping planar zone which intersects the vertical projection of the San Andreas fault trace at 8- to 10-km depth, approximately the inferred base of the gabbro of Logan (fig. 13).

As discussed in the subsection above entitled "Block Boundaries Southwest of the San Andreas Fault," magnetic data indicate that magnetic sedimentary rocks of the Purisima Formation in the Logan block extend in the shallow subsurface as far as 1 km northeastward of the San Andreas fault trace (see pl. 3A; fig. 8). Therefore, the shallowest part of the San Andreas fault must here dip northeast, even though aftershocks indicate that the main section of the fault dips steeply southwest. A consequence of this shallow northeastward dip is that locally the upper part of the main San

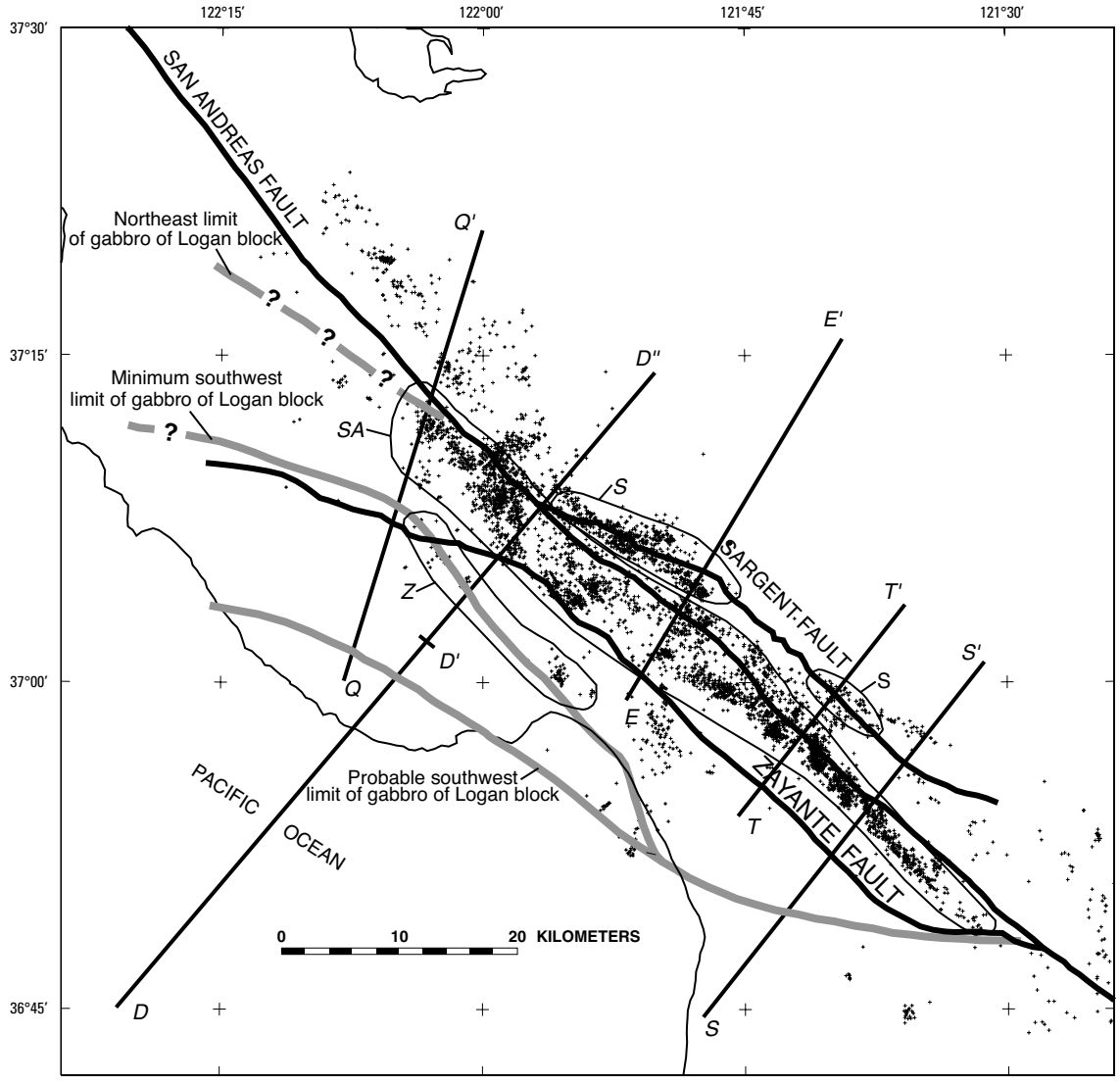

Figure 11.—Loma Prieta region, Calif., showing distribution of aftershocks (pluses) and locations of major faults, and profiles discussed in figures 12 through 16.

Andreas fault surface must lie northeast of the fault trace, in a position that could reasonably explain some of the shallow aftershocks northeast of the fault trace as seismicity associated with the main section of the San Andreas fault (fig. 13).

Of the rest of the aftershocks unaccounted for in the above discussion, a few could reflect movement on the poorly defined north boundary of the Logan block (fig 11), whereas others northeast of the San Andreas fault in the northern part of the map area (fig. 11) probably are associated with a suite of southwest-dipping thrust faults (for example, the Monte Vista, the northern section of the Berrocal, the Shannon, and related faults; Sorg and McLaughlin, 1975; see McLaughlin and Clark, this chapter), although our modeling does not extend far enough northward to relate block boundaries to seismicity. The aftershocks located northeast of the San Andreas fault about 5 km northwest of the magnetic profile along line *D–D′* (fig. 12*A*), and the north-dipping zone of aftershocks that lies 2 to 5 km southeast of the southwest end of the magnetic

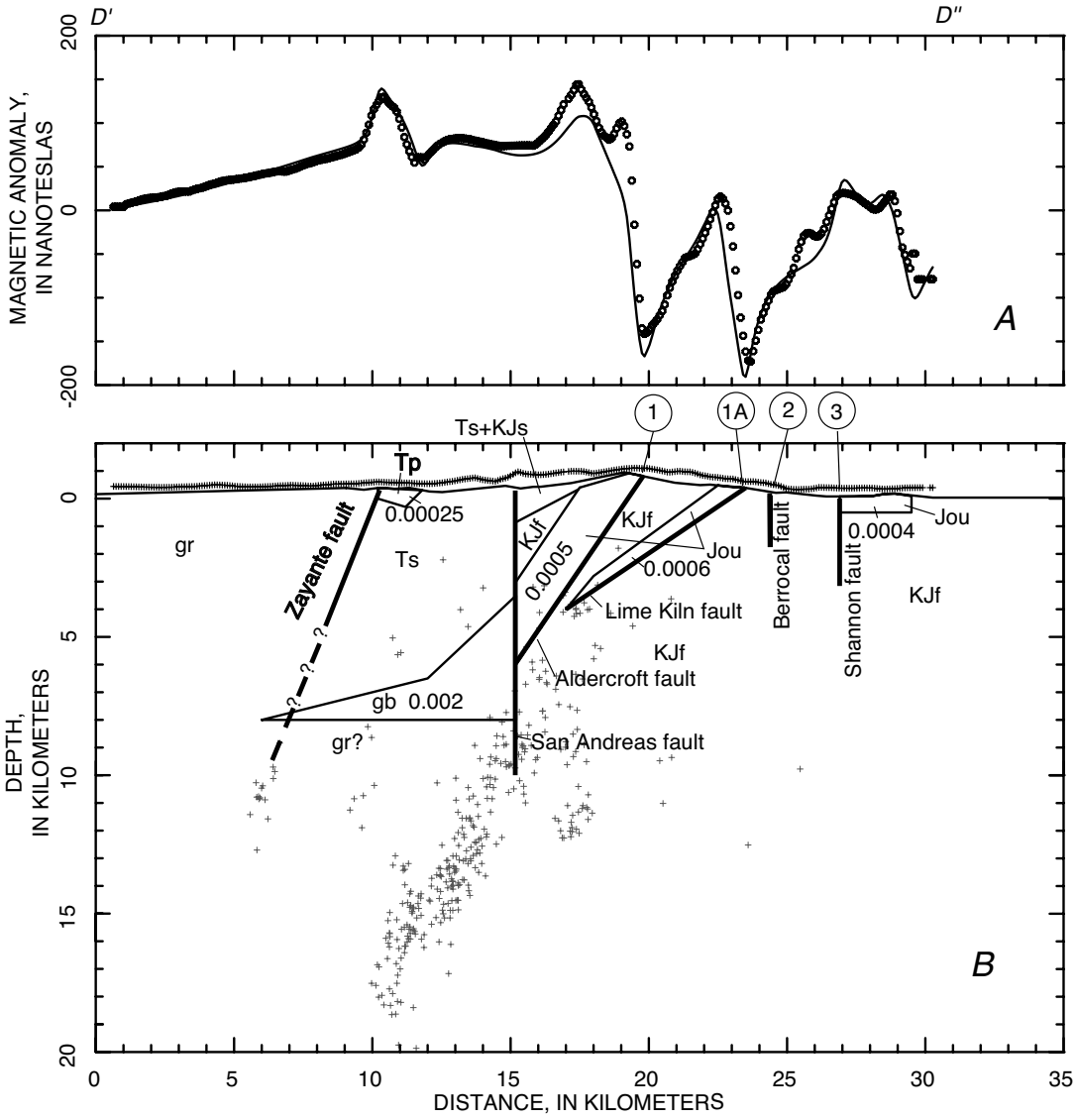

Figure 12.—Magnetic profile (*A*) (circles, measured data; curve, calculated values) and magnetic model (*B*) along line *D′–D″* (pl. 3) across the Logan block and area northeast of the San Andreas fault. Pluses along top of magnetic model, locations of magnetic observations; pluses in body of magnetic model, aftershocks that occurred within 2.5 km of line *D′–D″*. Numbers on units are magnetizations (in electromagnetic units per cubic centimeter). Circled numbers, magnetic boundaries. No vertical exaggeration. gb, gabbro; gr, granitic and older metamorphic rocks; Jou, Jurassic ultramafic rocks and serpentinite of the Coast Range ophiolite; KJf, Cretaceous and Jurassic Franciscan complex; KJs, Cretaceous and Jurassic sedimentary rocks; Tp, Pliocene Purisima Formation; Ts, Tertiary sedimentary rocks.

profile along line *E–E′* (fig. 13*B*), do not correlate with any of the structures defined by our gravity and magnetic modeling.

Finally, we point out an apparent relation between the distribution of aftershocks and the crustal structure for which we have no good explanation. Analysis of the distribution of aftershocks with depth relative to the inferred crustal structure of the Logan block (figs. 12–16) shows that the gabbroic basement of this block is mostly devoid of seismicity and that the major southwest-dipping planar distribution of aftershocks effectively passes just beneath the lower northeast edge of the block. Although seismicity on the San Andreas fault must lie at the eastern margin of the gabbroic basement, we believe that

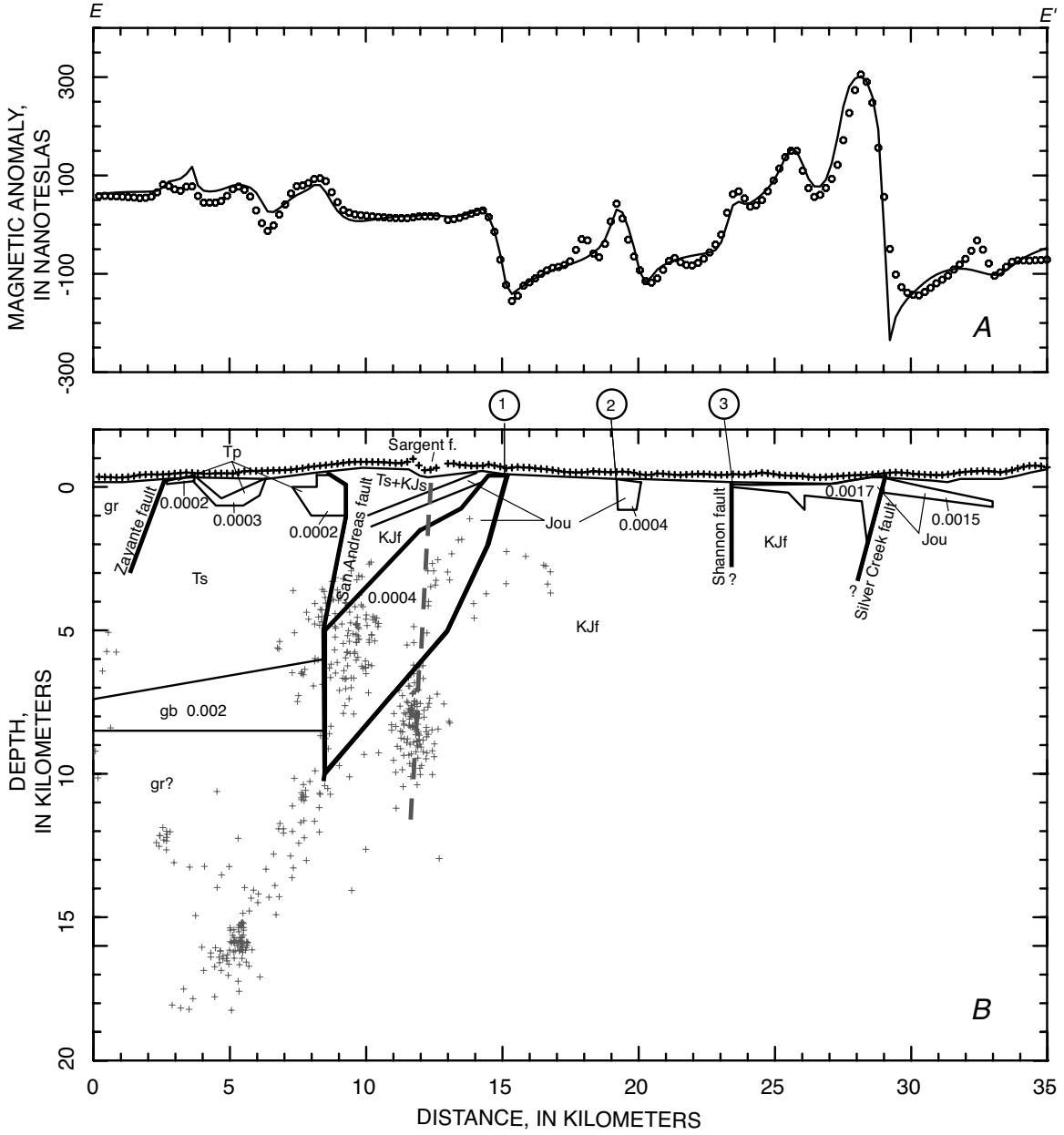

Figure 13.—Magnetic profile (*A*) (circles, measured data; curve, calculated values) and magnetic model (*B*) along line *E–E′* (pl. 3) across the Logan block and area northeast of the San Andreas fault. Pluses along top of magnetic model, locations of magnetic observations; pluses in body of magnetic model, aftershocks that occurred within 2.5 km of line *E–E′*. Numbers on units are magnetizations (in electromagnetic units per cubic centimeter). No vertical exaggeration. gb, gabbro; gr, granitic and older metamorphic rocks; Jou, Jurassic ultramafic rocks and serpentinite of the Coast Range ophiolite; KJf, Cretaceous and Jurassic Franciscan complex; KJs, Cretaceous and Jurassic sedimentary rocks; Tp, Pliocene Purisima Formation; Ts, Tertiary sedimentary rocks. Circled numbers, magnetic boundaries.

the aftershock patterns shown in figure 13 (where the zone of aftershocks appears to change dip at the depth of the gabbroic basement) and in figure 16 (where the aftershocks are distributed throughout the volume of crust below the gabbroic basement from approx 16-km depth upward to the inferred base of the gabbro, but not into the gabbro except at its lower northeast corner) indicate that the basement block exerted some control over the seismicity. (Recall that the northeast edge of the basement of the Logan block, which coincides with the San Andreas fault at depth, is poorly constrained by magnetic data along the reach where this body abuts the highly magnetic slab northeast of the San Andreas fault and southwest of magnetic boundary 1.) A possibly related observation (see pl. 3B) is that the north end of the constraining "Loma Prieta" bend in the San Andreas fault coincides with the northernmost contact of the basement of the gabbro of Logan with the San Andreas fault and that this basement abuts the fault along about 70 percent of the length of this bend. Although it is difficult to understand how a gabbroic basement block that in places is only a few kilometers thick could exert a major influence on the local behavior of the San Andreas fault, the crust of the Logan block below the gabbro may differ sufficiently from the lower crust in the surrounding blocks to account for the seeming influence of the gabbro.

CONCLUSIONS

Our analysis of gravity and magnetic anomalies, coupled with firm geologic constraints, produces a structural and compositional image of the midcrust and upper crust in the Loma Prieta region that helps define the major structural elements in the upper 10 km of the crust, provides clues and constraints on the tectonic development of the region, and suggests a framework for associating most aftershocks with known major faults. This crustal model is limited both by being focused on those features that are expressed mainly in the gravity and magnetic

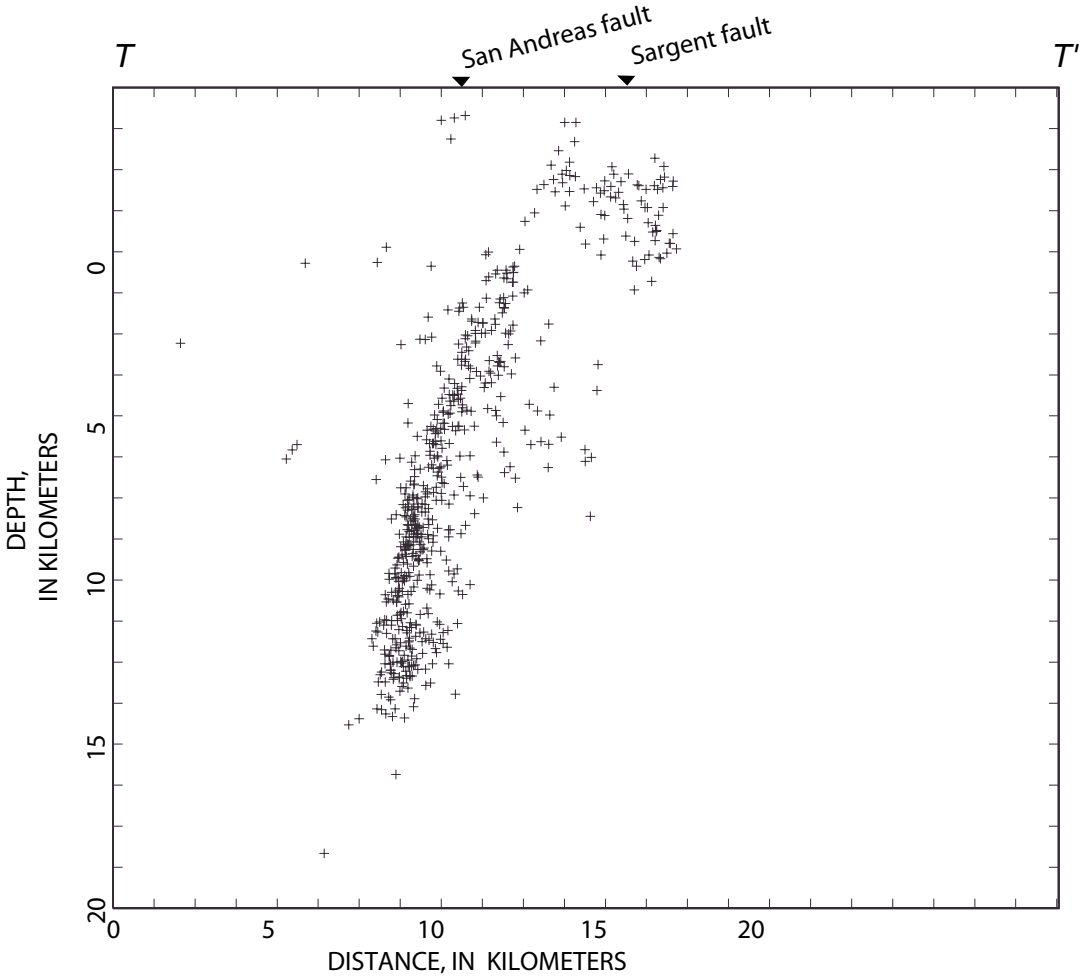

Figure 14.—Distribution of aftershocks (pluses) that occurred within 2.5 km of line *T*–*T′*. Note cluster of aftershocks beneath trace of the Sargent fault.

fields and by being confined to approximately the upper 10 km of the crust by the resolution limits of these techniques. In many places, movements on major faults, that in the past have controlled the tectonic evolution of the region and that today are responsible for the local seismicity, have juxtaposed rocks with different densities and (or) magnetic properties. The gravity and magnetic anomalies produced by these juxtapositions have served as the basis for our analysis.

The crust in the Loma Prieta region is divided into seven major basement blocks on the basis of characteristic geology, bounding structures, gravity and magnetic signatures, and internal structural style. Many of these blocks probably represent tectonostratigraphic terranes. From southwest to northeast, the blocks are defined as follows.

1. The Ben Lomond block, bounded on the southwest by the northeast-dipping San Gregorio fault and on the northeast by the southwest-dipping Zayante fault, is floored mostly by Cretaceous plutonic rocks that are exposed in the northern Gabilan Range and the Ben Lomond pluton (see pls. 3B, 3C).
2. The Logan block, bounded by the Zayante fault on the southwest, by the San Andreas fault on the northeast, by the

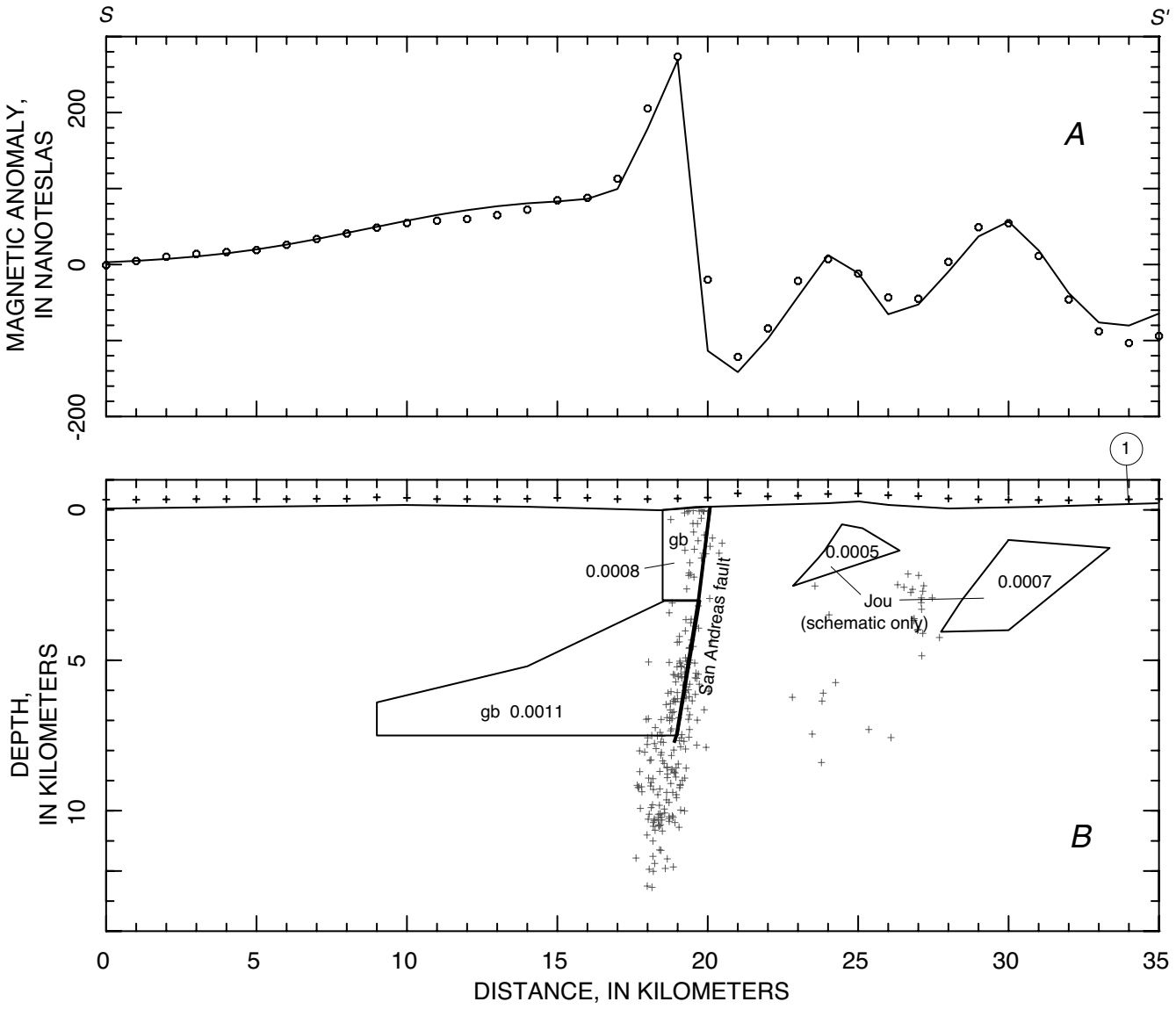

Figure 15.—Magnetic profile (*A*) (circles, measured data; curve, calculated values) and magnetic model (*B*) along line *S*–*S*′ (pl. 3) across the Logan block between the Zayante and San Andreas faults. Pluses along top of model, locations of magnetic observations; pluses in body of model, aftershocks that occurred within 2.5 km of line *S*–*S*′. Numbers on units are magnetizations (in electromagnetic units per cubic centimeter). No vertical exaggeration. gb, gabbro: Jou, Jurassic ultramafic rocks and serpentinite of the Coast Range ophiolite. Circled 1, magnetic boundary 1.

San Gregorio fault at its extreme northwest end, and by an unknown, completely concealed structure, probably a fault, on the north, is characterized by a thick section of Tertiary sedimentary rocks (La Honda Basin) resting on a gabbroic basement with affinities to rocks exposed at the south end of the Sierra Nevada batholith. Plutonic rocks of the Ben Lomond block were thrust northeastward over rocks of the Logan block along the Zayante fault, with total convergence of at least 10 km in places. We propose that the Zayante fault is a reactivated fault possibly left over from the suturing event which attached the basement of the Logan block to the North American Continent, or, alternatively, is a pre-Tertiary fault which juxtaposed the gabbro of Logan against more felsic crystalline rocks by large-scale, dominantly dip slip movement. This proto-Zayante fault may have as its counterpart the south-dipping contact (as interpreted from magnetic data) between the gabbro of Eagle Rest Peak and overlying granitic and high-grade metamorphic rocks of the southern Sierra Nevada. Although geologic evidence indicates that most movement on the Zayante fault had ended by early Miocene time, the spatial coincidence between some aftershocks and the inferred subsurface position of the Zayante fault suggests some ongoing movement. Most aftershocks define a southwest-dipping, crudely planar rupture zone that probably reflects the position of the main section of the San Andreas fault at depth. In contrast, magnetic anomalies

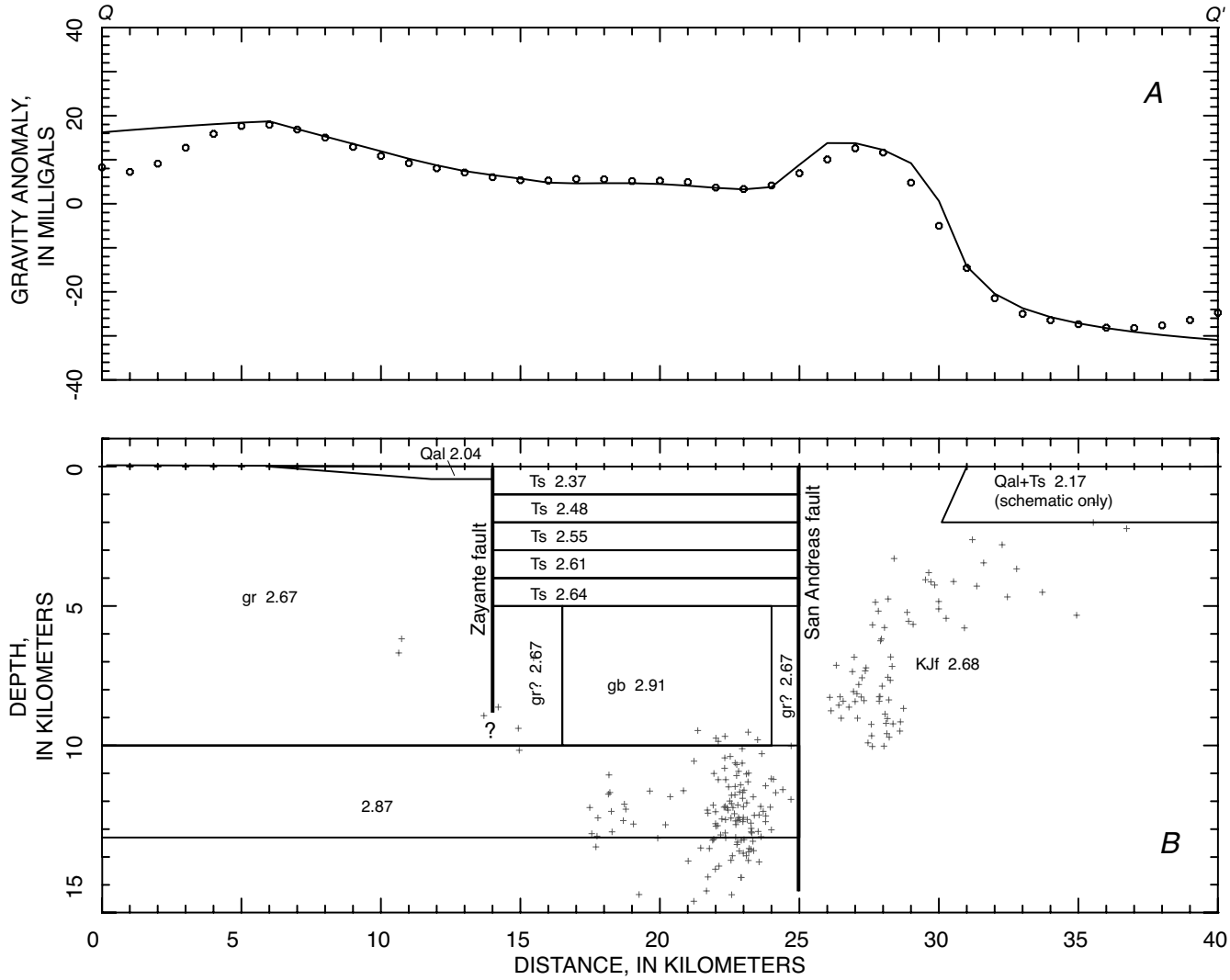

Figure 16.—Isostatic-residual-gravity profile (*A*) (circles, measured data sampled from gridded gravity map; curve, calculated values) and density model (*B*) along line *Q*–*Q′* (pl. 3) across the Logan block between the Zayante and San Andreas faults. Pluses along top of density model, locations where gravity was calculated; pluses in body of density model, aftershocks that occurred within 2.5 km of line *Q*–*Q′*. Numbers on units are densities (in grams per cubic centimeter). No vertical exaggeration. gb, gabbro; gr, granitic and older metamorphic rocks; KJf, Cretaceous and Jurassic Franciscan complex; Qal, Quaternary alluvium; Ts, Tertiary sedimentary rocks.

over younger sedimentary rocks of the Logan block cut by the San Andreas fault indicate that locally the uppermost part of the fault must dip gently northeast. These two facts indicate that, in places, a cross section normal to the fault would show a curved San Andreas fault surface, with the deepest part of the seismically active fault projecting from southwest of the trace toward the surface at a point northeast of the trace, and that only in the uppermost part of the cross section would the fault surface bend backward to the southwest to emerge at the mapped fault trace. We speculate that the San Andreas fault has this shape in the central part of the Loma Prieta "bend" and that some of the shallow aftershocks which appear to be located northeast of the fault actually are associated with the main section of the San Andreas fault at shallow depth.

3. A largely unknown block north of the Logan block and west of the San Andreas fault may be floored by Cretaceous plutonic rocks similar to those of the Montara pluton at lat 37°30′ N.
4. A block immediately northeast of the San Andreas fault has its northeast boundary defined primarily by the northeast border of a strong magnetic anomaly. We interpret the block to be made up of large, coherent packages of Franciscan rocks, Great Valley sequence, and overlying younger strata and to be bounded at its base by a thick, southwest-dipping slab of serpentinite of the Coast Range ophiolite. Because the normal, undeformed structural position of the Coast Range ophiolite is at the base of the Great Valley sequence, and because of similarities between the structure of this block and that of the Franciscan-Great Valley contact on the east side of the Coast Ranges, we interpret the presence of Franciscan rocks between Coast Range ophiolite and Great Valley sequence as evidence for past tectonic wedging by Franciscan rocks into the Coast Range-Great Valley contact. This block, after wedging, was transported northward from the southern Great Valley by strike-slip movement on the San Andreas fault system, which for part of the time included the Calaveras and Silver Creek faults. The Sargent fault cuts vertically through this block and into the block below. Although many aftershocks appear to be associated with movement on the Sargent fault, its failure to noticeably offset magnetic gradients caused by the underlying Coast Range ophiolite suggests that cumulative strike-slip offset on this fault totals no more than a few kilometers.
5. A block between magnetic boundaries 1 and 2 is composed of Franciscan rocks of the Permanente and Bald Mountain-El Sombroso terranes. The northeast limit of the block correlates with a shear zone of melange that also marks a change in structural style, from southwest-dipping units on the southwest to regionally flat lying units on the northeast. This block is denser than most Franciscan rocks, and it causes a gravity high.
6. A block between magnetic boundaries 2 and 3 is composed of Franciscan volcanic and sedimentary rocks with abundant small, isolated masses of serpentinite. This block is defined mostly on the basis of its characteristic magnetic signature, generated by serpentinite. The block is composed of regionally flat lying units, an inference based on the presence of thin serpentinite masses and the observation that the large masses of dense volcanic rocks fail to cause gravity highs.
7. A block immediately southwest of the southwest-dipping Silver Creek fault is composed predominantly of magnetic serpentinite with mafic components of the Coast Range ophiolite, together with sedimentary rocks of the Franciscan Complex and some sedimentary rocks of the Great Valley sequence. Magnetic modeling indicates that the block contains a nearly continuous, subhorizontal sheet of serpentinite which extends across the Santa Clara Valley beneath a thin cover of alluvium. The sheet may once have extended southwestward of magnetic boundary 3 to magnetic boundary 2 but has since been faulted at magnetic boundary 3 and eroded, leaving only thin patches of serpentinite southwest of the fault. The contact between this serpentinite sheet and underlying Franciscan rocks is interpreted to be a wedge fault.

Comparison of this crustal model with the distribution of aftershocks suggests that most aftershocks were associated with movement on three major faults—the Zayante, San Andreas, and Sargent faults—and that the gabbroic body which composes the basement of the Logan block is mostly devoid of aftershocks, in marked contrast to the surrounding rocks. This gabbroic body appears to have played a role in controlling the distribution of aftershocks, although the precise mechanism is unknown.

ACKNOWLEDGMENTS

This study benefited greatly from extensive discussions with Bob McLaughlin about the geology of the Santa Cruz Mountains northeast of the San Andreas fault, and from numerous other discussions about the general geology of the study area with Clark Blake, Joe Clark, Bob Coleman, Carl Wentworth, and many other of our USGS colleagues. Dave Oppenheimer generously supplied the seismicity catalog covering the aftershock sequence, along with the software needed to manipulate it. We thank Bill Ellsworth, Bob McLaughlin, Dave Ponce, and Carl Wentworth for their reviews of the manuscript.

REFERENCES CITED

Abrams, G.A., Kucks, R.P., and Bracken, R.E., 1991, Aeromagnetic gridded data for a portion of the San Jose 1°×2° quadrangle, California: U.S. Geological Survey Open-File Report 91–30, 5 p., 5¼-in. diskette.

Bailey, E.H., and Everhart, D.L., 1964, Geology and quicksilver deposits of the New Almaden district, Santa Clara County, California: U.S. Geological Survey Professional Paper 360, 206 p.

Bailey, E.H., Irwin, W.P., and Jones, D.L., 1964, Franciscan and

related rocks, and their significance in the geology of western California: California Division of Mines and Geology Bulletin 183, 177 p.

Bishop, C.C., and Chapman, R.H., 1967, Santa Cruz sheet *of* Bouguer gravity map of California: Sacramento, California Division of Mines and Geology, 3 p., scale 1:250,000.

Blake, M.C., Jr., Howell, D.G., and Jayko, A.S., 1984, Tectonostratigraphic terranes of the San Francisco Bay region, *in* Blake, M.C., Jr., ed., Franciscan geology of northern California: Los Angeles, Society of Economic Paleontologists and Mineralogists, Pacific Section Field Trip Guidebook, v. 43, p. 5–22.

Blake, M.C., Jr., Zietz, Isidore, and Daniels, D.L., 1977, Aeromagnetic and generalized geologic map of parts of central California: U.S. Geological Survey Geophysical Investigations Map GP–918, scale 1:1,000,000.

Blakely, R.J., and Simpson, R.W., 1986, Approximating edges of source bodies from magnetic or gravity anomalies: Geophysics, v. 51, no. 7, p. 1494–1498.

Brabb, E.E., 1960, Geology of the Big Basin area, Santa Cruz Mountains, California: Stanford, Calif., Stanford University, Ph.D. thesis, 192 p.

Carle, S.F., and Langenheim, V.E., 1990, Isostatic residual gravity map of the Palo Alto 7.5′ quadrangle, California, sheet 2 *of* Oliver, H.W., ed., Preliminary ground water quality data and the extent of the ground water basin from drill hole, seismic, and gravity data in the Palo Alto 7.5′ quadrangle, California: U.S. Geological Survey Open-File Report 90–74, scale 1:24,000.

Chapman, R.H., and Bishop, C.C., compilers, 1968, Bouguer gravity map of California, San Francisco sheet: Sacramento, California Division of Mines and Geology, 3 p., scale 1:250,000.

Chase, Gordon, and Youngs, L.G., 1979, Aeromagnetic map of the Santa Rosa 1°×2° quadrangle, California: California Division of Mines and Geology Open-File Report 89–22, scale 1:250,000.

Christensen, N.I., 1982, Seismic velocities, *in* Carmichael, R.S., ed., Handbook of physical properties of rocks: Boca Raton, Fla., CRC Press, v. 2, p. 1–228.

Clark, J.C., and Rietman, J.D., 1973, Oligocene stratigraphy, tectonics, and paleogeography southwest of the San Andreas fault, Santa Cruz Mountains and Gabilan Range, California Coast Ranges: U.S. Geological Survey Professional Paper 783, 18 p.

Cordell, Lindrith, and Grauch, V.J.S., 1985, Mapping basement magnetization zones from aeromagnetic data in the San Juan Basin, New Mexico, *in* Hinze, W.J., ed., The utility of regional gravity and magnetic anomaly maps: Tulsa, Okla., Society of Exploration Geophysicists, p. 181–197.

Cummings, J.D., Touring, R.M., and Brabb, E.E., 1962, Geology of the northern Santa Cruz Mountains, California, *in* Bowen, O.E., Jr., ed., Geologic guide to the gas and oil fields of northern California: California Division of Mines and Geology Bulletin 181, p. 179–220.

Dietz, L.D., and Ellsworth, W.L., 1990, The October 17, 1989, Loma Prieta, California, earthquake and its aftershocks; geometry of the sequence from high-resolution locations: Geophysical Research Letters, v. 17, no. 9, p. 1417–1420.

Eberhart-Phillips, D.M., and Michael, A.J., 1991, The 1991 active seismic experiment in the Loma Prieta, California region; shallow seismicity and fault structure: Eos (American Geophysical Union Transactions), v. 72, no. 44, supp., p. 311.

Ernst, W.G., 1970, Tectonic contact between the Franciscan melange and the Great Valley sequence—crustal expression of a late Mesozoic Benioff zone: Journal of Geophysical Research, v. 75, no. 5, p. 886–901.

Foxall, Williams, Michelini, Alberto, and McEvilly, T.V., 1993, Earthquake traveltime tomography of the southern Santa Cruz Mountains; control of fault rupture by lithological heterogeneity of the San Andreas fault zone: Journal of Geophysical Research, v. 98, no. B10, p. 17691–17710.

Gardner, G.H.F., Gardner, L.W., and Gregory, A.R., 1974, Formation velocity and density—the diagnostic basics for stratigraphic traps: Geophysics, v. 39, no. 6, p. 770–780.

Griscom, Andrew, 1966, Magnetic data and regional structure in northern California, *in* Subcrustal structure, chap. 9 *of* Bailey, E.H., ed., Geology of northern California: California Division of Mines and Geology Bulletin 190, p. 407–417.

———1982, Magnetic interpretation of ophiolites and batholiths in California [abs.]: Geological Society of American Abstracts with Programs, v. 14, no. 7, p. 503.

———1983, The contact between the Great Valley Sequence and the Franciscan Assemblage, California, from magnetic data [abs.]: Eos (American Geophysical Union Transactions), v. 64, no. 45, p. 867–868.

Griscom, Andrew, and Jachens, R.C., 1989, Tectonic history of the north portion of the San Andreas fault system, California, inferred from gravity and magnetic anomalies: Journal of Geophysical Research, v. 93, no. B4, p. 3089–3099.

———1990, Tectonic implications of gravity and magnetic models along east-west seismic profiles across the Great Valley near Coalinga, California, *in* Rymer, M.J., and Ellsworth, W.L., eds., The Coalinga, California, earthquake of May 2, 1983: U.S. Geological Survey Professional Paper 1487, 417 p.

Hamilton, Warren, 1969, Mesozoic California and the underflow of Pacific mantle: Geological Society of America Bulletin, v. 80, no. 12, p. 2409–2430.

Heiskanen, W.A., and Moritz, Helmut, 1967, Physical geodesy: San Francisco, W.H. Freeman and Co., 364 p.

Howell, D.G., Jones, D.L., and Schermer, E.R., 1985, Tectonostratigraphic terranes of the circum-Pacific region, *in* Howell, D.G., ed., Tectonostratigraphic terranes of the circum-Pacific region (Circum-Pacific Council for Energy and Mineral Resources Earth Science Series, no. 1): Houston, Tex., p. 3–30.

Jachens, R.C., and Griscom, Andrew, 1985, An isostatic residual gravity map of California—a residual map for interpretation of anomalies from intracrustal sources, in Hinze, W.J., ed., The utility of regional gravity and magnetic anomaly maps: Tulsa, Okla., Society of Exploration Geophysicists, p. 347–360.

Jachens, R.C., Griscom, Andrew, Blake, M.C., McLaughlin, R.J., and Wentworth, C.M., 1990, Cross-fault compression inferred from southwest dips of strike-slip faults in the San Francisco Bay region, California [abs.]: Geological Society of America Abstracts with Programs, v. 22, no. 3, p. 31.

Jachens, R.C., and Roberts, C.W., 1993, Aeromagnetic map of the San Francisco Bay area, California: U.S. Geological Survey Geophysical Investigations Map GP–1007, scale approximately 1:286,500.

James, E.W., 1992, Cretaceous metamorphism and plutonism in the Santa Cruz Mountains, Salinian block, California, and correlation with the southernmost Sierra Nevada: Geological Society of American Bulletin, v. 104, no. 10, p. 1326–1339.

James, E.W., Kimbrough, David, and Mattinson, J.J., 1986, Evaluation of pre-Tertiary piercing points along the northern San Andreas Fault using U-Pb zircon dating, initial Sr and common Pb isotopic ratios [abs]: Geological Society of America Abstracts with Programs, v. 18, no. 2, p.121.

Jennings, C.W., and Burnett, J.L., compilers, 1961, San Francisco sheet *of* Geologic map of California: Sacramento, California Division of Mines and Geology, scale 1:250,000.

Jennings, C.W., and Strand, R.G., compilers, 1958, Santa Cruz sheet *of* Geologic map of California: Sacramento, California Division of Mines and Geology, scale 1:250,000.

Johnson, C.M., and O'Neil, J.R., 1988, Constraints on Pre-Tertiary movement on the San Andreas fault system (SAF); stable and radiogenic isotope and trace element data from Jurassic gabbros [abs]: Geological Society of America Abstracts with Programs, v. 20, p. A381.

Lewis, S.D., 1996, Fault and fold map of the central California continental margin, San Francisco Bay/Monterey Bay region, *in* Jayko, A.S., and Lewis, S.D., Toward assessing the seismic risk associated with blind faults, San Francisco Bay region, California: U.S. Geological Survey Open-File Report 96–267, p. 28–29.

McCulloch, D.S., and Greene, H.G., 1990, Geology, map 5A *of* Geologic map of the central California continental margin, in Greene, H.G., and Kennedy, M.P., eds., Geology of the central California continental margin, California continental margin geologic map series: Sacramento, California Division of Mines and Geology, scale 1:250,000.

McLaughlin, R.J., Blake, M.C., Jr., Griscom, Andrew, Blome, C.D., and Murchey, Bonita, 1988a, Tectonics of formation, translation, and dispersal of the Coast Range ophiolite of California: Tectonics, v. 7, no. 5, p. 1033–1056.

McLaughlin, R.J., Clark, J.C., and Brabb, E.E., 1988b, Geologic map and structure sections of the Loma Prieta 7½′ quadrangle, Santa Clara and Santa Cruz Counties, California: U.S. Geological Survey Open-File Map 88–762, 2 sheets, scale 1:24,000.

McLaughlin, R.J., Clark, J.C., Brabb, E.E., and Helley, E.J., 1991, Geologic map and structure sections of the Los Gatos 7½′ quadrangle, Santa Clara and Santa Cruz Counties, California: U.S. Geological Survey Open-File Map 91–593, 3 sheets, scale 1:24,000.

Michael, A.J., and Eberhart-Phillips, D.M., 1991, Relations among fault behavior, subsurface geology, and three-dimensional velocity models: Science, v. 253, no. 5020, p. 651–654.

Pavoni, Nazario, 1973, A structural model for the San Andreas fault zone along the northeast side of the Gabilan Range, *in* Kovach, R.L., and Nur, Amos, eds., Proceedings of the conference on tectonic problems of the San Andreas fault system: Stanford, Calif., Stanford University Publications in the Geological Sciences, v. 13, p. 259–274.

Robbins, S.L., Oliver, H.W., and Holden, K.D., compilers, 1976, San Jose sheet *of* Bouguer gravity map of California: Sacramento, California Division of Mines and Geology, 10 p., scale 1:250,000.

Roberts, C.W., and Jachens, R.C., 1993, Isostatic residual gravity map of the San Francisco Bay area, California: U.S. Geological Survey Geophysical Investigations Map GP–1006, scale approximately 1:286,500.

Roberts, C.W., Jachens, R.C., and Oliver, H.W., 1990, Isostatic residual gravity map of California and offshore southern California: California Division of Mines and Geology Geologic Data Map 7, scale 1:750,000.

Rogers, T.H., compiler, 1966, San Jose sheet *of* Geologic map of California: Sacramento, California Division of Mines and Geology, scale 1:250,000.

Ross, D.C., 1970, Quartz gabbro and anorthositic gabbro; markers of offset along the San Andreas fault in the California Coast Ranges: Geological Society of America Bulletin, v. 81, no. 12, p. 3647–3662.

———1972, Petrographic and chemical reconnaissance study of some granitic and gneissic rocks near the San Andreas fault from Bodega Head to Cajon Pass, California: U.S. Geological Survey Professional Paper 698, 92 p.

———1978, The Salinian block—a Mesozoic granitic orphan in the California Coast Ranges, *in* Howell, D.G., and McDougall, K.A., eds., Mesozoic paleogeography of the Western United States (Pacific Coast Paleogeography Symposium 2): Los Angeles, Society of Economic Paleontologists and Mineralogists, Pacific Section, p. 509–522.

———1984, Possible correlations of basement rocks across the San Andreas, San Gregorio-Hosgri, and Rinconada-Reliz-King City faults, California: U.S. Geological Survey Professional Paper 1317, 37 p.

Sorg, D.H., and McLaughlin, R.J., 1975, Geologic map of the Sargent-Berrocal fault zone between Los Gatos and Los Altos Hills, Santa Clara County, California: U.S. Geological Survey Miscellaneous Field Investigations Map MF–643, scale 1:24,000.

Stanley, R.G., 1987, New estimates of displacement along the San Andreas fault in central California based on paleobathymetry and paleogeography: Geology, v. 15, no. 2, p. 171–174.

Telford, W.M., Geldart, L.P., Sheriff, R.E., and Keyes, D.A., 1976, Applied geophysics: London, Cambridge University Press, 860 p.

Wagner, D.L., Bortugno, E.J., and McJunkin, R.D., 1991, Geologic map of the San Francisco-San Jose quadrangle: California Division of Mines and Geology Regional Geologic Map Series Map 5A, scale 1:250,000.

Walter, A.W., 1990, Upper-crustal velocity structure near Coalinga, as determined from seismic-refraction data, *in* Rymer, M.J., and Ellsworth, W.L., eds., The Coalinga, California, earthquake of May 2, 1983: U.S. Geological Survey Professional Paper 1487, p. 23–40.

Wentworth, C.M., Blake, M.C., Jr., McLaughlin, R.J., and Graymer, R.W., 1999, Preliminary geologic map of San Jose 30×60-minute quadrangle, California: U.S. Geological Survey Open-File Report 98–795, scale 1:100,000.

Wentworth, C.M., Blake, M.C., Jr., Jones, D.L., Walter, A.W., and Zoback M.D., 1984, Tectonic wedging associated with emplacement of the Franciscan assemblage, California Coast Ranges, *in* Blake, M.C., Jr., ed., Franciscan geology of northern California: Society of Economic Paleontologists and Mineralogists, Pacific Section Field Trip Guidebook, v. 43, p. 163–173.

Wentworth, C.M., and Zoback, M.D., 1990, Structure of the Coalinga region and thrust origin of the earthquake, *in* Rymer, M.J., and Ellsworth, W.L., eds., The Coalinga, California, earthquake of May 2, 1983: U.S. Geological Survey Professional Paper 1487, p. 41–68.

Youngs, L.G., 1989, Aeromagnetic map of the Bakersfield 1°×2°

quadrangle, California: California Division of Mines and Geology Open-File Report 89–24, scale 1:250,000.

Youngs, L.G., and Mattison, Elise, 1989, Aeromagnetic map of the Los Angeles 1°×2° quadrangle, California: California Division of Mines and Geology Open-File Report 89–22, scale 1:250,000.

EARTHQUAKE OCCURRENCE

DEEP GEOELECTRICAL STRUCTURE OF THE LOMA PRIETA REGION

By Brian D. Rodriguez, Victor F. Labson, William D. Stanley, and Jay A. Sampson, U.S. Geological Survey

CONTENTS

ABSTRACT

A magnetotelluric-sounding profile in the Loma Prieta region was completed before the earthquake. An electrical-resistivity model calculated for the magnetotelluric profile indicates (1) a large, high-resistivity structure within 2 km of the surface between the San Andreas and Sargent faults at seismogenic depths that may have played an important role in stress buildup; and (2) a region of anomalously low resistivity at midcrustal depths near the San Andreas fault that may have been caused by fluids in the deeper parts of the fault-gouge zone, which could have reduced the shear stress required for sliding and thus promoted the M=7.1 earthquake. The anomalously low resistivity region was a key and required element of the model, even though the model was insensitive to dip, shape, and distribution. The structure interpreted from this profile will provide constraints on future geologic interpretations of the Loma Prieta region. High-resistivity units southwest of the San Andreas fault may represent Salinian-block granitoids of Mesozoic age. High-resistivity units, below 4-km depth, northeast of the San Andreas fault could be related to the Franciscan complex. Low-resistivity rocks between the Zayante and Sargent faults in the uppermost 4 to 7 km of crust are interpreted from drill-hole data as mostly Tertiary marine sedimentary rocks exposed in tightly folded structures in the Loma Prieta region. Low-resistivity units, above 4-km depth, northeast of the San Andreas fault are believed to represent Mesozoic units of the Franciscan assemblage. The resistivity model agrees well with the three-dimensional seismic-velocity model of the Loma Prieta region derived by using raypaths from aftershocks recorded by the U.S. Geological Survey seismic network. The resistivity model is also consistent with gravity and magnetic models of the Loma Prieta region. The San Andreas fault and adjoining subparallel Sargent and Zayante faults appear to juxtapose diverse deep geologic structures spanning the seismogenic zone in the Loma Prieta region, suggesting that local geologic structures may have played a role in triggering the earthquake and may control the overall seismicity on the San Andreas and Sargent faults. Another magnetotelluric-sounding profile about 35 km southeast, traversing the northwest end of the Gabilan Range, shows a distinctly different structure. Low-resistivity units there appear to be more spatially uniform and limited to the uppermost 4 km of crust. This type of geoelectrical structure may indicate stable fault slip on the central section of the San Andreas fault.

INTRODUCTION

The Loma Prieta earthquake associated with the San Andreas fault was unusual in its depth of focus (18 km) and the thrust component evident in first motions. Because the Loma Prieta region is complex, it needs interpretative input from every applicable field of study if we are ever to really understand its structure, dynamics, and tectonic history. Few published accounts of geoelectrical measurements across the San Andreas fault exist (Mazzella, 1976; Phillips and Kuckes, 1983; Mackie and others, 1988; Park and others, 1991). The absence of geoelectrical results is partly explainable by the difficulty of acquiring data in the region. Deep-penetrating electrical soundings measure extremely small magnetic and electrical fields and are prone to interference from such cultural features as powerlines, television and radio transmitters, and pipelines.

Two magnetotelluric (MT) profiles have been used to characterize the deep-crustal electrical structure of the San

Andreas fault in the Loma Prieta region and northern Gabilan Range as part of the U.S. Geological Survey (USGS)'s National Geologic Mapping and Deep Continental Studies programs. The MT method is used to determine the electrical-resistivity structure of the subsurface (see app. 1). Two MT profiles that define the subsurface resistivity to below 10-km depth indicate the geometry of faulting that is complementary to seismic and other geophysical techniques. In combination with geologic information and the results of other geophysical methods, lithologic distributions may be inferred. We hope that our interpretation of the MT data will not only lead to a more accurate understanding of the faulting mechanism but also assist other workers in their efforts to understand how the 1989 Loma Prieta earthquake actually fits into the larger scope of studies on the San Andreas fault.

MAGNETOTELLURIC COVERAGE

One north-by-northeast profile of MT soundings (Loma Prieta profile, fig. 1) near the Loma Prieta region was completed in May 1989. Later, MT coverage on this profile was expanded, and a northeast profile (Gabilan Range profile, fig. 1) across the northwest end of the Gabilan Range was completed in May 1990. Stations were then added to the Loma Prieta profile in June 1992 to provide more MT coverage in geologically complex areas (see app. 2).

The Loma Prieta profile (fig. 1) was positioned along the south end of the locked 1906 segment of the San Andreas fault, and the Gabilan Range profile was positioned along the transition from the locked segment to stable fault slip on the central section of the San Andreas fault near San Juan Bautista. A main objective of the study was to investigate deep structures associated with seismic-stress release so as to aid in understanding earthquake mechanisms along the San Andreas fault.

MAGNETOTELLURIC MODELS

LOMA PRIETA PROFILE

The 14 MT soundings on the Loma Prieta profile (fig. 1) were modeled with an interactive, finite-element algorithm to calculate the tensor resistivities and phases for two-dimensional structures (Wannamaker and others, 1987). The finite-element grid used in this model consisted of 263 by 40 variable-dimension cells extending to several hundred kilometers horizontally and 70 km vertically to minimize edge effects. The seawater of the Pacific Ocean was simulated at the southwest end of the model. We manually perturbed the starting two-dimensional model (see app. 3) more than 100 times; the best-fit model is shown in figure 2.

The gross structure of our model came from fitting the transverse-magnetic data (see app. 1). Wannamaker and others (1987) showed that finite strike-length structure is better resolved with the transverse-magnetic mode and that the transverse-electric mode is highly insensitive to gross resistivity structure. We noted, however, that we needed to add conductance in the depth range 4–16 km near the San Andreas fault so as to adequately fit the observed transverse-electric data in the low to midband frequencies. Thus, the dip, shape, and precise distribution of this added conductance were irresolvable, even though its presence was a major requirement of the model. We determined that, in its absence, we had no other solution to adequately fit the observed transverse-electric data (see app. 3). The deeper conductive zones could conceivably have numerous variations and still be consistent with the observed data, although our model requires some degree of lateral inhomogeneity in resistivity in the uppermost 16 km of crust across the Loma Prieta region (see app. 3).

In the uppermost 4 km of crust, resistivities ranged from 3 to 1,000 Ω-m. The conductive material beneath these stations could vary somewhat in thickness, distribution, and depth from what we consider to be our best discrete two-dimensional resistivity model, though probably not without adversely affecting the computed fit to the observed data. The thickness, distribution, and depth of the more resistive material, however, are poorly constrained and probably could vary somewhat. For example, the thickness of the 100 Ω-m material northeast of station 3 (fig. 1) could be increased to at least 19-km depth; however, the observed data do not require this increase in our models.

The key features of the Loma Prieta MT model are as follows:

(1) high resistivities (approx 100–1,000 Ω-m) above 2-km depth beneath stations 3 and 16 (fig. 1);
(2) high resistivities (approx 1,000 Ω-m) at 4- to 7-km depth over much of the profile southwest of the San Andreas fault and at 10-km depth northeast of the San Andreas fault;
(3) low resistivities of 3 to 30 Ω-m above 4-km depth southwest of the San Andreas fault and of 1 to 100 Ω-m above 10-km depth northeast of the San Andreas fault; and
(4) low-resistivity (approx 3 Ω-m) bodies in the depth range 4–19 km near the San Andreas fault, with their dip, shape, and precise distribution irresolvable.

The resolution of the resistivity boundaries used for the model is somewhat subjective. If different resistivities are used, then boundary positions and layer depths would have to be adjusted to achieve similar fits to the observed data. The extreme case would be to use a model with a "continuous" resistivity gradient from low to high resistivities. The resolution of the resistivity boundaries also is partly a function of our model grid-mesh design. We have attempted to keep the model simple. Our final model is, in our opinion, the best discrete two-dimensional model that fits the observed data.

GABILAN RANGE PROFILE

The six MT soundings on the Gabilan Range profile (fig. 1) were modeled with the same interactive, two-dimensional finite-element algorithm as the one used on the Loma Prieta profile. The finite-element grid used in this model consisted of 239 by 48 variable-dimension cells extending to several hundred kilometers horizontally and vertically; the best-fit model is shown in figure 3. This model indicates large contrasts in resistivity in the uppermost 4 km of crust across this region.

The key features of the Gabilan Range MT model are as follows:

(1) a high-resistivity (1,000 Ω-m) basement at about 4-km depth,
(2) a central low-resistivity (3–10 Ω-m) anomaly to about 4- to 7-km depth beneath stations 1, 5, and 6 (fig. 1), and
(3) an adjacent low-resistivity (1–3 Ω-m) anomaly southwest of station 4 to about 4-km depth.

Like the Loma Prieta MT model, the resolution of the resistivity boundaries used for the Gabilan Range MT model is somewhat subjective. We again have attempted to keep the model simple. Our final model is, in our opinion, the best discrete two-dimensional model that fits the observed data.

DISCUSSION OF MODELS

LOMA PRIETA PROFILE

Electrical resistivity can be reduced by fracturing, conductive pore fluids, and alteration minerals. Unaltered, unfractured crystalline rocks normally are highly resistive; marine sedimentary rocks and clay-rich alluvium normally are highly

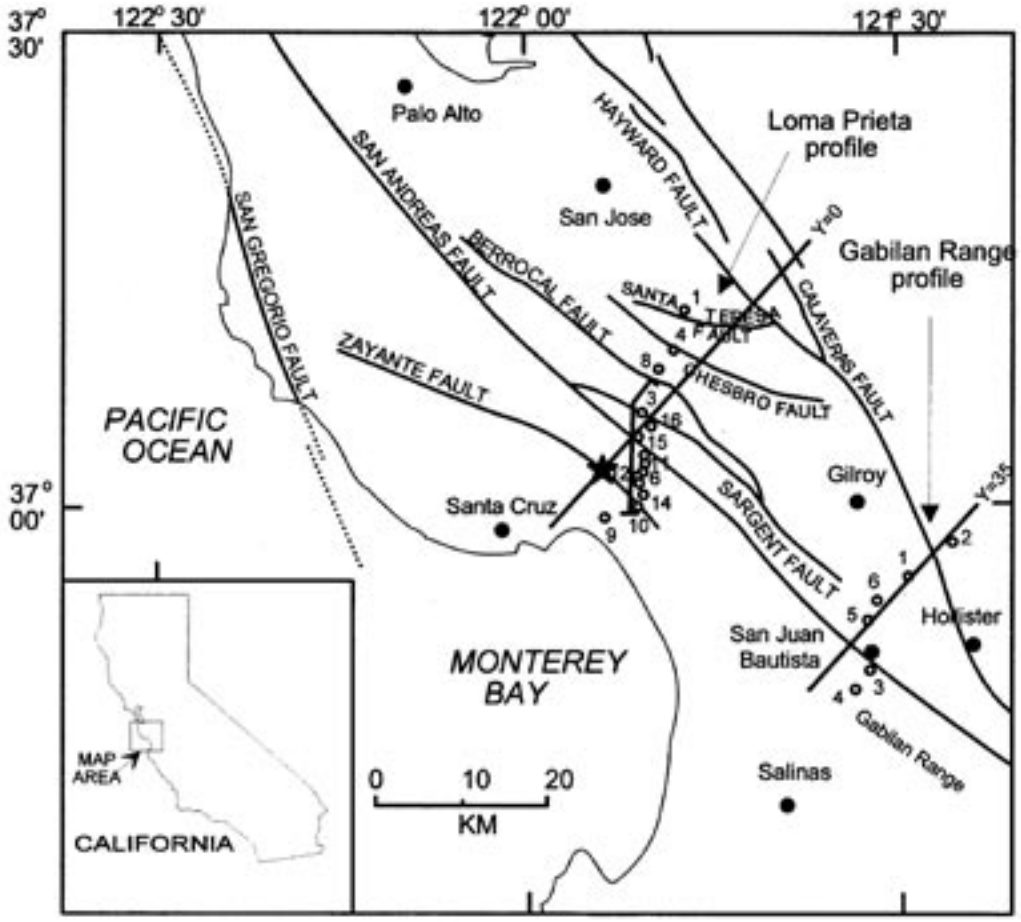

Figure 1.—Index map of the Loma Prieta region, Calif., showing locations of two magnetotelluric (MT) profiles used in resistivity modeling. Numbered dots, stations where MT soundings were made; star, epicenter of October 17, 1989, main shock. *Y*=0 line overlaying Loma Prieta MT profile is projection used for three-dimensional velocity-inversion vertical model slice (Eberhart-Phillips and others, 1990) at *Y*=0 km; *Y*=35 line overlaying Gabilan Range MT profile is projection used for Gabilan Range model 35 km southeast of *Y*=0 line. Irregular line with end points is profile of geologic cross section shown in figure 8.

conductive; and metamorphic rocks, including gneiss, schist (nongraphitic), and marble, are moderately to highly resistive. In general, low resistivity, low density, and low velocity are correlative because they all are associated with increasing porosity and water content. Exceptions to this behavior in the Loma Prieta region may be high-velocity, low-resistivity serpentinized mafic rocks.

The three-dimensional velocity model of the Loma Prieta region, derived using raypaths from aftershocks recorded by the U.S. Geological Survey seismic network (Eberhart-Phillips and others, 1990), includes a low-velocity (3.2–5.9 km/s) wedge of material between the Zayante and San Andreas faults that extends below 8-km depth, and a high-velocity (6.3–6.4 km/s) zone at depth between the San Andreas and Sargent faults. Some striking similarities in the velocity and resistivity models are visible in figure 4. The high-resistivity anomaly in the uppermost 10 km of crust beneath the San Andreas and Sargent faults coincides with high velocities, whereas the low-resistivity anomaly in the uppermost 8 km of crust between stations 10 and 5 (fig. 1) coincides with a low-velocity zone. We also note that a low-resistivity branch extends into the much higher velocity part of the velocity model. The thick, 10- to 100-Ω-m-resistivity units northeast of the Sargent fault correspond to velocities of less than 6 km/s. Readers of Eberhart-Phillips and others (1990) will notice minor differences between our current and previously published resistivity models. Reprocessing of the original six stations, the inclusion of nine additional stations (station 14 replacing station 7), and improved fits to the observed data account for these minor differences.

Although the high-resistivity units southwest of the San Andreas fault are believed to represent Salinian-block granitoids of Mesozoic age (Clark and Rietman, 1973), they could be any other granitic or metamorphic-rock units. Similar resistivities have been measured in granitic rocks worldwide, including granitoids in the Gabilan Range (southeast of the Loma Prieta region) by Phillips and Kuckes (1983). The high-resistivity unit in our model that occurs between the San Andreas and Berrocal faults could be related to a highly metamorphosed section of Franciscan complex (Brabb and Hanna, 1981; McLaughlin and others, 1988); this unit appears to be limited in strike length relative to the rest of the geoelectrical structure (see app. 2).

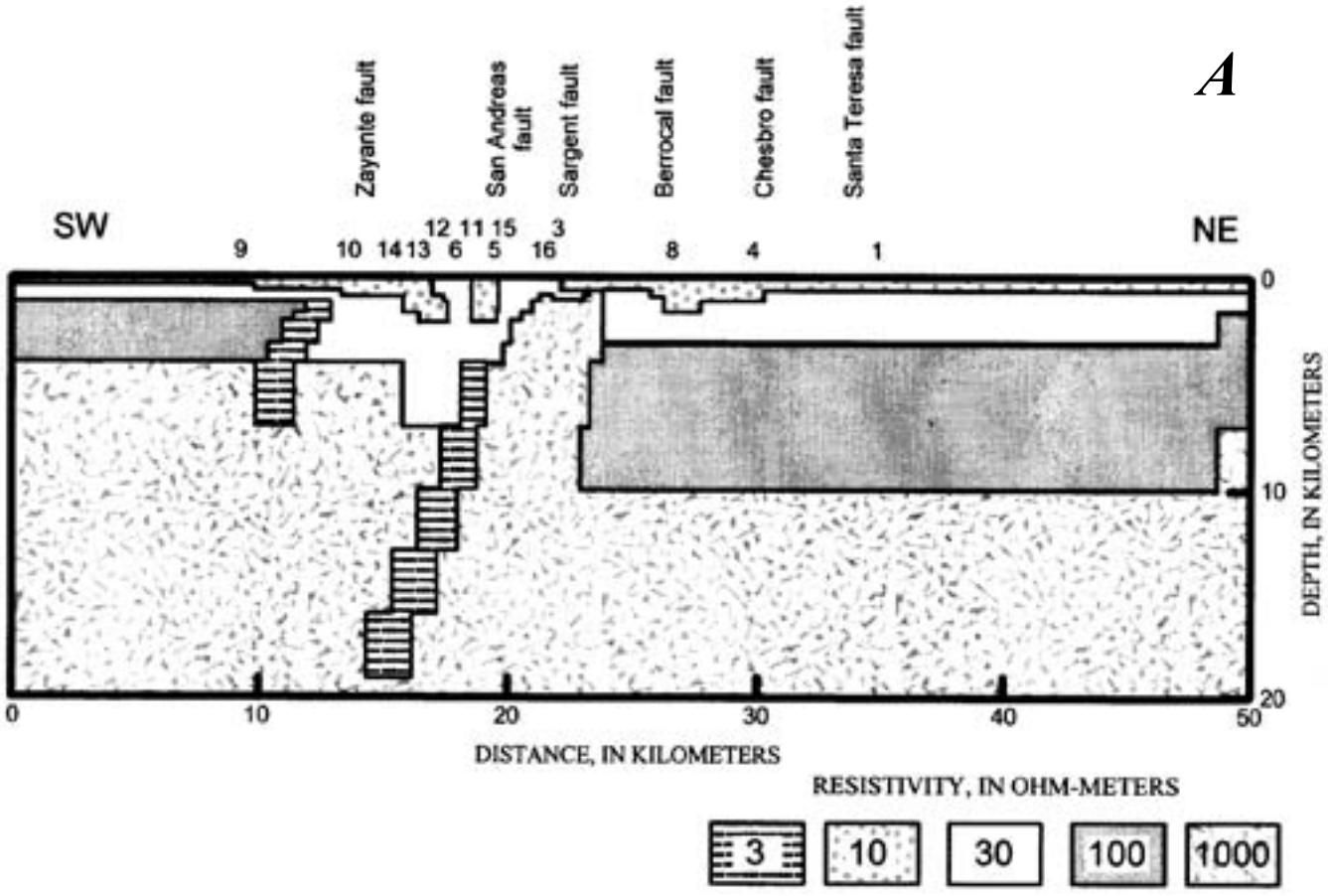

Figure 2.—Loma Prieta magnetotelluric (MT) profile (see fig. 1 for locations). *A*, Two-dimensional finite-element MT model. Numbers denote stations shown in figure 1. *B*, Resistivity data. *C*, Phase data. Observed data: crosses, transverse electric (TE); circles, transverse magnetic (TM). Calculated data: solid curves, TE; dashed curves, TM.

We interpret the 3- to 30-Ω-m-resistivity rocks between the Zayante and Sargent faults in the uppermost 4 to 7 km of crust as mostly Tertiary marine sedimentary rocks, which are exposed in tightly folded structures in the Loma Prieta region (McLaughlin and others, 1988). Jachens and Griscom (this chapter) state that the total Tertiary marine section is about 6 to 7.5 km thick between the Zayante and San Andreas faults beneath our Loma Prieta profile. The Loma Prieta MT model shows a conductive (3–30 Ω-m) section, about 4 to 7 km thick; however, this section extends only between station 14 (fig. 1) and the San Andreas fault (fig. 2). Extending this conductive section to the Zayante fault increases the transverse-magnetic curve misfit significantly at station 14; however, if we use a resistivity of 100 Ω-m in the depth range 4–7 km, extending this conductive section to the Zayante fault increases the transverse-magnetic curve misfit only slightly at station 14.

Although the conductive material that extends to 19-km depth may be partly explainable with altered basement rocks and fault gouge, we find it geologically difficult to accept 3-Ω-m-resistivity material at these depths. However, serpen-

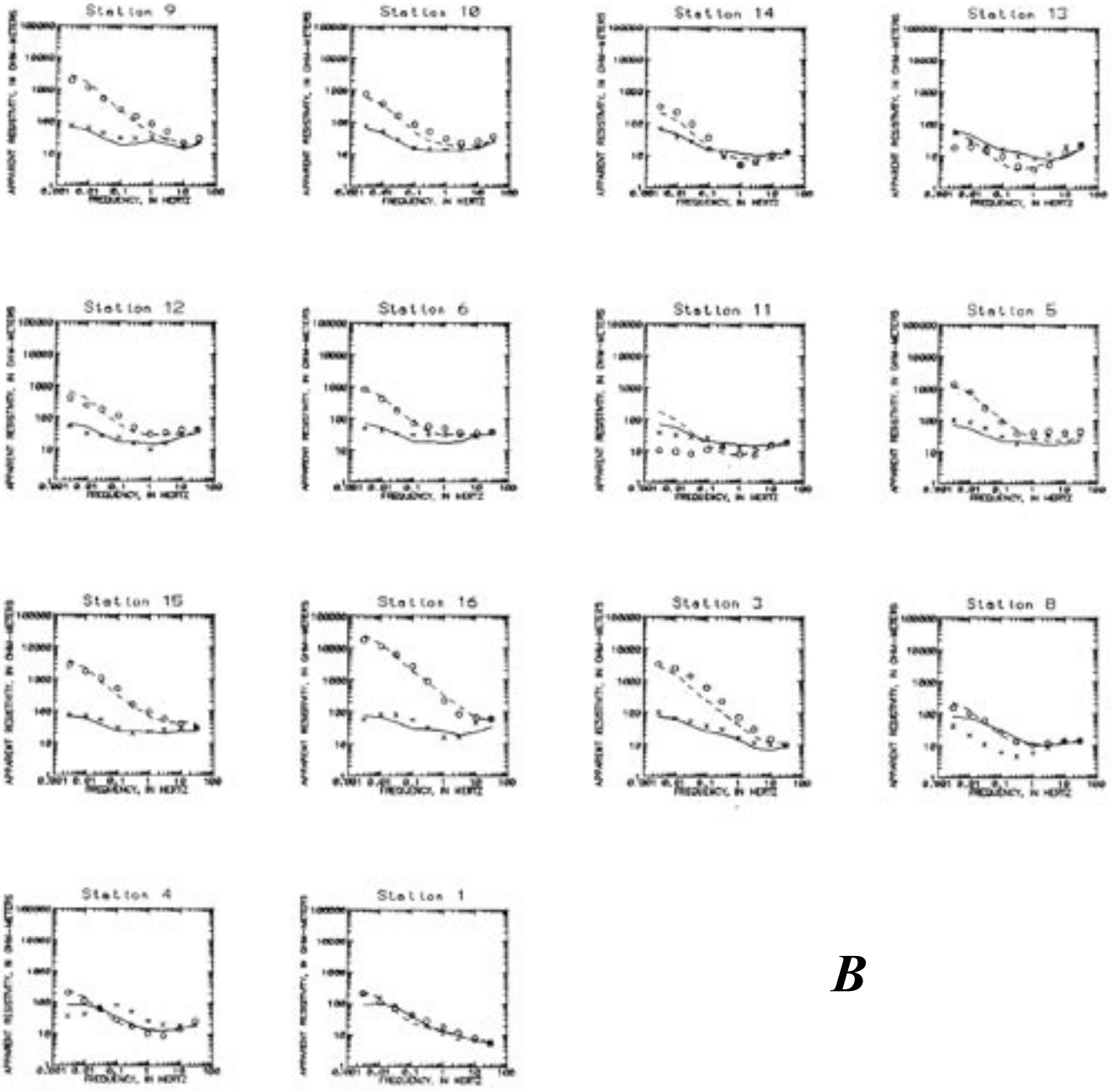

Figure 2.—Continued

tinization of mafic rocks reduces their resistivities to the range 5–40 Ω-m (Parkhomenko, 1967). Also, Stesky and Brace (1973) reported laboratory samples of serpentinite to have a steady 3-Ω-m resistivity when subjected to pressures of 0 to 6 kbars and that the resistivity of a serpentinized gabbro is 100 to 1,000 times lower than that of a serpentine-free gabbro. C.S. Cox (in Stesky and Brace, 1973, p. 7619) inferred a resistivity 10 times that of seawater for rocks within 30 km of the sea bottom. A 10- to 13-km-thick section of 10-Ω-m-resistivity rocks mapped under the east edge of the Gabilan Range (southwest of the San Andreas fault) by Phillips and Kuckes (1983), using controlled-source electromagnetic soundings, was interpreted by them to be either fault gouge or serpentinized oceanic crust. Serpentinite, however, is not known to exist anywhere in the Salinian block (Jachens and Griscom, this chapter). Therefore, resistivities in these deep rocks must be almost entirely related to fracturing and fluid content (see app. 1).

The 10-, 30-, 100-, and 1,000-Ω-m-resistivity units beneath stations 1, 4, and 8 on the Loma Prieta profile (fig. 1) are

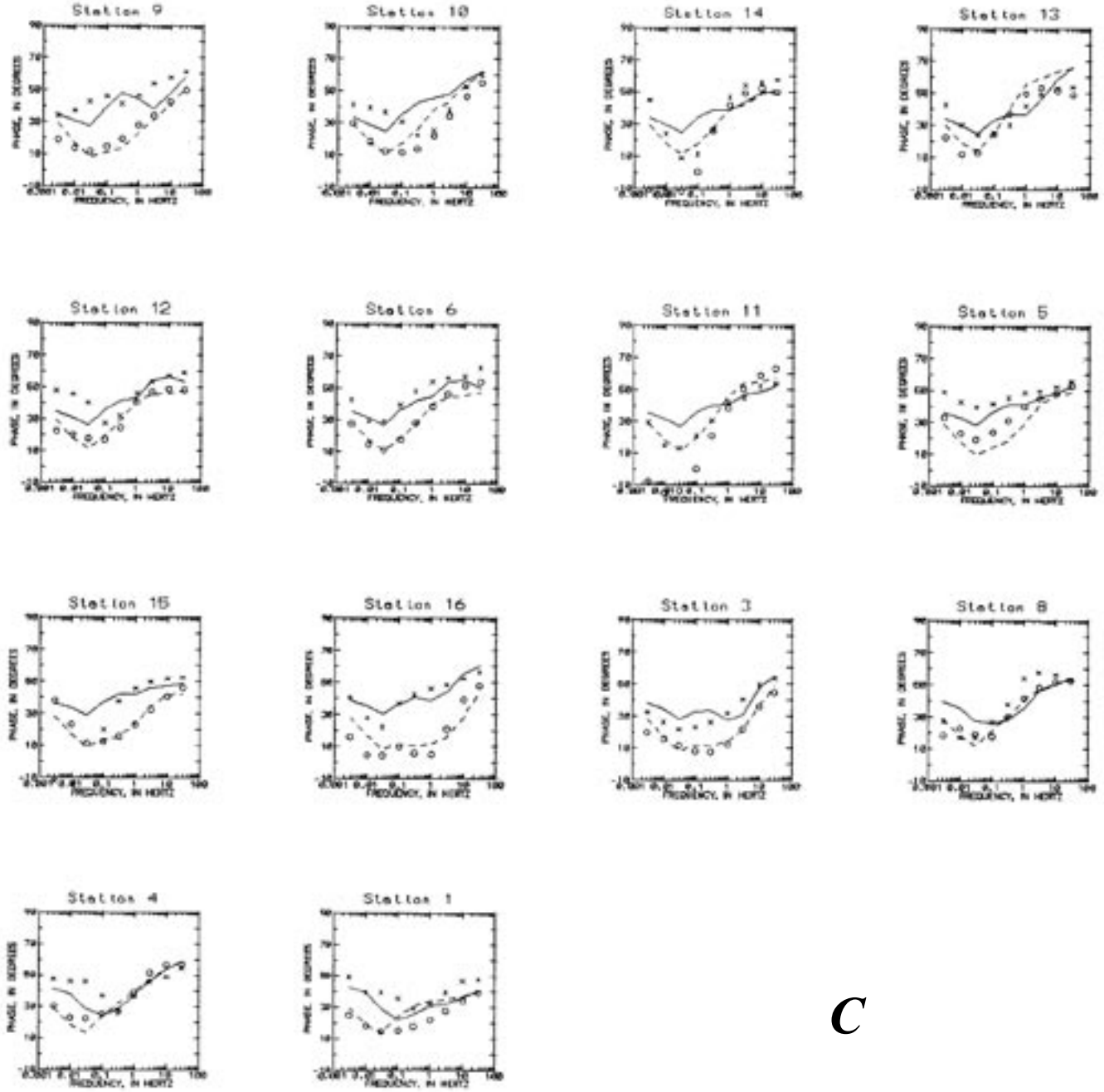

Figure 2.—Continued

believed to represent Mesozoic Franciscan rocks, which consist of a highly sheared assemblage of sandstone and shale, with lesser amounts of chert, limestone, greenstone, serpentine, and interbedded basalt flows (Alt and Hyndman, 1975; Cole and others, 1989). Mazzella (1976) measured similar resistivities for these units in the Hollister area (fig. 1). Velocities of less than 6.0 km/s coincident with this 100-Ω-m-resistivity section (fig. 4) are compatible with interpreted velocities for the Franciscan Formation in similar three-dimensional inversions and refraction surveys at Coalinga, Calif. (Eberhart-Phillips, 1989; Walter, 1990). The southwest edge of the 100-Ω-m-resistivity Franciscan wedge from 4- to 10-km depth approximately correlates with the position of the Berrocal fault, if its fault plane dips southwest. The interpreted wedge also appears to be limited in strike length relative to the rest of the geoelectrical structure (see app. 2), which we could not determine without additional data for our three-dimensional MT modeling. The northeast edge of the 10-Ω-m-resistivity unit under station 4 (fig. 1) correlates with the position of the Chesbro fault. The Santa Teresa fault is not apparent in the resistivity data at these depths.

A plot of aftershocks (main-shock section Y=0; Dietz and Ellsworth, 1990) along the Loma Prieta MT model cross section (fig. 5) shows a southwest-dipping main-shock plane below 10-km depth that approximately coincides with the deeper parts of the 3-Ω-m-resistivity material below stations 12 and 14 (fig. 1), but above that depth the seismicity is more diffuse and shifts northeastward, with seismicity patterns that are spatially associated with the San Andreas and Sargent faults. A distinct vertical pattern from 8- to 11-km depth also appears to be associated with the Sargent fault.

Given the small contrasts in the gravity and magnetic models of Jachens and Griscom (this chapter), we found our resistivity model to be consistent with the gross structure of their models near our MT profile.

Although the following information is given as an aid in correlating the various geologic units with the Loma Prieta MT model, the reader should remember that the drill-hole data have been projected twice, first onto the geologic cross section and then onto the Loma Prieta MT model (fig. 2), which is a two-dimensional model of finite-strike-length structures (see Jachens and Griscom, this chapter). Thus, the two moderately deep (1–2 km) drill holes between stations 10 and 14 (fig. 1) and surface geologic data (McLaughlin and others, 1988) were used to help geologically constrain the uppermost 2 km of crust in the Loma Prieta MT model (fig. 6) during our modeling efforts. On the basis of the geologic interpretation based on the drill-hole data (McLaughlin and others, 1988) near stations 10 and 14, the following correlation of resistivity with lithology is generally assumed in our interpretation of the MT data:

Unit	*Resistivity (Ω-m)*
Tertiary shale, mudstone, siltstone, and sandstone	3–30
Cretaceous shale, sandstone, and conglomerate	10–100
Jurassic Coast Range ophiolite	3–30

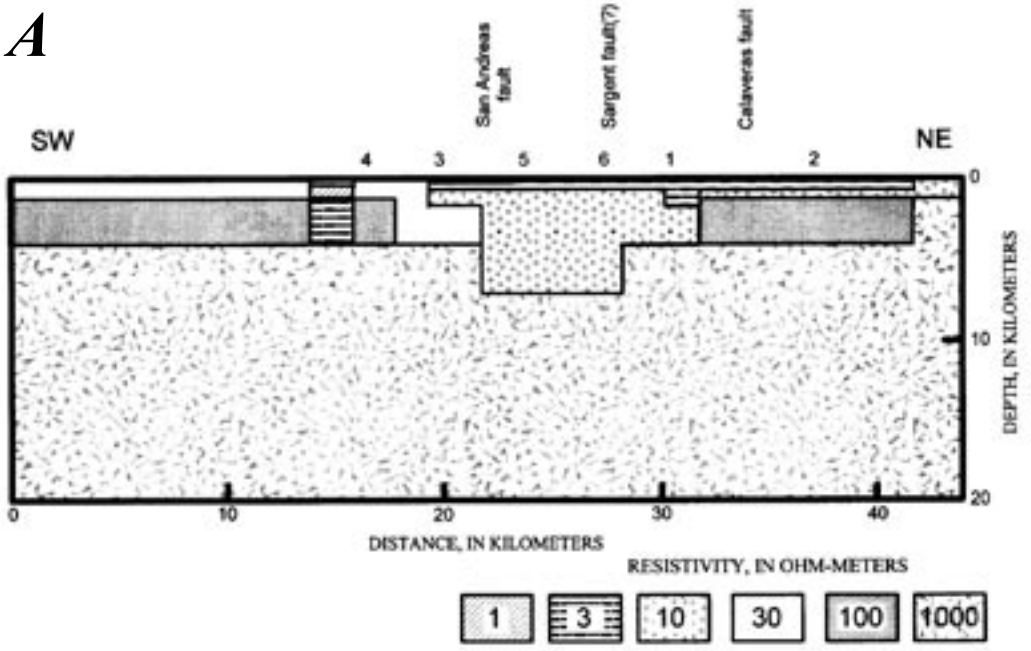

Figure 3.—Gabilan Range magnetotelluric (MT) profile (see fig. 1 for locations). *A*, Two-dimensional finite-element MT model. Numbers denote stations shown in figure 1. *B*, Resistivity data. *C*, Phase data. Same symbols as in figure 2.

Franciscan complex	30–1,000
Granitic rocks (quartz diorite)	30–1,000

The resistivities of all these rock types overlap, although some rock types appear to favor the low end of the resistivity spectrum (Tertiary and Jurassic), whereas others appear to favor the high end (Franciscan and granitic). The reader is, therefore, cautioned that our MT model boundaries are somewhat insensitive to precise lithologic boundaries.

We find it peculiar that the Salinian-block granitoids beneath station 10 (fig. 1) would have resistivities as low as 30 Ω-m; however, the close proximity of the Zayante fault may be responsible for the low resistivity here because of fault gouge, altered rocks, and an increase in fluid content in the fault zone. This low-resistivity zone also reduces the MT model resolution of determining both the depth and lateral boundaries of resistive granitoids near the fault. A perplex-

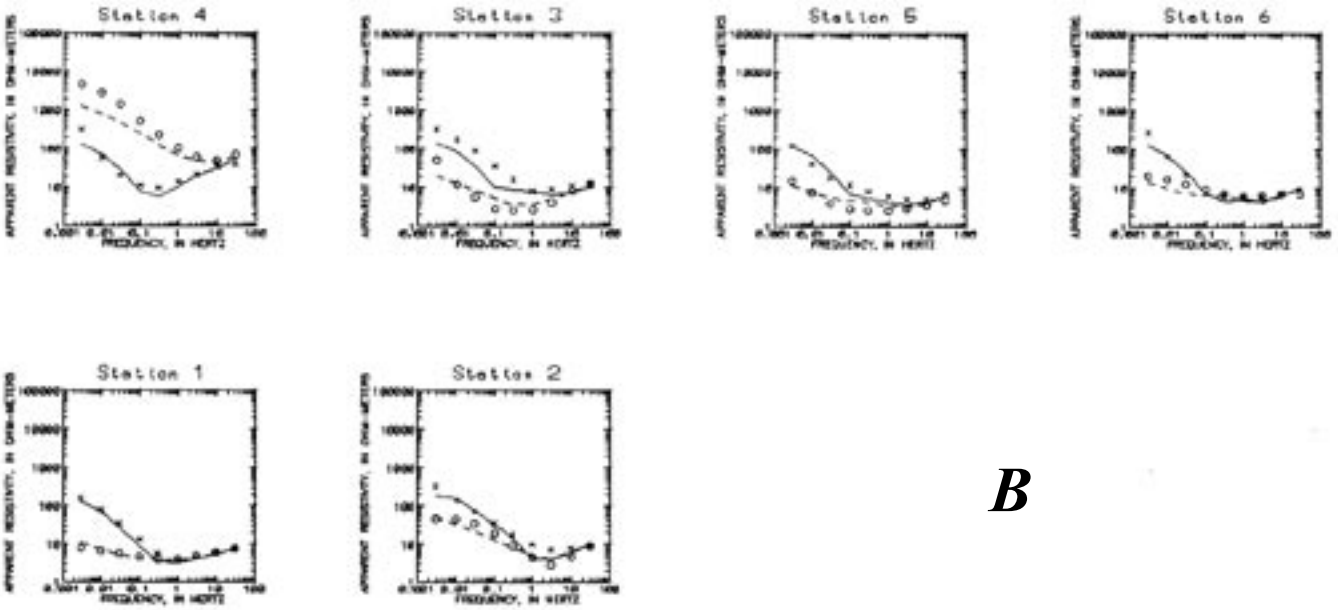

Figure 3.—Continued.

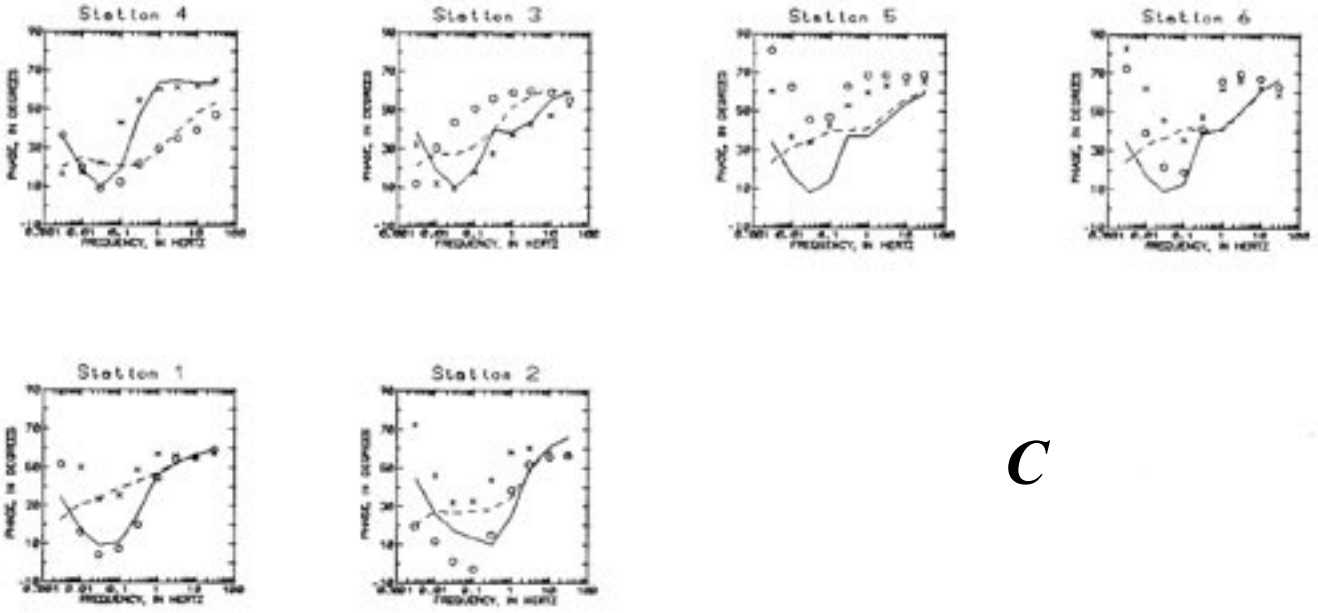

Figure 3.—Continued

ing anomaly is the low-resistivity body that apparently dips northeast beneath stations 12 and 13, where the surficial geology indicates that the subsurface structure should dip southwest. Either the geologic extrapolation of McLaughlin and others (1988) is invalid here, or the data could indicate the uncertainty in determining the lithologic boundaries with our resistivity measurements. We also find it peculiar that the Butano sandstone northeast of station 11 has a lower resistivity than the same unit southwest of station 11. The close proximity of the San Andreas fault zone northeast of station 11 may be responsible for the lower resistivity because of fault gouge, altered rocks, and an increase in fluid content within the fault zone; or the data could also indicate the uncertainty in determining the lithologic boundaries with our resistivity measurements. The close proximity of the Sargent fault zone may be responsible for the wide variation in resistivities in the Franciscan complex because of fault gouge, altered rocks, and an increase in fluid content within the fault zone.

The interpreted underlying structures southwest of the San Andreas fault evidently have different strain responses from the metamorphic rocks interpreted to occur between the San Andreas and Sargent faults. This contrast in strain response could have played a major role in stress buildup of the locked zone before the 1989 Loma Prieta earthquake, and it seems to have been instrumental in post-main-shock stress release controlling the aftershock distribution. A buildup of overpressured fluids in the deeper parts of the fault-gouge zones could have reduced the shear stress required for sliding to trigger the earthquake (Blanpied and others, 1992).

GABILAN RANGE PROFILE

Profiles across the San Andreas fault at Loma Prieta and in the Gabilan Range (fig. 1) show a distinctly different structure, especially for the San Andreas fault zone. Low-resistivity units appear to be more spatially uniform and limited to the uppermost 4 km of crust. This type of geoelectrical structure may indicate stable fault slip on the central section of the San Andreas fault. The Zayante, Chesbro, and Santa Teresa faults were not detected on the Gabilan Range profile probably because the profile did not cross them, a result consistent with surface geologic mapping (fig. 1). The 7-km-thick, low-resistivity (10 Ω-m) zone beneath station 6 (fig. 1) appears to correlate with a projection of the Sargent fault. The Calaveras fault, however, is not apparent in the resistivity data at these depths. The 10-km-thick, 100-Ω-m-resistivity Franciscan wedge on the Loma Prieta profile is only about 4 km thick on the Gabilan Range profile.

On the Gabilan Range profile (fig. 1), the 1- to 100-Ω-m-resistivity units in the uppermost 4 km of crust southwest of

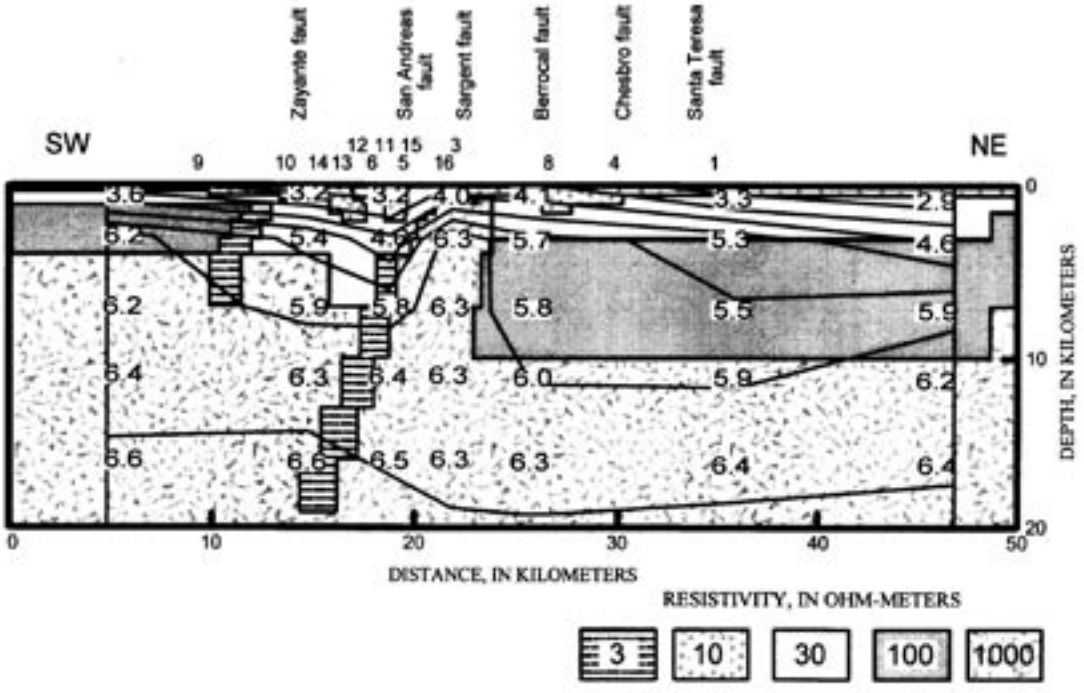

Figure 4.—Loma Prieta magnetotelluric profile (fig. 2; see fig. 1 for locations), with representative seismic velocities (in kilometers per second) from three-dimensional velocity-inversion model slice (Eberhart-Phillips and others, 1990) superimposed.

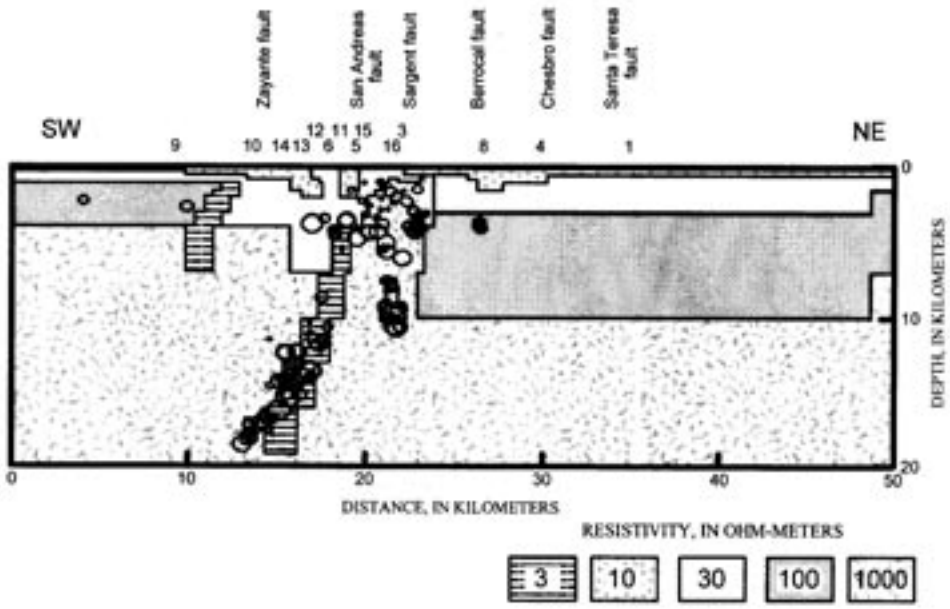

Figure 5.—Loma Prieta magnetotelluric profile (fig. 2; see fig. 1 for locations), with locations of 1989 main shock (star) and aftershocks (circles; size relative to magnitude) within 5 km of $Y=0$ line.

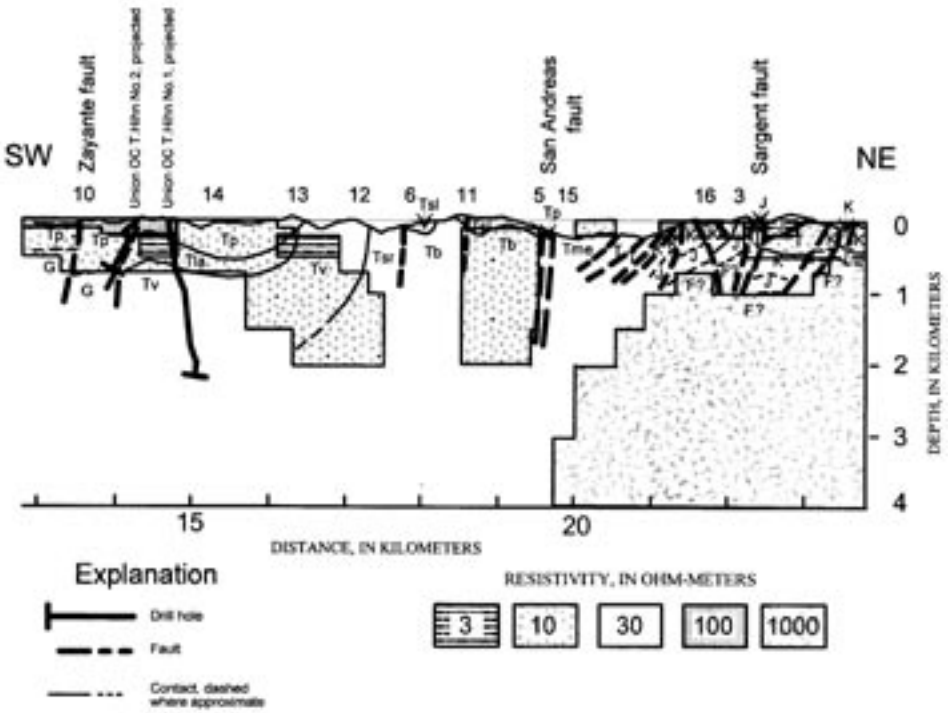

Figure 6.—Loma Prieta magnetotelluric profile (fig. 2; see fig. 1 for locations), with geologic cross section of McLaughlin and others (1988) superimposed. Irregular line at top of profile is topography; thick dashed lines are inferred faults. Units: F, Franciscan complex; G, granitic rocks (quartz diorite); J, Jurassic Coast Range ophiolite; K, Cretaceous sandstone, shale, and conglomerate of Sierra Azul; T, Tertiary marine sandstone, shale, and mottled marine mudstone and sandstone of Mount Chual; Tb, Tertiary sandstone and siltstone (Butano sandstone); Tla, Tertiary mudstone, siltstone, sandstone (Lambert shale); Tme, Tertiary marine shale and sandstone (Highland Way); Tp, Tertiary siltstone and sandstone (Purisima formation); Tsl, Tertiary shale and sandstone (San Lorenzo formation); Tsr, Tertiary mudstone and sandstone (Rices Mudstone member); Tv, Tertiary sandstone (Vaqueros sandstone).

the San Andreas fault are believed to represent Tertiary marine sedimentary rocks. The 1- to 10-Ω-m-resistivity units in the uppermost 4 km of crust northeast of the San Andreas fault are believed to represent Mesozoic Great Valley sedimentary rocks (Irwin, 1990). The 1,000-Ω-m-resistivity material may represent Salinian-block granitoids of Mesozoic age, Coast Range ophiolite, and Mesozoic units of the Franciscan assemblage in some combination, irresolvable because of masking by the thick (4 km) conductive (1- to 10-Ω-m-resistivity) overburden.

CONCLUSION

Our resistivity modeling suggests that details of the local deep structure can be mapped by using magnetotelluric surveys to assist in understanding the dynamics of the San Andreas fault system. The interpreted structure from our two profiles will provide constraints on future geologic interpretations of the Loma Prieta region. Resistivities in these deep rocks are almost entirely related to fracturing and fluid content; thus, the deep geoelectrical structure adds significant new information toward understanding seismic-stress release in the region. The Loma Prieta MT model indicates (1) a large, high-resistivity body within the upper 2 km of crust between the San Andreas and Sargent faults at seismogenic depths that may have played an important role in seismic-stress buildup; and (2) a low-resistivity anomaly at midcrustal depths near the San Andreas fault that may have been caused by a buildup of overpressured fluids in the deeper parts of the fault-gouge zone, which reduced the shear stress required for sliding and, subsequently, triggered the earthquake. The presence of this low-resistivity anomaly was a key and required element of our model, even though the model was insensitive to the dip, shape, and distribution of the anomaly. High-resistivity units southwest of the San Andreas fault may represent Salinian-block granitoids of Mesozoic age. High-resistivity units below 4-km depth northeast of the San Andreas fault could be related to the Franciscan complex. Low-resistivity rocks between the Zayante and Sargent faults in the uppermost 4 to 7 km of crust are interpreted from drill-hole data as mostly Tertiary marine sedimentary rocks exposed in tightly folded structures in the Loma Prieta region. Low-resistivity units above 4-km depth northeast of the San Andreas fault are believed to represent Mesozoic units of the Franciscan assemblage. The resistivity model agrees well with the three-dimensional seismic-velocity model, revealing distinctive velocity and resistivity variations in the Loma Prieta region associated with seismicity and fault-rupture patterns. The resistivity model is also consistent with gravity and magnetic models of the Loma Prieta region. The San Andreas fault and adjoining subparallel Sargent and Zayante faults appear to juxtapose diverse deep geologic structures spanning the seismogenic zone in the Loma Prieta region, suggesting that local geologic structures may have played a role in triggering the earthquake and may control the overall seismicity on the San Andreas and Sargent faults. Another MT-sounding profile about 35 km southeast, traversing the northwest end of the Gabilan Range, shows a distinctly different structure. Low-resistivity units there appear to be more spatially uniform and limited to the uppermost 4 km of crust. This type of geoelectrical structure may indicate stable fault slip on the central section of the San Andreas fault.

REFERENCES CITED

Alt, D.D., and Hyndman, D.W., 1975, Roadside geology of northern California: Missoula, Mont., Mountain Press, 244 p.

Brabb, E.E., and Hanna, W.F., 1981, Maps showing aeromagnetic anomalies, faults, earthquake epicenters, and igneous rocks in the southern San Francisco Bay region, California: U.S. Geological Survey Geophysical Investigations Map GP–932, scale 1:125,000, 3 sheets.

Blanpied, M.L., Lockner, D.A., and Byerlee, J.D., 1992, An earthquake mechanism based on rapid sealing of faults: Nature, v. 358, no. 6387, p. 574–576.

Clark, J.C., and Rietman, J.D., 1973, Oligocene stratigraphy, tectonics, and paleogeography southwest of the San Andreas fault, Santa Cruz Mountains and Gabilan Range, California Coast Ranges: U.S. Geological Survey Professional Paper 783, 18 p.

Cole, W.F., Cotton, W.R., and Fowler, W.L., 1989, Engineering geology of the San Francisco Bay region, *in* Engineering geology of Western United States urban centers: American Geophysical Union Field Trip Guidebook T181, 85 p.

Dietz, L.D., and Ellsworth, W.L., 1990, The October 17, 1989, Loma Prieta, California, earthquake and its aftershocks; geometry of the sequence from high-resolution locations: Geophysical Research Letters, v. 17, no. 9, p. 1417–1420.

Eberhart-Phillips, D.M., 1989, Investigations of crustal structure and active tectonic processes in the Coast Ranges, central California: Stanford, Calif., Stanford University, Ph.D. thesis, 216 p.

Eberhart-Phillips, D.M., Labson, V.F., Stanley, W.D., Michael, A.J., and Rodriguez, B.D., 1990, Preliminary velocity and resistivity models of the Loma Prieta earthquake region: Geophysical Research Letters, v. 17, no. 8, p. 1235–1238.

Gamble, T.D., Goubau, W.M., and Clarke, John, 1979, Magnetotellurics with a remote magnetic reference: Geophysics, v. 44, no. 1, p. 53–68.

Irwin, W.P., 1990, Geology and plate-tectonic development, chap. 2 *of* Wallace, R.E., ed., The San Andreas fault system, California: U.S. Geological Survey Professional Paper 1515, p. 61–80.

Kaufman, A.A., and Keller, G.V., 1981, The magnetotelluric sounding method (Methods in Geochemistry and Geophysics, no. 15): New York, Elsevier, 595 p.

Keller, G.V., and Frischknecht, F.C., 1966, Electrical methods in geophysical prospecting (International Series of Monographs in Electromagnetic Waves, v. 10): New York, Pergamon, 517 p.

Mackie, R.L., Bennett, B.R., and Madden, T.R., 1988, Long-period magnetotelluric measurements near the central California coast; a land-locked view of the conductivity structure under the Pacific Ocean: Royal Astronomical Society Geophysical Journal, v. 95, no. 1, p. 181–194.

Mazzella, A.T., 1976, Deep resistivity study across the San Andreas fault zone: Berkeley, University of California, Ph.D. thesis, 145 p.

McLaughlin, R.J., Clark, J.C., and Brabb, E.E., 1988, Geologic map and structure sections of the Loma Prieta 7½′ quadrangle, Santa Clara and Santa Cruz Counties, California: U.S. Geological Survey Open-File Map 88–752, 31 p., scale 1:24,000, 2 sheets.

Nelson, P.H., and Anderson, L.A., 1992, Physical properties of ash flow tuff from Yucca Mountain, Nevada: Journal of Geophysical Research, v. 97, no. B5, p. 6823–6841.

Park, S.K., Biasi, G.P., Mackie, R.L., and Madden, T.R., 1991, Magnetotelluric evidence for crustal suture zones bounding the southern Great Valley, California: Journal of Geophysical Research, v. 96, no. B1, p. 353–376.

Parkhomenko, E.I., 1967, Electrical properties of rocks: New York, Plenum, 314 p.

Phillips, W.J., and Kuckes, A.F., 1983, Electrical conductivity structure of the San Andreas fault in central California: Journal of Geophysical Research, v. 88, no. B9, p. 7467–7474.

Sheriff, R.E., 1991, Encyclopedic dictionary of exploration geophysics (3d ed.): Tulsa, Okla., Society of Exploration Geophysicists, 376 p.

Smith, J.T. and Booker, J.R., 1988, Magnetotelluric inversion for minimum structure: Geophysics, v. 53, no. 12, p. 1565–1576.

———1991, Rapid inversion of two and three-dimensional magnetotelluric data: Journal of Geophysical Research, v. 96, no. B3, p. 3905–3922.

Stacey, F.D., 1977, Physics of the earth (2d ed.): New York, John Wiley & Sons, 414 p.

Stesky, R.M., and Brace, W.F., 1973, Electrical conductivity of serpentinized rocks to 6 kilobars: Journal of Geophysical Research, v. 78, no. 32, p. 7614–7621.

U.S. Geological Survey, 1980, Soquel [Calif.] quadrangle: 7.5-minute series (topographic) map, scale 1:24,000.

———1981, State of California: Denver, Colo., scale 1:500,000, 2 sheets.

Vozoff, Keeva, 1991, The magnetotelluric method, chap. 8 of Nabighian, M.N., ed., Electromagnetic methods in applied geophysics (Investigations in Geophysics, no. 3): Tulsa, Okla., Society of Exploration Geophysicists, v. 2, pt. B, p. 641–711.

Walter, A.W., 1990, Velocity structure near Coalinga, California, *in* Rymer, M.J., and Ellsworth, W.L., eds., The Coalinga, California, earthquake of May 2, 1983: U.S. Geological Survey Professional Paper 1487, p. 23–40.

Wannamaker, P.E., Hohmann, G.W., and SanFilipo, W.A., 1984, Electromagnetic modeling of three-dimensional bodies in layered earths using integral equations: Geophysics, v. 49, no. 1, p. 60–74.

Wannamaker, P.E., Stodt, J.A., and Rijo, Luis, 1987, PW2D; finite element program for solution of magnetotelluric responses of two-dimensional earth resistivity structure: Salt Lake City, University of Utah, Research Institute, 40 p.

APPENDIX 1. MAGNETOTELLURIC METHODOLOGY

The magnetotelluric (MT) method (Kaufman and Keller, 1981; Vozoff, 1991) is an electromagnetic-frequency-sounding method utilizing natural variations of the Earth's magnetic and electric fields originating from geomagnetic micropulsations over the frequency range 0.0001–1 Hz and from worldwide lightning activity over the frequency range 1–10,000 Hz. These natural electric and magnetic fields are recorded in two orthogonal, horizontal directions (and the vertical magnetic field is sometimes recorded as well) at the Earth's surface with a computer-based data acquisition and processing system. The resulting time-series signals are transformed into the frequency domain and used in a cross-spectral analysis to derive earth tensor resistivities and phases. Generally, a rotated coordinate system that corresponds to resistivity measured along electrical strike, called the transverse-electric direction (TE), and normal to strike, called the transverse-magnetic direction (TM), is used. Phase values for the complex earth impedances used to calculate resistivities are also computed and can be used in modeling. In two- and three-dimensional modeling, models are derived to fit both the TE and TM resistivities.

Measurement of earth resistivities can be an effective means of mapping geologic structures because of the wide variation in the electrical resistivity of rocks. The resistivity of geologic units largely depends on their fluid content, alteration, fracturing, carbon and other conductive-mineral contents, and temperature (Keller and Frischknecht, 1966). Formation fluids play a large role in reducing resistivities below those of the normally high resistivity rock matrix, especially when formation salinities and porosity are high. Resistivities can also be lowered by the presence of highly conductive clay minerals, graphitic carbon, and metallic mineralization. Volcanic rocks and fault zones commonly contain conductive authigenic minerals and gouge with resistivities 10 to 100 times lower than those of the surrounding rocks (Nelson and Anderson, 1992). Increasing temperatures cause higher ionic mobility and mineral-activation energy, reducing rock resistivities significantly. The MT method has distinct advantages over other geophysical methods in the study of complex geologic environments because of the wide variation in rock resistivities and the inherent tensor nature of the technique, which makes it sensitive to vertical structures. Furthermore, the method is capable of establishing whether the subsurface structures being measured are effectively one, two, or three dimensional in terms of their response to electromagnetic fields.

Originating from the naturally occurring sources that the MT method uses, time-varying magnetic fields induce current flow in the conductive Earth. The Earth's resistivity is determined from the relation of these time-varying magnetic and electric fields (electrical impedance). Because lower frequencies penetrate deeper, measurement of a spectrum of frequencies allows the creation of an electrical sounding, which is a measure of electrical resistivity versus frequency. In a plane-layered Earth, the MT sounding could be inverted to produce a plot of resistivity versus depth. However, the Earth is seldom plane layered, and the MT method responds to lateral variations in resistivity. For a two-dimensional Earth—that is, an Earth

that varies only with depth and in a direction perpendicular to strike—profiles of MT soundings may be inverted to produce electrical cross sections. Although much of the surrounding structure is finite and complex (see Jachens and Griscom, this chapter), the linearity of some geologic structures in the Loma Prieta region makes two-dimensional modeling useful for approximating the local geology. At present three-dimensional modeling is inadequately crude and prohibitively time consuming, and so we used two-dimensional modeling to construct the interpretative cross sections presented here.

APPENDIX 2. MAGNETOTELLURIC COVERAGE

Station spacing (fig. 1) ranged from 0.4 to 5 km. Frequencies sampled were from 0.001 to 300 Hz, using single-station recordings of both orthogonal horizontal components of the electric and magnetic fields. These data were measured with USGS-designed instrumentation and processed in real time with the computer that controls the MT system. The recorded time-series data were Fourier-analyzed to determine a two-dimensional resistivity and phase tensor at each station, which were then freely rotated to maximum- and minimum-resistivity directions so that propagation modes for the signals were decoupled into transverse-electric and transverse-magnetic modes that are equivalent to measurement of the Earth's resistivity with the electric field directed along and across geologic strike, respectively. This data-analysis method uses the crosspower method of Gamble and others (1979), which produces estimates of apparent resistivity that are unbiased by noise but are subject to large random errors when coherencies are less than 0.9. Therefore, the observed data were manually smoothed and digitized in an effort to reduce systematic and random errors and coherent noise. The observed data were also corrected for static shift from near-surface effects, such as thin localized conductors.

Plots of tensor resistivity and phase for the manually smoothed representations of the Loma Prieta data are shown in figures 2*A* and 2*B*, respectively, along with the model curves. Both resistivity and phase values are included in the modeling process. These data have been interpreted by using two-dimensional finite-element forward modeling, which resulted in an estimated variation in resistivity from 3 to 1,000 Ω-m for a cross section extending from about 0.1- to more than 10-km depth.

If the data are obtained over structures that are three dimensional, the skew of the tensor will be significant, whereas for a truly two dimensional Earth the skew will be zero. Most of the data from the Loma Prieta survey had low skews, 0.1 to 0.3; but near stations 3 and 8 (fig. 1), the skews for some frequencies ranged from 0.3 to 1. Associated with the low skews was a northwestward principal-axis rotation of the resistivity tensors (fig. 7). Associated with the high skews at stations 3 and 8 is a departure from the typical northwestward rotation of the tensor principal direction to an azimuth of 000° (north). The north principal direction suggests a three-dimensional geoelectrical structure at these stations, indicating that the underlying resistivity structure may be limited in strike length. The anomalous principal tensor direction of station 15 was north by northwest, yet had low skews. Most of the data from the Gabilan Range survey had low skews (typically, 0.1–0.5) except station 2, which had powerline interference and whose skews ranged from 0.1 to 1. All of these stations exhibited a northwestward principal-axis rotation of the resistivity tensors (fig. 7).

APPENDIX 3. MAGNETOTELLURIC MODELS

The following discussion provides a detailed account of our modeling approach not presented in the main body of text, for those readers interested in our starting models, assumptions, boundary conditions, biases, and alternative models.

LOMA PRIETA PROFILE

Initially, using the combined 1989, 1990, and 1992 data sets, we inverted the data with the two-dimensional inversion algorithm of Smith and Booker (1991), using a simple layer (4 km thick, 30-Ω-m resistivity) over a half-space (1,000 Ω-m) as the starting model. Their inversion method is called the rapid-relaxation inverse (RRI) because of similarities to classical relaxation solutions and because of its speed. Another advantage to the RRI method arises from the use of a minimum-structure criterion (Smith and Booker, 1988). The algorithm uses a selected number of iterations to achieve a fit to the observed data, and then applies another selected number of steps in which the model complexity is reduced while maintaining an overall goodness of fit. These subsequent steps substantially reduce nonessential model geometries in the final solution. The final inversion model (fig. 8) generally fitted the transverse-magnetic (TM) data better than the transverse-electric (TE) data (figs. 8*B* and 8*C*, respectively). The gross structure of our model came from fitting the TM data. Wannamaker and others (1987) showed that finite structure is better resolved with the TM mode and that the TE mode is highly insensitive to gross resistivity structure. We then used this minimum-resistivity-structure inversion as the starting model for our two-dimensional forward-modeling efforts to improve the computed fits to the observed TE data.

Although the inversion model gives an approximation to the minimum-resistivity structure, it does not adequately take into account the effect of the Pacific Ocean because of a limitation in the algorithm. We modeled the seawater of the Pacific Ocean by using a resistivity of 0.3 Ω-m (Stacey, 1977; Sheriff, 1991). The seawater thickness was varied from 20-m depth in Monterey Bay (U.S. Geological Survey, 1980) to 4-km depth at a distance of 200 km from the California coast (U.S. Geologi-

cal Survey, 1981). We modeled the oceanic crust beneath the Pacific Ocean by using a resistivity of 1,000 Ω-m at about 4-km depth. The conductive seawater had the effect of increasing the resistivity values on the TM curve by at least 10 percent of a log cycle at 0.01 Hz for stations as close as 2.5 km and at 0.003 Hz for stations as far away as 28.1 km and of decreasing the resistivity values on the TE curve by at least 10 percent at 0.01 Hz for stations as close as 2.5 km. Our forward modeling, we believe, adequately accounts for these effects.

In the minimum-resistivity-structure model (fig. 8), we see a resistivity low at about 5-km depth between stations 5 and 13 (fig. 1), a resistivity high beneath stations 3 and 16, and a broader resistivity low northeast of station 3. The model curves, overall, make a poor to fair fit to the observed data. At most stations, the TM curve was fitted satisfactorily, but the TE curve needed to be decreased at the low to midband frequencies. The only approach that seemed to achieve this effect was to put lower resistivities in the depth range 4–16 km near the San Andreas fault. Although the model was insensitive to this resistivity configuration (fig. 9), within that depth range the TE curves had to be decreased at stations 6, 9, and 10 through 14 (figs. 10, 11). This model sensitivity is consistent with the resolution inherent in the MT method, which decreases with penetration. Thus, both horizontal and vertical boundaries at these depths were imprecisely resolvable.

We used 3 Ω-m as our best choice for the conductive material at these depths. We also tried 1 Ω-m, 10 Ω-m, and higher resistivities, but the computed fit was generally worse. The 1-Ω-m resistivity tended to decrease the resistivities on the TE curve too much at low to midband frequencies, and the 10-Ω-m resistivity tended to increase the resistivity values on the TE curve too much at midband frequencies. We tried a single-body conductor beneath stations 6 and 11 through 13 (fig. 1), reducing its thickness to compensate for the decrease in resistance, but we lost the anisotropy that is needed to fit the splitting TE and TM curves at station 12. Increasing its thickness does not cause the computed curves to split, and only worsens the misfit to the TE curves at stations 6, 11, 15, and

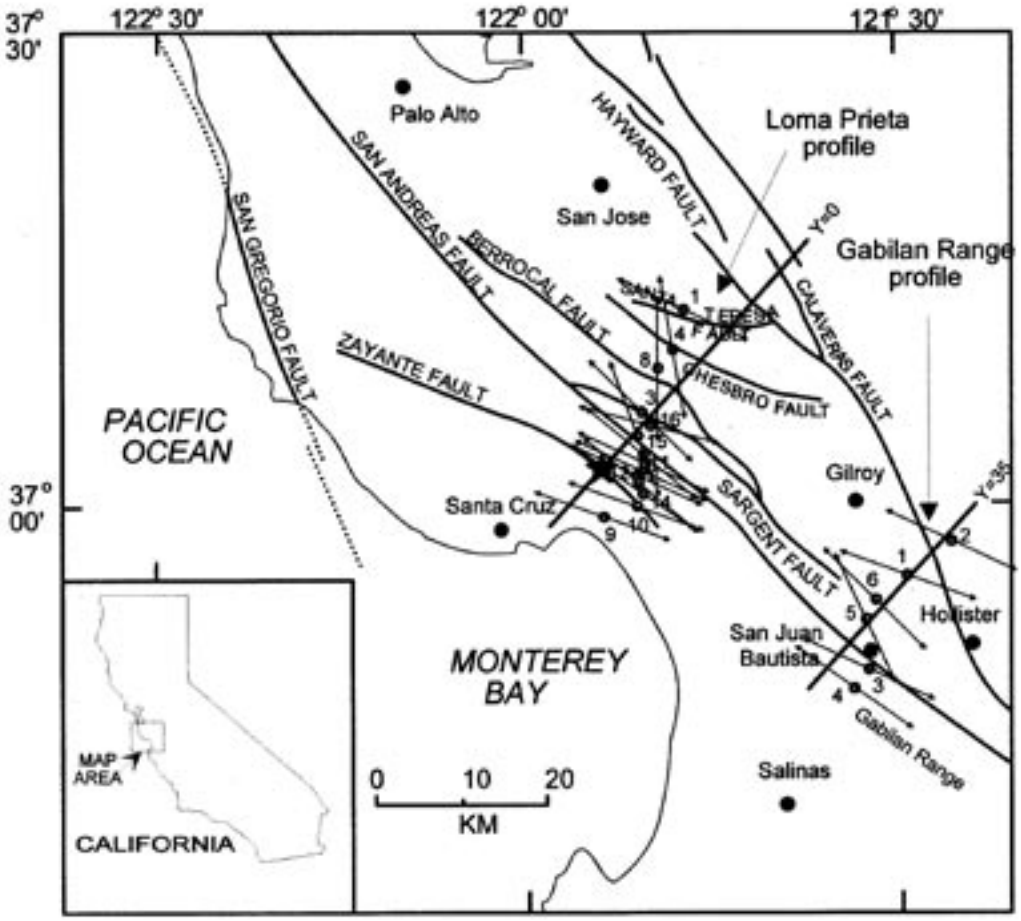

Figure 7—Index map of the Loma Prieta region, Calif., showing electrical-resistivity strike directions (double-headed arrows) at stations (numbered dots) where magnetotelluric soundings were made. Same symbols as in figure 1.

16 by decreasing the resistivities too much. Modeling vertical 3-Ω-m conductors closer to the surface expression of the San Andreas fault decreased the resistivities on the TE curves too much at midband frequencies at stations 15 and 16.

The resistivity high beneath stations 3 and 16 (fig. 1) is within 2 km of the surface. Modeling this geoelectrical structure at greater depths decreased the resistivities on the TM curve at low to midband frequencies at stations 3 and 16. We noted, however, that we could move the northeast edge of the resistive interface southwest as much as 0.5 km without adversely misfitting the observed data. The 100-Ω-m-resistivity material northeast of station 3 could be increased in thickness to at least 19-km depth; however, the observed data do not require such an increase in our models.

We manually perturbed the starting two-dimensional model more than 100 times. The best-fit model is shown in figure 2. Fits to the observed data were generally within measurement errors in the data. Significant misfits included the TE data at station 8 (fig. 1) at low to midband frequencies and the TM data at station 11 at low frequencies. Wannamaker and others (1984) showed in three-dimensional MT modeling that approximating three-dimensional structure beneath a sounding with two-dimensional modeling is best achieved by fitting the TM curve even at the expense of fitting the TE curve. This result is what our model achieves at station 8, where the data denoted an underlying three-dimensional structure (see app. 2). The misfit to the TM curve at low frequencies for station 11 most likely indicates a problem with the data at this station—that is, a data-acquisition error occurred at this station.

In summary, we found that we had to decrease the resistivities in the depth range 4–16 km near the San Andreas fault to bring the TE curve down at low to midband frequencies. The dip, shape, and precise distribution of this low-resistivity body were irresolvable, even though its presence was a major requirement of our model. We found that, in its absence, no other solution adequately fitted the observed TE data. The low-resistivity zones at deeper levels could conceivably have numerous variations and still be consistent with the observed data, although our model requires some degree of lateral inhomogeneity in resistivity within the uppermost 16 km of crust across the Loma Prieta epicentral region.

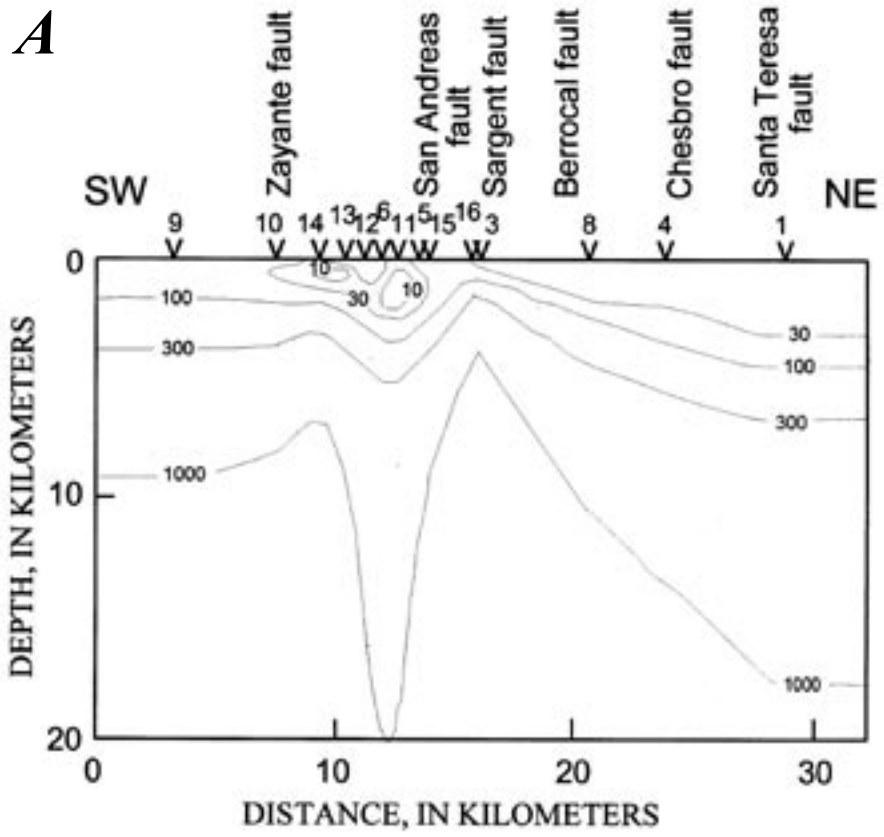

Figure 8.—Loma Prieta magnetotelluric (MT) inversion model (see fig. 1 for location) with contours of resistivity (in ohm-meters). *A*, Two-dimensional MT inversion model. Numbers denote stations shown in figure 1. *B*, Resistivity data. *C*, Phase data. Same symbols as in figure 2.

GABILAN RANGE PROFILE

Initially, we inverted the data with the two-dimensional inversion algorithm, using a simple layer (4 km thick, 30-Ω-m resistivity) over a half-space (1,000 Ω-m) as the starting model. The final inversion model generally fitted the data. We then used this minimum-structure inversion as the starting model in our two-dimensional forward-modeling efforts to improve the computed fits to the observed data. We determined that we needed to add a low-resistivity body southwest of station 4 (fig. 1) in the uppermost 4 km of crust to better fit the structure required by both modes of the

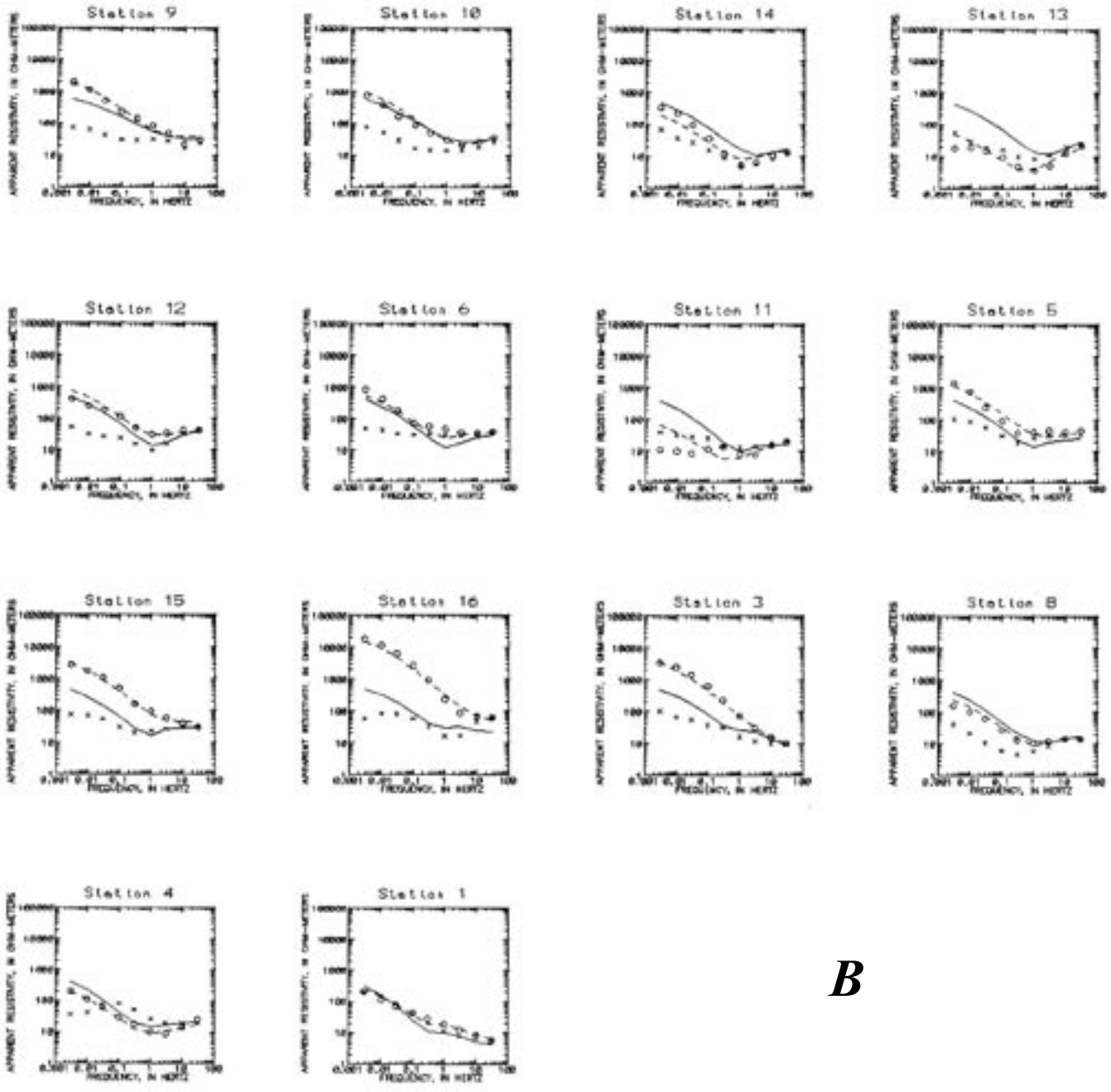

Figure 8.—Continued

observed data, deepen the central low-resistivity anomaly beneath stations 5 and 6 to better fit the TE data, and add low-resistivity material in the uppermost 4 km of crust beneath station 1 to better fit the TM data. The dip, shape, and precise distribution of this low-resistivity material were partly irresolvable because of the wide spatial sampling of the stations and because of the thick near-surface low-resistivity material. We manually perturbed the starting two-dimensional model more than 100 times. The best-fit model is shown in figure 3.

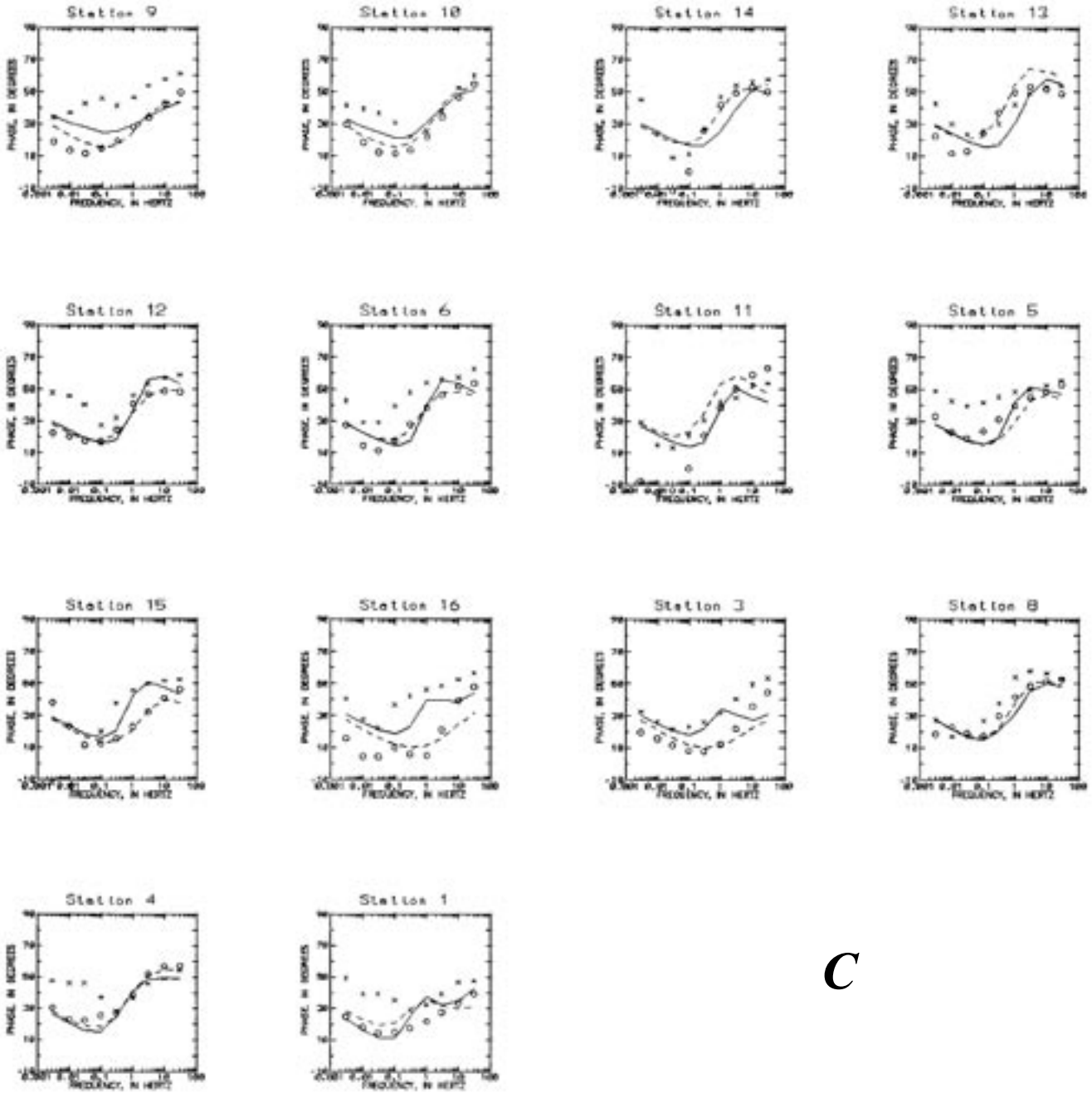

C

Figure 8.—Continued

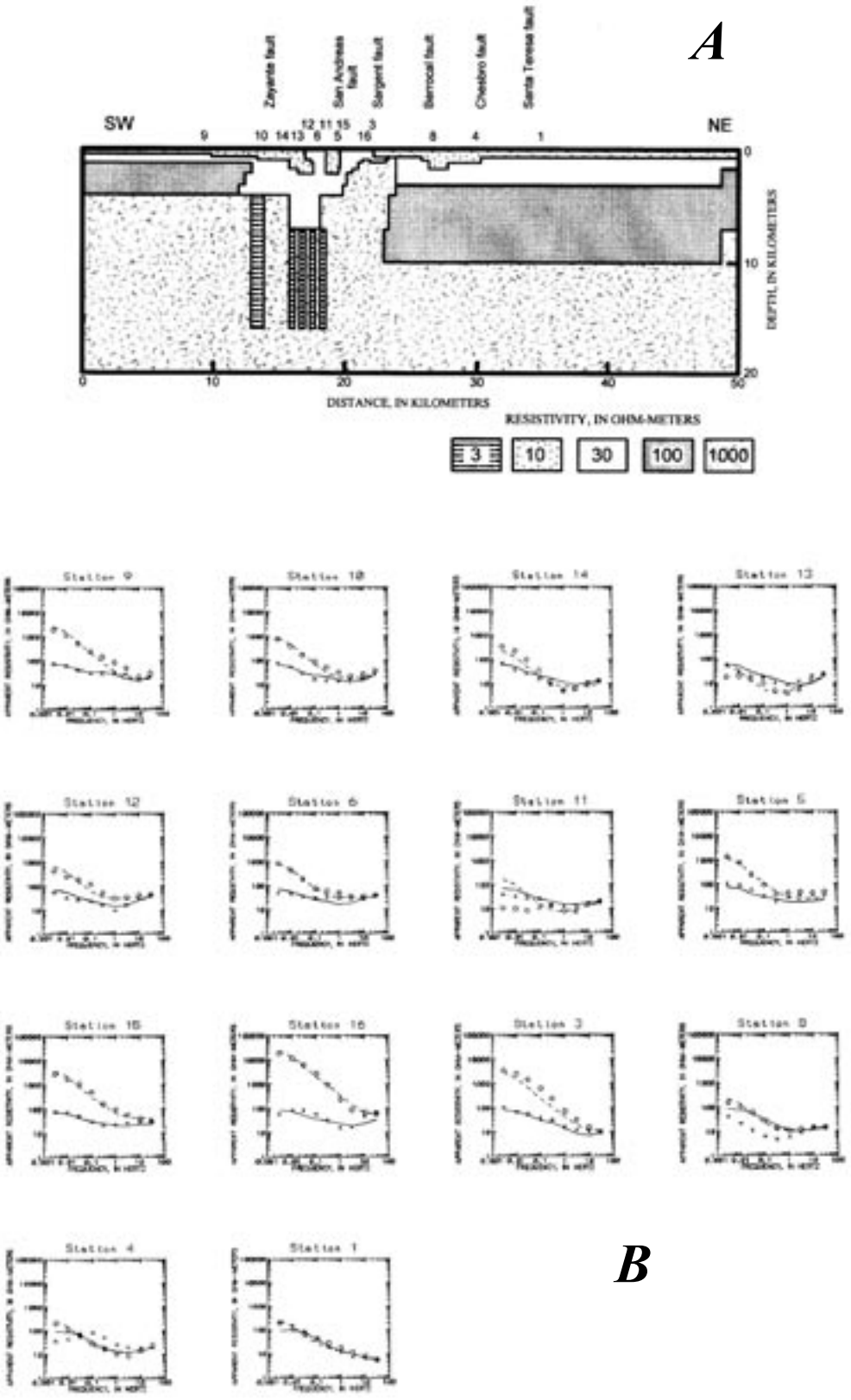

Figure 9.—Loma Prieta magnetotelluric (MT) profile (fig. 2; see fig. 1 for locations), with alternative variation of low-resistivity case of two-dimensional finite-element MT model. *A*, Two-dimensional finite-element MT model. Numbers denote stations shown in figure 1. *B*, Resistivity data. *C*, Phase data. Same symbols as in figure 2.

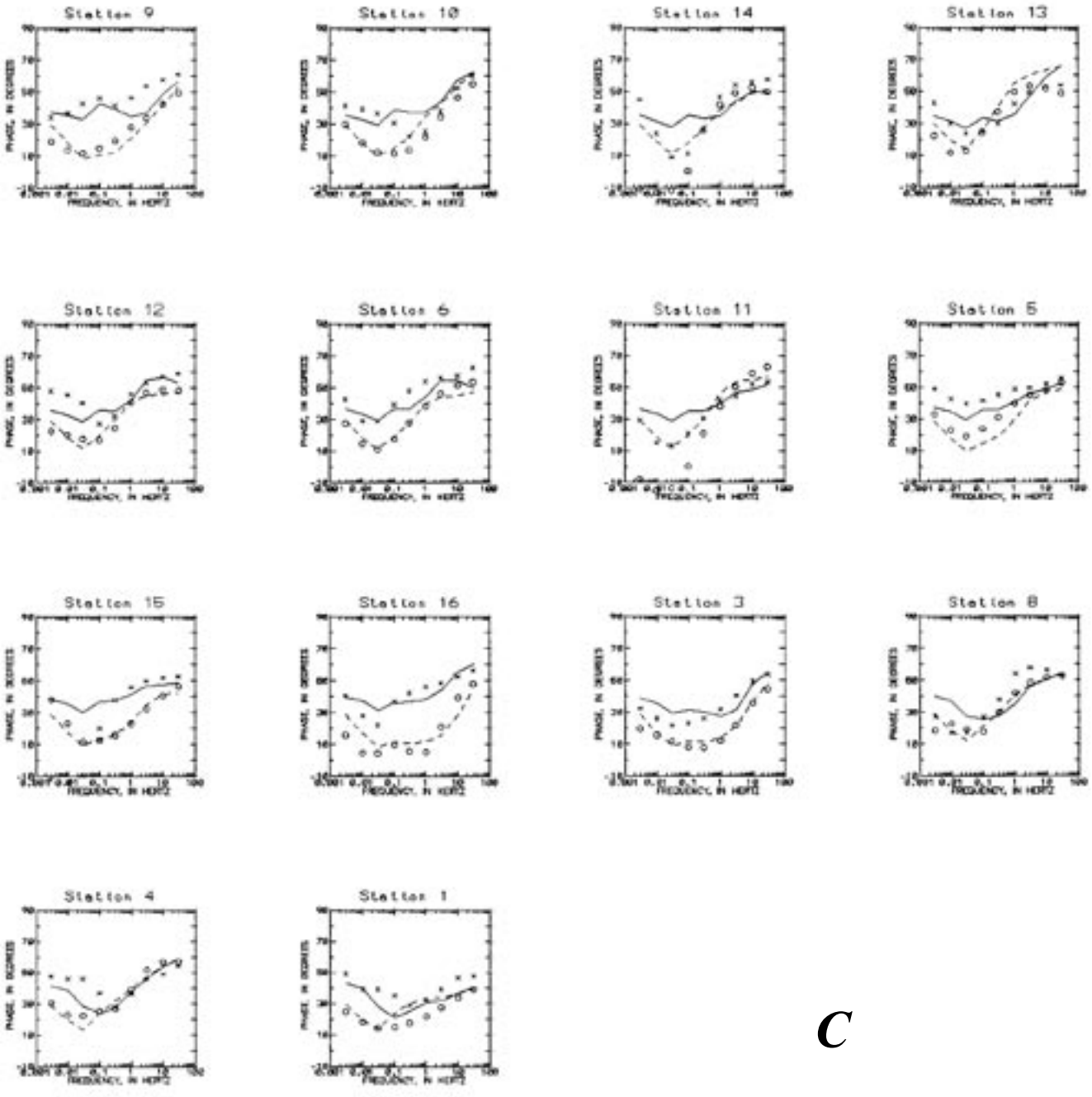

C

Figure 9.—Continued

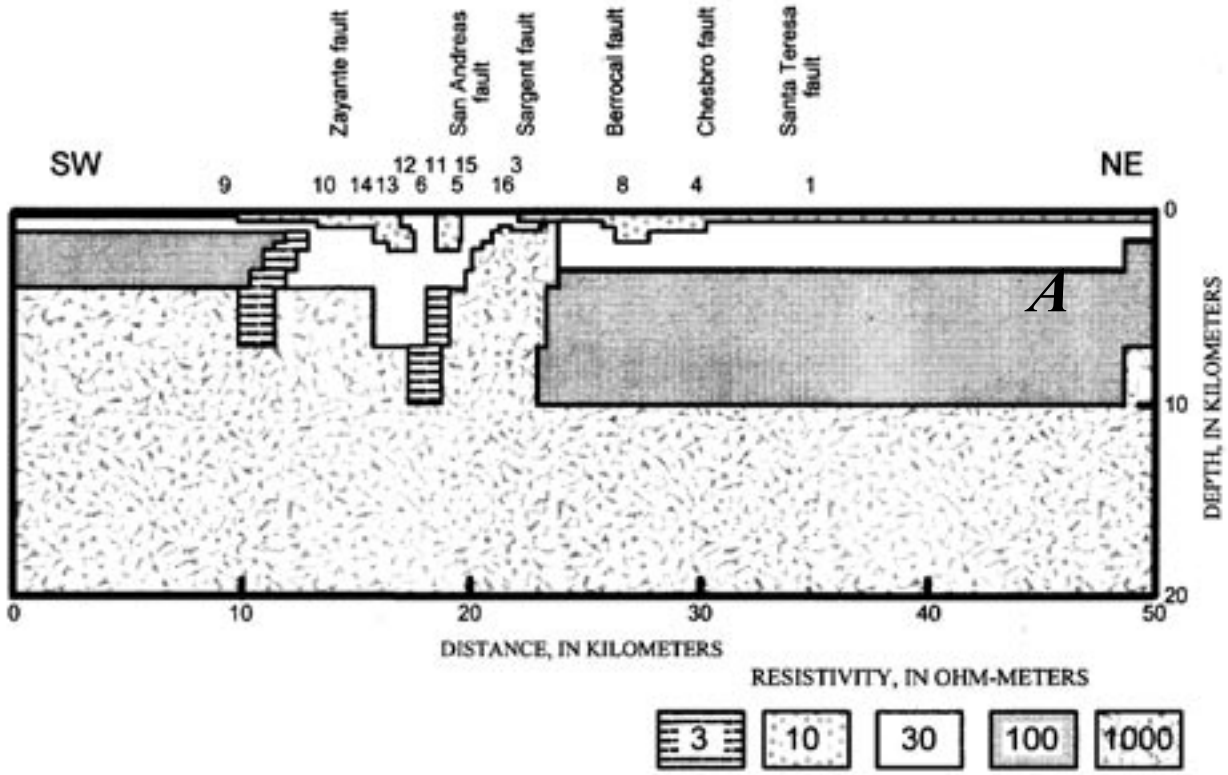

Figure 10.—Loma Prieta magnetotelluric (MT) profile (fig. 2; see fig. 1 for locations), with moderate depth extension of low-resistivity case of two-dimensional finite-element MT model. *A*, Two-dimensional finite-element MT model. Numbers denote stations shown in figure 1. *B*, Resistivity data. *C*, Phase data. Same symbols as in figure 2.

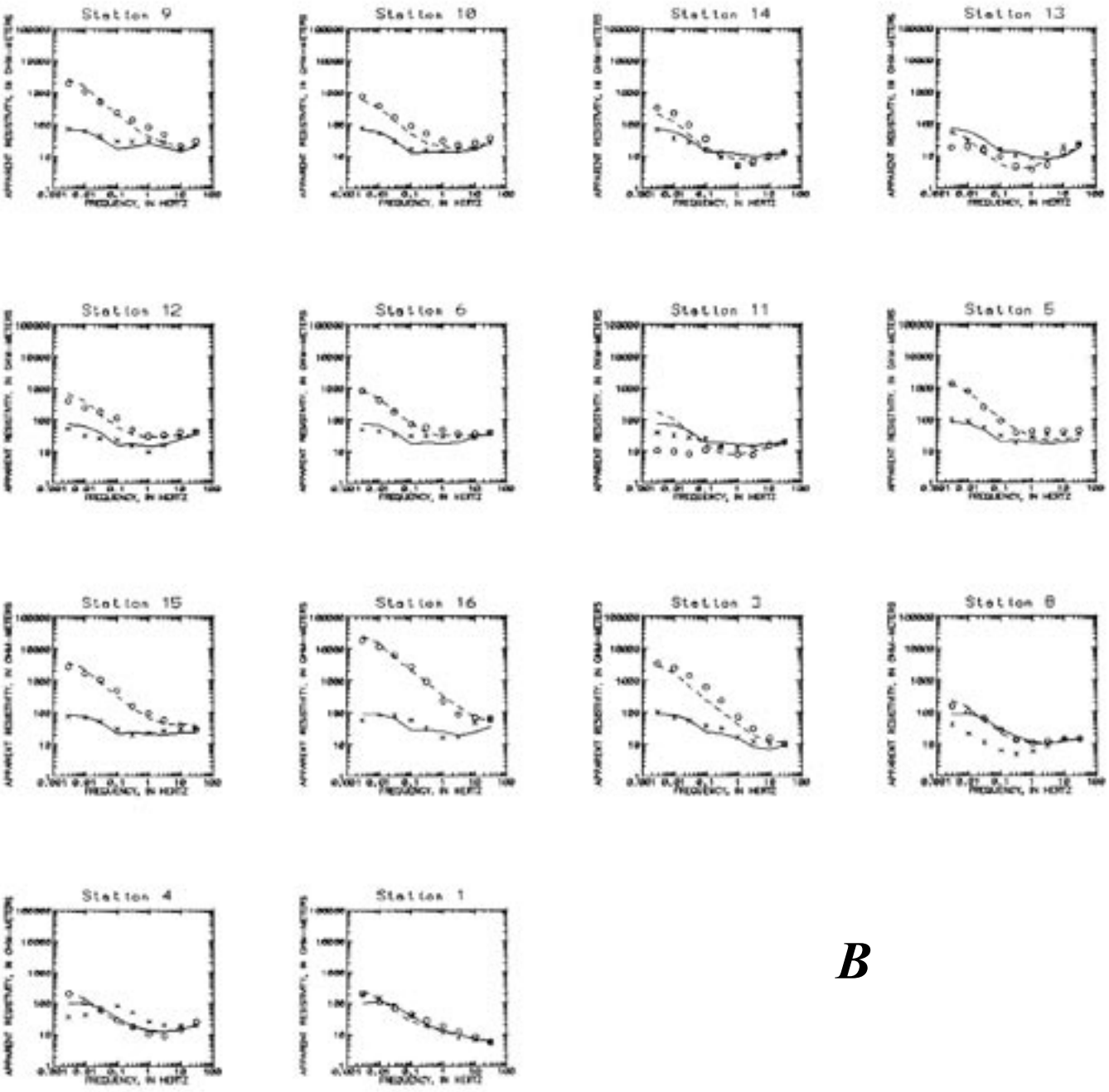

Figure 10.—Continued

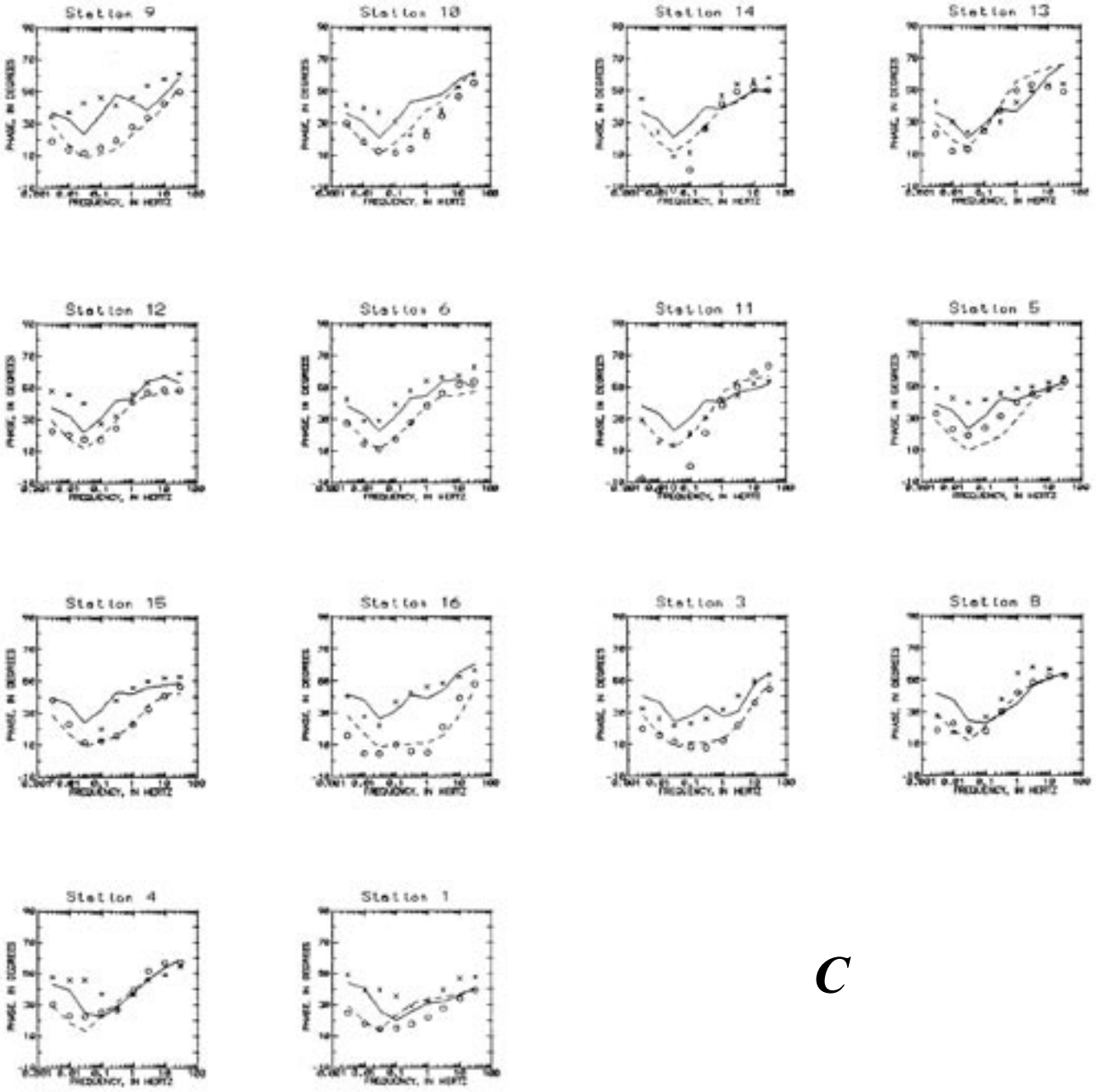

C

Figure 10.—Continued

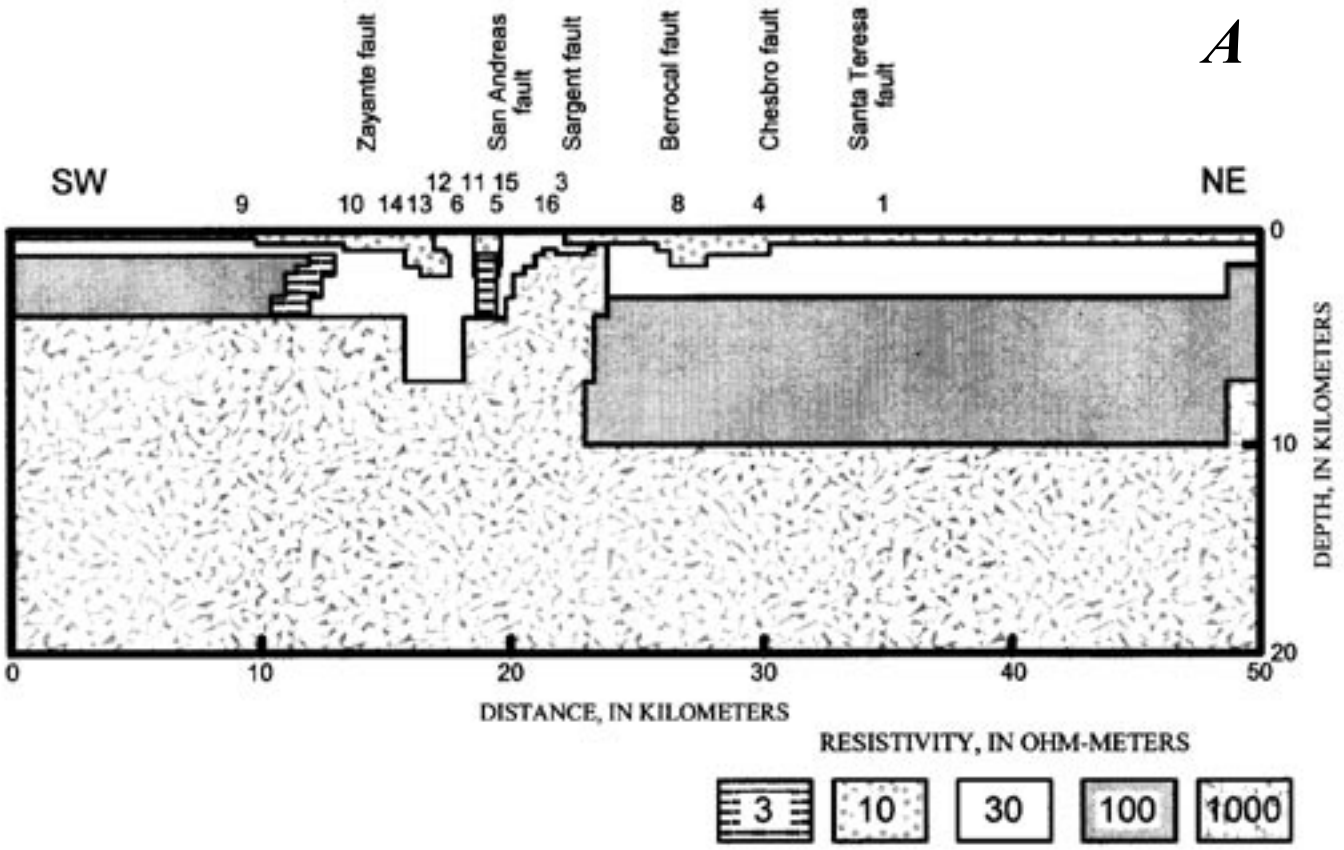

Figure 11.—Loma Prieta magnetotelluric (MT) profile (fig. 2; see fig. 1 for locations), with shallow depth extension of low-resistivity case of two-dimensional finite-element MT model. *A*, Two-dimensional finite-element MT model. Numbers denote stations shown in figure 1. *B*, Resistivity data. *C*, Phase data. Same symbols as in figure 2.

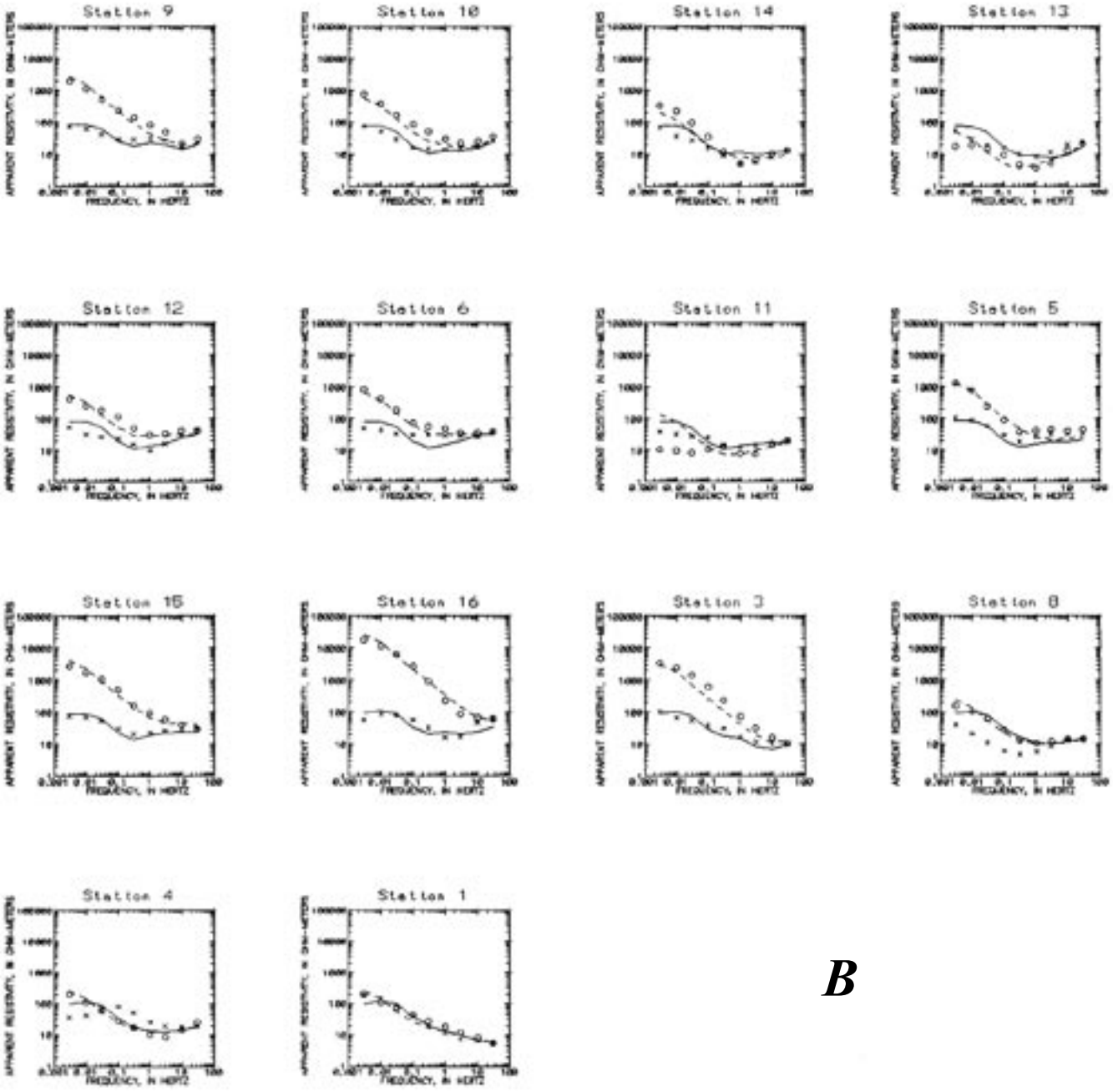

Figure 11.—Continued

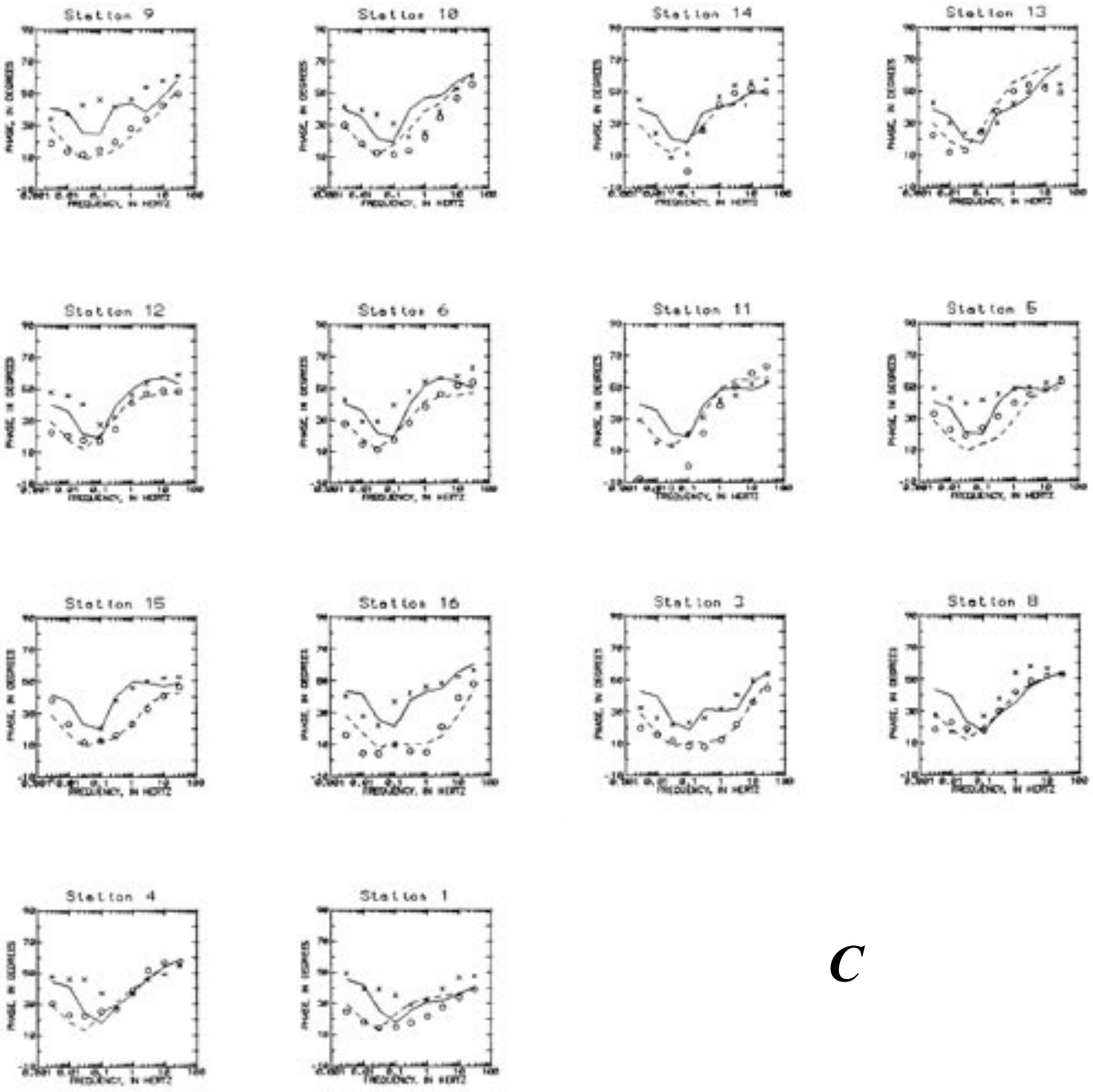

Figure 11.—Continued

EARTHQUAKE OCCURRENCE

EVIDENCE FOR OCEANIC CRUST BENEATH THE CONTINENTAL MARGIN WEST OF THE SAN ANDREAS FAULT FROM ONSHORE-OFFSHORE WIDE-ANGLE SEISMIC RECORDINGS

By Thomas M. Brocher, Michael J. Moses, and Stephen D. Lewis, U.S. Geological Survey

CONTENTS

ABSTRACT

Wide-angle seismic-reflection/refraction data obtained in the vicinity of the epicenter of the 1989 Loma Prieta earthquake provide evidence for a slab of oceanic crust extending from the deep-sea floor to the San Andreas fault. During marine seismic-reflection profiling of the north-central California margin in May 1990, two onshore recording arrays were deployed transverse to and straddling the San Andreas fault in the Santa Cruz Mountains and the Diablo Range. Wide-angle reflections recorded by these arrays define the top and bottom of oceanic crust as far eastward as the San Andreas fault. The wide-angle refraction data obtained by the arrays provide evidence that the oceanic crust, apparently connected to and inferred to represent Pacific plate, is overlain by a seaward-tapering wedge of rocks with velocities of 6.0 to 6.6±0.1 km/s. We interpret this wedge as composed of slivers of San Simeon and Salinian (and, possibly, other) rocks. The wide-angle data are consistent with a landward dip on the oceanic crust of 8°–11°. The velocity model inferred from these data suggests that the hypocenter of the earthquake was located near the base of the interpreted wedge of Salinian rocks beneath the continental margin but above the oceanic crust. On the basis of this geometry, we infer that the top of oceanic crust represents a detachment surface accommodating oceanward movement of North America. This oceanward movement mirrors the eastward-directed tectonic wedging observed beneath the Diablo Range and the western part of the Great Valley. An observed concave-upward geometry of the Moho in the vicinity of the San Andreas fault should strongly focus wide-angle reflections from the Moho that travel along the fault from earthquake sources on or near the fault.

INTRODUCTION

Knowledge of the structure of the midcrust to lower crust offshore central California is fundamental to our understanding of the tectonic processes associated with, and the earthquake hazards posed by, ongoing transpression of the California margin. Since early studies of the continental margin off California (Uchupi and Emery, 1963; Curray, 1966), workers have recognized that an Andean-type continental magmatic-arc/trench system existed during the Mesozoic throughout the region of present central California. That system was disrupted by Cenozoic strike-slip faulting, which included a period of transtension (Miocene) and transpression (Pliocene and Quaternary) (for example, Dickinson, 1970; Ernst, 1971; Saleeby, 1986; McCulloch, 1987). Major anticlinal-fold structures in the offshore Santa Maria Basin have been dated at Pliocene (3–5 m.y.), suggesting that compressional forces related to Pacific plate-motion changes began at that time (McCulloch, 1987; Clark and others, 1991). Present transpression across the margin has been inferred from geodetic, focal-mechanism, stress-measurement, and other data (Zoback and others, 1987). Although the ongoing transpressional tectonics favors thrust and strike-slip faults (for example, Namson and Davis, 1988), the existence and geometry of these thrust faults in north-central California, and their relation to the San Andreas fault, are poorly known because most of the faults are buried (Wentworth and others, 1984). In the vicinity of Morro Bay, south of Monterey, seismic-reflection/refraction profiling

by the Pacific Gas and Electric Co. (PG&E) and EDGE (a consortium of university investigators) suggests that the outer margin and shelf are underlain at midcrustal levels by oceanic crust, possibly of the Farallon plate, and that the top of this oceanic crust may act or have acted as a subhorizontal detachment surface (Ewing and Talwani, 1991).

The 1989 Loma Prieta earthquake served both as a reminder of the active transpression occurring along the San Andreas fault and as a catalyst for framework studies aimed at better understanding the crustal structure in the vicinity of the fault (U.S. Geological Survey staff, 1990). Large-amplitude reflections from the midcrust to the lower crust and the top of the upper mantle may have increased the ground motions generated by the earthquake at some distant sites (Somerville and Yoshimura, 1990) and provide additional motivation for the delineation of subhorizontal structures in the midcrust to lower crust. We report here the primary results of an onshore-offshore seismic-reflection/refraction investigation of the crustal structure of the California continental margin in the Loma Prieta region. We present seismic evidence for oceanic crust underlying the margin and extending continuously from the present deep-sea floor as far eastward as the San Andreas fault. We describe evidence favoring the presence of a sliver of Salinia terrane overlying the oceanic crust and propose a speculative tectonic model based on the observed crustal structure.

GEOLOGIC SETTING

The seismic profiles presented here nearly coincide with the C2 transect of central California (fig. 1; Saleeby, 1986; Fuis and Mooney, 1990). We therefore refer the reader to these studies for a detailed summary of geologic relations and provide here only a brief review of the main geologic structures crossed by the seismic survey.

As described by Fuis and Mooney (1990), the central California margin consists of an inactive, early Tertiary accretionary prism that is overlain by Oligocene to Holocene sedimentary rocks (Uchupi and Emery, 1963; Silver and others, 1971; Mullins and Nagel, 1981; McCulloch, 1987). On the basis of dredging results and geophysical data, parts of the margin have been interpreted to be underlain by Franciscan complex (Silver and others, 1971; Mullins and Nagel, 1981). The margin is believed to be floored by oceanic crust dated at 20 to 26 m.y., on the basis of an identification of magnetic anomalies on the Pacific plate (Atwater and Menard, 1970; Atwater, 1989; Fernandez and Hey, 1991; Lonsdale, 1991). Near the coast, the inactive Tertiary accretionary prism is juxtaposed against the Salinian block, which consists of granitic and high-temperature-metamorphic rocks overlain by Upper Cretaceous, Paleogene, and Neogene sedimentary rocks. At the latitude of our study (fig. 1), the Salinian block is bounded on the west by the San Gregorio-Hosgri fault and on the east by the San Andreas fault (U.S. Geological Survey and California Division of Mines and Geology, 1966; Jennings and others, 1977; Ross, 1978) and here includes mafic basement adjacent to the San Andreas fault.

Franciscan rocks lie between the San Andreas fault and a subsurface boundary beneath the San Joaquin Valley and in the Diablo Range (U.S. Geological Survey and California Division of Mines and Geology, 1966; Jennings and others, 1977; Ross, 1978). According to Wentworth and Zoback (1990, p. 44):

> The Franciscan assemblage, * * * of Late Jurassic to Late Cretaceous age, is an accretionary prism that consists principally of oceanic sedimentary and lesser volcanic rocks. Some tectonostratigraphic units in the Franciscan consist of well-bedded, albeit variously folded, rocks, whereas others are a melange of various kinds and sizes of blocks in a matrix of sheared mudstone (Blake and others, 1984). Most of the rocks have varyingly undergone high-pressure, low-temperature metamorphism to blueschist grade. The structural base of the Franciscan is nowhere exposed at the surface.

In the study area (fig. 1), two quite different types of Franciscan rocks are involved: in the Santa Cruz Mountains, graywacke, melange, and much greenstone, with a shallow high-velocity "basement" (pumpellyite to blueschist grade); and in the Diablo Range, metasandstone and melange (all blueschist, locally containing jadeite), with a thickness based on seismic-refraction velocities of 12 to 15 km.

Fuis and Mooney's (1990) compilation of existing seismic refraction and reflection studies along the C2 transect is modified in figure 2. Seismic-refraction profiling by Shor and others (1971) found oceanic crust of the Pacific plate just to the west of the base of the continental slope in deep water. Onshore seismic-refraction profiles, which were acquired along the strike of the San Andreas fault to the south of Loma Prieta, indicate that the Moho lies at 24- to 26-km depth just west of the San Andreas fault and that the crust may be about 30 km thick in the Diablo Range (Walter and Mooney, 1982; Blümling and Prodehl, 1983; Blümling and others, 1985).

DATA ACQUISITION AND PROCESSING

In May 1990, the U.S. Geological Survey (USGS) conducted a marine multichannel-seismic-reflection investigation of the central California margin (Lewis, 1990). The 10-element airgun array used by the research vessel *S.P. Lee* for the seismic-reflection profiling, totaling 40 L, was simultaneously recorded by two temporary onshore arrays of recorders deployed transverse to and straddling the San Andreas fault in the Santa Cruz Mountains and the Diablo Range (fig. 1*B*; Brocher and others, 1992). The Loma Prieta array consisted of 13 stations stretching from the coast landward 94 km to the San Joaquin Valley. A shorter array, located 25 km northeast of Loma Prieta, consisted of six stations stretching landward about 70 km from Año Nuevo to Cedar Mountain in the Diablo

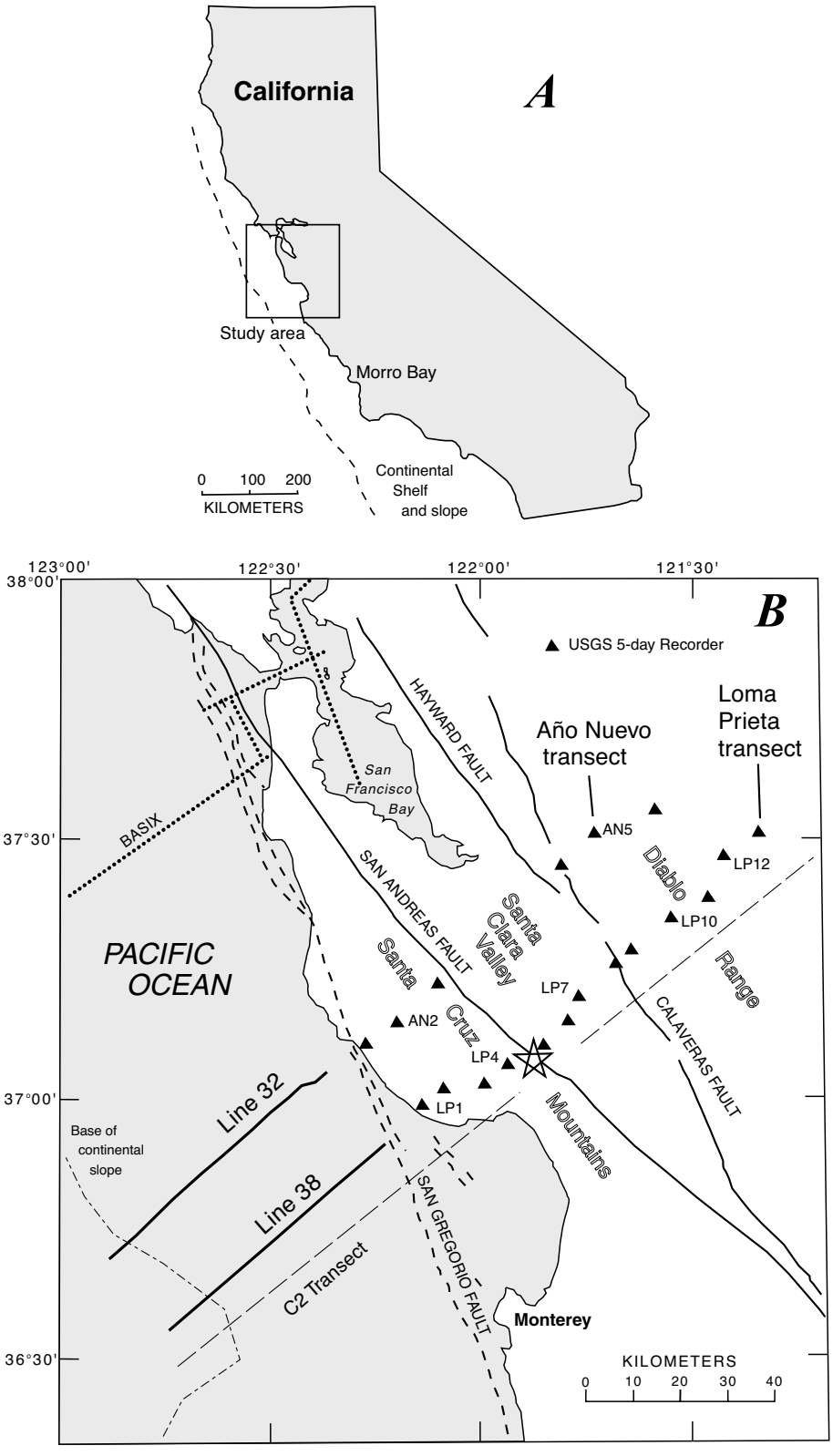

Figure 1.—Loma Prieta region, Calif. *A*, California, showing locations of study area and base of the Continental Shelf and slope (dashed line). *B*, Central California, showing locations of marine seismic-reflection lines 32 and 38, temporary recording stations (triangles), selected faults, 1991 BASIX lines (Holbrook and others, 1996), and C2 transect of Saleeby (1986). Star, epicenter of October 17, 1989, *M*=7.1 Loma Prieta, Calif., earthquake.

Range. These temporary arrays were deployed to record two parallel 61-km-long seismic-reflection lines (32, 38, fig. 1*B*) from source-receiver offsets ranging from 11 to 165 km. The goals of the wide-angle recording were to constrain the mid-crustal to lower-crustal structure in the Loma Prieta region and to look for variations in this structure along the strike of the San Andreas fault.

The wide-angle data were acquired with analog three-component, 5-day seismic recorders, as described by Criley and Eaton (1978). The 5-day recorders were deployed along access roads and were turned on before acquiring the marine seismic-reflection lines (Brocher and others, 1992). At four stations (AN2, LP1, LP9, LP11, fig. 1*B*), seismic signals from a vertical-component seismometer were telemetered to an adjacent 5-day recorder for data acquisition.

The digitization of the 5-day analog tapes, the conversion of the digitized data into SEG–Y format, and the subsequent processing of the wide-angle record sections were described by Brocher and others (1992). Record sections reduced by a velocity of 6 km/s were generated by this procedure.

DATA DESCRIPTION

Marine seismic-reflection lines 32 and 38 (fig. 1*B*) image similar structural elements on the central California Continental Shelf and slope (fig. 3). Seaward of Santa Cruz and the Outer Santa Cruz Basin high on the Continental Shelf, these lines image a thick slope basin locally containing more than 2,000 m of sedimentary deposits, probably of Oligocene to Holocene age. The slope deposits thin over, and are deformed by growth of, an unnamed anticline at the base of the continental slope. Sedimentary deposits of the Monterey deep-sea fan thin against, onlap, and appear to be uplifted by this unnamed anticline. Moderately dipping reflections from within the core of the anticline probably represent splay thrust faults that dip landward. Low-frequency and diffractive reflections beneath the Neogene sedimentary deposits, which we infer to represent the top of subducted oceanic crust of the Pacific plate, can be traced about 20 km landward of the base of the slope.

All of the wide-angle records obtained along the Loma Prieta and Año Nuevo transects were presented by Brocher and others (1992). These records indicate five crustal and upper-mantle arrivals, as shown in figure 4. The first of these arrivals represent refractions from the upper crust (*Pg*), which differ noticeably on records from the two transects. On the Loma Prieta transect, *Pg* arrivals have apparent velocities of 4 to 5 km/s and grade smoothly with arrivals with velocities closer to 6 km/s at greater ranges. On the Año Nuevo transect, *Pg* arrivals have an apparent velocity close to 6 km/s and are abruptly truncated near model coordinate 30 km. Modeling suggests that a group of secondary arrivals at the

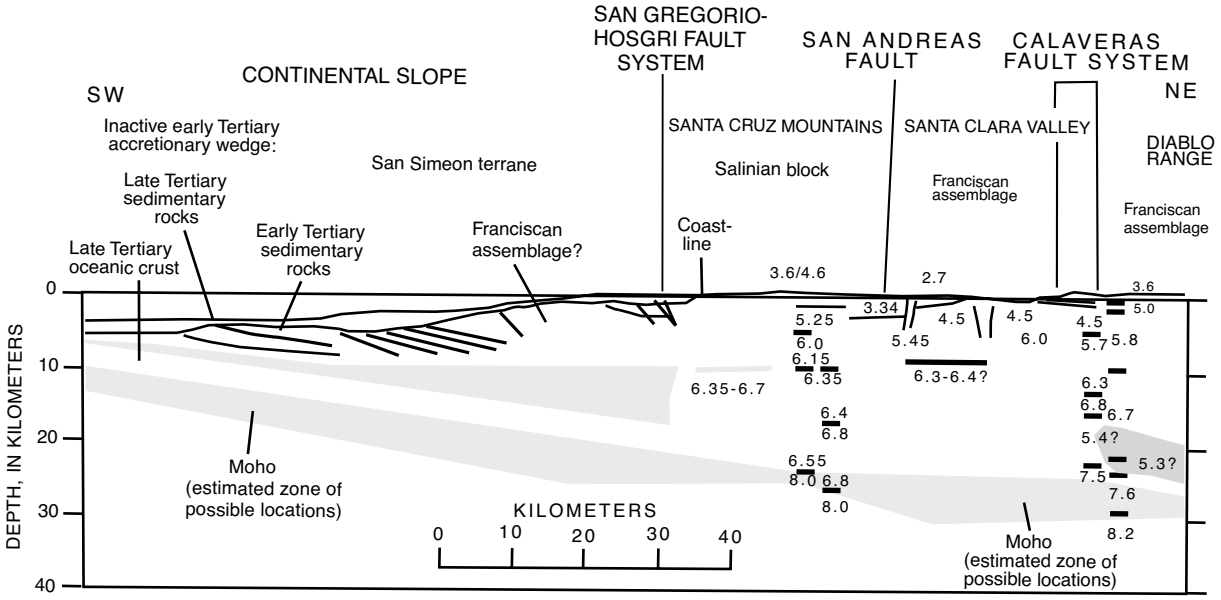

Figure 2.—Compilation of seismic refraction and reflection studies along C2 transect (modified from Fuis and Mooney, 1990). The San Simeon terrane west of the San Gregorio-Hosgri fault system is inferred to be composed of the Cretaceous Franciscan assemblage. The Salinian block in the Santa Cruz Mountains is composed mostly of upper Cretaceous granitic, high-temperature-metamorphic, and Tertiary sedimentary rocks. The Franciscan assemblage in the Santa Clara Valley is composed of the Permanente terrane, which is overlain by Tertiary sedimentary rocks and outliers of Coast Range ophiolite and Great Valley sequence. Shaded areas indicate uncertainties in locations of midcrustal and Moho discontinuities. No vertical exaggeration.

farthest source-receiver ranges represent refractions from a slab with velocities of 6.6 to 7.1 km/s. In the nomenclature of seismic-refraction profiling of the oceanic crust, these arrivals represent P_3 refractions from the gabbroic layer, although to our knowledge this nomenclature has not previously been applied to continental margins. A third group of arrivals represents wide-angle reflections (*PiP*) from the midcrust. On the Loma Prieta transect, these arrivals are fairly weak and generally observed only at small source-receiver offsets and on the highest quality profiles; these wide-angle reflections have much larger amplitudes on the Año Nuevo transect. A fourth group of arrivals represents large-amplitude reflections from the top of the upper mantle, the Moho, and is designated as *PmP*. *PmP* arrivals are curved strongly downward on the reduced record sections, indicating a landward-dipping Moho or a seaward-thinning crust (fig. 4). *Pn* arrivals, which represent refractions from the upper mantle, are generally faint and have complex traveltime curves due to the complex structure.

The low signal-to-noise ratio of the recorded data and the reverberant-airgun-array source result in a greater uncertainty of the traveltime observations than is normally reported for wide-angle seismic experiments. Here, we believe that absolute traveltime uncertainties, though widely varying, are generally as great as 0.1 to 0.2 s, owing to the reverberant waveform and low signal levels. Relative traveltime uncertainty, however, is only 0.01 to 0.05 s. Thus, inferred phase velocities are believed to be more accurate than inferred layer thicknesses.

FORWARD MODELING

We forward-modeled observed *P*-wave traveltimes and amplitudes by using the ray theory of ervený and others (1977) and the computer algorithms of McMechan and Mooney (1980) and Luetgert (1988) for two-dimensional velocity-depth structures. The velocity model consists of layers with linear velocity gradients and velocity discontinuities of varying magnitude between layers. The traveltime modeling proceeded by first fitting direct arrivals and then the refractions recorded nearest each receiver. These arrivals

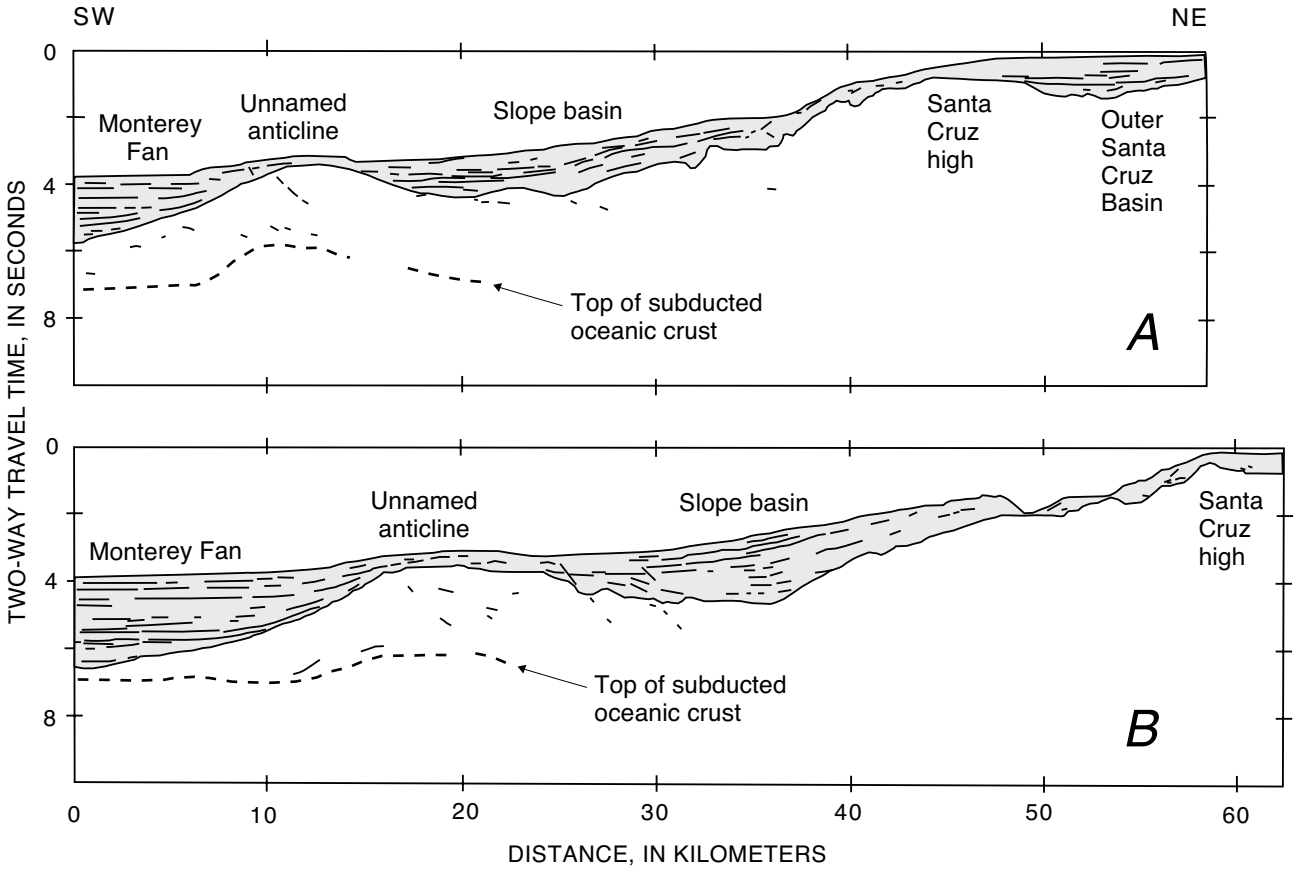

Figure 3.—Line-drawing interpretations of seismic-reflection lines 32 (*A*) and 38 (*B*) (see fig. 1*B* for locations), showing major Neogene basins and other structural elements revealed by these profiles. Seismic data have been migrated; for 2-km/s velocity appropriate for Neogene sedimentary deposits (shaded), sections are plotted with a vertical exaggeration of about 1.78.

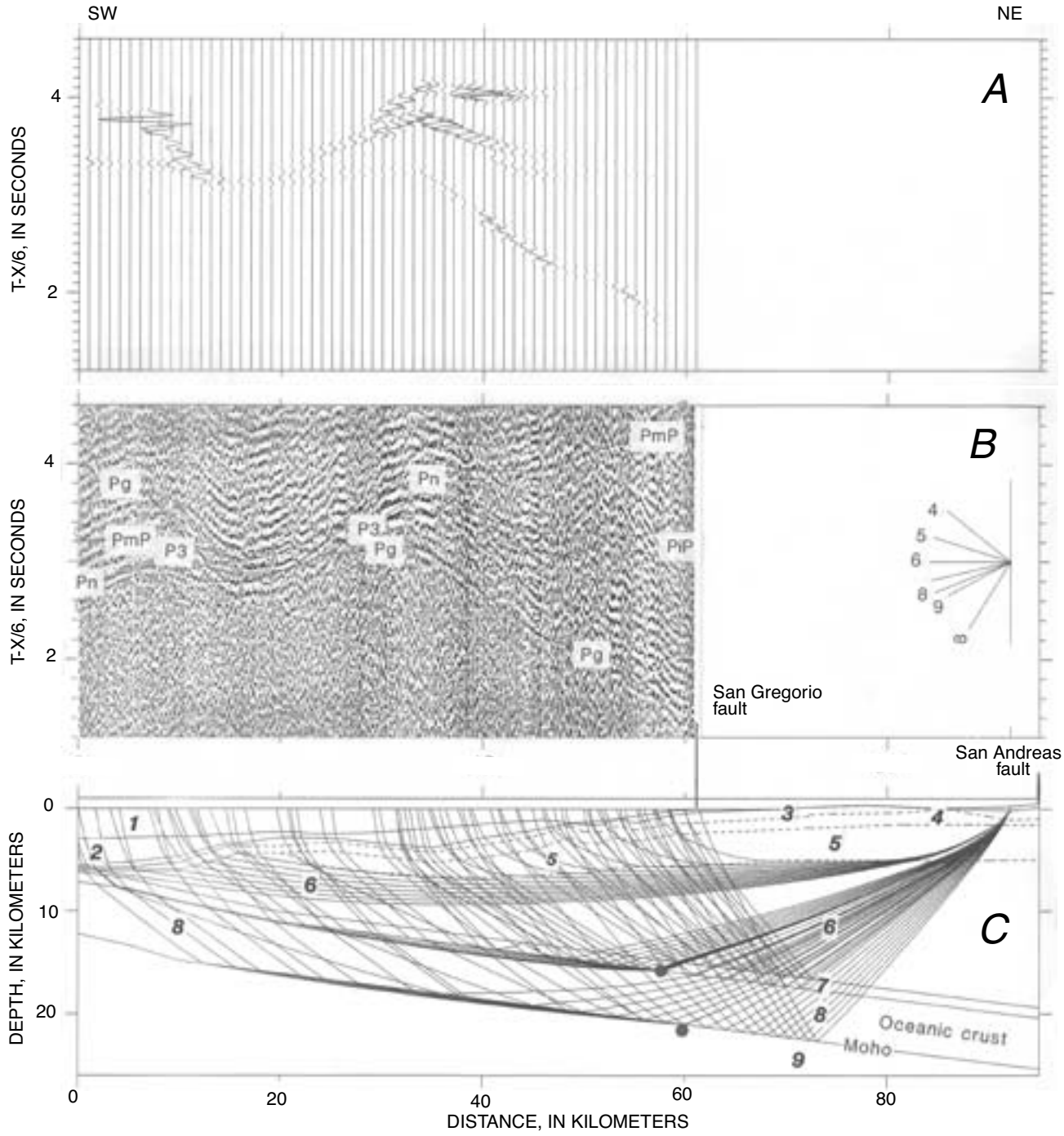

Figure 4.—Synthetic (*A*) and observed (*B*) record sections and ray diagram (*C*) for receiver at station LP4 on the Loma Prieta transect (see fig. 1*B* for location). Receiver was located at model coordinate 92 km. Synthetic seismograms in figure 4*A* were calculated from velocity model shown in figure 5*B*, using ray-theoretical method of McMechan and Mooney (1980); synthetic seismograms are plotted in true-relative-amplitude format, using a correction for geometric spreading of $(\text{Range})^{0.5}$. Record section shown in figure 4*B* is plotted showing true relative amplitudes, using a correction for geometric spreading of $(\text{Range})^{0.7}$. Velocity rosette on right indicates apparent phase velocities of arrivals. Calculated traveltimes along the Loma Prieta transect are superposed on record section and are queried where predicted branch does not correspond to clear arrivals in data. Arrivals include refractions from upper crust (*Pg*) and upper-mantle (*Pn*), and midcrustal (*PiP*) and upper mantle (*PmP*) reflections, all keyed to velocity model through layer numbers of model shown in figure 4C. *Pg* arrivals are refractions from layer 6, *PmP* is a postcritical reflection from top of layer 9, *PiP* is a postcritical reflection from top of layer 8, P_3 is a refraction from layer 8, and *Pn* is a refraction from layer 9. Critical points are indicated by dots along tops of layers 8 and 9. Velocity model in figure 4*C* is plotted without vertical exaggeration.

are used to determine the velocities and thicknesses of the uppermost layers of the model near each receiver, which, when interpolated between receivers, yield a two-dimensional velocity model for the entire receiver array. Subsequent arrival times are then fitted, always working downward through the model, to ensure that all previous, earlier arrivals are matched by the model. Velocity discontinuities between layers are introduced to replicate observed reflection arrivals. Because the velocity models are two dimensional, we assumed that the seismic-reflection lines and recording geometry could be approximated by a straight line. From figure 1*B*, this assumption is reasonable. Final velocity models obtained by this analysis for seismic-reflection lines 32 and 38 are shown in figure 5.

Observed *Pg* traveltimes were generally matched to within 0.10 s by forward modeling. We estimate from trial-and-error perturbations of model parameters that *P*-wave velocities are resolved to within ±0.1 km/s by this forward-modeling procedure, particularly in the center of the velocity model, and that the depths of interfaces are resolved to within 5 to 10 percent. The horizontal resolution varied along the model. On the seaward end, the shot spacing was 50 m, and the shortest

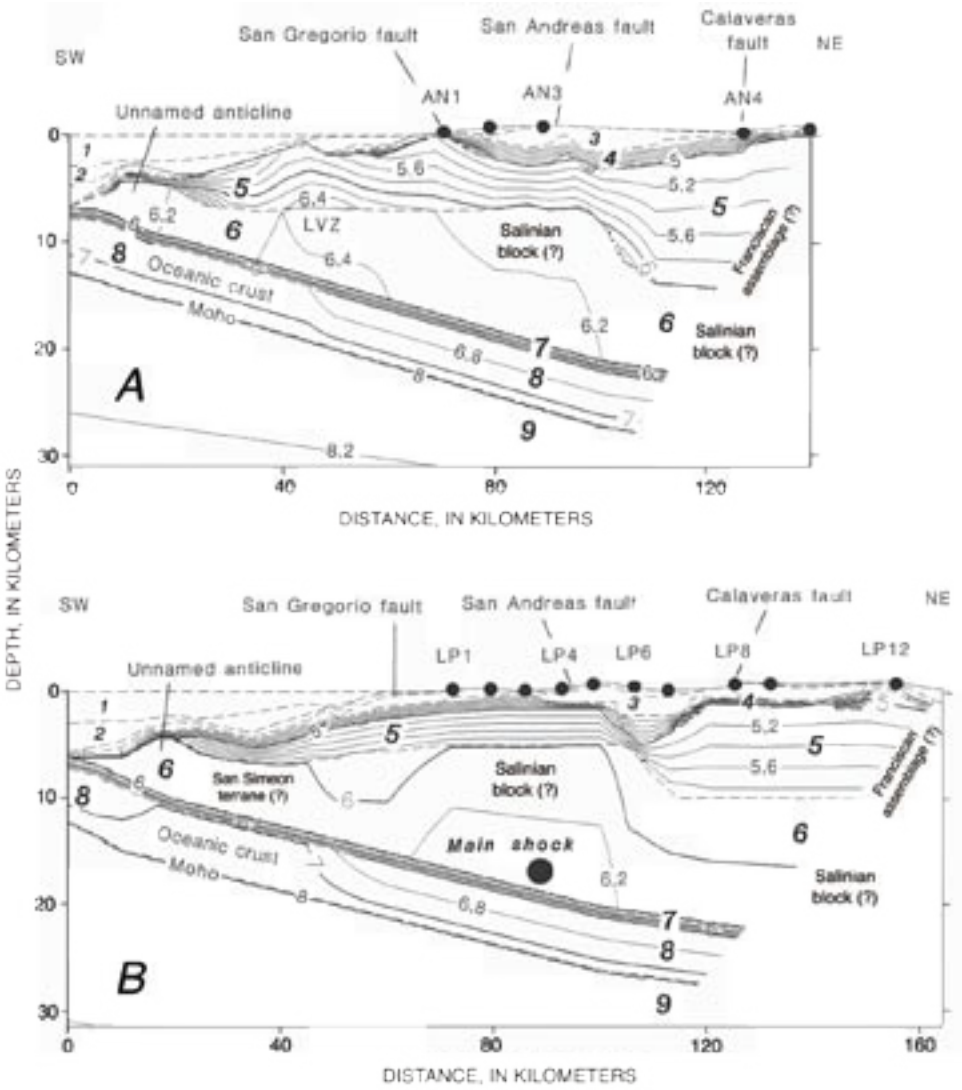

Figure 5.—Velocity models inferred from forward modeling of *P*-wave traveltimes and amplitudes for the Año Nuevo transect along seismic-reflection line 32 and Año Nuevo (AN) deployment (*A*), and for the Loma Prieta transect along seismic-reflection line 38 and Loma Prieta (LP) deployment (*B*). Isovelocity contours between 4 and 8.2 km/s are plotted every 0.2 km/s. Dots, temporary recording stations (see fig. 1*B* for locations); dashed lines, layer boundaries. Layers: 1, ocean water, with a velocity of 1.5 km/s; 2, Neogene sedimentary deposits, with a velocity of 2 km/s; 3, Neogene sedimentary deposits, with a velocity of 3 to 4 km/s. Note low-velocity zone (LVZ) between layers 5 and 6 near model coordinates 40 km on Año Nuevo transect. Vertical exaggeration, 2:1.

wavelengths of observed *P* waves were about 400 m, suggesting a horizontal resolution of less than 1 to 2 km for the offshore region. Onshore, the receiver spacing averaged 8 km, suggesting that the horizontal resolution in upper-crustal structure onshore is closer to 8 to 10 km. Ray diagrams, showing *P*-wave raypaths through the model, indicate that the resolution of the procedure varies along the model, depending on the density of raypaths. In particular, the landward end of the model lacks ray coverage, owing to the absence of sources there, thus degrading the resolution of our forward-modeling procedure. For a more detailed description of model parameterization and error estimates in this type of forward modeling, the reader is referred to Hill and others (1985) and Fuis and others (1991). Recent comparisons between velocity models obtained from forward modeling and inverse methods of traveltime analysis suggest that the first-order features obtained from forward modeling are robust (Brocher and others, 1991). Synthetic seismograms were calculated from the velocity models by using asymptotic-ray theory (McMechan and Mooney, 1980), as implemented at the USGS (Luetgert, 1988).

VELOCITY MODELS

Velocity models were constructed from forward modeling of traveltimes and amplitudes for both the Loma Prieta and Año Nuevo transects, which are defined by seismic-reflection lines 38 and 32, respectively (fig. 1*B*). The initial velocity models used for forward modeling were derived from several data sets, including multichannel-seismic-reflection lines 32 and 38 (fig. 3), earthquake tomography of the shallow crust in the vicinity of the San Andreas and Calaveras faults, and onshore seismic-refraction studies (fig. 2).

Seismic-reflection lines 32 and 38 provide important constraints on the sea-floor bathymetry and geometry of Neogene basins along the line of sources. Sea-floor topography and Neogene sedimentary-basin thicknesses in terms of two-way traveltime were obtained from a time-migrated version of seismic-reflection lines 32 and 38 (fig. 3); to convert these estimates to depths, we assumed a seawater velocity of 1.5 km/s and a velocity in the Neogene sedimentary deposits of 2 km/s. The seismic-reflection lines allowed us to determine the geometry of the Outer Santa Cruz Basin, the Santa Cruz high near the seaward edge of the Continental Shelf southwest of the Outer Santa Cruz Basin, a slope basin lying seaward of the Santa Cruz high, the unnamed anticline, and, farthest seaward, sedimentary deposits of the Monterey deep-sea fan (fig. 3). The unnamed anticline on seismic-reflection lines 32 and 38 is a major structural feature, displaying nearly 2 km of relief on the base of the Neogene sedimentary deposits. Mafic volcanic rocks dredged from the Santa Cruz high suggest that it may be cored either by Franciscan basement or Tertiary accretionary rocks (Silver and others, 1971; Mullins and Nagel, 1981). Diffractive reflections from the top of oceanic crust can be traced with confidence about 20 km landward of the relic trench on these seismic-reflection lines (fig. 3). The presence of reflections from the oceanic Moho in these data, however, is equivocal.

We forward-modeled vertical-incidence two-way traveltimes predicted by our model of the sea-floor bathymetry and Neogene sedimentary basin thickness for model coordinates 0 to 60 km. The model was adjusted until the calculated two-way traveltimes matched the observed two-way traveltimes on the seismic-reflection profiles to within 0.05 s. Similar modeling of the reflection from the top of oceanic crust was performed from model coordinates 0 to 20 km (where this reflection is observed), and the model was adjusted until the calculated two-way traveltimes matched the observed two-way traveltimes on the seismic-reflection profiles to within 0.075 s.

The initial model for the shallow (0–15-km depth) crustal structure onshore (model coordinates 70–165 km) was taken from a tomographic study of the San Andreas and Calaveras faults using microearthquakes (Michael, 1988; Eberhart-Phillips and others, 1990a, b). This structure displays pronounced velocity contrasts across the San Andreas and Calaveras faults, as well as across low-velocity zones associated with these faults. Michael's (1988) and Eberhart-Phillips and others' (1990a, b) structures had to be significantly modified during our forward modeling to improve the fit to the observed traveltimes. Generally speaking, the modifications reduced the complexity of the velocity structure and minimized the size of lower-velocity basinlike structures. These modifications included the addition of a layer of surficial sedimentary deposits, as much as several hundred meters thick, with a velocity of 2.0 km/s. Estimates of crustal thickness east of the San Andreas fault and in the Diablo Range are those of Walter and Mooney (1982), Blümling and Prodehl (1983), and Blümling and others (1985).

In the absence of offshore receivers, we made several assumptions in constructing the initial velocity model beneath the continental margin. First, we projected the 4-, 5-, and 6-km/s contours of Eberhart-Phillips and others (1990a, b) across the Continental Shelf and slope by assuming that these contours are subparallel to the base of the Neogene sedimentary deposits. Second, on the basis of our interpretation of the seismic-reflection data and in agreement with models for the C2 transect (Fuis and Mooney, 1990), we assumed that oceanic crust underlies the entire Continental Shelf and slope. Given our lack of control on the structure to the east of the San Andreas fault, and for convenience during forward modeling, we assumed that the oceanic crust is continuous across the fault. Third, following Shor and others (1971), we assumed that the oceanic crust is 6 km thick and that it can be adequately modeled by using the same structure as that determined by Tréhu (1991) for subducted oceanic crust in the vicinity of Morro Bay. Tréhu divided the oceanic crust into two layers with different thicknesses and velocity gradients. Thus, oceanic layer 2, consisting of extrusive volcanic rocks and sheeted dikes, is modeled as 1 km thick, with a linear-velocity gradient of 5.5 to 6.4 km/s; and oceanic layer 3, consisting

of gabbro, is modeled as 5 km thick, with a linear-velocity gradient of 6.6 to 7.1 km/s (fig. 5). Fourth, we assumed that the upper-mantle velocity is 8 km/s, in agreement with the Pn velocity determined by using Calnet data (Oppenheimer and Eaton, 1984) and with the upper-mantle velocity reported by Walter and Mooney (1982).

Velocity models inferred for the Loma Prieta and Año Nuevo transects differ significantly within the upper crust, although the overall structural elements are similar (fig. 5). The three major structural features resolved by the data include (1) a slab of oceanic crust with velocities of 5.5 to 7.1 km/s that dips landward and can be traced as far eastward as the San Andreas fault and possibly farther, (2) a midcrust with velocities of 6.0 to 6.5 km/s, and (3) lower average crustal velocities east than west of the San Andreas fault. The major difference in the velocity models for the two transects is the presence of upper-crustal velocities higher than 6.5 km/s west of the San Gregorio fault on the Año Nuevo transect but which are absent on the Loma Prieta transect to the south.

Before providing a detailed description of the velocity model obtained from each recorder array, we briefly summarize the evidence for the three major features of these models. The first feature, an east-dipping slab of oceanic crust, is primarily constrained by wide-angle reflections (*PiP*) observed from both the top and bottom of a 6.6- to 7.1-km/s layer. In addition, at greater source-receiver offsets, large-amplitude secondary arrivals are modeled as refractions from oceanic layer 3 that arrive earlier than refractions from within the midcrust with velocities of 6.0 to 6.5 km/s. The second feature, a low vertical-velocity gradient in the midcrust west of the San Andreas fault, is needed to match the large source-receiver ranges to which *Pg* arrivals are observed. If larger velocity gradients are used, the ranges to which these arrivals are observed cannot be matched, owing to the more rapid turning of rays with depth. The third feature, lower average crustal velocities east of the San Andreas fault, is consistent with velocity models obtained by inverting microearthquake traveltimes (Michael, 1988; Eberhart-Phillips and others, 1990a, b). These inversion results along the Loma Prieta transect indicate that velocities within the Franciscan Complex to the east of the San Andreas fault are lower than in the Salinian block to the west, as also determined by seismic-refraction profiling (Walter and Mooney, 1982). In the next section, we review in greater detail the constraints on velocity models for both the Loma Prieta and Año Nuevo transects.

LOMA PRIETA TRANSECT

The wide-angle seismic data recorded southwest of the San Andreas fault (stas. LP1–LP5, fig. 1*B*), between Loma Prieta and the coast, provide the best available information on the geometry of the oceanic crust and on upper-crustal velocities southwest of the San Andreas fault. Because these five stations provided nearly identical record sections, spanning a distance of only 28 km, we describe the modeling of these profiles as an ensemble rather than individually. An example of our modeling of these profiles is shown in figure 4. First arrivals observed from airgun shots nearest the receiver at stations LP1 to LP3 are explained by refractions within layer 5 (fig. 4*C*). At greater source-receiver offsets, large-amplitude Pg arrivals are modeled by using raypaths that sample layer 6 to about 10-km depth. First arrivals observed at greater ranges are more than 1 s too early to be explainable as refractions from layer 6 but are well matched by P_3 and *Pn* refractions from layers 8 and 9. Undulations in observed traveltimes on the southwest ends of the profiles between model coordinates 0 and 30 km are modeled by a pronounced structural relief of velocity contours across the unnamed anticline. The unusual moveout of reflected *PmP* arrivals on these profiles requires a seaward-thinning crust because a flat or substantially more gently dipping Moho beneath the continental margin does not predict the observed strong curvature of *PmP* arrivals (fig. 4). In turn, seaward thinning of the crust further constrains velocity gradients within the midcrust; deeply diving rays produced by the large velocity gradients in layer 6 would intersect the shoaling Moho, thereby truncating *Pg* arrivals prematurely. *PmP* arrivals and a faint wide-angle *PiP* reflection from the midcrust observed as far landward as the coastline (fig. 4*B*) are consistent with the 5-km modeled thickness of layer 8.

The records from stations LP6 to LP8 (fig. 1*B*), located between the San Andreas and Calaveras faults, are consistent with the presence of a small low-velocity body between these faults at model coordinates 105 to 120 km (fig. 6). First-arrival times require a large time delay modeled by replacing velocities of 4 to 5 km/s in layers 4 and 5 with velocities of 3 to 4 km/s: no arrivals that turn within this low-velocity region are observed. Observed *Pg* first arrivals with apparent velocities of 4.4 km/s are closely matched by refractions from layer 6. Large-amplitude secondary arrivals from model coordinates 0 to 30 km with phase velocities higher than 6 km/s are modeled as P_3 refractions from layer 8. The predicted amplitudes of reflected *PiP* arrivals are much weaker than the predicted amplitudes of *PmP* arrivals. The *Pn* arrivals predicted by refractions from layer 9 are very faint and not clearly observed.

Arrivals recorded at stations LP10, LP12, and LP13 (fig. 1*B*), located east of the Calaveras fault, provide only limited constraints on the crustal structure near the San Andreas fault. The data recorded at stations LP9 and LP11 were of significantly lower quality than at the others (Brocher and others, 1992) and so were not used to constrain the velocity model. Large-amplitude *Pg* arrivals with apparent velocities of 4 to 6 km/s are modeled by refractions from layer 6 (fig. 7*C*). The calculated *Pg* raypaths (1) match the maximum source-receiver range to which *Pg* arrivals are observed (approx. 130 km), (2) sample the crust down to about 15-km depth beneath the coastline and San Gregorio fault, and (3) support the existence of a weak velocity gradient within the midcrust to lower crust. Weak *Pn* arrivals observed on the record from station LP12 can be modeled by refractions that sample the Moho to the east of the San Andreas fault (fig. 7). Strong secondary arrivals

between model coordinates 40 and 60 km are modeled as wide-angle reflections and refractions from layer 8. We interpret the large velocity gradient in layer 8 as evidence that a slab of oceanic crust extends as far eastward as the San Andreas fault, although alternative explanations, such as magmatic underplating of the North American Continent, could also produce the modeled velocity gradient.

AÑO NUEVO TRANSECT

Recordings of seismic-reflection line 32 at stations AN1 to AN5 (fig. 1*B*) were used to construct a velocity model along the Año Nuevo transect. The data recorded at Station AN6 were of significantly lower quality than at the others (Brocher and others, 1992) and so were not used to constrain the velocity model.

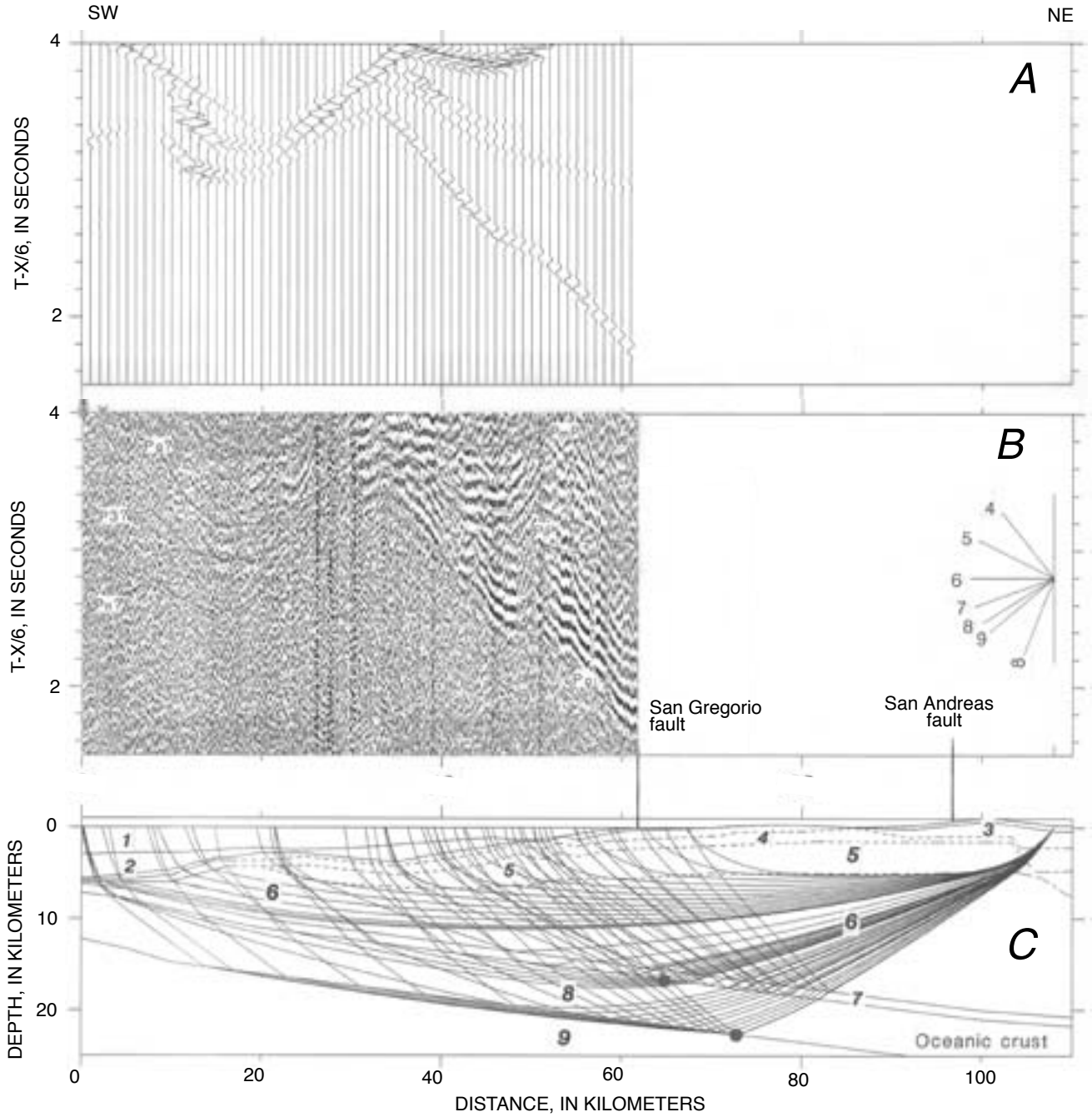

Figure 6.—Synthetic (*A*) and observed (*B*) record sections and ray diagram (*C*) for receiver at station LP6 on the Loma Prieta transect (see fig. 1*B* for locations). Receiver was located at model coordinate 108 km. Same format as in figure 4. Note large time separation between *Pn*, P_3, and *Pg* branches at largest source-receiver offsets.

Stations AN1 to AN3 (fig. 1*B*) all recorded wide-angle data southwest of the San Andreas fault in the Salinian block. The following discussion focuses on the high-quality data from station AN1 plotted in figure 8. Records from stations AN1 to AN3 require an upper-crustal velocity structure noticeably different from that along the Loma Prieta transect. *Pg* arrivals along the Año Nuevo profile show evidence of a rapid decay in amplitude, indicating a conspicuous low-velocity zone (fig. 8). These *Pg* arrivals are modeled as refractions within layer 5 with a velocity of 5.3 to 6.6 km/s and a thickness of about 7 km. We model the *Pg* arrivals as cut off at greater ranges by a low-velocity zone in layer 6 beginning at 7-km depth. At this low-velocity zone, velocities of 6.6 km/s overlie a region with velocities of 6.3 to 6.5 km/s between model coordinates 40 to

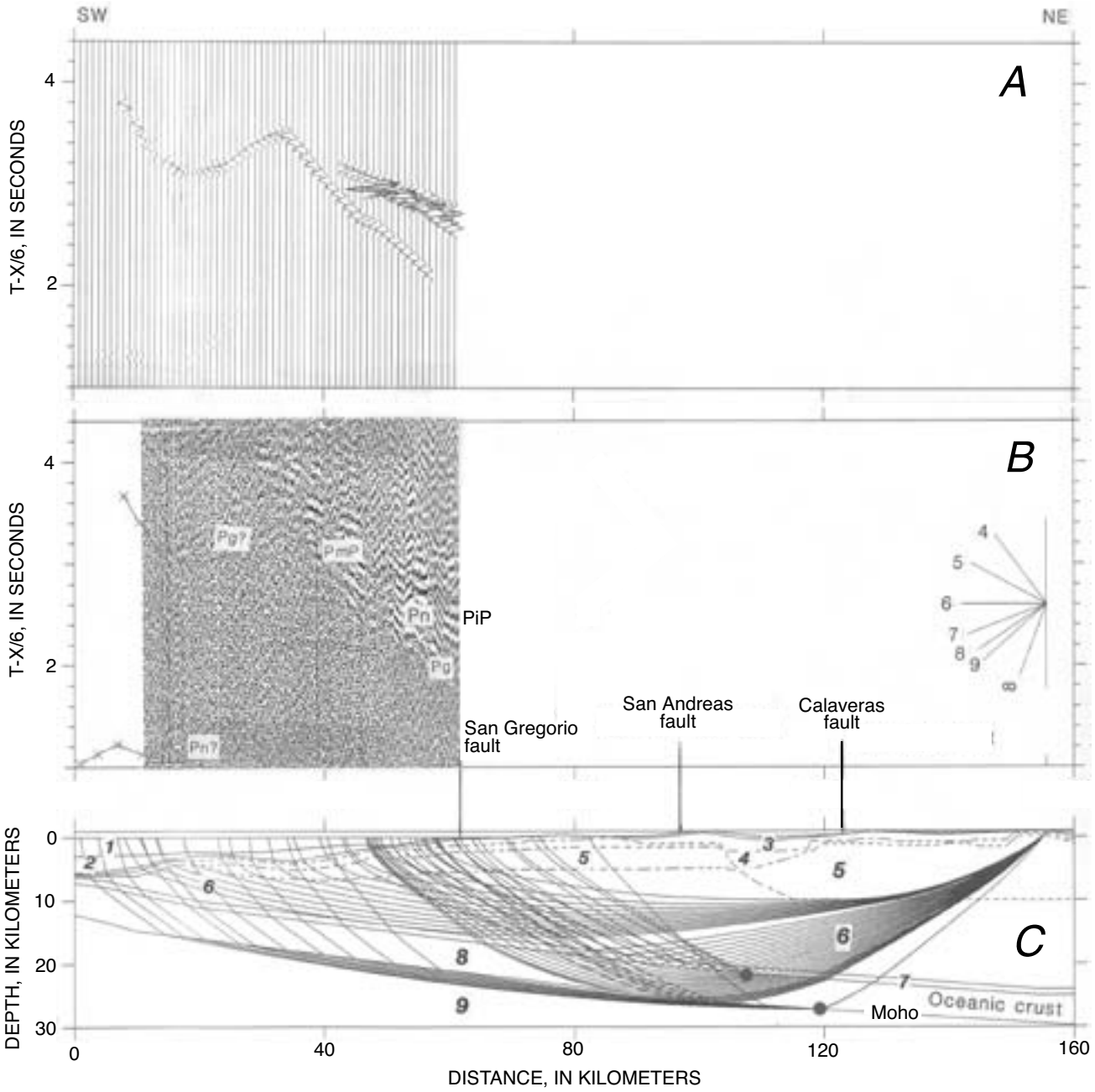

Figure 7.—Synthetic (*A*) and observed (*B*) record sections and ray diagram (*C*) for receiver at station LP12 on the Loma Prieta transect (see fig. 1*B* for locations). Receiver was located at model coordinate 156 km. Same format as in figure 4. *Pg* arrivals are modeled by refractions from layer 6 that turn upward in vicinity of the San Gregorio fault. Large-amplitude secondary arrivals are modeled by reflections and refractions from layers 7 and 8 in region between the San Gregorio and San Andreas faults. A weak *Pn* arrival is predicted by velocity model.

60 km. This narrow low-velocity zone is bounded to the east by the San Gregorio fault (fig. 5). At greater source-receiver ranges, large-amplitude first arrivals are modeled as wide-angle reflections from the top of layer 8 and define this layer as extending eastward of the San Gregorio fault (fig. 8). It is difficult to trace these wide-angle reflections to smaller offsets at precritical angles of incidence. First arrivals at increasing ranges are modeled as P_3 and *Pn* refractions from layers 8 and 9. *PmP* arrivals are observed only at wide angles and cannot easily be traced to smaller offsets; the synthetic seismograms indicate that both *PiP* and *PmP* reflections will have small amplitudes at small offsets.

The wide-angle data recorded at stations AN4 and AN5 (fig. 1*B*), both located in the Diablo Range to the northeast of the Calaveras fault, constrain structures in the vicinity of the San Andreas fault. The data recorded at these stations, separated by only 10 km, are nearly identical, and so we focus our discussion on station AN4 (fig. 9). The large-amplitude first arrivals on the profile from station AN4 were modeled as *Pg* refractions from layer 6 and, as on the Loma Prieta transect, provide evidence for a weak velocity gradient within the midcrust. Faint but clearly observed Pn arrivals (fig. 9) are consistent with the inferred Moho geometry and assumed upper-mantle velocity. A spatially limited set of secondary arrivals observed at about model coordinate 40 km are explainable by P_3 refractions from layer 8. Faint *PiP* reflections are well matched by reflections from the top of layer 8 within 10 km of the San Andreas fault. The strongly dipping, large-amplitude reflected arrivals at the nearest source-receiver ranges (model coordinates 40–60 km, fig. 9) are modeled as *PmP* reflections from the top of layer 9. These *PmP* reflections sample the Moho in the immediate vicinity of the San Andreas fault and, in combination with midcrustal *PiP* reflections, are consistent with the presence of oceanic crust underneath the entire Continental Shelf and slope.

LIMITATIONS OF THE VELOCITY MODELS

Uncertainties in the velocity models for the Loma Prieta and Año Nuevo transects are introduced primarily by (1) the absence of reversed raypaths caused by the absence of receivers on the sea floor and sources on land, and (2) the weakness of *PiP* reflections from the top of the 6.6- to 7.1-km/s layer. In the next subsections, we discuss the implications of both uncertainties.

ABSENCE OF REVERSAL

The unreversed raypaths make it impossible to distinguish between layer velocity and dip and to uniquely locate velocity anomalies along raypaths. A thicker low-velocity (2.0 km/s) layer beneath stations LP6 to LP8 (fig. 1*B*), for example, could be used to model time delays introduced by the basinlike structure between the San Andreas and Calaveras faults on the Loma Prieta transect. Because of the constraints introduced by the multichannel-seismic-reflection lines, we do not view this absence of reversal as a major limitation in the upper crust in the offshore region, where structures are reasonably well known and layer dips appear to be low; however, the uncertainties introduced by the absence of reversal are far more significant in the midcrust to lower crust. An inherent tradeoff, for example, exists between the velocities within the midcrust beneath the Continental Shelf and slope, and those within the unnamed anticline and the 6.6- to 7.1-km/s layer. Decreasing velocities within the midcrust require increasing velocities in the unnamed anticline and oceanic crust, and conversely. Furthermore, velocities within the midcrust are unlikely to be significantly lower than those shown (6.0 and 6.5±0.1 km/s) because this difference would require velocities within the 6.6- to 7.1-km/s layer to be increased above 7 km/s in the middle of this layer.

The dip of and depth to the Moho, and the average velocity within the crust above the Moho, are well determined from *PmP* reflections. *PmP* and midcrustal reflections constrain an inherent tradeoff between the dip and velocity of the oceanic crust. Decreasing the dip of the Moho requires increasing the velocities of the oceanic crust. *PmP* reflection times limit the range of permissible Moho dips to 8°–11°, in turn limiting the range of permissible velocities within the oceanic crust.

The absence of source points near the east end of the Loma Prieta transect introduces a major uncertainty into the presence or absence of significant midcrustal to lower-crustal differences across the San Andreas fault. The presence and position of a near-vertical velocity boundary across the San Andreas fault is poorly determined from the available onshore-offshore data. Because of the weak velocity gradient in the midcrust, the near-vertical 6-km/s isovelocity contour near the San Andreas fault on the Loma Prieta transect (bottom of fig. 5) can be moved horizontally several kilometers in either direction without noticeable effect on the calculated traveltimes.

Finally, the available onshore-offshore data simply do not allow us to determine the geometry of the Moho east of the San Andreas fault. The inferred 26-km crustal thickness in the vicinity of the San Andreas fault, however, agrees closely with that reported from seismic-refraction profiling (Walter and Mooney, 1982). The crustal thickness west of the San Andreas fault is thought to be reliable and accurate to within 2 to 3 km. The implied presence of oceanic crust east of the fault is undetermined and is shown only to suggest that the wide-angle data are consistent with, but do not require, the presence of this layer. This apparent continuity of oceanic crust is an intriguing aspect of our model that deserves to be tested by additional seismic profiling. Interpretation of explosion data recorded onshore confirms that the top of oceanic crust may be traceable as far landward as the San Andreas fault (Catchings and Kohler, 1996), and suggests that a reflection from the top of oceanic crust may extend eastward beneath the fault.

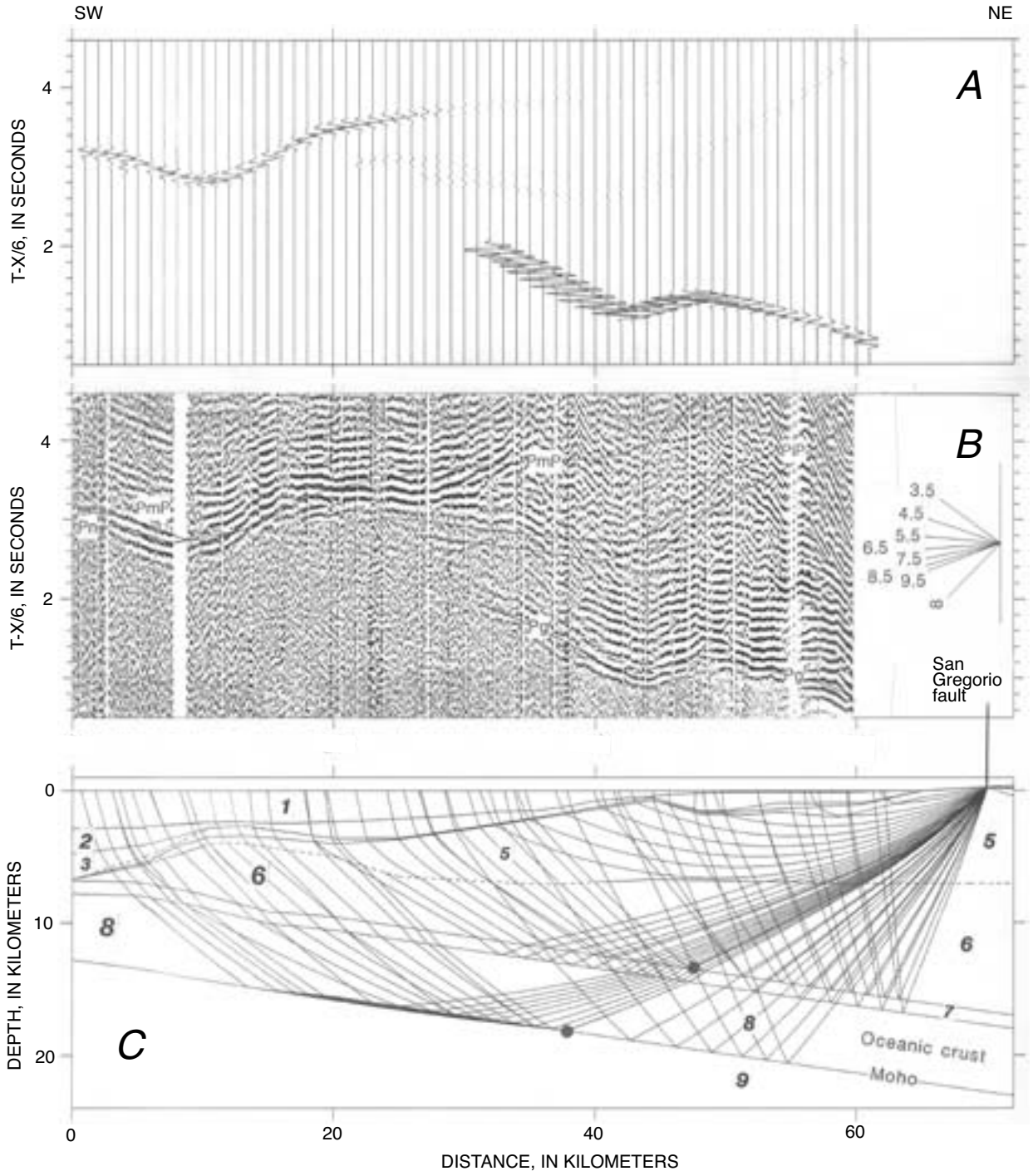

Figure 8.—Synthetic (*A*) and observed (*B*) record sections and ray diagram (*C*) for receiver at station AN1 on the Año Nuevo transect (see fig. 1*B* for locations). Receiver was located at model coordinate 70 km. Same format as in figure 4. *Pg* arrivals are modeled as refractions from layer 5 that are truncated at depth by a low-velocity zone. Synthetic seismograms for these *Pg* arrivals are much too large, suggesting a weaker vertical-velocity gradient in layer 5 than that used to model data. Strong *PiP* reflections are modeled by precritical reflections from tops of layers 7 and 8. Large-amplitude arrivals at greater ranges are modeled by postcritical reflections and refractions from layer 9.

FAINT *PiP* REFLECTIONS

The *PiP* reflection is the most compelling argument in favor of the existence of a 6.6- to 7.1-km/s layer beneath the Continental Shelf and slope. If these reflections are ignored, first arrivals can be fitted to the conspicuous wide-angle *PmP* reflection from a landward-dipping Moho with the same dip as that shown in figure 5 but located about 3 km higher than shown in figure 5. This Moho depth assumes that the 6.0- to 6.4-km/s-velocity midcrust extends downward to the Moho. For many of the records at the farthest ranges, P_3, *Pn*, and even *Pg* arrivals show little time separation, and so we argue that they do not provide the most compelling argument in favor of a 6.6- to 7.1-km/s layer. For stations at and east of the San Andreas fault, the calculated traveltimes indicate a significant time separation between these three arrivals (fig. 6); however, the quality of the data from these stations is generally insufficient to allow unequivocal identification of all three of these branches.

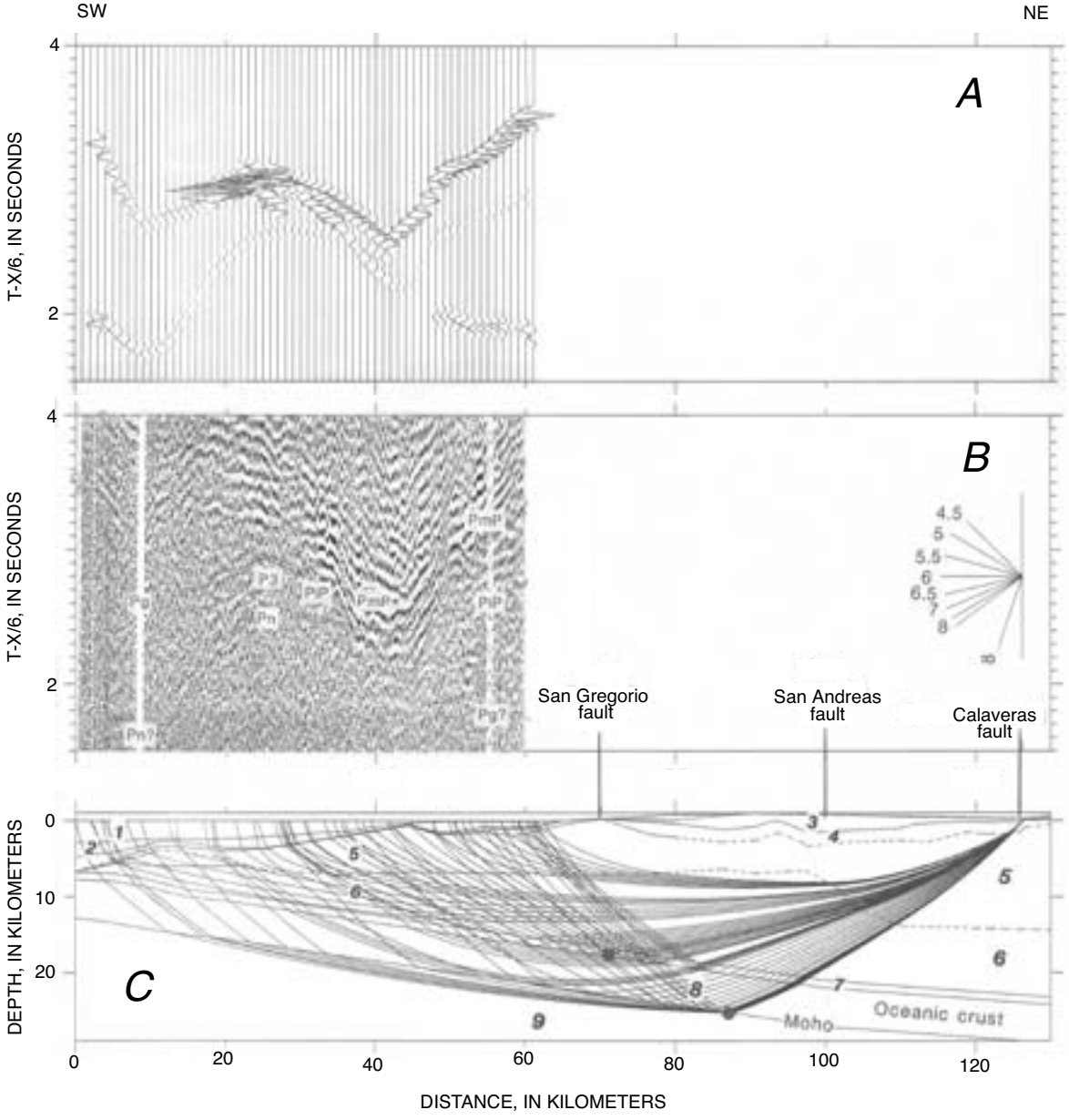

Figure 9.—Synthetic (*A*) and observed (*B*) record sections and ray diagram (*C*) for receiver at station AN4 on the Año Nuevo transect (see fig. 1*B* for locations). Receiver was located at model coordinate 126 km. Same format as in figure 4. *Pg* arrivals are modeled by refractions from layer 6. Weak *PiP* reflections are explained by precritical reflections from tops of layers 7 and 8 used to model oceanic crust. *PmP* arrivals are modeled as reflections from top of layer 9 to west of the San Andreas fault in vicinity of the San Gregorio fault.

The records from stations LP1 to LP5 and from stations AN1 to AN3 (fig. 1*B*) provide the best evidence for the *PiP* reflection. Synthetic seismograms for the models shown in figure 5 suggest that *PiP* and *PmP* reflections have similar amplitudes at identical ranges (figs. 4, 6, 8) and that locally at wide angles the amplitudes of *PiP* reflections exceed those of *PmP* reflections. The predicted amplitudes of *PiP* and *PmP* reflections at precritical incidence are much smaller than those of *Pg* arrivals. Both of these predicted amplitudes agree closely with the observed amplitudes.

The case for the presence and depth of oceanic crust between model coordinates 0 and 20 km is probably best made by seismic-reflection lines 32 and 38 (fig. 3). The depth of oceanic crust near model coordinate 10 km can be moved, on the basis of the wide-angle data themselves, a few kilometers up or down. The vertical seismic-reflection data, however, constrain the depth of oceanic crust to within 1 km.

DISCUSSION

The primary elements of the velocity structures inferred from forward modeling of *P*-wave-arrival traveltimes on onshore-offshore wide-angle data are (1) a landward-thickening wedge of rocks with velocities of 6.0 to 6.5 km/s and a low velocity gradient west of the San Andreas fault, corresponding to layer 6 (figs. 4–9); (2) a landward-dipping layer with velocities of 6.6 to 7.1 km/s extending as far eastward as the San Andreas fault and, possibly, farther (layer 8), also imaged by seismic tomography (Hole and others, 2000); (3) a landward decrease in average crustal velocities east of the San Andreas fault, in agreement with seismic-tomography models (for example, Hole and others, 2000); and (4) a crustal thickness of about 26 to 28 km beneath the San Andreas fault. These major structural elements, as well as the amplitude-versus-range characteristics of the arrivals, have important ramifications for the modeling of strong ground motions generated by earthquakes along the San Andreas fault and along subsidiary faults in the offshore region.

A well-constrained result of our modeling is a major difference in the upper-crustal structure west of the San Gregorio fault observed along the Loma Prieta and Año Nuevo transects. Velocities in layers 5 and 6 (figs. 4–9) west of the San Gregorio fault are significantly higher (max 1 km/s) along the Año Nuevo transect than along the Loma Prieta transect (fig. 5). One possible explanation for this difference in velocity is that at the latitude of Año Nuevo, the shelf and upper slope are underlain by rocks of the Salinian block, whereas at the latitude of Loma Prieta, the shelf and upper slope are underlain by rocks of the San Simeon terrane, which is composed of Franciscan rocks.

Our preferred interpretation of the near-uniform velocities (from 6.0 to 6.5±0.1 km/s) within the structural wedge beneath the continental margin between the San Gregorio and San Andreas faults is that they represent a sliver of Salinian basement. These velocities are reasonable for quartz monzonite of the Salinian block but apparently too high for typical metamorphosed graywacke of the Franciscan Complex (Lin and Wang, 1980). Likewise, bearing in mind that these velocities are minimums for the wedge, they are also too high to be representative of Tertiary rocks of the accretionary wedge (Stewart and Peselnick, 1981). We note, however, that previous workers have placed the west boundary of the Salinian block at the Sur-Nacimiento fault, which on our transect is offset along the San Gregorio-Hosgri fault (Silver and others, 1971; Mullins and Nagel, 1981). The lower (5.9–6.2 km/s) velocities in the block west of the San Gregorio fault on the Loma Prieta transect are more consistent with Franciscan rocks, as proposed by these workers.

Possibly the most surprising result of our experiment is the evidence for a 5-km-thick slab with velocities of 6.8 to 7.1 km/s beneath the Continental Shelf and slope extending as far landward as the San Andreas fault. We interpret this slab (layers 7, 8, figs. 4–9) as oceanic crust, owing to its thickness and velocity structure. Alternatively, it may represent a layer of material magmatically underplated to the base of the crust during subduction of the ridgecrest (Holbrook and others, 1996). We prefer the first interpretation, however, because of the coincidence requiring that the layer's thickness and velocity structure produced by magmatic underplating should resemble that of oceanic crust so strongly.

The presence of a slab of oceanic crust beneath the central California margin appears to conflict with the lithospheric-slab-window hypothesis (Dickinson and Snyder, 1979). That hypothesis, however, neither predicts nor requires a slab window west of the San Andreas fault, because it predicts a slab window only east of the fault. Our evidence, in conjunction with evidence for subducted oceanic crust from deep seismic profiling by PG&E and EDGE off central California (Ewing and Talwani, 1991; Tréhu, 1991), and permissive evidence for oceanic crust from the BASIX line near San Francisco (fig. 1*B*; Holbrook and others, 1996), suggests that the outer continental margin of California is underlain by oceanic crust from Morro Bay to as far north as San Francisco, a distance of more than 250 km. This relation is important because it demonstrates that the observed oceanic crust underneath central California cannot be explained simply as a local feature associated with subduction of the Monterey fragment of the Farallon plate, which is found to the south of Santa Cruz (Ewing and Talwani, 1991). The wide-angle *PmP* reflections observed during our experiment are consistent with a landward dip of the oceanic crust of about 8°–11°.

We cannot, however, determine the identity of the oceanic crust from the seismic data alone. Nonetheless, because the oceanic crust imaged at wide angles appears to be continuous with the Pacific plate imaged by multichannel-seismic-reflection data on the west end of the profile, the oceanic crust beneath the continental margin probably represents crust of the Pacific plate. Page (1991) and Page and Brocher (1993) proposed that at least part of this oceanic crust was thrust beneath North

America during Pliocene-Quaternary plate reorganization and extension in the Basin and Range Province. They calculated that at least 15 to 25 km of convergence between the Pacific plate and North America occurred during this interval.

We suggest that the Salinian block and Franciscan rocks are in thrust contact with the underlying slab of oceanic crust. We postulate that this thrust accommodates overthrusting of the oceanic crust by North America (fig. 10), as suggested on the basis of observed incipient overriding of the sedimentary deposits in the trench by the toe of the continental margin (McCulloch, 1987; Page, 1991; Page and Brocher, 1993). This tectonic wedge is the structural mirror image of the tectonic wedge observed east of the San Andreas fault, composed of Franciscan rocks, above which rocks of the Great Valley sequence have been uplifted (Wentworth and others, 1984; Wentworth and Zoback, 1989). We support the model of Eaton and Rymer (1990) that on either side of the San Andreas fault, tectonic wedges accommodate fault-normal compression in the crust by outward thrusting of large, rigid blocks along low-angle decollement surfaces. Onlap relations of the young sedimentary deposits on the unnamed anticline along seismic-reflection lines 32 and 38 (figs. 1*B*, 3) provide evidence for active thrusting within the unnamed anticline, supporting the inference that fault-normal compression is accommodated by low-angle thrusts. The inferred mirror symmetry of tectonic wedges across the San Andreas fault is consistent with the observation of fold-and-thrust belts on both sides on the fault that have opposite senses of vergence (Namson and Davis, 1988). Indeed, the opposite senses of thrusting on either side of the fault require material flow toward the fault, consistent with the proposed tectonic-wedge model of Eaton and Rymer (1990).

Comparison of the velocity structure derived from forward modeling with the hypocentral and aftershock data (U.S. Geological Survey staff, 1990) suggests that the Loma Prieta rupture initiated near the base of this structural wedge. The hypocenter apparently ruptured the highest velocity rocks near the base of the Salinian block at about 18-km depth (fig. 5). This observation agrees with previous spatial correlations of high-velocity anomalies and earthquake rupture zones (Michael and Eberhart-Phillips, 1991).

The wave-propagation characteristics of the wide-angle data and complex crustal structure revealed by our analysis of these data have important implications for the modeling of strong ground motions produced by earthquakes along the San Andreas and subsidiary faults. The concave-upward geometry of the Moho strongly focuses seismic amplitudes and thus will locally enhance ground motions in ways that can be anticipated by knowing the likely locations of future earthquakes (fig. 11). Upper-mantle *PmP* reflections are conspicuous and generally of greater amplitude than *Pg* arrivals, and so understanding the propagation of *PmP* arrivals is vital for understanding strong ground motions (Somerville and Yoshimura, 1990; Catchings and Kohler, 1996). (*PiP* amplitudes are generally smaller than *PmP* arrivals but locally can be quite strong.) The complex Moho geometry may help explain the localization of strong ground motion observed in northern San Francisco and Oakland during the 1989 Loma Prieta earthquake (Somerville and Yoshimura, 1990) and in subsequent seismic-refraction studies (Catchings and Kohler, 1996).

SUMMARY

We have used onshore recordings of airgun profiling offshore Santa Cruz and Año Nuevo to develop a model for the major structural elements beneath the continental margin west of the San Andreas fault in the Loma Prieta region. Our most important result is that wide-angle seismic-reflection data provide evidence for a slab of oceanic crust extending landward beneath the continental margin as far eastward as the San Andreas fault. These data require a landward-dipping oceanic crust and Moho dipping 8°–11° E. We interpret this oceanic crust as a slab of Pacific plate that was overthrust by North America during recent oceanward thrusting probably related to crustal extension in the Basin and Range Province. The data are consistent with the presence of a block of Salinian rocks, with velocities consistent with either granite or quartz monzonite, above the slab of oceanic crust, between the San Gregorio and San Andreas faults. This block forms part of a structural wedge composed of a sliver of Salinian rocks, the Tertiary accretionary prism, and, possibly, a piece of Franciscan terrane. Our interpretation is consistent with a mirror image across the San Andreas fault with respect to the existence and geometry of tectonic wedges and fold-and-thrust belts. Oceanic crust is also observed beneath the continental margin to the south near Morro Bay, and so a tectonic wedge west of the San Andreas may extend along the fault for hundreds of kilometers. The concave-upward geometry of the Moho in the vicinity of the San Andreas fault should strongly focus those wide-angle reflections from the Moho that travel along the fault from earthquake sources on the San Andreas and subsidiary faults.

ACKNOWLEDGMENTS

This research was supported by the National Earthquake Hazards Reduction Program and the Offshore Geologic Framework Program. Numerous private landowners kindly gave us permission to locate 5-day recorders on their property. Kevin Shea of the East Bay Regional Park District and Chief Lucky of the California Department of Forestry provided access to property under their jurisdiction. John Coakley and others of the USGS in Menlo Park, Calif., deployed the 5-day recorders. Donna Eberhart-Phillips projected the three-dimensional velocity models from earthquake tomography onto our sections for incorporation into our two-dimensional velocity model. Gary Fuis, Jill McCarthy, Ben Page, and Carl Wentworth provided useful reviews of the manuscript. This paper is dedicated to the memory of Ben Page.

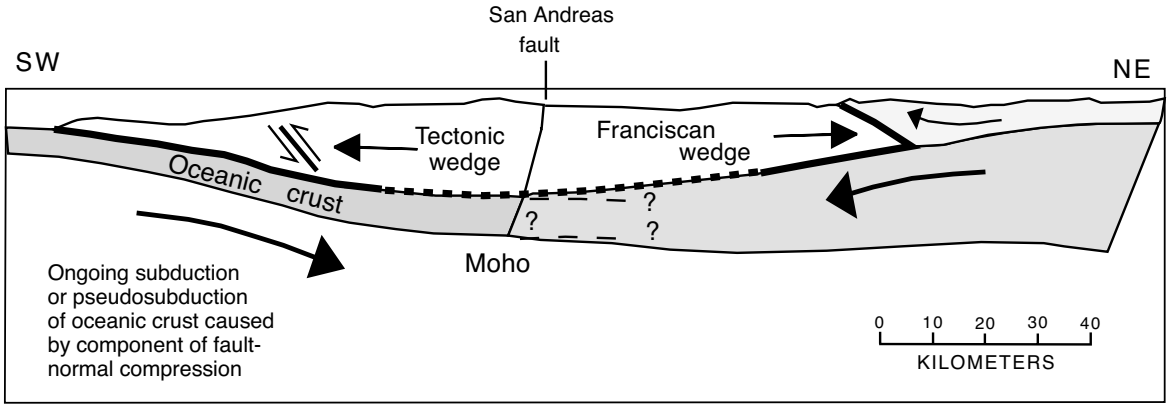

Figure 10.—Tectonic model of velocity structure, showing westward-directed tectonic wedge west of the San Andreas fault, similar to that proposed by Eaton and Rymer (1990). This wedge is inferred to be in thrust contact with underlying oceanic crust, which is undergoing subduction or pseudosubduction (Page, 1991; Page and Brocher, 1993) beneath North America. Also shown is eastward-directed Franciscan wedge east of the San Andreas fault, as described by Wentworth and others (1984) and Wentworth and Zoback (1989). This wedge uplifts rocks of the overlying Great Valley sequence. Eastward extent of oceanic crust, east of the San Andreas fault, is unknown. Heavy solid lines, seismogenic parts of crustal wedges; heavy dashed line, aseismic ductile/brittle transition. Vertical projection of the San Andreas fault downward through oceanic crust is unknown and purely speculative. No vertical exaggeration.

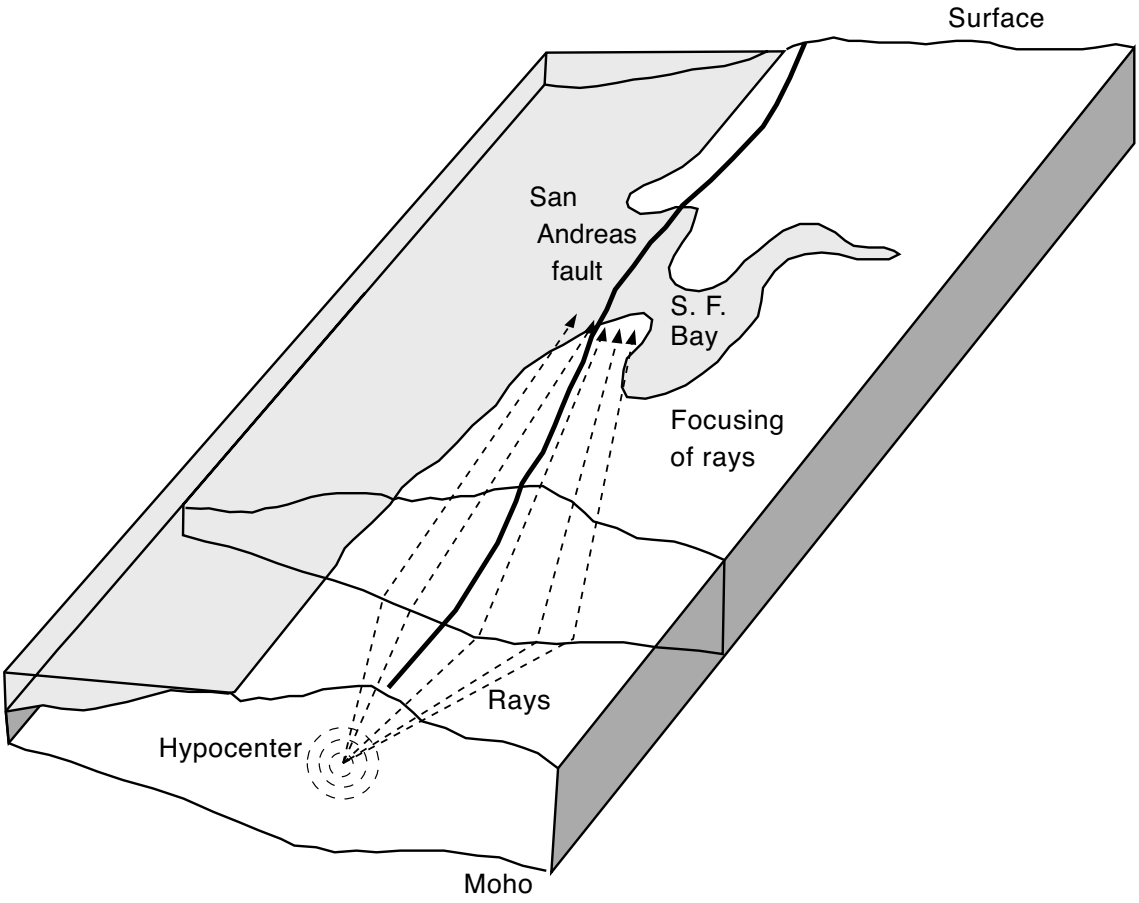

Figure 11.—Schematic perspective view of the Moho in central coastal California, showing earthquake-generated rays propagating along the San Andreas fault. These rays, which initially diverge away from hypocenter of 1989 Loma Prieta earthquake, are reflected by curved Moho and become focused close to the San Andreas fault. Ground motions will thus be amplified near the San Andreas fault because of curved Moho geometry beneath fault.

REFERENCES CITED

Atwater, Tanya, 1989, Plate tectonic history of the northeast Pacific and western North America, chap. 4 *of* Winterer, E.L., Hussong, D.M., and Decker, R.W., eds., The eastern Pacific Ocean and Hawaii, v. N *of* The geology of North America: Boulder, Colo., Geological Society of America, p. 21–72.

Atwater, Tanya, and Menard, H.W., 1970, Magnetic lineations in the northeast Pacific: Earth and Planetary Science Letters, v. 7, no. 5, p. 445–450.

Blake, M.C., Jr., Howell, D.J., and Jayko, A.S., 1984, Tectonostratigraphic terranes of the San Francisco Bay Region, *in* Blake, M.C., Jr., ed., Franciscan geology of northern California (book 43): Los Angeles, Society of Economic Paleontologists and Mineralogists, Pacific Section, p. 5–22.

Blümling, Peter, Mooney, W.D., and Lee, W.H.K., 1985, Crustal structure of the southern Calaveras fault zone, central California, from seismic refraction investigations: Seismological Society of America Bulletin, v. 75, no. 1, p. 193–209.

Blümling, Peter, and Prodehl, Claus, 1983, Crustal structure beneath the eastern part of the Coast Ranges (Diablo Range) of central California from explosion seismic and near earthquake data: Physics of the Earth and Planetary Interiors, v. 31, no. 4, p. 313–326.

Brocher, T.M., Moses, M.J., and Lewis, S.D., 1992, Wide-angle seismic recordings obtained during seismic reflection profiling by the S.P. Lee offshore the Loma Prieta epicenter: U.S. Geological Survey Open-File Report 92–245, 63 p.

Brocher, T.M., Nokleberg, W.J., Christensen, N.I., Lutter, W.J., Geist, E.L., and Fisher, M.A., 1991, Seismic reflection/refraction mapping of faulting and regional dips in the eastern Alaska Range: Journal of Geophysical Research, v. 96, no. B6, p. 10233–10249.

Catchings, R.D., and Kohler, W.M., 1996, Reflected seismic waves and their effect on strong shaking during the 1989 Loma Prieta, California, earthquake: Seismological Society of America Bulletin, v. 86, no. 5, p. 1401–1416.

ervený, Vlastislav, Molotkov, I.A., and Pšen ik, Ivan, 1977, Ray method in seismology: Prague, Karlova University, 214 p.

Clark, D.H., Hall, N.T., Hamilton, D.H., and Heck, R.G., 1991, Structural analysis of late Neogene deformation in the central offshore Santa Maria Basin, California: Journal of Geophysical Research, v. 96, no. B4, p. 6435–6457.

Criley, Ed, and Eaton, J.P., 1978, Five-day recorder seismic system: U.S. Geological Survey Open-File Report 78–266, 85 p.

Curray, J.R., 1966, Geologic structure on the continental margin, from subbottom profiles, northern and central California, *in* Bailey, E.H., ed., Geology of northern California: California Division of Mines and Geology Bulletin 190, p. 337–342.

Dickinson, W.R., 1970, Relations of andesites, granites, and derivative sandstones to arc-trench tectonics: Reviews of Geophysics and Space Physics, v. 8, no. 4, p. 813–860.

Dickinson, W.R., and Snyder, W.S., 1979, Geometry of subducted slabs related to San Andreas transform: Journal of Geology, v. 87, no. 6, p. 609–627.

Eaton, J.P., and Rymer, M.J., 1990, Regional seismotectonic model for the southern Coast Ranges, *in* Rymer, M.J., and Ellsworth, W.L., eds., The Coalinga, California, earthquake of May 2, 1983: U.S. Geological Survey Professional Paper 1487, p. 97–111.

Eberhart-Phillips, D.M., Labson, V.F., Stanley, W.D., Michael, A.J., and Rodriguez, B.D., 1990a, Preliminary velocity and resistivity models of the Loma Prieta earthquake region: Geophysical Research Letters, v. 17, no. 8, p. 1235–1238.

Eberhart-Phillips, D.M., Michael, A.J., Fuis, G.S., and Luzitano, R.D., 1990b, Three-dimensional crustal velocity structure in the region of the Loma Prieta, California, earthquake sequence from inversion of local earthquake and shot arrival times [abs.]: Seismological Research Letters, v. 61, no. 1, p. 48.

Ernst, W.G., 1971, Do mineral parageneses reflect unusually high-pressure conditions of Franciscan metamorphism?: American Journal of Science, v. 270, no. 2, p. 81–108.

Ewing, John, and Talwani, Manik, 1991, Marine deep seismic reflection profiles off central California: Journal of Geophysical Research, v. 96, no. B4, p. 6432–6433.

Fernandez, L.S., and Hey, R.N., 1991, Late Tertiary evolution of the seafloor spreading system off the coast of California between the Mendocino and Murray fracture zones: Journal of Geophysical Research, v. 96, no. B11, p. 17955–17979.

Fuis, G.S., Ambos, E.L., Mooney, W.D., Christensen, N.I., and Geist, E.L., 1991, Crustal structure of accreted terranes in southern Alaska, Chugach Mountains and Copper River Basin, from seismic refraction results: Journal of Geophysical Research, v. 96, no. B3, p. 4187–4227.

Fuis, G.S., and Mooney, W.D., 1990, Lithospheric structure and tectonics from seismic-refraction and other data, chap. 8 *of* Wallace, R.E., ed., The San Andreas fault system, California: U.S. Geological Survey Professional Paper 1515, p. 207–236.

Hill, D.P., Kissling, Edy, Luetgert, J.H., and Kradolfer, Urs, 1985, Constraints on the upper crustal structure of the Long Valley-Mono Craters volcanic complex, eastern California, from seismic refraction measurements: Journal of Geophysical Research, v. 90, no. B13, p. 11135–11150.

Holbrook, W.S., Brocher, T.M., ten Brink, U.S., and Hole, J.A., 1996, Crustal structure of a transform plate boundary; San Francisco Bay and the central California continental margin: Journal of Geophysical Research, v. 101, no. B10, p. 22311–22334.

Hole, J.A., Brocher, T.M., Klemperer, S.L., Parsons, Tom, Benz, H.M., and Furlong, K.P., 2000, Three-dimensional seismic velocity structure of the San Francisco Bay area: Journal of Geophysical Research, v. 105, no. B6, p. 13859–13874.

Jennings, C.W., Strand, R.G., and Rogers, T.H., compilers, 1977, Geologic map of California: Sacramento, California Division of Mines and Geology, scale 1:750,000.

Lewis, S.D., 1990, Deformation style of shelf sedimentary basins seaward of the San Gregorio fault, central California [abs.]: Eos (American Geophysical Union Transactions), v. 71, no. 43, p. 1631.

Lin, Wunan, and Wang, C.-Y., 1980, *P*-wave velocity in rocks at high pressure and temperature and the constitution of the central California crust: Royal Astronomical Society Geophysical Journal, v. 61, no. 2, p. 379–400.

Lonsdale, P.F., 1991, Structural patterns of the Pacific floor offshore of Peninsular California, *in* Dauphin, J.P., and Simoneit, B.R.T., eds., Gulf and Peninsula Provinces of the Californias: American Association of Petroleum Geologists Memoir 47, p. 87–125.

Luetgert, J.H., 1988, Users manual for RAY83/R83PLT; interactive

two-dimensional raytracing/synthetic seismogram package: U.S. Geological Survey Open-File Report 88–262, 52 p.

McCulloch, D.S., 1987, Regional geology and hydrocarbon potential of offshore central California, *in* Scholl, D.W., Grantz, Art, and Vedder, J.G., eds., Geology and resource potential of the continental margin of western North America and adjacent ocean basins—Beaufort Sea to Baja California (Earth Science Series, v. 6): Houston, Circum-Pacific Council for Energy and Mineral Resources, p. 353–401.

McMechan, G.A., and Mooney, W.D., 1980, Asymptotic ray theory and synthetic seismograms for laterally varying structures; theory and application to the Imperial Valley, California: Seismological Society of America Bulletin, v. 70, no. 6, p. 2021–2035.

Michael, A.J., 1988, Effects of three-dimensional velocity structure on the seismicity of the 1984 Morgan Hill, California, aftershock sequence: Seismological Society of America Bulletin, v. 78, no. 3, p. 1199–1221.

Michael, A.J., and Eberhart-Phillips, D.M., 1991, Relations among fault behavior, subsurface geology, and three-dimensional velocity models: Science, v. 253, no. 5020, p. 651–654.

Mullins, H.T., and Nagel, D.K., 1981, Franciscan-type rocks off Monterey Bay, California; implications for western boundary of Salinian Block: Geo-Marine Letters, v. 1, no. 2, p. 135–139.

Namson, J.S., and Davis, T.L., 1988, Seismically active fold and thrust belt in the San Joaquin valley, central California: Geological Society of America Bulletin, v. 100, no. 2, p. 257–273.

Oppenheimer, D.H., and Eaton, J.P., 1984, Moho orientation beneath central California from regional earthquake traveltimes: Journal of Geophysical Research, v. 89, no. B12, p. 10267–10282.

Page, B.M., 1991, Hypothetical origin of mid-crustal sub-horizontal boundaries in west-central California [abs.]: Geological Society of America Abstracts with Programs, v. 23, no. 2, p. 86.

Page, B.M., and Brocher, T. M., 1993, Thrusting of the central California margin over the edge of the Pacific plate during the transform regime: Geology, v. 21, no. 7, p. 635–638.

Ross, D.C., 1978, The Salinian block; a Mesozoic granitic orphan in the California Coast Ranges, *in* Howell, D.G., and McDougall, K.A., eds., Mesozoic paleogeography of the western United States (Pacific Coast Paleogeography Symposium 2): Los Angeles, Society of Economic Paleontologists and Mineralogists, Pacific Section, p. 509–522.

Saleeby, J.B., 1986, C–2; central California offshore to Colorado Plateau: Geological Society of America Centennial Continent/Ocean Transect 10, 63 p., scale 1:500,000, 2 sheets.

Shor, G.G., Jr., Menard, H.W., and Raitt, R.W., 1971, Structure of the Pacific basin, chap. 1 *of* Regional Observations, pt. 2 *of* New concepts of sea floor evolution, v. 4 *of* Maxwell, A.E., ed., The sea; ideas and observations on progress in the study of the seas: New York, John Wiley & Sons, p. 3–27.

Silver, E.A., Curray, J.R., and Cooper, A.K., 1971, Tectonic development of the continental margin off central California, *in* Lipps, J.H., and Moores, E.M., eds., Geologic guide to the Northern Coast Ranges, Point Reyes Region, California: Geological Society of Sacramento Annual Field Trip Guidebook, p. 1–10.

Somerville, P.G., and Yoshimura, Joanne, 1990, The influence of critical Moho reflections on strong ground motions recorded in San Francisco and Oakland during the 1989 Loma Prieta earthquake: Geophysical Research Letters, v. 17, no. 8, p. 1203–1206.

Stewart, R.M., and Peselnick, Louis, 1977, Velocity of compressional waves in dry Franciscan rocks to 8 kbar and 300°C: Journal of Geophysical Research, v. 82, no. 14, p. 2027–2039.

Tréhu, A.M., 1991, Tracing the subducted oceanic crust beneath the central California continental margin; results from ocean bottom seismometers deployed during the 1986 Pacific Gas and Electric EDGE experiment: Journal of Geophysical Research, v. 96, no. B4, p. 6493–6506.

Uchupi, Elazar, and Emery, K.O., 1963, The continental slope between San Francisco, California and Cedros Island, Mexico: Deep-Sea Research, v. 10, no. 4, p. 397–447.

U.S. Geological Survey and California Division of Mines and Geology, compilers, 1966, Geologic map of California: U.S. Geological Survey Miscellaneous Geologic Investigations Map I–512, scale 1:2,500,000.

U.S. Geological Survey staff, 1990, The Loma Prieta, California, earthquake; an anticipated event: Science, v. 247, no. 4940, p. 286–293.

Walter, A.W., and Mooney, W.D., 1982, Crustal structure of the Diablo and Gabilan Ranges, central California; a reinterpretation of existing data: Seismological Society of America Bulletin, v. 72, no. 5, p. 1567–1590.

Wentworth, C.M., Blake, M.C., Jr., Jones, D.L., Walter, A.W., and Zoback, M.D., 1984, Tectonic wedging associated with emplacement of the Franciscan assemblage, California Coast Ranges, *in* Blake, M.C., Jr., ed., Franciscan geology of northern California (book 43): Los Angeles, Society of Economic Paleontologists and Mineralogists, Pacific Section, p. 163–173.

Wentworth, C.M., and Zoback, M.D., 1989, The style of Late Cenozoic deformation at the eastern front of the California Coast Ranges: Tectonics, v. 8, no. 2, p. 237–246.

———1990, Structure of the Coalinga region and thrust origin of the earthquake, *in* Rymer, M.J., and Ellsworth, W.L., eds., The Coalinga, California, earthquake of May 2, 1983: U.S. Geological Survey Professional Paper 1487, p. 41–68.

Zoback, M.D, Zoback, M.L., Mount, V.S., Suppe, John, Eaton, J.P., Healy, J.H., Oppenheimer, D.H., Reasenberg, P.A., Jones, L.M., Raleigh, C.B., Wong, I.G., Scotti, Oona, and Wentworth, C.M., 1987, New evidence on the state of stress of the San Andreas fault system: Science, v. 238, no. 4830, p. 1105–1111.

EARTHQUAKE OCCURRENCE

THREE-DIMENSIONAL TOMOGRAPHIC ANALYSIS OF THE LOMA PRIETA REGION

By Eylon Shalev, Duke University;
and
Jonathan M. Lees, University of North Carolina, Chapel Hill

CONTENTS

ABSTRACT

A high-resolution tomographic study, using cubic B-spline parametrization, provided a three-dimensional *P*-wave-velocity map of the Loma Prieta region. A total of 11,977 high-quality raypaths from 844 aftershocks of the 1989 Loma Prieta earthquake were used in the inversion. The velocity model exhibits a low-velocity feature between the San Andreas and Zayante-Vergeles faults in the uppermost 10 km of the crust. This low-velocity feature is interpreted as a sedimentary unit exposed to the northwest and separated from the Salinian block by the Zayante-Vergeles fault. Below 10-km depth, no consistent change in velocity is observed between the Salinian and Franciscan blocks. A high correlation exists between aftershock activity and localized high-velocity anomalies southeast of the main shock. Whereas these anomalies may represent brittle rocks associated with a fault-zone asperity that failed after the main shock, they also suggest a body of serpentinite. The serpentinite exhibits high seismic velocities and is potentially less competent than the surrounding country rock, thus providing a sector along the fault more likely to be associated with many smaller earthquakes or creep behavior.

INTRODUCTION

The 1989 Loma Prieta earthquake has provided the seismological community with a unique opportunity to investigate the relation between seismic-velocity distributions, earthquake seismicity, and geologic structures along the San Andreas fault. The velocity distributions provide insight into the structural details of the subsurface, in addition to serving as the basis for future analyses of wave propagation in regions of major strike-slip faults. An integrated analysis, using seismic structures, geologic interpretation, and statistical analysis of seismicity, may ultimately provide a model for seismic-hazard estimation. In this paper, we present a detailed, three-dimensional tomographic analysis of *P*-wave-velocity variations, suggest several possible interpretations, and discuss the implications of these interpretations with regard to seismic hazard.

GEOLOGIC SETTING

The geology of the Loma Prieta region has been summarized in recent literature (Aydin and Page, 1984; Saleeby, 1986; Fuis and Mooney, 1990), and so we provide only a brief overview here. Central California crustal structure consists of parallel northwest-striking fault-bounded blocks (fig. 1). The San Andreas fault near Loma Prieta separates the Salinian block from an internally complex block that is composed mostly of rocks of the Franciscan assemblage, a late Mesozoic complex (Fuis and Mooney, 1990). The Salinian block is an orphaned granitic-basement terrane that was transported at least 500 km northwestward by the San Andreas fault system (Ross, 1978). The part of the Salinian block between the San Andreas and Zayante-Vergeles faults is considered different from the main part of the Salinian block. Ross postulated that this part is a gabbroic subdivision of the Salinian block. Clark and Rietman (1973) suggested a structure of sandstone and mudstone reaching 4 to 5 km deep. Between the San Andreas and Calaveras faults, Franciscan rocks of oceanic origin are overlain by a thin sliver of Coast Range ophiolite and Great Valley sequence (McLaughlin and others, 1988).

Seismic-refraction profiles of the Loma Prieta region were summarized by Fuis and Mooney (1990). In the Salinian block, the crust can be divided into layers, with a midcrustal interface at 10-km depth (Walter and Mooney, 1982). An alternative interpretation, also offered by Walter and Mooney, is a subdivision of the crust below 10-km depth into two sublayers. Ross and McCulloch (1979) postulated that the uppermost 10 km of crust of the Salinian block is detached from the basement

and that the crust below 10-km depth might correspond to the Franciscan complex. Fuis and Mooney noted, on the basis of the seismic velocity below 10-km depth, that the midcrustal and lower-crustal rocks are most likely not Franciscan. A seismic-refraction profile across the San Andreas, Sargent, and Calaveras faults 15 km southeast of Loma Prieta (Mooney and Colburn, 1985) shows heterogeneous upper-crustal velocities in the uppermost 3 km of the crust. No velocity change across the San Andreas fault was noted in that study. A strong reflector at 8- to 9-km depth is visible, but the seismic velocity below this depth was unresolvable.

After the 1989 Loma Prieta earthquake, Dietz and Ellsworth (1990) used the main shock and 89 aftershocks, evenly distributed with a maximum depth of 20 km, to calculate a joint hypocenter-velocity inversion for the two sides of the San Andreas fault. Their two velocity models differ in the uppermost 9 km of the crust, where the velocities southwest of the fault are lower. Below 9-km depth, the two models are nearly identical. Velocities below 18-km depth were poorly resolved because of inadequate sampling.

Previous three-dimensional tomographic studies of the study area (fig. 1) were conducted by using aftershocks of the 1989

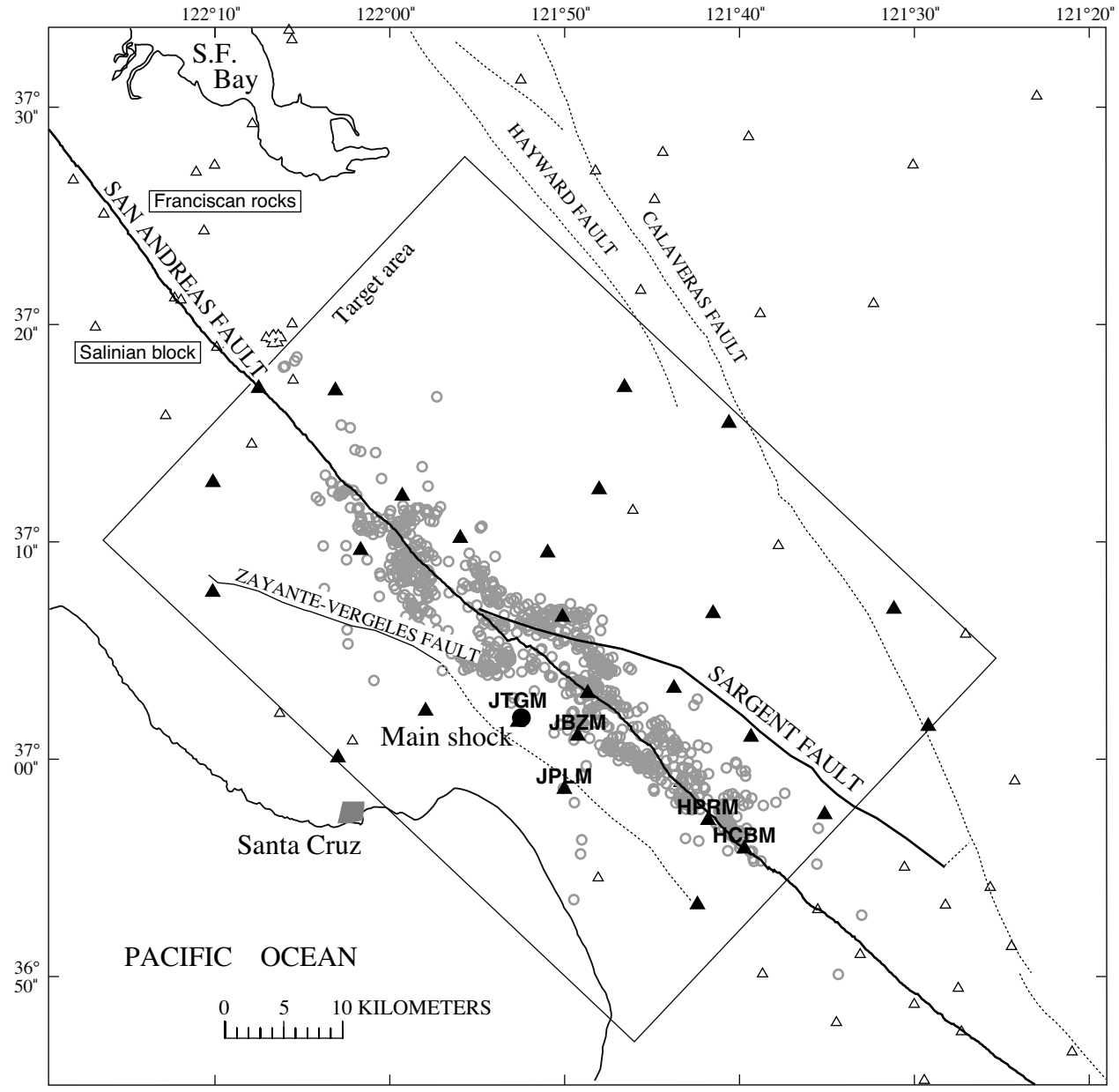

Figure 1.—Loma Prieta region, Calif., showing locations of major faults and study area (rectangle). Circles, epicenters; triangles, recording stations; solid triangles, stations used in inversion. Five named stations had unusually large station corrections (asterisks, table 1).

Loma Prieta earthquake (Eberhart-Phillips and others, 1990; Lees, 1990; Michael and Eberhart-Phillips, 1991; Lees and Shalev, 1992; see Eberhart-Phillips and Michael, this chapter). Those studies showed a marked variation in *P*-wave velocity across the San Andreas fault in the vicinity of the main shock from the surface to 10-km depth. The northeast side of the fault has seismic velocities nearly 1.0 km/s higher than the southwest side, with the highest contrast extending to 4- to 6-km depth. This pattern changes below 10-km depth, where the two sides of the fault appear to be similar. The velocity contrast across the fault is noticeable mainly in the vicinity of the main shock and is not observed elsewhere along the fault.

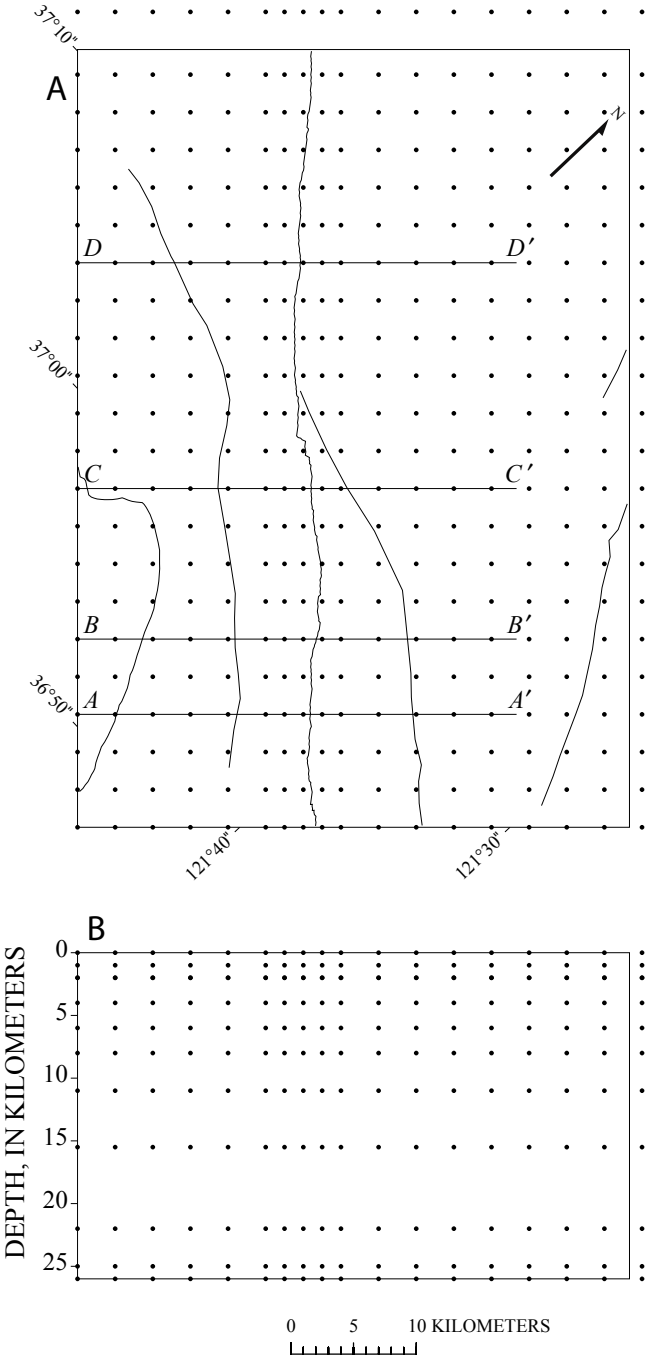

Figure 2.—Distribution of nodes (dots) in study area (fig.1): map view (*A*) and across-strike cross section (*B*). Lines *A–A′* through *D–D′* are traces of cross sections shown in figure 10.

DATA SELECTION

The data used in this study were selected from the U.S. Geological Survey (USGS) catalog of 2,775 events recorded from October through December 1989. All traveltime picks and observation weights were made by USGS scientists. We chose only those events that were located inside our target volume which had at least 10 readings from among the 27 recording stations included in the study area (fig. 1). Events with root-mean-square (rms) residuals of greater than 0.15, horizontal errors of greater than 1.0 km, and vertical errors of greater than 2.0 km were excluded, as were all observations marked by the original observer as poor-quality picks. The remaining 844 events produced 11,977 high-quality raypaths suitable for tomographic inversion.

METHOD

MODEL PARAMETRIZATION

The slowness structure of the target volume was parametrized by using cubic B-spline functions (Firbas, 1987; Michelini and McEvilly, 1991; Lees and Shalev, 1992; Shalev, 1993a), which have an implicit smoothness and no artificial discontinuities of velocity (as in block models) or velocity gradients (as in linear-interpolation models). The B-spline model is defined by a discrete number of spatially distributed points (nodes), and the slowness field at the points provides the coefficients for B-spline interpolation. A total of 64 points are needed to calculate the slowness at any given position inside the target volume. One advantage of using cubic B-splines is the ability to represent a complex structure with only a few nodes (Firbas, 1987); one disadvantage is that the locality of B-spline functions may entail underparametrization of the model in places where the raypaths are highly concentrated. To address this problem, we used a large concentration of nodes in the vicinity of the San Andreas fault, with a smaller node spacing than in the rest of the target volume. Furthermore, closer spacing in the vicinity of the fault allows a cubic B-spline structure to display rapid gradient changes (Shalev, 1993b). We used 18×22×12 nodes in *x*-coordinates (perpendicular to the fault), *y*-coordinates (along the fault), and depth coordinates, respectively, for a total of 4,752 nodes, to model the 45×65×25-km target volume (fig. 2). The coordinate system was rotated so that the San Andreas fault trends primarily in the *y*-coordinate direction (fig. 1). Regular node spacing in the *x* (perpendicular)- and

y (strike)-coordinates was 3 km, with 1.5-km spacing on the *x*-coordinate near the fault.

Rays in the three-dimensional model were traced by using a modified version of the ray-bending algorithm of Um and Thurber (1987). Using their algorithm, we found it important that the same model parametrization be used for both ray tracing and tomographic inversion. If we use a velocity structure for ray tracing and a slowness structure for tomographic inversion, an additional nonlinearity is introduced (Shalev, 1993a). Therefore, we modified the original ray-bending algorithm to work with slowness.

NONLINEAR TOMOGRAPHIC INVERSION

P-wave-arrival data were used in a joint hypocenter, station-correction, and three-dimensional slowness inversion. We added station-correction parameters to the linearized equation of Thurber (1983) relating the traveltime residual of the *k*th ray, r_k, to the model parameters:

$$r_k = \Delta t_s + \Delta t_e + \frac{\partial t_k}{\partial x_e}\Delta x_e + \frac{\partial t_k}{\partial y_e}\Delta y_e + \frac{\partial t_k}{\partial z_e}\Delta z_e + \sum_{n=1}^{N}\frac{\partial t_k}{\partial a_n}\Delta \mathbf{a}_n, \quad (1)$$

where Δt_s is the perturbation to the station correction (positive station correction=low velocity near the station or at higher elevation); Δt_e, Δx_e, Δy_e, and Δz_e are the perturbations to the hypocenter parameter; $\partial t/\partial x_e$, $\partial t/\partial y_e$, and $\partial t/\partial z_e$ are the partial derivatives of the traveltime with respect to hypocenter coordinates; N is the number of slowness parameters; and $\Delta \mathbf{a}_n$ is the perturbation to the slowness parameter n. The partial derivative of the traveltime with respect to the slowness parameter $\partial t_k/\partial \mathbf{a}_n$ (Shalev, 1993a) is defined as

$$\frac{\partial t_k}{\partial \mathbf{a}_n} = \int_{\text{ray}_k} b_n(\mathbf{a})\,dl, \quad (2)$$

where the integration is along the path of *k*th ray and the three-dimensional cubic B-spline function $b_n(\mathbf{a})$ is defined as

$$b_n(\mathbf{a}) = \sum_{i=1}^{N_1}\sum_{j=1}^{N_2}\sum_{l=1}^{N_3} B_i(x)B_j(y)B_l(z), \quad (3)$$

where $\mathbf{a}$ is the position vector; N_1, N_2, and N_3 are the number of nodes (functions) in *x*-, *y*-, and *z*-coordinates; and the *B* terms are the one-dimensional B-spline functions defined by de Boor (1978).

Station-correction parameters were added to the model space to automate the iterative, nonlinear inversion. Without a station-correction adjustment after each iteration, some of the data that could have been attributed to station-correction perturbations are mapped to structural perturbations directly beneath the stations. Because cubic B-spline structures are less local than block or linear-interpolation structures, those structural perturbations could propagate downward through the model.

To minimize the adverse affects of mapping noise into the models, we employed a damped-least-square approach (Crosson, 1976; Van Der Sluis and Van Der Vorst, 1987). Equation 1 includes three different types of model parameter: station correction, hypocenter location, and slowness. We found no theoretical justification for using the same damping parameter for each of these three types of model parameter. Following Spencer and Gubbins (1980), we chose three different damping parameters for each of the three types of model parameter. Each parameter class can be made more significant by lowering its damping, and less significant by increasing its damping. For example, setting the damping of the hypocenter location and the station correction to infinity leads to a damped-least-square slowness inversion. The tradeoff of this approach is the difficulty in determining the correct damping for each parameter class.

In addition to damping, we further constrained the slowness model by requiring the three-dimensional Laplacian of the model (that is, the slope of local gradients) to be small (Lees and Crosson, 1989; VanDecar, 1991), effectively smoothing the model. Without Laplacian smoothing, the slowness model can develop a random-noise appearance, alternating small areas of low and high velocity (Herman, 1980). This phenomenon is important primarily when using a large number of model parameters where individual parameters may be less constrained by the data. Because we are smoothing in three dimensions, the Laplacian constraint introduces three smoothing parameters. Although it is reasonable to assume that the two horizontal smoothing weights may be the same, choosing the same weight for the depth dimension appears to oversmooth the model vertically. The Laplacian is a local constraint, and so we expect that, at least on local scales, there may be more vertical heterogeneity than horizontal. We therefore differentiated between horizontal and vertical smoothing by using different parameters for each smoothing. This approach leads to a block-matrix equation with five different damping and smoothing parameters: station-correction damping, hypocenter damping, slowness damping, horizontal smoothing, and vertical smoothing.

Not all the observations have the same accuracy, and so some downweighting of data with high uncertainties is desirable. Following the standard approach (Crosson, 1976; Menke, 1984), we multiplied each row of the matrix equation by the inverse of the estimated uncertainty of observation. The final weighted block-matrix equation is

$$\begin{vmatrix} \mathbf{WA} & \mathbf{WB} & \mathbf{WC} \\ \mathbf{I}\lambda_1 & 0 & 0 \\ 0 & \mathbf{I}\lambda_2 & 0 \\ 0 & 0 & \mathbf{I}\lambda_3 \\ 0 & 0 & \mathbf{L}(\lambda_4,\lambda_5) \end{vmatrix} \begin{vmatrix} x_1 \\ x_2 \\ x_3 \end{vmatrix} = \begin{vmatrix} \mathbf{Wr} \\ 0 \\ 0 \\ 0 \\ 0 \end{vmatrix}, \quad (4)$$

where $\mathbf{W}$ is the weighting matrix; $\mathbf{A}$, $\mathbf{B}$, and $\mathbf{C}$ are the partial-derivative matrices of station corrections, hypocenter parameters, and slowness parameters; $\mathbf{I}$ is the identity matrix; x_1, x_2, and x_3 are the perturbations to the station corrections,

hypocenter parameters, and slowness parameters, respectively; λ_1, λ_2, and λ_3 are damping parameters; λ_4 and λ_5 are the horizontal and vertical smoothing parameters, respectively; and **r** the traveltime-residual vector. To illustrate the Laplacian operator **L**, consider one row of this operator associated with node $c_{i,j,k}$ in Cartesian coordinates:

$$\lambda_4\left(c_{i-1,j,k}+c_{i+1,j,k}\right)+\lambda_4\left(c_{i,j-1,k}+c_{i,j+1,k}\right) +\lambda_5\left(c_{i,j,k-1}+c_{i,j,k+1}\right)-\left(4\lambda_4+2\lambda_5\right)c_{i,j,k}=0 \quad (5)$$

Objectively choosing five independent damping and smoothing parameters for a large inversion is a complex problem. To avoid a totally subjective choice (which may be severely biased), a penalty function is sought that represents the merit of choosing a particular combination of these five parameters. A simple χ^2 test will not work because the minimum χ^2 score corresponds to no damping. Instead, we chose a crossvalidation score (Golub and others, 1979; Inoue and others, 1990) as a penalty function. The crossvalidation function can be used to choose the best model among competing models (Davis, 1987), and can indicate how well the computed model may predict traveltimes in the model area. The data are randomly divided into two subsets, say, S1 and S2. Subset S1 is excluded from the inversion, and subset S2 is used to conduct a full nonlinear inversion for a given set of damping parameters λ. After the inversion, the crossvalidation score is computed from subset S1:

$$f(\lambda)=\left\{\frac{1}{N}\sum_{i=1}^{N}\left[d_i^{o}-d_i^{e}(\lambda)\right]^2\right\}^{\frac{1}{2}}, \quad (6)$$

where $f(\lambda)$ is the crossvalidation score, N is the number of data in subset S1, d_i^{o} is the observed traveltime, and d_i^{e} is the estimated traveltime in the model associated with λ.

The crossvalidation score displayed a monotonic increase with respect to the horizontal smoothing parameter (λ_4) and therefore failed to provide an estimate for this parameter. For this reason, we chose the horizontal smoothing parameter (λ_4) to be the smallest value that appears to eliminate the random model fluctuations discussed above. The other four damping parameters that minimized $f(\lambda)$ were found by conducting a multiparameter search with a genetic algorithm (Goldberg, 1989; Sen and Stoffa, 1991; Stoffa and Sen, 1991; Shalev, 1993a), which is an efficient method of optimization that searches a multiparameter space of unknown shape, seeking a minimum (or maximum), using a small number of model evaluations relative to such arbitrary searches as Monte Carlo techniques. We used binary strings of 25 bits to represent models with four parameters. With a population size of 30 and 25 generations, an average genetic-algorithm run was completed in 10 days on a Sun SPARC–2 computer. The damping and smoothing that parameters that minimized the crossvalidation score for this data set were λ_1=46, λ_2=70, λ_3=6, λ_4=30, and λ_5=11. The numerical values of the damping parameters depend on the scaling of the matrices in equation 4.

The large number of raypaths, model parameters, and damping parameters yielded a very large system of simultaneous equations (28,820×10,123 in our case), which were solved with the LSQR algorithm (Paige and Saunders, 1982; Nolet, 1987). After solving these equations, we retraced rays from the relocated events in the new, three-dimensional structure, computed a new set of equations, and iterated. The iterations were carried out until the time-residual-variance reduction of the last step was less than 2 percent (typically, four iterations). Peterson and Davey (1991) suggested that crossvalidation methods are superior to change of variance as an indicator for convergence of a nonlinear inversion. Our method incorporates the two methods by finding, through a crossvalidation technique, the best set of dumping parameters that fits the data when the stopping criteria is the change in variance reduction. The total variance reduction from the best one-dimensional starting models was 49 percent.

RESOLUTION AND VARIANCE

Providing a measure of the reliability of inversion models entails the formation and analysis of resolution and covariance matrices (Aki and Richards, 1980). In this study, however, the large size of the matrix equation makes an explicit calculation of resolution and covariance prohibitive. Furthermore, since the nonlinear inversion is iterative, the standard matrix approach to resolution and error estimates is inappropriate. For this reason, we must estimate the resolution and variance by other, approximate means. One such approach is to examine the impulse response (point-spread function) of the matrix system for each individual slowness parameter as an estimate of the resolution for those parameters (Humphreys and Clayton, 1988). Because this procedure would require thousands of inversions, we compromised by considering a response to a checkerboard test pattern (Spakman and Nolet, 1988; Inoue and others, 1990) augmented by impulse responses for two individual slowness parameters at locations of interest in the model (fig. 3). A checkerboard test pattern with a 12-km horizontal wavelength was tested with the same source-receiver geometry and damping and parameters used in the real data inversion. We observed that in the vicinity of the San Andreas fault, where the ray coverage is high, the test pattern is reproduced with little distortion. Using this synthetic test, we found that the average event relocation was approximately 0.001 km, with an origin-time perturbation of 0.001 s and an average station correction of 0.004 s. These errors are smaller by a factor of 10 than the hypocenter relocations and station-delay corrections calculated in the real data inversion. These small values indicate that very little of the slowness-perturbation signal is mapped into the parameters associated with hypocenter locations and station delays. The small size of these corrections is due primarily to the heavy damping

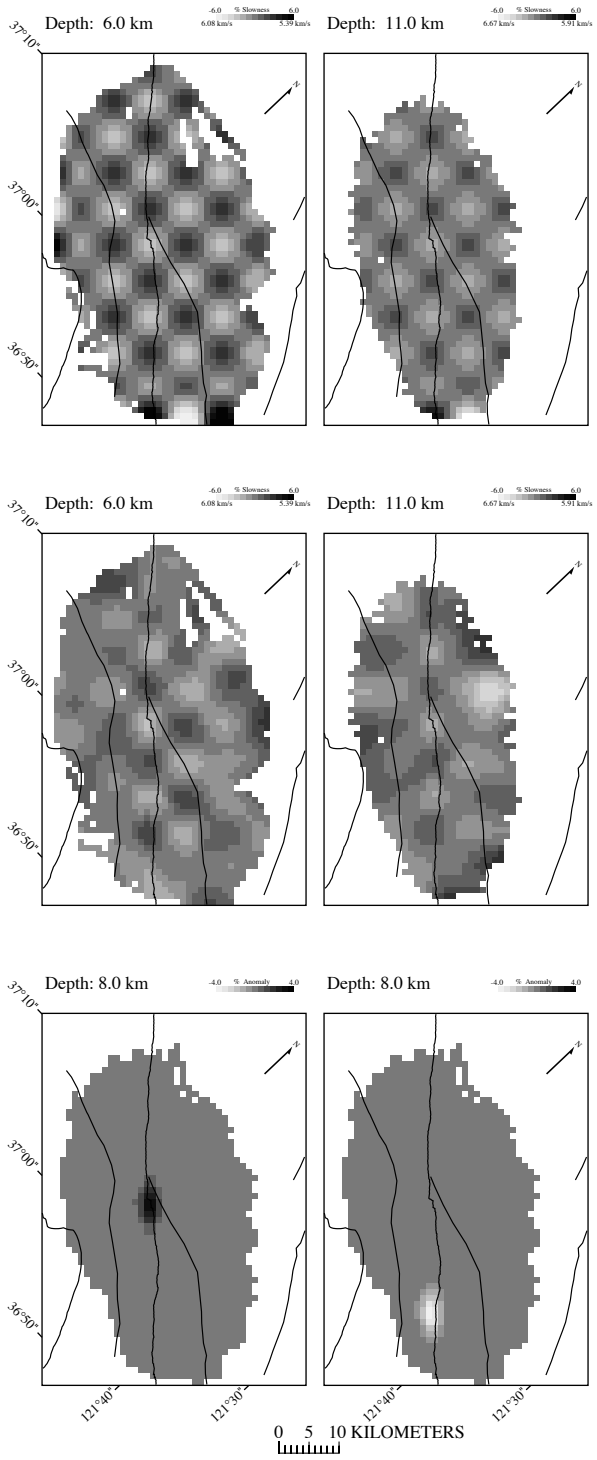

Figure 3.—Resolution-test results. Model is displayed as percentage of perturbation from reference slowness, where darker regions represent lower velocity and lighter regions represent higher velocity. Top row shows synthetic checkerboard model at 6- and 11-km depth. Center row shows results of nonlinear inversion for the same depths; scale for checkerboard perturbation is ±6 percent. Bottom row shows two impulse responses at 8-km depth; scale for impulse-response perturbation is ±4 percent.

imposed on the hypocenter and station-correction parameters, providing an estimate of the coupling noise between the slowness parameters and the other model parameters. We conclude that only a small part of the signal in the hypocenter locations comes from coupling to the slowness parameters and that the rest is due to the signal required by the data.

Estimation of the model variance is accomplished by using a statistical resampling technique called the jackknife (Efron, 1982). This technique has been used previously to estimate the slowness-parameter variance in linear inversions (Lees and Crosson, 1989). Extending the jackknife to nonlinear analysis is straightforward. The complete nonlinear inversion analysis, including all the intermediate linear approximations, is treated as a single inversion, and the variances of all the model parameters are computed as described by Lees and Crosson (1989). We partitioned the data into 30 random, nonoverlapping subsets and performed each "mini- inversion" with the same constraining parameters as the main inversion. This approach produced variance estimates for the slowness parameters (fig. 4), as well as for event relocations and station corrections. The jackknife approach is advantageous in that it makes no assumptions regarding the statistical distributions of errors in the data or model parameters. Furthermore, consistent estimates of variance are provided for all model variables, regardless of the number of nonlinear iterations.

INITIAL MODEL

Although the San Andreas fault represents a major tectonic boundary separating two distinct blocks, we used a one-dimensional, vertically varying velocity model as a reference starting model because slowness contrast across the fault is not always evident. Some studies suggest a significant seismic-velocity variation across the fault (Dietz and Ellsworth, 1990), whereas others indicate little or no variation (Mooney and Colburn, 1985; Fuis and Mooney, 1990). Three-dimensional tomographic studies (Eberhart-Phillips and others, 1990; Lees, 1990; Michael and Eberhart-Phillips, 1991; Lees and Shalev, 1992) suggested a marked velocity contrast across the fault in some areas, but this contrast was inconsistent along the full length of the fault. For this reason, we selected a one-dimensional, vertically varying model, assuring that all horizontal variations of slowness are warranted by the earthquake data used in our study. The large number of raypaths in the vicinity of the San Andreas fault assures that the area of the fault is well sampled and has a high resolution. Lees and Shalev (1992) showed that when a large number of high-quality data from the Loma Prieta aftershock sequence are used, nonlinear tomographic-inversion results appear to be robust with respect to the initial reference model. The initial model has, however, a greater influence on those parts of the model that are more sparsely sampled. In our study, the initial model was one dimensional, and the associated station corrections that minimized the residuals of the full data set used

the USGS station correction (L.D. Dietz, written communs., 1992). This one-dimensional model (fig. 5) lies approximately between the two models previously constructed by Dietz and Ellsworth (1990).

RESULTS

Final perturbations to the initial station corrections are plotted in figure 6 and listed in table 1. We note a regional gradient associated with these corrections that varies linearly across the fault, from positive on the Franciscan side to negative in the Salinian block (fig. 6*A*). This pattern, which remained in the final station corrections, represents a broad regional variation across the San Andreas fault. Five stations were found to have large negative perturbations (fig. 1; table 1). The original station corrections had a positive correction in the vicinity of these five stations, and the inversion results all but removed this feature (fig. 6*C*). The inversion thus removed structures in the initial model associated with the station corrections and distributed that structure into the three-dimensional velocity model. We found that this result affected only the shallow part of our three-dimensional inversion results. Inversion models both with and without the station corrections differed only in the uppermost few kilometers near these five stations. We note that the deeper structure (2–10-km depth) in this region also exhibited an anomalously low velocity that was unaffected by including the station corrections.

The overall pattern of the station corrections can be interpreted as a possible long-wavenumber slowness variation that was mapped into the station corrections. To test this interpretation, we performed a synthetic test whereby we selected a model with a different velocity (Dietz and Ellsworth, 1990) for each side of the San Andreas fault. We traced rays through this model by using the same source-receiver geometry with zero station corrections. We also added random noise with 0.1-s standard deviation to the synthetic data. Starting from a one-dimensional velocity structure whose slowness lies between the two sides of the synthetic model, we ran two test inversions: one with the same damping parameters that we determined for the real inversion, and the other with a large damping on the slowness perturbation (to simulate overdamping of the slowness model and mapping of regional slowness variation into the station corrections). The results were a very small perturbation of the station corrections in the first test (fig. 7*A*) and a smooth regional gradient in the second test (fig. 7*B*).

The results of the damped synthetic run (fig. 7*B*) show, as expected, that higher velocities (Franciscan assemblage) mapped into negative station corrections, and lower velocities (Salinian block) mapped into positive station corrections, in contrast to the station corrections plotted in figure 6. Furthermore, the synthetic station corrections plotted in figure 7*B* are 25 to 40 percent of those plotted in figure 6. From the synthetic test, we can say that the station-correction gradient in figure 6*C* is a result of the data and not some large-wave-

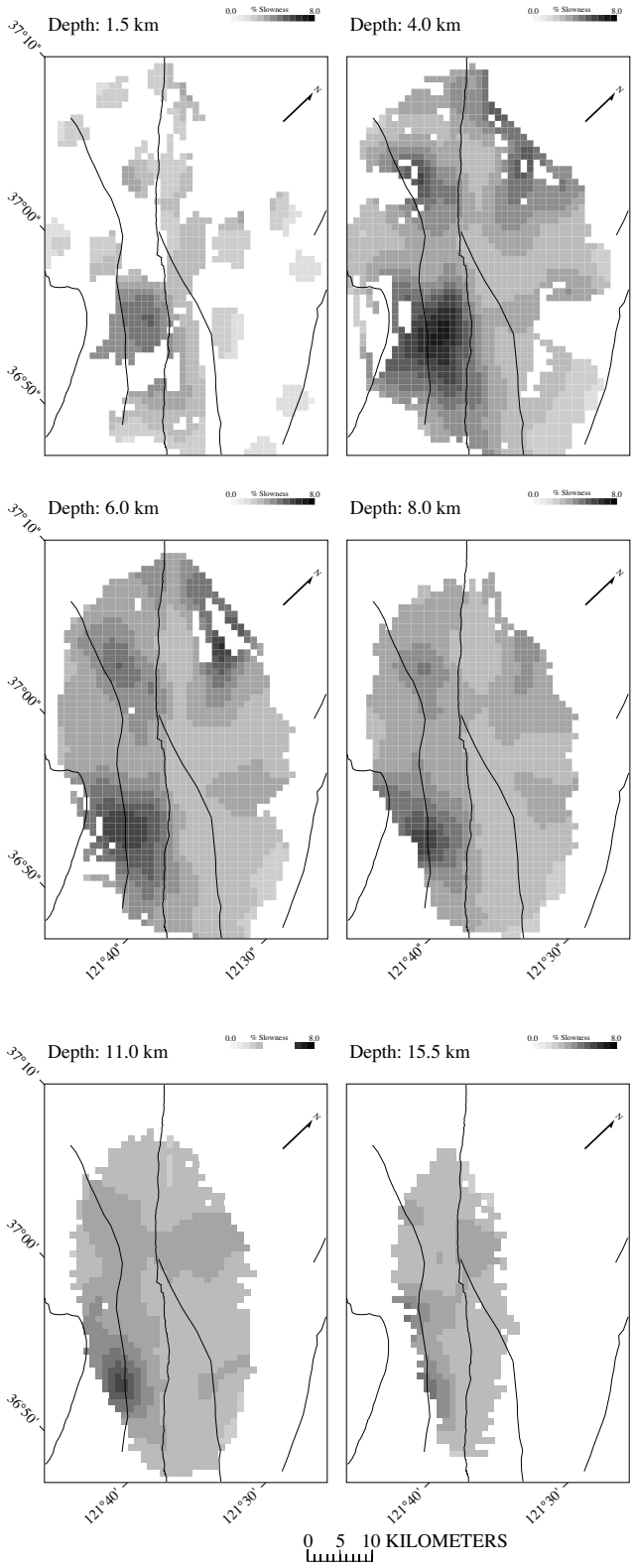

Figure 4.—Jackknife error estimates for different depths in study area (fig. 1). Size of estimated standard deviations is displayed as percentage of reference slowness, where darker regions represent higher standard deviation and lighter regions represent smaller standard deviation. Scale for each layer is from 0 to 8 percent.

length mapping of the regional velocity variation, and so we can resolve regional velocity change without adverse effect on the station corrections (fig. 7*C*).

The optimal choice of damping for hypocenter relocations (λ_1, eq. 4), using crossvalidation as a merit function, forced the hypocenters to be constrained close to their original locations (fig. 8). We found that the hypocenter-parameter perturbations averaged 0.03 km and 0.01 s. Relaxing this constraint, however, indicated that the structural features of our model are robust with respect to relocations. We attributed the small hypocenter corrections to the initial choice of events. Only raypaths from well-defined events, with small residual rms and hypocenter-location errors, were chosen for the inversion. Therefore, for small velocity perturbations, only small hypocenter corrections were expected. As a test, we ran the inversion with a large damping on the slowness and station corrections and no damping on the hypocenter corrections. This inversion allows the hypocenter to move as if the entire signal in the data set is the result of hypocenter mislocation. The average hypocenter perturbations were 0.24 km and 0.04 s, and none of the hypocenters moved more than 1 km. Variance reduction for this test was 7 percent, indicating that only a small part of the signal is attributable to hypocenter-location errors. Thus, the original hypocenter locations appear to be well defined.

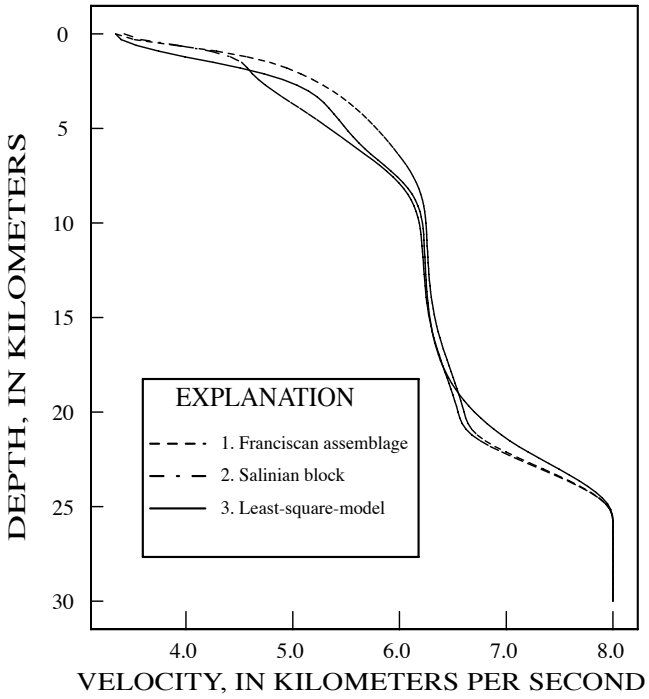

Figure 5.—Three velocity models for the Loma Prieta region (fig. 1): 1 and 2; velocity models for two sides of the San Andreas fault (Dietz and Ellsworth, 1990), translated to B-splines parametrization; 3, least-squares model used as initial model in this study.

To display the results of the tomographic inversion, we present plots of slowness perturbation both in horizontal slices (fig. 9), and in vertical cross sections perpendicular to the fault (fig. 10). For ease of interpretation, the vertical cross sections also display absolute velocity contours and projected hypocenter locations of events lying less than 3 km from the cross section.

The most outstanding feature present in the horizontal slices (fig. 9) is the velocity contrast across the San Andreas fault in the uppermost 4 km of the model. Velocities in the Salinian block are lower than in the Franciscan assemblage, in agreement with other tomographic studies in the Loma Prieta region (Eberhart-Phillips and others, 1990; Lees, 1990; Michael and

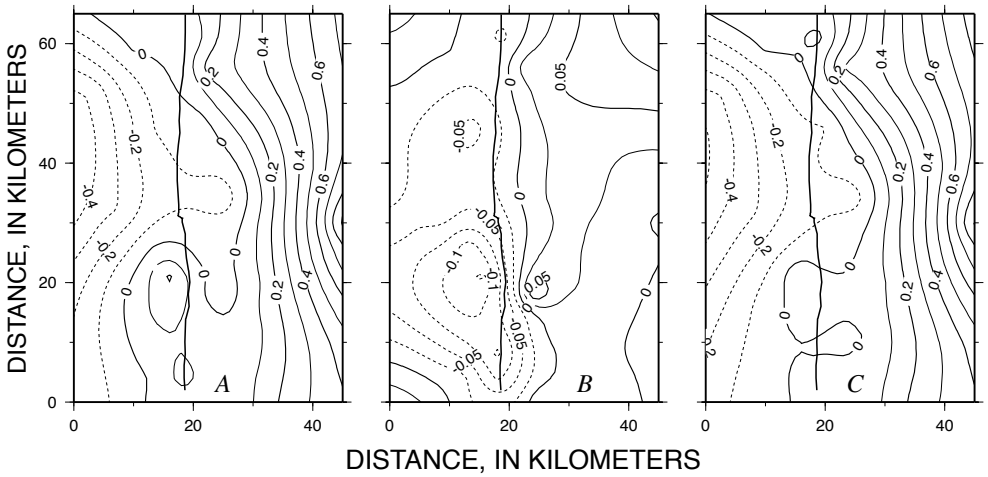

Figure 6.—Contour plots of station corrections in study area (fig. 1). *A*, Initial station corrections before inversion. *B*, Calculated perturbations from joint inversion. *C*, Final station corrections, which are sum of initial corrections and calculated perturbations. The San Andreas fault is shown as irregular heavy line on each contour plot for reference. Contour interval in figure 6*B* differs from that used in figures 6*A* and 6*C*.

Table 1.—*Station corrections for the 27 stations used in the inversion*

[Original correction, starting station correction as received from the U.S. Geological Survey; inversion correction cumulative correction of nonlinear inversion; total correction sum of the two former corrections; jackknife error standard deviation of inversion corrections as computed by jackknife method. Asterisks, station corrections that changed the most (see fig. 1 for locations)]

Station	Latitude (N.)	Longitude (W.)	Elevation (km)	Original correction (s)	Inversion correction (s)	Jackknife error (s)	Total correction (s)
CCOM	37°15.46′	121°40.35′	0.366	0.850	−0.001	0.006	0.849
CSCM	37°17.11′	121°46.35′	.128	.500	.017	.009	.517
HCAM	37°01.52′	121°29.02′	.332	.260	.009	.004	.269
HCBM	36°55.88′	121°39.63′	.219	.130	−.085*	.014	.045
HCOM	36°53.31′	121°42.34′	.129	−−	−.018	.012	−.018
HCRM	36°57.46′	121°35.01′	.241	.010	.012	.012	.022
HGWM	37°01.02′	121°39.20′	.133	−−	−.006	.009	−.006
HPRM	36°57.19′	121°41.70′	.094	.100	−.105*	.017	−.005
HSPM	37°06.91′	121°30.94′	.850	.370	−.005	.003	.365
JALM	37°09.50′	121°50.82′	.244	−.150	.022	.012	−.128
JBCM	37°09.62′	122°01.57′	.660	−.080	−.058	.013	−.138
JBLM	37°07.69′	122°10.08′	.792	−.370	−.005	.007	−.375
JBZM	37°01.07′	121°49.15′	.213	.220	−.132*	.022	.088
JCBM	37°06.71′	121°41.33′	.192	.100	.027	.006	.127
JECM	37°03.04′	121°48.56′	.438	.040	−.056	.015	−.016
JHLM	37°06.54′	121°49.99′	.908	−.050	−.008	.010	−.058
JLXM	37°12.11′	121°59.17′	.244	−.080	−.013	.009	−.093
JPLM	36°58.62′	121°49.93′	.158	.070	−.113*	.016	−.043
JRGM	37°02.22′	121°57.87′	.213	−.280	−.028	.008	−.308
JRRM	37°03.27′	121°43.61′	.408	−.070	.071	.011	.001
JSCM	37°17.07′	122°07.42′	.357	−−	−.032	.016	−.032
JSGM	37°16.96′	122°03.00′	.198	.260	−.041	.021	.301
JSMM	37°12.74′	122°10.06′	.262	−−	.000	.010	.000
JSSM	37°10.17′	121°55.84′	.946	−.060	−.004	.012	−.064
JSTM	37°12.41′	121°47.84′	.149	.130	.034	.011	.164
JTGM	37°01.71′	121°52.58′	.253	−−	−.112*	.011	−.112
JUCM	37°00.07′	122°02.91′	.177	−.470	−.017	.006	−.487

Eberhart-Phillips, 1991; Lees and Shalev, 1992; Eberhart-Phillips and Michael, 1997). At 4-km depth, the low-velocity zone in the Salinian block diminishes in size, and large velocity variations are not evident across the San Andreas fault at distances greater than 15 km in either direction along the fault from the main-shock epicenter. The low-velocity zone, shown as a southwesterly dipping low-velocity zone above the line of hypocenters in cross sections *B–B'* and *C–C'* (fig. 10), lies mainly between the San Andreas and Zayante-Vergeles faults. It decreases in size down to 10-km depth, where it appears as a small body, 4 to 6 km wide. Below 10-km depth, no clear velocity contrast across the San Andreas fault is evident.

An impulse-response test for a point 8 km deep beneath the San Andreas fault on cross section *C–C'* (at the location of the greatest velocity gradient across the fault, fig. 10) indicates approximately 3 km of spatial resolution perpendicular to the fault and about 6 km of spatial resolution parallel to the fault (fig. 3). Error analysis (fig. 4) shows only one major area with a large (>5 percent of the slowness size) standard deviation: at 4-km depth in the low-velocity zone between the San Andreas and Zayante-Vergeles faults. The perturbation there, however, is almost double the size of the standard deviation—14 and 8 percent, respectively—and so we conclude that a low-velocity zone is required by the data. The standard deviation in the rest of the model is less than 5 percent of the model slowness.

Another conspicuous feature in figures 9 and 10 is the high-velocity prism directly beneath the San Andreas fault along the southeast 10 km of the study area (cross section *A–A'*). This high-velocity prism, which separates two blocks of lower velocity, is visible from 6- to 14-km depth (there is no ray coverage below 14-km depth in this region). The high-velocity prism has a high correlation with hypocenter locations (fig. 10). The dip of the hypocenter plane changes from 70° in cross section *B–B'* to 85° in cross section *A–A'*, and the associated high-velocity prism appears to follow the same trend. An impulse-response test for a point at 8-km depth beneath the San Andreas fault in cross section *A–A'* (in the upper part of the high-velocity prism) indicates approximately 4 km of spatial resolution perpendicular to the fault and about 6 km of resolution parallel to the fault (fig. 3). We note that this high-velocity prism persists when different horizontal Laplacian parameters are used, in contrast to the shallower low-velocity feature discussed above, which apparently is sensitive to changes in the smoothing.

The zone adjacent to the main shock appears to have a slightly higher velocity than the surrounding rocks. We observe this high-velocity zone at 11- to 16-km depth, with the main shock to the southwest. This high-velocity zone is not directly beneath the low-velocity zone in the uppermost 10 km of the crust but is shifted about 3 km northeastward.

DISCUSSION

We emphasize that the absolute size of perturbations (and, therefore, the velocity) is partly a function of the particular damping parameters chosen (Lees and Shalev, 1992). We are therefore reluctant to associate specific rock types with given velocity anomalies. However, the spatial distribution of low- and high-velocity zones appears to be robust with respect to the initial model, damping parameters, and methods of parametrization. Thus, we believe that it is appropriate to interpret structural details relating to subsurface geology.

A schematic representation of a geologic interpretation of our results is shown in figure 11. The area between the San Andreas and Zayante-Vergeles faults has an apparent low-velocity anomaly down to 10-km depth, in the same area as an observed negative gravity anomaly (Clark and Rietman, 1973). The low velocity and negative gravity suggest that this section of the Salinian block consists of sedimentary rocks (Clark and Rietman, 1973). Below 10-km depth, no consistent difference between the two sides of the San Andreas fault is evident.

The high degree of correlation between seismicity and high velocity along the San Andreas fault has been noted previously (Lees, 1990; Lees and Malin, 1990; Nicholson and Lees, 1992). Cross section *A–A'*, on the southeast edge of the study area (fig. 10*A*), reveals a high-velocity prism (nearly 1-km/s anomaly) along the plane of aftershocks below 6-km depth. This high-velocity prism gradually becomes less noticeable 6 km to the northwest in cross section *B–B'* (fig. 10*B*). Farther northwest, in cross section *C–C'* (fig. 10*C*), the main shock is on the edge of a high-velocity anomaly restricted to greater than 11-km depth. In cross section *D–D'*, 18 km northeast of the main shock (fig. 10*D*), we see no correlation of high-velocity anomalies and seismicity. We also see no evidence for a low-velocity fault-gouge zone in our results. Because the resolution in our study is about 3 km, a fault-gouge zone several hundreds meters wide would be unresolvable.

Some workers have suggested that the high-velocity zone in the vicinity of the main shock and subsequent aftershocks is associated with brittle rocks more likely to sustain high stress (Lees, 1990; Lees and Malin, 1990; Nicholson and Lees, 1992). This suggestion implies that the high-velocity prism southeast of the main shock is an asperity and, as such, may represent the locus for future large earthquakes. This physical interpretation is based on the apparent pattern at several points along the fault. For the Loma Prieta region, however,

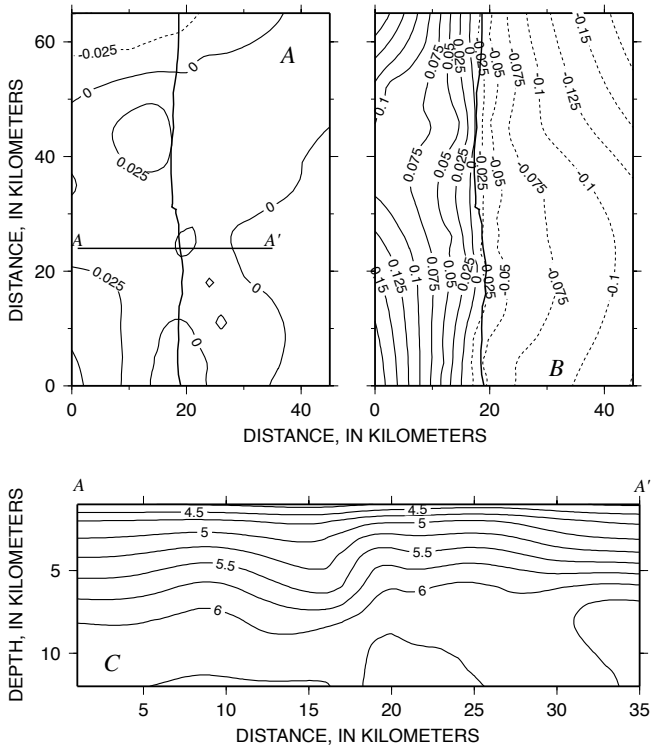

Figure 7.—Synthetic test of different velocity structures for each side of the San Andreas fault in study area (fig. 1). *A*, Contour plot of station corrections with same damping and smoothing parameters used in real data inversion. *B*, Contour plot of station corrections with strong damping of velocity, so that most of signal is mapped into station corrections. *C*, Cross section *A–A'* (fig. 2). Inversion with best damping reproduced velocity step at 18 km, same as in true (synthetic) data.

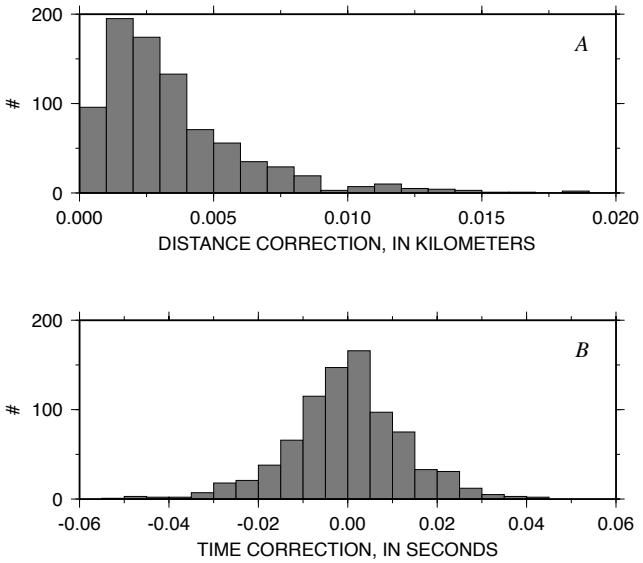

Figure 8.—Earthquake corrections. *A*, Total distance corrections. *B*, Time corrections.

an alternative explanation is that the high-velocity anomaly represents a prism of serpentinite (Allen, 1968).

Serpentinite is a common rock type, occurring in large sheets, in the Franciscan assemblage northeast of the San Andreas fault (Hanna and others, 1972). Although serpentinite samples from the Loma Prieta region exhibit *P*-wave velocities of only 5.5 to 5.6 km/s (N.I. Christensen, written commun., 1993), partially serpentinized ultramafic rock containing more than 50 volume percent serpentine showed higher *P*-wave velocities of 6.2 to 6.6 km/s (Christensen, 1966, 1982). Thoroughly serpentinized ultramafic rocks typically have a very low resistivity (Parkhomenko, 1982), and low resistivities have been observed between the San Andreas and Zayante faults in the vicinity of the Loma Prieta main shock (Eberhart-Phillips and others, 1990).

The most distinctive attribute of serpentinized rocks may be their high Poisson's ratio (Christensen, 1982; Gildner and Caruso, 1992), which can be detected with V_P/V_S inversion; however, a study of V_P/V_S structure in the Loma Prieta region (Thurber and Atre, 1993) does not have the resolution needed for accepting or rejecting the serpentinite-filled-fault model.

Wang (1984) dismissed the possible presence of serpentinite because of observed low velocities in gouge of the fault zone. Our study, however, reveals high velocities in the fault zone southeast of the main shock below 6- to 8-km depth, and so the serpentinite model is reasonable. If the high-velocity prism is, indeed, serpentinite, we recognize that this identification may contradict the fault-zone-asperity model suggested above, and so this high-velocity prism would represent a relatively weak part of the fault more likely to exhibit small earthquakes or

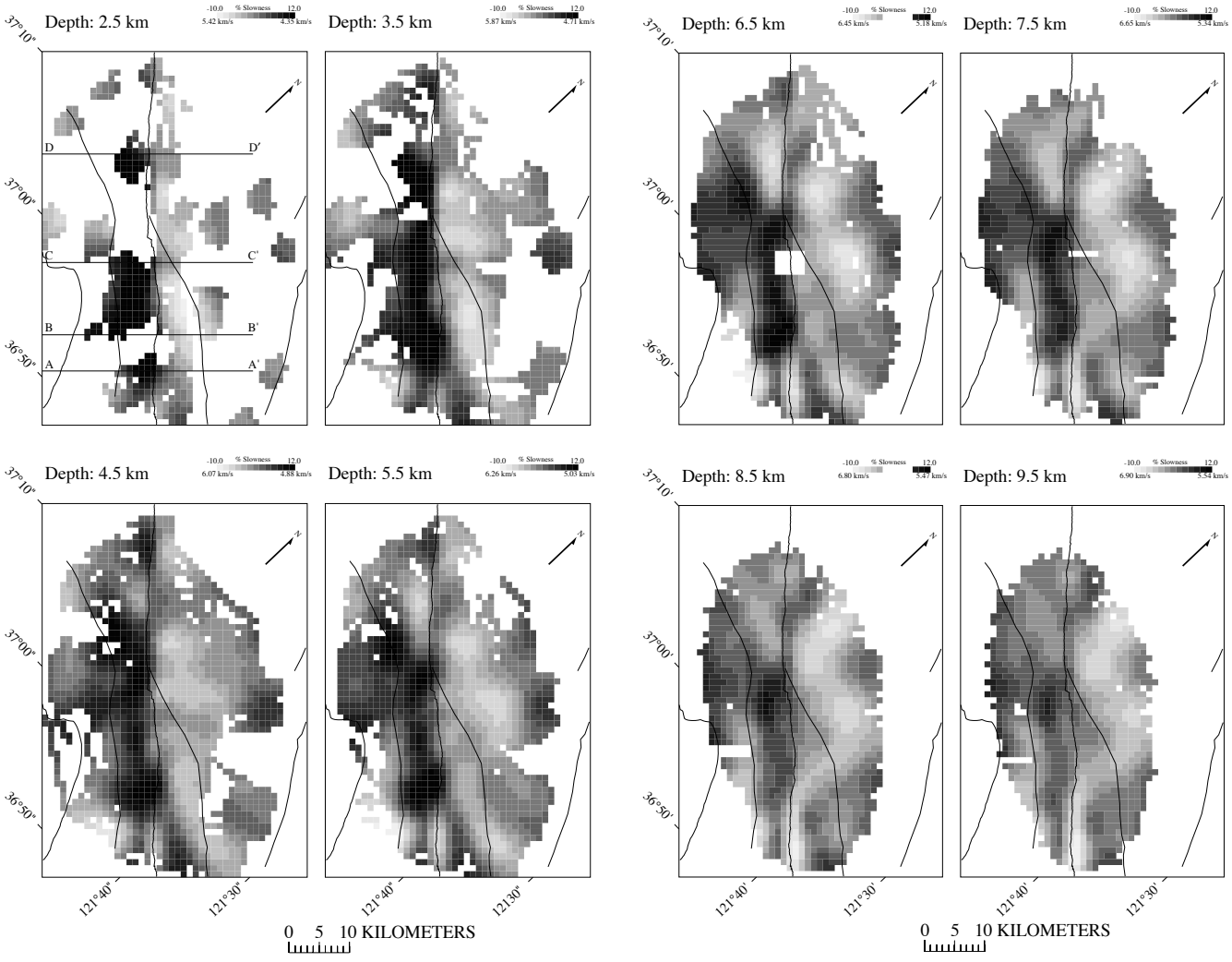

Figure 9.—Three-dimensional tomographic results of *P*-wave inversion in study area (fig. 1), displayed as horizontal slices 1 km apart. Model is represented as percentage of perturbation from initial slowness model, where darker regions represent lower velocity and lighter regions represent higher velocity. Scale for each slice is from constant −10 to 12 percent. See figure 2 for locations of cross sections in first slice.

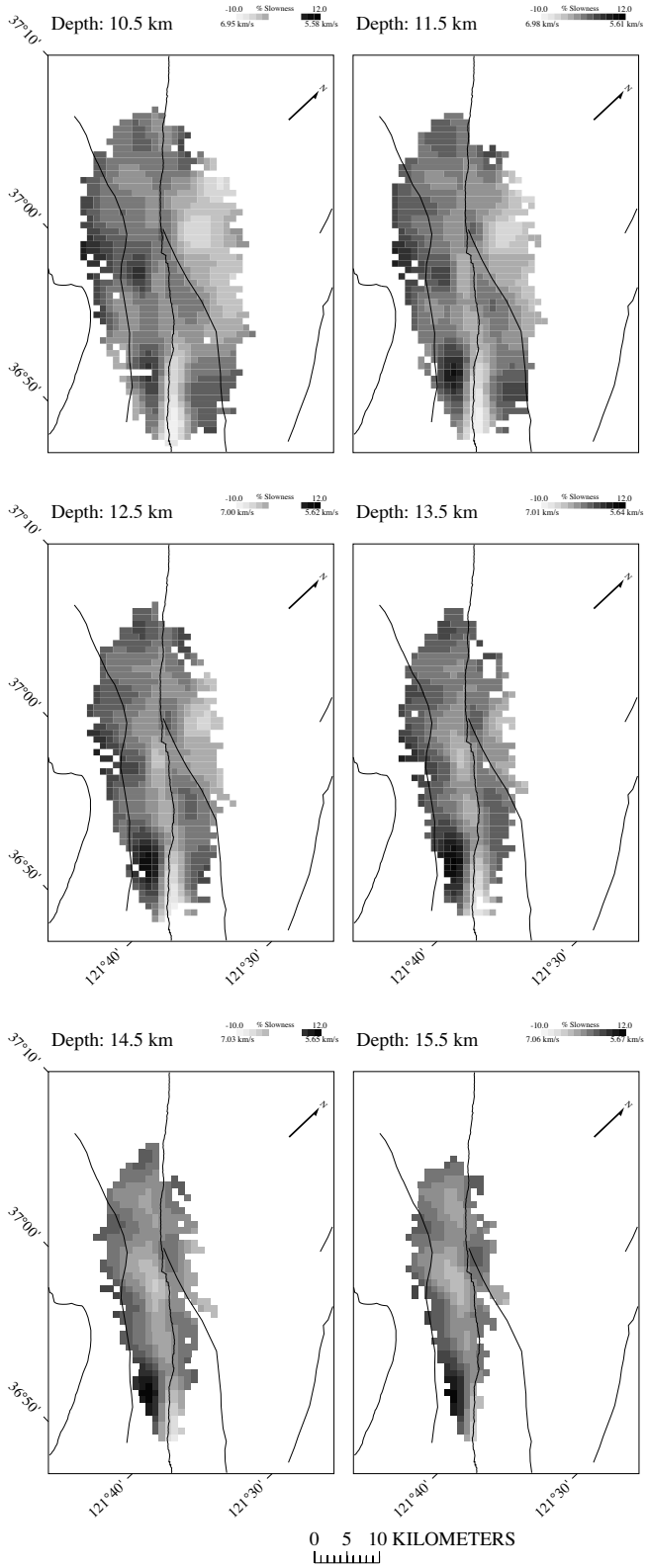

Figure 9.—Continued

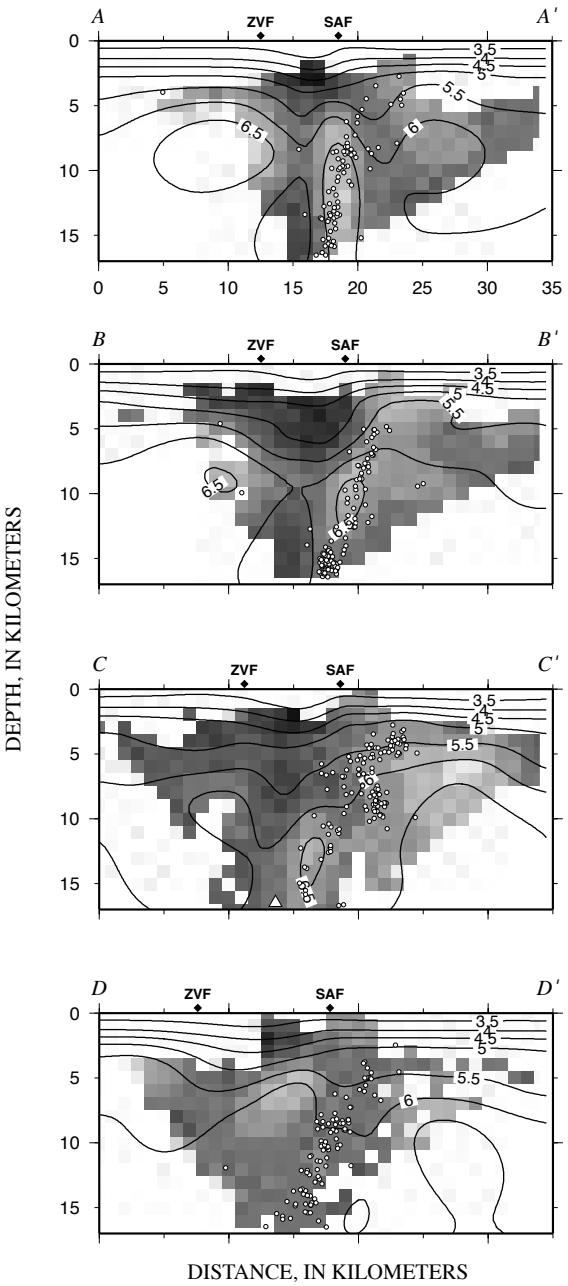

Figure 10.—Four cross sections perpendicular to the San Andreas fault in study area (fig. 1), from southeast (*A*–*A*') to northwest (*D*–*D*'). Shading represents percentage of perturbation from initial slowness model, where darker areas represent lower velocity and lighter areas represent higher velocity. Contour lines denote absolute velocity (that is, reference model plus perturbation) in cross section. Unshaded areas are those with no raypaths. Small circles, horizontally projected earthquakes in a ±3-km swath. SAF, San Andreas fault; ZVF, Zayante-Vergeles fault.

creeping behavior. By this interpretation, the aftershocks are concentrated in the weaker prism of serpentinite southeast of the main shock. A more detailed magnetic and resistivity investigation may be able to distinguish between those two alternative and apparently contradictory interpretations.

Rupture-model investigations (Beroza, 1991; Hartzell and others, 1991; Steidl and others, 1991; Wald and others, 1991) of the main shock showed different slip characteristics along the fault, from predominantly strike slip southeast of the hypocenter to predominantly dip slip northwest of the hypocenter. This change in slip direction, which occurs within a small distance of 12 to 20 km, has raised questions about the causative mechanism. The presence of serpentinite in the vicinity of the fault southeast of the main shock may be related to this phenomenon, and the change in slip direction may be the result of different rock types on the two sides of the fault. A high-velocity prism interpreted as serpentinite appears southeast of the main shock. This high-velocity prism does not exist northwest of the main shock (figs. 9, 10). The characteristics of the San Andreas fault may change in the Loma Prieta region, and the change of slip during the earthquake may have been geologically controlled. More detailed studies of the area southeast of the main shock are needed to confirm this change in the San Andreas fault.

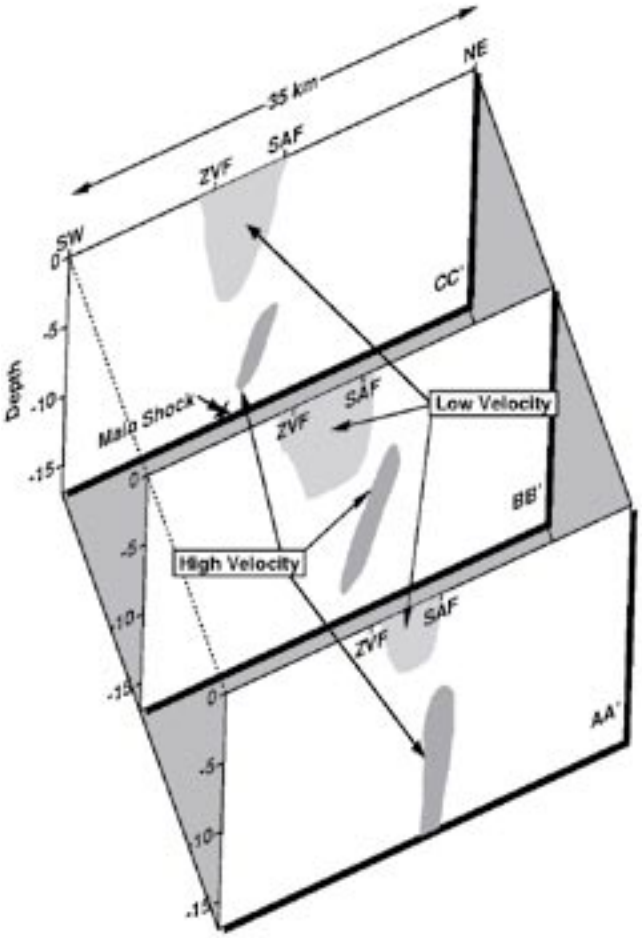

Figure 11.—Schematic representation of the low- and high-velocity regions in study area (fig. 1) along vertical cross sections *A*–*A*' through *C*–*C*' (fig. 2). SAF, San Andreas fault; ZVF, Zayante-Vergeles fault. Low-velocity region, sedimentary block between the San Andreas and Zayente-Vergeles faults; high-velocity region, thin prism of serpentinite that correlates with seismicity.

CONCLUSIONS

In this study, we have calculated and analyzed joint velocity, hypocenter, and station-correction inversions, using the traveltimes from aftershocks of the 1989 Loma Prieta earthquake. We found a regional gradient in station corrections across the fault, with particularly high negative station-delay perturbations occurring in the Salinian block near and southeast of the main shock. The shallow (3–4-km depth) region of our model exhibits a distinct velocity variation across the San Andreas fault, although in deeper sections the structures appear to be more heterogeneous.

The velocity model contains a low-velocity zone between the San Andreas and Zayante-Vergeles faults in the uppermost 10 km of the crust. This low-velocity zone is interpreted as a structure of sedimentary rocks exposed to the northwest and separated from the Salinian block by the Zayante-Vergeles fault. Below 10-km depth, no consistent change is observed between the Salinian block and the Franciscan assemblage.

There appears to be a high degree of correlation between aftershock activity and localized high-velocity anomalies in the area southeast of the main shock. Although this zone of high-velocity anomalies may represent brittle rocks associated with a fault-zone asperity that failed after the main shock, we observed no evidence to suggest that the zone may be a prism of serpentinite. The serpentinite exhibits high velocities and is potentially less competent than the surrounding country rock, providing a sector along the fault more likely to be associated with numerous smaller earthquakes or creep behavior.

We hypothesize that the geology of the San Andreas fault zone changes in the area of the main shock, from a serpentinite-filled zone southeast of the main shock to a hard-rock zone northwest of the main shock.

ACKNOWLEDGMENTS

This research was supported by U.S. National Science Foundation grants EAR–9011441 and EAR–8657206. We thank Lynn Dietz for her help in obtaining the original data, and Mark T. Brandon for helpful discussions and suggestions.

REFERENCES CITED

Aki, Keiiti, and Richards, P.G., 1980, Quantitative seismology; theory and methods: San Francisco, W.H. Freeman, 2 v.

Allen, C.R., 1968, The tectonic environments of seismically active and inactive areas along the San Andreas fault system, *in* Dickinson, W.R., and Grantz, Art, ed., Proceedings of the conference on geologic problems of San Andreas fault system: Stanford, Calif., Stanford University Publications in Geological Sciences, p. 70–80.

Aydin, Atilla, and Page, B.M., 1984, Diverse Pliocene-Quaternary tectonics in a transform environment, San Francisco Bay region, California: Geological Society of America Bulletin, v. 95, no. 11, p. 1303–1317.

Beroza, G.C., 1991, Near-source modeling of the Loma Prieta earthquake; evidence for heterogeneous slip and implications for earthquake hazard: Seismological Society of America Bulletin, v. 81, no. 5, p. 1603–1621.

Christensen, N.I., 1966, Elasticity of ultrabasic rocks: Journal of Geophysical Research, v. 71, no. 24, p. 5921–5931.

———1982, Seismic velocities, *in* Carmichael, R.S., ed., Handbook of physical properties of rocks: Boca Raton, Fla., CRC Press, p. 1–228.

Clark, J.C., and Rietman, J.D., 1973, Oligocene stratigraphy, tectonics, and paleogeography southwest of the San Andreas fault, Santa Cruz Mountains and Gabilan Range, California Coast Range: U.S. Geological Survey Professional Paper 783, 18 p.

Crosson, R.S., 1976, Crustal structure modeling of earthquake data 1. Simultaneous least squares estimation of hypocenter and velocity parameters: Journal of Geophysical Research, v. 81, no. 17, p. 3036–3046.

Davis, B.M., 1987, Uses and abuses of cross-validation in geostatistics: Mathematical Geology, v. 19, no. 3, p. 241–248.

de Boor, Carl, 1978, A practical guide to splines (Applied Mathematical Sciences, v. 27): New York, Springer-Verlag, 392 p.

Dietz, L.D., and Ellsworth, W.L., 1990, The October 17, 1989, Loma Prieta, California, earthquake and its aftershocks; geometry of the sequence from high-resolution location: Geophysical Research Letters, v. 17, no. 9, p. 1417–1420.

Eberhart-Phillips, D.M., Labson, V.F., Stanley, W.D., Michael, A.J., and Rodriguez, B.D., 1990, Preliminary velocity and resistivity models of the Loma Prieta earthquake region: Geophysical Research Letters, v. 17, no. 8, p. 1235–1238.

Efron, Bradley, 1982, The jackknife, the bootstrap and other resampling plans (CBMS–NSF Regional Conference Series in Applied Mathematics, no. 38): Philadelphia, Society for Industrial and Applied Mathematics, 92 p.

Firbas, Petr, 1987, Tomography from seismic profiles, *in* Nolet, Guust, ed., Seismic tomography with applications in global seismology and exploration geophysics: Dordrecht, D. Reidel, p. 189–202.

Fuis, G.S., and Mooney, W.D., 1990, Lithospheric structure and tectonics from seismic-refraction and other data, chap. 8 *of* Wallace, R.E., ed., The San Andreas fault system, California: U.S. Geological Survey Professional Paper 1515, p. 207–236.

Gildner, R.F., and Caruso, C.W., 1992, Limits on the interpretability of laboratory measurements of Poisson's ratio [abs.]: Eos (American Geophysical Union Transactions), v. 73, no. 43, p. 514.

Goldberg, D.E., 1989, Genetic algorithms in search, optimization, and machine learning: Reading, Mass., Addison Wesley, 412 p.

Golub, G.H., Heath, Michael, and Wahba, Grace, 1979, Generalized cross-validation as a method for choosing a good ridge parameter: Technometrics, v. 21, no. 2, p. 215–223.

Hanna, W.F., Brown, R.D., Ross, D.C., and Griscom, Andrew, 1972, Aeromagnetic reconnaissance along the San Andreas fault between San Francisco and San Bernardino, California: U.S. Geological Survey Geophysical Investigations Map GP–815, scale 1:250,000.

Hartzell, S.H., Stewart, G.S., and Mendoza, Carlos, 1991, Comparison of L_1 and L_2 norms in teleseismic waveform inversion for the slip history of the Loma Prieta, California, earthquake: Seismological Society of America Bulletin, v. 81, no. 5, p. 1518–1539.

Herman, G.T., 1980, Image reconstruction from projections; the fundamentals of computerized tomography: New York, Academic Press, 316 p.

Humphreys, Eugene, and Clayton, R.W., 1988, Adaptation of back projection tomography to seismic travel time problems: Journal of Geophysical Research, v. 93, no. B2, p. 1073–1085.

Inoue, Hiroshi, Fukao, Yoshio, Tanabe, Kunio, and Ogata, Yosihiko, 1990, Whole mantle *P*-wave travel time tomography: Physics of the Earth and Planetary Interiors, v. 59, no. 4, p. 294–328.

Lees, J.M., 1990, Tomographic *P*-wave images of the Loma Prieta earthquake asperity: Geophysical Research Letters, v. 17, no. 9, p. 1433–1436.

Lees, J.M., and Crosson, R.S., 1989, Tomographic inversion for three-dimensional velocity structure at Mount St. Helens using earthquake data: Journal of Geophysical Research, v. 94, no. B5, p. 5716–5728.

Lees, J.M., and Malin, P.E., 1990, Tomographic images of *P*-wave velocity variation at Parkfield, California: Journal of Geophysical Research, v. 95, no. B13, p. 21793–21804.

Lees, J.M., and Shalev, Eylon, 1992, On the stability of *P*-wave tomography at Loma Prieta; a comparison of parameterizations, linear and non-linear inversion: Seismological Society of America Bulletin, v. 82, no. 4, p. 1821–1839.

McLaughlin, R.J., Clark, J.C., and Brabb, E.E., 1988, Geological map and structure sections of the Loma Prieta 7½′ quadrangle, Santa Clara and Santa Cruz Counties: U.S. Geological Survey Open-File Report 88–752, 31 p., scale 1:24,000.

Menke, William, 1984, Geophysical data analysis; discrete inverse theory: Orlando, Fla., Academic Press, 260 p.

Michael, A.J., and Eberhart-Phillips, D.M., 1991, Relations among fault behavior, subsurface geology, and three-dimensional velocity models: Science, v. 253, no. 5020, p. 651–654.

Michelini, Alberto, and McEvilly, T.V., 1991, Seismological studies at Parkfield. I. Simultaneous inversion for velocity structure and hypocenters using cubic B-splines parametrization: Seismological Society of America Bulletin, v. 81, no. 2, p. 524–552.

Mooney, W.D., and Colburn, R.H., 1985, A seismic-refraction profile across the San Andreas, Sargent, and Calaveras faults, west-central California: Seismological Society of America Bulletin, v. 75, no. 1, p. 175–191.

Nicholson, Craig, and Lees, J.M., 1992, Travel-time tomography in the northern Coachella Valley using aftershocks of the 1986 M_L 5.9 North Palm Springs earthquake: Geophysical Research Letters, v. 19, no. 1, p. 1–4.

Nolet, Guust, 1987, Seismic wave propagation and seismic tomography, *in* Nolet, Guust, ed., Seismic tomography with appli-

cations in global seismology and exploration geophysics: Dordrecht, D. Reidel, p. 1–47.

Paige, C.C., and Saunders, M.A., 1982, LSQR; an algorithm for sparse linear equations and sparse least squares: Association for Computing Machinery Transactions on Mathematical Software, v. 8, no. 1, p. 43–71.

Parkhomenko, E.I., 1982, Electric resistivity of minerals and rocks at high temperature and pressure: Reviews of Geophysics and Space Physics, v. 20, no. 2, p. 193–218.

Peterson, J.E., Jr., and Davey, Amy, 1991, Crossvalidation method for crosswall seismic tomography: Geophysics, v. 56, no. 3, p. 385–389.

Ross, D.C., 1978, The Salinian block—a Mesozoic granitic orphan in the California coast ranges, *in* Howell, D.G., and McDougall, K.A., ed., Mesozoic paleogeography of the Western United States (Pacific Coast Paleogeography Symposium 2): Los Angeles, Society of Economic Paleontologists and Mineralogists, Pacific Section, p. 509–523.

Ross, D.C., and McCulloch, D.S., 1979, Cross section of the southern Coast Ranges and San Joaquin Valley from offshore Point Sur to Madera, California: Geological Society of America Map and Chart Series, no. MC–28H, scale 1:250,000.

Saleeby, J.B., 1986, C–2, central California offshore to Colorado plateau: Geological Society of America Centennial Continent/Ocean Transect 10, scale 1:500,000.

Sen, M.K., and Stoffa, P.L., 1992, Rapid sampling of model space using genetic algorithms; examples from seismic waveform inversion: Geophysical Journal International, v. 108, no. 1, p. 281–292.

Shalev, Eylon, 1993a, Three-dimensional seismic investigation of the crust in central New Hampshire and Loma Prieta, California: New Haven, Conn., Yale University, Ph.D. thesis, 143 p.

———1993b, Cubic B-splines; strategies of translating a simple structure to B-spline parameterization: Seismological Society of America Bulletin, v. 83, no. 5, p. 1617–1627.

Spakman, Wim, and Nolet, Guust, 1988, Imaging algorithms, accuracy and resolution in delay time tomography, *in* Vlaar, N.J., Nolet, Guust, Wortel, M.J.R., and Cloetingh, S.A.P.L., eds., Mathematical geophysics; a survey of recent developments in seismology and geodynamics: Hingham, Mass., D. Reidel, p. 155–187.

Spencer, Carl, and Gubbins, David, 1980, Travel-time inversion for simultaneous earthquake location and velocity structure determination in laterally varying media: Royal Astronomical Society Geophysical Journal, v. 63, no. 1, p. 95–116.

Steidl, J.H., Archuleta, R.J., and Hartzell, S.H., 1991, Rupture history of the 1989 Loma Prieta, California, earthquake: Seismological Society of America Bulletin, v. 81, no. 5, p. 1573–1602.

Stoffa, P.L., and Sen, M.K., 1991, Nonlinear multiparameter optimization using genetic algorithms; inversion of plane-wave seismograms: Geophysics, v. 56, no. 11, p. 1794–1810.

Thurber, C.H., 1983, Earthquake locations and three-dimensional crustal structure in the Coyote Lake area, central California: Journal of Geophysical Research, v. 88, no. B10, p. 8226–8236.

Thurber, C.H., and Atre, S.R., 1993, Three-dimensional V_P/V_S variations along the Loma Prieta rupture zone: Seismological Society of America Bulletin, v. 83, no. 3, p. 717–736.

Um, Junho, and Thurber, C.H., 1987, A fast algorithm for two-point seismic ray tracing: Seismological Society of America Bulletin, v. 77, no. 3, p. 972–986.

Van Der Sluis, Abraham, and Van Der Vorst, H.A., 1987, Numerical solution of large, sparse linear algebraic systems arising from tomographic problems, *in* Nolet, Guust, ed., Seismic tomography with applications in global seismology and exploration geophysics: Dordrecht, D. Reidel, p. 49–83.

VanDecar, J.C., 1991, Upper-mantle structure of the Cascadia subduction zone from non-linear teleseismic travel-time inversion: Seattle, University of Washington, Ph.D. thesis, 177 p.

Wald, D.J., Helmberger, D.V., and Heaton, T.A., 1991, Rupture model of the 1989 Loma Prieta earthquake from inversion of strong-motion and broadband teleseismic data: Seismological Society of America Bulletin, v. 81, no. 5, p. 1540–1572.

Walter, A.W., and Mooney, W.D., 1982, Crustal structure of the Diablo and Gabilan Ranges, central California; a reinterpretation of existing data: Seismological Society of America Bulletin, v. 72, no. 5, p. 1567–1590.

Wang, C.-Y., 1984, On the constitution of the San Andreas fault zone in central California: Journal of Geophysical Research, v. 89, no. B7, p. 5858–5866.

EARTHQUAKE OCCURRENCE

THREE-DIMENSIONAL VARIATIONS IN V_P/V_S RATIO IN THE LOMA PRIETA REGION[1]

By Shashank R. Atre and Clifford H. Thurber, University of Wisconsin, Madison

CONTENTS

ABSTRACT

We present a three-dimensional model for variations in the ratio of *P*- to *S*-wave velocity (V_P/V_S) along the Loma Prieta rupture zone, derived from portable-instrument *S*–*P* arrival times and earthquake locations determined in a three-dimensional *P*-wave-velocity model. We devoted significant effort to identifying *S*-to-*P*-converted waves, which were prevalent at a few of the stations used. The inversion method uses three-dimensional ray tracing in an existing laterally heterogeneous *P*-wave-velocity model and a constant V_P/V_S ratio to determine the initial paths for *S* waves. The model parametrization allows spatial variations in V_P/V_S ratio on a three-dimensional grid with node spacings of 3 to 15 km horizontally and 3 to 5 km vertically. The reduction in data variance is nearly 65 percent for the single-iteration inversion.

We interpret the V_P/V_S model in conjunction with other available geologic and geophysical information. Our major findings are (1) high V_P/V_S ratios along the rupture zone in the upper crust, indicative of upthrusted gabbroic rocks; (2) predominantly low V_P/V_S ratios in the lower crust, indicative of an underlying quartz-rich basement; and (3) two low-V_P/V_S-ratio areas in the near surface associated with known quartz-rich rock sequences, one of sandstone and the other of granite and (or) granodiorite. We also tentatively identify a boundary between areas of low and slightly high V_P/V_S ratio at depth in the immediate vicinity of the Loma Prieta main-shock hypocenter. Our results demonstrate the diagnostic power of a three-dimensional V_P/V_S model in combination with other geologic and geophysical information.

INTRODUCTION

The Loma Prieta earthquake sequence of October 17, 1989, provides an outstanding opportunity for detailed study of the structure and setting of a large California earthquake and its aftershocks. These events occurred within the U.S. Geological Survey (USGS)'s central California seismic network (Calnet), and so precise locations for the earthquake sequence are available. In addition, an array of three-component digital recorders densely covered much of the area above the aftershock sequence, mainly from the main shock toward the northwest (Simpson and field team, 1989). These data have been made available to the seismological community as part of the Program for Array Seismic Studies of the Continental Lithosphere (PASSCAL) of the Incorporated Research Institutions for Seismology (IRIS).

The data collected during the PASSCAL deployment, along with supplemental data from Calnet and other portable-instrument deployments, are well suited for the application of three-dimensional seismic-imaging techniques (Thurber, 1983; Thurber and Aki, 1987). The broadly distributed seismicity along the San Andreas and other nearby fault zones recorded at the PASSCAL and USGS stations (fig. 1), along with data from numerous portable-array, quarry-blast, and seismic-refraction studies (Wesson and others, 1973; Mooney and Luetgert, 1982; Bakun and McLaren, 1984; Mooney and Colburn, 1985), provides excellent spatial coverage for imaging. The three-dimensional *P*-wave-velocity structure was estimated by Eberhart-Phillips and others (1990) and Lees (1990). Owing to problems in the maintaining absolute time on the PASSCAL portable instruments (A.L. Lerner-Lam, oral commun., 1990) our present analysis utilizes *S*-minus-*P* (*S*–*P*) differential times only.

We used observed arrival-time differences between *P*- and *S*-wave first arrivals at the PASSCAL portable-array sites, augmented by some portable-instrument data from the University of California, Berkeley, and the USGS, to carry

[1]University of Wisconsin, Madison, Geophysical and Polar Research Center contribution 536.

out a single-step inversion for three-dimensional variations in the ratio of *P*- to *S*-wave velocity (V_P/V_S) along the Loma Prieta rupture zone. The analysis incorporates the preliminary three-dimensional *P*-wave-velocity model of Eberhart-Phillips and others (1990) to determine the initial raypaths. The assumptions built into the inversion for V_P/V_S ratio (rather than directly for *P*- and *S*-wave velocities) do not necessarily limit this analysis to a single-step inversion; however, a rigorous iterative inversion should also ultimately include hypocenter and *P*-wave-velocity perturbations. This endeavor will be undertaken with a greatly enlarged data set, including calibration-shot data obtained in 1991 by the USGS (D.M. Eberhart-Phillips, oral commun., 1991).

S–P DATA

The process of estimating the *S–P* time for an event simply involves picking the *P*-wave-arrival time, t_P, and the *S*-wave-arrival time, t_S, and then subtracting t_P from t_S. The identification of the *P* phase is generally easy, given adequate signal-to-noise ratio. Some workers have expressed concern

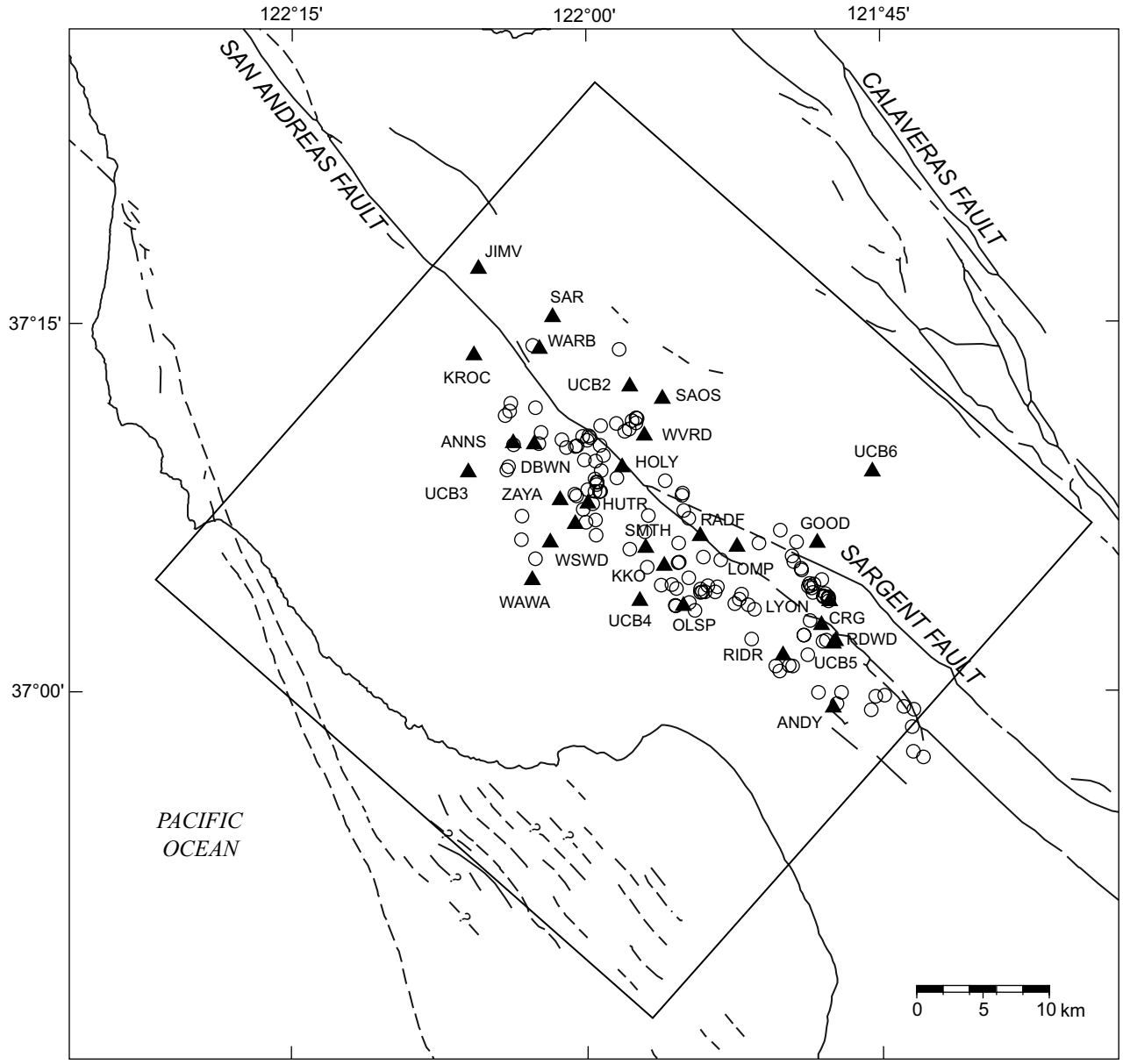

Figure 1.—Loma Prieta region, Calif., showing locations of study area (box), major faults, and epicenters (circles) of events used for V_P/V_S inversion. Triangles, seismic stations.

regarding the effect of the antialias filter of the PASSCAL instruments on the onset of *P* waves. A careful examination of representative data with varying signal-to-noise ratio indicates that the antialias filter does not affect our data (J.A. Fowler, oral commun., 1991). Typically, a *P*-wave arrival can be picked within ±10 ms, whereas picking the *S*-wave arrival is almost never easy. Because an *S*-wave arrives in the *P*-wave coda, the coda interferes with the *S*-wave. Thus, unlike for the *P* wave, no sharp and clear onset may be evident for the *S* wave.

Picking the *S* wave generally is subject to additional uncertainty because of the possible presence of anisotropy and (or) the generation of *S*-to-*P*-converted waves. The *S*-to-*P*-converted wave arrives before the actual *S* wave and, if not identified correctly, would result in too early an *S*-wave pick, causing an apparent increase in the *S*-wave velocity. Propagation of the *S* wave in an anisotropic medium depends on several factors, and if the effects of anisotropy are not considered, this dependence could also result in a mispick. In an anisotropic medium, the polarization vectors of the *S* wave are expected to be mutually orthogonal, with a degree of splitting dependent on the direction of propagation and the path length (Keith and Crampin, 1977; Babuska and Cara, 1991). If the horizontal components are rotated in this fixed direction of polarization, the *S* wave will split into a fast and a slow *S* wave, indicating the presence of anisotropy. We and other researchers from the University of California, Santa Cruz (Susan Schwarz, oral commun., 1990) have examined the data for anisotropy and found some evidence for weak splitting (max 50 ms), which is typically within our estimated *S*-wave-picking uncertainty.

Distinguishing the *S* wave from an *S*-to-*P*-converted wave requires that the horizontal-component seismograms (north-south and east-west) be rotated into the radial and transverse components. Examples of vertical-component, horizontal-radial-component, and horizontal-transverse-component seismograms for events recorded at PASSCAL stations, along with particle-motion plots for selected time windows, are plotted in figures 2 through 9.

An event almost directly south of station WARB (fig. 1) is shown in fig. 2*A*. The *P*-wave arrival is sharp enough to be picked with an estimated uncertainty of ±20 ms. To identify the *S*-wave arrival, we use the particle-motion plot, even though a clear arrival at approximately 22.8 s could be picked as the *S*-wave arrival. First, we plot the horizontal particle motion of the direct *P*-wave to confirm that the azimuth of the *P*-wave arrival is generally along the station-epicenter line. Here, the particle-motion plot shows the azimuth of the *P*-wave arrival to be orthogonal to the station-epicenter line. Similar plots of *P*-wave arrivals at this station from other events also showed the same phenomenon, leading us to believe that a channel flip may be present at this station. Thus, for station WARB, the horizontal components were rotated 90°, resulting in a radial *P*-wave first arrival (fig. 2*B*). A plot of a time window of the horizontal components within the expected range of the *S*-wave arrival is shown in figure 2*C*, and on the basis of its orthogonality to the *P* wave, this wave is identified as a direct *S* wave, arriving at approximately 22.82 s. Thus, what appears here to be the *S*-wave arrival on the raw seismograms is, indeed, the *S*-wave arrival. Another example for station WARB shows a strong phase at 21.9 s near the expected *S*-wave-arrival time (fig. 3*A*). A plot of the horizontal components (fig. 3*B*) shows that the azimuth of the direct *P* wave is close to the station-epicenter line once it is rotated 90°. A plot of the horizontal components within the time window expected for the *S*-wave arrival (fig. 3*C*) clearly shows that the initial particle motion of the phase on the radial component has nearly the same arrival azimuth as the direct *P* wave, and so this phase is identified as an *S*-to-*P* conversion. This phase is followed by a phase that is orthogonal to the *S*-to-*P*-converted phase and is identified as a direct *S* wave. The time difference between these two phases is about 100 ms.

Examples for station ZAYA (fig. 1) are plotted in figures 4 and 5. The seismograms in figure 4*A* show a sharp *P* wave on the vertical component and what appears to be a sharp *S* wave. In figure 4*B*, the azimuth of the direct *P*-wave arrival is a bit off the station-epicenter line, presumably owing to lateral heterogeneity. Once again, a plot of the horizontal components within the time window expected for the *S*-wave arrival (fig. 4*C*) shows that the initial particle motion is due to a phase with nearly the same arrival azimuth as the direct *P* wave. This phase is followed by a phase that is clearly orthogonal to the azimuth of the direct *P* wave. We interpret this later phase to be the direct *S* wave, and identify the earlier phase as an *S*-to-*P* conversion. The time difference between these two phases is only 36 ms, within the uncertainty we associate with our best *S*-wave picks. Another example for station ZAYA, from an event east-southeast of the station, again shows the *P* wave arriving off azimuth (fig. 5*B*). A plot of the horizontal components within the time window expected for the *S*-wave arrival (fig. 5*C*) shows a small phase identifiable as an *S*-to-*P* conversion.

More noteworthy examples of *S*-to-*P*-converted waves at stations WVRD and WAWA (fig. 1) are highlighted by the pairs of seismograms plotted in figures 6 and 7 and in figures 8 and 9, respectively. One example from station WVRD shows a strong phase on the radial component, arriving at 13.35 s (fig. 6*A*). A plot of the two horizontal components within a time window between 13.3 and 14 s (fig. 6*C*) clearly shows that the initial motion has the same azimuth as the direct *P* wave (fig. 6*B*). The *S* wave does not arrive until 13.7 s on the transverse component. The time difference between the onset of these two phases is about 350 ms, within the range of *S*–*P* time perturbations that we expect to quantify. Another example from station WVRD again shows a strong phase on the radial component (fig. 7*A*), arriving at 23.95 s, whereas the direct *S* wave apparently does not arrive until 24.25 s. Two examples from station WAWA for events to the north-northeast of the station each show a strong phase on the radial component,

arriving at 22.45 s (fig. 8*A*) and 12.72 s (fig. 9*A*). The direct *P*-wave arrival is off azimuth and has the same orientation (figs. 8*B*, 9*B*). The first-arriving phase on the horizontal components for both events is close to the station-epicenter line (figs. 8*C*, 9*C*). The direct *S* wave for both events arrives approximately 120 ms later, at approximately 22.57 and 12.84 s, respectively (figs. 8*A*, 9*A*). If ample care is not taken, such possible mispicks would result in an apparent increase in *S*-wave velocity and a decrease in V_P/V_S ratio.

We are confident that our picks were of the true *S* wave. We took great care to identify *S*-to-*P*-converted waves, as indicated above. We routinely used particle-motion plots to ascertain the characteristics of the *S* waves and reduce the uncertainty of each pick. The accuracy of a pick, however, still depends on the sharpness of the arrival. We assigned quality factors to our picks on the basis of the uncertainty of the arrival time. If the onset of the *S* wave had an estimated uncertainty of <50 ms, we assigned the pick a quality factor of 0. Similarly, for uncertainties of ±75, ±100, ±125, and ±200 ms in arrival time, we assigned a quality factor of 1, 2, 3, and 4, respectively. *S*–*P* times were weighted by a factor of $(1/2)^n$ in our inversions, where *n* is the quality factor, except that data with a quality factor of 4 were excluded from the inversion. The *S*–*P* data determined in this study were submitted to the Loma Prieta Data Archive Project of the National Information Service for Earthquake Engineering.

INVERSION METHOD

Our procedure of inverting for V_P/V_S ratios is similar in concept to that of Walck (1988), but with one major difference.

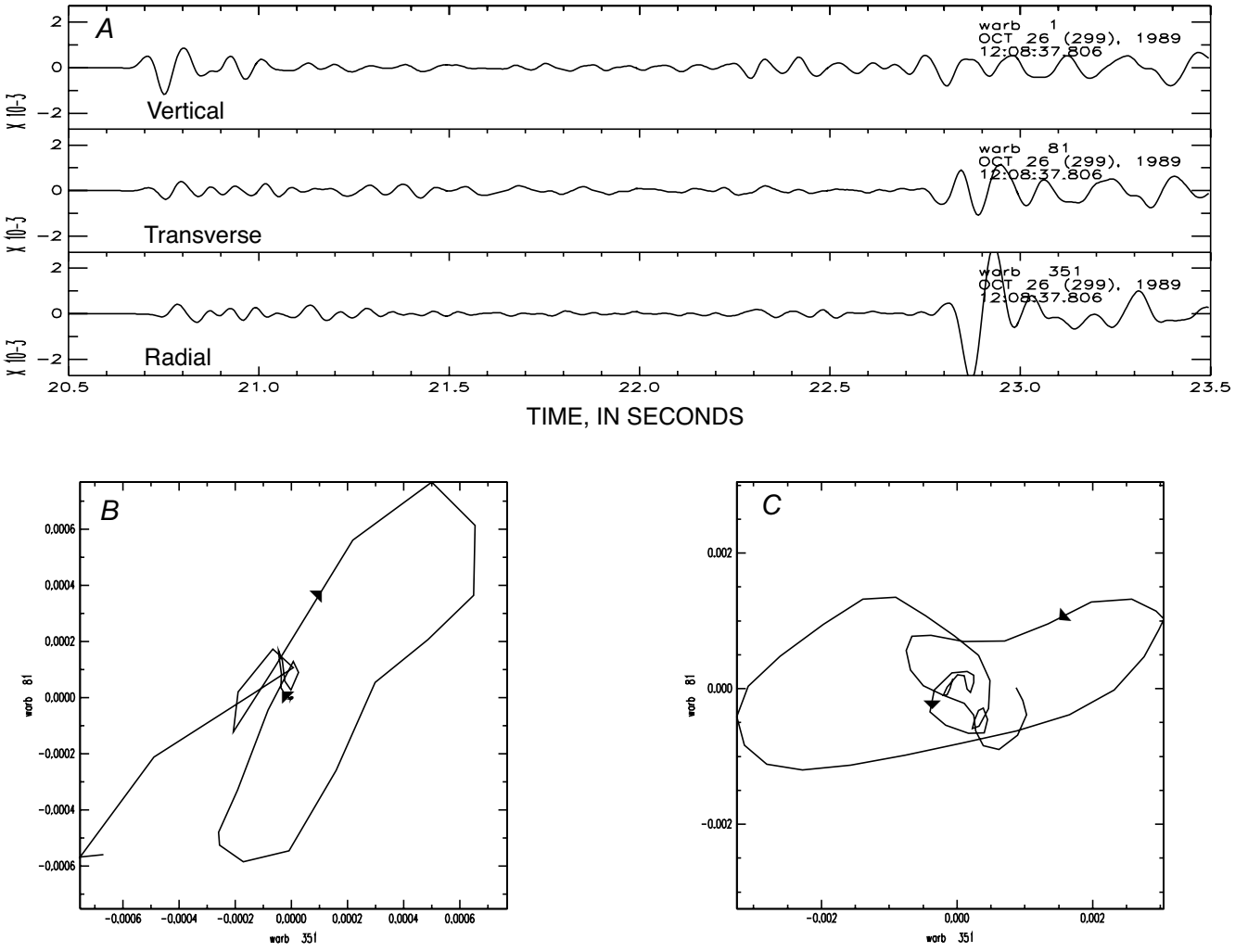

Figure 2.—Seismograph records from station WARB (fig. 1). *A*, *P*- and *S*-wave arrivals on vertical and two horizontal components from an event at lat 37°10.13′ N., long 122°2.51′ W., and 12.3-km depth. *B*, Particle-motion plot of direct *P* wave for a time window between 20.50 and 20.85 s. *C*, Particle-motion plot of direct *S* wave for a time window between 22.70 and 23.05 s.

The arrival time t_{ij} for a *P* or *S* wave at station *j* from event *i* is given by

$$t_{ij} = t_0 + \int_{\text{path}} u ds, \tag{1}$$

where t_0 is the event origin time and u is the *P*- or *S*-wave slowness ($1/V$). If the V_P/V_S ratio is treated as a constant initially, then the raypaths are identical for both *P* and *S* waves, and we can express the *S*–*P* time difference dt_{ij} as

$$dt_{ij} = \int_{\text{path}} \left(\frac{\frac{V_P}{V_S} - 1}{V_P} \right) ds. \tag{2}$$

Note the removal of dependence on event origin time, but the continued implicit dependence on event location as one end point of the path integral.

We can now develop a linearized inversion procedure for determining variations in V_P/V_S ratio. We begin by adopting a three-dimensional *P*-wave-velocity structure defined on a three-dimensional grid of nodes (Eberhart-Phillips and others, 1990), assuming an initially constant V_P/V_S ratio. We made a "reasonable" choice for an initial V_P/V_S ratio of 1.75 on the basis of the results of preliminary inversions and an analysis of Wadati diagrams. Observed *S*–*P* time differences dt_{ij} were determined for a substantial set of events in the PASSCAL data set that have also been accurately located

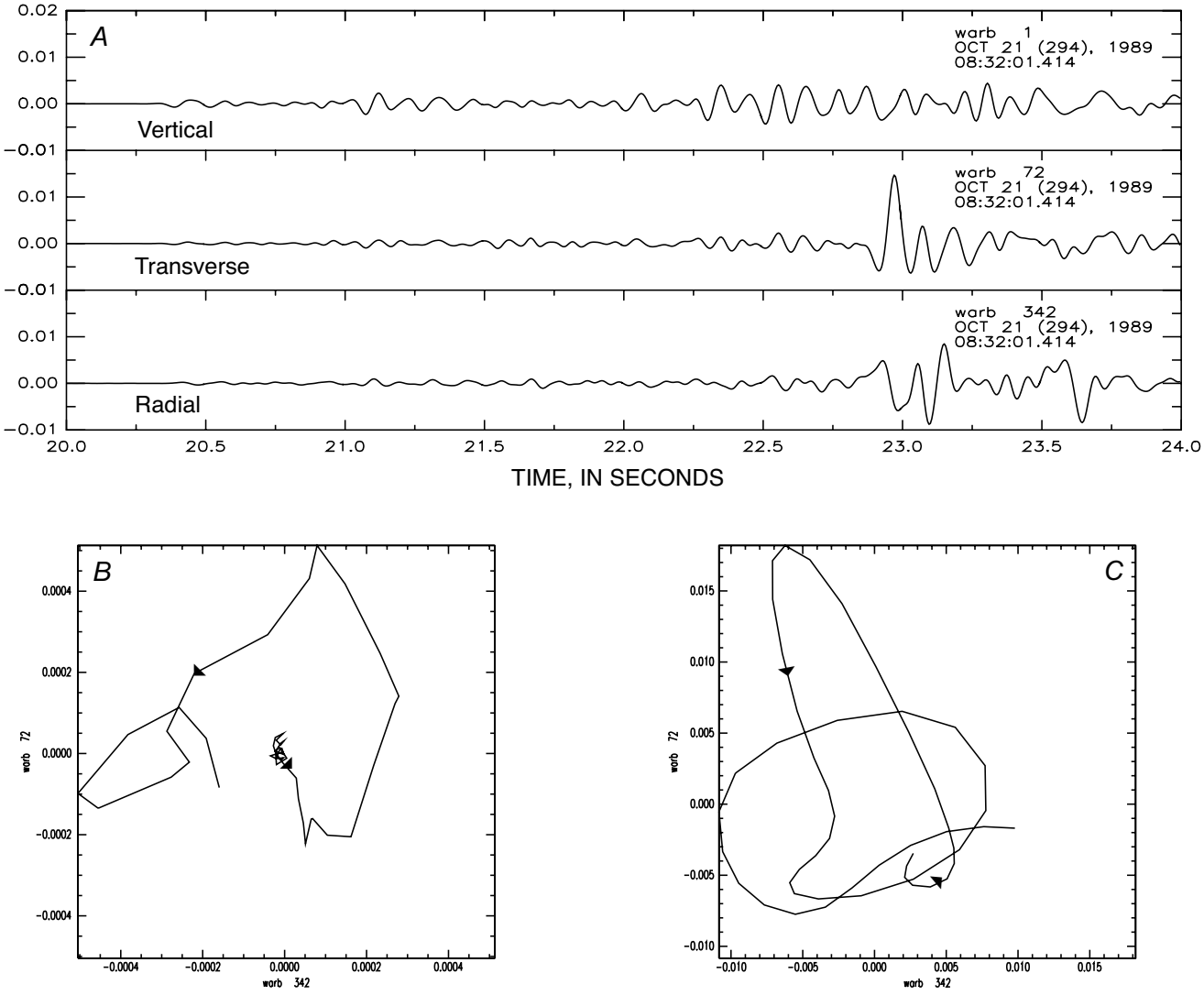

Figure 3.—Seismograph records from station WARB (fig. 1). *A*, *P*- and *S*-wave arrivals on vertical and two horizontal components from an event at lat 37°6.92′ N., long 122°0.01′ W., and 14.8-km depth. *B,* Particle-motion plot of direct *P* wave for a time window between 20.25 and 20.50 s. Note that azimuth of *P* wave is close to station-epicenter line. *C*, Radial-transverse particle-motion plot of direct *S* wave for a time window between 22.90 and 23.15 s. Note that initial particle motion is along nearly the same azimuth as direct *P* wave. Near 23.02 s, direct *S* wave arrives with a particle motion orthogonal to azimuth of initial phase, which is identified as *S*-to-*P* conversion.

by the USGS, using both "two dimensional" (Dietz and Ellsworth, 1990) and "three dimensional" velocity models (Eberhart-Phillips and others, 1990). We used both of these sets of velocity models and hypocenter locations to assess the sensitivity of the V_P/V_S inversion to assumed event locations and an initial velocity model. We calculated raypaths and expected S–P time differences dt_{ij}* by using the three (or two)-dimensional P-wave-velocity model and a constant V_P/V_S ratio, according to the pseudo-bending three-dimensional ray-tracing method of Um and Thurber (1987). This step is distinct from the approach of Walck (1988), who did not use the available three-dimensional P-wave-velocity model of Walck and Clayton (1987) to trace rays for the backprojection of S–P residuals. We then related the S–P time misfit $\Delta t_{ij}=dt_{ij}-dt_{ij}$* to perturbations in V_P/V_S ratio at the nodes of the three-dimensional grid, and inverted for V_P/V_S ratio in a single step, keeping the P-wave velocities and hypocenter locations fixed. Note that we can calculate revised S-wave traveltimes by first applying $\Delta(V_P/V_S)$ corrections to determine a grid of S-wave velocities for ray tracing and then redetermining the expected S–P times, thus directly assessing the improvement to the data fit, along with the usual measures of solution uncertainty and resolution.

This strategy for determining three-dimensional variations in V_P/V_S ratio is analogous to single-step inversion of earthquake P-wave-arrival-time residuals keeping the event loca-

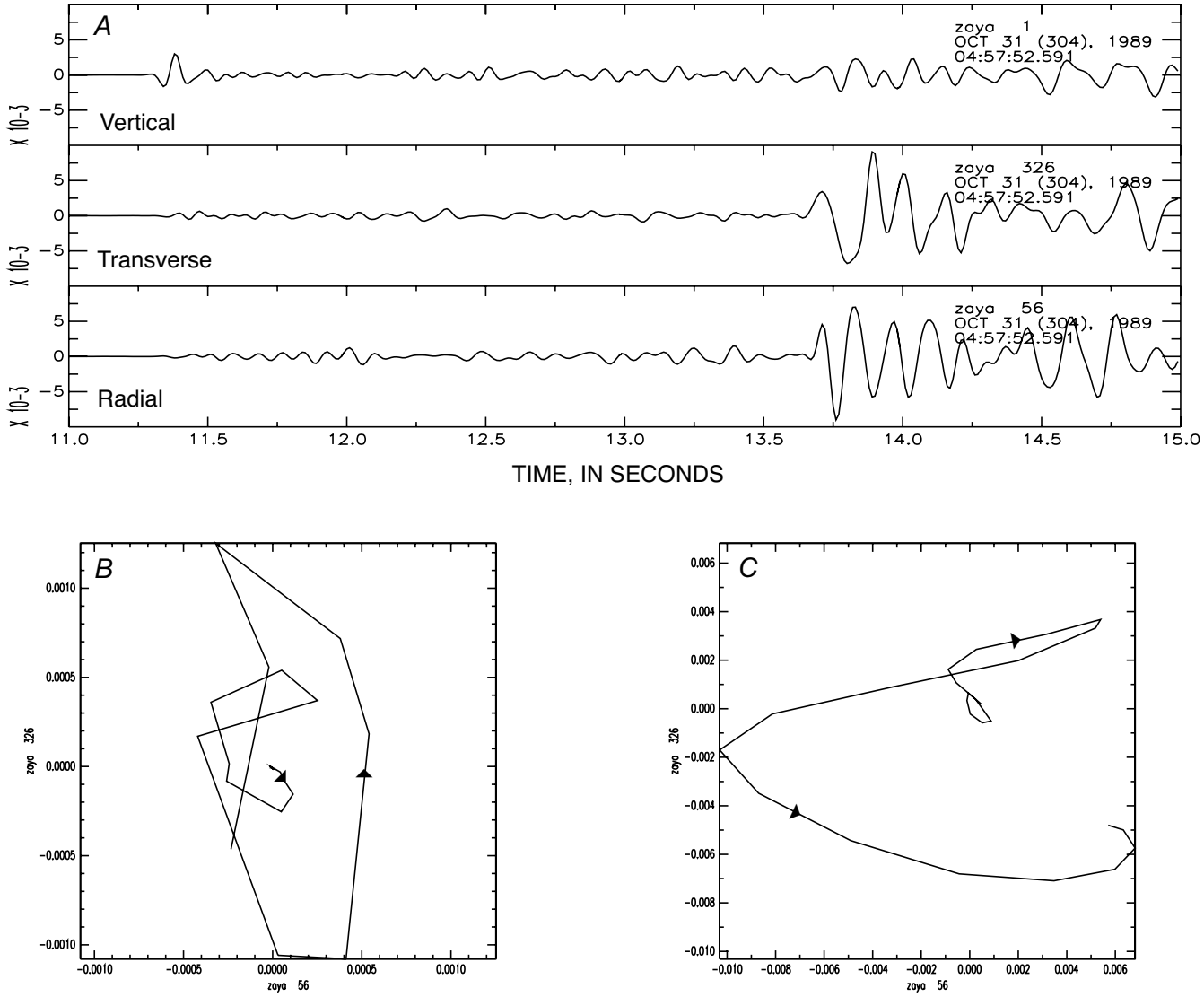

Figure 4.—Seismograph records from station ZAYA (fig. 1). *A*, *P*- and *S*-wave arrivals on vertical, radial, and transverse components from an event at lat 37°12.57′ N., long 122°5.15′ W., and 9.3-km depth. *B*, Radial-transverse particle-motion plot of direct *P* wave for a time window between 11.25 and 11.50 s. Note that azimuth of *P* wave is not along station-epicenter line. *C*, Radial-transverse particle-motion plot of direct *S* wave for a time window between 13.60 and 13.85 s. Note that initial particle motion is along same azimuth as direct *P* wave. Around 13.68 s, direct *S* wave arrives with a particle motion orthogonal to azimuth of initial phase, which is identified as *S*-to-*P* conversion.

tions fixed. We invoke Fermat's principle to justify the use of the (three dimensional) *P*-wave path to assess the spatial variation in V_P/V_S ratio, so that we neglect the variation of the "final" (*S* wave) path from the "initial" (*P* wave) path (which would be nil for a truly constant V_P/V_S ratio). These raypath differences should have only a second-order effect on our estimation of the variation in V_P/V_S ratio. Indeed, if spatial variations in V_P/V_S ratio are modest (say, max 5 percent), this assumption is quite valid. However, the complex geology of the Loma Prieta region (fig. 1), as well as the level of lateral *P*-wave-velocity variations determined by Eberhart-Phillips and others (1990) (>20 percent in places), leads us to suspect that the variation in V_P/V_S ratio may be substantial and an iterative solution will eventually be required. Thus, we view this single-step inversion as the first stage in our efforts, to be followed in the future by an iterative determination of *P*-wave-velocity structure, V_P/V_S structure, and event locations from *P*-wave-arrival and *S*–*P* times.

If we are interested in using variations in V_P/V_S ratio (or, equivalently, Poisson's ratio) to infer geologic structure and mechanical properties (including, for example, pore pressure), then the approach of inverting directly for variations in V_P/V_S ratio has certain significant advantages. It is well known that a direct comparison of three-dimensional *P*- and *S*-wave-velocity models to infer V_P/V_S ratios is hampered by the tendency for *S*-wave-velocity models to be more poorly

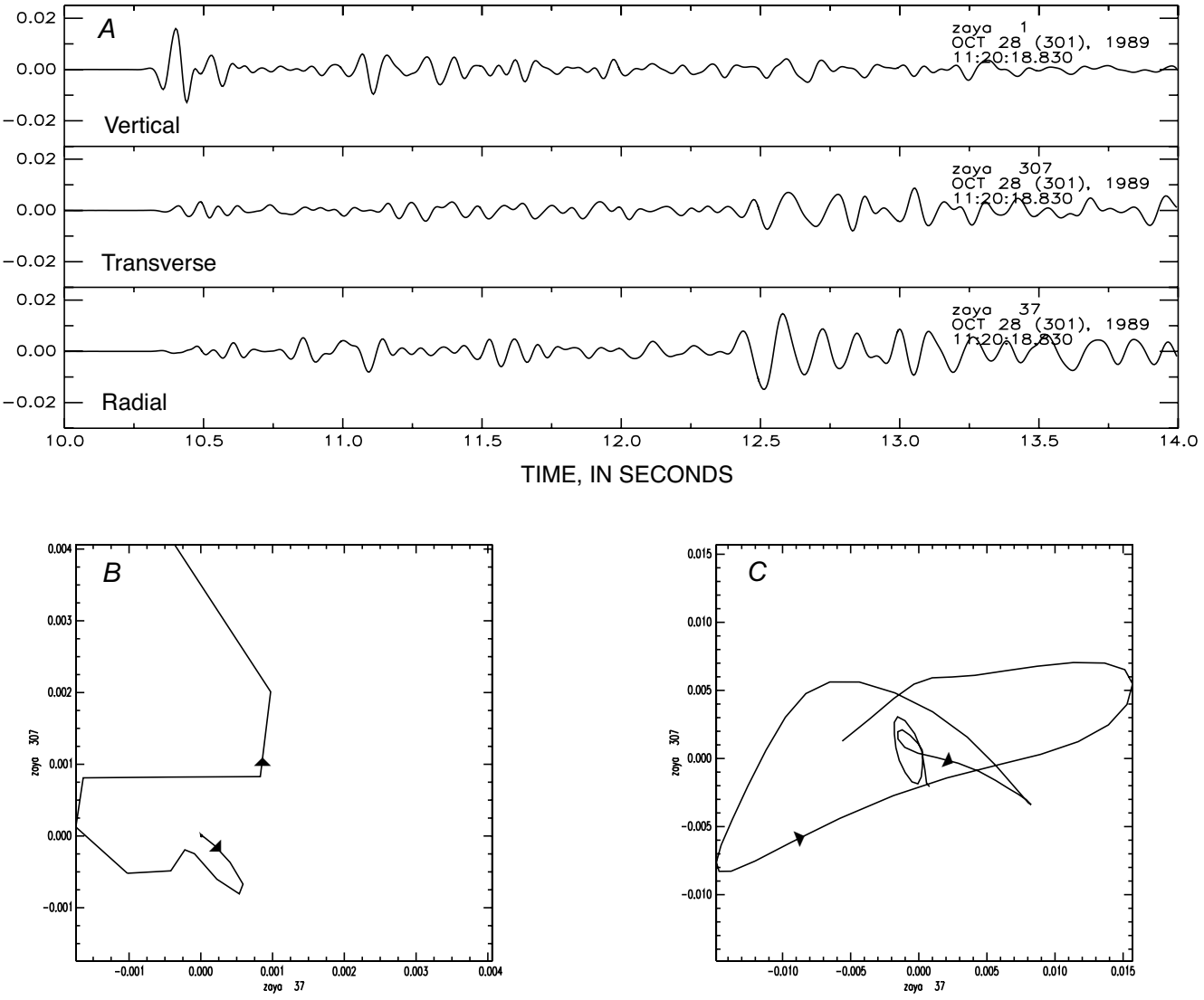

Figure 5.—Seismograph records from station ZAYA (fig. 1). *A*, *P*- and *S*-wave arrivals on vertical, radial, and transverse components from an event at lat 37°9.19′ N., long 122°4.06′ W., and 11.1-km depth. *B*, Radial-transverse particle-motion plot of direct *P* wave for a time window between 10.25 and 10.50 s. Note that azimuth of *P* wave is not along station-epicenter line. *C*, Radial-transverse particle-motion plot of direct *S* wave for a time window between 12.35 and 12.6 s. Note that initial particle motion is along same azimuth as direct *P* wave. Around 12.5 s, direct *S* wave arrives with a particle motion orthogonal to azimuth of initial phase, which is identified as *S*-to-*P* conversion.

resolved than *P*-wave-velocity models (Eberhart-Phillips, 1989). Thus, variations in the *P*-wave-velocity model tend to be more extreme, whereas variations in the *S*-wave-velocity model tend to be damped, resembling more closely the initial model. As a result, inferred V_P/V_S ratios might not reflect constraints that the data do (or do not) place on the variations in V_P/V_S ratio, but rather would tend to be controlled simply by the perturbation in *P*-wave velocity. If, instead, we invert directly for three-dimensional perturbations in V_P/V_S ratio, the solution will produce a relatively faithful representation of significant variations in V_P/V_S ratio where the data require it (and it is resolved), and elsewhere V_P/V_S ratios will be unperturbed, owing either to absence of heterogeneity or absence of resolution.

INVERSION TESTS

We made some tests to assess the need for a three-dimensional model to satisfy the data, and to examine the sensitivity of our results to the initial model (*P*-wave-velocity structure and corresponding hypocenters). Inversions for a one-dimensional (that is, vertically varying) model resulted in a structure with high near-surface and low midcrustal

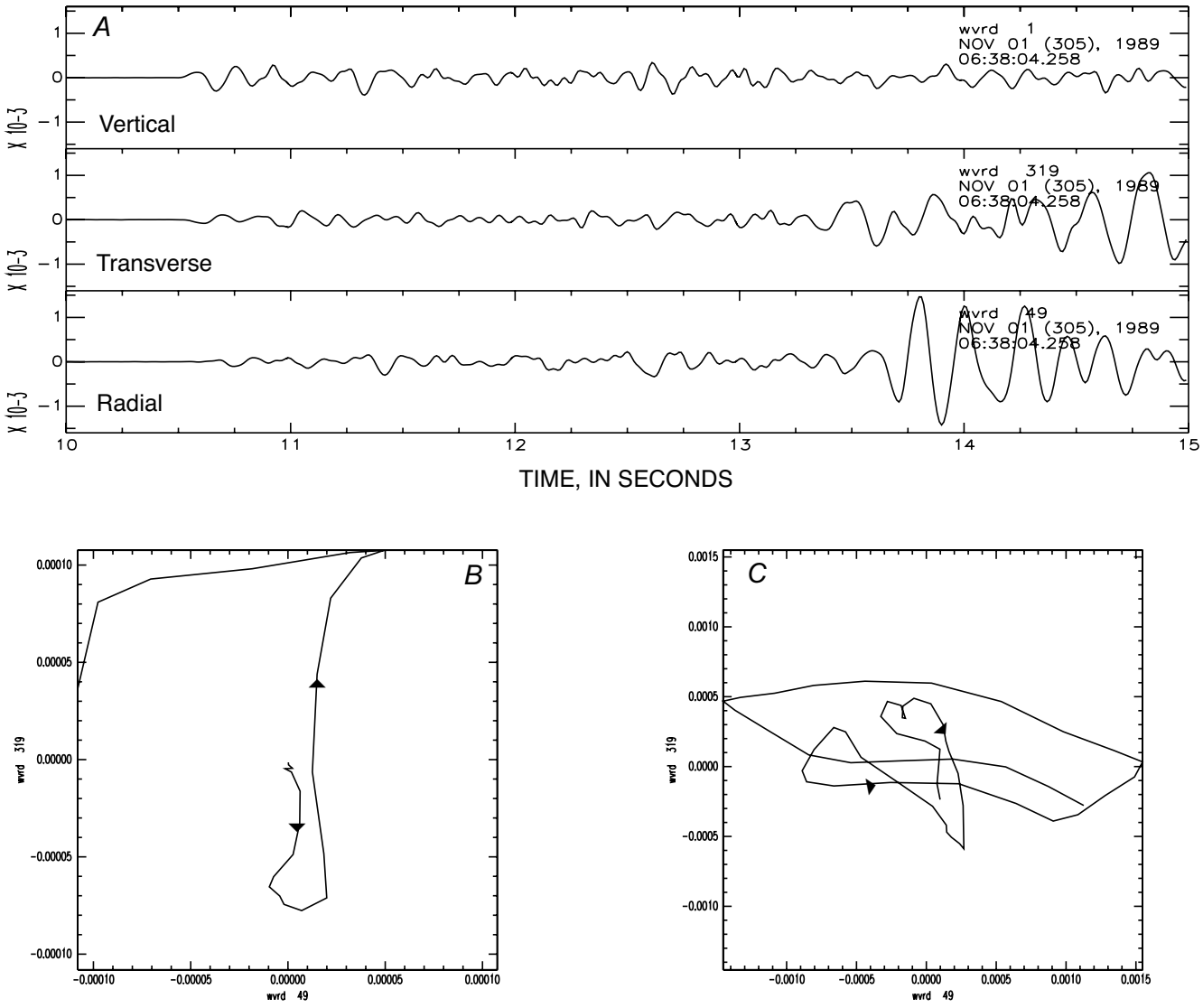

Figure 6.—Seismograph records from station WVRD (fig. 1). *A*, *P*- and *S*-wave arrivals on vertical, radial, and transverse components from an event at lat 37°2.32′ N., long 121°49.02′ W., and 4.0-km depth. *B*, Radial-transverse particle-motion plot of direct *P* wave for a time window between 10.40 and 10.80 s. *C*, Radial-transverse particle-motion plot of direct *S* wave for a time window between 13.35 and 14.00 s. Note that initial particle motion is along nearly the same azimuth as direct *P* wave. Near 13.70 s, direct *S* wave arrives with a particle-motion orthogonal to azimuth of initial phase, which is identified as *S*-to-*P* conversion.

V_P/V_S ratios (table 1). Including station corrections in the one-dimensional inversion resulted in a sharp reduction in the perturbation of near-surface V_P/V_S ratios and insignificant changes elsewhere. In both one-dimensional cases, variance reduction was less than 30 percent. Variance reduction should be significantly greater for a three-dimensional model to be justified.

We also examined the sensitivity of the inversion to the initial hypocenters and *P*-wave-velocity model. Preliminary three-dimensional V_P/V_S models were determined initially with a modest-size data set (31 earthquakes, 269 *S*–*P* times), using both the "three-dimensional initial" (Eberhart-Phillips and others, 1990) and "two-dimensional initial" (Dietz and Ellsworth, 1990) velocity models and corresponding hypocenters. The pattern of features in the two solutions were quite similar, but the "three-dimensional initial" velocity model yielded a slightly superior data fit (root-mean-square [rms] *S*–*P* time residual of 0.13 versus 0.14 s, from initial values of 0.20 and 0.21 s, respectively), with a lower rms amplitude of model perturbations (rms $\Delta(V_P/V_S)$ of 0.09 versus 0.11) relative to the "two-dimensional initial" velocity model. Thus, we adopt the "three-dimensional initial" velocity model as our preferred initial model and confine our discussion below to results derived from that model.

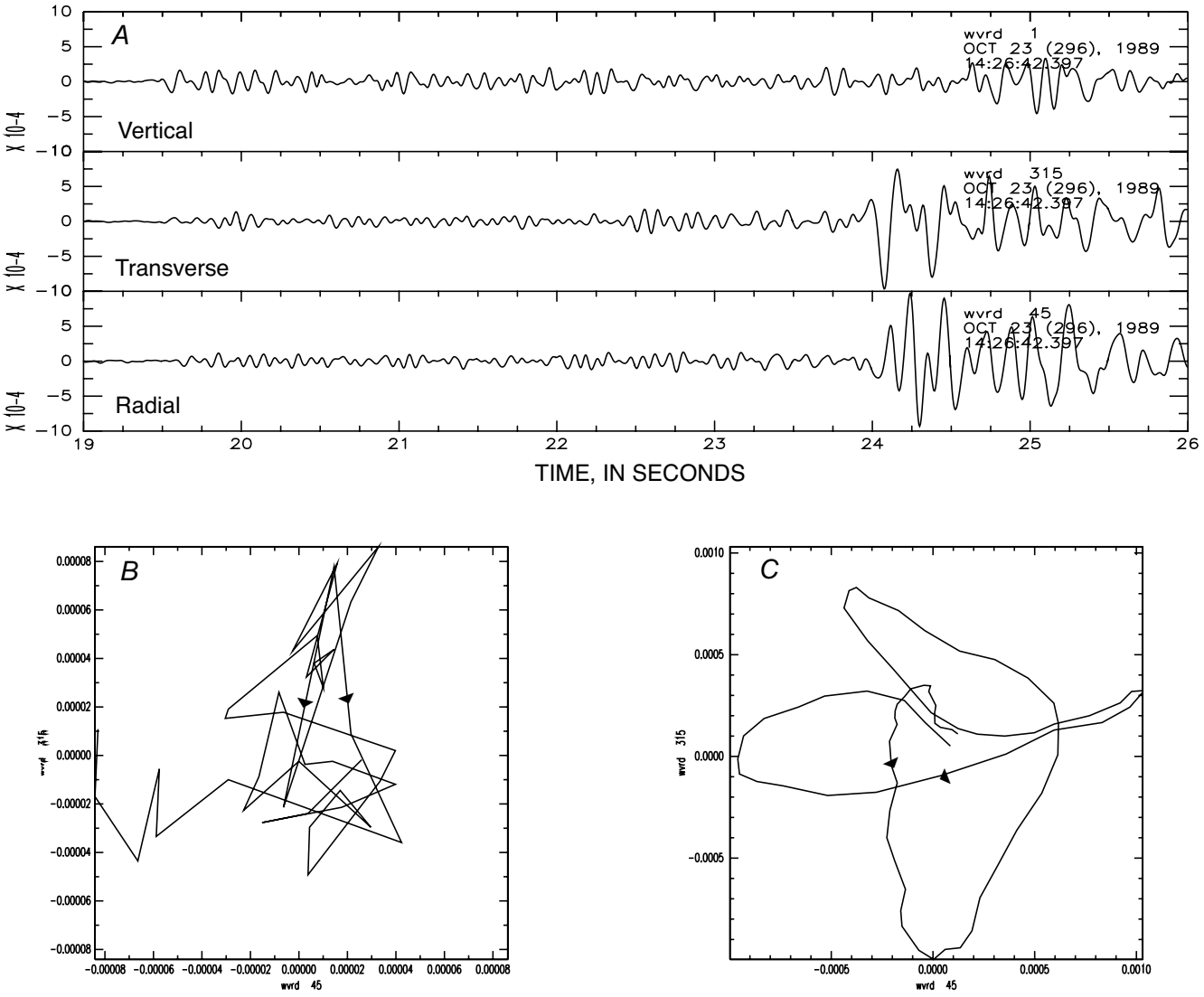

Figure 7.—Seismograph records from station WVRD (fig. 1). *A*, *P*- and *S*-wave arrivals on vertical, radial, and transverse components from an event at lat 36°57.35′ N., long 121°42.93′ W., and 13.4-km depth. *B*, Radial-transverse particle-motion plot of direct *P* wave for a time window between 19.45 and 19.65 s. *C*, Radial-transverse particle-motion plot of direct *S* wave for a time window between 23.95 and 24.35 s. Note that initial particle-motion is along nearly the same azimuth as direct *P* wave. Around 24.25 s, direct *S* wave arrives with a particle motion orthogonal to azimuth of initial phase, which is identified as *S*-to-*P* conversion.

Systematic errors in the initial *P*-wave-velocity model may still be propagated into biased perturbations in V_P/V_S ratio. The comparison above of two different sets of initial velocity models and their corresponding hypocenters suggests that our inversion is reasonably robust. The study by Schwartz and Nelson (1991) also indicates good stability of hypocenters, whether they are determined with *P*-wave-arrival times only (Calnet data) or *S*–*P* arrival times only (PASSCAL data), and whether a two-dimensional (Dietz and Ellsworth, 1990) or three-dimensional (Eberhart-Phillips and others, 1990) velocity model is used (both assuming a constant V_P/V_S ratio).

RESULTS OF THREE-DIMENSIONAL INVERSION

The results of the three-dimensional inversion from our complete *S*–*P* data set (128 earthquakes, 1,054 *S*–*P* times) are plotted in figure 10. Estimated V_P/V_S ratios range from 1.57 to 2.00, corresponding to a range of Poisson's ratios from 0.16 to 0.35. Note that these variations are significant relative to the uncertainty in V_P/V_S ratio of about 3 percent estimated from the inversion, corresponding to an uncertainty in V_P/V_S ratio about 0.05. This inversion used an initial V_P/V_S ratio of 1.75; using an initial V_P/V_S ratio of 1.80 resulted

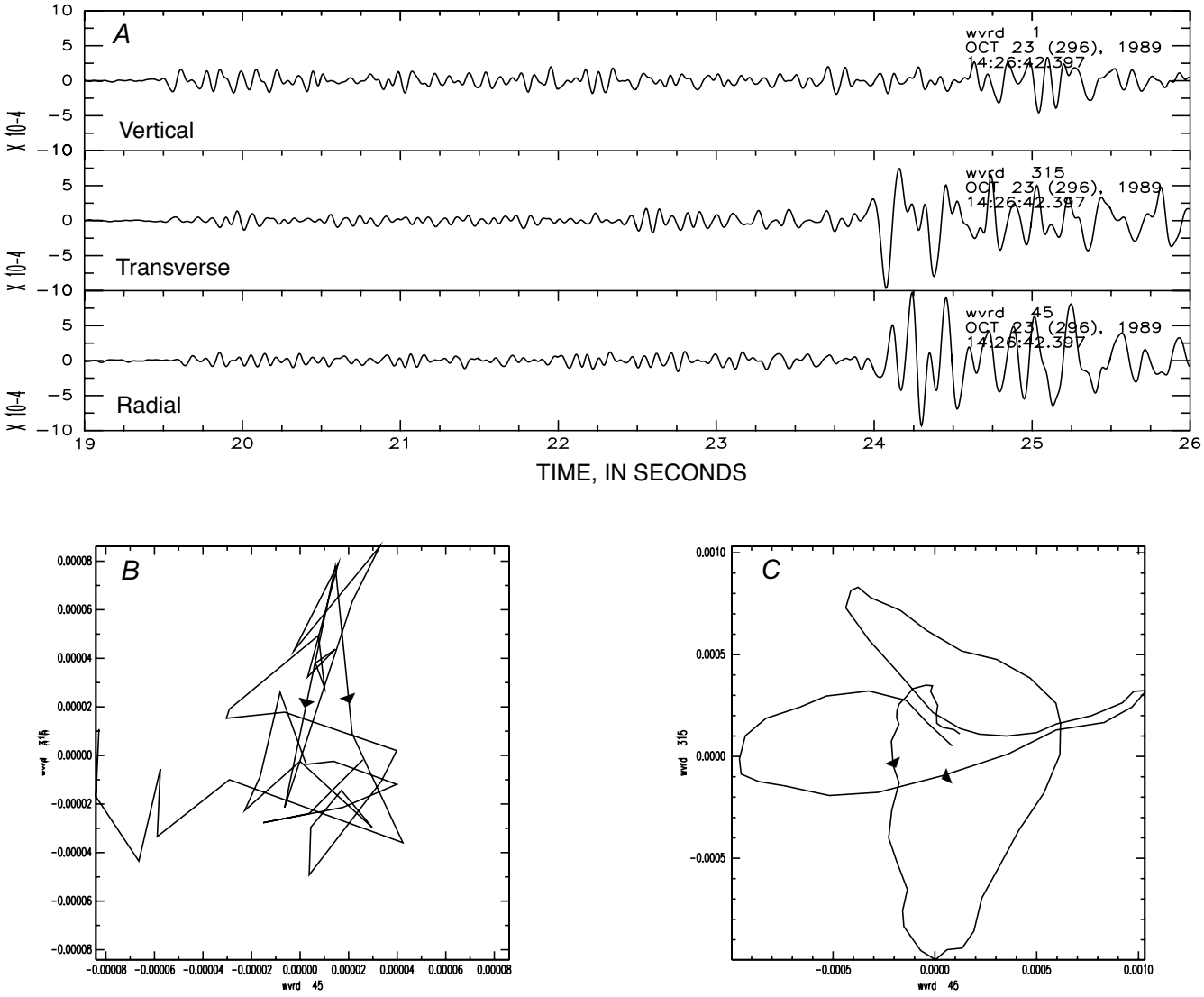

Figure 8.—Seismograph records from station WAWA (fig. 1). *A*, *P*- and *S*-wave arrivals on vertical, radial, and transverse components from an event at lat 37°10.95′ N., 121°58.56′ W., and 2.2-km depth. *B*, Radial-transverse particle-motion plot of direct *P* wave for a time window between 20.20 and 20.40 s. *C*, Radial-transverse particle-motion plot of direct *S* wave for a time window between 22.45 and 22.65 s. Note that initial particle motion is along nearly the same azimuth as direct *P* wave. Around 22.57 s, direct *S* wave arrives with a particle motion orthogonal to azimuth of initial phase, which is identified as *S*-to-*P* conversion.

in a solution that differed by no more than 0.02 from the model shown. We also performed a three-dimensional inversion with station corrections. As expected, the resulting V_P/V_S model differed significantly only in the near-surface grid layer, where most perturbations were cut approximately in half. Surprisingly, despite the greater number of parameters, the variance reduction of less than 60 percent was somewhat less than that for the three-dimensional inversion without station corrections (64 percent). Thus, we have adopted the three-dimensional model without station corrections as our best model.

In the shallow subsurface (layer 2, fig. 10*B*), V_P/V_S ratios are generally high (min 1.80), especially along the San Andreas fault zone. This result is not surprising because near-surface rocks typically have high V_P/V_S ratios (Nicholson and Simpson, 1985), owing in part to extensive microcracks (O'Connell and Budiansky, 1974). Two areas are exceptions: just west of the San Andreas fault, near stations OLSP (x=−5 km, y=0 km; V_P/V_S=1.57) and WAWA (x=−15 km, y=−10 km; V_P/V_S=1.67); and just east of the Sargent fault where it merges with the San Andreas fault, near stations WVRD and SAOS (x=2 km, y=−10 km; V_P/V_S=1.68) (see fig. 1 for locations). At shallow depths (layer 3, fig. 10*C*), V_P/V_S ratios are persistently high, though somewhat varying, along the San Andreas fault. A downward continuation of anomalously low V_P/V_S ratios also occurs at stations OLSP and WAWA.

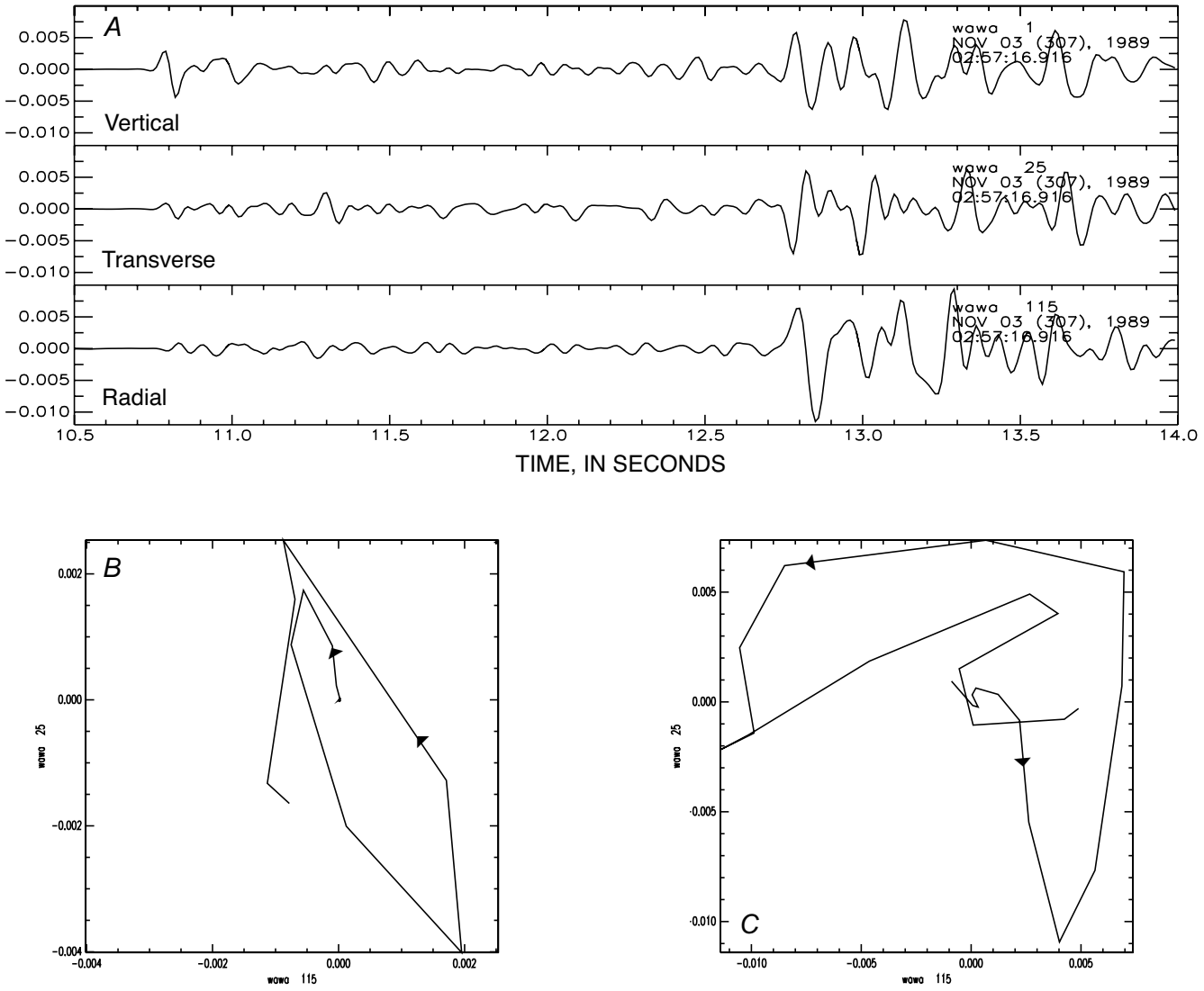

Figure 9.—Seismograph records from station WAWA (fig. 1). *A*, *P*- and *S*-wave arrivals on vertical, radial, and transverse components from an event at lat 37°9.46′ N., long 122°0.20′ W., and 10.10-km depth. *B*, Radial-transverse particle-motion plot of direct *P* wave for a time window between 10.70 and 10.90 s. *C*, Radial-transverse particle-motion plot of direct *S* wave for a time window between 12.7 and 12.90 s. Note that initial particle motion is along nearly the same azimuth as direct *P* wave. Around 12.84 s, direct *S* wave arrives with a particle motion orthogonal to azimuth of initial phase, which is identified as *S*-to-*P* conversion.

Table 1.— *One-dimensional V_P/V_S model without station corrections*

Node depth (km)	V_P/V_S ratio	Diagonal resolution	Uncertainty (percent)
0	1.95	0.88	5
3	1.77	.96	3
7	1.71	.97	3
11	1.71	.97	3
16	1.62	.91	4
24	1.79	.14	5

Table 2.—*Depth distribution of aftershocks used for inversion.*

Depth range (km)	Number of events
0–3	4
3–7	22
7–11	44
11–16	59
16–24	11

Layer 4 (fig. 10*D*) displays only one feature that we view as significant. An area of moderately high V_P/V_S ratio (1.80–1.87) is present along and just southwest of most of the San Andreas fault (x=−5 to 2 km, y=−20 to 0 km). Good model resolution becomes fairly restricted to the immediate vicinity of the seismically active fault-zone area in layer 5 (fig. 10*E*), and so we have little information on the V_P/V_S structure northeast of the San Andreas fault. However, we do find a pattern of low V_P/V_S ratios along and southwest of most of the San Andreas fault, in sharp contrast to the high V_P/V_S ratios along the fault at shallower depths. In layer 6 (fig. 10*F*), good resolution is quite limited; however, a strong V_P/V_S-ratio low occurs in the area just northwest of the main-shock epicenter (x=−5 km, y=−10 to 0 km; V_P/V_S=1.55–1.69).

Rows of the resolution matrix for selected nodes of our model are listed in tables 3 through 6. The patterns are quite typical: resolution is highest for the diagonal element, with two or three neighboring nodes having resolutions a factor of 2 to 5 smaller and the other nodes having resolutions a factor of 8 to 10 smaller or even less. We consider the model resolution to be quite satisfactory.

DISCUSSION

Our results indicate significant variations in V_P/V_S ratio laterally and with depth throughout the study area (fig. 1). We note that the V_P/V_S ratios in layer 2 (0-km depth, fig. 10*B*), layer 3 (3-km depth, fig. 10*C*), layer 4 (7-km depth, fig. 10*D*), layer 5 (11-km depth, fig. 10*E*), and layer 6 (16-km depth, fig. 10*F*) vary by 27, 15, 12, 7, and 17 percent, respectively. Previous studies have shown that V_P/V_S ratios are sensitive to pore-fluid pressure and crack or pore geometry, and are influenced by the distribution of crack aspect ratios (Tatham, 1982). V_P/V_S ratios in crystalline rocks, which are known to have significant porosity, are strongly affected by the degree of flatness of the cracks because *S*-wave velocity is more sensitive to aspect ratio than is *P*-wave velocity (Tatham, 1982). In sedimentary rocks, composition more than crack geometry may be the dominant factor in controlling the V_P/V_S ratio (Wilkens and others, 1984). V_P/V_S ratios are also influenced by confining pressure, pore pressure, pore-fluid saturation, and to a lesser degree, temperature. V_P/V_S ratios decrease with depth as microcracks close under increasing confining pressures (Nur and Simmons, 1969; O'Connell and Budiansky, 1974) because *S*-wave velocity increases faster than *P*-wave velocity, owing to closure of microcracks at depth. Studies suggest that most microcracks in crustal rocks close when confining pressures reach 1 to 2 kbars (at 3.5–7-km depth) and that further increases in pressure with depth have little effect on the V_P/V_S ratio (Wilkens and others, 1984). Thus, below 6- or 7-km depth, the composition and mineralogy of the rock strongly influences the V_P/V_S ratio.

For shallow crustal rocks, composition can still significantly affect inplace V_P/V_S ratios. In particular, laboratory studies show that free quartz has a low Poisson's ratio (0.077; Simmons and Wang, 1971)—that is, a V_P/V_S ratio of 1.48—and that even the bulk Poisson's ratio of a rock containing 20 to 40 volume percent free quartz is relatively low (Ukawa and Fukao, 1981). Kern and Richter (1981) and Christensen and Wepfer (1989) also concluded that quartz-rich rocks have low Poisson's ratios but that feldspar-rich rocks have high Poisson's ratios.

Clearly, V_P/V_S ratios depend on several factors, and the variation in V_P/V_S ratio in rocks is due to one or more these factors. The variations in V_P/V_S ratio for different rock types overlap, and so it is difficult to assign a unique V_P/V_S ratio to a given rock type. Thus, additional information is also necessary, such as independently estimated *P*-wave-velocity structure, as well as surface and subsurface geologic and geophysical information. The independently estimated *P*-wave-velocity structure in the study area (fig. 1; Eberhart-Phillips and others, 1990) also shows considerable variations in *P*-wave velocity laterally and with depth. We note that the *P*-wave velocities in layers 2, 3, 4, 5, and 6 of the model of Eberhart-Phillips and others (1990) vary by 57, 54, 12, 6, and 4 percent, respectively. This observation clearly shows that *P*-wave velocity varies significantly above 7-km depth. *P*-wave velocity, like V_P/V_S ratio, is sensitive to several factors, such as porosity, aspect ratio, pore-fluid composition, and fluid saturation. Thus, any interpretation of the geologic structure based only on *P*-wave velocity can be misleading

above 7-km depth. Below 7-km depth, however, lateral variations in *P*-wave velocity are significantly smaller (<12 percent) in the study area, probably because of closure of microcracks due to high confining pressures, resulting in a reduced influence of porosity and pore fluids. Thus, for 7-km depth and greater, *P*-wave velocity and V_P/V_S ratio together could provide some information about the mineralogy of the rock, whereas *P*-wave velocity alone might not.

The significance of V_P/V_S ratio as a diagnostic tool over *P*-wave velocity for geologic interpretation can be clearly noted below 10-km depth. In layer 5 (fig. 10*E*), the estimated *P*-wave-velocity structure of Eberhart-Phillips and others (1990) shows a mere 6-percent lateral variation in *P*-wave velocity, thus not providing much evidence about rock composition. In contrast, the V_P/V_S ratios clearly suggest that rocks with different mineralogies could be present at this depth. Studies by Molotova and Vassil'ev (1960), Press (1966), and Christensen (1989), however, indicate enough nonuniqueness in V_P/V_S ratios even for high *P*-wave velocities (below 7-km depth) that geologic interpretations based only on seismic-velocity information can be misleading. Thus, when making geologic interpretations in a region, it is crucial to incorporate information on (1) the density of specific rock types and their lateral variations, as inferred from gravity data; (2) the depth and position of rocks that produce anomalous magnetic fields, as inferred from magnetic data; and (3) surface geology. In combination with information from other geophysical and geologic investigations, variations in V_P/V_S ratio provide powerful diagnostic evidence regarding the geologic composition and structure of a region.

Magnetic and gravity anomalies in the study area (fig. 1), based on the maps by Brabb and Hanna (1981), Chuchel and Jachens (1990), and Jachens and Griscom (this chapter), are mapped in figures 11 and 12, respectively. These maps of geophysical anomalies are invaluable in our geologic interpretation.

Two conspicuous magnetic anomalies occur southwest of the San Andreas fault in the study area (fig. 1): near Boulder Creek and Corralitos (fig. 11). The Boulder Creek anomaly is a northwest-southeast-trending, elongate magnetic high with an amplitude of 120 γ between the Zayante and Butano faults, where Cenozoic sedimentary rocks are present at the surface. Magnetic-field gradients indicate that the source of the Boulder Creek anomaly is below about 1.5-km depth and may extend significantly deeper (Hanna and others, 1972). This magnetic high coincides with a region of average to high V_P/V_S ratios in layers 2, 3, and 4 (figs. 10*B*, 10*C*, and 10*D*, respectively) and is sandwiched between two north-south-striking gravity highs to the east and west (fig. 12). The Corralitos anomaly is somewhat more complex: two magnetic highs flank a magnetic low between the Zayante and San Andreas faults and a paired magnetic high and low southwest of the Zayante fault.

The Boulder Creek anomaly and the part of the Corralitos anomaly between the Zayante and the San Andreas faults resemble the Logan anomaly situated southeast of the study area (fig. 1). The Logan anomaly is associated with exposed quartz gabbro and anorthosite gabbro (Ross, 1970), which have relatively high densities (Clark and Rietman, 1973) and a strong normal magnetization (Brabb and Hanna, 1981). The map by Hanna and others (1981) also shows an outcrop of gabbro about 10 km southwest of the center of the Boulder Creek anomaly. A gabbroic source rock for the Boulder Creek and Corralitos anomalies that lies between the Zayante and San Andreas faults would also be consistent with the high V_P/V_S ratio of 1.81 to 2.0 in our model (V_P/V_S=1.84–1.96 for gabbro; Molotova and Vassil'ev, 1960; Press, 1966). A gravity low occurs over the magnetic high between the Zayante and San Andreas faults. The absence of a gravity high at the Corralitos anomaly may be due to the presence of a thick section of clastic marine sedimentary rocks at the surface (McLaughlin and others, 1988).

The magnetic low within the Corralitos anomaly southwest of the Zayante fault coincides with the regions of low V_P/V_S ratio in layers 2, 3, and 4 (figs. 10*B*, 10*C*, and 10*D*, respectively) and is close (2 km southeast) to an outcrop of granodiorite. Granodiorite also crops out in the Bald Mountains west-northwest of the magnetic low (Hanna and others, 1981). Thus, these granitoids are also present southwest of the Zayante fault. We note that the trace of the Zayante fault separates the low-V_P/V_S-ratio area to the southwest from the high-V_P/V_S-ratio area to the northeast in layer 2 (0-km depth, fig. 10*B*). The projection of the fault trace downward to layers 3 and 4 (figs. 10*C* and 10*D*, respectively) also shows a clear separation between the areas of low and high V_P/V_S ratio, suggesting that the Zayante fault extends downward to at least 7-km depth. A correlation of stratigraphic units in this area supports a downward extension of the Zayante fault to at least 6-km depth (R.J. McLaughlin, oral commun., 1992).

Granite and granodiorite commonly contain 20 to 40 volume percent quartz, a diamagnetic mineral, and so give rise to negative magnetic anomalies. The presence of quartz also helps to lower the V_P/V_S ratio of a rock. Laboratory studies on the granodiorite of Lakeside, Calif., yielded a V_P/V_S ratio of 1.54 (Press, 1966). Similarly, laboratory studies on the granodiorite of Weston, Mass., also yielded a V_P/V_S ratio of 1.54 (Birch and Bancroft, 1940); a study of the mineral composition of this granodiorite showed that it contained 33.5 volume percent quartz. The *P*-wave velocities in these two granodiorites were 4.88 and 4.78 km/s, respectively. The three-dimensional *P*-wave-velocity models of Eberhart-Phillips and others (1990) and Foxall and others (1993) at a depth (below mean sea level) of 3 km show *P*-wave velocities of 4.5 to 5.0 km/s southwest of the Zayante fault, similar to the *P*-wave velocities in granodiorite at very shallow depths, as cited above and elsewhere (Press, 1966). Thus, we interpret the anomalously low V_P/V_S ratios in layers 2, 3, and 4, (figs. 10*B*, 10*C*, and 10*D*, respectively), west of the Zayante fault, to be due to the presence of granodiorite and rocks of similar composition.

A second area of anomalously low V_P/V_S ratio is present in layer 2 (0-km depth, fig. 10*B*), just northeast of the Sargent fault. The area is underlain by a zone of average to high V_P/V_S

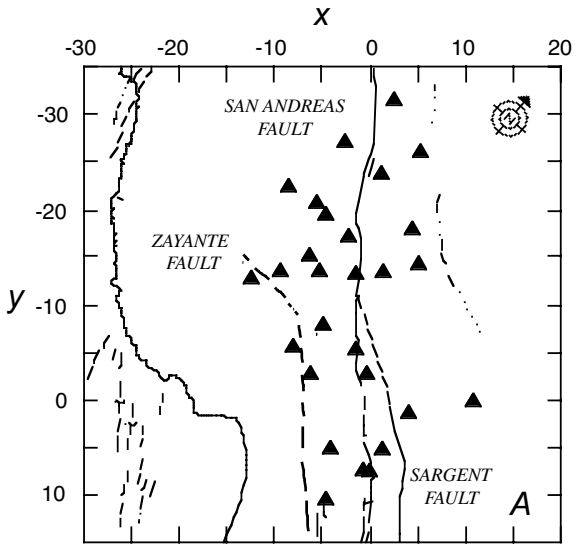
x
y
SAN ANDREAS FAULT
ZAYANTE FAULT
SARGENT FAULT
A

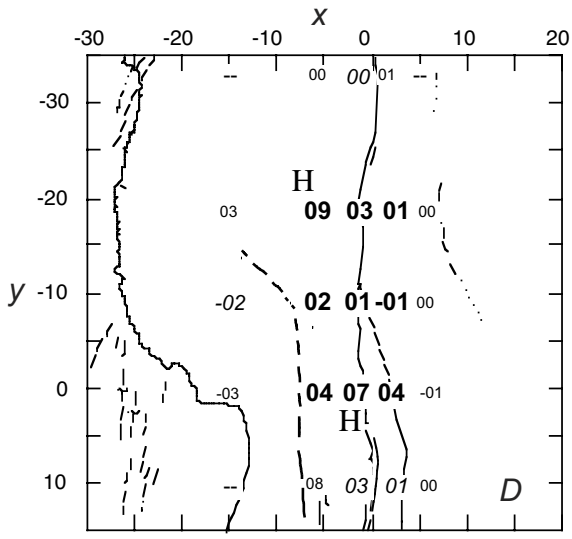
x
y
H
09 03 01
02 01 -01
04 07 04
H
D

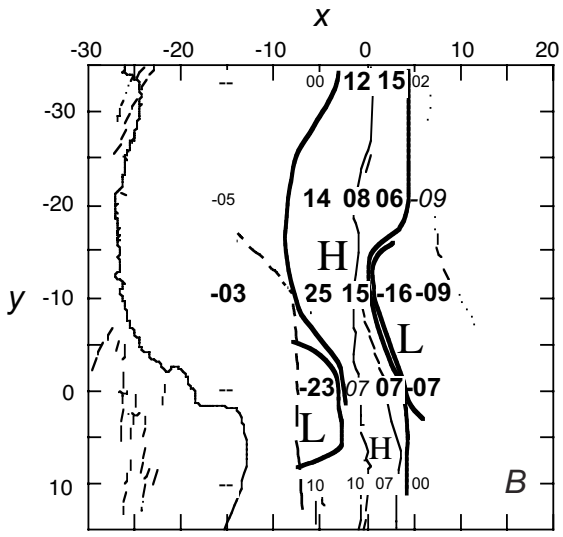
x
y
12 15
14 08 06 -09
H
-03
25 15 -16 -09
L
-23 07 07 -07
L
H
B

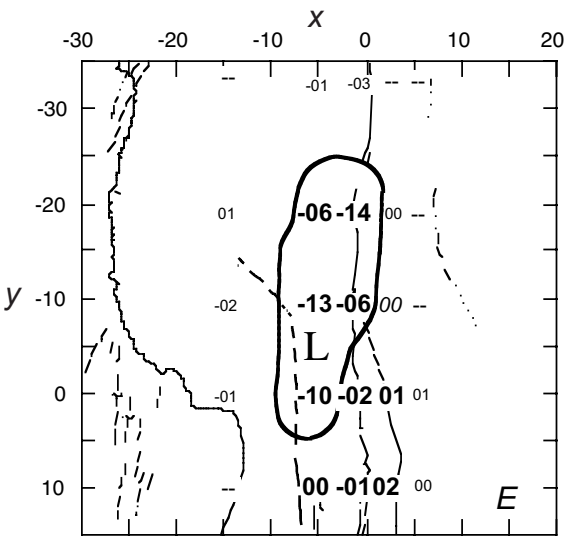
x
y
-06 -14
-13 -06
L
-10 -02 01
00 -01 02
E

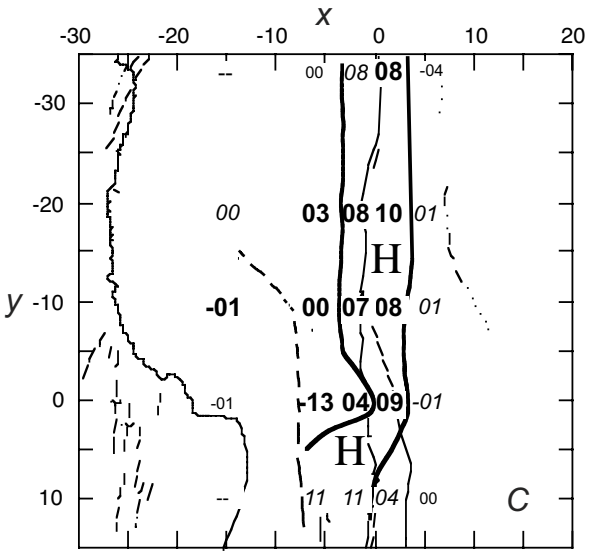
x
y
08 08
03 08 10
H
-01
00 07 08
-13 04 09
H
C

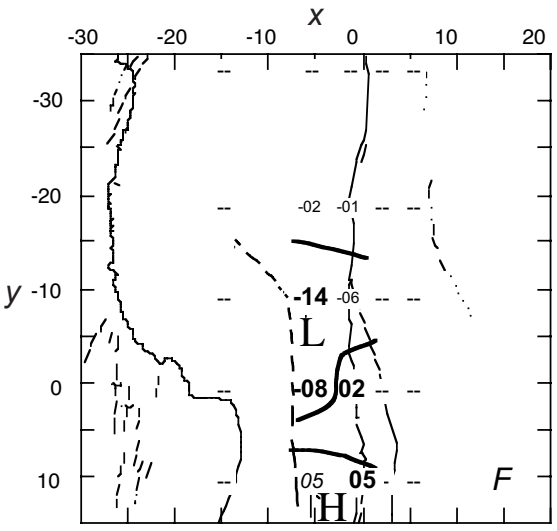
x
y
-14 -06
L
-08 02
H
F

Table 3.—*Resolution matrix for layer 2 node of three-dimensional inversion model.*

[Diagonal element is listed in bold]

0.0000	-0.0078	-0.0124	0.0123	-0.0037
-.0098	-.0500	.0414	-.0468	-.0266
-.0128	.0373	**.5108**	-.0018	-.0309
.0000	-.0648	.1139	.0068	-.0265
.0000	-.0054	-.0211	-.0251	.0000
.0000	.0000	-.0113	-.0002	.0000
-.0040	-.0081	-.0065	-.0052	.0453
-.0145	-.0378	.1685	.0248	.0038
.0000	-.0144	.0296	.0107	.0008
.0000	-.0054	-.0164	-.0276	.0000
.0000	.0000	-.0052	-.0011	.0000
.0027	.0186	.0192	-.0029	.0000
-.0047	.0268	.0204	-.0208	-.0033
.0000	.0251	.0085	.0237	.0039
.0000	.0070	.0015	.0016	.0000
.0000	.0000	.0006	.0000	.0000
.0000	.0049	.0101	-.0002	.0000
-.0017	.0131	-.0016	.0275	.0000
.0000	-.0019	.0013	-.0058	.0000
.0000	.0017	-.0001	.0021	.0000
.0000	.0000	.0000	.0000	.0000
.0000	.0002	.0007	.0000	.0000
.0000	.0005	-.0050	.0000	.0000
.0000	-.0005	.0048	.0000	.0000
.0000	.0023	.0060	.0000	.0000

ratio in layer 3 (fig. 10*C*). This low-V_P/V_S-ratio region coincides with a magnetic low and a moderate gravity high. These observations are consistent with the geologic interpretation by R.J. McLaughlin (oral commun., 1990) that this area has a 2- to 3-km-thick near-surface layer of quartz-rich sandstone underlain by underthrust ophiolitic basement. Studies by Christensen (1989) show that the Poisson's ratio of the Mount Simon and St. Simon sandstones of northern Illinois can be as low as 0.185 and 0.142, respectively, under moderate (1–2 kbars) confining pressures, corresponding to V_P/V_S ratios of 1.61 and 1.55. Sample mineralogic descriptions of these two rocks show that the Mount Simon sandstone contains 84 volume percent quartz and the St. Simon sandstone 91 volume percent quartz. Both of these rocks have a porosity of 8 to 9 percent and were from a depth of only 670 m. Here, the high quartz content of the rocks seems to control

◄ Figure 10.—Results of three-dimensional inversion. *A*, Schematic map of study area in Loma Prieta region, Calif. (fig. 1), showing locations of PASSCAL, University of California, Berkeley, and GEOS stations (triangles) and mapped faults for reference. *y*-axis of grid is rotated 41° west of north, following three-dimensional model of Eberhart-Phillips and others (1990). *B–F*, Final V_P/V_S ratios for model nodes in grid layers 2 through 6 at depths of 0, 3, 7, 11, and 16 km, respectively. Grid layer at 24-km depth was totally unresolved, and so no results are plotted for that layer. H, high; L, low. *x*- and *y*-axes in kilometers. Resolution of V_P/V_S ratio: large numbers, >0.45; medium-size numbers, 0.15–0.45; small numbers, <0.15. Contour interval, 0.10; dashed where resolution is poor. Lateral node spacing ranges from 3 to 15 km across strike (northeast-southwest) and from 10 to 15 km along strike (northwest-southeast) of the San Andreas fault. Variance reduction for single-step inversion, 64 percent, with a root-mean-square perturbation of 0.09 and an average estimated error of 3 percent for moderately well resolved nodes (diagonal element >0.15). Depth distribution of events is listed in table 2.

Table 4.—*Resolution matrix for layer 3 node of three-dimensional inversion model.*

[Diagonal element is listed in bold]

0.0000	0.0000	-0.0037	-0.0010	-0.0011
-.0070	-.0239	.0053	-.0041	-.0023
-.0162	.0392	-.0144	-.0039	-.0004
.0000	.2741	-.0215	-.0061	.0038
.0000	-.0029	-.0068	-.0009	.0000
.0000	.0000	-.0048	-.0012	.0000
.0108	-.0049	.0103	.0008	.0009
-.0548	.0130	-.0182	.0038	.0020
.0000	**.5955**	.0428	-.0178	.0038
.0000	-.0053	-.0125	-.0071	.0000
.0000	.0000	-.0012	.0002	.0000
.0060	.0056	.0005	-.0026	.0000
-.0144	-.0218	-.0038	.0069	.0003
.0000	.1529	.0713	.0004	-.0008
.0000	.0704	.0239	-.0014	.0000
.0000	. 0000	.0003	.0000	.0000
.0000	.0064	-.0025	-.0003	.0000
.0053	.0301	.0059	.0060	.0000
.0000	-.0330	-.0399	-.0156	.0000
.0000	.0143	.0177	-.0049	.0000
.0000	.0000	.0000	.0000	.0000
.0000	-.0054	.0005	.0000	.0000
.0000	-.0146	-.0054	.0000	.0000
.0000	.0268	.0067	.0000	.0000
.0000	.0035	.0170	.0000	.0000

the Poisson's ratio. Similarly, the high quartz content of the sandstone in the study area (fig. 1) appears to dominate the V_P/V_S ratios.

The V_P/V_S ratios in layer 2 (0-km depth, fig. 10*B*) range from 1.80 to 2.0. A correlation with the surface-geology map by Brabb and Hanna (1981) shows that the V_P/V_S ratio of 2.00 at x=−5 km, y=−10 km, occurs about 4 km southwest of outcrops of diabase and gabbro in contact with outcrops of serpentinite and Franciscan rocks. Similarly, the V_P/V_S ratios of 1.95 at x=−5 km, y=−20 km, of 1.91 at x=0 km, y=−10 km, and of 1.82 at x=0 km, y=−20 km, occur very close to (within 5 km of) outcrops of serpentinite and diabase. The outcrops of serpentinite and diabase near the nodes at x=−5 km, y=−10 km, and at x=0 km, y=−10 km, are surrounded by a thick section of Tertiary marine sedimentary rocks. The gravity low visible in figure 12, which extends from y=10 km to y=−10 km near x=−5 km, marks approximately the boundary of this sedimentary section. The outcrops of serpentinite and diabase near the nodes at x=0 km, y=−20 km, and at x=5 km, y=−20 km, are also surrounded by sedimentary rocks with *P*-wave velocities of 3.5 to 4.5 km/s (Eberhart-Phillips and others, 1991). The V_P/V_S ratios of diabase from eastern Siberia and from Centerville, Va., for example, range from 1.8 to 2.3. Similarly, the V_P/V_S ratios of serpentinite range from 2.0 to 2.1 (Press, 1966). Samples of serpentinite collected near Loma Prieta by N.I. Christensen (written commun., 1991) have a V_P/V_S ratio of 1.93 to 1.95 over a depth range of 0 to 3 km. Both diabase and serpentinite are rich in ferromagnetic minerals, and so a magnetic contribution to the Boulder Creek anomaly due to these outcrops and their subsurface extensions (if they exist) is possible. The range in V_P/V_S ratio of 1.8 to 2.0 for this area is also consistent with the V_P/V_S ratios of sedimentary rocks.

Comparing our model with those of Eberhart-Phillips and others (1990) and Foxall and others (1993) for layer 2 (0-km depth, fig. 10*B*), we note that a region of lower *P*-wave velocities (~4.0–4.5 km/s) in their models coincides with the high V_P/V_S ratios between y=10 km and y=−10 km near x=0 km in our model. This lower-*P*-wave-velocity region corresponds to the thick section of Tertiary marine sedimentary rocks. The *P*-wave velocities in a serpentinite and a diabase at shallow (<1 km) depths, however, were determined to range from 5.5 to 5.9 km/s and from 6.2 to 6.8 km/s, respectively

Table 5.—*Resolution matrix for layer 5 node of three-dimensional inversion model.*

[Diagonal element is listed in bold]

0.0000	0.0000	0.0031	0.0048	-0.0002
.0045	.0134	.0146	.0077	-.0031
-.0092	.0184	.0131	.0036	.0004
.0000	.0049	-.0020	.0054	.0060
.0000	.0001	.0005	.0000	.0000
.0000	.0000	.0037	.0030	.0000
.0090	.0182	-.0110	-.0043	-.0049
-.0068	-.0405	.0131	-.0026	.0042
.0000	.0301	.0000	.0013	-.0014
.0000	.0005	.0013	.0006	.0000
.0000	.0000	-.0009	-.0015	.0000
-.0062	-.0203	.0006	.0011	.0000
.0189	.1401	-.0316	.0021	.0005
.0000	-.0357	-.0127	.0006	-.0024
.0000	.0066	.0053	-.0009	.0000
.0000	.0000	-.0024	.0000	.0000
.0000	.0195	-.0103	-.0006	.0000
.0146	**.7302**	.0498	-.0156	.0000
.0000	.0037	-.0190	-.0057	.0000
.0000	-.0107	-.0079	.0025	.0000
.0000	.0000	.0000	.0000	.0000
.0000	.0290	.0015	.0000	.0000
.0000	.1935	.0161	.0000	.0000
.0000	.0258	.0121	.0000	.0000
.0000	-.0062	.0090	.0000	.0000

(Birch, 1960). The *P*-wave-velocity models of Eberhart-Phillips and others (1990) and Foxall and others (1993) do not show these variations in *P*-wave velocity in the near-surface rocks. Thus, the sedimentary section is apparently contributing significantly more to the high V_P/V_S ratios in layer 2, and so the contribution from the outcrops of serpentinite and diabase may be mostly confined to affecting the magnetic anomalies only. Notwithstanding, the low-V_P/V_S-ratio areas at x=2 km, y=−10 km, and at x=7 km, y=−10 km, in our model coincide with the higher-*P*-wave-velocity areas (4.5–5.2 km/s) in their models. The higher-*P*-wave-velocity area southwest of the San Andreas fault corresponds to outcrops of granodiorite and quartz diorite, which, because of their high quartz contents, can be expected to have lower V_P/V_S ratios, consistent with our results. The low-V_P/V_S-ratio area southwest of the Zayante fault in layer 3 (3-km depth, fig. 10*C*) probably indicates an extension of the granodiorite to depth. The corresponding *P*-wave velocity in this area ranges from 5.2 to 5.5 km/s (Eberhart-Phillips and others, 1990), within the expected range of *P*-wave velocities in granodiorites of 4.4 to 6.27 km/s at 0- to 3-km depth estimated from laboratory studies (Press, 1966). A broad high-V_P/V_S-ratio area also exists at 3-km depth along the San Andreas fault, consistent with the results of Eberhart-Phillips and others, who indicated the presence of high-*P*-wave-velocity rock at 3-km depth between the Sargent and San Andreas faults. They interpreted this rock to be a part of upthrust ophiolitic basement (presumably gabbro).

In layer 4 (7-km depth, fig. 10*D*), the V_P/V_S highs corresponding to the Boulder Creek and Corralitos anomalies are visible along the San Andreas fault, along with a low-V_P/V_S-ratio zone close to the coast. The presence of this low-V_P/V_S-ratio zone is consistent with the continued presence of such quartz-rich basement rocks as the quartz diorite, granodiorite, and granite that crop out on Ben Lomond and in the Bald Mountains to the northwest (Hanna and others, 1981). Below 7-km depth, V_P/V_S ratios are mostly average (1.72–1.77) to low (1.55–1.69). In particular, a distinct discontinuity is evident between 7- and 11-km depth that separates the high-V_P/V_S-ratio area along the fault zone that we have associated with shallower mafic rocks from the major V_P/V_S low visible in layer 5 (11-km depth, fig. 10*E*). This observation agrees quite well with the seismic-

Table 6.—*Resolution matrix for layer 6 node of three-dimensional inversion model.*

[Diagonal element is listed in bold]

0.0000	0.0000	0.0000	-0.0023	0.0009
-.0124	.0020	.0015	-.0013	.0024
.0105	.0011	-.0005	.0078	-.0013
.0000	.0008	.0191	.0090	.0016
.0000	.0036	.0069	.0035	.0000
.0000	.0000	-.0009	-.0015	.0000
-.0150	-.0036	.0008	.0001	-.0001
-.0017	.0019	-.0056	-.0002	-.0028
.0000	.0268	-.0030	-.0008	.0044
.0000	.0056	.0092	.0084	.0000
.0000	.0000	.0000	-.0007	.0000
-.0020	.0086	-.0018	.0020	.0000
.0114	-.0226	.0060	-.0023	.0005
.0000	-.0138	-.0018	-.0007	.0081
.0000	.0098	.0169	.0039	.0000
.0000	.0000	.0017	.0000	.0000
.0000	-.0150	-.0008	.0001	.0000
.0270	.0258	.0015	.0008	.0000
.0000	.1563	.0083	.0132	.0000
.0000	-.0794	-.0365	.0113	.0000
.0000	.0000	.0000	.0000	.0000
.0000	-.0263	-.0010	.0000	.0000
.0000	.1417	.0120	.0000	.0000
.0000	**.4937**	.0940	.0000	.0000
.0000	.0542	.0087	.0000	.0000

refraction studies by Fuis and Mooney (1990), who reported a midcrustal boundary at about 10-km depth, and by Foxall and others (1993), who also claim that rocks of different composition are present at 7- versus 11-km depth. However, the interpretation of a gneissic midcrust by Fuis and Mooney (1990) (V_P/V_S=1.75–1.94; Press, 1966) is inconsistent with the low V_P/V_S ratios (1.65–1.68) near the San Andreas fault between y=0 km and y=−20 km obtained in our study, but possibly consistent with the average V_P/V_S ratio (1.72–1.77) between y=0 km and y=10 km (fig. 10*E*). In any case, the V_P/V_S ratios between y=0 km and y=−20 km at 11- and 16-km depth are inconsistent with those typically observed for gabbro, which has been suggested by Foxall and others (1993) to be present at these depths. Our interpretation, based on V_P/V_S ratios, is that the midcrust in the study area (fig. 1) is composed mainly of granitic rocks; that is, it is a part of the Salinian block. Wide-angle seismic-reflection/refraction data obtained in the Loma Prieta region by Brocher and others (this chapter) showing that seismic velocities at 11- to 16-km depth range from 6.0 to 6.4 km/s also suggest that the rocks at these depths may be a part of the Salinian block.

In layer 6 (16-km depth, fig. 10*F*), we again observe a conspicuous V_P/V_S low along and southwest of the San Andreas fault near its intersection with the Sargent fault (fig. 10*F*), and possibly average to high V_P/V_S ratios slightly to the southeast. Resolution elsewhere at this depth is too poor to permit interpretation. Interestingly, these two anomalies bracket the 1989 Loma Prieta main-shock hypocenter, possibly indicating a major variation in rock type in the immediate vicinity of the main shock that may play a role in the mechanical behavior of the fault. One major goal of our future work will be to improve the model resolution within this depth range to determine the significance of these particular anomalies.

CONCLUSIONS

A model of the three-dimensional velocity structure along the Loma Prieta rupture zone indicates the presence of significant variations in V_P/V_S ratio both laterally and with depth. Our model can account for 64 percent of the original variation in S–P time (assuming a constant V_P/V_S ratio).

Using other geologic and geophysical information, we can interpret most of the anomalous features in our model. Two major findings are supporting evidence for the presence of mafic rocks at shallow depth along the fault zone (high V_P/V_S ratios) and for a crustal discontinuity at about 10-km depth (a transition from mostly high to mostly low V_P/V_S ratio with depth). Unanticipated V_P/V_S lows near the surface are accountable for by the presence of quartz-rich rocks. Our model supports the suggestion that the Zayante fault represents a major boundary to 7-km depth, with low V_P/V_S ratios (mostly granodiorite) to the southwest. Northeast of the San Andreas fault, a near-surface V_P/V_S anomaly supports the presence of a 2- to 3-km-thick sandstone sequence. At 16-km depth, a possible boundary between high- and low-V_P/V_S-ratio rocks coincides with the location of the Loma Prieta main-shock hypocenter. With additional data from recent USGS passive and active experiments in the Loma Prieta region, we expect to be able to improve the resolution of our image of the Loma Prieta rupture zone.

ACKNOWLEDGMENTS

This research was supported by U.S. National Science Foundation grants EAR–9011784 and EAR–9117464; computations at the University of Wisconsin-Madison's Geophysical and Polar Research Center computing facility were partly supported by U.S. National Science Foundation grant EAR–9019555. We thank Donna Eberhart-Phillips and Lynn Dietz for providing their *P*-wave-velocity models and event locations for our use; Bill Foxall and Susan Schwartz for sharing their data and ideas; Bob Jachens, Bob McLaughlin, and David Malone for helpful discussions; Bill Ellsworth and John Vidale for their reviews of the manuscript; Ray Wells for seeing the chapter to completion; and the IRIS Data Management Center staff for assistance in accessing the PASSCAL data.

REFERENCES CITED

Bakun, W.H., and McLaren, Marcia, 1984, Microearthquakes and the nature of the creeping-to-locked transition of the San Andreas fault zone near San Juan Bautista, California: Seismological Society of America Bulletin, v. 74, no. 1, p. 235–254.

Babuska, Vladislav, and Cara, Michel, 1991, Seismic anisotropy in the earth (Modern Approaches in Geophysics, v. 10): Dordrecht, Kluwer, 217 p.

Birch, A.F., 1960, The velocity of compressional waves in rocks to 10 kilobars: Journal of Geophysical Research, v. 65, no. 4, p. 1083–1102.

Birch, A.F., and Bancroft, Dennison, 1940, New measurements of the rigidity of rocks at high pressure: Journal of Geology, v. 48, no. 7, p. 752–766.

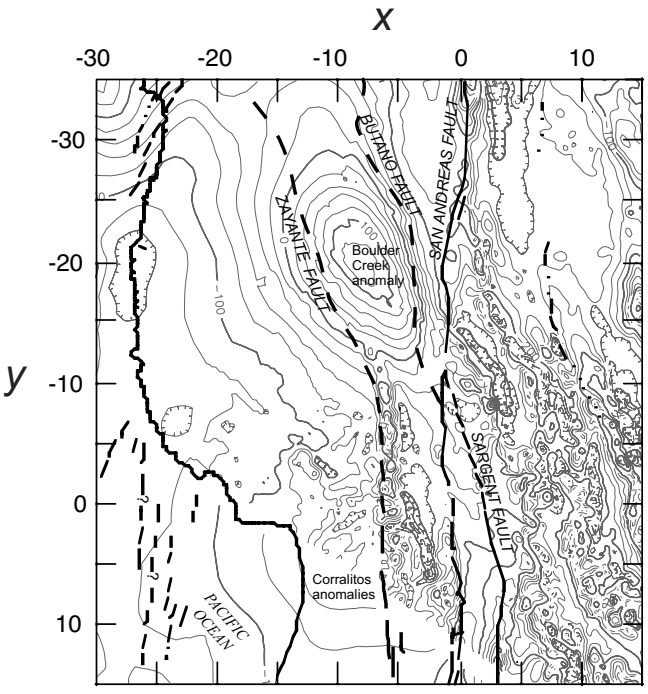

Figure 11.—Magnetic-anomaly map of study area in Loma Prieta region, Calif. (see fig. 1 for location), based on map by Brabb and Hanna (1981) and Jachens and Griscom (this chapter). *x*- and *y*-axes in kilometers; contour values in gammas.

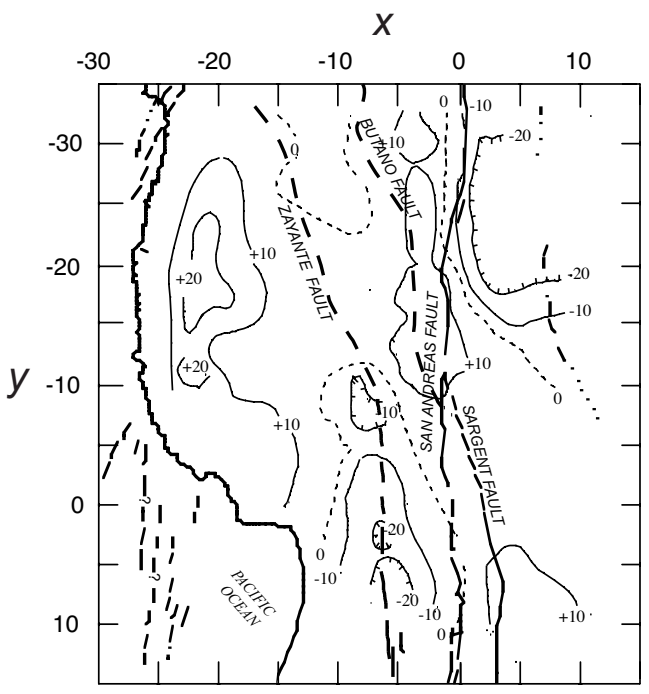

Figure 12.—Isostatic-gravity-anomaly map of study area in Loma Prieta region, Calif. (see fig. 1 for location), based on map by Chuchel and Jachens (1990). *x*- and *y*-axes in kilometers; contour values in milligals.

Brabb, E.E., and Hanna, W.F., 1981, Maps showing aeromagnetic anomalies, faults, earthquake epicenters, and igneous rocks in the southern San Francisco Bay region, California: U.S. Geological Survey Geophysical Investigations Map GP–932, sale 1:125,000, 3 sheets.

Christensen, N.I., 1989, Pore pressure, seismic velocities, and crustal structure, chap. 32 *of* Pakisev, L.C., and Mooney, W.D. eds., Geophysical framework of the continental United States: Geological Society of America Memoir 172, p. 783–798.

Christensen, N.I., and Wepfer, W.W., 1989, Laboratory techniques for determining seismic velocities and attenuations, with applications to the continental lithosphere, chap. 7 *of* Pakiser, L.C., and Mooney, W.D., eds., Geophysical framework of the continental United States: Geological Society of America Memoir 172, p. 91–101.

Chuchel, B.A., and Jachens, R.C., 1990, Preliminary isostatic residual gravity map of the San Jose 1:100,000 scale quadrangle, California: U.S. Geological Survey Open-File Report 90–55, scale 1:100,000.

Clark, J.C., and Rietman, J.D., 1973, Oligocene stratigraphy, tectonics and paleogeography southwest of the San Andreas, Santa Cruz Mountains and Gabilan Range, California Coast Ranges: U.S. Geological Survey Professional Paper 783, 18 p.

Dietz, L.D., and Ellsworth, W.L., 1990, The October 17, 1989, Loma Prieta, California, earthquake and its aftershocks; geometry of the sequence from high-resolution locations: Geophysical Research Letters, v. 17, no. 9, p. 1417–1420.

Eberhart-Phillips, D.M., 1989, Investigations of crustal structure and active tectonic processes in the Coast Ranges, central California: Stanford, Calif., Stanford University, Ph.D. thesis, 209 p.

———1990, Three-dimensional *P* and *S* velocity structure in the Coalinga region, California: Journal of Geophysical Research, v. 95, no. B10, p. 15343–15363.

Eberhart-Phillips, D.M., Labson, V.F., Stanley, W.D., Michael, A.J., and Rodriguez, B.D., 1990, Preliminary velocity and resistivity models of the Loma Prieta earthquake region: Geophysical Research Letters, v. 17, no. 8, p. 1235–1238.

Foxall, William, Michelini, Alberto, and McEvilly, T.V., 1993, Earthquake tomography of the southern Santa Cruz mountains; control of rupture by lithological heterogeneity of the San Andreas fault zone: Journal of Geophysical Research, v. 98, no. B10, p. 17691–17710.

Fuis, G.S., and Mooney, W.D., 1990, Lithospheric structure and tectonics from seismic-refraction and other data, chap. 8 *of* Wallace, R.E., ed., The San Andreas fault system, California: U.S. Geological Survey Professional Paper 1515, p. 207–236.

Hanna, W.F., Brabb, E.E., and Le Compte, J.R., 1981, Map showing aeromagnetic anomalies and igneous rocks, sheet 1 *of* Brabb, E.E., and Hanna, W.F., Map showing aeromagnetic anomalies, faults, earthquake epicenters, and igneous rocks in the southern San Francisco Bay region, California: U.S. Geological Survey Geophysical Investigations Map GP–932, scale 1:125,000.

Hanna, W.F., Brown, R.D., Jr., Cross, D.C., and Griscom, Andrew, 1972, Aeromagnetic reconnaissance and generalized geologic map of the San Andreas fault between San Francisco and San Bernardino, California: U.S. Geological Survey Geophysical Investigations Map GP–815, 8 p., scale 1:250,000.

Keith, C.M. and Crampin, Stuart, 1977, Seismic body waves in anisotropic media; reflection and refraction at a plane interface: Royal Astronomical Society Geophysical Journal, v. 49, no. 1, p. 181–208.

Kern, Hartmut, and Richter, A.E., 1981, Temperature derivatives of compressional and shear wave velocities in crustal and mantle rocks at 6 Kbar confining pressure: Journal of Geophysics, v. 49, no. 1, p. 47–56.

Lees, J.M., 1990, Tomographic *P*-wave velocity images of the Loma Prieta earthquake asperity: Geophysical Research Letters, v. 17, no. 9, p. 1433–1436.

McLaughlin, R.J., Clark, J.C., and Brabb, E.E., 1988, Geologic map and structure sections of the Loma Prieta 7½′ quadrangle, Santa Clara and Santa Cruz counties, California: U.S. Geological Survey Open-File Report 88–752, 32 p., scale 1:24,000, 2 sheets.

Molotova, L.V., and Vassil'ev, Y.I., 1960, Velocities ratio of longitudinal and transverse waves in rocks, II: USSR Academy of Sciences Bulletin, Geophysics Series, p. 731–743.

Mooney, W.D., and Colburn, R.H., 1985, A seismic-refraction profile across the San Andreas, Sargent, and Calaveras faults, west-central California: Seismological Society of America Bulletin, v. 75, no. 1, p. 175–191.

Mooney, W.D., and Luetgert, J.H., 1982, A seismic refraction study of the Santa Clara Valley and southern Santa Cruz Mountains, west-central California: Seismological Society of America Bulletin, v. 72, no. 3, p. 901–909.

Nicholson, Craig, and Simpson, D.W., 1985, Changes in V_P / V_S with depth; implications for appropriate velocity models, improved earthquake locations, and material properties of the upper crust: Seismological Society of America Bulletin, v. 75, no. 4, p. 1105–1123.

Nur, Amos, and Simmons, Gene, 1969, The effect of saturation on velocity in low porosity rocks: Earth and Planetary Science Letters, v. 7, no. 2, p. 183–193.

O'Connell, R.J., and Budiansky, Bernard, 1974, Seismic velocities in dry and saturated cracked solids: Journal of Geophysical Research, v. 79, no. 35, p. 5412–5426.

Press, Frank, 1966, Seismic velocities, *in* Clark, S.P., Jr. ed., Handbook of physical constants: Geological Society of America Memoir 97, p. 195–218.

Ross, D.C., 1970, Quartz gabbro and anorthositic gabbro; markers of offset along the San Andreas fault in the California Coast Ranges: Geological Society of America Bulletin, v. 81, no. 12, p. 3647–3661.

Schwartz, S.Y., and Nelson, G.D., 1991, Loma Prieta aftershock relocations with *S–P* travel times; effects of 3-D structure and true error estimates: Seismological Society of America Bulletin, v. 81, no. 5, p. 1705–1725.

Simmons, Gene, and Wang, Herbert, 1971, Single crystal constants and calculated aggregated properties; a handbook (2d ed.): Cambridge, Mass., MIT Press, 370 p.

Simpson, D.W., and field team, 1989, Field activities of the IRIS/PASSCAL and NCEER teams recording aftershocks of the October 17, 1989 earthquake: American Geophysical Union annual meeting, 1989, poster session.

Tatham, R.H., 1982, V_P / V_S and lithology: Geophysics, v. 47, no. 3, p. 336–344.

Thurber, C.H., 1983, Earthquake locations and three-dimensional crustal structure in the Coyote Lake area, central California: Journal of Geophysical Research, v. 88, no. B10, p.

8226–8236.

Thurber, C.H., and Aki, Keiiti, 1987, Three-dimensional seismic imaging: Annual Review of Earth and Planetary Sciences, v. 15, p. 115–139.

Ukawa, Motoo, and Fukao, Yoshio, 1981, Poisson's ratios of the upper and lower crust and the sub-Moho mantle beneath central Honshu, Japan: Tectonophysics, v. 77, no. 3–4, p. 233–256.

Um, Junho, and Thurber, C.H., 1987, A fast algorithm for two-point seismic ray tracing: Seismological Society of America Bulletin, v. 77, no. 3, p. 972–986.

Walck, M.C., 1988, Three-dimensional V_P/V_S variations for the Coso region, California: Journal of Geophysical Research, v. 93, no. B3, p. 2047–2052.

Walck, M.C., and Clayton, R.W., 1987, *P*-wave velocity variations in the Coso region, California, derived from local earthquake travel times: Journal of Geophysical Research, v. 92, no. B1, p. 393–405.

Wesson, R.L., Roller, J.C., and Lee, W.H.K., 1973, Time-term analysis and geological interpretation of seismic travel-time data from the Coast Ranges of central California: Seismological Society of America Bulletin, v. 63, no. 4, p. 1447–1471.

Wilkens, R.H., Simmons, Gene, and Caruso, Lou, 1984, The ratio of V_P/V_S as a discriminant of composition for siliceous limestones: Geophysics, v. 49, no. 11, p. 1850–1860.

EARTHQUAKE OCCURRENCE

SEISMOTECTONICS OF THE LOMA PRIETA REGION DETERMINED FROM THREE-DIMENSIONAL *P*-WAVE VELOCITIES, V_P/V_S RATIOS, AND SEISMICITY

By Donna M. Eberhart-Phillips[1] and Andrew J. Michael, U.S. Geological Survey

CONTENTS

ABSTRACT

Three-dimensional models from *P*-wave velocities and the ratio of *P*- to *S*-wave velocity (V_P/V_S) for the Loma Prieta region were developed from the inversion of local traveltime data (21,925 *P*-wave arrivals and 1,116 *S*-wave arrivals) from earthquakes, seismic-refraction shots, and blasts recorded at 1,700 stations in the U.S. Geological Survey's Northern California seismic network (Calnet) and numerous portable-seismograph deployments. The velocity and density models and microearthquake hypocenters reveal a complex structure that includes a San Andreas fault extending to the base of the seismogenic layer. A high-*P*-wave-velocity body extends the length of the Loma Prieta rupture zone and fills the 5-km-wide volume between the main-shock rupture and the San Andreas and Sargent faults. We suggest that this body controls both the pattern of background seismicity on the San Andreas and Sargent faults and the extent of rupture during the main shock, thus explaining how the background seismicity outlined the along-strike and depth extent of the main-shock rupture on a different fault plane 5 km away. New aftershock focal mechanisms, based on three-dimensional ray tracing through the velocity model, support a heterogeneous postseismic-stress field and cannot resolve a uniform fault-normal compression. Both the subvertical (or steeply dipping) San Andreas fault and the fault surfaces that ruptured in the 1989 Loma Prieta earthquake are parts of the San Andreas fault zone, this section of which does not have a single type of characteristic earthquake.

INTRODUCTION

At first glance, the 1989 Loma Prieta earthquake appeared to be an expected and easily understood event. By filling a gap in the background seismicity along the San Andreas fault with right-lateral slip, it fit the forecasts by Moths and others (1981), and the initial epicentral location to the west of the San Andreas fault was attributable to a mislocation of the main shock caused by across-fault velocity contrasts. With further investigation, however, it soon became clear that the earthquake occurred on a dipping structure, west of the surface trace of the San Andreas fault, and that it was an oblique-slip event with a thrust component and a spatially varying amount of slip and rake angle. Considering the varying strike of the San Andreas fault trace, Dietz and Ellsworth (1990 and this chapter) inferred that the Loma Prieta slip-and-rupture geometry is ideal for accommodating plate motion and that an additional subvertical San Andreas fault segment at the depth of the Loma Prieta rupture is not needed. Schwartz and others (1990) also presented a model without a subvertical San Andreas fault segment, but they instead required a 65° NE.-dipping fault in addition to the 65° SW.-dipping Loma Prieta rupture. Olson (1990) examined background seismicity and inferred an active subvertical San Andreas fault in addition to the southwest-dipping Loma Prieta rupture.

These observations lead to several questions that we investigate in this paper by inverting local-earthquake and controlled-source arrival-time data to determine a detailed three-dimensional velocity model for the Loma Prieta region. How does the fault surface for this earthquake relate to the San Andreas fault and the major geologic units? Can spatially varying material properties account for the spatial variations in the amount of slip? Why did the main shock fill a micro-

[1]Current affiliation: Institute of Geological and Nuclear Sciences, Dunedin, New Zealand.

seismicity gap despite occurring on a subparallel surface several kilometers from the background seismicity? Was the post-main-shock state of stress heterogeneous or simple fault-normal compression?

Several previous studies have focused on the problems of the three-dimensional velocity structure in the Loma Prieta region (fig. 1). Eberhart-Phillips and others (1990a, b) discussed an inversion of primarily aftershock data recorded by the U.S. Geological Survey (USGS)'s permanent northern California seismic network (Calnet). Lees (1990) and Shalev and Lees (this chapter) used Calnet aftershock data to produce a tomographic image of velocity contrasts in the aftershock zone. Their approach, however, did not include new ray tracing through the three-dimensional structure, a step that Kissling and others (1994) showed to be critical when the sources are inside the structure, as is the case here. Foxall and others (1993) included three-dimensional ray tracing in their inversions of Calnet aftershock data to determine the *P*-wave-velocity structure of the Loma Prieta region. In this paper, we seek to improve the spatial resolution and, most importantly, to obtain a model based on V_P/V_S ratios. These goals require combining the largely vertical component Calnet data with data from varied portable-instrument deployments. To improve the spatial distribution of sources and to remove some of the tradeoffs between velocity and hypocentral location, we also use various active sources, including explosions, throughout the Loma Prieta region and airguns deployed to the southwest. This expanded data set yields not only V_P/V_S ratios in addition to *P*-wave velocities, but also a more complete image of the crust, instead of focusing only on the region within and above the zone of seismicity. A velocity model with a larger volume than just the aftershock zone is important for such purposes as including realistic crustal rheology in numerical models (for example, Eberhart-Phillips and Stuart, 1992).

Using the new three-dimensional velocity model, we relocated 8,577 events that occurred in the aftershock zone from 1968 through September 1993. We determined new focal mechanisms for 3,964 of these events, about 2,600 of which we judged to be sufficiently reliable to use in seismotectonic and stress interpretations. With this new data set, we now determine whether the three-dimensional ray tracing requires

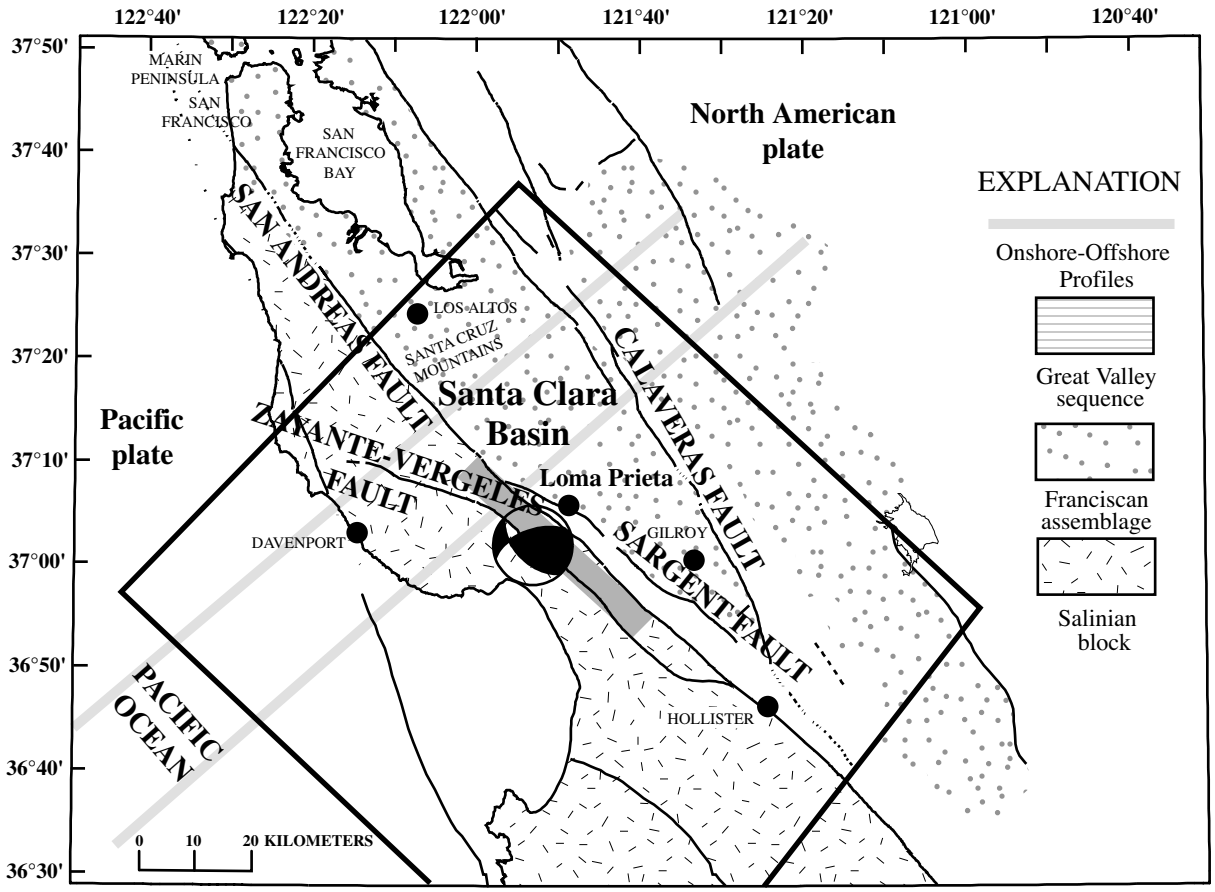

Figure 1.—Loma Prieta region, Calif., showing generalized geology (adapted from Irwin, 1990), locations of major faults (dotted where inferred), approximate surface projection of rupture zone (shaded area), and velocity grid for three-dimensional model (within rectangle). Main-shock focal mechanism is plotted at hypocenter.

any changes in previous tectonic interpretations. We use the new seismicity catalog to reevaluate the stress state before and after the main shock by considering the stress inferred from focal mechanisms. Finally, we combine the velocity models with the seismicity results to interpret faults and consider the relations between seismic velocity and seismogenic behavior.

GEOLOGIC SETTING

The Loma Prieta region is dominated by the Pacific-North American plate boundary (fig. 1), of which the major element is the San Andreas transform fault. Over the past 23 m.y., as much as 315 km of strike-slip movement has occurred on this fault, so that the Salinian block of plutonic rocks on the southwest is juxtaposed against the Franciscan subduction complex on the northeast (Page, 1990). During the fault's history, however, various factors have caused the geology to be more complex than a simple strike-slip fault separating uniform blocks of material. The fault has changed its position, at times stranding slivers of material (Sims, 1993). The plate motion changed slightly about 3.5 Ma, so that a compressional component exists (Harbert and Cox, 1989), generally taken up off the San Andreas fault (Zoback and others, 1987).

The Loma Prieta region is transitional between the San Francisco Bay region and the narrower creeping section of the San Andreas fault. In the San Francisco Bay region, geodetic analysis of velocity data shows that the plate boundary extends approximately 50 km northeastward of the San Andreas fault (Lisowski and others, 1991). In contrast, the geometry of the plate boundary in the creeping section is considered to be relatively simple with the deformation through the lithosphere centered below the surface trace of the San Andreas fault (Furlong and others, 1989). The velocity field in the transitional region is not well modeled by block motion (Lisowski and others, 1991), and a bend in the fault has formed in the Loma Prieta region.

Fuis and Mooney (1990) summarized the crustal structure and geology of this transitional region. Northeast of the San Andreas fault, mafic crust is inferred at 8-km depth below the Franciscan assemblage. Directly northeast of the fault, several thrust faults complicate the picture by bringing in slivers of ophiolite and sedimentary rock, as described by McLaughlin and Clark (this chapter). Southwest of the San Gregorio fault lies an inactive accretionary prism consisting of the San Simeon terrane (Franciscan assemblage) and Tertiary sedimentary rocks. Page (1990) inferred that Salinian basement lies on both sides of the San Gregorio fault, so that the San Gregorio fault does not consistently bound the Salinia terrane. Page and Brocher (1993) and Brocher and others (this chapter) further delineated the crustal structure and tectonic history of the transitional region by showing that oceanic crust underlies the accretionary prism and Salinian block. They inferred that oceanic crust extends from the deep-sea floor to the San Andreas fault, dipping landward 8°–10°. Holbrook and others (1996) interpreted wide-angle profiles across the fault near San Francisco and parallel to San Francisco Bay. They also inferred that active fault zones extend throughout the crust and that Pacific oceanic crust may not extend under the Salinian block.

The structure of the San Andreas fault at depth in the Loma Prieta region is unclear from surface geology. Just as evidence of near-surface heterogeneity exists from slivers of rock, other slivers or blocks of material may exist at greater depth along the fault that influence fault behavior. To study the plate boundary and understand seismic deformation, the fault zone needs to be better defined within the larger-scale setting of crustal blocks.

TRAVELTIME DATA

For this study, we tried to assemble the most complete traveltime data set possible (fig. 2). In previous studies, we used primarily Calnet data and solved for *P*-wave velocity only (Eberhart-Phillips and others, 1990a; Michael and Eberhart-Phillips, 1991). To increase the variety of raypaths and, therefore, the resolution of the three-dimensional inversion, we now include data from the temporary stations that were deployed after the Loma Prieta main shock and from three-component stations, so that we can solve for V_P/V_S ratio in addition to *P*-wave velocity.

Several arrays of temporary instruments were deployed after the main shock. A total of 60 seismic cassette recorders were deployed by the USGS. These instruments are normally used for recording seismic-refraction shots, can record only for a maximum of 13-minute intervals, and can record a maximum of 30 minutes on a single tape (Murphy, 1988). With a field crew changing tapes, the instruments recorded for six 13-minute periods on October 19, 1989, and during those 78 minutes of operation they recorded 59 aftershocks. The University of California, Berkeley (UCB), deployed six DR100 recorders from October 19 to November 16. The USGS deployed General Earthquake Observing System (GEOS) recorders at 94 different sites from October 17, 1989, to March 14, 1990 (Mueller and Glassmoyer, 1990). Reftek recorders were deployed by the Program for Array Seismic Studies of the Continental Lithosphere (PASSCAL) of the Incorporated Research Instruments for Seismology (IRIS) at 21 sites from October 27 to November 6, and at six sites from November 7 to November 23. We obtained *P*-wave-arrival and *S*–*P* times for PASSCAL, UCB, and selected GEOS stations from C.H. Thurber (written commun., 1993).

The best spatially distributed three-component array was deployed in fall 1990 by Takauchi and Evans (1995) for the purpose of recording teleseisms; however, numerous aftershocks were also recorded during the deployment. A total of 29 sites were occupied for 5 months, using 25 5-day analog

recorders, 3 GEOS recorders, and 2 Reftek recorders. For this study, we used 69 events that form a spatially well distributed data set from the 1990 array. To improve the spatial distribution of sources, we also used 85 events that were recorded on Calnet before the Loma Prieta main shock.

To reduce the tradeoff between hypocentral location and the velocity model, we also used arrival-time data from known sources, including 19 quarry blasts recorded on Calnet and seven shots recorded on both Calnet and seismic-refraction arrays before 1989. Those seismic-refraction data cross the San Andreas fault near Gilroy (Mooney and Colburn, 1985), traverse the Santa Clara Valley 15 km south of Gilroy (Mooney and Luetgert, 1982), and run southwest of the San Andreas fault from Los Altos to Davenport (Boken and Mooney, 1982).

In May 1991, the USGS conducted a seismic-refraction profile across the Zayante-Vergeles, San Andreas, and Sargent faults (Murphy and others, 1992). Six shots were recorded on a 75-station distributed array reoccupying sites of temporary earthquake stations; at most of these stations, horizontal seismometers were deployed in addition to vertical seismometers. Three shots were recorded on a 25-km-long across-fault profile with a 150-m station spacing. Three shots were recorded on a long profile from the Marin peninsula, along the San Francisco peninsula, through the Loma Prieta region. We include *P*-wave-arrival times (and *S*-wave-arrival times, where available) from all of the shots and stations in the study area (fig. 1).

The onshore/offshore data collected by Brocher and others (1992) provide another valuable data set, particularly for the Salinian/southwestern block (fig. 1), which is poorly sampled by the aftershock data and onshore stations. Brocher and others (1992) deployed 5-day recorders onshore to record offshore airgun profiles. In their analysis, the recording site is considered the shotpoint, and the source locations are considered the receivers. They interpreted both first and later arrivals to infer that the crust southwest of the San Andreas fault has a northeast-dipping Moho with a layer of subducted oceanic

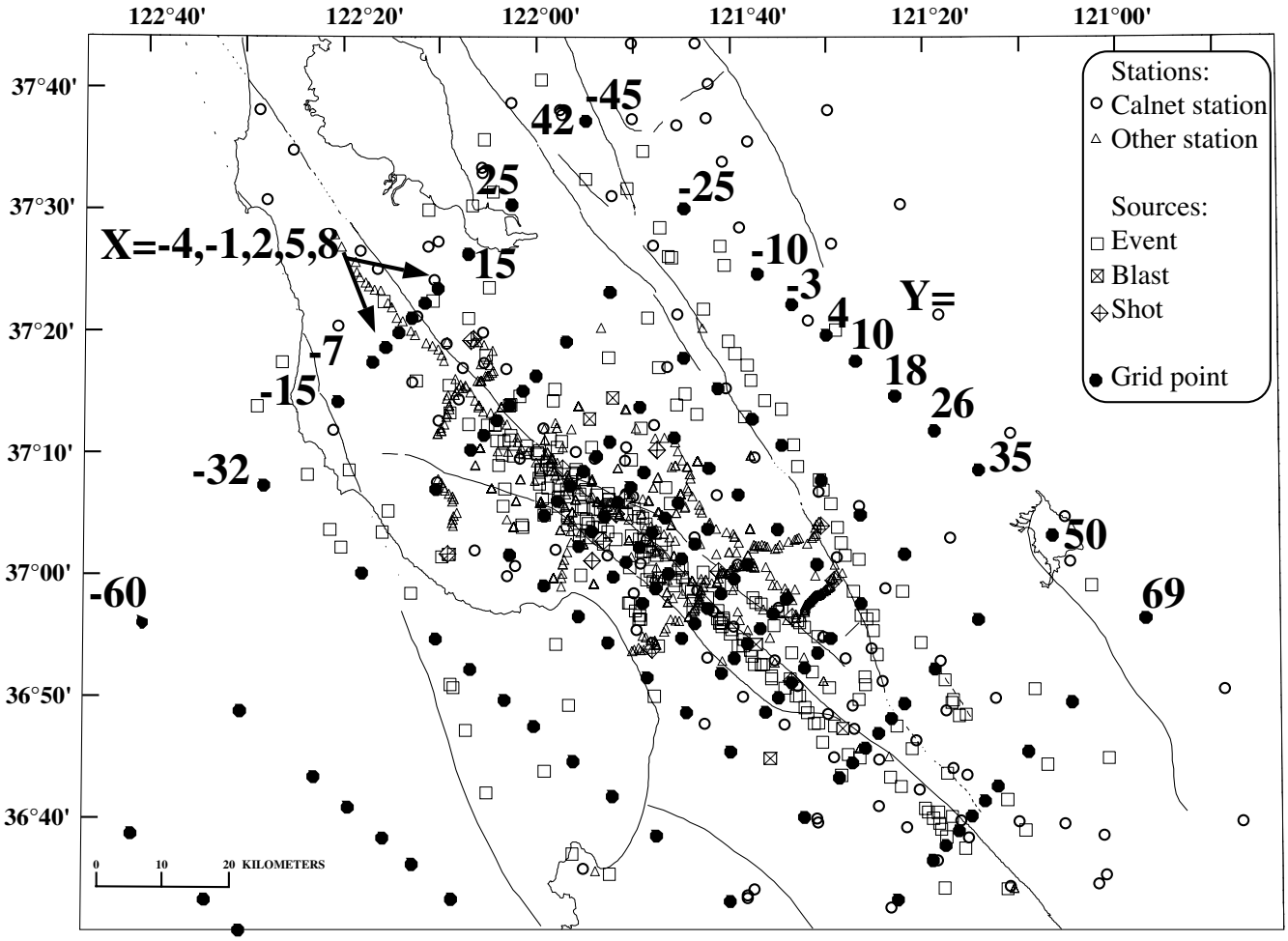

Figure 2.—Loma Prieta region, Calif., showing locations of sources and receiver stations superimposed on fault base map. Dots, velocity grid. Origin of grid is at the San Andreas fault near main-shock hypocenter (fig. 1). *x* is parallel to fault, positive to northeast; *y* is normal to fault, positive to southeast.

crust (see Brocher and others, this chapter). From the seismic-reflection lines, they were able to carefully map the bathymetry and the bottom of the Neogene sedimentary deposits along the airgun profiles. To use their data in our inversions, we stripped off the water and sedimentary layers. We traced rays in their models and then adjusted the traveltimes by the time traveled in the water and sedimentary layers, and changed the "receiver" locations to be at the raypath location at the base of the Neogene sedimentary deposits. To allow for some uncertainty in this correction process, we treated these shots as blasts by allowing the origin time to be free.

Our data set thus includes 1,700 stations. We use 273 events with 20,284 observations, and 54 shots and blasts with 2,757 observations, including 21,925 *P*-wave arrivals and 1,116 *S*-wave arrivals.

INVERSION PROCEDURE

The local aftershock arrival-time data are simultaneously inverted for hypocenters and three-dimensional velocity structure, as developed by Thurber (1983) and Eberhart-Phillips (1990) and described by Thurber (1993) and Eberhart-Phillips (1993). The algorithm has been revised to solve simultaneously for *P*-wave velocity and V_P/V_S ratio, using the same formulation as that of Thurber and Atre (1993). We prefer to obtain *P*-wave-velocity and V_P/V_S-ratio models rather than *P*- and *S*-wave-velocity models because V_P/V_S ratio is similar to Poisson's ratio and is an important parameter in characterizing rock properties and rheology. Particularly, in such cases as ours where *S*-wave-velocity data are less numerous and of poorer quality than *P*-wave-velocity data, *S*-wave velocities would be poorly resolved relative to *P*-wave velocities, making the interpretation of V_P/V_S-ratio variations difficult (Eberhart-Phillips, 1990). We assume that, given a three-dimensional heterogeneous *P*-wave-velocity model and unknown *S*-wave velocities, estimating an *S*-wave-velocity model from *P*-wave velocities using a constant V_P/V_S ratio would be more useful than assuming a homogeneous or one-dimensional *S*-wave-velocity model. Alternatively, we could assume a crustal lithology with only one-dimensional variations in rigidity, despite known three-dimensional variations in compressibility, implying large variations in Poisson's ratio wherever the three-dimensional pattern differed from the one-dimensional pattern.

The velocity of the medium is parametrized by assigning velocities at the intersections (gridpoints) of a three-dimensional grid. The raypaths are calculated with an approximate three-dimensional ray-tracing algorithm that produces curved, nonplanar raypaths which are defined by points more closely spaced (1 km) than the velocity gridpoints (3–20 km). The solution is obtained by iterative damped least-squares inversion. For each iteration, new raypaths are determined, the hypocenter solution is included, and parameter separation is carried out. Throughout the inversion, weighting is applied to each observation on the basis of both the size of the traveltime residual and the source-receiver distance. The full-resolution matrix is then calculated.

The damping parameter for each inversion is chosen empirically by evaluating a tradeoff curve of data variance and solution variance, because the damping will vary with the model grid and the data set (Eberhart-Phillips, 1986). This selective damping greatly reduces the data variance, with only a moderate increase in solution variance. Note that for a damped-least-squares inversion, any significantly large damping parameter will reduce the resolution, so that the diagonal resolution will be far from 1. Thus, the resolution matrix must be evaluated by other means than simply by inspecting the diagonal elements.

We performed a series of simultaneous hypocenter-velocity inversions, progressively increasing the complexity of the model (Eberhart-Phillips and Michael, 1993). This procedure obtains a reasonable estimate of velocities throughout the entire volume. We aimed at obtaining a velocity model that would be useful for other purposes, such as inclusion of three-dimensional crustal rheology in numerical modeling of deformation. Thus, we preferred an inversion procedure that provides simple but reasonable velocities outside the high-resolution area, rather than giving either undefined velocities or uninterpretable velocity artifacts outside the immediate aftershock zone. The pattern of subsurface velocity variations probably will resemble the overall distribution of lithologic units and faults that are mapped at the surface. Thus, we assume greater variation in material properties in the direction normal than parallel to the major faults, and we treat the traveltime data so as to optimize structures subparallel to the San Andreas fault. Using tectonic knowledge to parametrize a velocity model is a widely used strategy. For example, Abers and Roecker (1991), Foxall and others, (1993), Thurber and others (1997), and Shalev and Lees (this chapter) all used grids designed to maximize the resolution of across-fault velocity heterogeneity. Alternatively, an even grid spacing or smoothing can be used. Parsons and Zoback (1997) used 10-km horizontal smoothing for a San Francisco Bay model that included the northwestern part of our model, and Dorbath and others (1996) used an even 5-km grid spacing for a Hollister velocity model that included the southeastern part of our model (fig. 1). Both of these models show a similar along-strike extent of velocity features; however, they do not resolve across-fault velocity gradients so sharply.

We do not incorporate theoretical velocity information into the model, but obtain initial models from the data with progressive inversions (Kissling and others, 1994). For a synthetic example with a sharp across-fault gradient, the true model was recovered more accurately and with fewer artifacts when progressive inversions were done (Eberhart-Phillips and others, 1995). An alternative single-step inversion with evenly spaced grid points across the San Andreas fault is discussed below in the section entitled "Results." The grid area is shown

in figure 2. For all inversions, stations outside the grid are allowed station corrections to avoid smearing external velocity anomalies into the grid.

We begin with a one-dimensional inversion of the entire data set for *P*-wave velocities and hypocenters. We position a sharp velocity gradient to approximate the Moho at 25-km depth, with *P*-wave velocity fixed at 8 km/s at 26-km depth. The position of the Moho is poorly constrained, but the 25-km depth fits the data slightly better than do other depths (data variance, 2 percent lower than for 22- or 28-km depth), consistent with the modeling of wide-angle data by Holbrook and others (1996). Brocher and others (this chapter) determine a dipping Moho from later arrivals. Thus, we assume a Moho that dips from 15-km depth at 85 km southwest of the San Andreas fault to 25-km depth at the fault and then is flat farther northeast (fig. 3*A*), and we evaluate this location with two-dimensional inversions, using only onshore-offshore data. A dipping Moho fits the data slightly better but is poorly constrained by first-arrival data.

We next obtain an approximately two-dimensional *P*-wave-velocity model of regional variations across the plate boundary. We use the onshore-offshore data, which provide almost all of our raypath coverage southwest of the Loma Prieta region (fig. 1), together with a subset of 71 spatially distributed earthquakes, so that the two-dimensional inversion does not overly focus on the aftershock zone. The inversion is not purely two dimensional but allows for some variation in velocity along the fault, using two *y*-grids, one at *y*=–45 km (45 km northwest) and the other at *y*=69 km (69 km southeast). The *z*-grids are at 0-, 2-, 4-, 6-, 8-, 10-, 12-, 15-, and 18-km depth. We use a constant V_P/V_S ratio with the two-dimensional-inversion results as our initial three-dimensional model. The *S*-wave data come almost entirely from events and stations in the aftershock zone and so do not sample regional variations. We selected a uniform V_P/V_S ratio of 1.74 from Wadati plots. The two-dimensional model has a 24-percent reduction in variance from the one-dimensional model.

The coarse three-dimensional grid has 20- to 34-km spacing in the *y*-direction, and the initial *P*-wave-velocity model is interpolated from the two-dimensional *P*-wave-velocity model. The three-dimensional inversions use the full set of earthquakes and shots. The coarse three-dimensional inversion

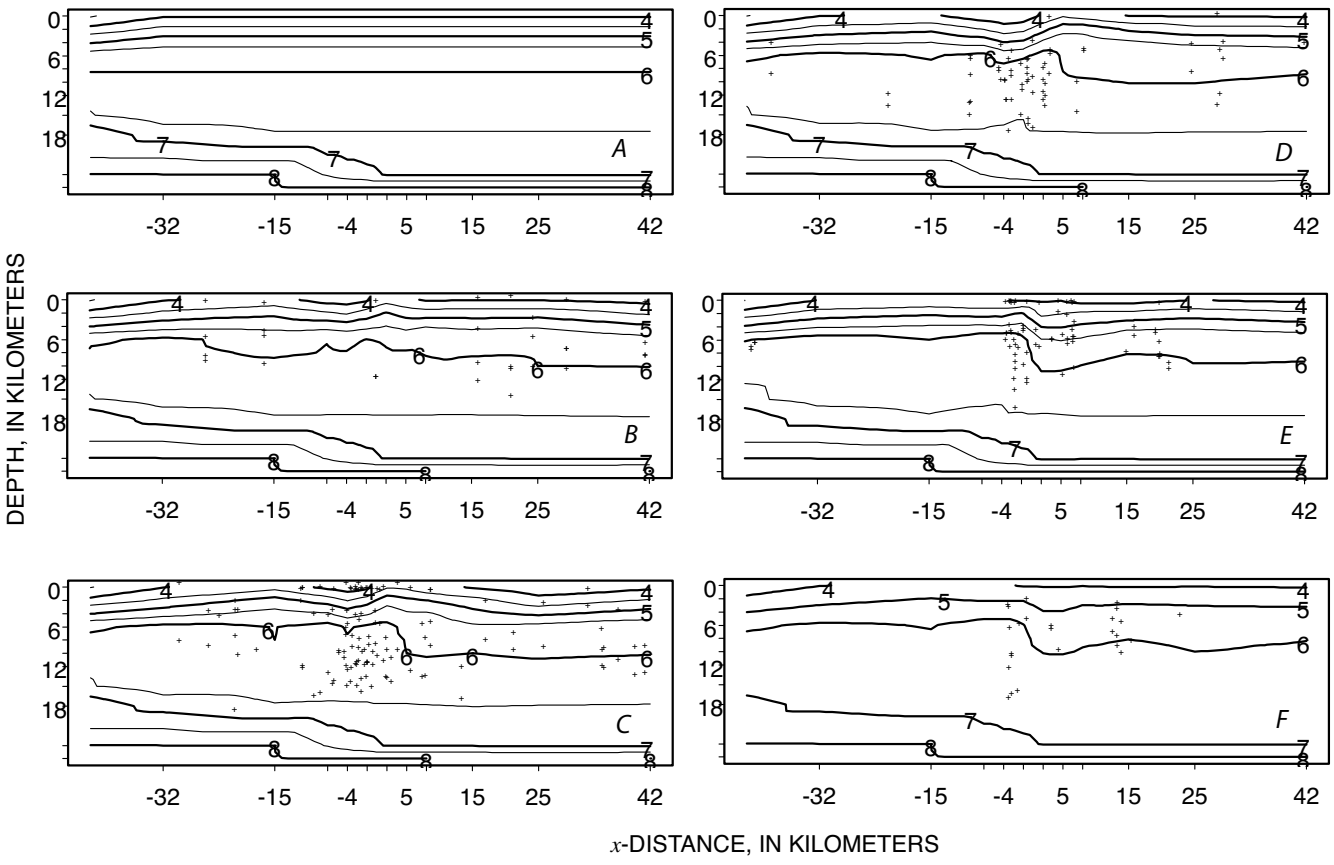

Figure 3.—Initial one-dimensional *P*-wave-velocity model (*A*), with a dipping Moho estimated from Brocher and others (1992), and southwest-northeast cross sections of coarse three-dimensional *P*-wave-velocity model for grid layers at *y*=–45 km (*B*), *y*=–10 km (*C*) *y*=10 km (*D*), y=35 km (*E*), and y=69 km (*F*). Contour interval, 0.25 km/s. Crosses in figures 3*B* through 3*F*, hypocenters of events used in inversion.

reduces the variance by a further 22 percent relative to the one-dimensional model; the fine three-dimensional inversion has a y-grid spacing of 6 to 20 km, and the initial P-wave-velocity and V_P/V_S-ratio models are interpolated from the coarse three-dimensional inversion. Only the well-sampled central part of our model, from x=−7 to x=15 km, is free in the fine three-dimensional inversion; outside this area, velocities are fixed to the coarse three-dimensional values. The fine three-dimensional inversion reduces the variance by a further 27 percent relative to the one-dimensional model.

Some near-surface variations in velocity may not be resolvable with our relatively smooth three-dimensional gridded model, and so they should be included to improve the locations of the hypocenters. Using the fine three-dimensional results, we use additional iterations with lower damping where we solve only for velocities in the upper 2 km within the finely gridded central area and allow station corrections for stations located outside of this area. This procedure reduces the variance by a further 5 percent relative to the one-dimensional model, so that the progressive three-dimensional inversion reduces the variance by a total of 78 percent. The final root-mean-square (rms) traveltime residual is 0.118 s.

Hypocenter locations will be most accurate in the central part of the model, where most of the inversion hypocenters occur. To evaluate the spatial variation in hypocenter-location accuracy, we relocated the shots and blasts, using the three-dimensional model and only the Calnet data. The four shots in the profile across the San Andreas fault near the main shock locate within 0.27 km of their true epicenters. Shots near the fault at y=−36 km and across the fault at y=15 km locate within 0.36 km of their true epicenters. At the southeast end of the model, blast relocations are not so accurate, mislocating 1 km southwest at y=35 km and 1.7 km southwest at y=45 km. Thus, some of the apparent offset between the southeastern epicenters and the San Andreas fault trace may be due to lower hypocentral accuracy in the southeastern part of the model. A set of station corrections determined solely for this area would likely move the events back onto the San Andreas fault, but we chose to keep the location process consistent for the entire data set, rather than to use multiple sets of station corrections.

RESULTS

VELOCITY AND RESOLUTION

The resolution matrix describes the distribution of information for each node, such that each row is the averaging vector for a given parameter. The relative size and pattern of the offdiagonal elements show how the information is smeared. For a node to be adequately resolved, its resolution should be peaked and have no significant contribution from nonadjacent nodes. For a succinct way of comparing the resolution, we calculate the spread function (Michelini, 1991; Michelini and McEvilly, 1991), which compresses each row of the resolution matrix into a single number which describes how strong and peaked the resolution is for that node. As described in detail by Toomey and Foulger (1989), the spread function is a better way to describe the resolution than by examining only the diagonal element, because the diagonal resolution depends strongly on grid spacing and damping. As defined by Michelini and McEvilly (1991), the spread function S_j for a given node is computed from all the elements s_{kj} of the corresponding row of the resolution matrix, weighted by their distance D_{jk} from the node, and S_j is the diagonal element S_{jj}:

$$S_j = \log\left[\frac{1}{|s_j|}\sum_{k=1}^{N}\left(\frac{s_{jk}}{|s_j|}\right)^2 D_{jk}\right].$$

This relation combines two issues in evaluating resolution: the amount of information and the amount of smearing. The first factor makes the spread function small for nodes with large diagonal resolutions. The summed terms make the spread function large for nodes that have significant averaging from other nodes, and particularly large if the contributing nodes are more distant. Because the spread function combines these factors, it does not have such physical units as kilometers, similar to the resolution matrix, which also does not have physical units. The range of values obtained for the same data set will vary, depending on the chosen grid spacing and damping.

We also illustrate the pattern of image blurring in low-resolution areas by showing contours of the averaging vectors for nodes with significant smearing. For local earthquake tomography, this procedure is more useful than showing ellipses because the smearing commonly is in only one direction and ellipses would wrongly imply that the averaging is centered on the node. Each node has a row of the resolution matrix, with offdiagonal elements for all other nodes, showing the spatial averaging for that node. For each row of the resolution matrix, we plot where the resolution is 70 percent of the diagonal element. The resolution for the coarse three-dimensional model is plotted in figure 4. Resolution contours are shown for only those nodes with such smearing that the resolution contour extends beyond an adjacent node; at other nodes, we would expect the spatial averaging to be represented by the grid spacing.

For small values (<2) of the spread function, the model velocity is representative of the volume surrounding a given node, that is, the volume between that node and adjacent nodes. For moderate values (2–4) of the spread function, the velocity may be averaging a larger volume, and so small features may not be imaged or may appear as broader features. The largest values (>4) of the spread function indicate little or no information, and the associated velocity in the damped-least-squares inversion remains close to that in the initial model.

A comparison of the coarse three-dimensional model and inversion hypocenters (fig. 3) with the resolution plots (fig. 4) indicates that the resolution is best where the density of

events is highest. The resolution is generally poor below 12-km depth, except where deeper events occurred. The surface nodes generally are not constrained by raypaths independent of the 2-km-deep nodes. The resolution of V_P/V_S ratio is generally low, and virtually no information is obtainable outside the central area with three-component aftershock stations. Because the damping allows only small velocity perturbations in areas of low resolution, velocity features that are artifacts are avoided. However, the spatial shape of velocity features may be inexact, and spatially small velocity features will not be imaged in poorly resolved areas. For example, the southwestern part (x=−32 to −15 km) of the y=69 km grid (fig. 3*F*) shows a higher velocity than that in the initial model at 0- to 12-km depth; however, the resolution contours are

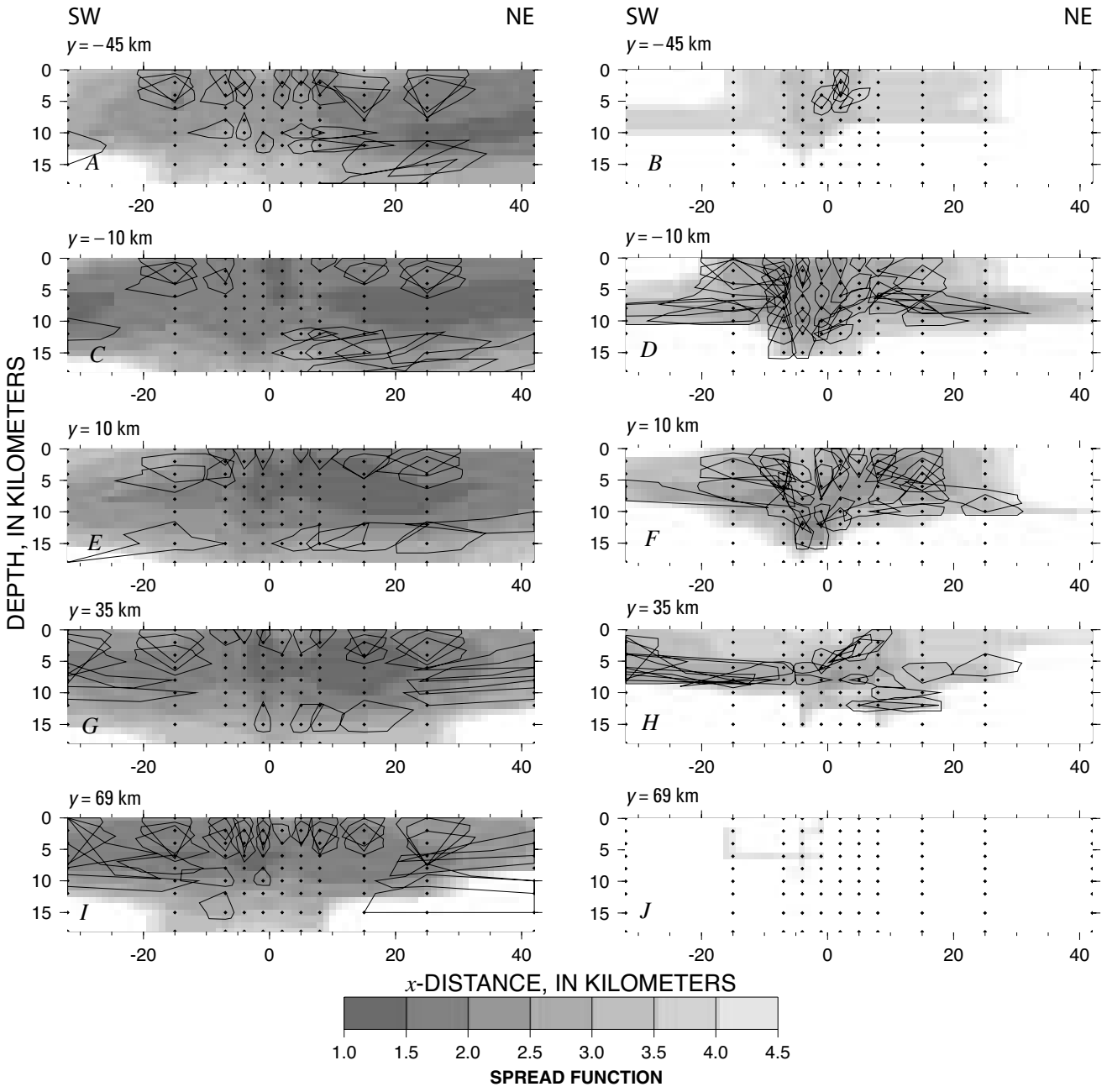

Figure 4.—Resolution plots of *P*-wave velocity (*A*, *C*, *E, G, I*) and V_P/V_S ratio (*B*, *D*, *F*, *H*, *J*) for coarse three-dimensional *P*-wave-velocity model (figs. 3*B*–3*F*) of velocity grid in the Loma Prieta region (figs. 1, 2) for grid layers at y=−45 km (*A*, *B*), y=−10 km (*C*, *D*) y=10 km (*E*, *F*), y=35 km (*G*, *H*), and y=69 km (*I*, *J*). Spread function is shown with contours of averaging vector (row of resolution matrix) for nodes with smearing greater than grid spacing. Contours, which are 70 percent of diagonal resolution, are plotted where resolution contour extends farther than adjacent nodes, but not for nodes with near-zero resolution.

vertically smeared. Thus, velocities may be high below 4-km depth and relatively low in the uppermost few kilometers of the crust, but any shallow, moderately low velocity cannot be imaged distinct from a deeper high velocity.

P-wave velocities in the southwestern part of our model range from 6.1 to 6.35 km/s at 5- to 15-km depth and vary only slightly from northwest to southeast. Overall, the range of *P*-wave velocities in this Salinian material is similar to the range of 6.0 to 6.4 km/s at 5- to 15-km depth modeled by Holbrook and others (1996) from wide-angle data near San Francisco. The central part of our model (x=−7 to 8 km) shows more complexity, with distinct gradients and high velocity features.

In the northeastern part our model, the area between the Calaveras and San Andreas faults (x=15 km) contains a large volume of material at 2- to 10-km depth with a *P*-wave velocity ranging from 5.1 to 5.9 km/s (fig. 5). Along the Santa Clara Basin (fig. 1; x=15 km, y=−45 to −25 km), however, the shallow velocities are lower, and the deeper velocities are higher, with 6.25-km/s material at 10-km depth. Some velocity contrast is evident across the Calaveras fault, with higher *P*-wave velocities on the northeast side below 6-km depth. *P*-wave velocities in the northeastern part of our model are also similar to those in Holbrook and others' (1996) block model of San Francisco Bay, except that Holbrook and others inferred a discontinuity that does not appear in our model; they also showed material with *P*-wave velocities ranging from 5.5 to 6.1 km/s at 3- to 17-km depth overlying material with *P*-wave velocities ranging from 6.9 to 7.3 km/s at 17- to 24-km depth.

Cross sections of the fine three-dimensional model are shown in figure 6, and the resolution is plotted in figure 7.

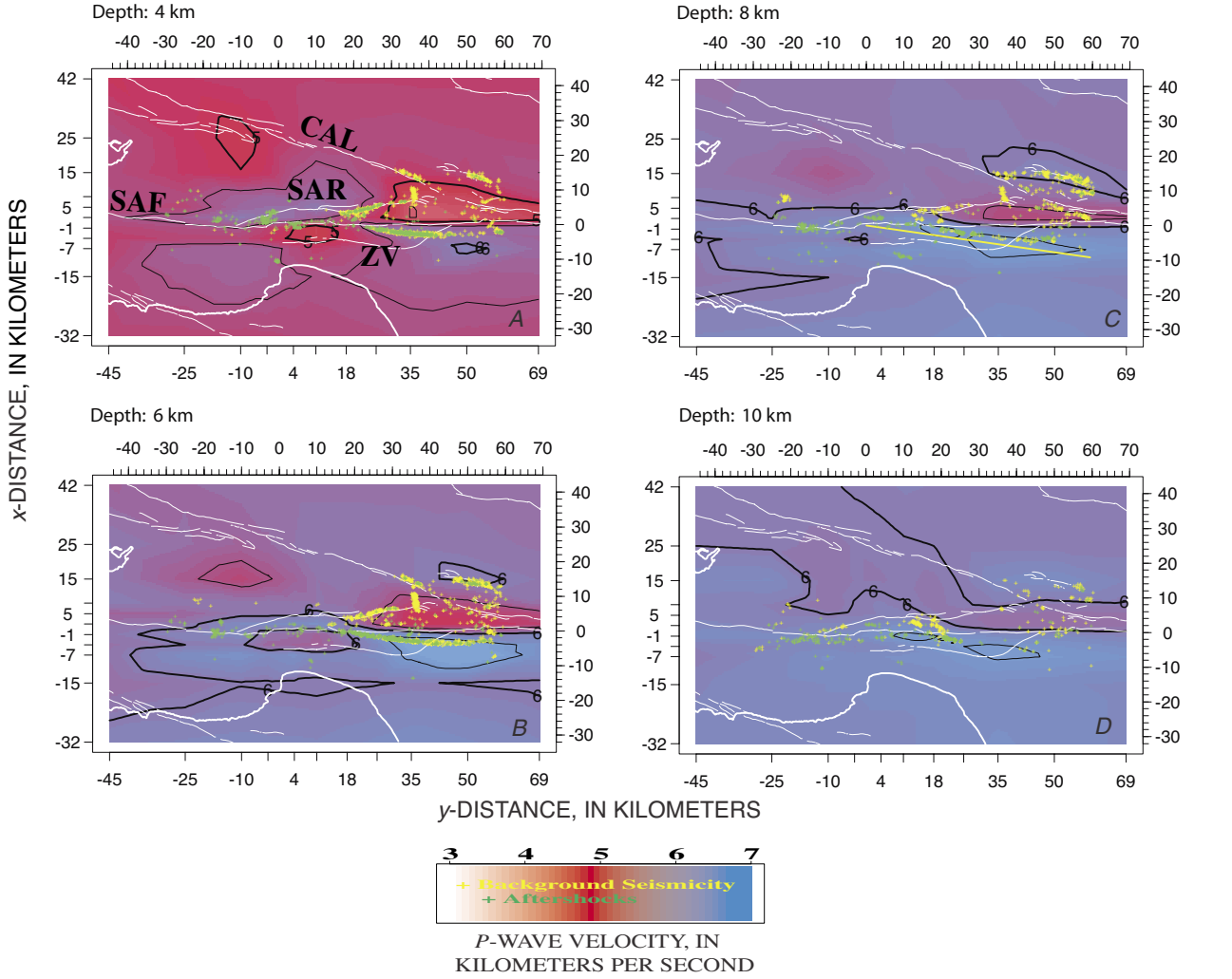

Figure 5.—Map views of final three-dimensional model of velocity grid in the Loma Prieta region (figs. 1, 2), showing surface traces of faults (thin white lines) and locations of hypocenters (crosses) within 1 km of each layer for grid layers at 4-km (*A*), 6-km (*B*), 8-km (*C*), and 10-km (*D*) depth. Faults: CAL, Calaveras; SAF, San Andreas; SAR, Sarmiento; ZV, Zayante-Vergeles. *P*-wave-velocity contour interval, 0.5 km/s, with 5.0- and 6.0-km/s contours in bold. Yellow heavy straight line in figure 5*C* denotes location of cross section in figure 12*E*.

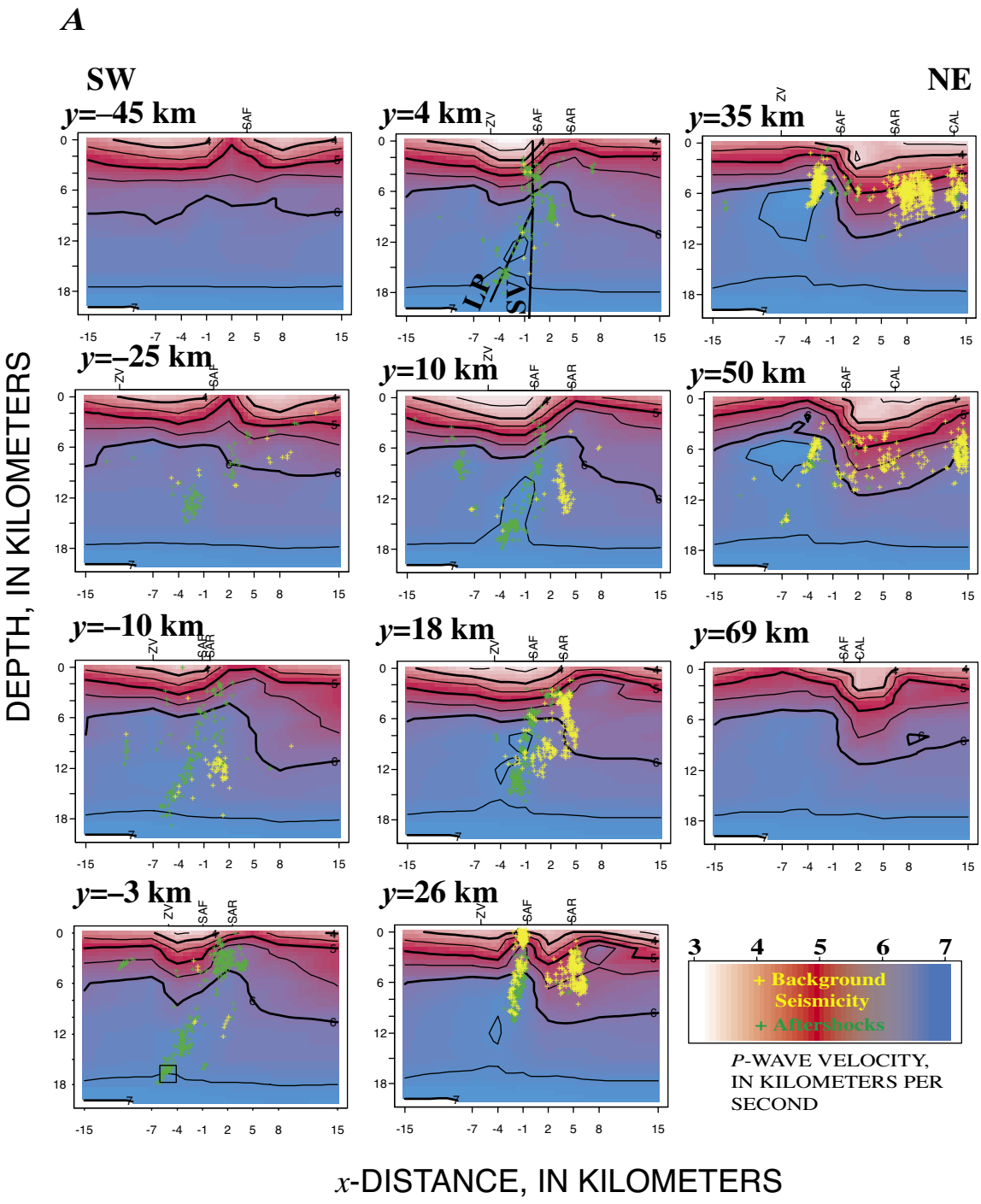

Figure 6.—*P*-wave-velocity (*A*) and V_P/V_S-ratio (*B*) cross sections of final three-dimensional model of velocity grid in the Loma Prieta region (figs. 1, 2), showing locations of mapped fault traces and of hypocenters within 3 km of each layer. Faults: CAL, Calaveras; SAF, San Andreas; SAR, Sarmiento; ZV, Zayante-Vergeles. Contour intervals: *P*-wave velocity, 0.5 km/s, with 4.0-, 5.0-, 6.0-, and 7.0-km/s contours in bold; V_P/V_S ratio, 0.05, with 1.7, 1.8, and 1.9 contours in bold. In cross sections for $y=4$ km, estimated locations of southwest-dipping fault surface (LP) and the subvertical San Andreas fault (SV) are shown; both LP and SV are considered parts of the San Andreas fault system at depth.

The velocity images (fig. 6) extend farther southwestward than the nodes in the fine three-dimensional inversion (x=−7 to 15 km) so as to plot all of the relocated aftershocks. The resolution is generally good at 4- to 12-km depth. Key features of the *P*-wave-velocity model are a large low-velocity body in the southwest, a deep high-velocity body in the southwest, and several small, shallow high-velocity bodies. The low-velocity body parallels the San Andreas fault from the northwest to y=20 km and is most conspicuous at y=4 km (fig. 6), where it is clearly bounded on the northeast by the San Andreas fault and its *P*-wave velocity ranges from 2.8 km/s at the surface to 5.7 km/s at 6-km depth. This low-velocity body appears to be bounded by a vertical fault on the southwest, as shown in the y=−3 km and y=4 km cross

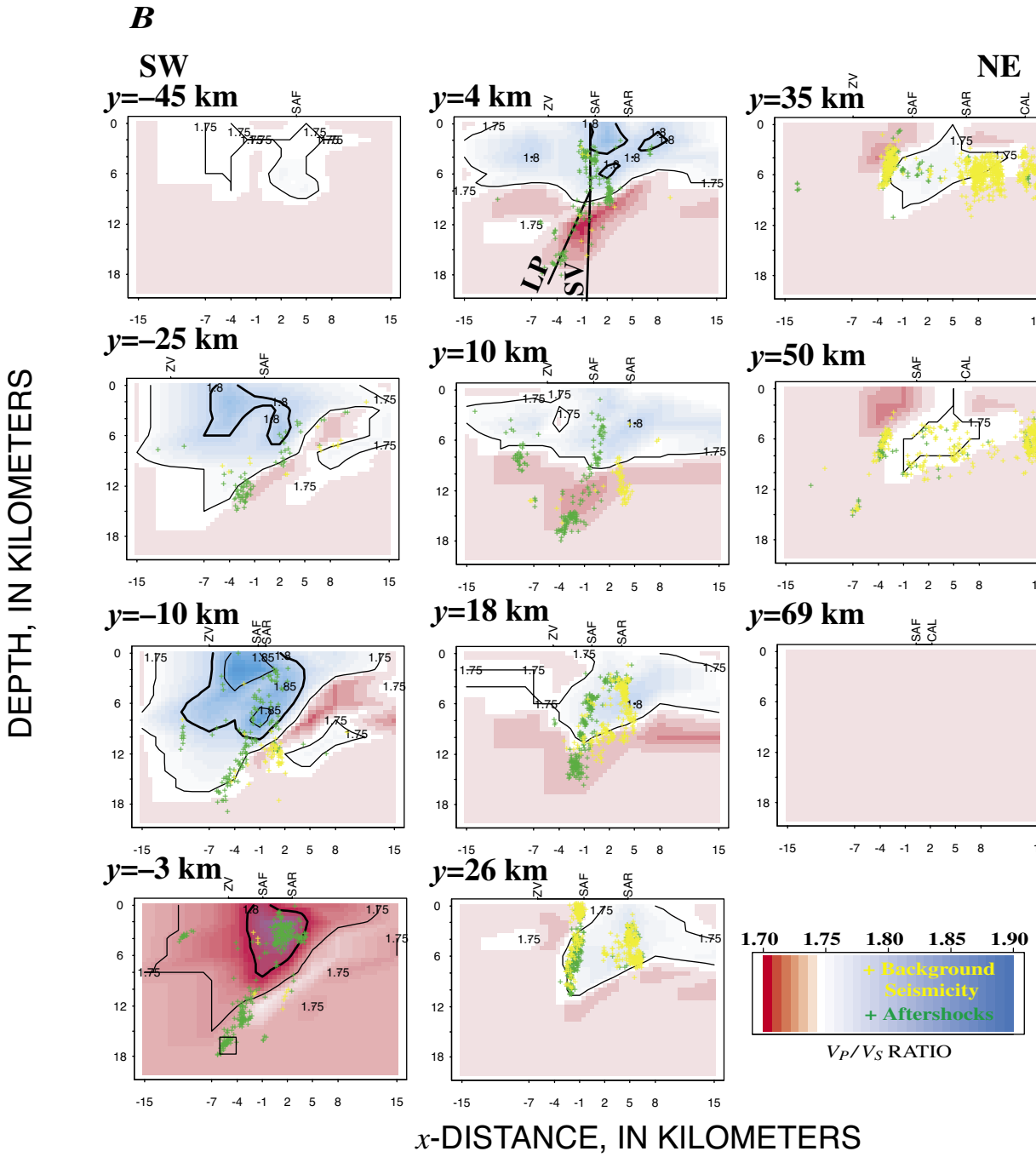

Figure 6.—Continued

sections (fig. 6). Given the resolution and grid spacing, however, this boundary could as well dip southwest. The resolution is fairly even over the length of the low-velocity body, and so we can be confident of its location centered near y=4 km.

Below 6-km depth, the three-dimensional model shows an overall higher P-wave velocity on the southwest side of the vertical projection of the San Andreas fault trace, as well as several distinct high-velocity bodies. One high-velocity body parallels the fault on the southwest, is centered at y=10 km, and ranges in P-wave velocity from 6.5 to 6.6 km/s. This high-velocity body is about 20 km long and dips southwest at 8- to 12-km depth. The resolution is fairly even in this vicinity, and so the high-velocity body is most likely a distinct feature, rather than reflecting the uniformly high velocity on

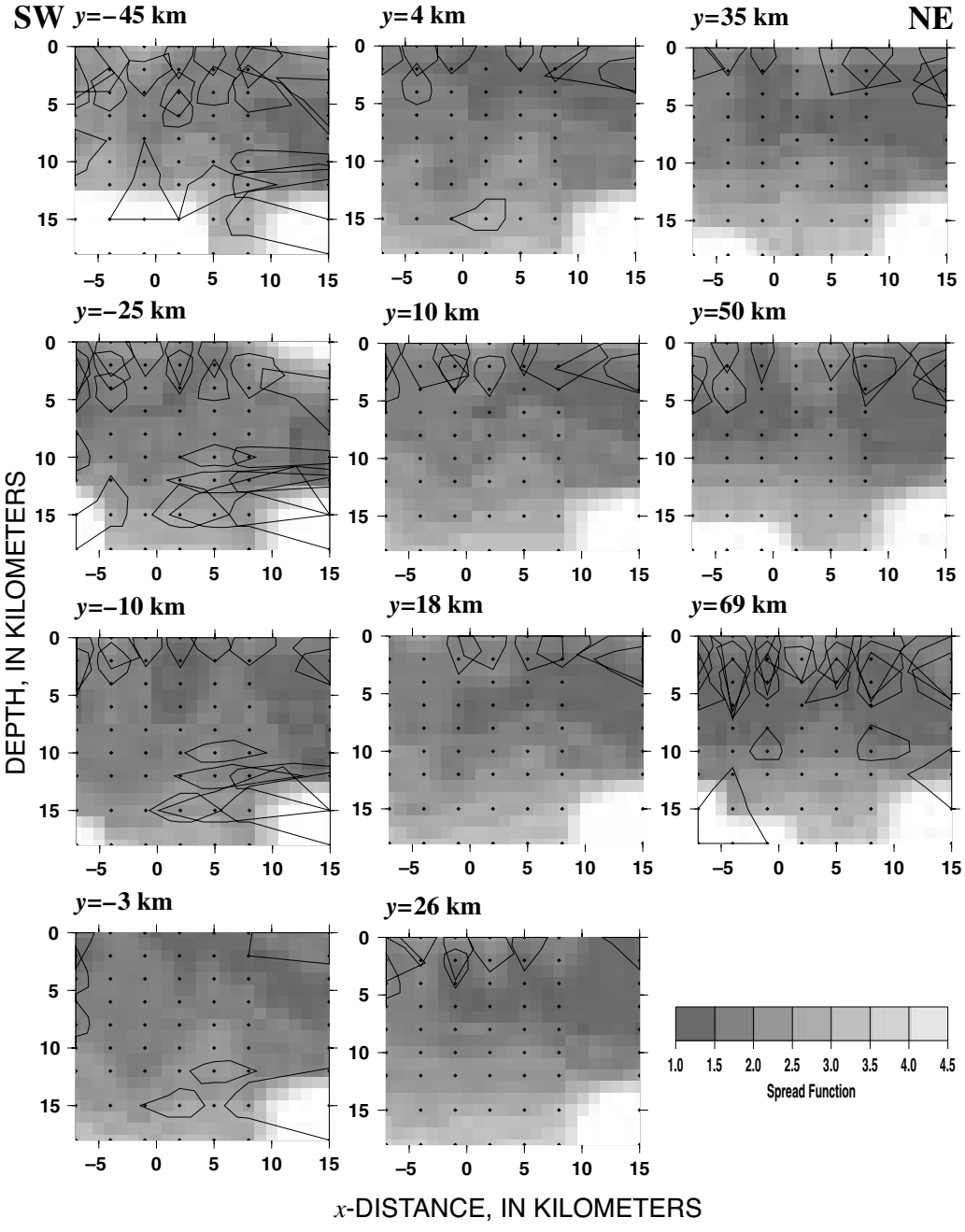

Figure 7.— Resolution plots of V_P/V_S ratio for final three-dimensional model (fig. 6) of velocity grid in the Loma Prieta region (figs. 1, 2). Spread function is shown with contours of averaging vector (row of resolution matrix) for nodes with smearing greater than grid spacing. Contours, which are 70 percent of diagonal resolution, are plotted where resolution contour extends farther than adjacent nodes but not for nodes with near-zero resolution.

the southwest side of the fault. The high-velocity body appears to be about 3 km thick, although the resolution decreases below 8-km depth. A synthetic test of a subset of these data was performed by Kissling and others (1994). Below 10-km depth, the high-velocity side of their inversion model had a 10-km-thick high-velocity feature in addition to the expected overall high velocity. Thus, below 10-km depth, the southwestern high-velocity body could be part of a broader feature extending farther southwestward. For example, Brocher and others (this chapter) describe a high-velocity feature below 10-km depth that extends 35 km southwestward to the San Gregorio fault.

On the northeast side of the San Andreas fault is a moderately high velocity zone (6.1–6.3 km/s) extending from

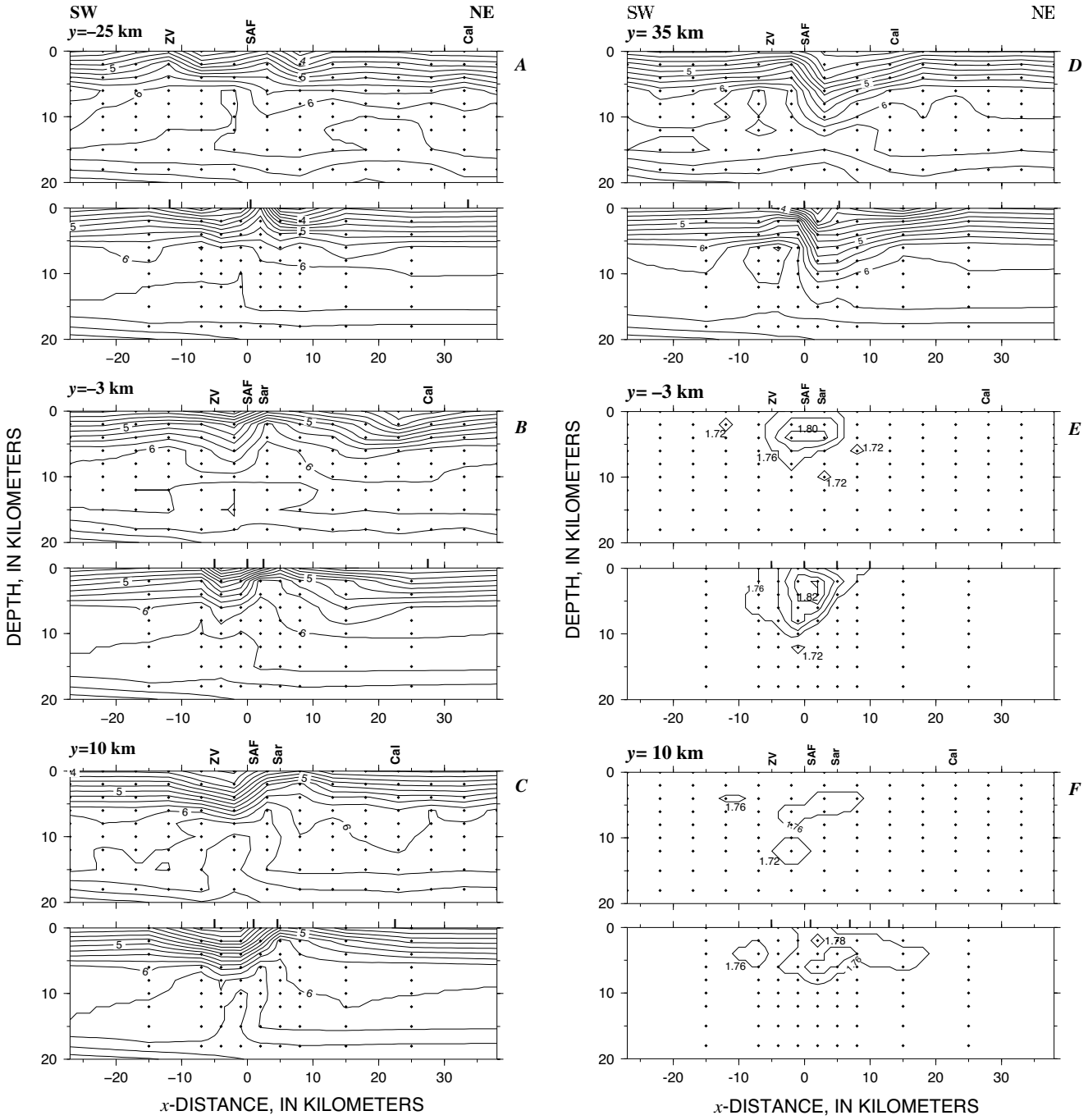

Figure 8.— Comparison of three-dimensional inversion (upper plots), with even across-fault grid spacing and one-dimensional initial model, with progressive inversion of three-dimensional model (lower plots), showing *P*-wave velocity in grid layers at y=–25 km (*A*), y=–3 km (*B*), y=10 km (*C*), and y=35 km (*D*) and V_P/V_S ratio in grid layers at y=–3 km (*E*) and y=10 km (*F*). Dots, inversion grids. Contour intervals: *P*-wave velocity, 0.25 km/s; V_P/V_S ratio, 0.02. Faults: CAL, Calaveras; SAF, San Andreas; SAR, Sarmiento; ZV, Zayante-Vergeles.

y=−18 to y=20 km at 6- to 12-km depth. The resolution in this area is adequate, and some hypocenters occur within it, and so this feature is not caused simply by smearing from the southwestern high-velocity body. In the uppermost 4 km of crust, shallow high-velocity features, with a *P*-wave velocity of 5.9 km/s at 2-km depth, follow the Sargent fault from y=10 to y=18 km; these features are well imaged at y=−3 km, where the shallow resolution is best.

In the southeastern part of our model (y=26–69 km), the velocity structure is simpler, with uniformly higher velocity on the southwest. Within the general southwestern high-velocity body is a distinct narrow high-velocity zone, with a *P*-wave velocity of 6.8 to 7.0 km/s at 6-km depth, that is 15 km long and extends from y=35 to y=50 km. We note that the resolution is poor below 12-km depth, and so we are uncertain of the depth extent of this high-velocity zone.

The V_P/V_S model has a moderate resolution from y=−25 to y=−3 km, and the most conspicuous feature is a high V_P/V_S ratio (max 1.89) within the large low-*P*-wave-velocity area southwest of the San Andreas fault. At y=−3 km, the high V_P/V_S ratio is centered on the fault, rather than in the low-velocity material. This feature would be intriguing if it were imaging some property of the fault zone itself, but it is just as likely to be a smearing of high V_P/V_S ratios on both sides of the fault. Apparently, the various high-velocity features have different V_P/V_S ratios: the high-velocity zone northeast of the fault has a high V_P/V_S ratio, and the high-velocity body on the southwest has a low V_P/V_S ratio.

As described above in the section entitled "Inversion Procedure," we take into account the general pattern of geology and the uneven data distribution by using a series of inversions, with more closely spaced nodes near the San Andreas fault, where most events occur. To evaluate the effect of these assumptions on the resulting velocity features, we also compute an inversion with evenly spaced nodes in the across-fault direction and the one-dimensional initial crustal model (fig. 3*A*), without two-dimensional or coarse three-dimensional inversion steps. These results are compared with our progressive-inversion results in figure 8. No velocity features are evident in our progressive model that are not evident in the evenly spaced model; however, the features appear broader in the evenly spaced model because their spatial position cannot be defined so well by the coarser spacing near the San Andreas fault. The evenly spaced model also differs in having many single-point velocity anomalies and low-velocity zones in its poorly resolved parts. Only a couple of these differences appear to be reasonable, such as the more distinct low-velocity zone associated with the Calaveras fault at y=10 km (fig. 8*C*). In general, the differences do not appear to be believable features that could be interpreted to represent crustal structure. For example, the low-velocity zone on the southwest edge at y=−25 km (fig. 8*A*) and the velocity complexity below 10-km depth at y=10 km (fig. 8*C*) are more likely to be inversion artifacts. Therefore, the evenly spaced model would be less useful for other applications, such as providing three-dimensional rheology in numerical modeling.

RELOCATION OF EVENTS

To improve the image of the seismicity with respect to the new velocity model, we relocated 8,577 events with the final three-dimensional model and station corrections. These events, which occurred from 1968 through September 8, 1993, were recorded by Calnet, have hand-timed arrival times, are all of $M \geq 1.5$, and were located in the central part of our model. The standard Calnet catalog uses four different one- and two-dimensional velocity models with station corrections to locate events in this area and achieves an average rms traveltime-residual misfit of 0.13 s. With the single three-dimensional velocity model, the average rms misfit drops by 25 percent to 0.096 s.

In the figures that follow, we plot only the best located of the new hypocenters. Each hypocentral location uses at least 15 stations and has an rms misfit of less than 0.12 s. In general, the hypocenter locations do not differ substantially from those in other studies (Dietz and Ellsworth, this chapter), but they do provide a self-consistent comparison between the hypocenter locations and the three-dimensional velocity structure. These hypocenters were also used in figures 5 and 6.

DETERMINATIONS OF FAULT-PLANE SOLUTIONS

For the events located with the three-dimensional model, first-motion fault-plane solutions are determined with the program FPFIT (Reasenberg and Oppenheimer, 1985), using the three-dimensional raypaths. Requiring 25 or more hand-timed readings, and rejecting solutions that did not converge well or had multiple possible minimums, reduces the number of solutions to 3,964 events, of which 2,624 are considered to be well determined because they have 30 or more observations. The 90-percent-confidence limits in strike, dip, and rake were limited to 40°, 43°, and 50°, respectively; the observations were well distributed over the focal sphere, and the rms misfit was less than 0.24. These values were picked by making histograms of the various functions and then selecting values to keep most of the solutions while rejecting the tails of the distributions. A review of the solutions shows that these criteria are adequate. The average 90-percent-confidence limit on the three angles for the selected solutions is 23°.

The distribution of focal mechanisms is illustrated in figure 9 by maps of the different types of mechanisms in the background seismicity and in the aftershocks. The strike-slip mechanisms were divided into right and left lateral, signify-

ing the type of slip on the nodal plane most nearly parallel to the San Andreas fault. Thus, the events plotted as right lateral are consistent with the stress field expected in the Loma Prieta region; however, an event plotted as right lateral could be left lateral on a plane subperpendicular to the San Andreas fault. The *P*-axes are shown for thrusting events, and the *T*-axes for normal events. Right-lateral and thrust solutions predominate, with a greater proportion of thrusting events in the north half of the aftershock zone, as might be expected from the main-shock slip distribution, which indicates a higher proportion of reverse slip for the northern part of the rupture (Beroza, 1991; Wald and others, 1991). Numerous left-lateral and normal aftershocks, however, are not inconsistent with the main-shock slip. The left-lateral and normal aftershocks are not on isolated structures but are distributed throughout areas of right-lateral and thrusting events, similar to the one-dimensional mechanisms of Oppenheimer (1990).

STRESS FIELD INFERRED FROM FOCAL MECHANISMS

Focal-mechanism data were inverted by the method of Michael (1984) to obtain the uniform component of the stress field under the assumption that the constitutive relation is linear and isotropic. The uniform-stress tensor that best explains the focal mechanisms in a data set is expressed by the three axes

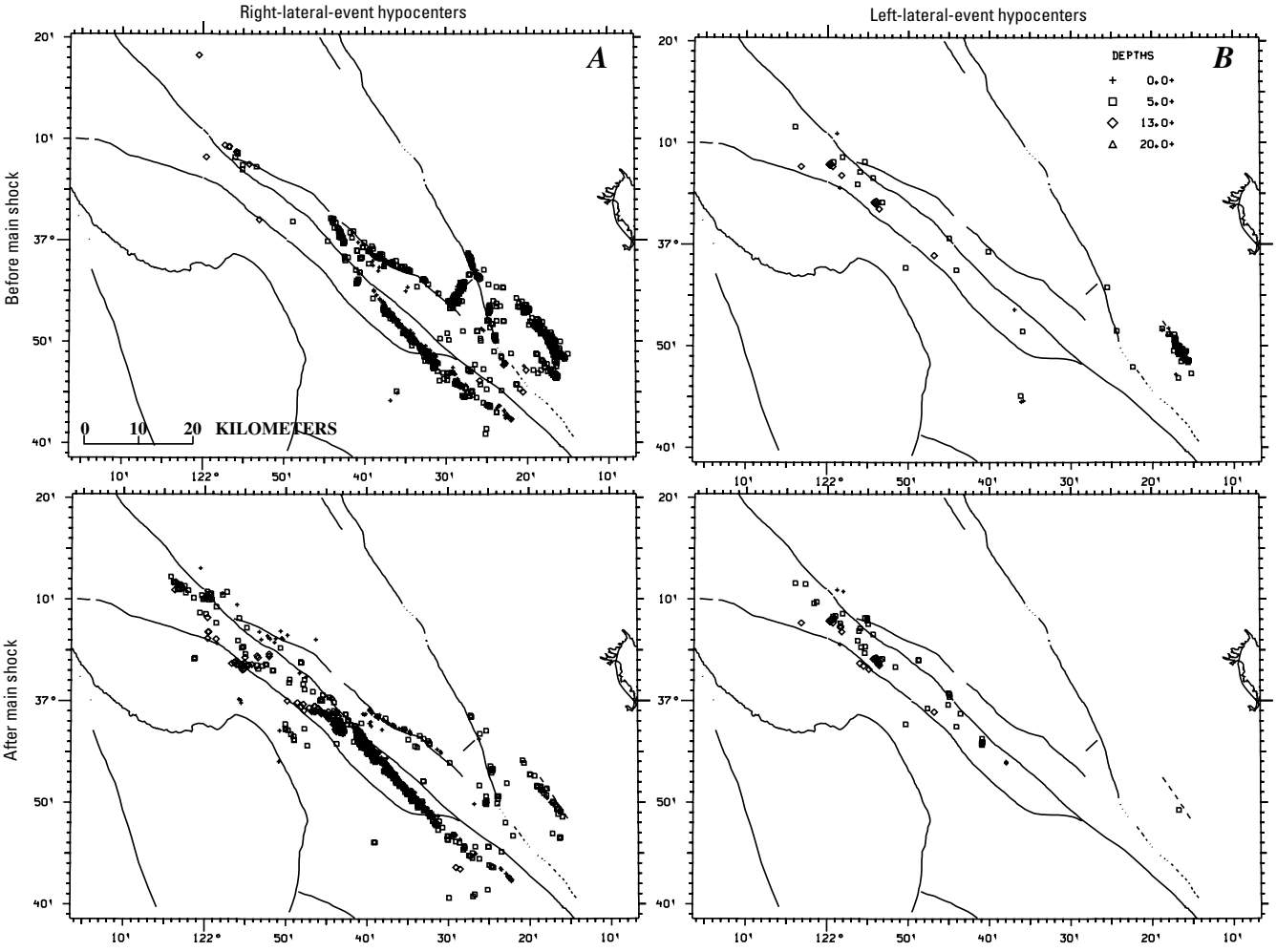

Figure 9.—Distribution of focal mechanisms in the Loma Prieta region (fig. 1) before (upper plots) and after (lower plots) October 17, 1989, main shock, calculated using three-dimensional raypaths. *A*, Events with focal mechanisms consistent with right-lateral slip on a nodal plane subparallel to the San Andreas fault. *B*, Events with focal mechanisms consistent with left-lateral slip on a nodal plane subparallel to the San Andreas fault. *C*, *P*-axes of events with thrust mechanisms. *D*, *T*-axes of events with normal mechanisms. Note that because we categorize strike-slip events on the basis of a nodal plane subparallel to the San Andreas fault, events on cross-structures may be misclassified, for example, in figure 9*A*, where an intermediate fault links the Sargent and Calaveras faults.

of principal stress and the stress ratio $\phi=(S_2-S_3)/(S_1-S_3)$, where S_1, S_2, and S_3 are the principal stresses numbered from most to least compressive. The 95-percent-confidence regions were determined by the bootstrap method (Michael, 1987a), and an average misfit angle β (angle between observed and predicted slip directions) was computed that measures the difference between the observed slip direction and the predicted direction of maximum tangential traction. The angle β can be used as a measure of the success of inversion; if it exceeds 47°, then the inversion has failed to find a uniform-stress tensor, most likely because the true stress field is highly heterogeneous (Michael, 1991).

The data set is divided into two time periods, before and after the main shock, and four hypocentral volumes for a total of eight subsets, as was done for the preliminary Loma Prieta data set by Michael and others (1990). The four hypocentral volumes were obtained by first dividing the epicenters into three areas: the central area, which contains the main-shock rupture; and the areas to the north and south of this central area. The main-shock rupture did not extend to the surface, and so the central area was further subdivided at 5-km depth into shallow and deep volumes, with the deep volume containing the main-shock rupture. For each event, the nodal plane oriented closer to a strike of northwest-southeast was selected to represent the slip plane. Owing to the complexity of these mechanisms, however, when computing the confidence limits, the odds of choosing the wrong fault plane from the two nodal planes were estimated at 50 percent (Michael, 1987b).

The major coseismic change is found in the main-shock rupture area (deep central area, fig 10). Before the main shock, the motion on fault planes subparallel to the San Andreas fault was primarily right-lateral strike slip due to a uniform stress field with the axis of principal stress S_1 oriented slightly east of north. The aftershocks in the deep central area, however, are a completely heterogeneous set of focal mechanisms that cannot be explained by a uniform-stress

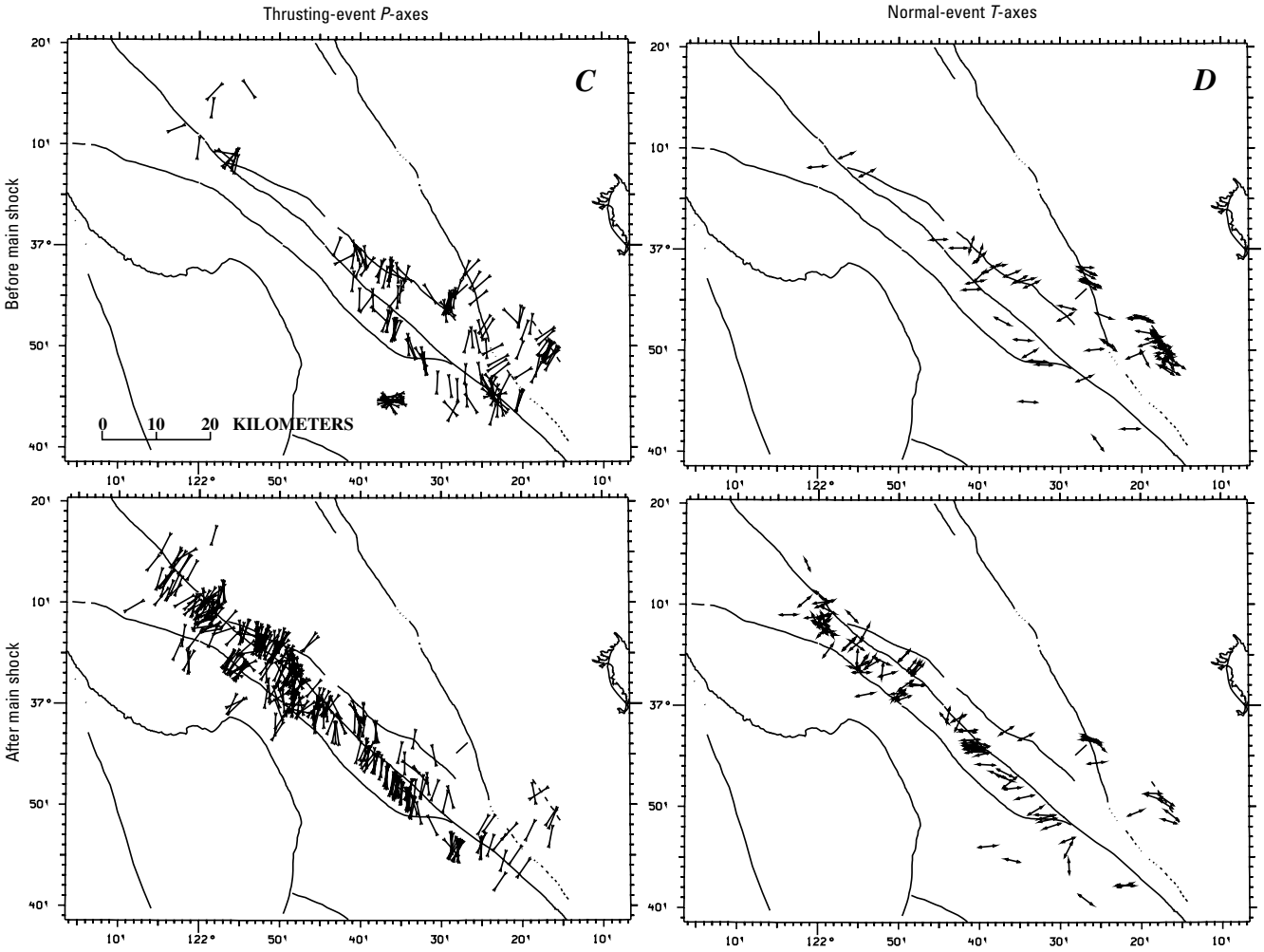

Figure 9.—Continued

tensor, as evidenced by the extremely high misfit, (β=61°). These results from the three-dimensional focal mechanisms are similar to those of the initial study by Michael and others (1990), and thus continue to support their conclusion that the stress field in the rupture zone became highly heterogeneous after the main shock.

Above the main-shock rupture zone (shallow central area, fig. 10), the number of data is insufficient to determine the previous stress field, but aftershocks show a stress field with the axis of principal stress S_1 oriented east-northeast and the axis of principal stress S_3 vertical, consistent with thrusting. The northern area has a similar absence of background seismicity, but the aftershocks consisted primarily of fault-parallel thrusts due to fault-normal compression. In the southern area, right-lateral strike-slip events dominate both time periods, and the stress regime shows approximately north-southward compression, with the axis of principal stress S_2 vertical both before and after the main shock. Michael and others (1990) suggested that the main shock increased the stress in the southern area, leading to a lower β value during the aftershocks, but this conclusion is not supported by the three-dimensional mechanisms.

The high β value of 61° in the main-shock rupture zone suggests that the uniform component of the stress field, which is what the stress inversions attempt to recover, is smaller than the spatially varying component, which the inversions treat as noise. Although some nonzero uniform component to the stress field is likely, we cannot recover it within the 95-percent-confidence limits of the inversion results (Michael, 1991). Zoback and Beroza's (1993) conclusion that the total stress drop on the main-shock fault plane (Michael and others, 1990) will lead to a uniform component

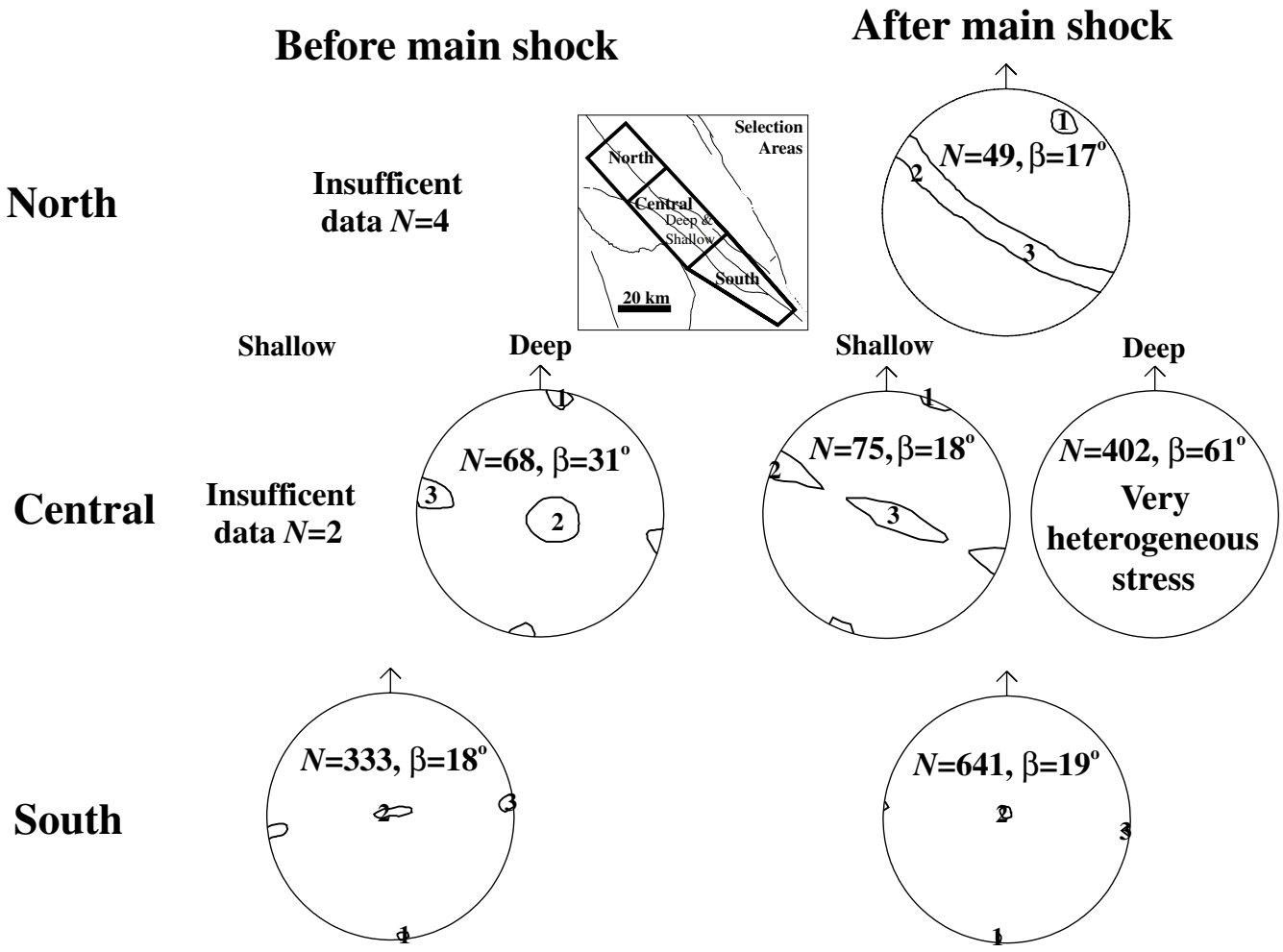

Figure 10.—Results of stress inversion before and after October 17, 1989, main shock for four areas originally defined by Michael and others (1990): north of main-shock rupture (north), south of main-shock rupture (south), above main-shock rupture (shallow central), and near main-shock rupture (deep central). 1–3, three axes of principal stress from most compressional to most extensional, with their 95-percent-confidence areas; *N*, number of inverted events; β, average misfit angle between observed and predicted slip directions.

of fault-normal compression during the aftershocks is reasonable, but we consider this conclusion to be unresolvable with the data.

DISCUSSION

The aftershocks show a fault dipping southwest to near the base of the crust, but could there also be a subvertical fault that extends below the surface trace of the San Andreas fault? The aftershock zone would intersect a subvertical San Andreas fault at 5- to 6-km depth. Above that hypothetical intersection, the San Andreas fault is indicated by a subvertical lateral velocity contrast in the 0- to 4-km grids. In the northwestern and central parts of our model, from y=−45 to y=18 km, the P-wave velocity in the higher shallow material is on the northeast side; and in the southeastern part of our model, from y=26 to y=69 km, the P-wave velocity is higher on the southwest side (fig. 5*A*). With the station array and velocity grid we used, we are unable to discern whether or not an additional narrow low-velocity zone is present at the fault.

Does the San Andreas fault extend below 6-km depth? In the southeastern part of our model, the fault is defined by a lateral-velocity contrast down to 15-km depth, with a high P-wave velocity on the southwest (y=35–50 km, fig. 6). The resolution plots (y=35–50 km, fig. 7) show that whereas the spread function increases below 10-km depth, the nodes near the San Andreas fault are not dominated by smearing from other areas. Therefore, they should show a weaker, broader fault image than the actual fault, but not be artifacts. A synthetic example of a simple fault model with a subset of the event data set showed that a velocity gradient across the fault could be determined down to 15-km depth but that it was much weaker than in the true model (Kissling and others, 1994). In the density model of Jachens and Griscom (this chapter), a narrow, high-density (2.91 g/cm^3) fragment adjacent to the San Andreas fault broadens with depth into a large, 5-km-thick high-density body (fig. 11*C*) that corresponds to the large high-velocity zone we image on the southwest side (figs. 5, 6). They suggested that the shallow high-density fragment, a mapped gabbro, is a small piece that has been splintered off the larger deeper body.

Northwest of y=18 km, below 6-km depth, the San Andreas fault is not simply defined in the P-wave-velocity image. A relatively high velocity is measured on both sides of a subvertical San Andreas fault, and several distinct high-velocity bodies are present. The V_P/V_S ratio varies across the fault, implying the high-velocity body is not a single feature: the high P-wave velocity on the northeast side has a high V_P/V_S ratio, but the deeper high P-wave velocity on the southwest side has a low V_P/V_S ratio. Additionally, Jachens and Griscom's (this chapter) density model near y=−3 km shows that the high-velocity features have different densities

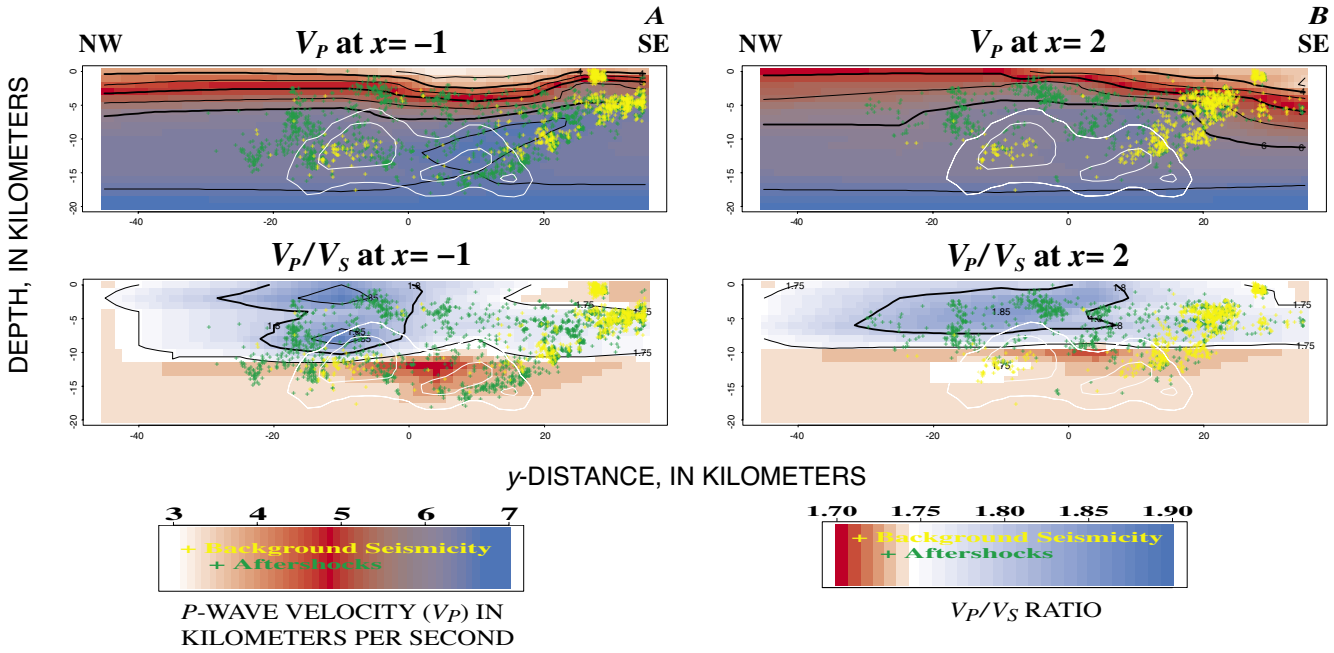

Figure 11.—P-wave-velocity (upper plots) and V_P/V_S ratio (lower plots) cross sections for grid layers at x=−1 km (*A*) and x=2 km (*B*), showing hypocenters within 3 km of each cross section. Contour intervals: P-wave velocity, 0.5 km/s, with 4.0-, 5.0-, 6.0-, and 7.0-km/s contours in bold; V_P/V_S ratio, 0.05, with 1.7, 1.8, and 1.9 contours in bold. Irregular white outlines, 1- and 2-m-slip contours of Wald and others (1991).

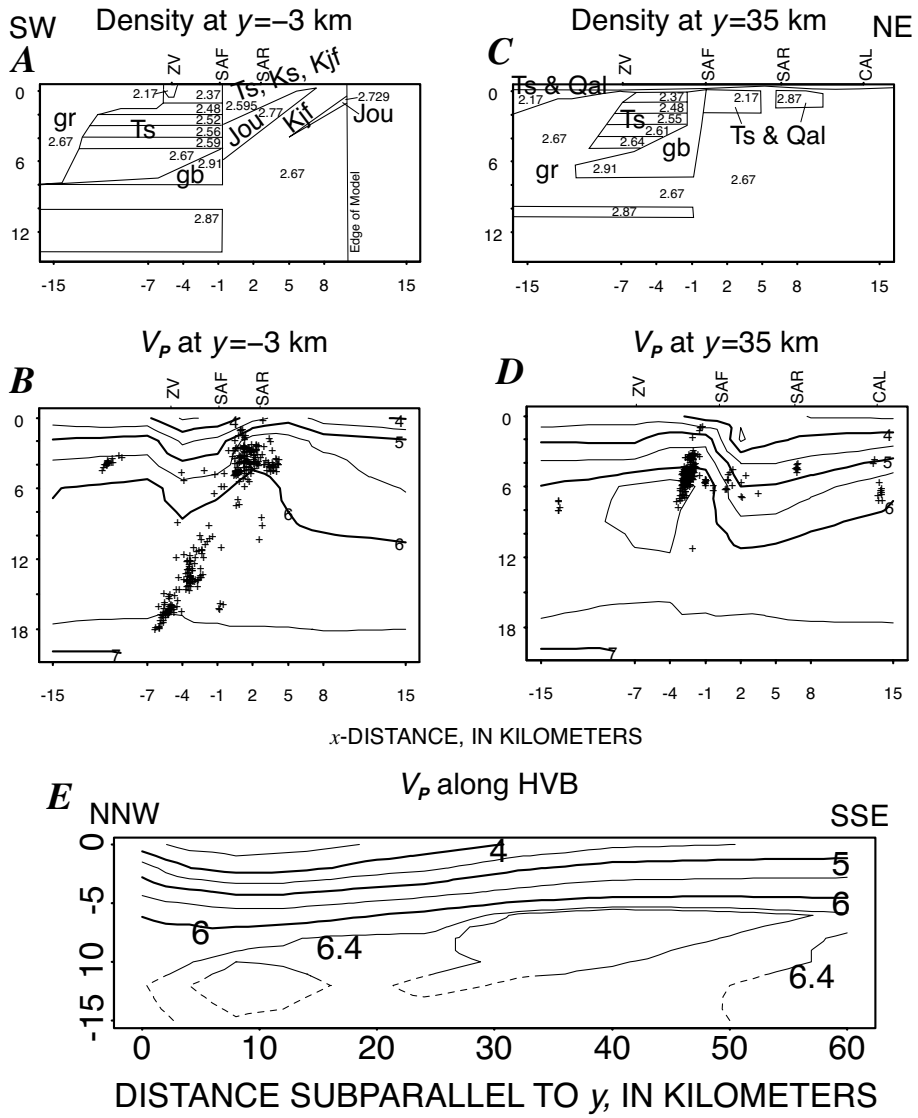

Figure 12.— Comparison of density models of Jachens and Griscom (this chapter) with three-dimensional *P*-wave-velocity (V_P) model, showing density (*A*, *C*; all values in grams per cubic centimeter) and *P*-wave velocity (*B*, *D*; all values in kilometers per second) for grid layers at y=–3 and 35 km. *P*-wave-velocity contour interval, 0.5 km/s, with 4.0-, 5.0-, 6.0-, and 7.0-km/s contours in bold. Faults: CAL, Calaveras; SAF, San Andreas; SAR, Sarmiento; ZV, Zayante-Vergeles. gb, gabbro; gr, granitic and older metamorphic rocks; Jou, Coast Range ophiolite; Kjf, Jurassic and Cretaceous Franciscan complex; Ks, Cretaceous sedimentary rocks; Qal, Quaternary alluvial deposits; Ts, Tertiary sedimentary rocks. *E*, Cross section along length of main high-velocity body (HVB; see fig. 5*C*), which trends slightly more northerly than the San Andreas fault. Cross section is subparallel to y-axis, starting at origin and ending at y=–9 and y=59 km. *P*-wave-velocity contour interval, 0.5 km/s, with 4.0-, 5.0-, 6.0-, and 7.0-km/s contours in bold; 6.4-km/s *P*-wave-velocity contour is added to better delineate high-velocity body. Dashed contours emphasize lack of resolution at depth and therefore our inability to delineate bottom of high-velocity body.

across the fault and that the deeper southwestern feature has a higher density (fig. 11*A*).

Thus, the high-velocity slivers adjacent to the San Andreas fault on the northeast at 6- to 8-km depth and on the southwest at 8- to 15-km depth have different material properties and so are different rock types separated by the fault and are not a single feature that crosses it. Other studies that developed only a *P*-wave-velocity model interpreted the high-velocity body as a single body that would cross a subvertical San Andreas fault (Foxall and others, 1993; see Shalev and Lees, this chapter).

We infer that the most likely boundary of the southwestern high-velocity body is the San Andreas fault extending from the surface throughout the seismogenic zone. A few aftershocks and previous microearthquakes are consistent with the San Andreas fault (as also noted by Olson, 1990). We cannot determine the fault dip accurately with our grid spacing and resolution, and so the fault may be either subvertical or steeply southwest dipping in the Loma Prieta region. We are confident, however, the San Andreas fault is distinct from the Loma Prieta rupture surface and that it does not dip northeast. The fault surfaces can be visualized from aftershock locations. We cannot define them exactly, and so we prefer not to draw the faults on every velocity cross section, but for illustration purposes the two faults are sketched in the y=4 km section (fig. 6).

In addition to a subvertical San Andreas fault, other faults are also imaged in the velocity model. A southwest-dipping thrust fault is correlated with the southwestern Santa Clara Valley thrust belt that has emplaced the Sierra Azul block (see McLaughlin and Clark, this chapter). This thrust fault is not defined by a lineation of seismicity but seems to bound the seismicity such that aftershocks in this area occur primarily in the hanging-wall material (y=–3 km, fig. 6). Most of the aftershocks within this volume have thrust mechanisms (fig. 9*B*).

No single clear feature in the velocity model reveals the fault segment that ruptured in the 1989 Loma Prieta earthquake (fig. 6), although small velocity variations might be missed below 10-km depth as the spread function increases (fig. 7). Along the segment from y=–10 to y=–3 km, the rupture zone has the appearance of a thrust, with higher velocities in the upthrown block. Farther southeast from y=4 to y=10 km, the plane defined by aftershocks is centered in the high-velocity block, not below it. The Loma Prieta fault segment thus appears to vary in its characteristics in the velocity image along the length of rupture. The slip also varies: the earthquake was an oblique-slip event, with at least two patches of slip with different proportions of reverse- and strike-slip motion (Beroza, 1991; Wald and others, 1991).

Michael and Eberhart-Phillips (1991) showed that geologic structure as imaged in three-dimensional velocity models is related to seismogenic behavior, on the basis of models of four earthquakes, including preliminary results from the 1989 Loma Prieta earthquake. In the asperities with greatest moment release, higher-velocity material is in contact with the fault, and the velocity image of the fault is more complex than in creeping sections, where the fault is imaged as a simple strong across-fault velocity contrast. Although our model is coarse at the southeast end, other studies focusing on the creeping section also image the fault with a relatively uniform velocity contrast. For example, Dorbath and others (1996), using a uniform 5-km grid spacing in their study of the intersection of the Calaveras and San Andreas faults, also characterized the San Andreas fault by an across-fault velocity contrast at y=26 km and farther southeast.

In our final model (fig. 11), we can consider details of the high-velocity body and the Loma Prieta rupture zone. The southeastern rupture patch is correlated with a large, distinct high-velocity body within the general southwestern high-velocity feature. The deepest part of the high-slip patch is correlated with the deepest part of the high-velocity body, although the resolution is weak below 10-km depth and the high-velocity body may extend to 18-km depth all along its length to the southeast. The high-velocity body is a more nearly linear feature than the Loma Prieta rupture (figs. 5, 12*E*). It trends slightly more northerly than the San Andreas fault and is closest to the fault near the main shock. Southeast of the main shock, aftershock locations show that the Loma Prieta rupture bends toward the subvertical San Andreas fault (fig. 6). Thus, the rupture is nonplanar and consists of at least two different fracture surfaces. The high-velocity body cannot be an undeformed block with earthquake displacements only on the block boundaries. Instead, we propose that the high-velocity body adjoining the San Andreas fault at depth has many internal fracture surfaces that could sustain rupture in different earthquakes. The high-velocity body may have been built up of many fragments over time coming off the mafic oceanic crust below, or it may have been emplaced as a large coherent fragment that developed internal structure as it was transported into the San Andreas fault bend in the Santa Cruz Mountains.

The primary feature in our final model is a volume of higher-than-normal V_P/V_S ratio in the hanging wall of the Loma Prieta rupture zone at the northwest end of the mainshock rupture. This feature, also seen by Thurber and others (1995), is associated with low *P*-wave velocity and low density. The low-velocity material on the southwest corresponds to a 9-km-wide, 8-km-deep low-density (2.37–2.67 g/cm^3) body (figs. 12*A*, 12*B*). The horizontal base of the high-V_P/V_S-ratio zone at about 8-km depth may be a lithologic boundary between marine sedimentary rocks above and gabbroic basement below (see McLaughlin and Clark, this chapter). Because high V_P/V_S ratios correlate with high pore pressures (Nur and Simmons, 1969), this correlation may provide an explanation for the northwest termination of the Loma Prieta asperity. High pore pressure in that volume of material could reduce the effective pressure, possibly causing velocity-strengthening behavior. Thus, as the rupture began to propagate upward into the sedimentary rocks, it could have undergone a change in frictional behavior and had difficulty propagating farther.

In light of the aftershock locations and velocity features, we suggest that the fault surface which ruptured in the 1989 Loma Prieta earthquake should not be considered as the only active fault segment, or as a tectonic fault independent of the subvertical San Andreas fault; instead, the approximately 5-km-wide zone could be considered as the active San Andreas fault zone. Some events may rupture the subvertical San Andreas fault, which bounds the southwestern high-velocity mafic fragment. This high-velocity mafic fragment probably contains various fracture surfaces, any of which might rupture in an earthquake that would release the strain built up on the San Andreas fault zone. For any particular event, the exact rupture surface may depend on such factors as the residual-stress pattern after previous events. This model of the San Andreas fault zone explains how the Loma Prieta rupture could fill in a microseismicity gap that had been observed on the subvertical San Andreas fault (Moths and others, 1981; U.S. Geological Survey staff, 1990). Given the various fault structures, however, this section of the San Andreas fault zone does not consistently rupture in a single type of characteristic earthquake but rather in varied events, such as the 1906 and 1989 earthquakes (for example, Segall and Lisowski, 1990).

CONCLUSIONS

Defining the spatial extent of lithologic units and material-property changes in the subsurface is a challenge best met by combining several geophysical parameters. In this study, we have developed new three-dimensional models for the Loma Prieta region. Inverting for V_P/V_S ratios circumvents the problems associated with determining V_P/V_S ratios from separate *P*- and *S*-wave-velocity models that have different resolution patterns.

To reasonably estimate velocities throughout the model, taking into account the overall pattern of mapped geology, we performed a series of inversions of progressively increasing complexity. An alternative model with even grid spacing across the fault, and a one-dimensional initial model, show similar but broader velocity features in the aftershock zone but also many single-point velocity anomalies and low-velocity zones in poorly resolved areas.

We interpret subvertical San Andreas fault through the Loma Prieta region from an examination of *P*-wave velocities, V_P/V_S ratios, microearthquake hypocenters, and densities. In the section southeast of the Loma Prieta rupture, the fault is simply defined by an across-fault *P*-wave-velocity gradient with higher velocity on the southwest at all depths. The velocity image is more complex near the Loma Prieta rupture, with low velocities on the southwest side above 7-km depth and relatively high velocities on both sides of the fault below that depth.

Relocated aftershocks help define fault surfaces and show that the Loma Prieta rupture is associated with a high-velocity body, likely to be a mafic fragment, although the rupture surface does not bound this high-velocity body.

Fault-plane solutions computed with three-dimensional raypaths show a range of focal mechanisms similar to that in previous one-dimensional fault-plane solutions. Inversions of focal mechanisms for uniform-stress tensors in subregions are also similar to those in previous one-dimensional results. The aftershocks in the main-shock rupture zone cannot be fitted by a uniform-stress tensor and provide evidence for a coseismic-stress change resulting from a near-total stress drop during the main shock that left a small heterogeneous residual-stress field.

The high-velocity fragment appears to be a key feature in controlling the pattern of slip and the length of the fault segment that ruptured, as well as the distribution of background seismicity on the subvertical San Andreas fault. Thus, the fault surface that ruptured in the 1989 Loma Prieta earthquake, and the subvertical San Andreas fault, do not behave independently and could both be considered parts of the active San Andreas fault zone.

ACKNOWLEDGMENTS

Use of all the data collected after the earthquake turned out to be a large task, and we understand why so many data are commonly overlooked when excellent Calnet data are also available and already analyzed. Cliff Thurber and Shashank Atre combined forces and helped with this task by timing some of the data from portable instruments. We are also indebted to Bill Foxall for the UCB data, Chuck Mueller for the GEOS data, Gary Fuis for data from seismic cassette recorders, John Evans for the 5-day data from the teleseismic network, Cliff Thurber and Shashank Atre for the PASSCAL data, Tom Brocher for the onshore-offshore profiles, and Walter Mooney for his seismic-refraction profiles. Still, most of the data came from the USGS Calnet team, who completely timed and analyzed the records from the prolific aftershock sequence. Without the permanent network, our view of the Loma Prieta region would be hazy and grossly limited in time. Jim Luetgert, Bruce Julian, and John Evans all provided software to help analyze these data sets. The 1991 field experiment required too many personnel from both the USGS and Stanford University to name. We enjoyed many useful discussions with Greg Beroza, Tom Brocher, Rufus Catchings, Bill Ellsworth, Lynn Dietz, John Gephart, Bob Jachens, Will Kohler, Al Lindh, Bob McLaughlin, Dave Oppenheimer, Dal Stanley, Cliff Thurber, Mark Zoback, and Mary Lou Zoback. We thank Tom Brocher, Dave Oppenheimer, and Stephanie Ross for their reviews of the manuscript. We dedicate this paper to Ben Page, who, with his keen insight and unflagging enthusiasm for investigating the tectonics of the San Andreas fault system, pushed us to make the most geologically relevant interpretations of seismic-velocity inversions.

REFERENCES CITED

Abers, G.A., and Roecker, S.W., 1991, Deep structure of an arc-continent collision; earthquake relocation and inversion for upper mantle *P* and *S* wave velocities beneath Papua New Guinea: Journal of Geophysical Research, v. 96, no. B4, p. 6379–6401.

Beroza, G.C., 1991, Near-source modeling of the Loma Prieta earthquake; evidence for heterogeneous slip and implications for earthquake hazard: Seismological Society of America Bulletin, v. 81, no. 5, 1603–1621.

Boken, Annette, and Mooney, W.D., 1982, A refraction study of the Santa Cruz Mountains, west-central California [abs.]: Eos (American Geophysical Union Transactions), v. 63, no. 45, p. 1036.

Brocher, T.M., Moses, M.J., and Lewis, S.D., 1992, Wide-angle seismic recordings obtained during seismic reflection profiling by the *S.P. Lee* offshore the Loma Prieta epicenter: U.S. Geological Survey Open-File Report 92–245, 63 p.

Dietz, L.D., and Ellsworth, W.L., 1990, The October 17, 1989, Loma Prieta, California, earthquake and its aftershocks; geometry of the sequence from high-resolution locations, Geophysical Research Letters, v. 17, no. 9, p. 1417–1420.

Dorbath, Catherine, Oppenheimer, David, Amelung, Falk, and King, Geoffrey, 1996, Seismic tomography and deformation modeling of the junction of the San Andreas and Calaveras faults: Journal of Geophysical Research, v. 101, no. B12, p. 27917–27941.

Eberhart-Phillips, D.M., 1986, Three-dimensional velocity structure in northern California Coast Ranges from inversion of local earthquake arrival times: Seismological Society of America Bulletin, v. 76, no. 4, p. 1025–1052.

———1990, Three-dimensional *P*- and *S*-velocity structure in the Coalinga region, California: Journal of Geophysical Research, v. 95, no. B10, p. 15343–15363.

———1993, Local earthquake tomography; earthquake source regions, *in* Iyer, H.M., and Hirahara, Kazuro, eds., Seismic tomography; theory and practice: London, Chapman and Hall, p. 614–643.

Eberhart-Phillips, D.M., Labson, V.F.D., Stanley, W.D., Michael, A.J., and Rodriguez, B.D., 1990a, Preliminary velocity and resistivity models of the Loma Prieta earthquake region: Geophysical Research Letters, v. 17, no. 8, p. 1235–1238.

Eberhart-Phillips, D.M., and Michael, A.J., 1993, Three-dimensional velocity structure, seismicity, and fault structure in the Parkfield region, central California: Journal of Geophysical Research, v. 98, no. B9, p. 15737–15758.

Eberhart-Phillips, D.M., Michael, A.J., Fuis, G.J., and Luzitano, R.D., 1990b, Three-dimensional crustal velocity structure in the region of the Loma Prieta, California, earthquake sequence from inversion of local earthquake and shot arrival times [abs.]: Seismological Society of America Bulletin, v. 61, no. 1, p. 48.

Eberhart-Phillips, D.M., Stanley, W.D., Rodriguez, B.D., and Lutter, W.J., 1995, Surface seismic and electrical methods to detect fluids related to faulting: Journal of Geophysical Research, v. 100, no. B7, p. 12919–12936.

Eberhart-Phillips, D.M., and Stuart, W.D., 1992, Material heterogeneity simplifies the picture; Loma Prieta: Seismological Society of America Bulletin, v. 82, no. 4, p. 1964–1968.

Foxall, William, Michelini, Alberto, and McEvilly, T.V., 1993, Earthquake travel time tomography of the southern Santa Cruz Mountains; control of fault rupture by lithological heterogeneity of the San Andreas fault zone: Journal of Geophysical Research, v. 98, no. B10, p. 17691–17710.

Fuis, G.S., and Mooney, W.D., 1990, Lithospheric structure and tectonics from seismic-refraction and other data, chap. 8 *of* Wallace, R.E., ed., The San Andreas fault system, California: U.S. Geological Survey Professional Paper 1515, p. 207–236.

Furlong, K.P., Hugo, W.D., and Zandt, George, 1989, Geometry and evolution of the San Andreas fault zone in northern California: Journal of Geophysical Research, v. 94, no. B3, p. 3100–3110.

Harbert, William, and Cox, Allan, 1989, Late Neogene motion of the Pacific plate: Journal of Geophysical Research, v. 94, no. B3, p. 3052–3064.

Holbrook, W.S., Brocher, T.M., ten Brink, U.S., and Hole, J.A., 1996, Crustal structure of a transform plate boundary; San Francisco Bay and the central California continental margin: Journal of Geophysical Research, v. 101, no. B10, p. 22311–22334.

Irwin, W.P., Geology and plate-tectonic development, chap. 3 *of* Wallace, R.E., ed., The San Andreas fault system, California: U.S. Geological Survey Professional Paper 1515, p. 61–80.

Kissling, Edi, Ellsworth, W.L., Eberhart-Phillips, D.M., and Kradolfer, Urs, 1994, Initial reference models in local earthquake tomography: Journal of Geophysical Research, v. 99, no. B10, p. 19635–19646.

Lees, J.M., 1990, Tomographic *P*-wave velocity images of the Loma Prieta earthquake asperity: Geophysical Research Letters, v. 17, no. 9, p. 1433–1436.

Lisowski, Michael, Savage, J.C., and Prescott, W.H., 1991, The velocity field along the San Andreas fault in central and southern California: Journal of Geophysical Research, v. 96, no. B5, p. 8369–8389.

Michael, A.J., 1984, Determination of stress from slip data; faults and folds: Journal of Geophysical Research, v. 89, no. B13, p. 11517–11526.

———1987a, Stress rotation during the Coalinga aftershock sequence: Journal of Geophysical Research, v. 92, no. B8, p. 7963–7979.

———1987b, Use of focal mechanisms to determine stress; a control study: Journal of Geophysical Research, v. 92, no. B1, p. 357–368.

———1991, Spatial variations in stress within the 1987 Whittier Narrows, California, aftershock sequence; new techniques and results: Journal of Geophysical Research, v. 96, no. B4, p. 6303–6320.

Michael, A.J., and Eberhart-Phillips, D.M., 1991, Relations among fault behavior, subsurface geology, and three-dimensional velocity models: Science, v. 253, no. 5020, p. 651–654.

Michael, A.J., Ellsworth, W.L., and Oppenheimer, D.H., 1990, Coseismic stress changes induced by the 1989 Loma Prieta, California earthquake: Geophysical Research Letters, v. 17, no. 9, p. 1441–1444.

Michelini, Alberto, 1991, Fault zone structure determined through the analysis of earthquake arrival times: Berkeley, University of California, Ph.D. thesis, 191 p.

Michelini, Alberto, and McEvilly, T.V., 1991, Seismological studies at Parkfield. I. Simultaneous inversion for velocity structure

and hypocenters using cubic B-splines parameterization: Seismological Society of America Bulletin, v. 81, no. 2, p. 524–552.

Mooney, W.D., and Colburn, R.H., 1985, A seismic-refraction profile across the San Andreas, Sargent, and Calaveras faults, west-central California: Seismological Society of America Bulletin, v. 75, no. 1, p. 175–191.

Mooney, W.D., and Luetgert, J.H., 1982, A seismic refraction profile in the Santa Clara Valley and southern Santa Cruz Mountains, west-central California: Seismological Society of America Bulletin, v. 72, no. 3, p. 901–909.

Moths, B.L., Lindh, A.G., Ellsworth, W.L., and Fluty, L., 1981, Comparison between the seismicity of the San Juan Bautista and Parkfield regions, California [abs.]: Eos (American Geophysical Union Transactions), v. 62, no. 45, p. 958.

Murphy, J.M., 1988, USGS FM cassette seismic-refraction recording system: U.S. Geological Survey Open-File Report 88–570, 43 p.

Murphy, J.M., Catchings, R.D., Kohler, W.M., Fuis, G.S., and Eberhart-Phillips, D.M., 1992, Data report for 1991 active-source seismic profiles in the San Francisco Bay area, California: U.S. Geological Survey Open-File Report 92–570, 45 p.

Mueller, Charles, and Glassmoyer, Gary, 1990, Digital recordings of aftershocks of the October 17, 1989 Loma Prieta, California, earthquake: U.S. Geological Survey Open-File Report 90–503, 147 p.

Nur, Amos, and Simmons, Gene, 1969, The effect of saturation on velocity in low porosity rocks: Earth and Planetary Science Letters, v. 7, no. 2, p. 183–193.

Olson, J.A., 1990, Seismicity in the twenty years preceding the Loma Prieta, California earthquake: Geophysical Research Letters, v. 17, no. 9, p. 1429–1432.

Oppenheimer, D.H., 1990, Aftershock slip behavior of the 1989 Loma Prieta, California earthquake: Geophysical Research Letters, v. 17, no. 8, p. 1199–1202.

Page, B.M., 1990, Evolution and complexities of the transform system in California, U.S.A.: Annales Tectonicae, v. 4, no. 2, p. 53–69.

Page, B.M., and Brocher, T.M., 1993, Thrusting of the central California margin over the edge of the Pacific plate during the transform regime: Geology, v. 21, no. 7, p. 635–638.

Parsons, Tom, and Zoback, M.L., 1997, Three-dimensional upper crustal velocity structure beneath San Francisco Peninsula, California: Journal of Geophysical Research, v. 102, no. B3, p. 5473–5490.

Reasenberg, Paul, and Oppenheimer, D.H., 1985, FPFIT, FPPLOT, and FPPAGE; Fortran computer programs for calculating and displaying earthquake fault-plane solutions: U.S. Geological Survey Open-File Report 85–739, 109 p.

Schwartz, S.Y., Orange, D.L., and Anderson, R.S., 1990, Complex fault interactions in a restraining bend on the San Andreas fault, southern Santa Cruz Mountains, California: Geophysical Research Letters, v. 17, no. 8, p. 1207–1210.

Segall, Paul, and Lisowski, Michael, 1990, Surface displacements in the 1906 San Francisco and 1989 Loma Prieta earthquakes: Science, v. 250, no. 4985, p. 1241–1244.

Sims, J.D., 1993, Chronology of displacement on the San Andreas fault in central California; evidence from reversed positions of exotic rock bodies near Parkfield, California, *in* Powell, R.E., Weldon, I.R.J., and Matti, J.C., eds., The San Andreas fault system; displacement, palinspastic reconstruction, and geologic evolution: Geological Society of America Memoir 178, p. 231–256.

Takauchi, Yoko, and Evans, J.R., 1995, Teleseismic tomography of the Loma Prieta earthquake region, California; implications for strain partitioning: Geophysical Research Letters, v. 22, no. 16, p. 2203–2206.

Thurber, C.H., 1983, Earthquake locations and three-dimensional crustal structure in the Coyote Lake area, central California: Journal of Geophysical Research, v. 88, no. B10, p. 8226–8236.

———1993, Local earthquake tomography; velocities and V_P/V_S—theory, *in* Iyer, H.M., and Hirahara, Kazuro, eds., Seismic tomography; theory and practice: London, Chapman and Hall, p. 563–583.

Thurber, C.H., and Atre, S.R., 1993, Three-dimensional V_P/V_S variations along the Loma Prieta rupture zone: Seismological Society of America Bulletin, v. 83, no. 3, p. 717–736.

Thurber, C.H., Atre, S.R., and Eberhart-Phillips, D.M., 1995, Three-dimensional V_P and V_P/V_S structure at Loma Prieta, California, from local earthquake tomography: Geophysical Research Letters, v. 22, no. 22, p. 3079–3082.

Thurber, C.H., Roecker, S.W., Ellsworth, W.L., Chen, Y.-H., Lutter, W.J., and Sessions, Robert, 1997, Two-dimensional seismic image of the San Andreas fault in the northern Gabilan Range, central California; evidence for fluids in the fault zone: Geophysical Research Letters, v. 24, no. 13, p. 1591–1594.

Toomey, D.R., and Foulger, G.R., 1989, Tomographic inversion of local earthquake data from the Hengill-Grensdalur central volcano complex, Iceland: Journal of Geophysical Research, v. 94, no. B12, p. 17497–17510.

U.S. Geological Survey staff, 1990, The Loma Prieta, California, earthquake; an anticipated event: Science, v. 247, no. 49, p. 286–293.

Wald, D.J., Helmberger, D.V., and Hanks, T.H., 1991, Rupture model of the 1989 Loma Prieta earthquake from the inversion of strong-motion and broadband teleseismic data: Seismological Society of America Bulletin, v. 81, no. 5, p. 1540–1572.

Zoback, M.D., and Beroza, G.C., 1993, Evidence for near-frictionless faulting in the 1989 (*M* 6.9) Loma Prieta, California, earthquake and its aftershocks: Geology, v. 21, no. 2, p. 181–185.

Zoback, M.D., Mount, V.S., Suppe, John, Eaton, J.P., Healy, J.H., Oppenheimer, D.H., Reasenberg, P.A., Jones, L.M., Raleigh, C.B., Wong, I.G., Scotti, Oona, and Wentworth, C.M., 1987, New evidence on the state of stress of the San Andreas fault system: Science, v. 238, no. 4830, p. 1105–1111.

EARTHQUAKE OCCURRENCE

TELESEISMIC TOMOGRAPHY OF THE LOMA PRIETA REGION: IMPLICATIONS FOR STRAIN PARTITIONING

By Yoko Takauchi and John R. Evans, U.S. Geological Survey

CONTENTS

ABSTRACT

From teleseismic traveltime residuals, we derive three-dimensional velocity models of the Loma Prieta region to 71-km depth. We use an extended ACH inversion process that minimizes parametrization artifacts while retaining an explicit resolution matrix. We also "strip" upper-crustal structure from our data, inverting the remaining teleseismic traveltime residuals to test the robustness of the deeper structures we image. For stripping, we use three methods: wave-front tracing through each of two local-earthquake-tomography models, and an iterative technique that maximally removes the upper-crustal signature from our data. Absent stripping, the shallow crustal structure we determine generally agrees with local-earthquake-tomography results, with discrepancies consistent with resolution effects and wave effects at strong velocity contrasts across some faults. Deeper structures are not significantly affected by crustal stripping, indicating that they are not much affected by smearing of shallow, large-magnitude velocity anomalies. We observe many horizontal velocity gradients beneath the San Andreas fault at all depths, including in the upper mantle. These gradients suggest that the fault was a deep, narrow shear locus at least at one time. Low velocities are observed beneath the Loma Prieta highlands near the Moho; this feature probably is caused by a crustal root, approximately 2 to 5 km thick and 10 to 30 km across. We also resolve two conspicuous upper-mantle low-velocity features between 45- and 70-km depth, separated right laterally along the San Andreas fault by about 45 km. The San Andreas fault (or its adjacent predecessor, the Pilarcitos fault) formed in this region by at least 6 Ma. Estimated slip rates along the San Andreas fault system suggest that this 45-km offset is comparable to the amount of shear occurring within just a few million years. If this pair of upper-mantle low-velocity features preserves the total upper-mantle slip at a locus beneath the San Andreas fault, this result is consistent with a model that posits rapid cooling of this volume after passage of the Mendocino Triple Junction and a current, broad locus of upper-mantle shear centered beneath the Hayward/Calaveras fault system to the northeast.

INTRODUCTION

The lithospheric structure of the Loma Prieta region of central California (fig. 1) is complicated by major and minor reverse- and strike-slip faults that together form the San Andreas fault system. Although the San Andreas fault is a manifestation of the northwest-striking boundary between the Pacific and North American plates at the surface, the deeper structure and position of the plate boundary are matters of debate.

The 1989 Loma Prieta earthquake (M_W=6.9) was unusual for its relatively great depth and oblique reverse rupture. Furlong and Langston (1990) concluded that relatively low observed heat flow and thin upper crust in the region lead to strain accumulation at the base of the brittle crust (18–20-km depth), where the Loma Prieta rupture commenced. Below this depth, the lowermost Pacific crust can deform ductilely. They attributed this strain to a discrepancy in the displacement directions between the crustal and mantle parts of the Pacific plate where the crust moves relatively westward around a bend in the San Andreas fault, creating a basal traction toward the fault. If, as they proposed, the crust between sections of the fault is detached from the mantle somewhere in the lower crust, then crustal compressive strain will accumulate near the fault.

Zandt (1981) did the first comprehensive teleseismic-tomography study of central California, achieving 10- to 25-km

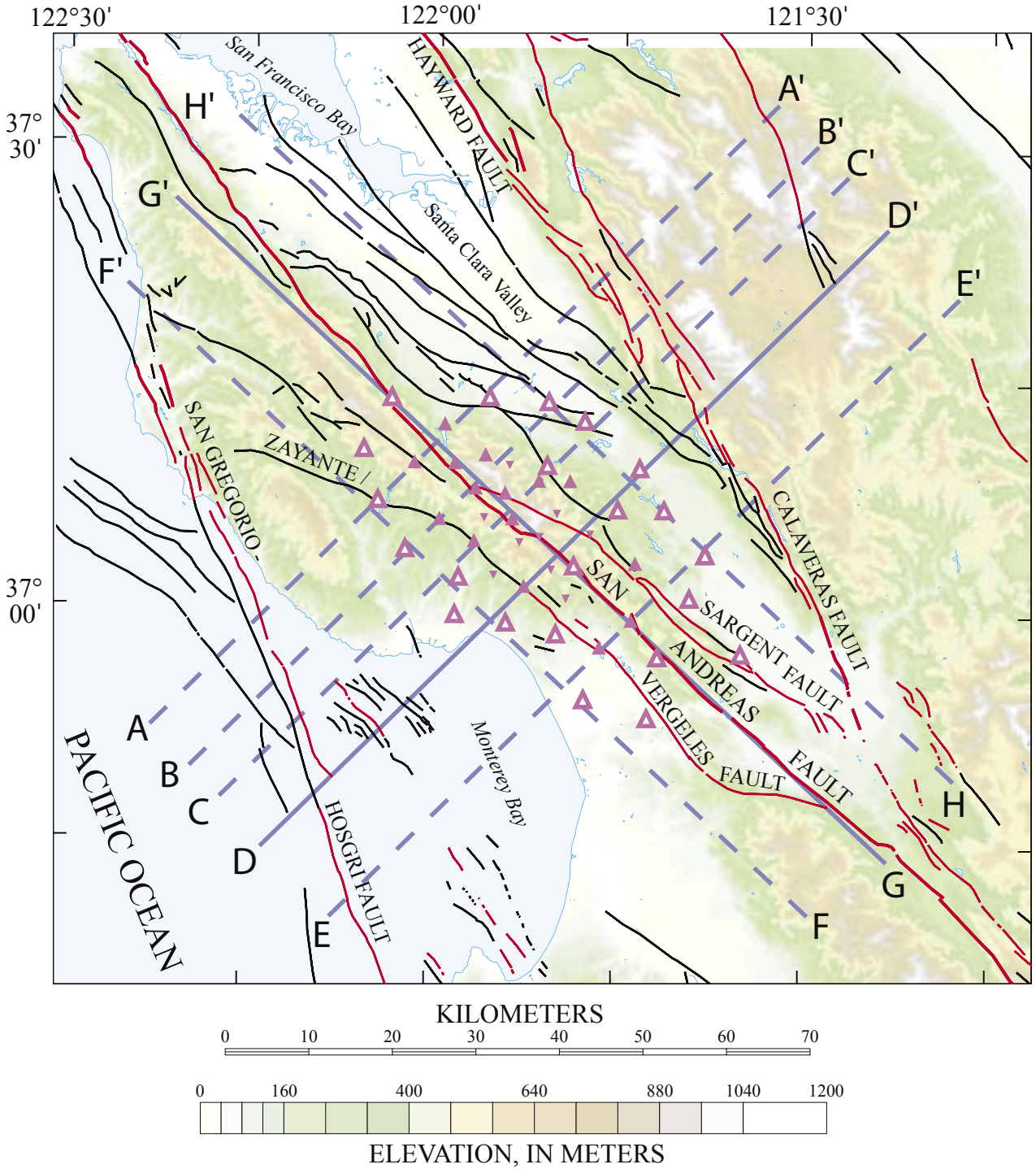

Figure 1.—Loma Prieta region, Calif., showing locations of major faults and cross sections *A–A′* through *H–H′*. Dashed-line cross sections were shown only by Takauchi (1994). Both types of upright triangles, seismic stations used for principal-model series; both types of solid triangles, seismic stations used for detailed-model series.

horizontal resolution from teleseismic *P*-wave-traveltime data recorded on the Northern California Seismic Network (NCSN) operated by the U.S. Geological Survey (USGS). His main findings include (1) correlation of a Tertiary marine sedimentary block between the San Andreas and Zayante faults with a modeled upper-crustal low-velocity feature, and (2) a low-velocity body in the lower crust (10–30-km depth) beneath Loma Prieta that he attributed to variation in the depth to the Moho.

Local-earthquake-tomography models by Eberhart-Phillips and others (1990) and Lees (1990) similarly reveal a low-velocity wedge between the San Andreas and Zayante faults, extending to 8-km depth, that they interpreted as Tertiary marine sedimentary rocks. It also has a low Q value (Lees and Lindley, 1994). Both Lees (1990) and Eberhart-Phillips and others (1990) imaged a high-velocity body northeast of the San Andreas fault. In the near-surface, Eberhart-Phillips and others (1990) modeled it between the San Andreas and Sargent faults, whereas Lees placed it mostly northeast of the Sargent fault. This high-velocity body dips southwest to at least 18-km depth, where it underlies the previous low-velocity body in both models and includes the hypocenter of the 1989 Loma Prieta earthquake. Lees inferred a relation between this high-velocity body and aftershock locations. Foxall and others (1993), who also derived a local-earthquake-tomography model of the southern Santa Cruz Mountains, inferred that the high-velocity body is the site of a stress concentration which caused the earthquake. Seismic-refraction studies (for example, Fuis and Mooney, 1990) also reveal the structure of the crust in this area, showing it thinning toward the Pacific Ocean and about 25 km thick beneath the Loma Prieta region (fig. 1).

Although previous local-earthquake-tomography models are useful for understanding the structure of the seismogenic crust, they do not reveal the lower-crustal or upper-mantle structure of the region because rays observed from local earthquakes do not penetrate that deeply. Previous teleseismic-tomography studies were of relatively low resolution, limited by the spacing of NCSN permanent stations. In this paper, we describe teleseismic-tomography models that resolve this deeper structure and allow inferences regarding the tectonics of the San Andreas fault system.

METHOD

DATA

Teleseisms used in our study were recorded from August to December 1990, using 27 temporary seismic stations to augment NCSN stations. The combination is a much denser array than that available to Zandt (1981). In this paper, we treat this array as two subarrays, with many stations shared between subarrays (fig. 1). The first subarray was for a study of the whole area to 60- to 70-km depth at ~6-km horizontal resolution. This less dense subarray comprised 20 temporary stations and 17 NCSN stations; the models derived from it are called the principal-model series. The second subarray was for a study in the vicinity of the intersection of the San Andreas and Sargent faults, where structure is particularly complex. This subarray comprised 14 temporary stations and 10 NCSN stations; the models derived from it, which are called the detailed-model series, reach 30- to 40-km depth at ~3-km horizontal resolution. (A larger, regional-model series spanning the principal-model series, presented by Takauchi, 1994, does not add much to the principal models and those by Zandt, 1981, and so is not described further here.)

The epicenters of the teleseisms we used are mapped in figure 2. The resulting distribution of rays within our target volumes is reasonably homogeneous, although events with northeastward backazimuths were far fewer than those with other backazimuths, as is typical in the Western United States (for *P* phases: 4 events from the northeast, 25 from the southeast, 11 from the southwest, and 23 from the northwest; for *PKPdf* phases: 5 events).

Relative arrival times of compressional *P* and *PKPdf* phases were picked from filtered traces by a visual correlative method. Each pick was assigned a subjective quality based on noise and signal coherence, using the guideline that 3σ for "a"-quality picks should be about ±0.05 s, for "b"-quality picks about ±0.10 s, and for "c"-quality picks about ±0.25 s. We also reviewed the data in slowness-backazimuth space to identify errors, basing any corrective actions on the seismograms themselves. The final data set has 2,705 picks from 68 teleseisms, including 544 "a"-quality, 1,193 "b"-quality, and 968 "c"-quality picks.

INVERSION TECHNIQUE

Traveltime residuals R_{ij} at the ith station for the jth event are calculated with respect to a known one-dimensional Earth model (Herrin, 1968). This "raw" residual includes the effects of origin-time uncertainty, hypocenter mislocation, and velocity heterogeneity outside the modeled volume. To mitigate these effects, relative residuals RR_{ij} are calculated by subtracting some reference residual R_j:

$$RR_{ij} = R_{ij} - R_j.$$

For R_j, we use a weighted mean residual

$$R_j = \frac{\sum_i w_{ij} R_{ij}}{\sum_i w_{ij}}$$

where w_{ij} is a weight derived from the pick qualities.

To invert these data for velocity structure, we used the ACH inversion method of Aki and others (1977) as extended by Evans and Achauer (1993) to include (1) an offset-and-

average horizontal-smoothing technique; (2) a layer-thinning vertical-smoothing technique; and (3) representation of the resolution matrix **R** in terms of "volume metrics," irregular volumes of approximately the size, shape, and orientation of the smallest resolvable features. We use the more mature ACH method because its behavior is well understood and it produces an explicit resolution matrix **R**.

The target volume beneath the receiver array is divided into layers of approximately equal teleseismic traveltime, where each layer is subdivided into rectilinear blocks whose horizontal width is about equal to the mean station spacing. This dimension is the smallest horizontal size validly modeled by ACH tomography. Each block has an unknown fractional slowness deviation from the initial model's (layer) slowness. The total thickness of the modeled volume approximately equals the aperture of the receiver array because below this depth, *P*-wave rays diverge significantly, no longer crisscrossing, so that deeper objects are poorly resolvable.

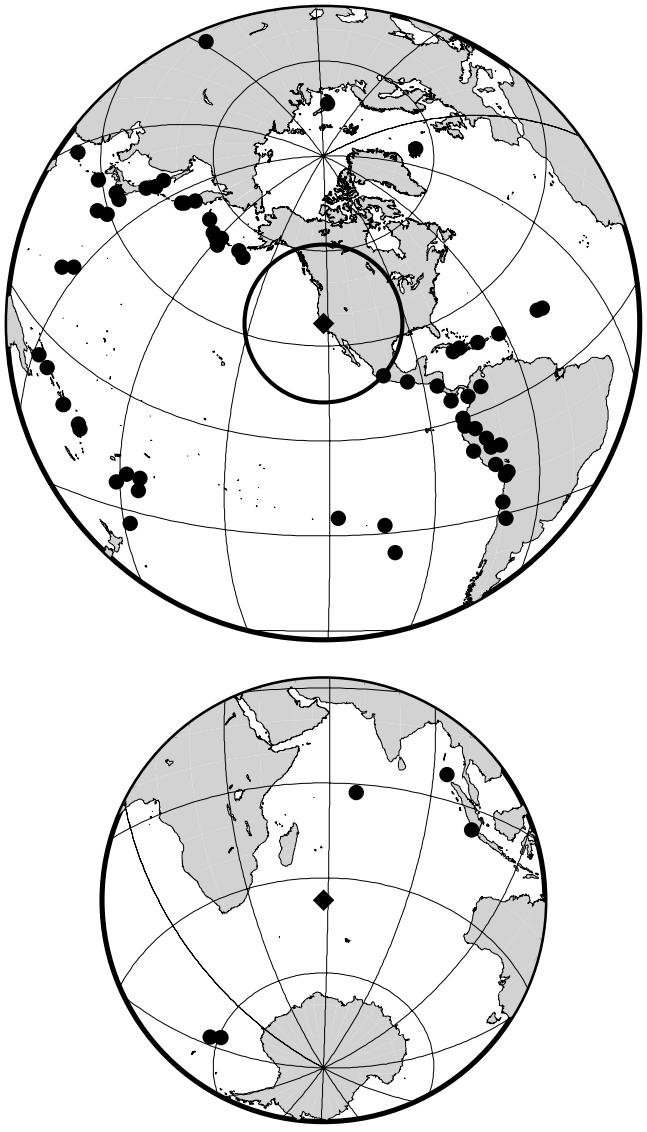

Figure 2.—Azimuthal equidistant maps of earthquake epicenters for this study (dots). Diamond in upper map is study area; diamond in lower map is its antipode. Dark circles in upper map are 025° and 100° distant from center of study area; dark circle in lower map is 110° distant from study area (thus, 070° distant from antipode).

Succinctly, following Evans and Achauer (1993), we linearize the problem through block parametrization, disregarding refraction by the slowness perturbations (a second-order term because our rays do not have turning points within the model):

$$b = \mathbf{G}m,$$

where b is a vector derived from the traveltime residuals RR_{ij}, m is a vector containing the unknown fractional slowness deviations of each block (that is, the velocity model we seek), and **G** is a matrix derived from the unperturbed traveltimes of ray ij in block k. (Here, we leave out details related to data-quality weighting and parameter separation for the source term.) To estimate m, we use damped least squares to regularize the problem:

$$\hat{m} = (\mathbf{G} + \theta\mathbf{I})^{-1}b.$$

The solution, $m\hat{}$, is not iterated, since refraction is a second-order effect. More modern methods use higher-order regularization, which is arguably more physical, but the smoothing procedures that we next apply obviate this advantage.

We chose an appropriate damping value by plotting tradeoff curves between damping, data fit, and model complexity (the Euclidean norm of $m\hat{}$). The optimal damping value is near a residual data variance that is comparable to the square of expected reading errors, and where neither data fit nor model complexity dominates the solution (fig. 3). Finally, the Moho is near 25-km depth in this region (for example, Fuis and Mooney, 1990). To improve ray-tracing accuracy, we ensure that a layer boundary falls at this depth. Horizontal block widths are ~6 and ~3 km for principal- and detailed-model series, respectively.

The processes of horizontal and vertical smoothing proceed in several steps, beginning with a "base" model and proceeding through layer-thinning and offset-and-average steps (as explained below). For the base model in each series, we chose layer thicknesses about 1.5 times the block width, a choice designed to yield fairly "well resolved" individual blocks. For initial crustal velocities, we used the average of the velocity models of Dietz and Ellsworth (this chapter) for the southwest and northeast sides of the San Andreas fault. Mantle velocities are those of Herrin (1968), joined to the crustal model by a linear gradient between 25- and 45-km depth. To this velocity structure we applied an Earth-flattening transform to trace rays more accurately. (The ACH inversion that we use is Cartesian.) Our choice of damping value was for this base model. We also used the base models to compute diagonal

elements of the resolution matrix **R** and associated standard errors, because subsequent layer thinning invalidates these items (Evans and Achauer, 1993).

We incorporated vertical smoothing into the model by dividing each layer of the base model, except for the shallowest layer, into three sublayers of equal traveltime (tables 1, 2). Evans and Achauer (1993) showed that this layer-thinning method is a legitimate means of obtaining vertical smoothing in ACH teleseismic tomography, as long as the damping value is reduced in proportion to the increase in the number of unknowns (that is, in the number of modeled blocks).

One effect of layer thinning is to drastically reduce the values of the diagonal elements of the resolution matrix **R**. Although these diagonal elements are in no case an adequate exposition of resolution characteristics, with layer thinning that inadequacy is manifold, and so we clearly need a more complete description. For this purpose, Evans and Achauer (1993) introduced the "volume metric," which is a figure of merit derived from any single column of the resolution matrix

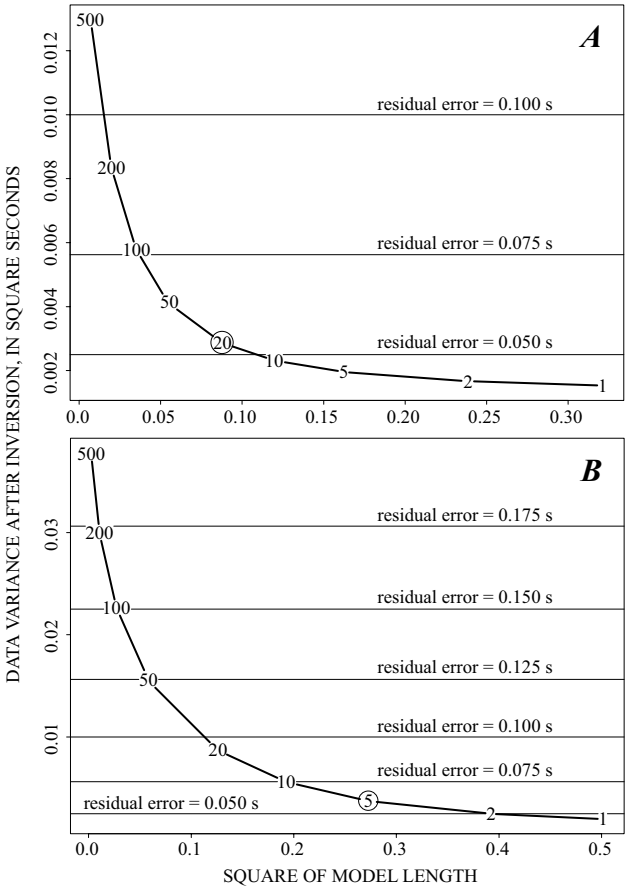

Figure 3.—Damping tradeoff curves for principal model (*A*) and detailed model (*B*). Circled damping value was selected for use, on the basis of shape of curve (trading data fit against model complexity) and residual error after inversion, which should approximate reading error.

Table 1.—*Initial parameters for principal inversion model*

[Datum is sea level]

Base model		Thinned-layer model	
Depth to top (km)	Velocity (km/s)	Depth to top (km)	Velocity (km/s)
Station elevation	4.86	Station elevation	4.86
6.90	6.23	6.90	6.12
		9.81	6.22
		12.75	6.33
15.75	6.52	15.75	6.40
		18.78	6.57
		21.89	6.57
25.00	8.05	25.00	8.03
		28.80	8.05
		32.60	8.07
36.40	8.11	36.40	8.09
		40.22	8.11
		44.03	8.12
47.85	8.14	47.85	8.13
		51.67	8.14
		55.50	8.15
59.32	8.16	59.32	8.15
		63.15	8.16
		66.97	8.17
70.80	– – –	70.80	– – –

R by summing its largest positive values until they reach some acceptable "equivalent diagonal-element value," for example, 0.75. The volume metric is the irregular portion of the model spanned by these summed blocks. Thus, each volume metric is a simple representation of the size, shape, and orientation of the model's "impulse response" at the site of the diagonal element's block—that is, it shows how far and in what directions any very small feature would be smeared out. Evans and Achauer showed that such volume metrics are effectively invariant under adjusted-damping layer thinning.

For horizontal smoothing, we applied an offset-and-average scheme. Each layer of the thinned-layer model is shifted horizontally in increments of $^1/_n$th the block width (in our model, ⅓ the block width), and the shifted model is inverted. Every nonduplicating permutation of block shift is used, and so there are n^2 (nine) shifted models. Models with each of these block-shift permutations are produced and averaged within each ⅓-by-⅓-width block overlap (Evans and Achauer, 1993, fig. 13.2). Between layer thinning and offset-and-average smoothing, then, the block volume is reduced to $^1/_{27}$th that of the base model, although the resolvable volume remains nearly constant. We gain presentation quality and reduce the side effects of block parametrization, which can be significant and unintuitive.

Table 2.—*Initial parameters for detailed inversion model*

[Datum is sea level]

Base model		Thinned-layer model	
Depth to top (km)	Velocity (km/s)	Depth to top (km)	Velocity (km/s)
Station elevation	4.06	Station elevation	4.06
2.90	5.67	2.90	5.42
		4.15	5.61
		5.48	5.98
6.90	6.16	6.90	6.03
		8.35	6.22
		9.82	6.22
11.31	6.30	11.31	6.22
		12.75	6.32
		14.27	6.34
15.77	6.46	15.77	6.35
		17.29	6.46
		18.84	6.57
20.41	6.57	20.41	6.57
		21.97	6.57
		23.48	6.57
25.06	8.04	25.05	8.03
		26.96	8.04
		28.86	8.05
30.78	8.07	30.77	8.06
		32.66	8.07
		34.59	8.08
36.51	– – –	36.50	– – –

CRUSTAL CORRECTION

We also addressed the issue of possible smearing of shallow velocity anomalies to greater depth, using the two methods of Dawson and others (1990). Because the shallowest layer generally has the largest velocity perturbations (unconsolidated sedimentary deposits, high porosity, weathering) and resolution is never perfect, the perturbations caused by these shallow upper-crustal structures might distort deeper images by smearing downward. To examine these effects, we (1) used iterative stripping of shallow structure and (2) separately corrected our data for two upper-crustal models derived by local-earthquake tomography.

Iterative stripping refers to an iterative inversion for velocities in the shallowest layer by itself. At each step, the velocity model resulting from inversion for this top layer is added back into the starting model of the next iteration, until velocity perturbations converge. The intent is to explain as many of the data as possible by this one-layer shallow model alone. The final, iterated velocity model is then used as the first layer of the starting model for a fully layered inversion of the entire target volume. Below the shallowest layer, this new starting model has the one-dimensional starting velocities of the original, whereas the shallowest layer is the heterogeneous model taken from the iteration scheme. This starting model effectively "corrects" the data, removing all residuals that can be (but not necessarily are) explained by shallow structure, thus allowing inversions of deeper layers to proceed with a minimum of smearing. We call such models iteratively stripped.

Although the iterative-stripping method is useful, it may overcorrect for shallow structure (Dawson and others, 1990) and so should be considered an end member in a continuum of models. (The unstripped model is the other end member.) Not all data that *can* be explained by shallow structure necessarily *should* be. To explore this issue, we used two recently derived local-earthquake-tomography models, those of Eberhart-Phillips and Michael (this chapter) and Harley Benz (digital commun., 1995).

Eberhart-Phillips and Michael (this chapter) derive detailed three-dimensional *P*-wave-velocity and V_P/V_S-ratio models of the Loma Prieta region from data recorded on NCSN stations and our temporary array, and from seismic refraction or other explosion data. They use the damped-least-squares method originated by C.H. Thurber (see Evans and others, 1994). Eberhart-Phillips and Michael's model ("crustal model A") is specific to the Loma Prieta region and includes station-correction terms for many of our stations. Harley Benz determined *P*-wave velocities in a broad stretch of northern California ("crustal model B"); he used NCSN data for local earthquakes, applying the wave-front-tracing method of Podvin and Lecomte (1991) and a least-squares inversion with smoothness constraints.

To incorporate crustal models A and B into ours, we computed traveltimes through both models for our teleseismic wave fronts, using the method of Podvin and Lecomte (1991). First, we extracted the appropriate part of each model, creating a slowness mesh of 0.5-km block dimension. (Teleseismic wavelengths are ~6 km in the crust.) This remeshing was unambiguous for model B because it was derived with the same wave-front tracer; for model A, we simply made a trilinear interpolation to the center of each mesh cell from the nearest eight nodes of the crustal model. The mesh extends from the middle crust (10 km below sea level) to above the highest station. Except locally, the local-earthquake models are unreliable below the middle crust. In any case, most of the traveltime perturbation associated with these models comes from shallower structure.

Rather than initializing our plane-wave front on three sides of this mesh (the bottom and both sides facing the teleseism), we extracted a volume broad enough to initialize only the bottom without affecting the seismic array with diffractions along the uninitialized sides. We calculated the teleseismic traveltime through the slowness mesh (crustal model) and interpolated it to each station from the nearest time nodes (corners of 0.5-km mesh blocks). We converted these

traveltimes to traveltime residuals by removing the initial wave-front slowness. The residuals were reduced to relative residuals by removing an appropriate mean residual.

Finally, we subtracted these "crustal relative residuals" from our observed teleseismic relative residuals and inverted the difference; we call these deterministically stripped inversions, or A- or B-stripped models. The result, if the crustal models were perfect and directly applicable, would be our estimate of deeper structure based on the teleseisms. However, differing resolution, different wavelengths (differing diffraction or evanescence effects near faults), and, possibly, anisotropy result in some fraction of the upper-crustal contribution to our teleseismic relative residuals being undercorrected or overcorrected. Our experience matches that of Dawson and others (1990)—that iteratively stripped models probably overestimate the crustal correction, whereas deterministically stripped crustal models derived from nonteleseismic sources commonly underestimate the crustal correction.

RESULTS

UNSTRIPPED MODELS

Maps and cross sections of our velocity models (fully smoothed by layer-thinning and offset-and-average steps) for the principal- and detailed-model series are shown in figures 4 and 5, respectively. For each series, unstripped models are shown in the first position, iteratively stripped models in the last position, and models deterministically stripped by crustal models A and B in between. In this subsection, we discuss the unstripped models.

In general, our unstripped models of upper-crustal velocity structure agree with the results from earlier local-earthquake tomography (models A, B; Lees, 1990). We confirm thick low-velocity material southwest of the San Andreas fault (for example, figs. 4*D*, 5*C*), previously identified by teleseismic and local-earthquake-tomography studies and interpreted as Tertiary marine sedimentary deposits. Although the bottom of this low-velocity body reaches as deep as 20 km in our models (figs. 4*D*, 5*C*), its thickness is not well constrained by teleseismic tomography. A high-velocity body northeast of the Sargent fault also appears in our models (figs. 4*A*, 5*A*) and in the local-earthquake results of Lees. The equivalent feature reaches the surface between the San Andreas and Sargent faults in the model of Eberhart-Phillips and others (1990).

Many upper-mantle velocity gradients fall beneath the surface trace of the San Andreas fault (for example, figs. 4*B*, 4*C*, 5*B*). We compared the subjective coincidence of such gradients with the coincidences along arbitrary lines. For this comparison, we used a set of lines passing through the center of the model at various azimuths. The linear sum of such gradient coincidences is in most cases larger for the real San Andreas fault than for these arbitrary lines. Therefore, we infer that the coincidence is real (see Takauchi, 1994).

In figures 4*B*, 4*D*, 5*B*, and 5*C*, a large, low-velocity body (feature L), centered at 25- to 35-km depth, is the most conspicuous feature. Although the depth to the center of this low-velocity body is greater than the nominal average Moho depth of 25 km and its thickness outwardly appears to be about 25 km, its true thickness may be much smaller, and its depth uncertain by as much as 10 km. (Exaggeration of the vertical dimensions of subhorizontal features is a well-known artifact in teleseismic tomography, according to Evans and Achauer, 1993.) For example, the low-velocity body could well be caused by a horizontal, lenticular feature near the depth where the velocity anomaly appears to be widest (25–35-km depth). Indeed, many geometries of a low-velocity body with the width of the imaged feature and fitting within its vertical range could cause this anomaly. Thus, it could be caused by topography on the Moho, a crustal "root," as suggested by Zandt (1981).

Near 58-km depth, we note two conspicuous low-velocity features adjacent to the San Andreas fault (M1, M2, figs. 4*C*, 4*E*). Oceanic-plate geometry was complex enough during the final stages of subduction here (for example, Skaer, 1989) to create such a velocity variation in many ways. For example, these two low-velocity features could be caused by one or more subducted ridge segments (still hot or relatively enriched) or by asthenospheric upwelling through weak or open parts of the subducted slab. Whatever their origin, these two low-velocity features are separated from one another by about 45 km right laterally along the San Andreas fault. If they were once contiguous, which we cannot determine, then they create a piercing point, a strain marker.

The outward "dips" of low-velocity features M1 and M2 suggested by figure 4*E* are almost certainly artifacts of the inversion caused by smearing along the dominant ray direction (Evans and Achauer, 1993); M1 and M2 probably are caused by the presence of more compact bodies near the depths of their maximum velocity anomalies. Similarly, these two low-velocity features lie along common *P*-wave raypaths with the shallower low-velocity feature, L, and so we may ask whether they are artifacts of that shallower low-velocity feature. We summed offdiagonal elements of the resolution matrix **R** to estimate this smearing, and found that smearing of low-velocity feature L can contribute only a minority fraction of low-velocity feature M2 and actually mutes the velocity contrast of low-velocity feature M1 slightly. Thus, low-velocity features M1 and M2 in figures 4*C* and 4*E* appear to represent real features, lying mainly between 45- and 70-km depth.

Other features of our model, particularly around the edges, are poorly resolved. The high-velocity feature near the south edge of our principal model (for example, fig. 4*B*) is consistent with the results of Zandt (1981), who interpreted it as Salinian basement, which has higher velocities than surrounding Franciscan rocks. However, the depth of this high-velocity feature is very poorly resolved here, and so further interpretation is inappropriate.

STRIPPED MODELS: UPPER-CRUSTAL STRUCTURE

In this subsection, we describe some of the differences between our four models, interpreting those that are of well-understood origin. More speculative issues are relegated to the section below entitled "Discussion."

Differences between the stripped and unstripped models are minor throughout the upper mantle and, for the most part, in the lower crust. Thus, the effects of shallow crustal structure on our results are insignificant at such depths, including for low-velocity features L, M1, and M2 (figs. 4, 5). However, upper-crustal structure does vary greatly between the various models, and unsettlingly large anomalies remain in both our A- and B-stripped models.

Differences at the periphery of the modeled volumes are easily understood as the effects of poor resolution and differing styles of this weakness for the different data sets, local and teleseismic. These rays have differing incidence angles, and their numbers differ in given areas. The most noteworthy example of a mismatch at the periphery of the teleseismic model (most intense anomaly, fig. 4*A*) is at the southeast edge of our array. We have one station modeled at a much higher velocity than in either local-earthquake model. Indeed, the local-earthquake models indicate somewhat low velocities in this area, intensifying the high-velocity feature in our A- and B-stripped models. This feature may be related to Salinian rocks at depth, as inferred by Zandt (1981); local earthquakes presumably sense shallower low-velocity material, with that near the San Andreas having an inordinate influence because of the concentration of sources there. In another example, the B-stripped principal model has a low-velocity area (−11 percent) in the west corner, an area of exposed Salinian igneous and metamorphic rocks.

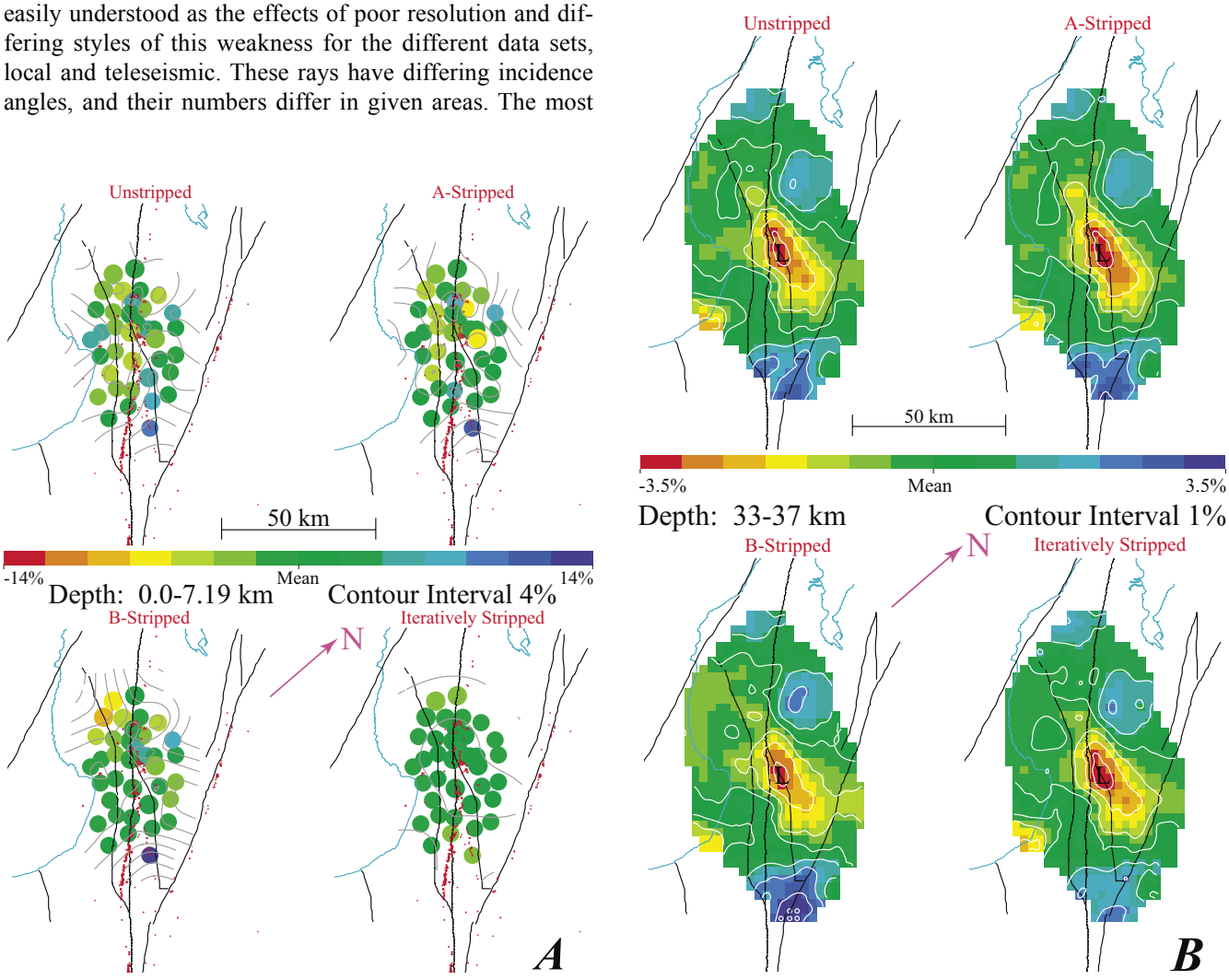

Figure 4.—Maps (*A*–*C*) and cross sections (*D*, *E*) of compressional-wave velocity perturbation in thinned, smoothed principal model. *A*–*C*, Blue lines, coast; black lines, faults; gray or white lines, velocity contours. Plan views of layers are centered at about 4-km depth (*A*), 35-km depth (*B*), and 58-km depth (*C*); datum is mean station elevation (290 m). Layer depths are slightly exaggerated by flat-earth transformation used. Small red dots, local earthquakes from January 1, 1990, through May 31, 1994, occurring within depth range of each layer; L, M1, and M2, low-velocity features discussed in text. *D*, *E*, Contour lines are black. Small red dots, earthquakes occurring within 5 km of cross-section plane.

This mismatch is absent in the A-stripped principal model. We infer a weakness in local-earthquake model B, probably owing to the low seismicity of that area and to our not having used data from temporary stations in the area (as we did with model A). In a similar example, the high-velocity feature at the northernmost station (blue dot nearest the Santa Clara Valley, fig. 4*A*) in the unstripped principal model is also present in the A- and B-stripped models, and even accentuated. The velocity anomalies in model A are northwest-southeast elongated (for example, Eberhart-Phillips and Michael, this chapter, fig. 5), presumably partly representing the resolution effects of high concentrations of sources and receivers along the San Andreas fault. Teleseismic features streak subvertically for equivalent reasons, thus at right angles to the streaking in crustal model A. Teleseisms probably are sensing deeper-crustal high-velocity ultramafic rocks of the Franciscan Formation.

Contradictions in the central parts of our model—for example, along the Sargent fault in crustal model B, along the Zayante fault in crustal model A, and near (northeast of) the intersection of the Sargent and San Andreas faults in both models—are interpreted below in the section entitled "Discussion."

RESOLUTION

The diagonal elements of the resolution matrix **R** for the base models, as a general indicator of the spatial variation in resolution, are shown in figure 6. These diagonal elements and associated standard errors are typical of well-sampled

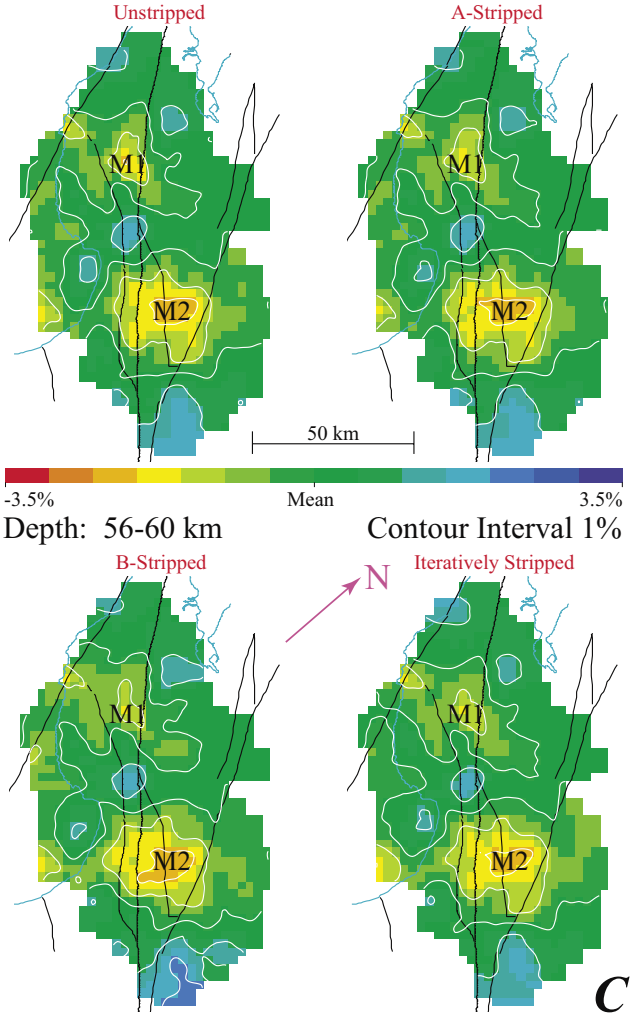

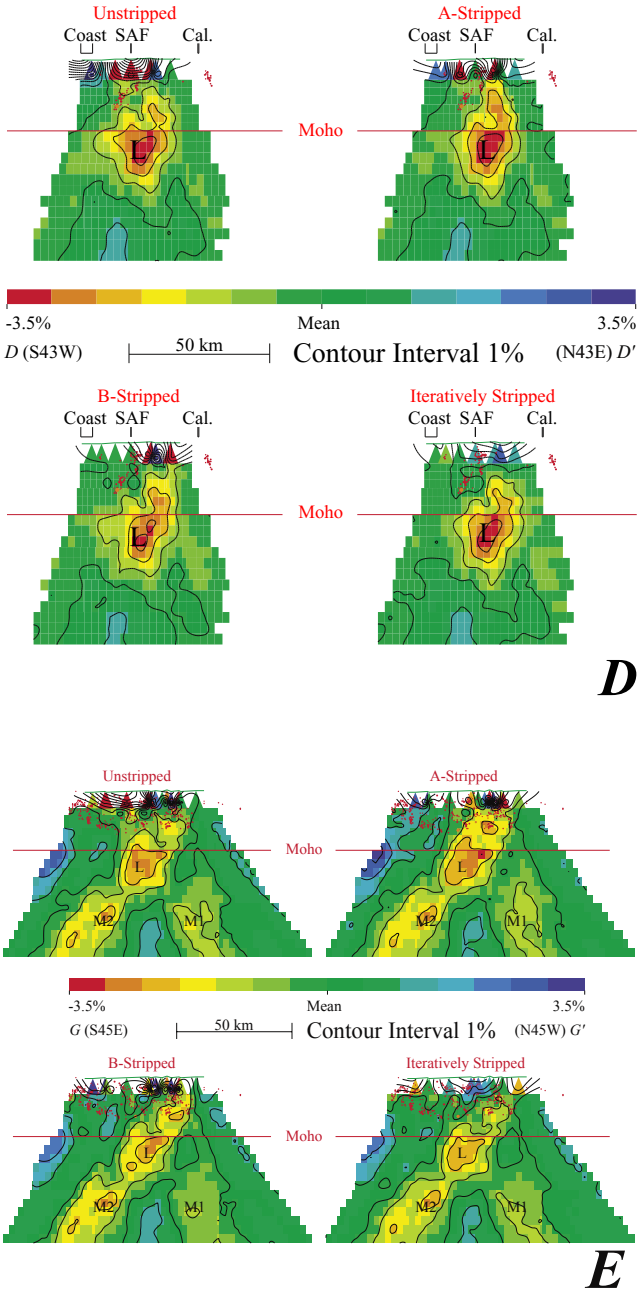

Figure 4.—Continued

teleseismic models; the diagonal elements are as large as 0.77 for the principal model and 0.69 for the detailed model in the best-resolved areas. Because the ray sets are essentially identical between unstripped and stripped models (with trivial variations due to first-layer velocity differences changing the raypaths slightly), figure 6 is representative of all four models. Worst-case standard errors in these areas are about 0.5 percent for the unstripped principal model and 1.2 percent for the unstripped detailed model. As expected, the resolution is fair to good at the centers of the modeled volumes and gradually decreases toward the peripheries.

To help readers visualize resolution effects in more detail, including the directions and lengths of smearing, volume metrics for selected blocks are plotted in perspective in figure 7. Volume metrics are described above in the section entitled "Inversion Technique" but, succinctly, should be thought of as the "impulse responses" of our tomographic imaging process—the sizes and shapes of very small, intense, point anomalies once we have imperfectly imaged them.

Volume metrics for blocks near the centers of the modeled volumes generally are more compact than for blocks near the peripheries. Indeed, some edge blocks smear over a large part of the model (for example, fig. 7*B*) and are largely meaningless. The shape and orientation of smearing generally is radially away from the seismograph array, in the direction of the most plentiful (*P* wave) rays. These characteristics are also typical of well-sampled teleseismic-tomography models.

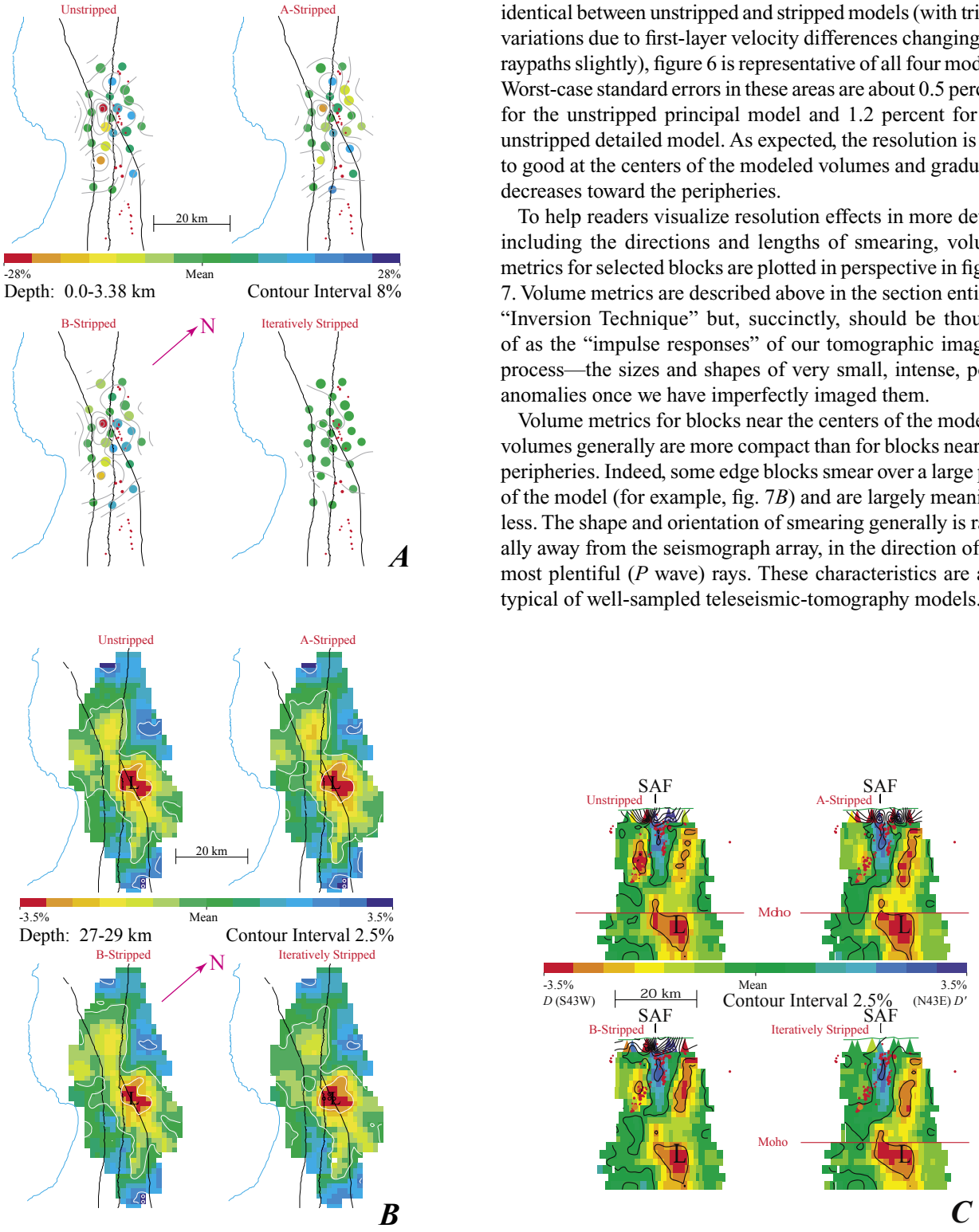

Figure 5.—Maps (*A*, *B*) and cross sections (*C*, *D*) of compressional-wave-velocity perturbation in thinned, smoothed detailed model. Same symbols as in figure 4. Datum is mean station elevation (476 m). Plan views of layers are centered at about 2-km depth (*A*) and 28-km depth (*B*).

DISCUSSION

Differences in modeled upper-crustal structure between figures 4*A* and 5*A* and among the various stripping methods shed light on what is "real" in the upper crust. Two low-velocity features (yellow dots) northeast of the Sargent fault in the A-stripped principal model imply that model A velocities are higher there than we modeled with teleseisms. Crustal model B leaves a similar but weaker feature (that is, is closer to our result). We suspect that complexity near the intersection of the Sargent and San Andreas faults and the steepness of thrust faults in this area are contributing to this mismatch, and that higher velocity material underlying a shallower velocity low may be present. (This area contains many slivers of ultramafic rock, commonly fault bounded.) For the uppermost crust, we consider the local-earthquake models more reliable.

Disagreement also exists between the local-earthquake-tomography models of Eberhart-Phillips and others (1990) and Lees (1990) on the location of the high-velocity body near the Sargent fault. Their results and ours all contain strong velocity gradients near these faults (for example, ±28.0-percent velocity perturbation in our detailed model), although the location of the responsible high-velocity body northeast of the San Andreas fault is poorly constrained. In particular, it is unclear on which side of the Sargent fault it lies in the uppermost crust. It appears to dip southwest and probably is an ophiolitic fragment bounded above or below by the Sargent fault.

Along the Zayante fault, the A-stripped principal model leaves systematically lower velocities than the unstripped or B-stripped models. In our detailed models, the core of the low-velocity body lies between the San Andreas and Zayante faults (unstripped model, fig. 5*A*). The A-stripped model effectively corrects for this low-velocity feature, except at a station at the intersection of the Sargent and San Andreas faults. The B-stripped model is less effective—no surprise, given that model's regional scale. We conclude that crustal model A compensates well for the core of the low-velocity marine sedimentary rocks between these faults but that the A-stripped principal teleseismic model shows some mismatch of the Zayante fault boundary of this feature. If the low-velocity wedge dips southwest, teleseismic rays at the surface would have traversed some of it, making the feature look wider to us than to Eberhart-Phillips and Michael (this chapter). Similarly, our results are more subject to diffraction and evanescence than theirs, a difference that is likely to matter along a fault or other major contact, and so we defer to their model (A).

Leaving the upper crust, the likely cause of low-velocity feature L (figs. 4*B*, 4*D*, 4*E*, 5*B*–5*D*) is a crustal "root," as suggested above and by Zandt (1981). Bürgmann and others (1994) evaluated fission-track dates, geomorphology, and geodesy in the Santa Cruz Mountains, concluding that the region northeast of the San Andreas fault has undergone rapid uplift of about 3 to 4 km over the past 4.6 m.y., whereas both the current uplift rate and total uplift since 10 Ma southwest of the San Andreas fault are much lower. Bürgmann and others also concluded that the locus of uplift has remained about fixed in the Loma Prieta region on the northeast side of the fault, whereas the southwest side was uplifted mainly as it passed the fault bend near Loma Prieta, leaving a trail of moderate uplift to the northwest. Therefore, a significant

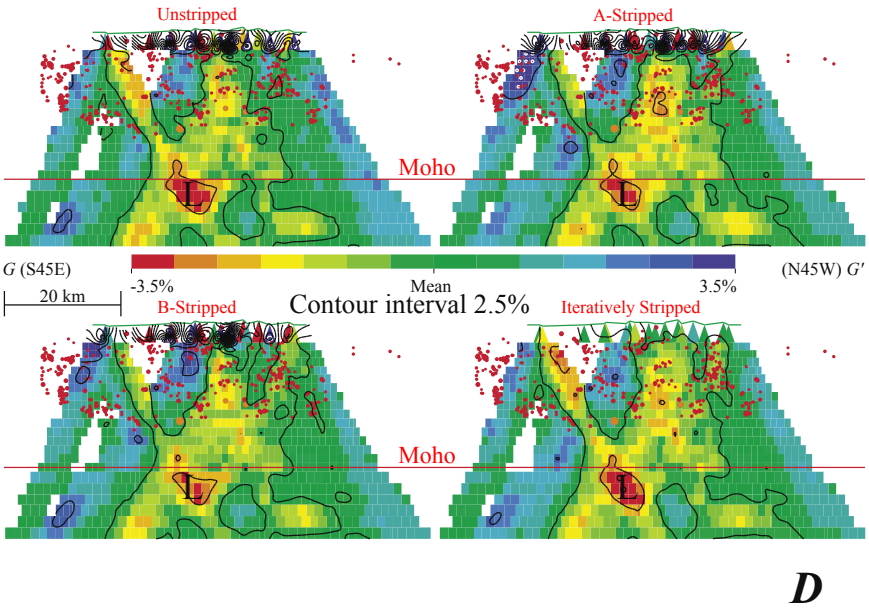

Figure 5.—Continued

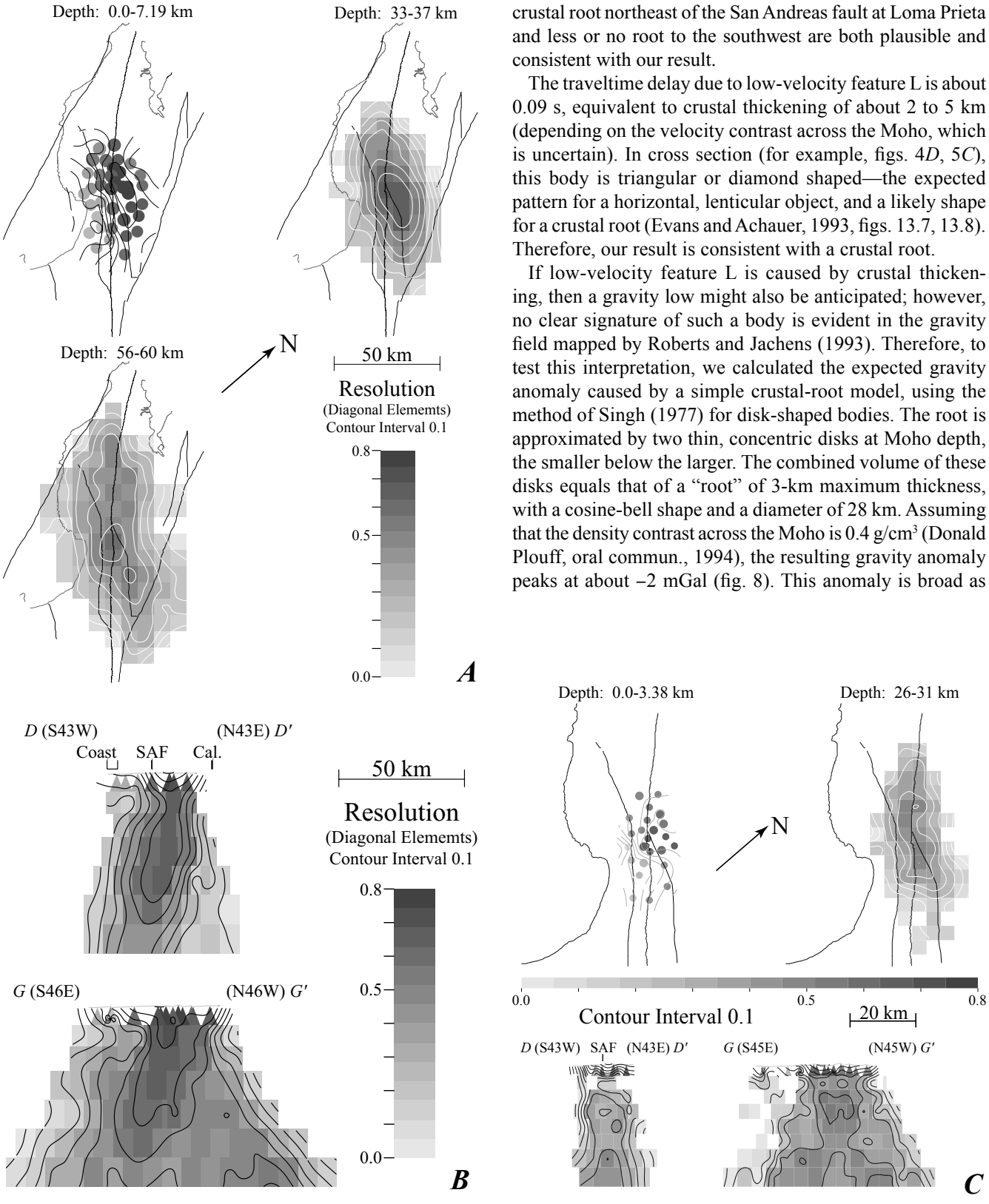

Figure 6.—Diagonal elements of resolution matrix of base models. *A*, Plan views of principal model. *B*, Cross sections of principal model. *C*, Plan and cross-sectional views of detailed model. Plan views are for layers containing thinned layers shown in compressional-wave velocity-perturbation maps (figs. 4, 5); that is, layer shown here is subdivided into three layers, one of which is shown in figures 4 and 5. Cross sections match those in figures 4 and 5.

crustal root northeast of the San Andreas fault at Loma Prieta and less or no root to the southwest are both plausible and consistent with our result.

The traveltime delay due to low-velocity feature L is about 0.09 s, equivalent to crustal thickening of about 2 to 5 km (depending on the velocity contrast across the Moho, which is uncertain). In cross section (for example, figs. 4*D*, 5*C*), this body is triangular or diamond shaped—the expected pattern for a horizontal, lenticular object, and a likely shape for a crustal root (Evans and Achauer, 1993, figs. 13.7, 13.8). Therefore, our result is consistent with a crustal root.

If low-velocity feature L is caused by crustal thickening, then a gravity low might also be anticipated; however, no clear signature of such a body is evident in the gravity field mapped by Roberts and Jachens (1993). Therefore, to test this interpretation, we calculated the expected gravity anomaly caused by a simple crustal-root model, using the method of Singh (1977) for disk-shaped bodies. The root is approximated by two thin, concentric disks at Moho depth, the smaller below the larger. The combined volume of these disks equals that of a "root" of 3-km maximum thickness, with a cosine-bell shape and a diameter of 28 km. Assuming that the density contrast across the Moho is 0.4 g/cm^3 (Donald Plouff, oral commun., 1994), the resulting gravity anomaly peaks at about –2 mGal (fig. 8). This anomaly is broad as

well as weak (~ 42-km half-width) and so it would be difficult to identify among anomalies from shallower features in this structurally complex region.

Many other explanations are possible for this velocity low, including complexities in the last-subducted material that may underlie the region. Because the low-velocity body in figures 4*B* and 5*B* is elongate parallel to the Sargent and San Andreas faults, we should also consider possible local upper-mantle shear heating. Few heat-flow data are available in this region (Lachenbruch and Sass, 1980), and any surface heat-flow anomaly from such shear heating would still be far below equilibrium values (for example, Lachenbruch and others, 1976). Therefore, the shear-heating model cannot be dismissed. However, (1) the absence of the low-velocity anomaly beneath other sections of the San Andreas fault and (2) the great nucleation depth of the 1989 Loma Prieta earthquake (suggesting that the adjacent lower crust is cold) argue against shear heating.

The presence of velocity gradients along the San Andreas fault in the upper mantle suggests that the fault was at least at one time a deeply penetrating feature present in the upper mantle as a narrow shear locus. As mentioned above, simple coincidence tests suggest that the San Andreas fault is more closely correlated with such gradients than most arbitrary lines that can be drawn through the centers of figures 4 and 5, or equivalent plots at other depths. The inference of a deep, narrow shear locus beneath the fault during some interval is the first major result of our study. We may ask when this locus was active, and we address that question next in reference to low-velocity features M1 and M2 (fig. 4*C*).

With the complexity of subducted material in the Loma Prieta region, low-velocity features M1 and M2 may not have originated as contiguous. Certainly, we can say little about what they are. R.J. McLaughlin (oral commun., 1997) suggested that low-velocity feature M2 could be the source volume for volcanism and its associated hydrothermal alteration and mineralization at New Almaden, whereas low-velocity feature M1 could be the source for the Mindego Volcanics in the La Honda Basin. He noted that these thermal events are of different ages and suggested that low-velocity features M1 and M2 may also be of different age. In our view, the complexity of crustal tectonics in the region and its likely control of volcanism suggests that being the heat sources for different-age volcanic rocks does not imply that the two mantle anomalies are of different ages. We also note that the preservation of low-velocity upper-mantle anomalies beneath volcanoes (presumably, regions of basaltic partial melt) for more than 10 m.y. is, at least, rare. The oldest such anomaly known to us is the ≥6-Ma anomaly beneath the eastern Snake River Plain (Evans, 1982). Beneath the Miocene southwestern Nevada Volcanic Field is a deep high-velocity anomaly interpreted as the cooled and (or) depleted mafic rock of a dead magma source (Evans and Smith, 1995). Although the correlation of low-velocity features M1 and M2 with Neogene volcanism is intriguing, it is uncertain.

If we assume that low-velocity features M1 and M2 were contiguous when formed, then, regardless of their origin, they constitute a marker for strain partitioning—a piercing point. Although this assumption is certainly not required, it is plausible. If correct, however, it has important implications.

The northward passage of the Mendocino Triple Junction and consequent inception of the transform boundary at this part of the North American plate occurred from as early as about 8 Ma (Atwater, 1989) to as late as about 6.5–5.5 Ma (Riddihough, 1984). At this part of the Pacific plate, it occurred much earlier, at 30–20 Ma (Atwater, 1989). The position of the plate boundary also has moved laterally over time, but it probably has always been diffuse and generally moving northeastward, inland (Atwater, 1989). Some evidence exists that it has also moved southwestward at least once, with east-bay faults dominating from 8 to 6 Ma, then primary shear returning to the San Andreas fault and its adjacent predecessor, the Pilarcitos fault (McLaughlin and others, 1996). Because we do not know what low-velocity features M1 and M2 are, we do not know with which plate to associate them, and so we do not know which time interval is appropriate for estimating San Andreas fault shearing of a piercing point at low-velocity features M1 and M2. However, even using the shortest time period (6 m.y.), motion across the San Andreas/Pilarcitos ranges from about 150 to 200 km, possibly more (fig. 9; Dickinson and others, 1972; Sedlock and Hamilton, 1991; R.J. McLaughlin, oral commun., 1997). Thus, the 45-km offset between low-velocity features M1 and M2 (fig. 4*C*) is much too small to have been caused by a narrow, persistent shear locus beneath the San Andreas fault. Therefore, if low-velocity features M1 and M2 are a valid piercing point, then this discrepancy implies that the San Andreas fault was a deep, narrow shear locus for only a small part of that time.

As much has been proposed by Furlong and others (1989), who inferred a midcrustal or lower-crustal detachment fault connecting the San Andreas fault with the Hayward/Calaveras fault system, and a deeper, broad lithospheric boundary now centered beneath the Hayward/Calaveras fault system. Beneath the initial plate boundary, they modeled uppermost-mantle shearing as a transient pattern, frozen into place within a few million years after passage of the Mendocino Triple Junction. This model is consistent with the limited offset that we observe between low-velocity features M1 and M2 if shearing at their depth "froze in" within 2 to 3 m.y. of the inception of faulting (fig. 9). This consistency is the second major result or our study.

An alternative interpretation of the 45-km offset between low-velocity features M1 and M2, still assuming that they originated as a single feature, is that mantle shear has always been broadly distributed at this depth, rather than constrained to a narrow locus. A broad shear locus might be similar to the modern surface displacements measured by Lisowski and Savage (1992), a fault-parallel band about 85 km across. If so, the fraction of the plate motion taken up between M1 and M2 (centered ~17 km apart in the northeast direction)

would be less than or equal to about $^{17}/_{85}$, or 20 percent of the total plate motion since 8 Ma. That total motion is ~370 km (Atwater and Molnar, 1973), yielding an expected separation of as much as ~74 km between low-velocity features M1 and M2 in the northwest direction. The match would be closer if we accounted for the fraction of plate motion taken up elsewhere in the Western United States. However, the resulting shape of low-velocity features M1 and M2 would probably be elongate and still contiguous. Therefore, we prefer the frozen-in narrow-shear-locus model described first, or some composite model.

Finally, we emphasize that low-velocity features M1 and M2 might simply be unrelated. They could have originated in any spatial configuration, from their current one to a large, fortuitous, left-lateral offset now erased and reversed by motion on the San Andreas fault; they may also be of different age. We cannot rule out any of these interpretations without further study.

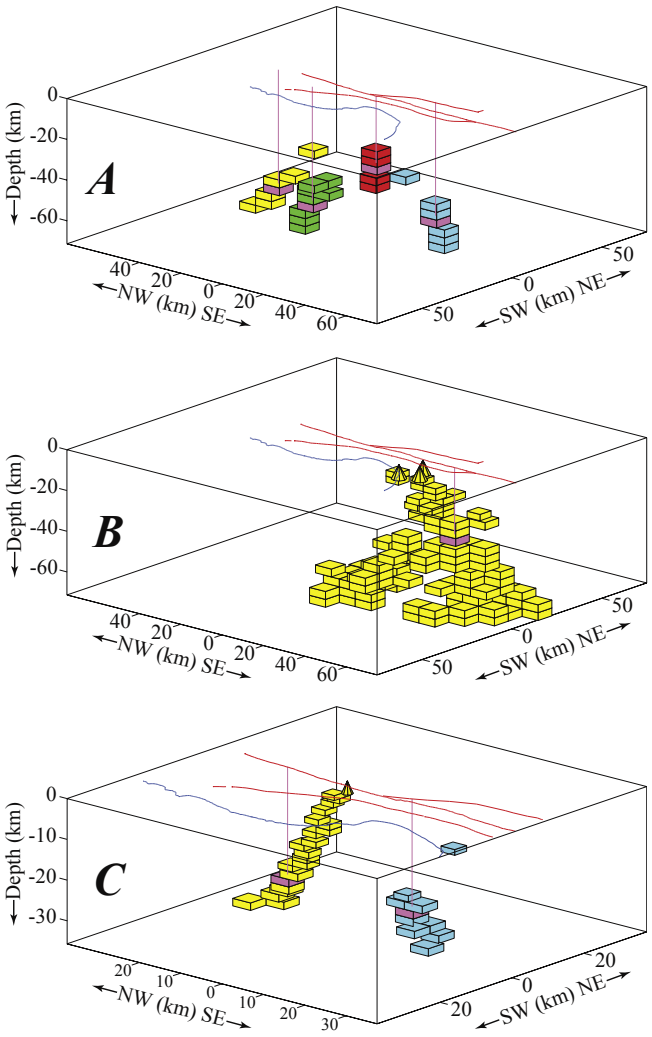

Figure 7.—Perspective views of representative volume metrics from the thinned principal model (*A*, *B*) and the thinned detailed model (*C*). View is northward from an elevation angle of 40°. Equivalent diagonal-element resolution is 0.75 in figures 7*A* and 7*C* but 0.60 in figure 7*B*. Metrics are plotted together to save space, each being a more or less contiguous set of model blocks of one color (except diagonal-element block, which is magenta in each figure). In figure 7*A*, red is for a block near center of low-velocity feature L, green for low-velocity feature M1, cyan for low-velocity feature M2, and yellow for a fairly well resolved block near northwest edge of model (see fig. 4 for locations). Figure 7*B* shows example of a very poorly resolved edge block—it cannot be interpreted meaningfully. In figure 7*C*, cyan is for center of low-velocity feature L, and yellow is for a typical edge block. For perspective, center of each magenta diagonal-element block is connected to surface by a magenta vertical line. Coastline (blue) and the San Andreas, Zayante, and Sargent faults (red) are shown at surface.

CONCLUSIONS

Our teleseismic-tomography images of the San Andreas and related faults in the vicinity of the Loma Prieta earthquake rupture generally agree with previous local-earthquake tomography for the upper crust and with earlier, less detailed teleseismic tomography. Beneath the Loma Prieta highlands, we model a large, low-velocity body near the Moho. This anomaly is most likely due to a crustal root of about 2- to 5-km thickness beneath those highlands. Alternatively, it may be caused by complexities in late-subducted material or by laterally discontinuous shear heating in the upper mantle beneath the San Andreas fault.

We find many velocity gradients coincident with the San Andreas fault at all depths. These coincidences are more common than for most other, arbitrary lines drawn through the center of the model, and so we consider the coincidence meaningful. In addition, we find a right-lateral offset between two low-velocity bodies in the upper mantle beneath the San Andreas. If these features were contiguous before the initiation of strike-slip faulting in the Loma Prieta region, then they are markers for strain partitioning since that time—a piercing

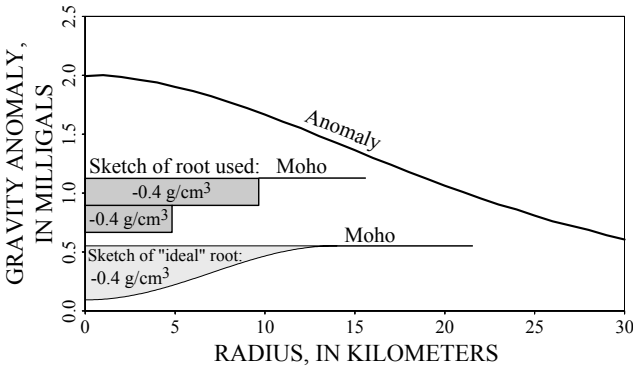

Figure 8.—Estimated gravity anomaly due to a cylindrically symmetric lenticular "crustal root" comparable to low-velocity feature L (see figs. 4 and 5 for location). Root is approximated by two thin disks centered at 0-km radius, each with 0.4-g/cm^3 density contrast. Roughness of gravity anomaly is numerical noise.

point. In particular, the small size of the offset would imply that the San Andreas/Pilarcitos fault could not have been a narrow upper-mantle shear locus for the entire period since 6 Ma—indeed, not for more than a few million years. This result is consistent with the detachment-fault model of Furlong and others (1989) if upper-mantle shear in this region "froze in" within a few million years after passage of the Mendocino Triple Junction, as predicted by their model.

ACKNOWLEDGMENTS

We thank Art Lachenbruch, Bob Jachens, and Don Plouff for their assistance with heat-flow and gravity data. Don Reed and Richard Sedlock of San Jose State University gave invaluable feedback and support at every stage. Reviews by Harley Benz, Phil Dawson, and Bob McLaughlin significantly improved the manuscript. Hitoshi Saito provided both moral and practical support to the first author. This research was partly supported by the Earthquake Hazards Reduction Program. The first author was partly supported by a San Jose State University foreign-student tuition waiver, by an Association for Women Geoscientists' Chrysalis Scholarship, by a scholarship from the Geology Department of San Jose State University, and by the USGS.

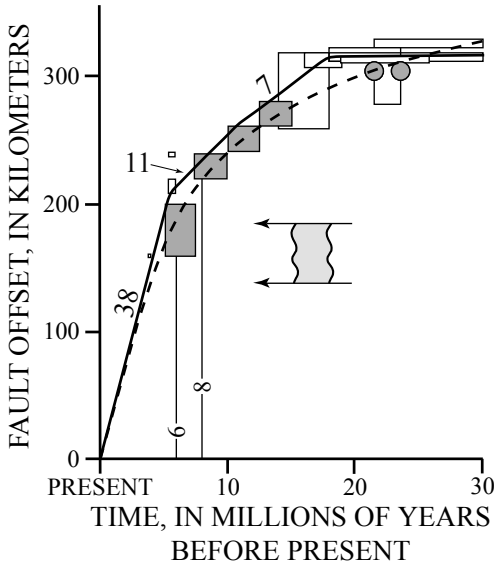

Figure 9.—Offset versus age for various geologic units along the San Andreas fault. Dashed curve and dark-gray boxes modified from Dickinson and others (1972); solid line and open boxes modified from Sedlock and Hamilton (1991); offset rates are in millimeters per year. Boxes show estimated uncertainties of age and offset. Vertical lines indicate arrival of the Mendocino Triple Junction relative to North America (8–6 Ma). Arrows spanned by irregular light-gray band show amount of offset observed between low-velocity features M1 and M2 (fig. 4*C*).

REFERENCES CITED

Aki, Keiiti, Christoffersson, Anders, and Husebye, E.S., 1977, Determination of the three-dimensional seismic structure of the lithosphere: Journal of Geophysical Research, v. 82, no. 2, p. 277–296.

Atwater, Tanya, 1989, Plate tectonic history of the northeast Pacific and western North America, chap. 4 *of* Winterer, E.L., Hussong, D.M., and Decker, R.W., eds., The eastern Pacific Ocean and Hawaii, v. N *of* The geology of North America: Boulder, Colo., Geological Society of America, p. 21–72.

Atwater, Tanya, and Molnar, Peter, 1973, Relative motion of the Pacific and North American plates deduced from sea-floor spreading in the Atlantic, Indian, and south Pacific Oceans, *in* Proceedings of conference on tectonic problems of the San Andreas fault system: Stanford Calif., Stanford University Publications in Geological Sciences, v. 13, p. 136–148.

Bürgmann, Roland, Arrowsmith, J.R., Dumitru, T.A., and McLaughlin, R.J., 1994, Rise and fall of the southern Santa Cruz Mountains, California, from fission tracks, geomorphology, and geodesy: Journal of Geophysical Research, v. 99, no. B10, p. 20181–20202.

Dawson, P.B., Evans, J.R., and Iyer, H.M., 1990, Teleseismic tomography of the compressional-wave velocity structure beneath the Long Valley region, California: Journal of Geophysical Research, v. 95, no. B7, p. 11021–11050.

Dickinson, W.R., Cowan, D.S., and Schweickert, R.A., 1972, Test of new global tectonics; discussion: American Association of Petroleum Geologists Bulletin, v. 56, no. 2, p. 375–384.

Eberhart-Phillips, D.M., Labson, V.F., Stanley, W.D., Michael, A.J., and Rodriguez, B.R., 1990, Preliminary velocity and resistivity models of the Loma Prieta earthquake region: Geophysical Research Letters, v. 17, no. 8, p. 1235–1238.

Evans, J.R., 1982, Compressional wave velocity structure of the upper 350 km under the eastern Snake River Plain near Rexburg, Idaho: Journal of Geophysical Research, v. 87, no. B4, p. 2654–2670.

Evans, J.R., and Achauer, Ulrich, 1993, Teleseismic velocity tomography using the ACH method; theory and application to continental-scale studies, chap. 13 *of* Iyer, H.M., and Hirahara, Kazuro, eds., Seismic tomography; theory and practice: London, Chapman & Hall, p. 319–360.

Evans, J.R., Eberhart-Phillips, D.M., and Thurber, C.H., 1994, User's manual for SIMULPS12 for imaging v_P and v_P/v_S; a derivative of the Thurber tomographic inversion SIMUL3 for local earthquakes and explosions: U.S. Geological Survey Open-File Report 94–431, 101 p.

Evans, J.R., and Smith, Moses, III, 1995, Teleseismic investigations, chap. 7 *of* Oliver, H.W., Ponce, D.A., and Hunter, W.C., eds., Major results of geophysical investigations at Yucca Mountain and vicinity, southern Nevada: U.S. Geological Survey Open-File Report 95–74, p. 135–156.

Foxall, William, Michelini, Alberto, and McEvilly, T.V., 1993, Earthquake travel time tomography of the southern Santa Cruz mountains; control of fault rupture by lithological heteroge-

neity of the San Andreas Fault zone: Journal of Geophysical Research, v. 98, no. B10, p. 17691–17710.

Fuis, G.S., and Mooney, W.D., 1990, Lithospheric structure and tectonics from seismic refraction and other data, chap. 8 *of* Wallace, R.E., ed., The San Andreas fault system, California: U.S. Geological Survey Professional Paper 1515, p. 207–238.

Furlong, K.P., Hugo, W.D., and Zandt, George, 1989, Geometry and evolution of the San Andreas fault zone in northern California: Journal of Geophysical Research, v. 94, no. B3, p. 3100–3110.

Furlong, K.P., and Langston, C.A., 1990, Geodynamic aspects of the Loma Prieta earthquake: Geophysical Research Letters, v. 17, no. 9, 1457–1460.

Herrin, Eugene, 1968, 1968 seismological tables for *P* phases: Seismological Society of America Bulletin, v. 58, no. 4, p. 1193–1241.

Lachenbruch, A.H., and Sass, J.H., 1980, Heat flow and energetics of the San Andreas fault zone: Journal of Geophysical Research, v. 85, no. B11, p. 6185–6222.

Lachenbruch, A.H., Sass, J.H., Munroe, R.J., and Moses, T.H., Jr., 1976, Geothermal setting and simple heat conduction models for the Long Valley caldera: Journal of Geophysical Research, v. 81, no. 5, p. 769–784.

Lees, J.M., 1990, Tomographic *P*-wave velocity images of the Loma Prieta earthquake asperity: Geophysical Research Letters, v. 17, no. 9, p. 1433–1436.

Lees, J.M. and Lindley, G.T., 1994, Three-dimensional attenuation tomography at Loma Prieta; inversion of t^* for Q: Journal of Geophysical Research, v. 77, no. B4, p. 6843–6863.

Lisowski, Michael, and Savage, J.C., 1992, The velocity field in the San Francisco Bay Area and the inferred depth of creep on the Hayward fault, *in* Framework and seismology of the East Bay, chap. 1 *of* Borcherdt, Glenn, Hirschfeld, S.E., Lienkaemper, J.J., McClellan, Patrick, Williams, P.L., and Wong, I.G., eds., Proceedings of the second conference on earthquake hazards in the eastern San Francisco Bay Area: California Division of Mines and Geology Special Publication 113, p. 39–44.

McLaughlin, R.J., Sliter, W.V., Sorg, D.H., Russell, P.C., and Sarna-Wojcicki, A.M., 1996, Large-scale right-slip displacement on the east San Francisco Bay region fault system, California; implications for location of late Miocene to Pliocene Pacific plate boundary: Tectonics, v. 15, no. 1, p. 1–18.

Podvin, Pascal, and Lecomte, Isabelle, 1991, Finite difference computation of traveltimes in very contrasted velocity models; a massively parallel approach and its associated tools: Geophysical Journal International, v. 105, no. 1, p. 271–284.

Riddihough, R.P., 1984, Recent movements of the Juan de Fuca plate system: Journal of Geophysical Research, v. 89, no. B8, p. 6980–6994.

Roberts, C.W., and Jachens, R.C., 1993, Isostatic residual gravity map of the San Francisco Bay area, California: U.S. Geological Survey Geophysical Investigations Map GP–1006, scale 1:286,500.

Sedlock, R.L., and Hamilton, D.H., 1991, Late Cenozoic tectonic evolution of southwestern California: Journal of Geophysical Research, v. 96, no. B2, p. 2325–2351.

Singh, S.K., 1977, Gravitational attraction of a circular disc: Geophysics, v. 42, no. 1, p. 111–113.

Skaer, L.E., 1989, Late Tertiary tectonic evolution of the seafloor spreading system off the coast of California between the Mendocino and Murray fracture zones: Honolulu, University of Hawaii, M.S. thesis, 91 p.

Takauchi, Yoko, 1994, Teleseismic tomography of the Loma Prieta region, central California: San Jose, Calif., San Jose State University, M.S. thesis, 263 p.

Zandt, George, 1981, Seismic images of the deep structure of the San Andreas fault system, central Coast Ranges, California: Journal of Geophysical Research, v. 86, no. B6, p. 5039–5052.